



Anchoring mechanism of the plant protein remorin to membrane nanodomains

Anthony Legrand

► To cite this version:

Anthony Legrand. Anchoring mechanism of the plant protein remorin to membrane nanodomains. Molecular biology. Université de Bordeaux, 2020. English. NNT : 2020BORD0285 . tel-03118537

HAL Id: tel-03118537

<https://theses.hal.science/tel-03118537>

Submitted on 22 Jan 2021

HAL is a multi-disciplinary open access archive for the deposit and dissemination of scientific research documents, whether they are published or not. The documents may come from teaching and research institutions in France or abroad, or from public or private research centers.

L'archive ouverte pluridisciplinaire **HAL**, est destinée au dépôt et à la diffusion de documents scientifiques de niveau recherche, publiés ou non, émanant des établissements d'enseignement et de recherche français ou étrangers, des laboratoires publics ou privés.



THÈSE PRÉSENTÉE
POUR OBTENIR LE GRADE DE
DOCTEUR DE
L'UNIVERSITÉ DE BORDEAUX

PAR

Anthony Thomas Pascal LEGRAND

**Anchoring mechanism of the plant protein remorin to
membrane nanodomains**

Sous la direction de
Dr Sébastien MONGRAND
Dr Birgit HABENSTEIN

Soutenue le 16 décembre 2020

Pr Sebastian HILLER
Dr Thomas STANISLAS
Dr Derek McCUSKER
Dr Luca MONTICELLI
Dr Sébastien MONGRAND
Dr Birgit HABENSTEIN

Professeur, Université de Bâle
Assistant professeur, Université de Tübingen
Directeur de recherche CNRS
Directeur de recherche CNRS
Directeur de recherche CNRS
Chargée de recherche CNRS

Rapporteur
Rapporteur
Examineur
Examineur
Invité
Invitée

Résumé

La rémorine du groupe 1 isoforme 3 de *Solanum tuberosum* (StREM1.3) est une protéine membranaire de la famille multigénique de protéines de plante appelée rémorines (REMs), impliquées dans l'immunité des plantes, la symbiose, la résistance aux stress abiotiques et la signalisation hormonale. La caractéristique la plus connue des REMs est leur capacité à se ségréger en nanodomaines au feuillet interne de la membrane plasmique (MP). Pour StREM1.3, ceci se fait via une interaction entre deux lysines de l'ancre C-terminale de la rémorine (RemCA) et le phosphatidylinositol 4-phosphate (PI4P) négativement chargé. Ainsi, RemCA modifie sa conformation et s'enfonce partiellement dans la MP, résultant en un accrochage membranaire intrinsèque. Capitalisant sur les données structurales déjà disponibles concernant cet isoforme, nous investiguons StREM1.3 davantage quant à ses propriétés d'interaction membranaire, en utilisant un large éventail de techniques, allant de la microscopie de fluorescence et de la RMN à l'état solide (ssNMR) à la microscopie de force atomique (AFM), la cryo-microscopie électronique (cryoEM) et la modélisation informatique. Nous souhaitons découvrir l'impact de l'oligomérisation et de la phosphorylation de StREM1.3 sur ses interactions membranaires et son activité biologique, ainsi que d'examiner son influence sur la dynamique des lipides et les lipides requis pour l'accrochage à la membrane et le regroupement en nanodomaines. Enfin, forts de toutes les données structurales disponibles, nous entreprendrons la reconstruction *in vitro* et la caractérisation de nanodomaines minimaux de StREM1.3.

Abstract

Group 1 isoform 3 remorin from *Solanum tuberosum* (StREM1.3) is a membrane protein belonging to the multigenic family of plant proteins called remorins (REMs), involved in plant immunity, symbiosis, abiotic stress resistance and hormone signalling. REMs' most well-known feature is their ability to segregate into nanodomains at the plasma membrane's (PM) inner leaflet. For StREM1.3, this is achieved by an interaction between two lysines of the remorin C-terminal anchor (RemCA) and negatively charged phosphatidylinositol 4-phosphate (PI4P). Thus, RemCA undergoes conformational changes and partially buries itself in the PM, resulting in an intrinsic membrane anchoring. Capitalising on pre-existing structural data about this isoform, we investigate StREM1.3's membrane-interacting properties further, using a wide array of techniques, ranging from fluorescence microscopy and solid-state nuclear magnetic resonance (ssNMR) to atomic force microscopy (AFM), cryo-electron microscopy (cryoEM) and computational modelling. We aim to discover the impact of StREM1.3's oligomerisation and phosphorylation on its membrane interactions and biological activity, and to assess its influence on lipid dynamics as well as its lipid requirements for membrane binding and nanoclustering. Finally, based on all available structural data, we will undertake the *in vitro* reconstruction and characterisation of minimal nanodomains of StREM1.3.

Acknowledgments

Dr Birgit Habenstein welcomed me as a master 2 intern to work with her on the project that would, in time, become the subject of my PhD thesis. Soon after, I met with Dr Sébastien Mongrand, and both helped me prepare for the doctoral school's ranked exam. Throughout the entirety of my internship-then-doctorate, I could count on their thoughtful insights, their patience and their nice words of encouragement. To their kindness I must extend my gratitude.

I should also acknowledge Dr Denis Martinez, Dr Paul Gouguet and Dr Ahmad Saad for their counselling, their support and, perhaps unknowingly, teaching me how to de-dramatise failure and performance anxiety. Special thanks also go to Mélanie Berbon for teaching me sample preparation and Axelle Grélard and Estelle Morvan for teaching me NMR spectroscopy – all the while bearing with my very clumsy self.

At last, I must also thank my office neighbours Gaëlle Lamon and Dr Arpita Tawani, as well as Mathilde Bertoni both for our scientific discussions and the pleasant atmosphere we created in IECB. My encouragements go to Marie-Dominique Jolivet who started working on the remorin about a year ago as a PhD student and to whom I wish her a happy and productive thesis. The working mood in LBM, which has always been exceptionally pleasant, has vastly improved with your arrival along with Marguerite Batsale, Marion Rocher, Delphine Bahammou and Julie Castets.

Working with all of you made me grow immensely, both as a scientist and as a person.

I am grateful to the jury for the time spent reviewing this manuscript.

Table of contents

LIST OF ABBREVIATIONS.....	9
INTRODUCTION	11
I. Biological membranes	11
A. The discovery of cell membranes	12
B. Towards the fluid mosaic model	12
C. The composition of lipid bilayers.....	14
1. Phospholipids.....	14
a. Generalities	14
b. Phosphoinositides (PIPs)	15
2. Glycolipids	16
3. Sterols.....	17
4. Lipid phase behaviour and sterols	19
5. Sphingolipids.....	21
6. Lipid composition and asymmetry of PMs.....	22
a. Of animal cells.....	22
b. Of plant cells.....	22
c. Of yeasts	22
d. Of <i>Bacillus</i>	23
D. Membrane proteins.....	23
1. Hydrophobic interactions	23
2. Hydrogen bonding.....	23
3. Electrostatic interactions	24
a. Polar residues within a membrane	24
b. Protein-lipid electrostatic interactions at the membrane's surface.....	24
4. Possible folds of membrane proteins	26
E. Membrane domains	28
1. Early observations	28
a. Coexistence of lipid phases.....	28
b. Caveolae, a visible heterogeneity.....	28

c. Detergent-insoluble membranes (DIM).....	29
d. Cell polarity.....	29
2. From lipid rafts to nanodomains.....	29
a. Birth of the lipid raft hypothesis	29
b. Restatements	31
c. Interdigitation and domain registration.....	31
d. Pinning	31
e. A clarification of terminology.....	33
II. Models of membrane nanodomains across Nature's clades	36
A. In animals	36
1. Ras	36
2. GM1	37
3. Caveolae.....	37
B. In yeasts: on different nanodomain distributions of many systems	38
C. In prokaryotes: flotillins	39
D. In plants: Rho of plants (ROP).....	40
III. Remorins.....	41
A. Phylogeny.....	41
B. Biological implications.....	43
1. Immunity	44
a. Against viruses	44
b. Against bacterial and fungal infections	44
2. Symbiosis	45
3. Stress resistance	45
4. Cell-to-cell communication.....	45
C. Biophysics of membrane anchoring and nanodomain formation, with a special attention to StREM1.3.....	45
1. Remorin C-terminal anchor (RemCA)	45
2. Oligomerisation domain	48
3. IDD.....	49
4. Towards a model of StREM1.3 nanoclustering.....	49
a. Remorin/lipid-lipid interactions: PIPs cluster on their own	49
b. Remorin-remorin interactions: remorins tether with their peers.....	50

c. Remorin-cytoskeleton interactions: the cytoskeleton directs nanoclustering	50
IV. Objectives	51
1. What is the nanoclustering mechanism of StREM1.3?	52
2. What is the minimal set of partners required to make StREM1.3 nanodomains?	52
3. How interactors of StREM1.3 may regulate its relationship with membranes and biological functions?	52
4. Professional context.....	52
V. Biophysical tools to study membrane nanodomains	52
A. Detergent insoluble membranes	52
B. Fluorescence microscopy	54
1. The fluorescence phenomenon.....	54
2. Confocal microscopy.....	54
3. Super-resolution microscopy.....	57
a. Airy scan.....	57
b. Stimulated emission depletion (STED)	57
c. Single-particle tracking photoactivated localisation microscopy (spt-PALM)	58
C. Electron microscopy (EM)	58
1. Negative staining TEM.....	61
2. Cryo-TEM	62
D. Atomic force microscopy (AFM).....	62
E. Computational modelling	63
F. Nuclear magnetic resonance (NMR).....	64
1. Spin.....	64
2. NMR spectrometer	65
3. Energy levels	66
4. The simplest NMR experiment.....	67
5. NMR spectrum	69
6. Liquid-state vs. solid-state NMR	69
7. ssNMR to study membrane nanodomains	70
8. ssNMR to elucidate protein structures	71
a. Cross polarisation (CP)	71

b. Proton Driven Spin Diffusion (PDSD)	72
c. Secondary chemical shifts	74
9. IsNMR to study soluble intrinsically disordered proteins	74
a. Generalities	74
b. On intrinsically disordered proteins (IDPs)	74
c. On folded proteins	75
10. ssNMR to monitor lipid dynamics: ² H ssNMR	75
11. ssNMR to monitor lipid dynamics: ³¹ P ssNMR	77
Article I.....	80
Article I: addendum.....	95
I. REM ₈₆₋₁₉₈ in liposomes by ssNMR.....	95
II. Structure of RemCA in micelles.....	96
A. Material and methods	96
B. Results.....	97
III. Structural analysis of RemCA in native-like conditions by ssNMR	100
IV. On a putative role of the N-terminal IDD of StREM1.3 on the structure of its filaments.....	103
V. Conclusion	103
Article II.....	105
Article II: addendum.....	147
Article III.....	150
Article IV	161
Article IV: addendum	187
Article V	189
I. Introduction.....	190
II. Material and methods.....	190
A. Protein purification	190
B. Preparation and observation of giant vesicles (GVs)	191
C. Nanodomain reconstitution for cryoEM.....	191
D. Agroninfiltration in <i>Nicotiana benthamiana</i>	191
E. Confocal microscopy	191
III. Results	191
A. StREM1.3 specifically binds to PA and PIPs, but not PS.....	191
B. StREM1.3 must be oligomerised to ensure a tight membrane binding	193

C. Close visual of synthetic remorin nanodomains.....	194
IV. Discussion.....	196
V. Conclusion	196
Conclusion.....	199
Annex: an up-to-date review on remorins.....	203
References	245

LIST OF ABBREVIATIONS

Bold symbols represent vectors. Regular symbols represent their modulus.

ASG: acylated steryl glucoside

AFM: atomic force microscopy

B₀: magnetic field induced by the spectrometer's superconducting magnet

CL: cardiolipin

CP: cross-polarisation

CS, σ : chemical shielding

CTF: contrast transfer function

CTX: *Vibrio cholerae*'s toxin

δ : chemical shift

DAG: diacylglycerol

DIM: detergent insoluble membrane

DLPC: di-linoleoyl-PC

DMPC: di-myristoyl-PC

DOPC: di-oleoyl-PC

POPC: palmitoyl-oleoyl-PC

DPC: dodecyl-PC

DPPC: di-palmitoyl-PC

DRM: detergent resistant membrane

DSM: detergent soluble membrane

EE: early endosome

EM: electron microscopy

ER: endoplasmic reticulum

FID: free induction decay

γ : gyromagnetic ratio

GIPC: glycosyl inositol phosphoryl ceramide

GluCer: glucosyl ceramide

GTP: guanosine triphosphate

HIV: human immunodeficiency virus

HMQC: homonuclear multiple quantum correlation

IDD: intrinsically disordered domain

IDP: intrinsically disordered protein

Ins: inositol

InsP: inositol phosphate

KO: knocked-out

L _{α} : liquid disordered phase

L _{β} : gel phase

LCB: long chain base

LE: late endosomes

L_o: liquid-ordered phase

lsNMR: liquid-state NMR
LUV: large unilamellar vesicle
M: magnetisation
MVB: multivesicular bodies
NA: numerical aperture
NMR: nuclear magnetic resonance
NOESY: nuclear overhauser spectroscopy
 ω : rotational frequency of a spin
 ω_0 : Larmor frequency
PA: phosphatidic acid
PALM: photoactivated luminescence microscopy
PC: phosphatidylcholine
PD: plasmodesmata
PDS: proton-driven spin diffusion
PE: phosphatidylethanolamine
PG: phosphatidylglycerol
PH: pleckstrin homology
PI: phosphatidylinositol
PI(3/4/5)P: phosphatidylinositol (3/4/5)-phosphate
PI(3,4/3,5/4,5)P₂: phosphatidylinositol (3,4/3,5/4,5)-bisphosphate
PI_{3,4,5}P₃: phosphatidylinositol 3,4,5-trisphosphate
PIP: phosphoinositide
PLC: phospholipase C
PM: plasma membrane
PP-IPPs: pyrophosphorylated (PP) inositol polyphosphates (IPPs)
PS: phosphatidylserine
PtdIns, PIP: phosphoinositide
REM: remorin
RemCA: remorin C-terminal anchor
ROP: Rho of plants
 σ , CS: chemical shielding
SE: steryl ester
SG: steryl glucoside
spt: single-article tracking
SNR: signal-to-noise ratio
STED: stimulated emission-depletion
SUV: small unilamellar vesicle
SV40: simian virus 40
ssNMR: solid-state NMR
TGN: trans-Golgi network
T_m: gel-liquid phase transition temperature
TOCSY: total correlated spectroscopy

INTRODUCTION

I. Biological membranes

The word membrane refers to a thin semi-permeable material separating two liquid compartments. In the context of biology, compartmentation using membranes is very common (van Meer et al., 2008): from the plasma membrane (PM), delimiting a cell's inside from its outside, the nuclear membrane, delimiting the nucleus from the cytoplasm, the mitochondrial double membrane, the chloroplast double membrane and thylakoids, to the endoplasmic reticulum (ER) membrane. Some viruses even envelope themselves in the plasma membrane of the infected cell they budded from (Chazal and Gerlier, 2003). A cell may or may not have all the organelles cited above but, at the very least, it has a PM: this one is ubiquitous. Indeed, encapsulation of some self-replicating RNA by a primitive membrane could have been at the origin of the first cell ever (Kamat et al., 2015).

Although the PM acts as a physical barrier between the cell and its environment, it must also, in terms of signalling and metabolism (i.e. signal transduction and exchange of molecules), take from the outside and release from the inside (Grecco et al., 2011; Groves and Kuriyan, 2010; Ray et al., 2016). This implies a great complexity in the PM's organisation, far from being a homogeneous and impenetrable wall.

In this section, we shall rewind the history of membrane discovery, starting from the first observation of a cell in the 17th century (Lombard, 2014). We shall see how the mere existence of the PM was debated, what was thought of its composition and how its structural organisation was depicted. Once the fluid mosaic model (Singer and Nicolson, 1972) will be introduced, we shall discuss about membrane composition and spatial heterogeneity, such as microdomains and nanodomains.

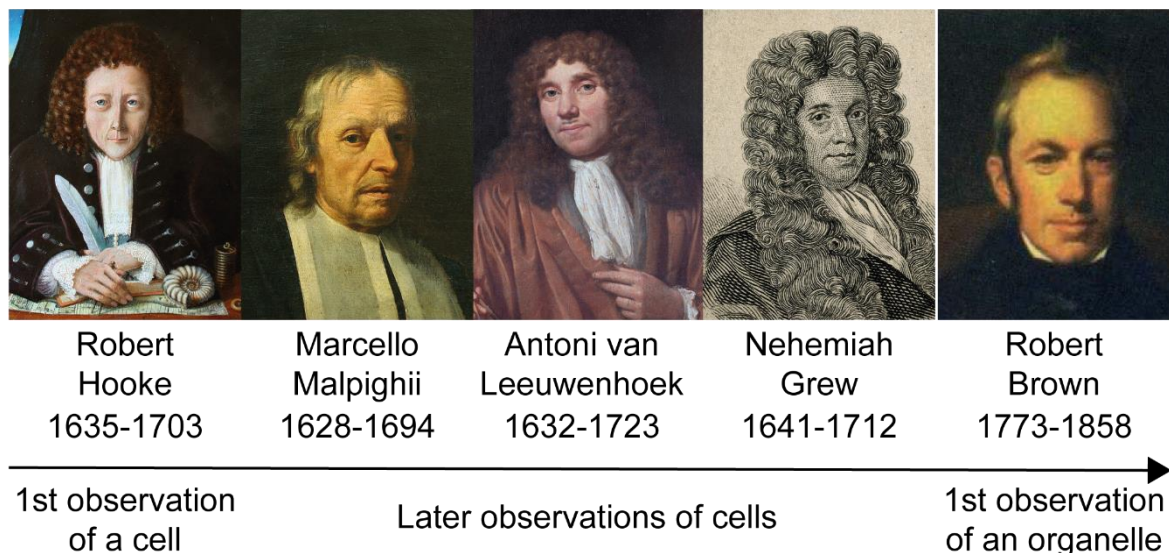


Figure 1
Trombinoscope of the pioneers of cell and organelle discovery.

A. The discovery of cell membranes

The emergence of the microscope unlocked the key to the microscopic realm for biologists of the 17th century and beyond. The first published observation of a cell dates back to 1665 when Robert Hooke ([Figure 1](#)) cut a thin slice of cork and observed, under a microscope ([Hooke, 1665](#)), an ensemble of cavities separated by a thick, solid and continuous structure. He named these cavities cells, likely as a reference to cells within a monastery, and referred to the cell wall as a wall. Later observations enforced the existence of cells as a basic unit of biological matter ([Grew, 1672](#); [Leeuwenhoek and Hoole, 1800](#); [Malpighii, 1675](#)). But if the cell exists, what about its frontier?

As shocking as it may be from our modern point of view, the very existence of membranes as physical barriers was questioned: some argued it was the mere optical manifestation of a liquid-liquid phase separation between two immiscible liquids, for example, in the case of the PM, a membrane-less cell and its environment. By the late 19th century, seminal work on cell osmosis, diffusion, electrophysiology and cytolysis managed to engrave the existence of cell membranes in the scientific discourse ([Lombard, 2014](#)). Meanwhile, the first report on the observation of an organelle, the nucleus, dates back to 1833 ([Brown, 1833](#)). Other organelles soon followed, as reviewed in ([Mullock and Luzio, 2013](#)).

B. Towards the fluid mosaic model

By the end of the 19th century, it was known that living matter was made of proteins, lipids (called fats back then), carbohydrates, nucleic acids and salts ([Dahm, 2008](#); [Loeb, 1906](#)). Charles Ernest Overton showed PMs to be apolar, by virtue of the fact that they allowed the diffusion of apolar molecules yet blocked the diffusion of polar ones ([Lombard, 2014](#)). Therefore, the best candidates to be membrane components were “lecithin and cholesterin” or, in modern terms, phospholipids and sterols (section I.C). But in which manner are they organised? The emergence of Langmuir trough, first developed by Agnes Pockels ([Pockels, 1891](#)), then popularised by Irving Langmuir ([Langmuir, 1917](#)), allowed *in vitro* surface measurements. Ratios between monolayer surface and cell surface at the PM ranged greatly: Gorter and Grendel found 2 ([Gorter and Grendel, 1925](#)), then Bar et al. found 1.3 ([Bar et al., 1966](#)). The use of different cell types, with variable protein content, and different purification protocol are obvious pitfalls that could explain such discrepancies. It should be noted that the last value, 1.3, is the most truthful for PMs, if we remind ourselves of the high amount of proteins within ([Cacas et al., 2016](#)). Nonetheless, electron microscopy of PMs showed a “railroad”-like structure: two thin and dense layers encasing a broader and lighter one, with a total thickness below 10 nm ([Robertson, 1957](#)), reinforcing the hypothesis of a phospholipid bilayer with hydrophilic parts exposed to water and hydrophobic parts buried.

By the 1960s, mainly three models subsisted ([Singer, 2004](#)): the Davson-Danielli-Robertson model ([Danielli and Davson, 1935](#)), where a phospholipid bilayer was sandwiched between two layers of unfolded proteins, the Benson model ([Benson, 1966](#)), where membranes were a juxtaposition of lipoproteins, and the lipid-protein mosaic model ([Lenard and Singer, 1966](#)), where folded membrane proteins would bury

their hydrophobic parts in a phospholipid bilayer while keeping their hydrophilic parts in contact with solvent water (Figure 2). Further refinements on the fold of membrane proteins led to the achievement of the fluid mosaic model (Figure 3) (Singer and Nicolson, 1972), which is, to this day, still the basis for the depiction of biological membranes in virtually any biology textbook.

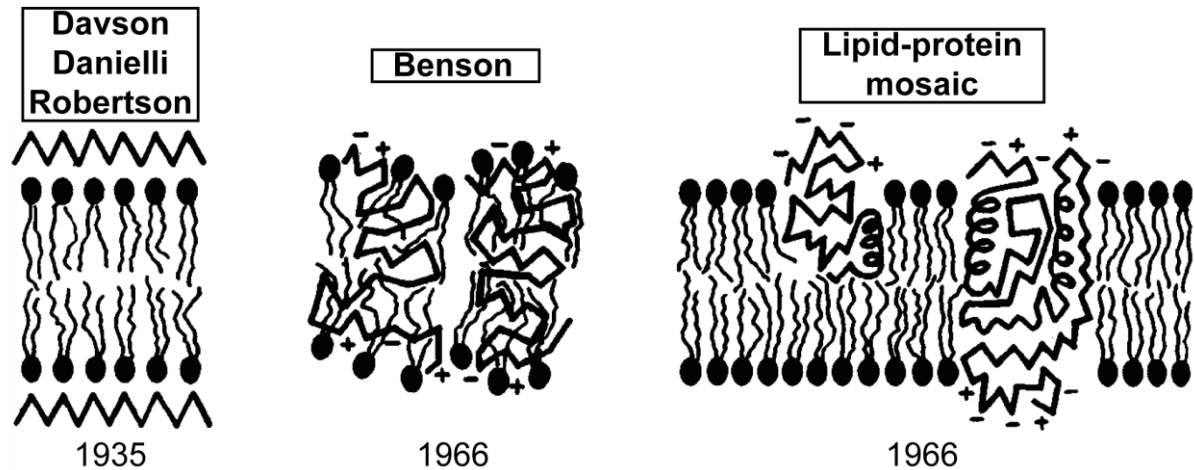


Figure 2

Before the fluid mosaic model (Singer and Nicolson, 1972), three models of membrane structure prevailed. The Davson-Danielli-Robertson model (Danielli and Davson, 1935) proposed a phospholipid bilayer with hydrophobic tails groups buried and hydrophilic ones exposed to solvent water, sandwiched between two layers of unfolded proteins. The Benson model pictured membranes as a juxtaposition of lipoproteins (Benson, 1966). The lipid-protein mosaic model (Lenard and Singer, 1966) is a prototype version of the fluid mosaic model with a less detailed description of membrane protein folding, although the schematic displayed here was used to illustrate both models. Adapted from (Singer, 2004).

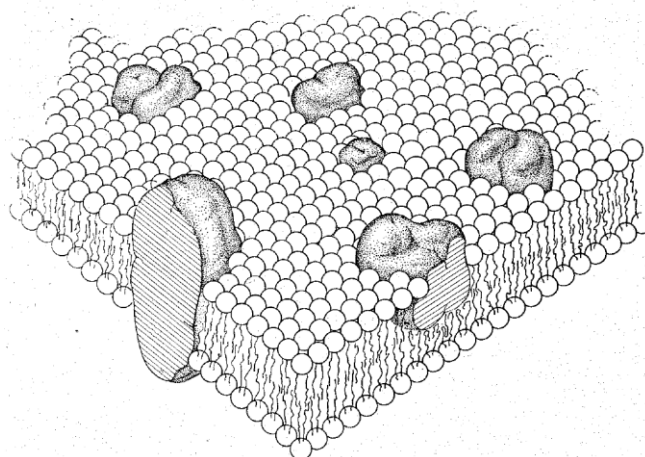


Figure 3

The fluid mosaic model. Biological membranes can be envisioned as two-dimensional bilayers of phospholipids and proteins with hydrophobic parts buried and hydrophilic parts exposed to solvent water. Membrane proteins must adopt particular conformations in order for their insertion to be thermodynamically stable. From (Singer and Nicolson, 1972).

C. The composition of lipid bilayers

The composition of biological membranes displays tremendous diversity. To remain concise, we shall restrain our description to the three major lipid classes: phospholipids, sterols and sphingolipids and the distribution of all three at the PM, with a special focus on plant membranes. Membrane proteins will be discussed in section I.D.

1. Phospholipids

a. Generalities

Phospholipids, whose full name are glycerophospholipids, share a common chemical structure: two acyl chains esterified in sn-1 and sn-2 of a glycerol moiety, and a polar head etherified in sn-3. The polar head starts with an inorganic phosphate. It is eventually followed by other moieties, the nature or absence of which defining the polarity and shape of the molecule (Figure 4). Depending on the organism, acyl chains may be 16 to 24 carbons long (Cacas et al., 2016; Sassa and Kihara, 2014; Villasmil et al., 2017), though longer chains exist (see sphingolipids), and may be desaturated (i.e. bearing C=C double bonds) (Nakamura, 2017; Wisnieski et al., 1973).

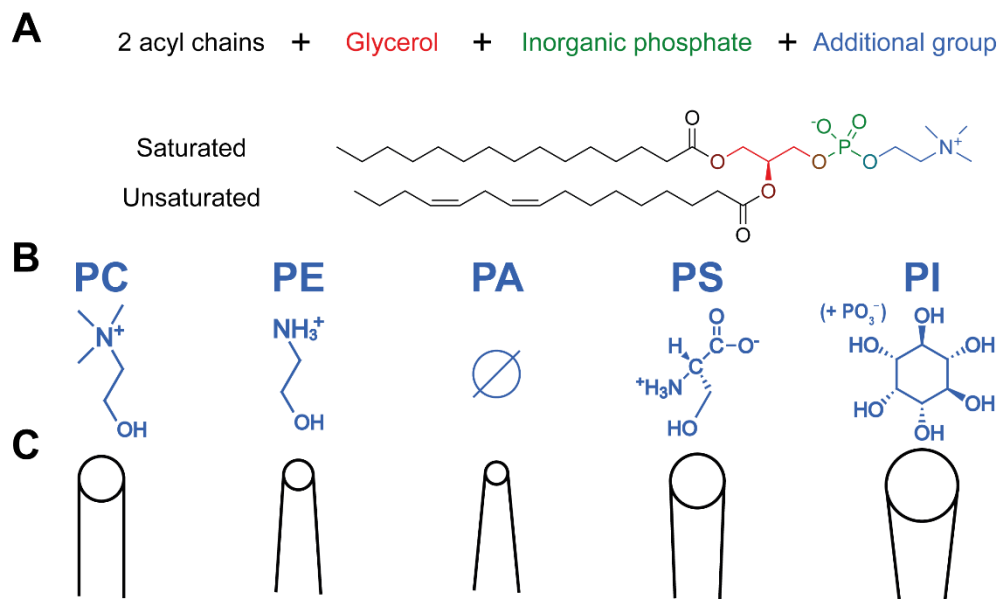


Figure 4

General description of phospholipids. (A) A phospholipid is made of two acyl chains, whether saturated or unsaturated, esterified in sn-1 and sn-2 and an inorganic phosphate etherified in sn-3 of a glycerol moiety. The inorganic phosphate may, or not, be grafted with an additional group, the nature of which defines the phospholipid class it belongs to. An oleoyl-linoleoyl-phosphatidylcholine is drawn as an example. (B) Chemical structure of the various additional groups and their abbreviations and (C) overall shape of the entire phospholipid (circle: polar head, sticks: acyl chains, not to scale). Inorganic phosphates may be added to PI, introducing new negative charges on the polar head and making it bigger.

b. Phosphoinositides (PIPs)

One class of phospholipids will be of particular interest to us: phosphoinositides (PIPs). They are characterised by their inositol sugar moiety to which inorganic phosphates are added (**figure 5**). They represent a minor class of all eukaryotic phospholipids, whose biological implications range from endo- and exo-cytosis to signal transduction and membrane targeting by proteins (**figure 6**) (Di Paolo and De Camilli, 2006; Heilmann, 2016). Prokaryotes do not bear PIPs but possess PIP-specific phosphatases as virulence factors (Heinz et al., 1998). Positions 3, 4 and 5 of the *myo*-inositol ring can be specifically phosphorylated or dephosphorylated, leading to a multitude of PIP species, whose localisations could be assigned as follows (**figure 7**) (Noack and Jaillais, 2017), leading to the concept that PIPs are signature lipids of a given cellular structure.

This manuscript will focus on plant PMs, where PI4P and PI4,5P₂ are the main PIPs (Noack and Jaillais, 2017; Simon et al., 2014). They are also found enriched in detergent insoluble membranes (DIMs, see section V.A) (Furt et al., 2010) and have a tendency to cluster with one another at the PM (Bilkova et al., 2017; van den Bogaart et al., 2011; Ji et al., 2015).

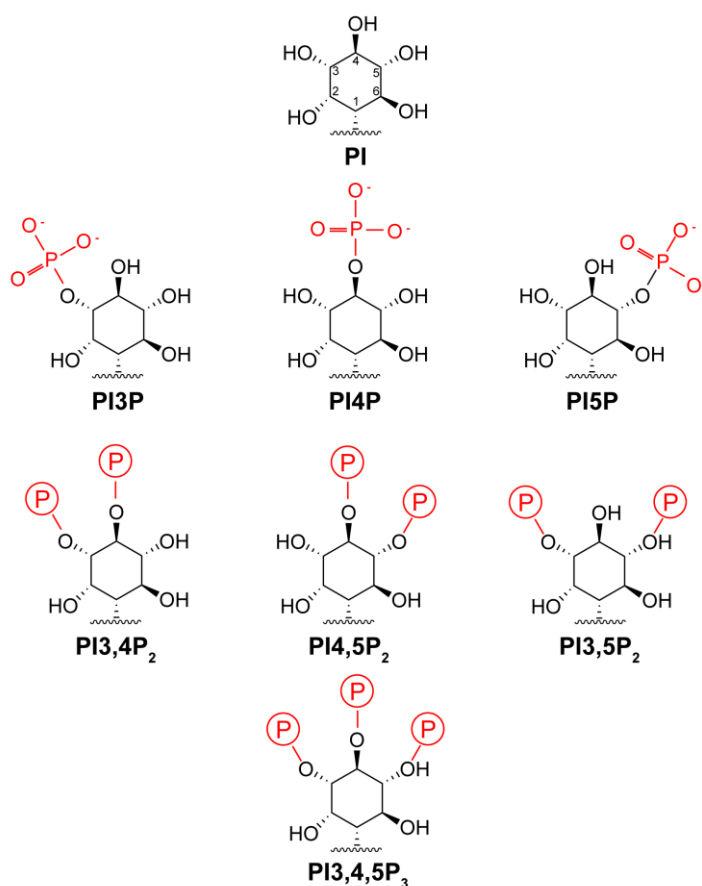


Figure 5

On the diversity of phosphoinositide polar heads. A phosphoinositide is a phospholipid with a terminal *myo*-inositol upon which one, two or three inorganic phosphates are grafted. Positions 2 and 6 cannot be phosphorylated.

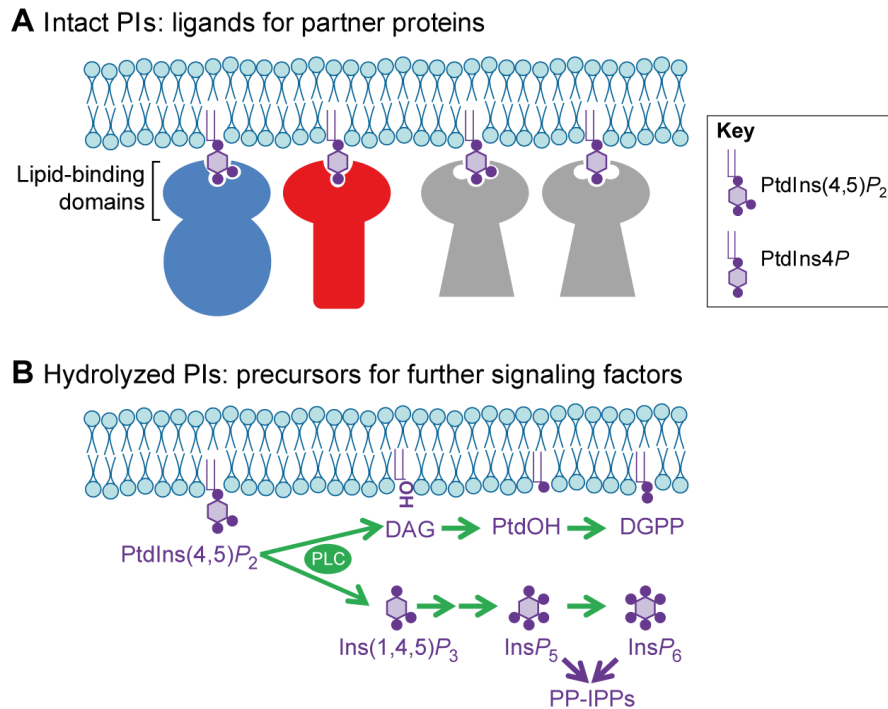


Figure 6

On the biological involvements of PIPs. (A) In a membrane, PIPs may serve as specific anchor for proteins. As the distribution of PIPs in all membranes is heterogeneous, this allows a fine addressing of organelles by specific membrane proteins. (B) Once hydrolysed, e.g. by phospholipase C (PLC), their products are substrates of major cell signalling pathways. Both products of hydrolysis may be phosphorylated further, up to all 6 positions in the case of the nascent inositol-1,4,5-trisphosphate (Ins(1,4,5) P_3), yielding Ins P_6 . PtdIns: PIPs; DAG: di-acyl glycerol; PtdOH: PA; DGPP: DAG pyrophosphate; Ins P_5 : inositol pentakisphosphate; Ins P_6 : inositol hexakisphosphate; PP-IPPs: pyrophosphorylated (PP) inositol polyphosphates (IPPs). From (Heilmann, 2016).

2. Glycolipids

Monogalactosyldiacylglycerol, digalactosyldiacylglycerol and sulfoquinovosyldiacylglycerol are galactolipids synthesised in chloroplasts and major constituents of their photosynthetic membranes, *in lieu* of phospholipids (Nakamura, 2017).

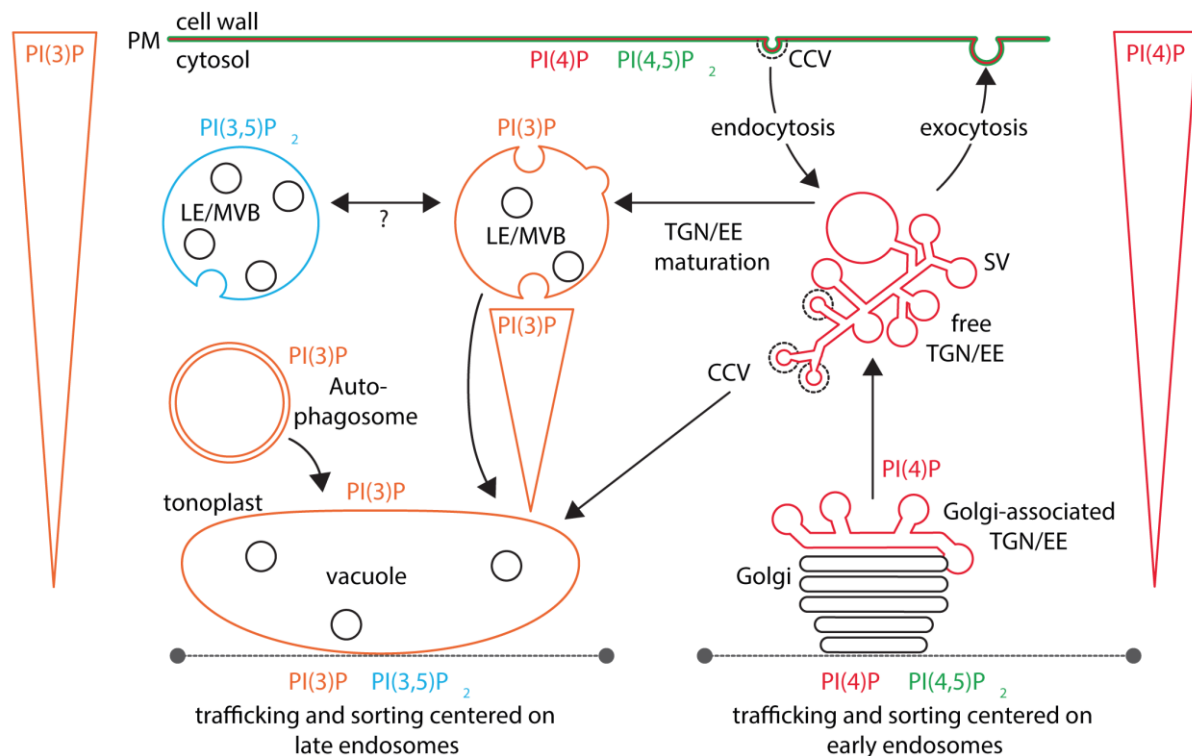


Figure 7

Distribution of PIPs in plant cells. There are two pools of PIPs: those phosphorylated at position 3 for late endosomes (LE), multivesicular bodies (MVB), tonoplasts, autophagosomes and vacuoles (*left*); those phosphorylated at position 4 for early endosomes (EE), the *trans*-Golgi network (TGN) and the PM (*top and right*). An increasing gradient of PI4P exists from the Golgi to the PM (*right*), and a similar increasing gradient of PI3P exists from tonoplasts to late endosomes (Simon et al., 2014). The PM is enriched in PI4P and PI4,5P₂. The nucleus is enriched in PI5P (not shown). Modified from (Noack and Jaillais, 2017).

3. Sterols

Unlike animals and yeasts that rely on cholesterol and ergosterol, respectively, plants possess a plethora of phytosterols. Sterol profiles may strongly vary between species. Later, we will be interested in *Solanum tuberosum* (potato), whose major sterols are sitosterol and stigmasterol, in an approximate 11/1 molar ratio (Figure 8) (Nyström et al., 2012; Wewer et al., 2011). Most chemical differences between phytosterols rely on their aliphatic part or substitution at position 4 (Moreau et al., 2018). Cholesterol may exist in plants but remains in minor quantities (Diener et al., 2000). Sterols may be conjugated via their hydroxyl group into steryl glycosides (SG), steryl esters (SE) and acylated steryl glycosides (ASG) (Figure 9) (Wewer et al., 2011). In lipid membranes, sterols are oriented perpendicular to the membrane plane, with their hydroxyl group at the height of the phospholipid glycerol backbones. This has been proved only for free cholesterol but is likely true for other sterols (Dufourc, 2008; Léonard et al., 2001).

Besides being crucial membrane components, phytosterols are involved in the biosynthesis of phytoecdysteroid, an anti-parasitic agent (Speranza, 2010) and

brassinosteroids, a plant growth hormone (Moreau et al., 2018). Similarly, cholesterol is at the basis of the steroid hormone metabolism. Evidence of biological function for sterol conjugates are scarce, though ASGs are involved in thermal shock response in plants (Grille et al., 2010).

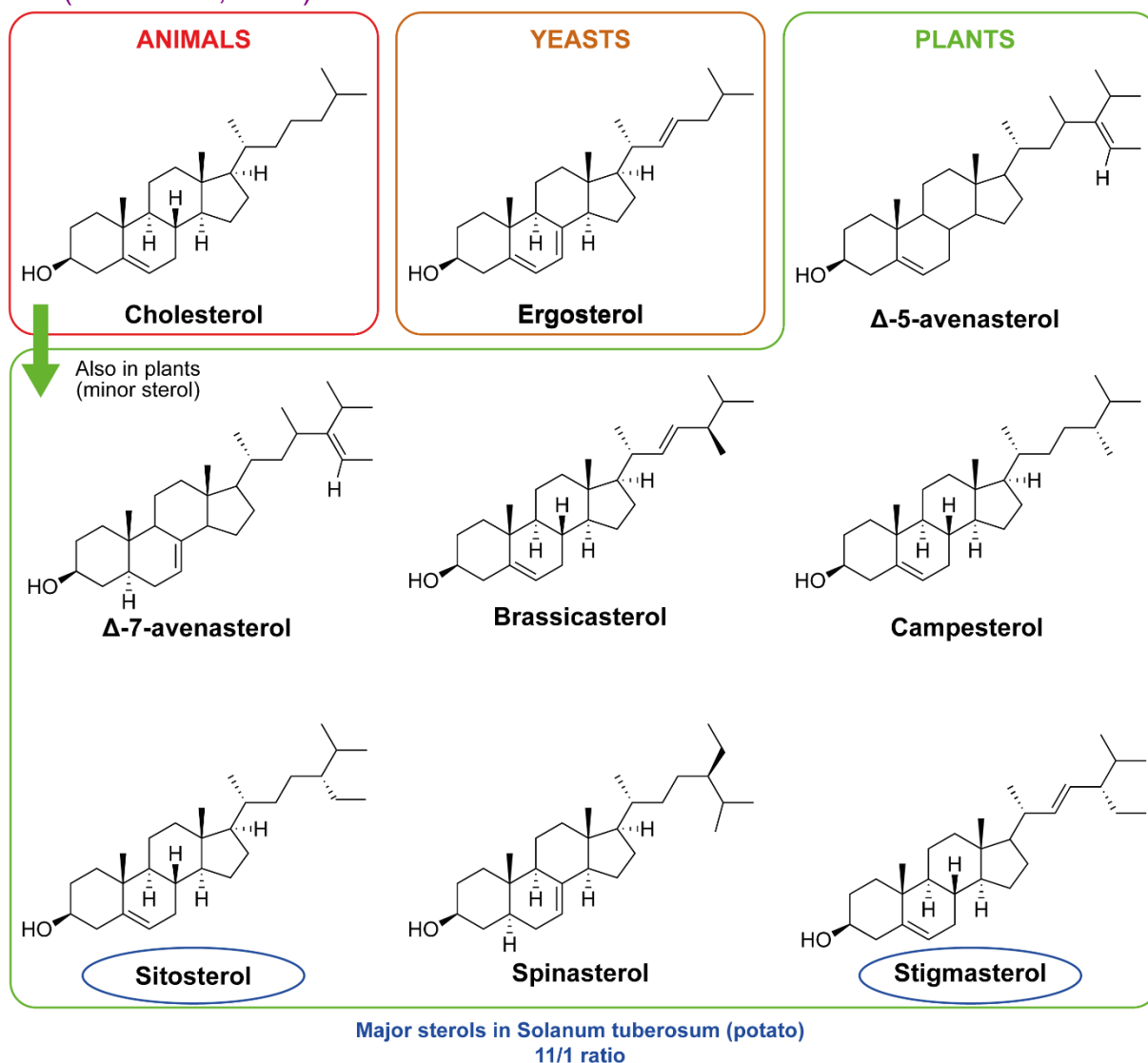


Figure 8

Chemical structures of common sterols. Animals and yeasts use only one sterol (cholesterol and ergosterol, respectively) while plants employ a multitude of them, among which cholesterol may be found in small quantities. In this manuscript, we will be interested in PMs of *Solanum tuberosum* (potato), whose main phytosterols (in blue) are sitosterol and stigmasterol in an 11/1 ratio (Nyström et al., 2012).

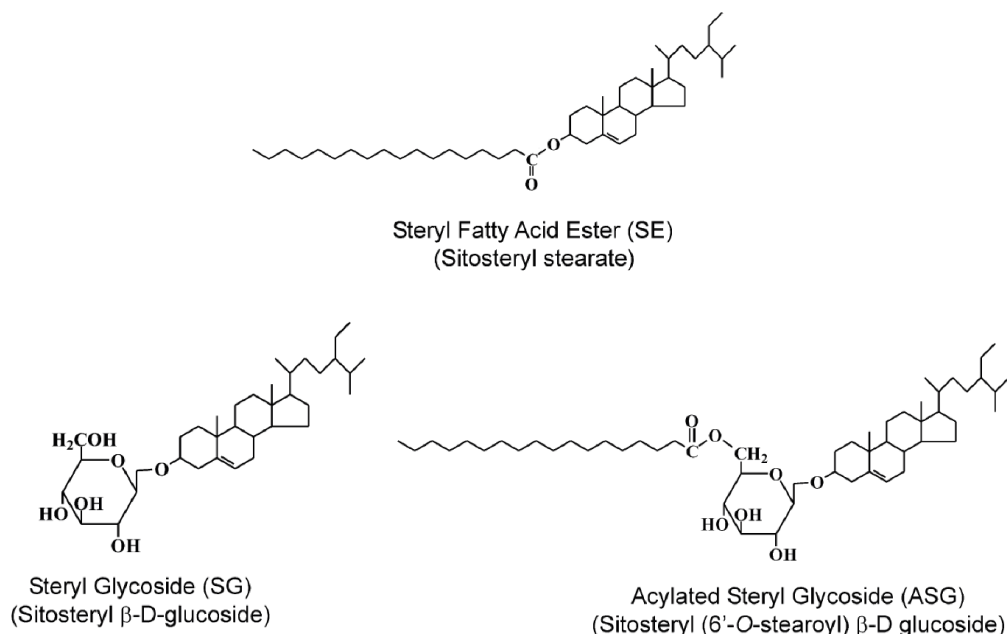


Figure 9

Display of the various types of phytosterol conjugates. Here, a simplified sitosterol is used as example. All conjugation rely on attaching an ester (sterol ester, SE), a sugar (steryl glycoside, SG) or an esterified sugar (acetylated steryl glycoside, ASG) to the sterol's hydroxyl function. Adapted from (Moreau et al., 2002).

Prokaryotes possess no sterol. Instead they produce hopanoids, pentacyclic sterol analogues (Bramkamp and Lopez, 2015). Although they are thought to behave similarly to sterols, the absence of hydroxyl group on the A ring implies that (1) hopanoids cannot be conjugated and (2) the polar and apolar regions are inverted compared to sterols, with rings being apolar and the tail being polar (Dufourc, 2008).

4. Lipid phase behaviour and sterols

Depending on their nature, phospholipids, glycolipids and sphingolipids may exhibit a variety of phase behaviours (Koynova and Tenchov, 2013). Yet, in the context of the fluid mosaic model, we are referring to a lipid bilayer, which is a lamellar phase (Figure 10). In addition, depending on lipid composition, temperature and hydration, the rate of diffusion of molecules within, the thickness and the acyl chain packing (hereafter called order) will vary (Feigenson, 2006; Koynova and Tenchov, 2013). Here, we will be interested in the phase behaviour of mixtures of phospholipids, sphingolipids and sterols at physiological temperature (i.e. 0-40°C). Here, phospholipids and sphingolipids (section I.C.4) have a phase transition temperature (T_m) above which they make a liquid-disordered ($L\alpha$) phase and below which they enter into a gel phase ($L\beta$ or $L\beta'$, depending on the lipids). T_m can reach rather extreme values, so that the concerned lipids are present almost exclusively in a $L\alpha$ - (e.g. unsaturated acyl chains) or a $L\beta$ - or $L\beta'$ -phase (saturated acyl chains). Briefly, lipids in a $L\alpha$ phase diffuse fast and are loosely ordered, while lipids in a $L\beta$ or $L\beta'$ phase diffuse slowly and are much more ordered. Another important phase is the sterol-enriched liquid-ordered phase (L_o) where lipids still diffuse fast but are more ordered.

How do free sterols compare to each other in terms of function? Cholesterol is known to fluidify membranes in the gel phase at low temperature and to rigidify them in the liquid phase at higher temperature. This latter effect is lessened for sitosterol and even inverted for stigmasterol, depending on the membrane composition, while campesterol retains properties similar to cholesterol (Beck et al., 2007; Grosjean et al., 2015). Conjugated sterols can order membranes further, with an increased efficiency in the case where free sterols are already present (Grosjean et al., 2015).

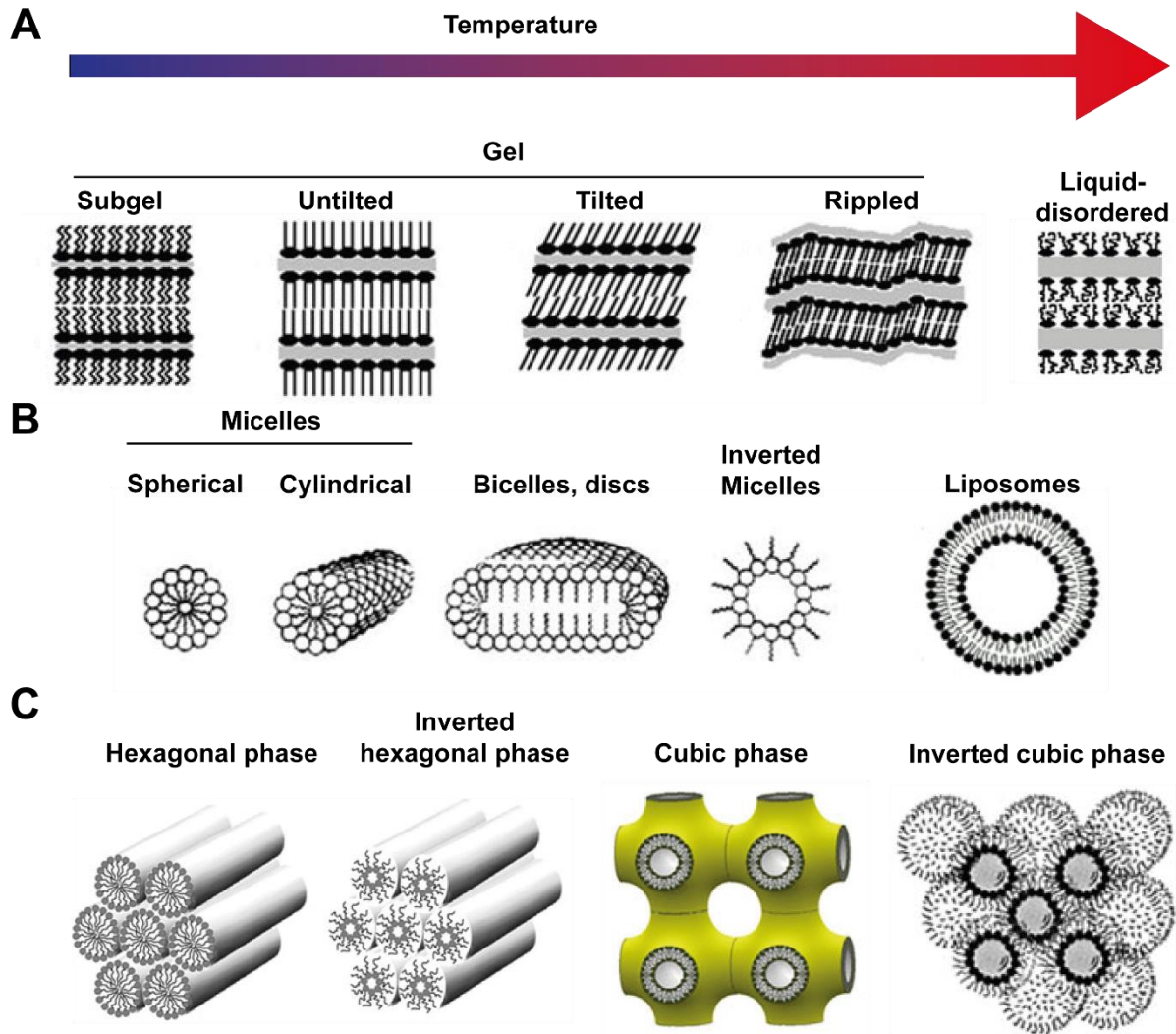


Figure 10

Representation of lipid phases. (A) Biological membranes are in lamellar phase. At the lowest temperature, a given phospholipid is in a subgel (L_c) phase with slow lateral diffusion and high acyl chain order. Upon temperature increase, it will transition to an untilted (L_β), then tilted (L_β'), then rippled (P_β') gel phase, depending on the nature of the lipid. Once a certain temperature T_m is reached, a gel-liquid-disordered (L_α) phase transition occurs. In this latter phase, lipids diffuse quickly and acyl chain order is lower. *In lieu* of the L_α phase, the sterol-enriched liquid-ordered phase (L_o) (not shown) may be reached: it retains a higher acyl chain order than the L_α phase. Lipids in water may spontaneously aggregate into spherical (B) and non-spherical structures (C). Adapted from (Koynova and Tenchov, 2013).

5. Sphingolipids

Plant sphingolipids are made of a long (acyl) chain base (LCB) amide linked to a FA to create a ceramide, with the eventual addition of phosphate and sugar moieties. In plants, four classes may be distinguished: free LCBs, ceramides, glucosylceramides (GluCers) and glycosyl inositol phospho-ceramides (GIPCs) (Figure 11). The first three classes are entirely synthesised in the ER while GIPC synthesis is pursued with ceramides in the Golgi apparatus. Animals cells contain no GIPCs but they possess sphingomyelin (Futerman and Hannun, 2004).

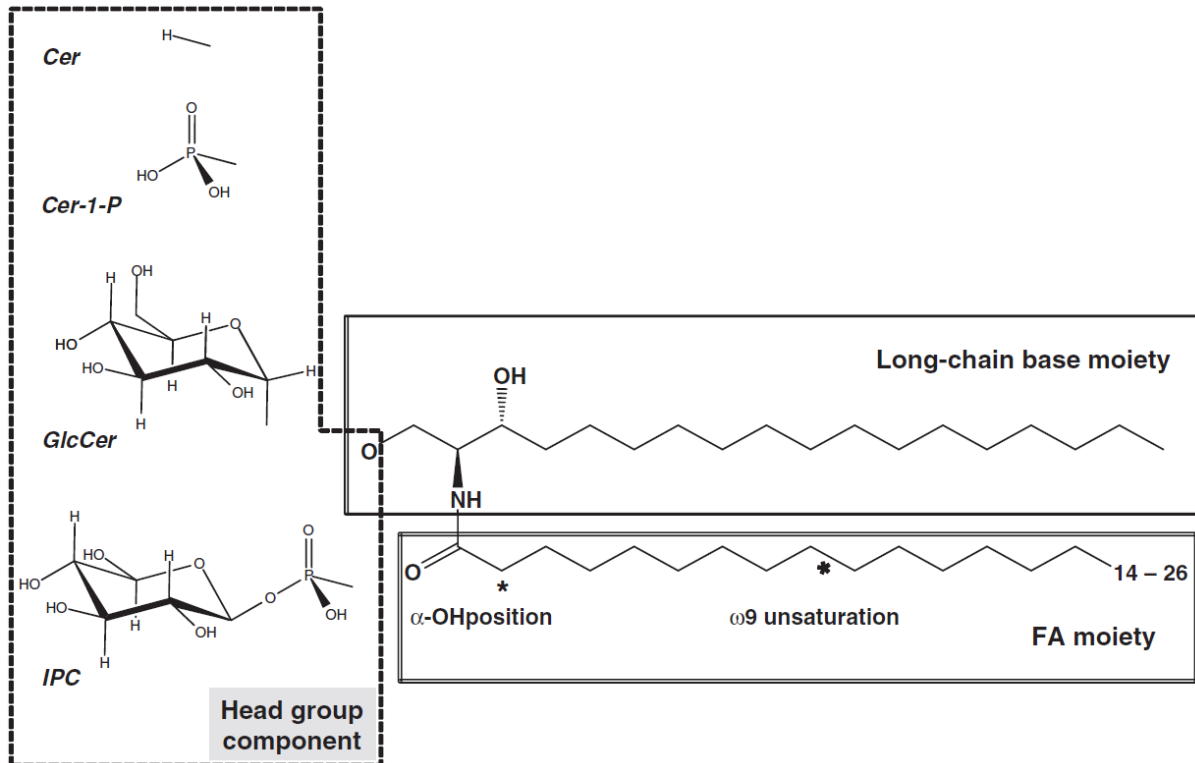


Figure 11

Display of plant sphingolipids. An FA, possibly hydroxylated, is grafted to an LCB. The primary hydroxyl can be functionalised with a head group, defining its sphingolipid class. From (Pata et al., 2010).

GIPCs are the most abundant sphingolipids in *Arabidopsis thaliana* leaves (Markham et al., 2006). GIPCs make up a wide class of molecules whose diversity relies on: (1) the LCB, its double bonds and hydroxylations, mostly t18:0 or t18:1 (where t means trihydroxylated); (2) the FA length, its double bonds and hydroxylations, most commonly a very long chain FA (VLCFA) or a 2-hydroxylated VLCFA up to 30 carbons ; (3) the glycans, their number, their nature and their glycosidic links (Buré et al., 2014; Cacas et al., 2016; Pata et al., 2010). The polar head composition defines the series to which a GIPC belongs (Mamode Cassim et al., 2019).

In synergy with phytosterols, sphingolipids can modulate membrane rigidity: GluCers fluidify membranes in presence of stigmasterol where GIPC would rigidify, while a 1/1 GluCer/GIPC mixture would strongly rigidify membranes in presence of

sitosterol or campesterol (Grosjean et al., 2015). Beside their structural role, GIPCs were also found to act as toxin receptors: necrosis and ethylene-inducing peptide 1-like (NLP) protein may bind GIPCs from series A, predominant in eudicotyledons and bearing two hexose moieties, but not those from series B, predominant in monocotyledons and bearing three hexose moieties. This explains why eudicotyledons plants are sensitive to NLPs while monocotyledons are not (Lenarčič et al., 2017).

Yeast sphingolipids have sphingolipids similar to plants', with the exception that GIPCs are replaced by mannosyl inositol phospho-ceramides (Marquês et al., 2018). Prokaryotes, with very few exceptions, bear no sphingolipids (Hannich et al., 2011).

6. Lipid composition and asymmetry of PMs

Understanding membrane organisation implies quantifying and situating all its compounds. This section will provide the necessary data about the PMs of the organisms discussed in this manuscript. The description of endomembranes (e.g. nuclear membranes, mitochondrial membranes, plastid membranes...) is out of the scope of this manuscript; the interested reader is referred to (Cheesbrough and Moore, 1980; Rolland et al., 2009; Schwertner and Biale, 1973; Zachowski, 1993; Zhendre et al., 2011).

a. Of animal cells

The erythrocyte, lacking a nucleus, is commonly used to study PM composition and asymmetry as the PM is the only membrane it possesses. Cholesterol represents about 40% of the whole PM (Steck and Lange, 2018), sphingolipids around 25% (Virtanen et al., 1998) while the remainder is made of phospholipids. Sphingolipids are almost exclusively in the outer leaflet along with PC while other phospholipids, particularly anionic ones, are in the inner leaflet (Zachowski, 1993). The repartition of cholesterol between both leaflets is still up to debate (Steck and Lange, 2018).

b. Of plant cells

Phospholipids account for 30-40% of the plant PM, sterols make up 20-30% of it while sphingolipids make up the remainder (Cacas et al., 2016). Although the PM's lipid distribution is well studied in animal cells (Zachowski, 1993), data in plant cells are scarce (Cacas et al., 2016; Tjellström et al., 2010). Recently, building upon these few articles, a model of PM's lipid asymmetry was proposed (Mamode Cassim et al., 2019): (1) GIPCs are exclusive to the outer leaflet, (2) GluCers and sterols, both free and conjugated, are enriched in the outer leaflet, (3) phospholipids, including glycolipids, are enriched in the inner leaflet and (4) PS, PA and PIPs are exclusive to the inner leaflet. We must remind ourselves it is only a model that remains to be tested.

c. Of yeasts

According to (Patton and Lester, 1991), the PM of *Saccharomyces cerevisiae* is made up of phospholipids for 34%, sphingolipids for 16%, cardiolipin for 2% and ergosterol for 48%. There again, aminophospholipids and PIPs remain mostly in the

inner leaflet while sphingolipids, ergosterol and PC are mostly in the outer leaflet (Mioka et al., 2014; Santos and Riezman, 2012; Solanko et al., 2018).

d. Of *Bacillus*

Bacteria of the *Bacillus* clade are Gram-positive bacteria, with one PM coated by a thick layer of polysaccharides. *Bacillus subtilis* was shown to contain PG/PE/CL in a 70/12/4 molar ratio (Clejan et al., 1986), while a study on the PM asymmetry in *Bacillus amyloliquefaciens* hints at an enrichment of 70% of all phospholipids in the outer leaflet while CL would remain in the inner leaflet. The amount and distribution of hopanoids at the PM remains an open question.

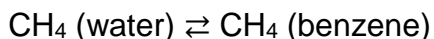
Overall, anionic- and amino-phospholipids remain in the inner leaflet while sphingolipids and PC remain in the outer leaflet. Sterol distribution may vary and is generally very disputed. Proteins of both leaflets are completely different, being either cytoplasmic, apoplasmic or transmembranous, in ways we will see in the next section.

D. Membrane proteins

(Singer and Nicolson, 1972) make a distinction between peripheral membrane proteins, which superficially interact with membranes, and integral ones, which bind tightly and may even span the entirety of the bilayer. Examples of the former would be pleckstrin domains (Lenoir et al., 2015a) while examples of the latter would be GPCRs (Katritch et al., 2013), ATP-synthases (Zhou et al., 2015), voltage-dependent ion channels (Hosaka et al., 2017) and remorins (section III). For an integral protein to interact with a membrane, thermodynamics tell us there are three types of interactions to consider: (1) hydrophobic interactions, (2) hydrogen bonding and (3) electrostatic interactions. Basing ourselves upon the lecture of (Singer, 2004), we shall comment all three then conclude on the kind of protein fold we may expect for membrane-interacting proteins.

1. Hydrophobic interactions

Let us consider the solubility of a typically hydrophobic molecule such as methane (CH₄) in both water and benzene:



with $\Delta G = -11.5 \text{ kJ/mol}$ (Kauzmann, 1959). The dielectric constant, i.e. the electric permeability of a material over that of the void, for a protein is $D_{\text{protein}} = 4$ and $D_{\text{water}} = 78.5$ (Dwyer et al., 2000), so $D_{\text{protein}} < D_{\text{water}}$, so proteins may bury their hydrophobic residues in their core. Alternatively, such hydrophobic residues may be buried in the core of the hydrophobic membrane whose $D_{\text{membrane}} = 2-3$ (Gramse et al., 2013; Huang and Levitt, 1977).

2. Hydrogen bonding

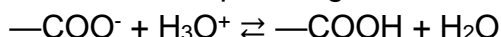
In addition to some residues' lateral chains, the peptide backbone itself is involved in hydrogen bonding. Solvent water may bond with such groups as well as other protein groups, but what if they are within the hydrophobic core of a bilayer? Absence of

hydrogen bonding costs about $\Delta G = + 18.5\text{kJ/mol}$ (Klotz and Franzen, 1962). The only H-acceptors there would be the protein's H-donors. This implies the integral part of a protein must be meticulously folded to be both thermodynamically stable and functional.

3. Electrostatic interactions

a. Polar residues within a membrane

Charges from polar residues (i.e. aspartate, glutamate, histidine, lysine and arginine) in the polar environment of solvent water (e.g. at $\text{pH} \approx 7$ in the cytosol) may be balanced by it or nearby polar solutes. Can polar residues find themselves stably inside a bilayer? All the above-mentioned residues are in exchange between a charged state and a discharged state. As an example, for glutamate:



with $\text{pK} = 4.25$ in 0.1 M NaCl water at 25°C (Thurkill et al., 2006). The interior of a protein is itself much less polar than water, as attested by their respective dielectric constants of $D_{\text{protein}} = 4$ and $D_{\text{water}} = 78.5$ (Dwyer et al., 2000). The thermodynamic cost to keep a glutamate in the discharged state at $\text{pH} = 7$ is $\Delta G = + 15.7\text{kJ/mol}$ in solvent water, making it unfavourable. Yet we must keep in mind that pK constants for aminoacids inside a protein may be heavily shifted, as exemplified in (Dwyer et al., 2000) where a buried glutamate had a $\text{pK} = 8.8$ with an unusually high $D_{\text{protein}} = 12$, in which case a substantial proportion of glutamates are discharged. Thus, we should remind ourselves that the peculiar environment of a protein's inside may impose behaviours on residues much different from solvent water. Yet, discharging a polar residue to bury it in a lipid bilayer seems unfavourable.

Counterbalancing a charged residue with another charged residue or an ion of opposite sign would be another mechanism to embed a polar residue in a bilayer. This mechanism finds its limit illustrated with the poor solubility of a zwitterionic glycine in acetone, whose $D_{\text{acetone}} = 21.0$, compared to water whose $D_{\text{water}} = 78.5$ (Lide, 2010). A lipid bilayer core has $D_{\text{membrane}} = 2\text{-}3$ (Gramse et al., 2013; Huang and Levitt, 1977). Since, as D decreases, the solubility of glycine decreases, it shows that counterbalancing a charge does not improve its solubility in an apolar environment.

The free energy cost of burying a residue was systematically assessed in (MacCallum et al., 2007). It strengthens the conclusion that, for a part of a protein to be embedded in a lipid membrane, polar residues should be avoided.

b. Protein-lipid electrostatic interactions at the membrane's surface

However, lipid polar head groups may favour the presence of polar residues at the membrane-water interface. In (MacCallum et al., 2007), free energy costs to bury a residue in a DOPC membrane were compared with the costs of keeping these residues at such an interface (Table 1). Arginine, asparagine, glutamine, threonine, and tyrosine are very costly to bury but are prone to stay at the membrane-water interface.

Residue	At interface	Buried
Leu	-14.1	-15.2
Ile	-20.6	-22.1
Val	-12.2	-13.8
Phe	-14.9	-12.8
Ala	-6.8	-8.4
Trp	-21.6	-4.9
Met	-10.5	-4.4
Cys	-6.6	-3.4
Tyr	-14	6.6
Thr	-4.2	13.9
Ser	-0.7	15.8
Gln	-8.9	20.2
Lys ¹	-18.6	19.9
Asn	-6.5	23.9
Glu ²	-1.68	21.1
Asp ²	1.6	31
Arg ³	-21.2	58.1

¹ Charged at interface, neutral if buried

² Neutral in both cases

³ Charged at interface, both states are equiprobable if buried

Table 1

Free energy cost (in kJ/mol) to bury a residue in a lipid bilayer or to keep it at the membrane-water interface. Values from (MacCallum et al., 2007).

This leads to the question: how much do electrostatic interactions with lipid polar groups contribute to the stabilisation of a membrane protein? We will consider the case of the peripheral pleckstrin homology (PH) protein domain, which is a well-known marker of phosphoinositides both *in vivo* and *in vitro* (Kavran et al., 1998). These domains merely touch the membrane to bind their target partner (Lenoir et al., 2015b, 2015a). In (Figure 12), we visualise the loop responsible for FAPP1-PH's membrane-interaction docked *in silico* to a micelle of dodecylphosphorylcholine (DPC) / phosphatidylinositol 4-phosphate (PI4P). It is only a few angstroms deep inside the micelle. Recalling (Table 1), the residues' positions are not surprising: L12 may favourably be buried deep within the micelle while other residues are more stable at the interface. This explains why mutations of W8 to a less hydrophobic residue (i.e. less prone to be at the interface) nullifies binding. A similar result is obtained for the mutant N10T, highlighting the necessity of a basic residue that is likely to interact with the negatively charged 4-phosphate moiety of the PI4P polar head group (Lenoir et al., 2015b).

The structural analysis of FAPP1-PH demonstrates that electrostatic interactions at the membrane-water interface can ensure a protein's tethering to a membrane.

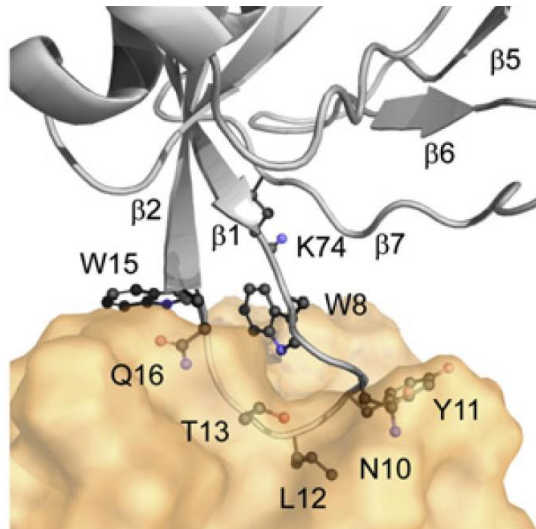


Figure 12

***In silico* structure of FAPP1-PH's loop** (grey) with a micelle (orange surface) of dodecylphosphorylcholine (DPC) / phosphatidylinositol 4-phosphate (PI4P). From (Lenoir et al., 2015a).

4. Possible folds of membrane proteins

In the example above, the interplay between hydrophobic and electrostatic interactions is blatant. Now that we are aware of the different types of interactions between a membrane protein and its membrane, we may wonder what they imply in terms of membrane protein fold.

A first consideration is that proteins will keep their polar residues in water and away from the apolar membrane core. For apolar residues, the opposite is true. In addition, we just saw that some residues, whether polar or not, may be found at the membrane-water interface and play a crucial role in membrane binding.

FAPP1-PH's membrane anchoring is shallow. What about integral protein domains? Most do fold in one of the following manners: (1) into helices spanning part of or all the membrane, lying in its plane or tilted (Katritch et al., 2013; Lins et al., 2008; Zickermann et al., 2015a). (2) Into β -strands, granted they are long enough to span the membrane and numerous enough to make a complete barrel, as in porins, forming a β -barrel (Figure 13) (Kefala et al., 2010).

Less canonical folds exist for peripheral membrane proteins. We already discussed FAPP1-PH. Another example would be the fusion protein gp41 from the human immunodeficiency virus (HIV), folding into a β -sheet in the host membrane, allowing membrane hemi-fusion (Figure 14) (Lee et al., 2019). We shall discuss, in section III.C.1, a less canonical fold of an integral membrane anchoring domain, in which a horizontal α -helix is only partially embedded in the membrane while one hydrophobic extended β -strand is deeply buried.

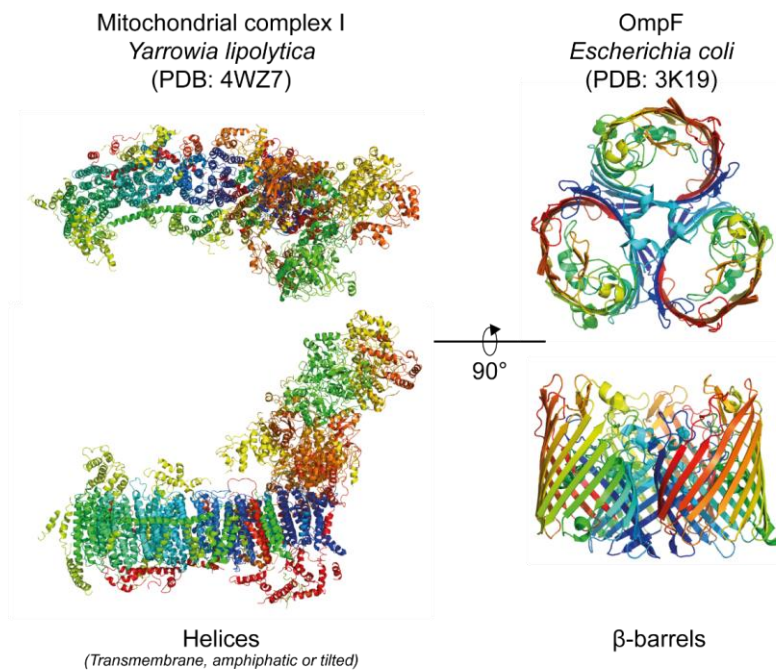


Figure 13

Display of the most common protein fold in membranes. *Left:* the mitochondrial complex I is embedded in the inner mitochondrial membrane via many helices. The majority of them are transmembrane (i.e. perpendicular to the membrane plane), some are tilted and a few are amphiphatic, thus lying in the membrane plane (Zickermann et al., 2015b). *Right:* OmpF is a pore granting passage of small molecules (< 600 Da) through *Escherichia coli*'s outer membrane. Each monomer is made of 16 β -strands folded in a β -barrel (Kefala et al., 2010).

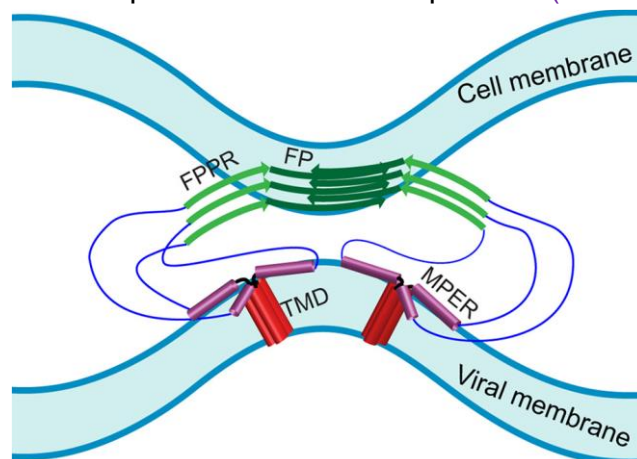


Figure 14

Schematic structure of gp41, a subunit of the HIV's envelope. The transmembrane domain (TMD, red) is made of helices spanning the viral membrane while the fusion peptide (FP) and the FP proximal region (FPPR) fold into β -strand in the targeted cell membrane. This fold promotes membrane fusion and viral entry into the cell. From (Lee et al., 2019).

E. Membrane domains

1. Early observations

We discussed the complex composition of membranes (sections I.C and I.D). The amount of possible interactions between all its components is gigantic. We also discussed that both leaflets of the PM possess different lipids (section I.C.6) and proteins (section I.D), creating a strong heterogeneity. Could there be heterogeneities within one leaflet of the PM?

a. Coexistence of lipid phases

We are already familiar with the concept of lipid phases (section I.C.4). Soon after the publishing of the fluid mosaic model, evidence of *in vitro* lipid phase separation in membranes were brought in (Stier and Sackmann, 1973) monitored, using paramagnetic electron resonance, the activity of the peripheral P450 cytochrome reductase on both a soluble spin label and a fatty acid one, embedded in liver microsomal membranes, at various temperatures. The Arrhenius plot showed a drop-in energy activation above 32°C only for the fatty acid label. Stier and Sackmann interpreted this as proof of the presence, below 32°C, of rigid membrane domains created by the interaction between the peripheral P450 cytochrome reductase and the otherwise fluid bulk membrane (Figure 15).

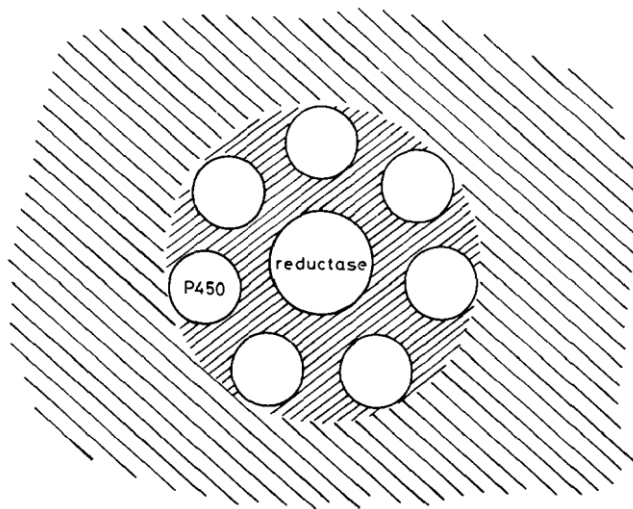


Figure 15

The earliest proof of coexistence of lipid phases. P450 cytochrome reductase is a peripheral protein. It was hypothesised to order the lipids in its vicinity (fine stripes), creating a rigid membrane domain in the otherwise fluid bulk membrane (large stripes). From (Stier and Sackmann, 1973).

b. Caveolae, a visible heterogeneity

In 1955, electron microscopy of mouse gall bladder epithelium cells showed small invaginations of about 50 to 90 nm (Figure 16) (Yamada, 1955). This is a visual example of spatial heterogeneity in biological membranes. Since these structures resemble cavities within the PM, they were named caveolae. Caveolae will be discussed in greater lengths in section II.A.3.

For now, we need only to remember that one could see, as early as 1955, that biological membranes were not homogeneous.

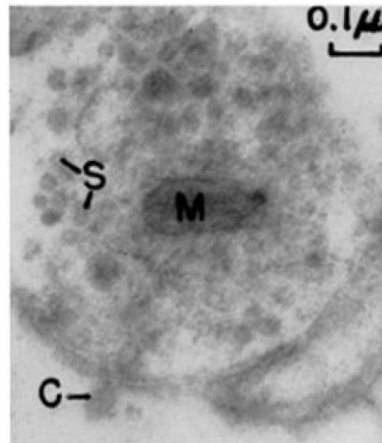


Figure 16

The earliest observation of a caveolae. Thin slice of a mouse's gall bladder epithelium by negative staining electron microscopy with osmium tetroxide. Scale bar: 1 μm. S: synaptic vesicle, M: mitochondria, C: caveolae. From (Yamada, 1955).

c. Detergent-insoluble membranes (DIM)

In parallel, lipids and membrane proteins of human erythrocytes treated by Triton X-100, a mild non-ionic detergent, at cold, followed by ultracentrifugation on a sucrose gradient, showed variable solubilities (Yu et al., 1973): detergent-solubilised material was pelleted while DIM remained in the supernatant. We may note that phospholipids were mostly soluble while sphingomyelin, an animal sphingolipid, was not. It was yet another hint that biological membranes may not be homogeneous.

Twenty years later, (Sargiacomo et al., 1993) purified DIM enriched in proteins bearing glycosyl-phosphatidyl-inositol (GPI) anchors and caveolin, the main protein component of caveolae (section II.A.3). The enrichment in such GPI-bearing proteins was a commonly explored feature of DIMs (Brown and Rose, 1992; Hooper and Turner, 1988). (Schroeder et al., 1994) pushed the lipidomic analysis of DIMs further by reconstituting minimal DIMs. Cholesterol and lipids with high T_m , such as sphingolipids and saturated phospholipids, were shown to promote the formation of DIMs, in the absence of any protein.

d. Cell polarity

Meanwhile, investigations on animal cell polarity, more specifically on animal epithelial cells, revealed differential lipid and protein composition between apical and basolateral membrane domains (Simons and Van Meer, 1988). This led to the formulation of putative lipid and protein sorting mechanisms for the specialisation of these membranes (Simons and Wandering-Ness, 1990)

2. From lipid rafts to nanodomains

a. Birth of the lipid raft hypothesis

Evidence stated above led to the formulation of the raft hypothesis: the existence of (1) small membrane domains, the size of a caveolae (50-90nm), (2) enriched in cholesterol, high-T_m lipids and GPI-anchored proteins (Figure 17) (Simons and Ikonen, 1997). It was proposed that lipid rafts could be purified in DIM fractions: they would float at the top of a sucrose gradient, hence their designation as rafts (Dupree et al., 1993). In this initial description, lipid rafts were regarded as sorters of membrane trafficking (Simons and Ikonen, 1997).

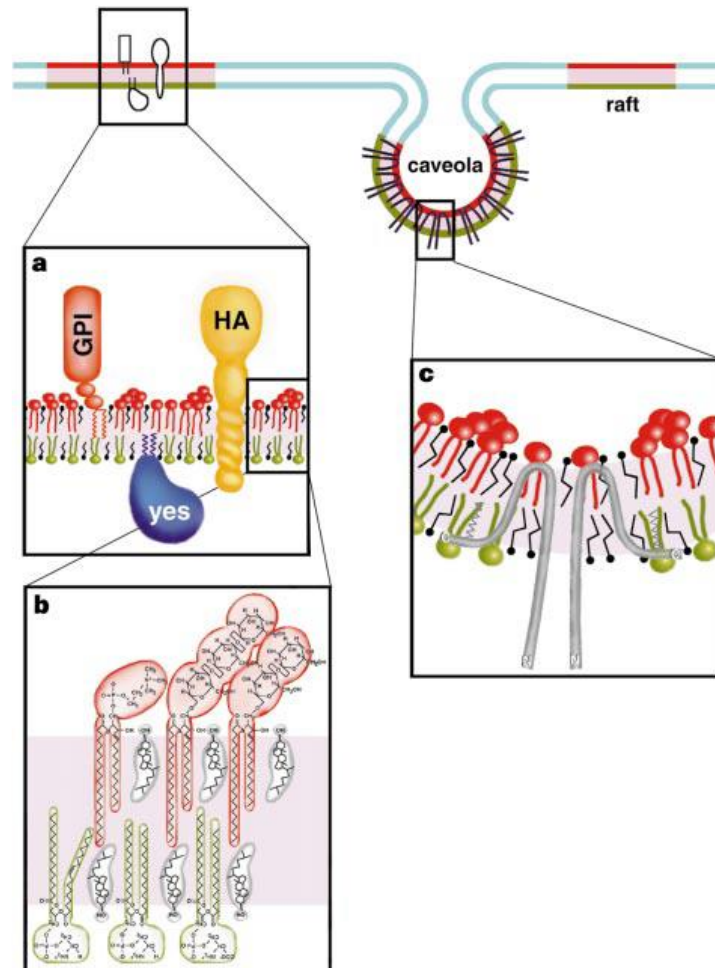


Figure 17

First hypothetical model of lipid rafts and caveolae at the animal PM, in 1997.

Rafts (red) segregate from the bulk PM (blue). Caveolae are proposed as a peculiar kind of raft-like structure. (a) A lipid raft enriched in cholesterol bearing some membrane proteins attached to one leaflet, a GPI-anchored protein (red) to the outer leaflet and the Src-family kinase Yes (blue) to the inner leaflet, or spanning the entire bilayer, here hemagglutinin (HA, yellow). (b) Asymmetry of the animal PM, as described in section I.C.6.a: sphingolipids and PC are in the outer leaflet while other lipids, particularly anionic ones, are the inner leaflet. (c) Caveolae are formed by self-associating caveolin proteins making a hairpin loop in the membrane. Interactions with raft lipids may be mediated by binding to cholesterol and by acylation of C-terminal cysteines. From (Simons and Ikonen, 1997).

b. Restatements

Many more observations of lipid rafts occurred, which did not relate on caveolae and GPI-anchored proteins (de Laurentiis et al., 2007; Mongrand et al., 2004; Yuan and Johnston, 2001), rendering the initial description of lipid rafts obsolete. In 2006, at the Keystone Symposium on Lipid Rafts and Cell Function, an updated, much broader definition was proposed (Pike, 2006). “Membrane rafts”, for it was accepted that proteins could also be involved in their formation, “are small (10-200nm), heterogeneous, highly dynamic, sterol- and sphingolipid-enriched domains that compartmentalise cellular processes. Small rafts can sometimes be stabilised to form larger platforms through protein-protein and protein-lipid interactions.” Major limitations of DIM purifications as indicators of membrane rafts were pointed out (Munro, 2003; Shogomori and Brown, 2003) and a clear distinction was made between simple *in vitro* system, where a distinction between phases may apply, and *in vivo* systems, where the multiplicity of interactors makes lipid phases harder to assess. The question of biological functions was deliberately left unanswered beyond the statement that “[membrane] rafts are involved in the compartmentalisation of cellular processes”, whatever they may be.

This led to a restatement, by one of the author of the initial lipid raft hypothesis, of what a raft should be (Lingwood and Simons, 2010) (Figure 18). In this view, lipid rafts (used as a synonym of membrane rafts) are also thicker, L_o phase membrane domains, something that was previously deemed too specific of simple *in vitro* systems (Pike, 2006).

c. Interdigitation and domain registration

This last redefinition also addressed the concept of interdigitation: if a lipid raft is in the outer leaflet, would a raft be recruited (registration) or chased away (antiregistration) from the inner leaflet (Figure 19)? Theoretical calculations oppose antiregistration to minimise membrane thickness variations to registration via interdigitation of aliphatic chains (Williamson and Olmsted, 2015). Works on planar (Collins and Keller, 2008) and supported (Lin et al., 2006; Rinia et al., 2001) model membranes, favour registration.

d. Pinning

The concept of interdigitation is often linked to the notion of pinning, as in pinning and keeping these registered membrane domains together. Such phenomena were observed *in vivo* between GPI-anchored proteins of lipid rafts of the PM's outer leaflet and actin bound to phosphoinositides of lipid rafts of the PM's inner leaflet (Dinic et al., 2013; Raghupathy et al., 2015).

(Tsuji and Ohnishi, 1986) were the first to demonstrate a pinning of the anion transporter Band 3 by the actin cytoskeleton in erythrocytes in a spectrin-dependent manner. A model of pinning was thus proposed (Figure 20), often referred to as the fence and picket model (Kusumi et al., 2005). Similar findings were obtained on transferrin and α_2 -macroglobulin upon disruption of actin filaments and microtubules (Sako and Kusumi, 1994).

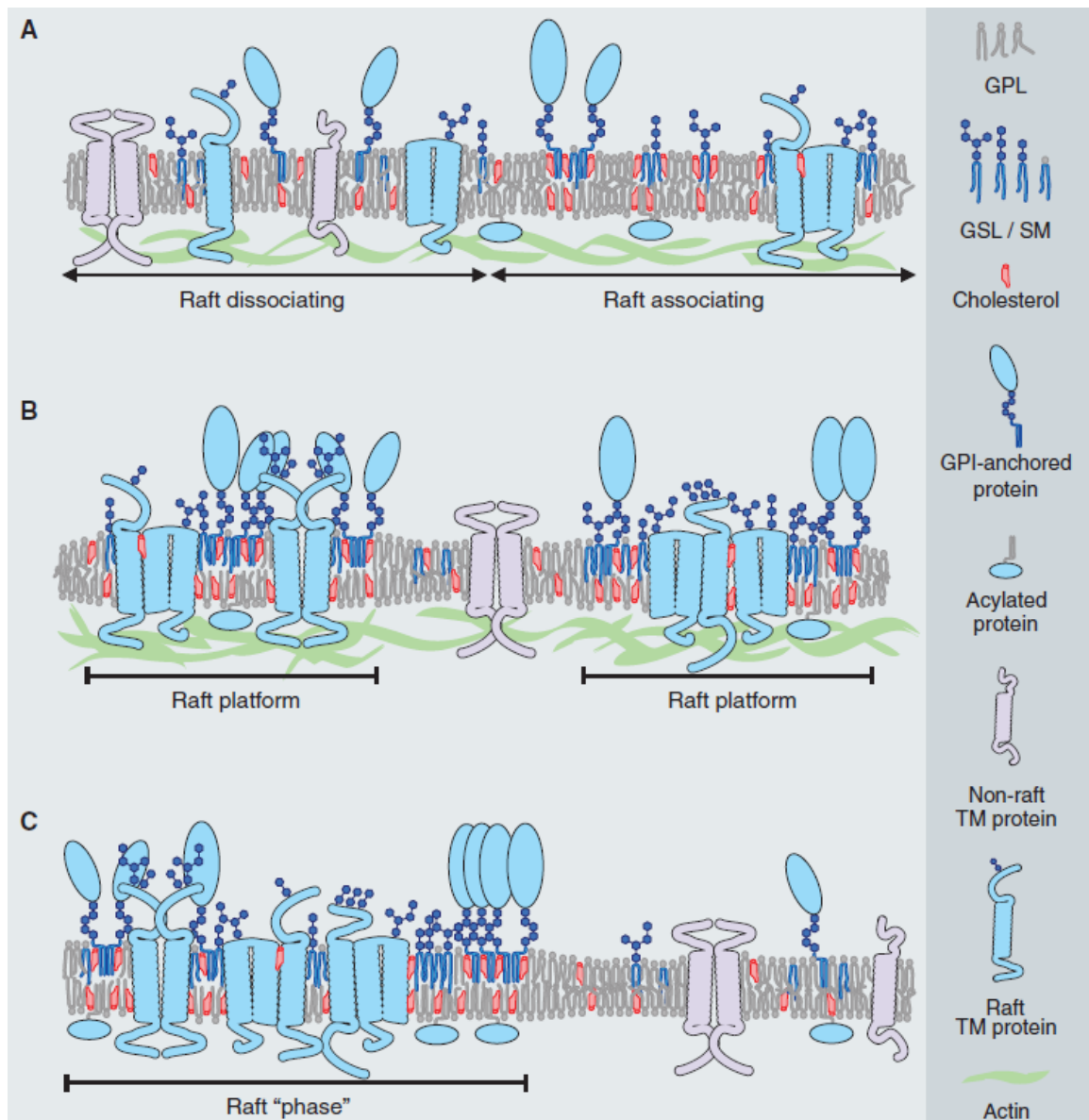


Figure 18

Restatement of the lipid raft hypothesis in 2010. Lipid rafts are liquid-ordered L_o membrane domains enriched in sterols, sphingolipids, some particular membrane proteins and among which some may interact with actin (green). They may exist in various membrane systems, even though most examples within relate to the PM and animals. (A) Lipid rafts are dynamic structures with particular lifetimes. They may fuse or dissociate. (B) Lipid rafts may have heterogeneous contents. Their formation may be triggered by lipid-lipid segregation, protein-lipid multivalent binding and protein-protein oligomerisation. Protein-actin interaction as a mechanism to initiate lipid raft formation by pinning (see section I.E.2.d) its component in place is also suggested. (C) Casting the concept of actin pinning aside, lipids and proteins may coalesce, or not, into lipid rafts by their sheer preference for a certain degree of membrane order, liquid-ordered L_o for lipid rafts or liquid-disordered L_d for the bulk membrane, and biochemical interactions. GPL: glycerophospholipid; GSL/SM: glycosphingolipid/sphingomyelin; TM: transmembrane. From (Lingwood and Simons, 2010).



Figure 19

The two leading behaviours of inter-leaflet membrane domain coupling. Inter-leaflet interactions between acyl chains favour domains in both leaflets to be registered (A) while hydrophobic mismatch favours domain anti-registration (B) to even membrane thickness. From (Fujimoto and Parmryd, 2017).

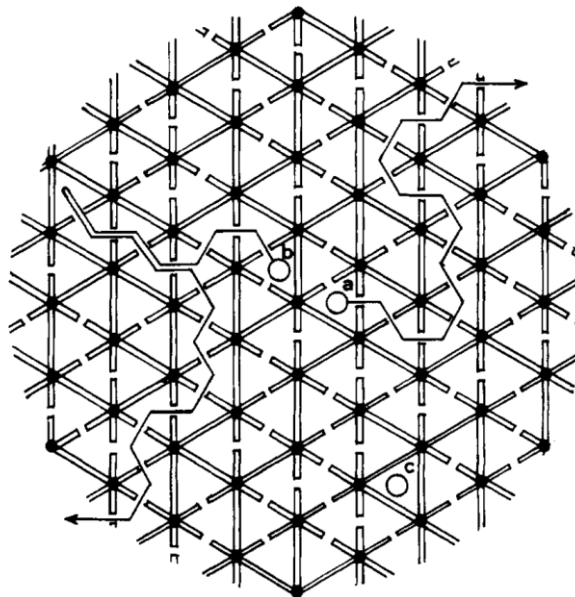


Figure 20

Pinning of membrane proteins. Pinning of band 3 (white circles) by the actin cytoskeleton, later termed the “membrane skeleton fence model” (Sako and Kusumi, 1994). Black dots represents actin and its associated band 4.1 protein, connected to six spectrins (white lines) at the PM’s inner leaflet. Each spectrin is either in a tetrameric state (full lines) or a dissociated dimeric state (broken lines), forming a mesh. The fate of three pinned band 3 molecules a, b and c trying to escape the membrane region of interest represented here is drawn. a diffuses through the mesh and escapes quickly. b encountered a dead-end in the mesh, so it escapes slowly. c is blocked and will never escape: it is pinned down until a neighbouring spectrin tetramer dissociates. From (Tsuji and Ohnishi, 1986).

e. A clarification of terminology

We must have noted that the nomenclature of membrane domains is quite heterogeneous: between DIMs (also synonymously called detergent resistant membranes, DRMs), lipid rafts, membrane rafts, microdomains and nanodomains. Now, we shall define each term with precision and decide on which to commit to.

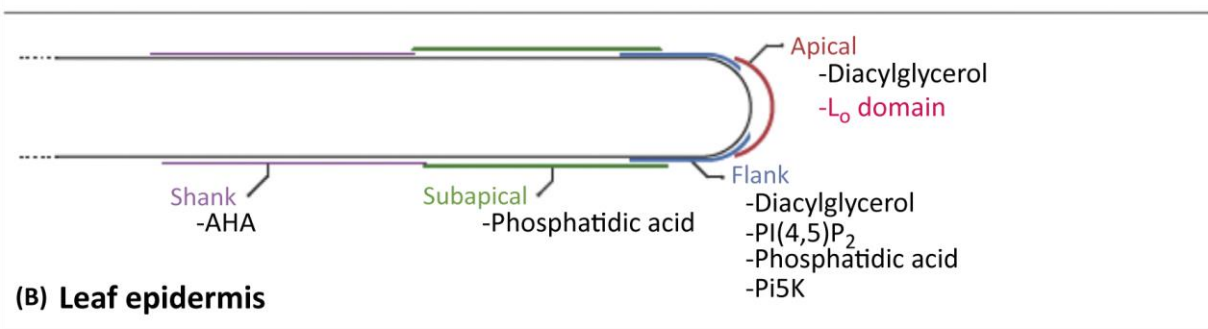
DIMs are the insoluble fraction of a biological membrane preparation treated with a mild detergent at cold temperature. They are separated from their soluble counterparts by ultracentrifugation on a sucrose gradient.

Lipid rafts and membrane rafts are synonymous, although the former is the historical and most remembered word. The term raft was a reference to DIMs that would float at the top of a sucrose gradient (Dupree et al., 1993). Although it is still used in scientific parlance, we prefer the broader designation of nanodomain (Gronnier et al., 2018).

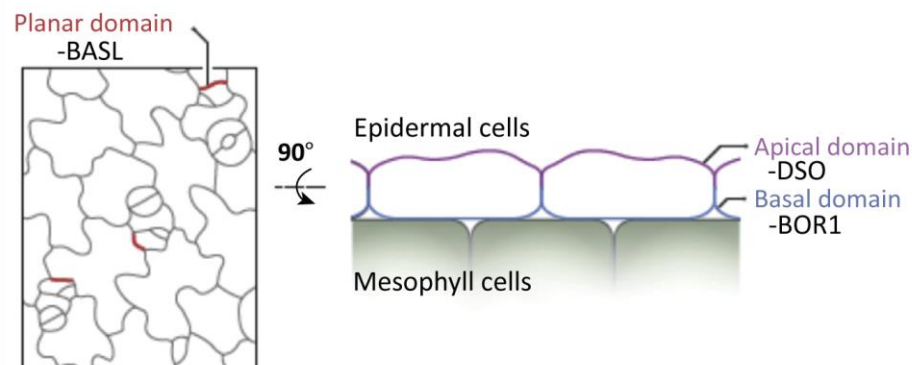
Nanodomains are small (10-200 nm) membrane domains of specific and independent compositions. This broad definition welcomes a wide variety of phenomena, some of which will be described in section II. Common features of nanodomains may include an enrichment in sterols and lipids with high T_m , such as sphingolipids and saturated PL, a higher acyl chain order parameter and, therefore, a slightly greater membrane thickness. This definition emphasises the spatial segregation of membrane components and avoids confusion with DIMs, whose physiological relevance can be questioned (see section V.A).

Microdomains are micrometric ($\geq 1\mu\text{m}$) membrane domains related to cell polarisation, fabricated through polarised secretion or endocytosis. A large patchwork of nanodomains may also be considered a microdomain. This distinction in size between nano- and micro-domains is capital to emphasise that the former is a sub-membrane specialisation while the latter concerns a whole portion of it (Figure 21). This implies that microdomains can be resolved by classic confocal microscopy while nanodomains cannot.

(A) Pollen tube



(B) Leaf epidermis



(C) Root

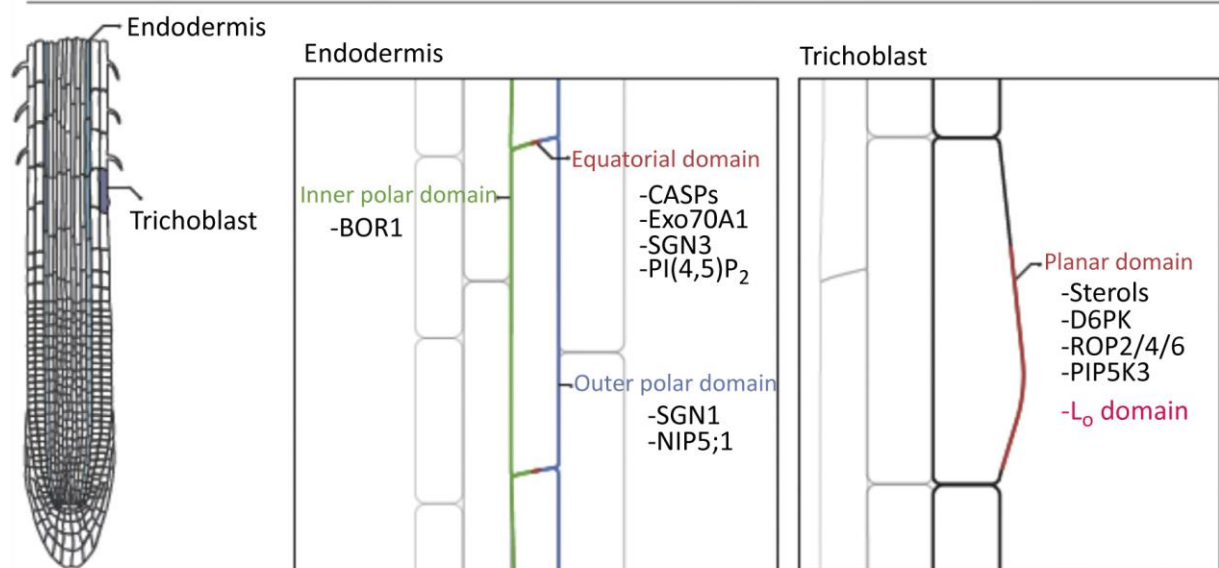


Figure 21

Examples of membrane microdomains in plants cells. (A) The four microdomain types in a pollen tube along with some respective components and characteristics: shank, subapical, flank and apical. (B) Schematic of a leaf epidermal cells highlighting three proteins with polar repartitions: Breaking of Asymmetry in the Stomatal Lineage (BASL, red) in planar microdomains, desperado (DSO, purple) in apical microdomains and the boron transporter 1 (BOR1, blue) in basal microdomains. (C) Schematic of endodermal root cells. There are planar, equatorial, inner and outer polar microdomains. Some typical components within and general characteristics are given. From (Gronnier et al., 2018).

II. Models of membrane nanodomains across Nature's clades

We wish to understand the structure, the formation and the dynamics of membrane nanodomains. This requires the study of a wide variety of membrane nanodomain systems before achieving a more general model. This section will provide details on a few well studied membrane nanodomain systems.

A. In animals

1. Ras

Ras proteins form a family of three proto-oncogene GTPases: H-Ras, K-Ras and N-Ras. They are ubiquitously expressed. Mutations of K-Ras and N-Ras are often found in human cancers (Prior et al., 2012). Ras are involved in two signalling pathways related to cell proliferation and survival: the mitogen-activated protein kinases (MAPK) pathway and the P13K/Akt pathway (Braicu et al., 2019). Their G-domains, responsible for the binding of guanine nucleotides and effectors, are highly similar while their C-termini vary greatly. Ras anchors include a carboxymethyl S-farnesylated cysteine for all isoforms, palmitoylations for H- and N-Ras, and a cluster of lysines for K-Ras (Zhou and Hancock, 2015).

It is through this extremity that Ras attaches to the inner leaflet of the PM (Hancock, 2003). A detailed structural and functional analysis of membrane anchor mutants of K-Ras4B highlighted the mechanisms behind its interactions with membranes what it entails in terms of cell signalling (Zhou et al., 2017). Nanoclustering of K-Ras4B with asymmetric PS species (one saturated acyl chain and one unsaturated acyl chain) relies on a delicate balance of H-bonds, hydrophobic and electrostatic interactions that can easily be shattered by a single mutation. Indeed, a membrane anchor mutant was shown to interact and cluster with PI4,5P₂ rather than PS, resulting in altered cell signalling. K-Ras4B is an example of an animal oncoprotein where just one mutation can impact nanoclustering and subsequent interactions with its protein partners (Figure 22).

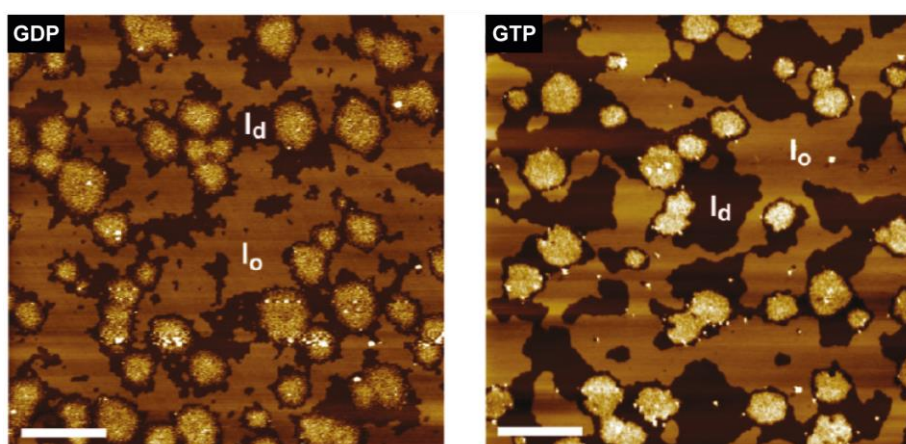


Figure 22

Atomic force microscopy (AFM) on K-Ras4B nanodomains. Bilayers of 20/5/45/5/25 DOPC/DOPG/DPPC/DPPG/cholesterol and K-Ras4B in a GDP-bound (left) or a GTP-bound state (right). K-Ras4B clusters in nanodomains ranging from 500 nm to 1µm only in the liquid-disordered (ld) phase, never in the liquid-ordered (Lo)

phase. Nanodomains appear thicker when K-Ras4B is loaded with GTP. Scale bar: 2 μm . Adapted from (Weise et al., 2011).

2. GM1

GM1 gangliosides (Figure 23) are sphingolipids critically involved in many metabolic and signalling pathways in animal cells, such as ion transport, neuronal differentiation, GPCRs, immune system reactions, neuroprotection, toxin and viral susceptibility (Ledeen and Wu, 2015). It is these latter aspects (toxin and viral susceptibility) that we will discuss now. Indeed, atomic force microscopy (AFM) reveals the formation of GM1 nanodomains in simple monolayer systems. Moreover, incubation with cholera toxin induces the formation of larger nanodomains, hinting at a direct interaction between GM1 and the cholera toxin (Yuan and Johnston, 2001). Similarly, the simian virus 40 (SV40) can target giant unilamellar vesicles (GUV) enriched in GM1 and produce invaginations, demonstrating the mean of entry of SV40 in animal cells exhibiting GM1 at their surface (Ewers et al., 2010).

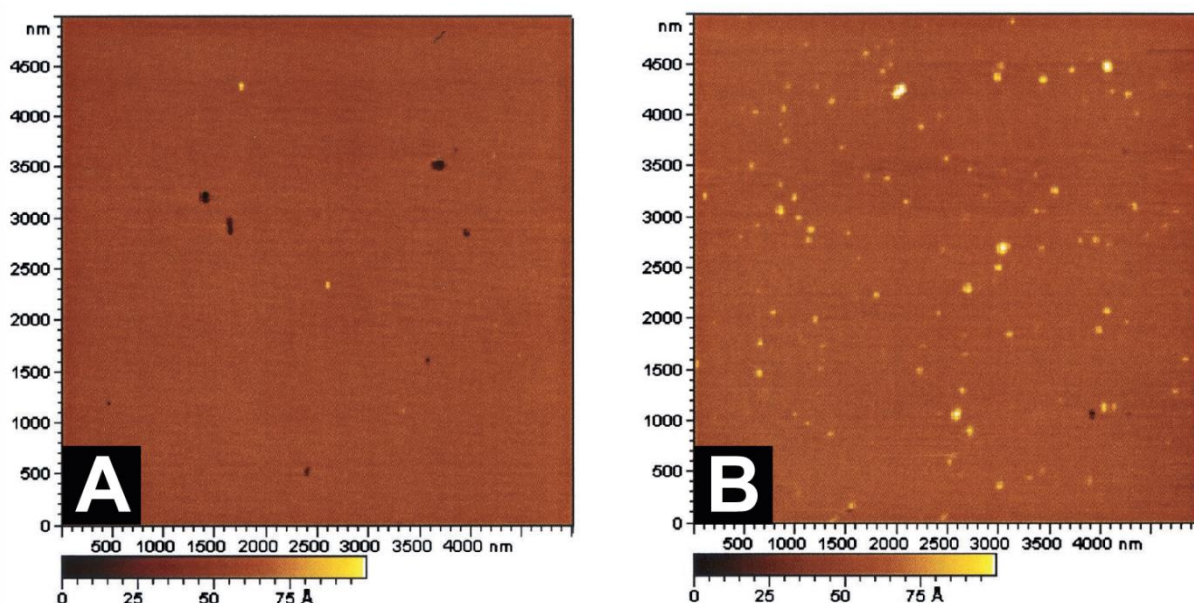


Figure 23

AFM on GM1 nanodomains. of 2/1 DPPC/cholesterol bilayers alone (A) or with 10% GM1 (w/v) (B). Adapted from (Yuan and Johnston, 2001).

3. Caveolae

Caveolae are invaginations of the PM. They were first observed in 1955, making it the first nanodomain system to be ever discovered (Yamada, 1955). Caveolae are formed by proteins called caveolins that bind to the PM's inner leaflet (figure 24). They are mainly involved in endocytosis, cell signalling (Lisanti et al., 1995; Williams and Lisanti, 2005) and cellular entry of pathogens such as SV40 (section II.A.2) and toxins like *Vibrio cholerae*'s toxin (CTX). Indeed, internalisation of SV40 utilises both GM1 gangliosides and caveolae nanodomain systems (Norkin and Kuksin, 2005; Pang et al., 2004; Parton, 1994). Drug-induced removal of cholesterol from the PM makes these initially relatively immobile structures quite mobile (Thomsen et al., 2002). Thus,

cholesterol seems not involved in their formation but may impact their biological activity. Lastly, caveolae are rigid structures: neighbouring caveolae tagged with different fluorophores do not mix, unless cholesterol is depleted (Tagawa et al., 2005).

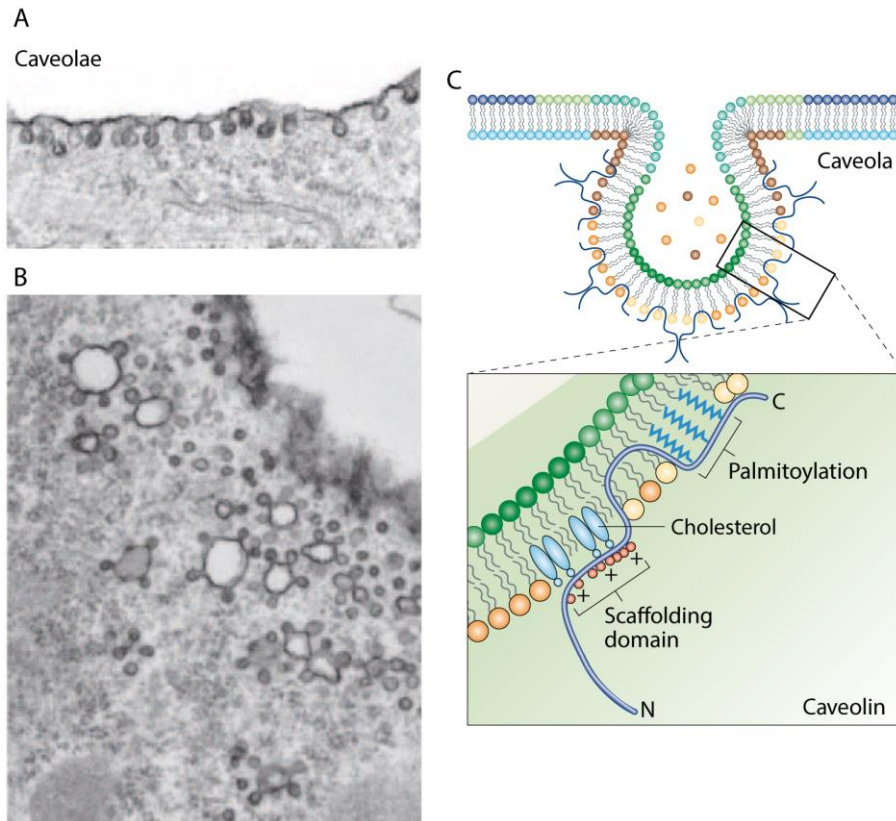


Figure 24

A general description of caveolae. (A-B) Electron micrographs of adipocytes showing invaginations at the PM: caveolae. Notice how some caveola appear to be interconnected to each other. (C) Schematic of a caveola. Insertion of caveolins (blue) in the PM provoke the formation of a caveola. Their N-termini scaffolding domains are putatively involved in interactions with cholesterol while their central part is embedded in the PM. In addition, their C-termini domains bear palmitoylation sites. Modified from (Parton and Simons, 2007).

B. In yeasts: on different nanodomain distributions of many systems

(Spira et al., 2012) described an ensemble of nanodomain systems in yeast with distinct localisations. A distinction was made between patch-like systems of punctate domains (i.e. nanodomains) and network-like systems displaying varying levels of connectivity, excluded from nanodomains (Figure 25). Some nanodomains appeared larger than for animals (up to 1 μm). This was attributed to a slower diffusion of membrane components compared to animal cells favouring their aggregation (Valdez-Taubas and Pelham, 2003). Knockoffs of ergosterol or sphingosine biosynthesis switched patch-like systems to network-like systems, indicating a loss of patch-like membrane repartition capability upon suppression of typical membrane nanodomain components (see section I.E.2.d), a proof that these patches could be nanodomains.

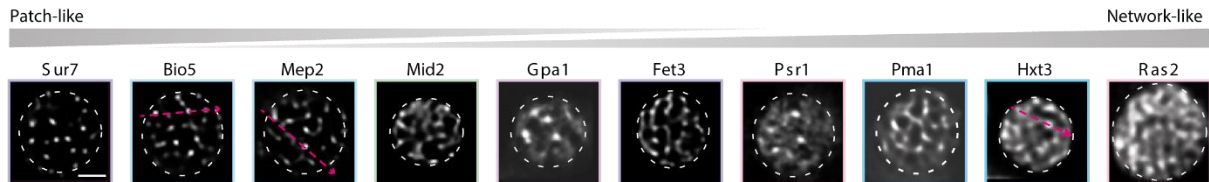


Figure 25

Screening the subcellular localisation of yeast proteins. Some cluster in patch-like domains while others adopt a network-like repartition, as if they were excluded from some membrane nanodomains. From (Spira et al., 2012).

C. In prokaryotes: flotillins

Flotillins and flotillin-like proteins are ubiquitous, appearing by convergent evolution in all clades of Nature (Rivera-Milla et al., 2006). YuaG is involved in the sporulation of *Bacillus subtilis*, localises at the PM's inner leaflet into nanodomains of size below 500 nm and is purified in DIMs enriched in PG and cardiolipin (Donovan and Bramkamp, 2009). Fluorescence microscopy with the lipid order-sensitive probe Laurdan demonstrated YuaG's ability to regulate membrane fluidity. Indeed, a knockoff of YuaG resulted in the coalescence of initially punctate ordered membrane domains into a cell-wide increase of lipid ordering. A similar phenotype was observed for a knockoff of squalene synthase, responsible for the synthesis of hopanoids, the bacterial equivalents of sterols (Bach and Bramkamp, 2013). This dependence on molecules with similar functions as sterols reinforces the idea of the existence of membrane nanodomains in bacteria. Finally, many of YuaG's interacting partners were found to co-cluster leading to propose a role for YuaG as maker of membrane hubs in various cell processes (Bramkamp and Lopez, 2015) (Figure 26).

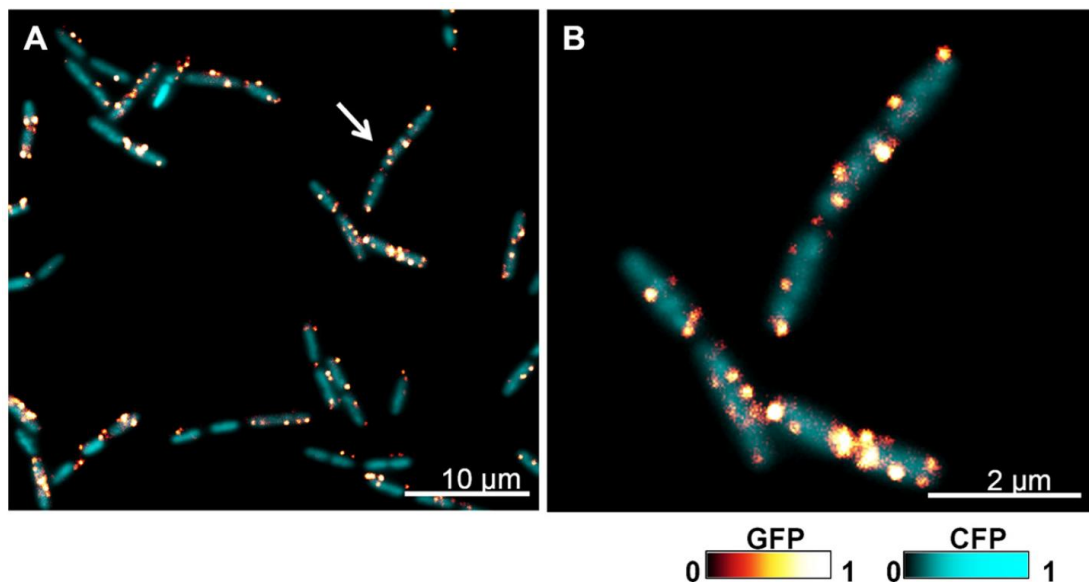


Figure 26

Epifluorescence microscopy of *Bacillus subtilis* expressing CFP and FloT-GFP. Images use false-colours. From (Bramkamp and Lopez, 2015).

D. In plants: Rho of plants (ROP)

Ras proteins in animals and Rho proteins in yeast have a plant vegetal equivalent with Rho of plants (ROP), which exist and cluster into nanodomains. The molecular basis of its membrane-interacting properties are similar to animal Ras proteins (see section II.A.1) (Nagawa et al., 2010; Platre et al., 2019; Zhou et al., 2017) and will not be re-discussed here. Rather, the involvement of membrane nanodomains in signal transduction will be detailed. Auxin, a plant hormone involved in growth and development (Leyser, 2018), can remodel cellular distribution of PS, activate ROP6 and promote its PS-dependent nanoclustering (Platre et al., 2019). Conversely, variations in PS levels at the PM define ROP6-mediated auxin response. As a result, co-clustering of ROP6 and PS is an obligatory step in auxin signalling, as part of an analogue-digital-analogue signal converter (Figure 27) (Jaillais and Ott, 2020; Tian et al., 2007): (1) a certain amount of auxin interacts with its cognate receptors; (2) resulting in a given level of ROP6 nanoclustering; (3) defining a particular signal output level. This model, which was first hypothesised for Ras proteins (Tian et al., 2007), was further expanded to ROP in a recent preprint (Smokvarska et al., 2020).

ROP11 is pinned by microtubules forming a fence preventing the free diffusion of the protein. These ROP11 microdomains were shown to define cell shapes (Oda and Fukuda, 2012).

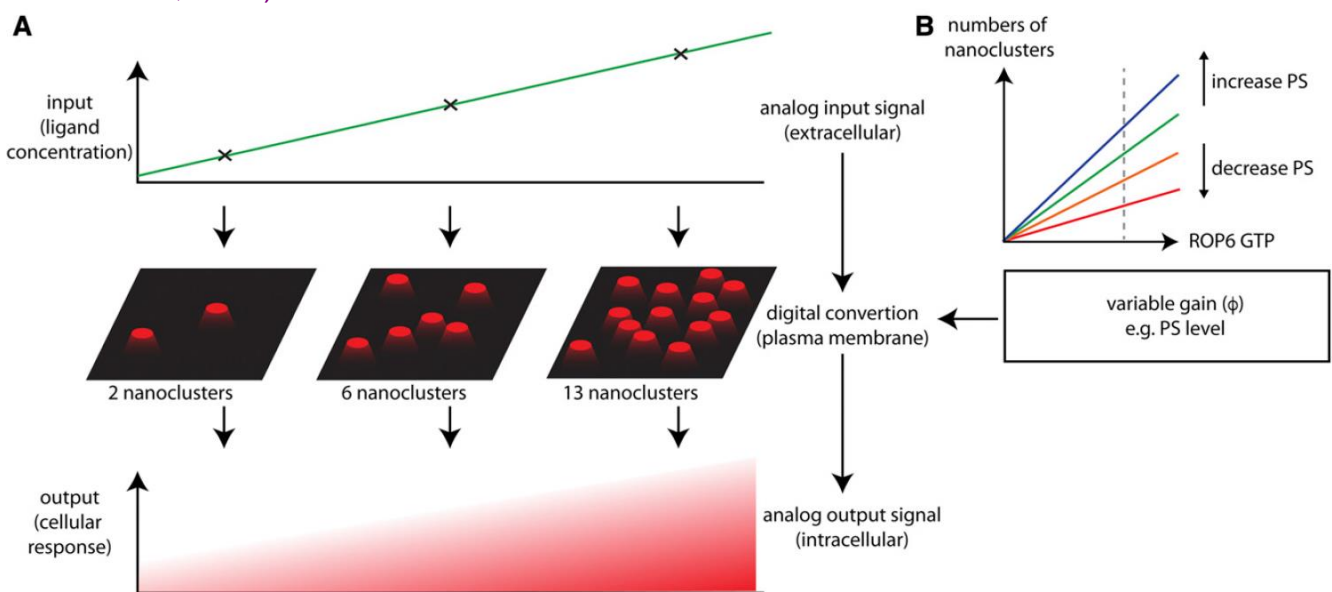


Figure 27

A model for the role of Ras and ROP nanodomains in cell signalling. (A) Let us assume that hormone receptors of the PM bind increasing concentrations of their ligand and subsequently recruit and activate ROP, which clusters in PM nanodomains, such as the more ligand is bound, the more ROP is clustered in nanodomains and the more of these nanodomains there are (analogue-to-digital conversion). Nanoclustering allows signal concentration, making the signalling pathway more efficient, such as the more ROP nanoclusters, the higher the signalling output (digital-to-analogue conversion). (B) ROP binds the PM via PS, the quantity of which, at the PM, positively regulates ROP signalling. From (Jaillais and Ott, 2020).

Another plant membrane nanodomain system will be the subject of this manuscript: the remorins.

III. Remorins

The multigenic, plant-specific, family of remorin proteins (Raffaele et al., 2007a) is a well-known marker of such nanodomains in plants (Demir et al., 2013; Gronnier et al., 2017; Mongrand et al., 2004; Raffaele et al., 2009a). Remorins were first discovered as soluble DNA-, oligogalacturonide- and pectin-binding phosphorylated receptors (Alliotte et al., 1989; Farmer et al., 1989; Jacinto et al., 1993) in tomato and potato plants. In the latter, this protein, having an apparent molecular weight of 34 kDa by SDS-PAGE, was named pp34 (Jacinto et al., 1993). It is only after it was cloned and turned out to be totally hydrophilic (albeit membrane bound) that it was renamed remorin, as a reference to the remora fish hanging up to boats or other fishes from *El Libro De Los Seres Imaginarios* (Borges and Guerrero, 1969), just like remorin is bound to the plasma membrane (Reymond et al., 1996).

To avoid spoiling this manuscript, contributions of articles in which I was involved were removed and replaced with their related interrogations and hypotheses as they were at the beginning of this PhD thesis.

A. Phylogeny

Remorins are split into six phylogenetic groups (Raffaele et al., 2007a). All bear a predicted C-terminal coiled-coil domain ended by a remorin C-terminal anchor (Perraki et al., 2012; Raffaele et al., 2013) and an N-terminal intrinsically disordered domain (IDD), where lie most differences between isoforms (Figure 28). It should be noted that group 3 remorins lack an IDD. In comparison, C-terminal domains have a well conserved size of about 110 residues. A brief overview of each group will be given.

Group 1 contains remorins from ancestral plants such as gymnosperms (i.e. naked seed plants such as conifers), ferns and early angiosperms (i.e. floral plants), from monocotyledons to eudicotyledons. These remorins possess proline-enriched IDDs (8.9% for group 1a and 14.4% for group 1b) of about 81 ± 11 residues with a high homology (Raffaele et al., 2007a). *In silico* analysis of group 1 IDDs reveals a propensity for phosphorylation, hinting at a putative regulatory mechanism and a functional diversity of these domains, as phosphorylation is a common mean to control and tune an IDD's function (Khan et al., 2017; Uversky, 2013). Group 1a remorins' gene expression is correlated with genes involved in cell wall biology and extracellular functions, while group 1b remorins' gene expression seems more related to genes involved with the Golgi apparatus or the PM (Raffaele et al., 2007a).

Group 2 contains isoforms coming mostly from legumes and poplars. Their IDDs are about 86 ± 7 residues long and bear no significant homology with group 1's IDDs. They are mainly expressed in eurosids, even though we should note that a REM2.1 has recently been evidenced in *Arabidopsis thaliana* (Gouguet et al., 2020).

Group 3 gathers remorins without IDD. As such, it could be labelled as the shortest remorin group. This absence of N-terminal domain could indicate a more restricted set of functions performed by remorins from this group, with all the biological activity originating from the coiled-coil C-terminal domain and its membrane anchor. They are expressed in rosids.

Group 4 remorins have IDD about 160 ± 31 residues long, which are notoriously longer and different from group 1 IDD, and these domains are enriched in both prolines and serines, highlighting a different set of biological functions. They are expressed in both monocotyledons and eudicotyledons.

Group 5 remorins have more divergent C-terminal domains in addition to a 91 ± 45 residues long IDD that is poor in prolines. This absence of conformation-restrictive aminoacids could be a hint at a higher order parameter of these N-terminal domains and a greater ability to form, upon interaction with a ligand, a complex structure.

Group 6 remorins are the longest with highly variable, 279 ± 89 residues long IDDs, for total lengths between 240 and 522 residues. Such discrepancies may indicate the existence of many yet uncharacterised subgroups.

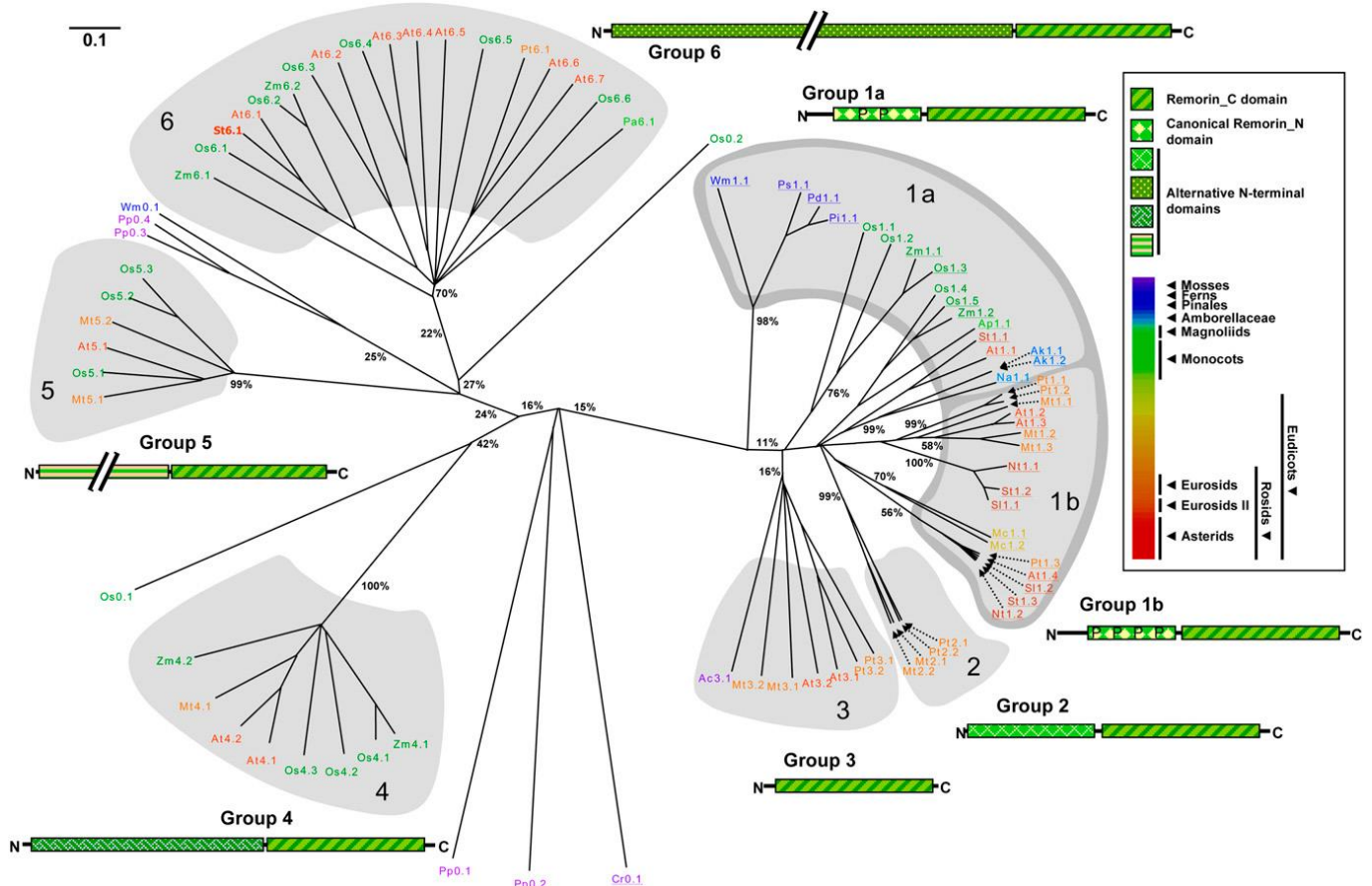


Figure 28

Phylogenetics of the remorin family. All remorins share a common C-terminal coiled-coil signature. Their classification relies on their distinct N-terminal domains. Organisms are colour-coded as described in the inlet. Abbreviations: *Ac*, *Adiantum capillus-veneris*; *Ak*, *Amborella trichopoda*; *Ap*, *Allium cepa*; *At*, *Arabidopsis thaliana* (thale cress); *Cr*, *Ceratopteris richardii*; *Mc*, *Mesembryanthemum crystallinum*; *Mt*,

Medicago truncatula (barrelclover); *Na*, *Nuphar advena*; *Nt*, *Nicotiana tabacum* (common tobacco); *Os*, *Oryza sativa* (rice); *Pa*, *Persea americana*; *Pd*, *Pinus taeda*; *Pi*, *Pinus pinaster*; *Pp*, *Physcomitrella patens*; *Ps*, *Picea sitchensis*; *Pt*, *Populus trichocarpa*; *Sl*, *Solanum lycopersicum* (tomato); *St*, *Solanum tuberosum* (potato); *Wm*, *Welwitschia mirabilis*; *Zm*, *Zea mays* (corn). From (Raffaele et al., 2007b).

B. Biological implications

The functions of remorins remain partly enigmatic although it is attributed some recurring roles such as in the regulation of cell-to-cell communication, plant immunity, symbiosis and stress resistance. Sections III.B.1 to III.B.4 are heavily inspired from the comprehensive bibliographic review of (Gouguet et al., 2020), currently in positive revision in Plant Physiology and of which I am co-author (see Annex). Thematics associated with remorins are summarised in (Figure 29), some of which will be discussed below. A complete list of known biological involvements is given at the end of Annex.

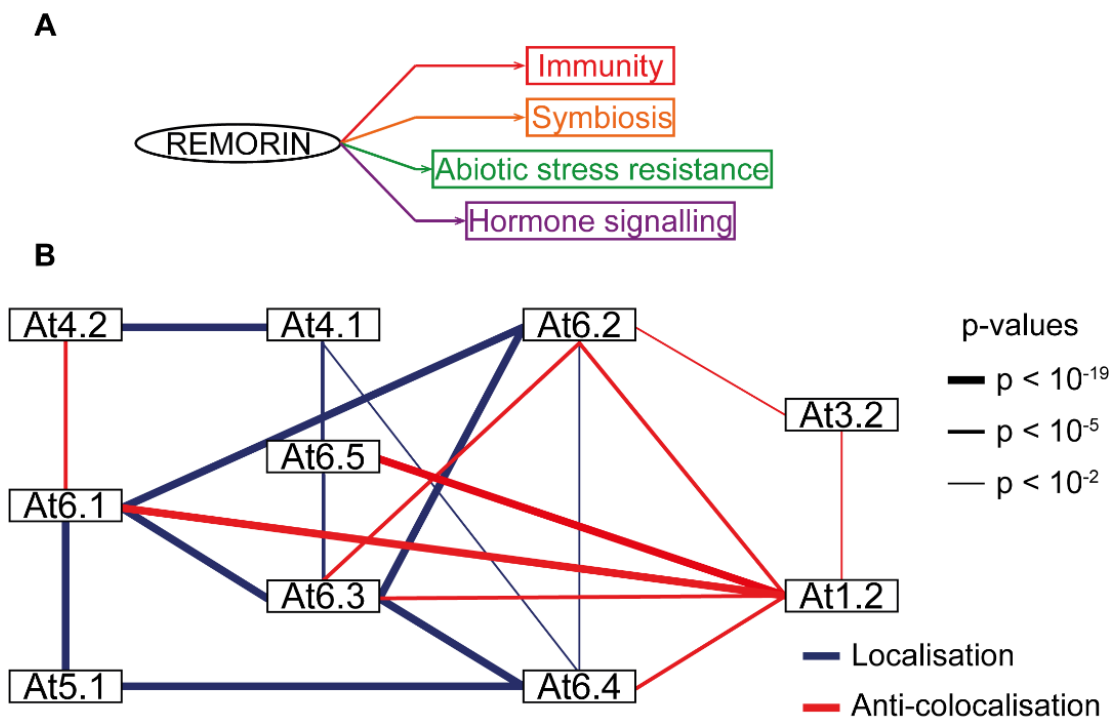


Figure 29

Summary of remorins biology. (A) Main biological roles of remorins (Gouguet et al., 2020). (B) Localisation (blue) or anti-colocalisation (red) of some remorins in nanodomains observed by spt-PALM (Jarsch et al., 2014).

1. Immunity

a. Against viruses

Plasmodesmata are membranous channels, about 20-40 nm large, connecting neighbouring cells, across PMs and cell wall. They are partially filled with ER from one side to another (Nicolas et al., 2017). Thus, they link the cytosols of virtually every plant cell, allowing the exchange of molecules. Consequently, PD are capital elements of plant development (Otero et al., 2016; Wu et al., 2016), metabolism (Ross-Elliott et al., 2017) and immunity (Benitez-Alfonso et al., 2010). On this last point, we should emphasise that, if metabolites and signalling molecules can travel from one cell-to-another, so can plant viruses by hijacking the PD to increase its size exclusion limit. It is on such a basis that we can grasp the role of remorins in viral immunity.

Overexpression of StREM1.3, slowed down the cell-to-cell propagation of the plant virus model Potato Virus X (PVX), as could be assessed by a decrease in PVX infection foci area. Conversely, underexpression of StREM1.3 increased the size of infection foci (Perraki et al., 2014; Raffaele et al., 2009a). The closure of PD is correlated with the deposition at their neck region of a 1,3- β -glucan named callose that seems to clog the pore. Conversely, the degradation of callose open the PD pore. The passage of the PVX through PD is made possible by its viral movement protein TGBp1 (Howard et al., 2004). Coincidentally, StREM1.3 interacts with TGBp1 and can be found at PD (Gronnier et al., 2017; Raffaele et al., 2009a). There are two non-exclusive hypothetical mechanism to explain these phenomenon: (1) StREM1.3 interacts with TGBp1 (Raffaele et al., 2009a) and prevents the passage of PVX components through PD; (2) StREM1.3 promotes callose deposition at PD, thus confining the PVX to the cells it already infected. This last mechanism is supported by the fact that co-expression of lone viral movement proteins TGBp1 from the PVX, or 30K from the *Tobacco Mosaic Virus* (TomV) or Hc-Pro from the *Potato Virus Y*, along with StREM1.3, restricted the cell-to-cell diffusion of free GFP, indicating PD closure (Perraki et al., 2014).

b. Against bacterial and fungal infections

Arabidopsis thaliana treated with flagellin 22, a short segment of a bacterial flagellin a known immune response elicitor, display a more phosphorylated AtREM1.3, on residues S14 and T58, but not AtREM1.2, which does not have these phosphorylation sites (Benschop et al., 2007). Yet, both AtREMs co-localise to the same nanodomains (Jarsch et al., 2014). Similarly, upon overexpression of the bacterial effector gene AvrRPM1 from *Pseudomonas syringae*, AtREM1.2's expression increases (Widjaja et al., 2010). In the fight between plants and pathogens, extracellular vesicles (EVs) are excreted from both sides, containing proteins, metabolites and interfering RNAs. Among these, we find again AtREM1.2, AtREM1.3 and RIN4, a known interactor of AtREM1.2 related to Pathogen-Associated Molecular Pattern (PAMP)-triggered immunity (PTI) against *Pseudomonas syringae* (Meyer et al., 2009; Micali et al., 2011). AtREM1.3 is also known to bind ergosterol, which happens to be toxic for plants (Khoza et al., 2019).

StREM1.4 is up-regulated against *Ralstonia solanaceum*, a pathogen of potato (Kong et al., 2016), while StREM1.3 is enriched in PMs near haustoria of *Phytophthora*

infestans, i.e. fungal protrusions into plant cells (Bozkurt et al., 2014; Lu et al., 2012). In maize, *ZmREM6.3* is genetically correlated to the resistance against *Steosphaeria turcica*, responsible for the northern leaf blight plant disease, and *ZmREM1.3* infers resistance against *Puccinia polyspora* (Bilska-Kos et al., 2016; Jamann et al., 2014).

2. Symbiosis

If remorins are involved in protecting the plant from harmful pathogens, it is equally involved in symbiotic relationship with bacteria. Indeed, *MtREM2.2* is expressed in roots, especially in nodules as a necessary response to nodulation factors sent by symbionts during nodulation initiation. It acts as a scaffold for receptor-like kinases NFP, DMI2 and LYK3, as well as flotillin 4, all involved in nodulation (Lefebvre et al., 2010; Liang et al., 2018). Overexpression of *LjSYMREM1*, a group 2 remorin, increases the number of nodules per root (Tóth et al., 2012). Finally, *QrREM4.1* is up-regulated in case of symbiosis with *Piloderma croceum* (Tarkka et al., 2013).

3. Stress resistance

We described remorins as organisers of symbiosis and biotic stress (i.e. defence against pathogens). They are also involved in abiotic stress. A first hint would be the ability of group 1 remorins to bind poly-galacturonic acid, a product of cell wall degradation (Reymond et al., 1996). A large bibliography records remorins from groups 1, 4 and 6 as inferring resistance to drought and salt-stress. Treatment with various plant hormones whose levels increase during biotic and abiotic stress, including abscisic acid, auxin, brassinosteroids, cytokinins, jasmonates and salicylic acid, also up-regulates these remorins, confirming a general link between remorins and stress resistance (Gouguet et al., 2020).

4. Cell-to-cell communication

In rice, *OsREM6.6* Grain Setting Defect 1 (GSD-1) mutant provokes an accumulation of starch and free sugars in leaf blades and a lack of starch in grains. This implies a correlation between this remorin and metabolite transfer across tissues. This can be corroborated to the presence of a subset of *StREM1.3* at PD (Gronnier et al., 2017; Raffaele et al., 2009a).

C. Biophysics of membrane anchoring and nanodomain formation, with a special attention to *StREM1.3*

The remorin family is vast, yet one isoform received much attention not only for its biological implications but also as a model to study its membrane anchoring and nanodomain formation mechanism: *StREM1.3*. Many structural data are already available, making this isoform a candidate of choice to further our understanding of remorins' biophysics. However, other remorins will be discussed in order to keep in mind the larger picture of learning about the biophysics of remorins.

1. Remorin C-terminal anchor (RemCA)

Removing the last 28 aminoacids of StREM1.3 turns it from an integral, tightly membrane-bound protein into a fully soluble protein (Perraki et al., 2012). This C-terminal feature, RemCA, is common to all remorins and has convergent analogues outside of plants sharing the same overall fold and aminoacid bias: a long helix lying at the membrane interface and a shorter C-terminal helix buried in the membrane, both linked by a small loop (Figure 29) (Raffaele et al., 2013). A comparison of RemCA domains between remorins of *Arabidopsis thaliana* and MtREM2.2 displays the extent of their diversity, some bearing many S-acylated cysteines while others none, most showing a strong pattern of hydrophobic residues at their C-terminal and basic residues towards their N-terminal, with the notable exceptions of At4g36970, At1g53860, At4g67590 and StREM1.3 (Konrad et al., 2014). However, all of them are detected in PM nanodomains, but not necessarily the same nanodomains: some do colocalise while others exclude one another (Jarsch et al., 2014). This could imply that: (1) remorins may bind different and specific target at the PM or (2) actively exclude one another on a yet unknown basis (section III.C.4).

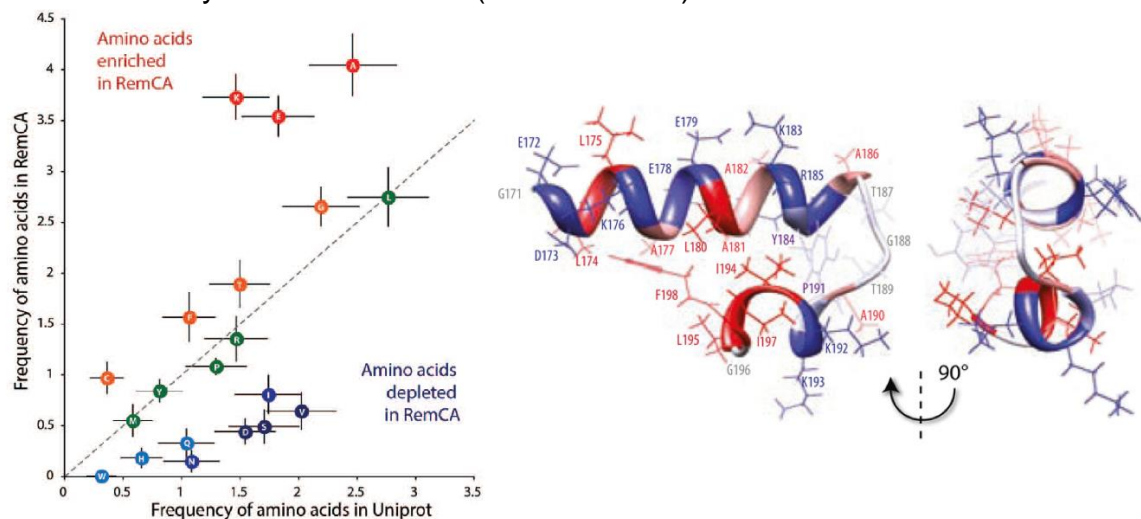


Figure 29

First structural studies on RemCA. Left: aminoacid composition bias of 117 RemCA from 26 species, compared to randomly selected 28 aminoacids long peptides from Uniprot. From (Raffaele et al., 2013). Right: first structural model of StREM1.3-RemCA from (Perraki et al., 2012).

A detailed biophysical analysis of StREM1.3's RemCA (StREM1.3-RemCA) and 16 mutants provided the structural basis for its PM nanodomain targeting (Gronnier et al., 2017). Lowering the PI4P content in the PM's inner leaflet of *Nicotiana benthamiana* by expressing the myristoylated/palmitoylated-phosphatidylinositol 4-phosphatase SAC1p enzyme, StREM1.3's PM targeting was largely abolished. Using a combination of solid-state nuclear magnetic resonance (ssNMR), Langmuir trough and infrared spectroscopy, StREM1.3-RemCA's fold was re-evaluated: the short C-terminal helix was replaced by an extended β -sheet (Figure 30). In this model, K192 and K193 (of the extended β -sheet) are positively charged and interact with PI4P through an electrostatic interaction with the inorganic phosphate in position 4 of the inositol.

Attempts at deciphering the aminoacid code responsible for StREM1.3-RemCA's membrane interacting properties, by mutant analysis followed confocal microscopy or super-resolution microscopy, revealed the anchor's net charge as an interesting parameter to follow: a shift from a non-charged WT anchor to negatively charge mutated anchor is correlated with a decrease in PM targeting. Surprisingly, a fine monitoring of some WT and mutated StREM1.3-RemCA, by single-particle tracking photoactivated localisation microscopy (spt-PALM), revealed that all variants were still able to make nanodomains, although with significantly different sizes, diffusion rates, relative areas and nanodomain localisation (Figure 31).

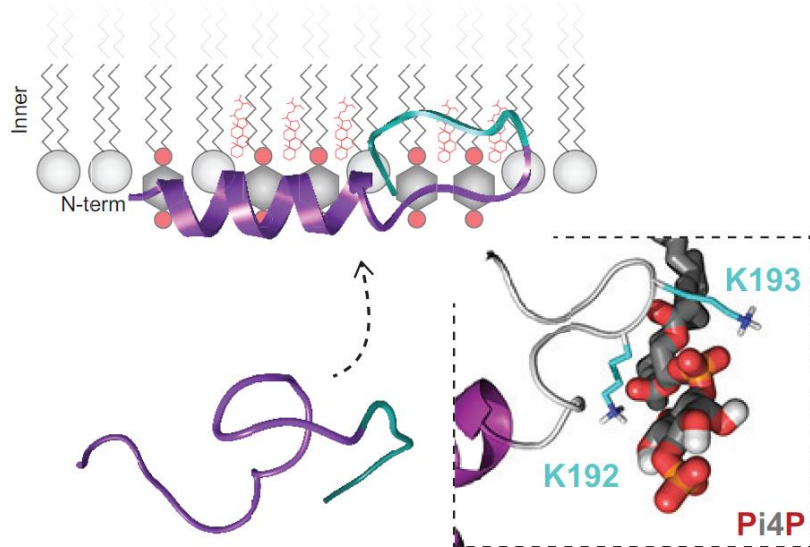


Figure 30

Structural model of StREM1.3's RemCA by molecular dynamics. Comparing to figure remca_2012_2013, the second helix of the latter is now an extended β -sheet in the former. In this model, PI4P specificity is explained by an electrostatic interaction between K192, K193 and the last inorganic phosphate of the polar head. From (Gronnier et al., 2017).

Critical mutations of StREM1.3-RemCA shown to abolish PM targeting decreased, if not cancelled, StREM1.3's ability to slow down cell-to-cell viral propagation (Perraki et al., 2014), proving the need of an optimal repartition of StREM1.3 at the PM localisation to ensure its anti-viral activity.

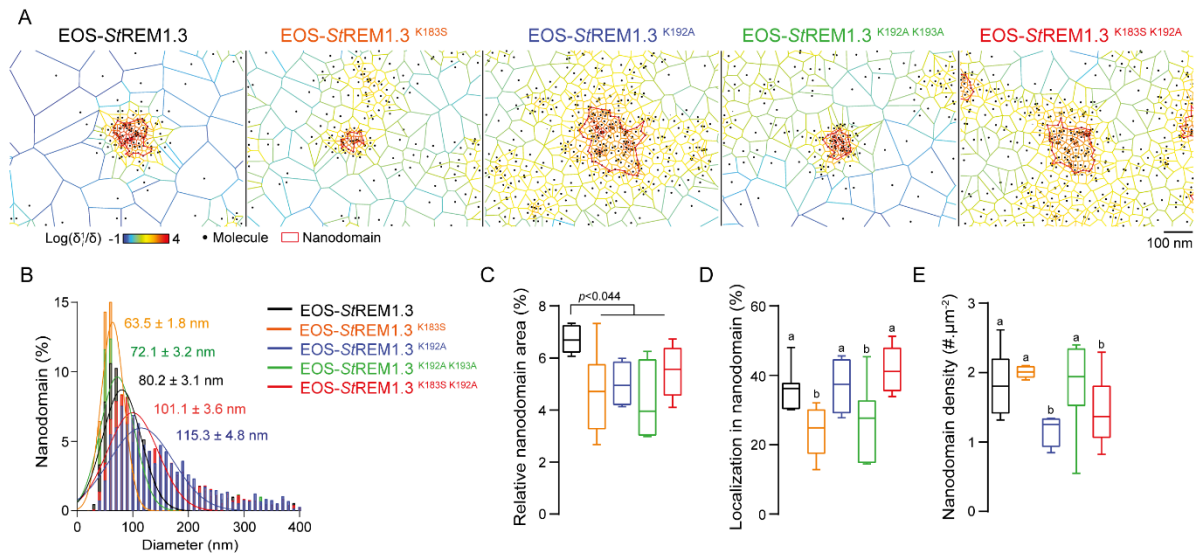


Figure 31

Spt-PALM analysis of EOS-tagged WT and mutated StREM1.3 in *Nicotiana benthamiana* leaves (EOS is a fluorophore suited for spt-PALM). (A) Representative PALM image analysis for each protein with tessellation-based automatic image segmentation (images are automatically fragmented so that only one remorin occupies a given tile). Nanodomains are circled in red. (B) Diameter distributions of nanodomains for each protein. (C) Percentage of the PM occupied by nanodomains. (D) Percentage of EOS-tagged StREM1.3 in nanodomains. (E) Number of nanodomains per μm². From (Gronnier et al., 2017).

2. Oligomerisation domain

Early on, some group 1 remorins, including StREM1.3, were shown to spontaneously assemble into filaments *in vitro* (Figure 32) (Bariola et al., 2004). Cross-linking experiments and analytical centrifugation (although the latter was labelled as “data not shown”) indicated a continuum of oligomeric states from degree 2, 4 and above. In opposition, size exclusion chromatography on StREM1.3 would indicate a homo-trimeric state (Perraki et al., 2012), but this experiment suffered from a poor choice of column and corresponding separation range. The ability of remorins to spontaneously make filaments certainly hinders the measurement of intermediate oligomeric states.

Beyond *in silico* analyses (Raffaele et al., 2007a; Raymond et al., 1996), the putative coiled-coil fold of the oligomerisation domain has yet to be proven.

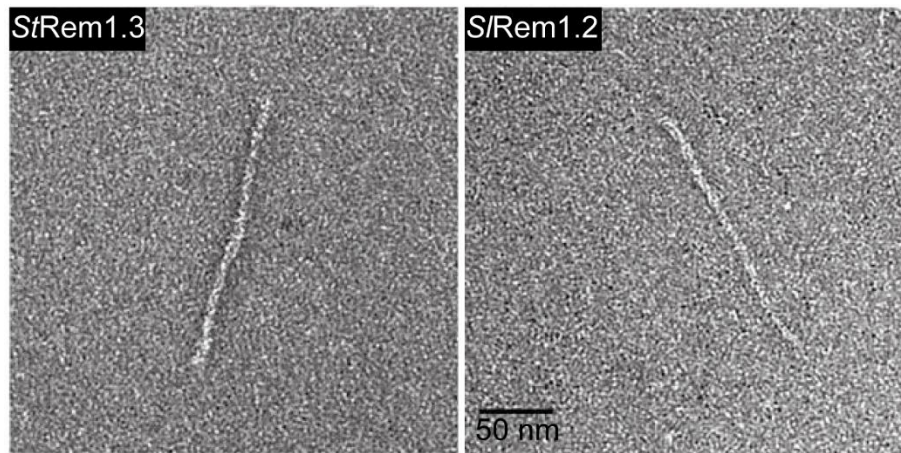


Figure 32

Negative-staining electron microscopy of StREM1.3 (from potato) and *SIREM1.2* (from tomato) filaments, *in vitro*. Adapted from (Bariola et al., 2004).

3. IDD

Bioinformatic tools predict remorins' N-termini as IDD (Raffaele et al., 2007a). Although no experimental structural investigation can confirm this yet, if it is taken for granted, the study of this domain in interactions with partners of remorins would allow to grasp the structural implications of such associations.

Phosphorylation is a recurrent mean to change an IDD's properties, or to switch it from an unfolded inactive state to a folded active state, or *vice versa* (Khan et al., 2017; Nishi et al., 2013; Uversky, 2013). Remorins' IDDs are no exception (Marín and Ott, 2012), so if a non-phosphorylated IDD is indeed unfolded, what about its phosphorylated state? There again, no structural study of a remorin's IDD is available beyond sequence analysis.

4. Towards a model of StREM1.3 nanoclustering

The study of (Gronnier et al., 2017) was the first to formulate a hypothetical membrane nanoclustering mechanism of a remorin: (1) cytosolic, homo-trimeric StREM1.3 would bind to PI4P of the PM's inner leaflet and (2) cluster with one another together with sterols. The bundling of three RemCA domains within a single trimer would confer the protein a higher avidity for PI4P, and maybe other PIPs, than a lone StREM1.3-RemCA.

Although the first step, the PM binding, is easy to accept, given the evidence at our disposal (section III.C.1), the second step remains elusive. What promotes nanoclustering?

a. Remorin/lipid-lipid interactions: PIPs cluster on their own

Due to their big negatively charged polar heads conferring an inverted conical shape, PIPs have the interesting property to promote a negative membrane curvature and cluster (Bilkova et al., 2017; van den Bogaart et al., 2011; Ji et al., 2015; Picas et al., 2016). This nano-environment is reminiscent of our definition of nanodomains. The

presence of sterols could be explained by the presence of a pool of saturated PIPs in DIMs of plants (Furt et al., 2010).

In this aspect, the mere binding of StREM1.3 would be enough to ensure its nanoclustering. However, StREM1.3 binds tightly to the PM, as salt- and high pH shocks cannot alter its binding (Perraki et al., 2012). In this regard, it is an integral protein. We may expect protein insertion to modify if not shatter this pre-existing organisation.

At last, this mechanism alone cannot explain the coexistence of many different remorin-enriched nanodomains (Jarsch et al., 2014).

b. Remorin-remorin interactions: remorins tether with their peers

Remorins are likely to make oligomers through their putative coiled-coil domains (Raffaele et al., 2007a; Reymond et al., 1996), and they can make filaments *in vitro* (Bariola et al., 2004). Although these have never been unambiguously observed *in vivo*, the underlying self-assembling behaviour could persist. This would explain why remorins with high homology, such as those within a given phylogenetic group, could cluster together while divergent remorins could not. The structural basis of such discrimination is unknown. It could originate either from the oligomerisation domain or the IDD. It could also be directed by pinning, as we will see in the next section.

c. Remorin-cytoskeleton interactions: the cytoskeleton directs nanoclustering

Disruption of microfilaments or microtubules changed the localisations of AtREM1.2 and AtREM1.3 from DIMs to detergent-soluble membranes (DSMs) (Figure 33) (Szymanski et al., 2015). Coincidentally, for AtREM1.2, the characteristic dot-like pattern of fluorescently-tagged remorins observed by confocal microscopy turned into a more homogeneous PM distribution upon disruption of microfilaments but not microtubules. We should remind ourselves that confocal microscopy cannot resolve remorin nanodomains of about ≈ 80 nm in diameter (section III) (Gronnier et al., 2017; Raffaele et al., 2009a), so we can only conclude that the overall PM organisation of this remorin has been modified. In any case, these observations indicate an interaction between remorins and cytoskeletal components, namely actin and microtubules, to pin remorins (Dinic et al., 2013; Raghupathy et al., 2015; Tsuji and Ohnishi, 1986). Disruption of the cytoskeletal network would unleash these remorins from their nanodomains and grant them freer movement.

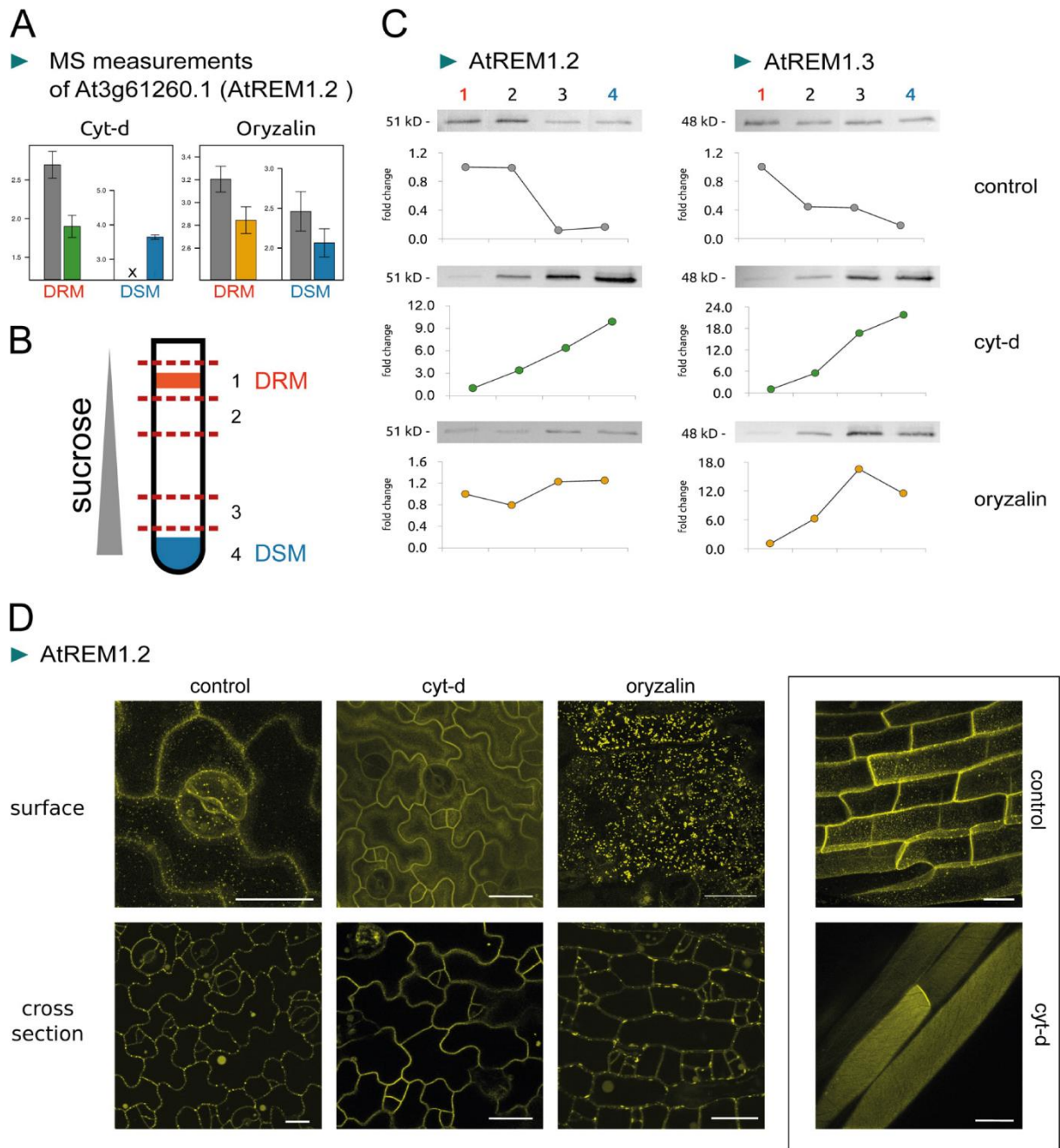


Figure 33

Relationship between the cytoskeleton and AtREM1.2 or AtREM1.3. (A) Mass spectrometry analysis of AtREM1.2 content of *Arabidopsis thaliana* seedlings. (B) Principle of DRM (or DIM) purification. (C) Analysis of DRM purification by western blot on untreated (control), disrupted for actin (cyt-d) or disrupted for microtubule (oryzalin). (D) Confocal microscopy of *Arabidopsis thaliana* seedlings expressing YFP-AtREM1.2 of untreated or treated with cyt-d or oryzalin. Scale bars: 20 μ m.

Adapted from (Szymanski et al., 2015).

IV. Objectives

As can be gauged from the previous section, a lot of unknowns hover in the realm of remorins. To work upon pre-existing knowledge, we will concern ourselves with the

biophysics of StREM1.3 in membranes. We will be interested in answering the following questions:

1. What is the nanoclustering mechanism of StREM1.3?

What is StREM1.3's impact on membrane dynamics? How does it oligomerise? Is oligomerisation relevant in understanding its membrane interactions? How does it make filaments? The seminal work of (Gronnier et al., 2017) must be pursued to test and further our model of StREM1.3's nanoclustering.

2. What is the minimal set of partners required to make StREM1.3 nanodomains?

Can we reconstruct such domains *in vitro*? If we achieved it, it would mean that: (1) we understood how StREM1.3 nanodomains are formed and (2) we would have a powerful *in vitro* tool to study the formation and the behaviour of such nanodomains.

3. How interactors of StREM1.3 may regulate its relationship with membranes and biological functions?

The interactors and the precise mechanism by which StREM1.3 can block the cell-to-cell propagation of the PVX remain to be elucidated.

4. Professional context

This doctoral work is the fruit of a joint effort by a team of biologists, biochemists and remorin specialists at the *Laboratoire de Biogenèse Membranaire*, UMR 5200, CNRS led by Dr Sébastien Mongrand and a team of biophysicists and NMR spectroscopists at the Institute of Chemistry and Biology of Membranes and Nano-objects, UMR 5248, CNRS led by Dr Birgit Habenstein. About a quarter of the work was performed in the "biology team" and the rest was done in the "NMR team", including protein production and purification. As such, and due to my student cursus, my outlook on the project is inherently focused on structural biology rather than plant biology. Nonetheless, I was trained to perform experiments belonging in either of these categories.

To achieve the aforementioned objectives, we disposed of many biophysical tools, whose description will be the subject of the next section.

V. Biophysical tools to study membrane nanodomains

The aim of this section is to list the biophysical tools of interest for the comprehension of this manuscript. Principles will be explained and relevance to our field of study indicated. It is not intended to be a full-length description of these tools.

A. Detergent insoluble membranes

Although no DIM purification will be performed in this manuscript, given the importance of this technique in membrane nanodomain research, it deserves to be discussed in more details.

Density gradient separation is a powerful biochemical tool to separate components of varying densities. Proteins have densities around 1.4 g/cm^3 (Fischer et al., 2004; Quillin and Matthews, 2000), lipid membranes have densities $\approx 1.05 \text{ g/cm}^3$, water's density is 0.997 g/cm^3 and a 60% (w/v) sucrose solution, a common maximum in such experiments, is 1.29 g/cm^3 . Here, proteoliposomes tend to behave, in terms of density, like pure liposomes. The membrane preparation is incubated at 4°C overnight in presence of 1% (v/v) Triton X-100. It is adjusted to 60% sucrose, covered with 40%, 35% then 30% sucrose and submitted to an ultracentrifugation. A short run of 2-3 h will maintain gradient discontinuity, while a longer run of 16h will turn the density gradient continuous. Solubilised proteins will be located at the bottom of the gradient while membrane proteins anchored to DIMs will float near the top of it (Figure 34) (Brown and Rose, 1992; Carter and Hakomori, 1981; Mongrand et al., 2004; Raffaele et al., 2009a; Yu et al., 1973).

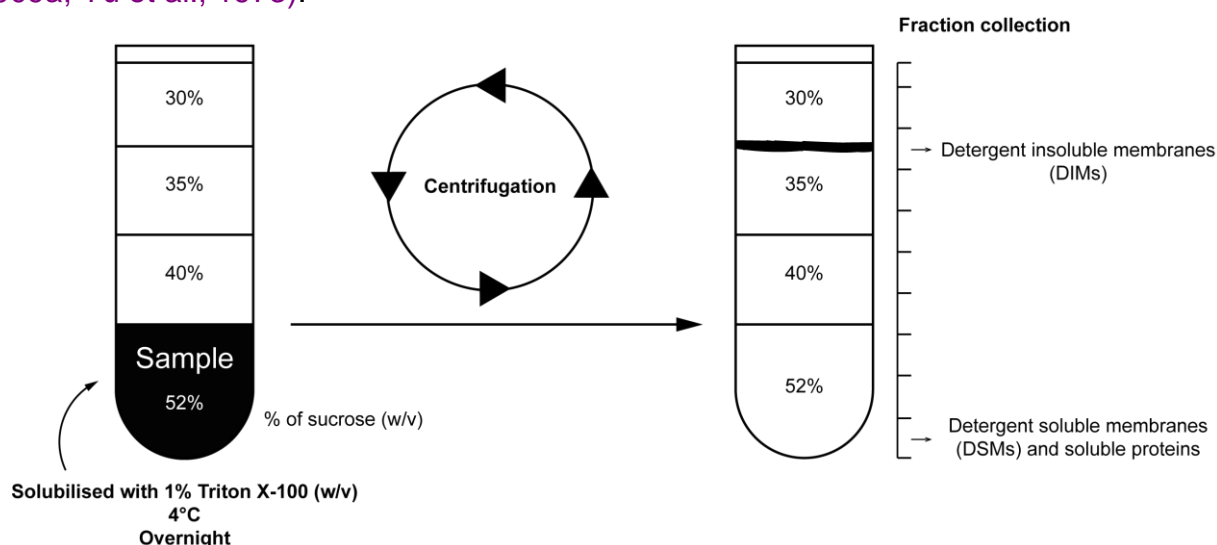


Figure 34

Schematic of a typical DIM purification. Purified membranes are incubated with 1% Triton X-100 (w/v) at 4°C overnight. The sample is then adjusted to 52% sucrose and covered with layers of sucrose of decreasing concentrations. After ultracentrifugation (200000 g for 16h), DIMs will float at one interface near the gradient's top while soluble material will be pelleted. Protocol based on (Raffaele et al., 2009b).

The formation of DIMs is correlated to the enrichment in high- T_m lipids, such as sphingolipids and saturated phospholipids, and sterols (Schroeder et al., 1994), which is, as we saw in section I.E.2.d, an expected feature of many membrane nanodomain systems. Moreover, DIM purification is the only technique amenable to lipidomic investigations (Furt et al., 2010; Schroeder et al., 1994). However, it does not inform on spatial segregation: just because two proteins are enriched in DIMs does not imply they are segregated in the same membrane nanodomains: we saw, in the case of remorins, that many remorins seem to exclude each other while being enriched in DIMs (Jarsch et al., 2014). Also, some membrane nanodomain systems are not particularly enriched in lipids suitable to behave as DIMs, such as the Ras system that relies on

PS in the fluid phase (section II.A.1). Finally, the appearance of DIMs depends on the choice of detergent (Schuck et al., 2003), casting doubt on the results this purification technique may provide. This is the main reason to explain its decline.

B. Fluorescence microscopy

Recent definitions of membrane nanodomains increasingly emphasize spatial segregation, which may only be observed by some kind of microscopy. Light microscopy allows the study of both *in vivo* and *in vitro* samples in native or native-like conditions. Since sample fixation is not mandatory, one can also observe time-dependent phenomena.

1. The fluorescence phenomenon

Suppose a fluorophore F, whose size is nanometric, (1) receives an incident light carrying an energy $E = h.c.\lambda^{-1}$ where $h = 6.626.10^{-34} \text{ m}^2.\text{kg}.\text{s}^{-1}$ is the Planck constant and $c = 299792458 \text{ m/s}$ the celerity of light (Bureau International des Poids et Mesures, 2006). λ is such that an electron may jump from a ground electronic state S_0 to an excited electronic state S_1 . Note the multiple vibrational energy states for each electronic state. Here, F is at the highest electronic and vibrational states $S_{1,3}$ of our diagram. (2) Following a process called interconversion, F will relax to the lowest vibrational state $S_{1,0}$ in about 10^{-12}s . (3) F will relax further by returning to S_0 by emitting a photon. Yet, F carries less energy in (3) compared to (1), so the photon's energy will be less: $E_{\text{excitation}} > E_{\text{emission}}$ so $\lambda_{\text{excitation}} < \lambda_{\text{emission}}$ (Figure 35) (Lakowicz, 2006). The whole process takes about 10^{-8}s and although excitation is done at a specific $\lambda_{\text{excitation}}$ via a laser, fluorescence emission covers a range of $\lambda_{\text{emission}}$.

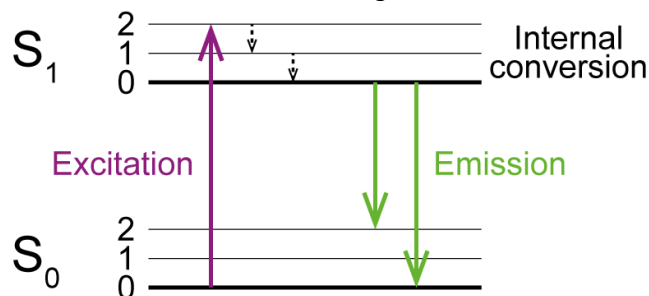


Figure 35

An explanation of the fluorescence phenomenon. A fluorophore F is in an electronic and vibrational state $S_{0,1}$ of lowest energy. Following an excitation with a photon of energy $h.\nu_{\text{excitation}}$, F is excited to the highest electronic and vibrational state $S_{1,2}$. F will lose some energy through a process called internal conversion, reaching the lowest vibrational state $S_{1,0}$. Finally, F will relax to S_0 by emitting a photon of energy $h.\nu_{\text{emission}}$, such that $h.\nu_{\text{excitation}} > h.\nu_{\text{emission}}$.

2. Confocal microscopy

Epifluorescence microscopy differs from confocal microscopy in that the former illuminates the whole sample at once and recovers the fluorescence signal across all of it. The latter illuminates one point of the sample at a time and recovers the

fluorescence signal from that point only (Figure 36). Due to a detection pinhole, photons will not bleed from nearby areas towards the detector, so the resolutions both in the (x,y) plane and along z are much higher. Assuming one can graft a fluorescent label without modifying the properties of a protein of interest, its membrane interacting properties can be studied. Lipid-binding fluorescent proteins can also be used to inquire on lipid repartition. Altogether, confocal microscopy allows the study of protein and lipid repartition at the cellular and sub-cellular scales. We already saw many examples of what this technique can do. We also saw it being replaced by techniques with higher resolutions. Indeed, let us discuss the resolution of confocal microscopy in the context of nanodomains.

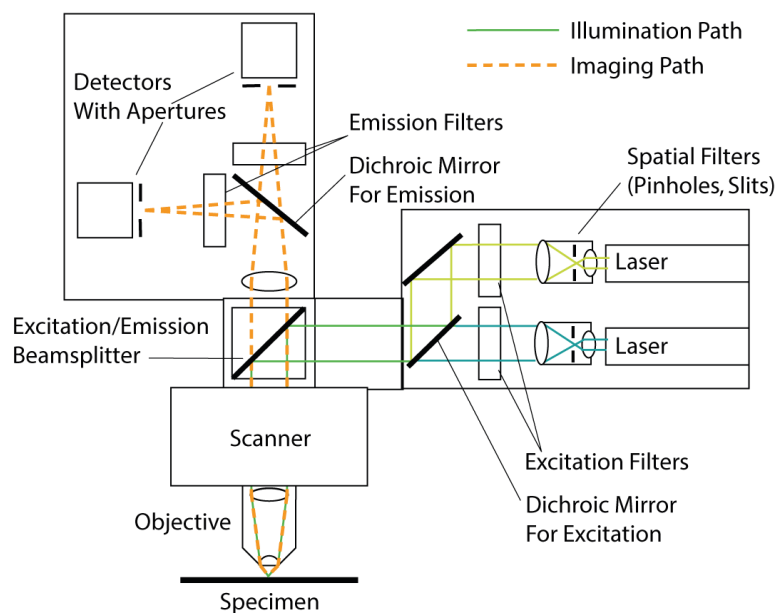


Figure 36

General schematic of a confocal microscope. Right: lasers send photons to the specimen. *Bottom:* the scanner ensures only one point of the sample is imaged at any given time. *Top:* the emitted fluorescence signal is directed to detectors. Note the use of pinholes the lasers and before the detectors: these ensure out-of-focus photons are not detected, effectively increasing the resolution. From (Reichman, 2013).

First, we shall differentiate the act of detecting from that of resolving (Figure 37). Presented with a clear sky, our eyes may detect Mars: all we would see is a brighter-than-usual spot. Yet, our eyes cannot resolve Mars: we cannot distinguish any of its many features, as we can do for the Moon which appears, not as a spot, but as a sphere of a certain diameter, littered with craters and various shades of grey. To resolve Mars, a telescope is needed: an apparatus with a higher resolution. It is the same issue with light microscopy and nanodomains.

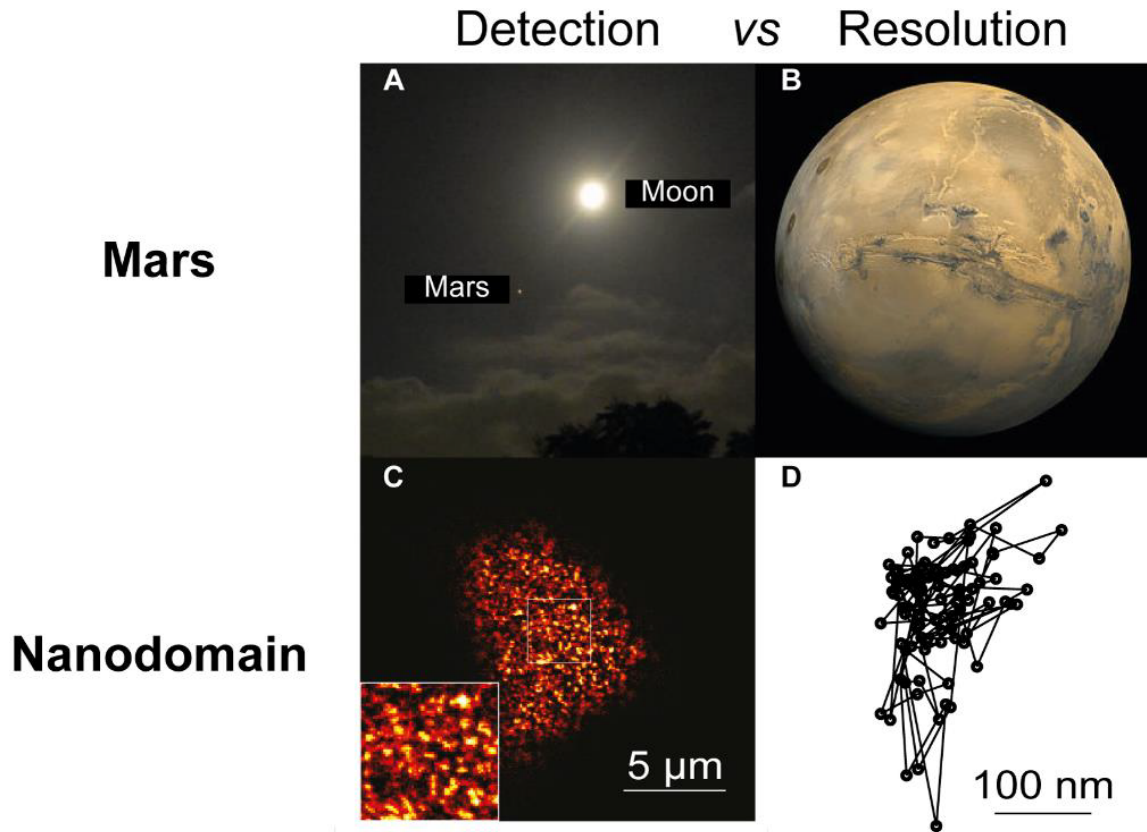


Figure 37

On the difference between detecting and resolving. (A) Moon and Mars seen from Earth. From (<https://earthsky.org/todays-image/photos-videos-mars-brightest-closest-2018>). (B) Mars seen 2500 km away from its surface by Viking 1 Orbiter, NASA, on the 22nd of February 1980 (MG07S078-334SP, NASA). (C) PM repartition of GFP-StREM1.3 by confocal microscopy in *Nicotiana benthamiana* leaves. (D) Spt-PALM of an EOS-StREM1.3 nanodomain microscopy in *Nicotiana benthamiana* leaves. (C) and (D) are adapted from (Gronnier et al., 2017).

Visible light, when meeting an obstacle or when passing through a hole of similar or smaller size than the light's wavelength, makes a diffraction pattern (Figure 38). This implies that even a perfectly focused beam of light will produce a diffraction pattern instead of a point. Moreover, no matter the fineness of the apparatus, its centre cannot be made smaller. John William Strutt Rayleigh found that this pattern's diameter d is defined by:

$$d = 0.61 \frac{\lambda}{NA} \quad (\text{Eq.1})$$

where λ is the wavelength, $NA = n \cdot \sin(\theta)$ is the numerical aperture, with n the immersion medium's refractive index, θ the half-angle from the image to one half of the cone of light reaching the photomultiplier, and $0.61 = 3.83/2\pi$ where 3.83 is the first minimum of a diffraction pattern behaving as a Bessel function J_0 :

$$J_0(x) = \frac{1}{\pi} \int_0^\pi \cos(x \cdot \cos(\theta)) d\theta \quad (\text{Eq.2})$$

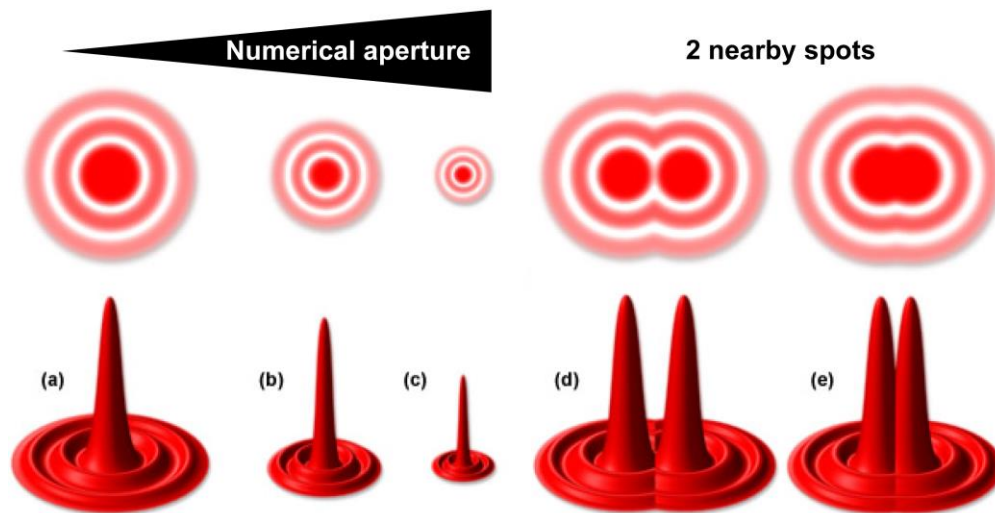


Figure 38

Illustrating the importance of Airy discs in light microscopy. *Top:* Airy discs are diffraction patterns of a perfectly focused beam of light through a given optical system. *Bottom:* 3D projection with intensity as height. (a-c) Increasing the microscope's numerical aperture (e.g. by switching from an air immersion objective of NA = 1 to an oil immersion objective of NA = 1.4). (d-e) When multiple spots (here two) are in proximity, it becomes difficult to assess the centre of each spot, making sample resolution harder. Adapted from (<http://zeiss-campus.magnet.fsu.edu/print/basics/imageformation-print.html>).

For example, one GFP, which is among the fluorophores with the smallest $\lambda_{\text{emission}}$ with $\lambda_{\text{emission}} (\text{GFP}) = 509 \text{ nm}$, observed with an oil-immersion objective whose NA = 1.40, yields a spot of size $d = 222 \text{ nm}$. d is also called the Airy unit (AU) for the GFP channel.

In the case of remorins, nanodomains are smaller than 100 nm (Demir et al., 2013; Gronnier et al., 2017; Raffaele et al., 2009a), so it would not be possible to resolve a GFP-REM nanodomain with confocal microscopy. Although confocal microscopy can be used to assess overall PM organisation (Spira et al., 2012; Szymanski et al., 2015), its resolution is too poor to resolve many nanodomain systems. Alternative methodologies must be employed, regrouped in what is called super-resolution microscopy.

3. Super-resolution microscopy

a. Airy scan

The Airy scan relies on the idea that, although a diffraction pattern has an immutable size, the area it covers can be finely scanned then de-convolved to break the resolution limit up to 120nm in (x,y) and 340nm in z (Huff et al., 2017). This is done by using a 32-channel photomultiplier array detector *in lieu* of a single photomultiplier detector.

b. Stimulated emission depletion (STED)

STED uses the concept that the electronic states of a Jablonski diagram can be manipulated in both directions. Thus, photons of a given energy are sent until every illuminated fluorophore reaches the excited state S_1 just before a third photon of slightly smaller energy returns fluorophores from a small central area to S_0 , all before fluorescence occurs, effectively depleting fluorescence from an area smaller than 1 AU, thus breaking the resolution limit (Hell and Wichmann, 1994). It is the oldest super-resolution methodology, reaching a maximal resolution of 40 nm (Vicidomini et al., 2018).

c. Single-particle tracking photoactivated localisation microscopy (spt-PALM)

Spt-PALM relies on the fact that if only a single fluorophore emits fluorescence at a given time, one could locate the centre of its diffraction pattern and call it the position of the fluorophore. This requires that (1) only a subset of fluorophores is excited during each acquisition, so any diffraction pattern is due to exactly one fluorophore, and (2) this subset of excited fluorophores must change over many acquisitions so all fluorophores are imaged (Betzig et al., 2006; Liu et al., 2015). Classical fluorophores, such as GFP, cannot be used: some of them must remain “dark” and not fluorescent while others are excited and fluoresce (Dempsey et al., 2011; Rust et al., 2006). This requires the use of photoactivable (PA) fluorophores, such as PA-GFP (Patterson and Lippincott-Schwartz, 2002), that can be switched, by irradiation at a specific wavelength, from an active to an inactive state. First, a laser activates a subset of all targeted fluorophores. Then, a second laser excites the activated fluorophores. As this cycle is repeated, new fluorophores will be activated while a fraction of already activated fluorophores will be de-activated (Betzig et al., 2006). A resolution around 20 nm can be reached, and time series can be used to track single particles and reconstitute their trajectories, granting unique insights into the dynamics of live cells (Gronnier et al., 2017; Liu et al., 2015).

Super-resolution microscopy is becoming increasingly common. Yet, other kinds of microscopies, whose methodologies are older, more commonly available and easier to perform exist.

C. Electron microscopy (EM)

Recalling (Eq.1), one way to improve resolution would be to decrease λ . Yet, lenses do not exist for every wavelength of the light spectrum: none for ultraviolets and x-rays. De Broglie states the wave-particle duality:

$$\lambda = \frac{h}{p} = \frac{h}{mv} \quad (\text{Eq.3})$$

The kinetic energy E_k of an electron is:

$$E_k = \frac{1}{2} m v^2 \quad (\text{Eq.4})$$

where $m = 9.1 \cdot 10^{-31}$ kg is the rest mass of an electron (Bureau International des Poids et Mesures, 2006). Combining (Eq.4) and (Eq.5):

$$\lambda = \frac{h}{\sqrt{2mE_k}} = \frac{h}{\sqrt{2meU}} \quad (\text{Eq.5})$$

where $e = 1.6 \cdot 10^{-19}$ C is the elementary electric charge (Bureau International des Poids et Mesures, 2006) and U the acceleration voltage applied to an electron. If we are to send an electron beam on a sample at acceleration voltage U , we will do so at a non-negligible proportion of the speed of light $c = 299792458$ m/s in vacuum. Thus, the special theory of relativity (Einstein, 1920) applies and eU must be corrected:

$$\lambda = \frac{h}{\sqrt{2meU(1 + \frac{eU}{2mc^2})}} \quad (\text{Eq.6})$$

If $U = 200$ kV then $\lambda = 2.51$ pm. Thus, electrons allow us to reach wavelengths in the picometre range, much below the length of a C-C bond (154 pm), and far below the few hundred nanometres of fluorescence microscopy, therefore providing a very high theoretical resolution.

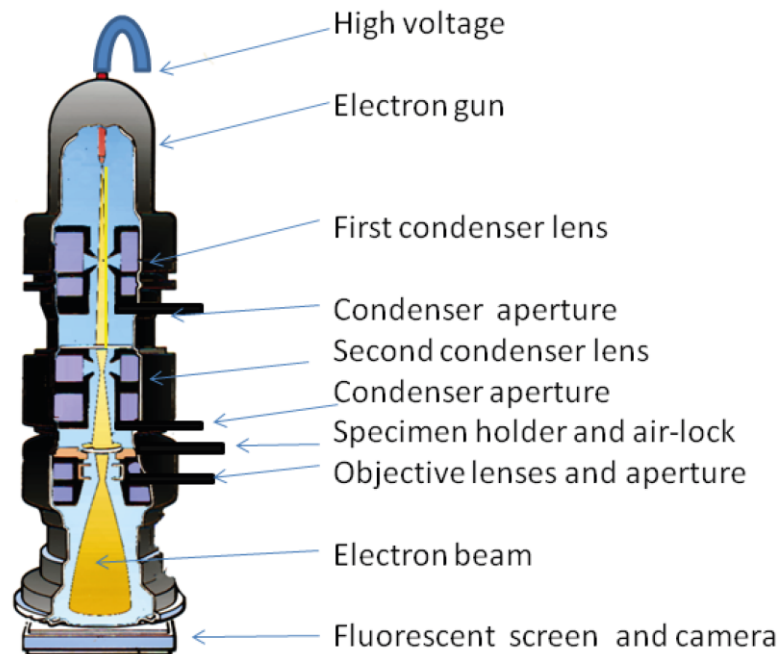


Figure 39

Schematic of transmission electron microscope. An electron gun shoots an electron beam accelerated to a high voltage (100-300 keV). A series of condenser lenses (electromagnetic lenses) and diaphragms focus the electron beam onto the sample. Electrons passing through will encounter the objective lens to magnify the electron beam. A fluorescent screen may be employed for direct visualisation (by the eye), or a CCD camera to record electron microscopy clichés. From Dr Graham Beards, published on Wikipedia (https://en.wikipedia.org/wiki/Electron_microscope).

However, the sample's nature, the quality of preparation and the instrumentation will be the most determining factors of the final resolution. The details of sample preparation will be discussed later. The sample is loaded onto a grid and inserted in an electron microscope, in vacuum, and bombarded with electrons (Figure 39). Note that the glass lenses of a fluorescent microscope are replaced here by electromagnetic

lenses. The possible fates of electrons when reaching the sample stage are many (Figure 40). Here, we deal with transmission electron microscopy (TEM), which makes use of transmitted and scattered electrons, even though we must acknowledge the existence of scanning electron microscopy (SEM), using back-scattered and Auger electrons and whose resolution is poorer. Electrons will reach a charge-coupled device (CCD) camera that will produce fluorescence upon excitation by transmitted electrons. This fluorescence will be recorded as a grayscale image, the brightness of a pixel being positively correlated to the amount of electrons received. It follows that a dark spot indicates electron absorption by the sample and thus the presence of a material of some kind blocking the electron's path.

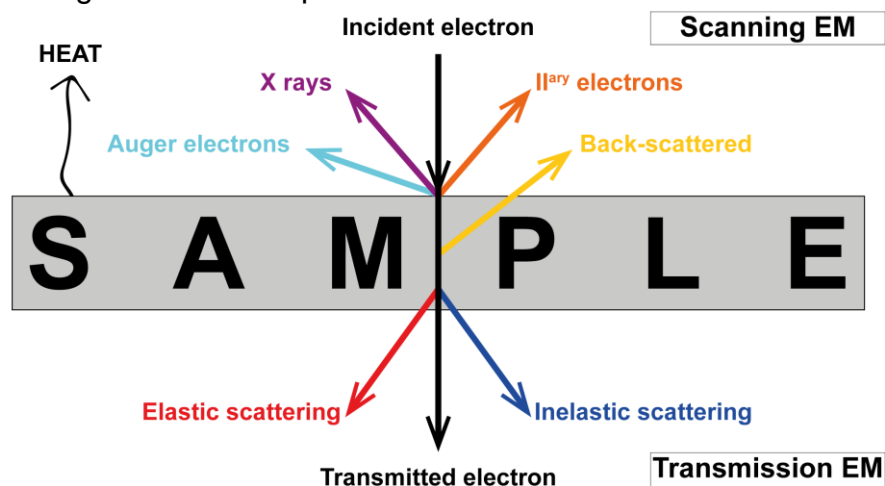


Figure 40

Illustrating the possible fates of electrons in an electron microscope. *Top:* An incident electron may elastically (without losing energy) back-scatter (yellow), non-elastically (with energy loss) be reflected back from the sample's surface (orange), excite an atom that will return to its ground by emitting X-rays (violet) or Auger electrons (cyan) to the incident side. These electrons are captured in scanning EM (surface observation, low resolution). The sample will heat upon beam exposure. *Bottom:* an incident electron may pass, undisturbed, through the sample (black) or be scattered elastically (red) or not (blue). Adapted from Prof. Alain Brisson's lecture on EM.

Biological matter is primarily made of light atoms such as hydrogens, carbons, nitrogens, oxygens, sulphurs and phosphorus, along with a handful of heavier atoms. These light atoms do not block much electrons, so we say that biological matter does not yield much amplitude contrast: most incident electrons are either transmitted (black arrows) or scattered (red and blue arrows). Scattered electrons are phase-shifted upon interaction with the sample, experience a longer path towards the detector compared to transmitted electrons and are finally refocused by the objective lens and sent to the CCD camera for detection. Phase interference between all transmitted and scattered electrons in the image plane increases contrast: this is phase contrast. It is defined by the contrast transfer function (CTF) (Erickson and Klug, 1970; Thuman-Commike and Chiu, 2000):

$$\text{CTF} = \sin \left[-\pi \Delta z \lambda k^2 + \frac{\pi C_s \lambda^3 k^4}{2} \right] \quad (\text{Eq.7})$$

where C_s represents spherical aberration (waves passing through the edges of the lens being refocused too far away from the focal plane), Δz is the defocus, λ is the electron's wavelength and k is the spatial frequency ($1/\text{\AA}$). CTF are plotted as functions of k ([figure 41](#)).

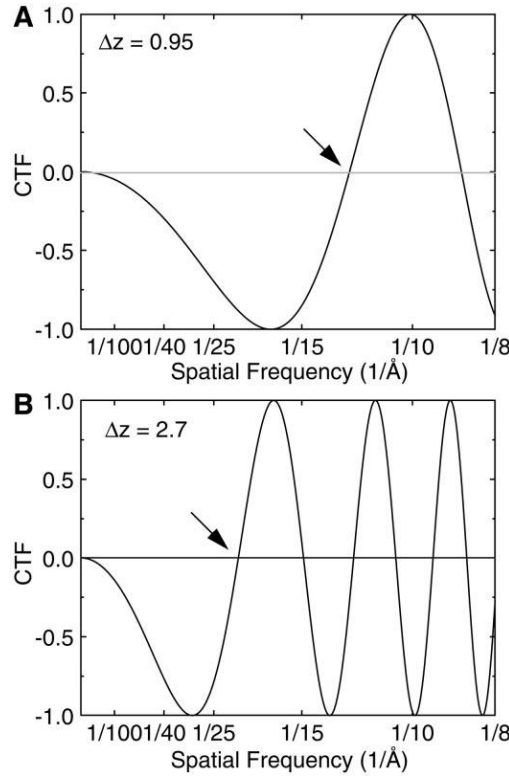


Figure 41

Simulation of the CTF for 400 kV electrons with an LaB6 gun and a $C_s = 4.1$ mm. The first zero of the contrast transfer function, denoted by the arrows, occurs at $1/12.5 \text{ \AA}^{-1}$ for a defocus Δz of (a) $0.95 \mu\text{m}$ and at $1/21 \text{ \AA}^{-1}$ for a defocus of (b) $2.7 \mu\text{m}$. From ([Thuman-Commike and Chiu, 2000](#)).

If $\text{CTF}(k) = 0$, no contrast is yielded for features of spatial frequency k . As $\text{CTF}(k)$ approaches 1 (or -1), k is imaged with a higher contrast (or a higher negative contrast). Thus, not all values of k may be represented, much less equally, in an EM image. If the defocus Δz is 0, phase contrast is minimal and there is not so much contrast at all in the final image. By increasing the defocus Δz , the CTF can be modified to gain contrast at the expense of resolution. Here, a higher Δz allows for an easier detection of the objects of interest, yet the resolution is lowered as many k values now have poor contrast. Hence one of the main issues of biological TEM: getting enough contrast.

In this manuscript, two methodologies will be employed: negative staining TEM and cryo-TEM.

1. Negative staining TEM

The idea is that, if the sample itself does not yield much contrast, an addition of heavy atoms to fill the empty spaces left by the sample on the grid will provide contrast instead. Therefore, electron absorption (i.e. dark spots) will be caused by the stain while the sample, which does not absorb much electrons, will remain light, hence the term of negative staining TEM: the object of interest will be light, not dark.

A sample, which may or may not be fixated (e.g. with glutaraldehyde), is blotted onto an electrically charged carbon-coated copper grid. Excess sample is removed by blotting against an absorbent paper then stained, typically with a uranyl acetate solution, and dried by blotting. The resolution, though heavily dependent on the sample's nature and the quality of the stain, can reach up to a few nanometres in the best cases (Scarff et al., 2018). As the sample is dehydrated and littered with heavy atoms, its shape may be deformed by the non-physiological conditions. Typically, liposomes observed by negative staining TEM can display a characteristic flat balloon shape (see Article IV).

2. Cryo-TEM

A way to maintain the physiological state of a biological object of interest and to reach atomic resolution exists: freezing the sample fast enough so it does not have time to react to the change of environment. This is cryo-TEM. Since there is no stain and biological matter is made of light atoms, contrast is lower compared to negative staining TEM. Nevertheless, the native-like state of the object of interest combined with the absence of stain to interact or hinder resolution made this technique famous over the past decades. By building image classes of an object of interest, which can be considered as 2D projections of such an object, a 3D model of it can be reconstructed. For a protein, a resolution as high as 1.8 Å can be reached (Merk et al., 2016).

In this manuscript, our use of cryo-TEM will be more modest: it will provide high-resolution clichés of protein assemblies and proteoliposomes in native-like conditions at a nanometric scale.

D. Atomic force microscopy (AFM)

The first technique to ever be able to provide an image of individual atoms was atomic force microscopy (AFM) (Figure 42). Here, the tip of a cantilever will touch or gently scrap the surface of a sample, yielding a height map (Figure 43). In the field of biology, spreading vesicles of chosen composition on a mica surface and measuring their height map upon various treatments is common (Frederix et al., 2009; Garcia-Manyes and Sanz, 2010; Jung et al., 2010; Whited and Park, 2014; Yuan and Johnston, 2001). More specific measurements concern the force needed to rupture a bilayer (Garcia-Manyes and Sanz, 2010) or that which is required to unfold a protein domain (Pimenta-Lopes et al., 2019), the latter being sometimes referred to as force spectroscopy.

In this manuscript, we will attempt to reconstitute supported bilayers of just enough components and remorin to form nanodomains.

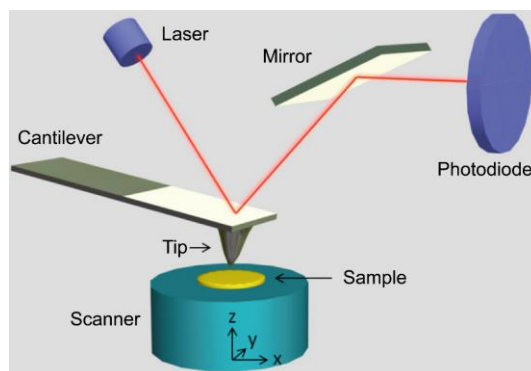


Figure 42

Principle of AFM. The sample (yellow) is placed atop a scanner that will move with high precision. A cantilever with a tip culminating with a single atom will tap or gently scratch the sample's surface. The tip's position is monitored by a laser pointed at the cantilever, which will reflect light onto another mirror then a photodiode. The cantilever will adjust its position to aim at the photodiode's centre. Thus, the sample's height map is generated. Adapted from (Zeng et al., 2012).

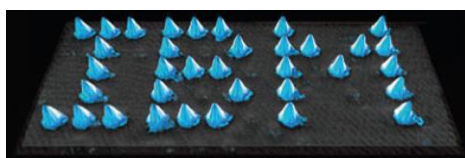


Figure 43

Xenon atoms (blue) on a mica surface (grey) manipulated to form the name IBM.
From (<https://www.ibm.com>).

E. Computational modelling

Computational methods are well suited to apprehend protein-lipid nano-objects, assuming one can correctly describe each interaction using the right software and parameters (Marrink et al., 2019). Atoms are considered as balls and interactions are described as springs linking two atoms together. In this classical picture, since quantum mechanics refutes the “balls and springs” analogy, every energy level of every interaction between two atoms has the following shape as a function of distance (Figure 44). The entire system evolves to minimise its energy and maximise its entropy (Smith, 2014).

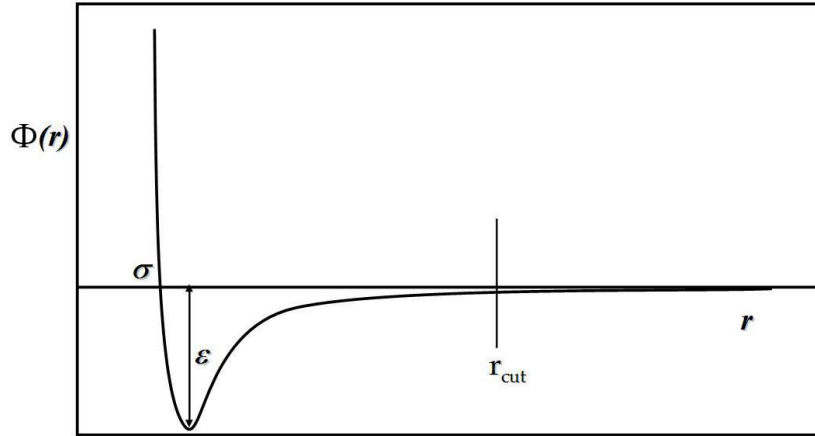


Figure 44

Lennard-Jones potential Φ as a function of distance r between two atoms. σ is the length scale, i.e. atoms' diameter. ϵ is the energy scale, i.e. interaction strength. r_{cut} is the value of r above which $\Phi = 0$.

The resolution issue is inverted: the bigger the system and the longer the simulation, the more computational power is required. A way to circumvent this issue is to lower the resolution of the modelled system: to replace a group of neighbouring atoms with similar properties by one single object. This methodology is called coarse grain (Chavent et al., 2016; Friedman et al., 2018). It allows the increase in size and time length of the modelled system. It has been thoroughly used to model lipid phase behaviour and nanoclustering (Ackerman and Feigenson, 2015; van den Bogaart et al., 2011; Gronnier et al., 2017; Javanainen et al., 2017; Koldsø et al., 2014). Moreover, it is becoming ever more successful at predicting protein structures (Baker, 2019).

F. Nuclear magnetic resonance (NMR)

Having performed many NMR experiments in the making of this work, I had the opportunity to delve further into the theoretical details of this technique. As a result, this subsection is a vulgarisation effort: an introductory lecture to NMR for beginners and particularly biologists, who may be interested in what this technique has to offer yet do not understand its functioning.

1. Spin

NMR deals with a fundamental property of particles called spin I , which is either positive or null. It denotes, if $I > 0$, an intrinsic angular momentum \mathbf{L} linked to a magnetic momentum $\boldsymbol{\mu}$ by:

$$\boldsymbol{\mu} = \gamma \mathbf{L} \quad (\text{Eq.8})$$

where γ is a constant called the gyromagnetic ratio. If $I = 0$, the particle has no spin and it follows that \mathbf{L} and $\boldsymbol{\mu}$ are null vectors. As its name suggests, NMR deals with magnetic nuclei whose spin $I > 0$, a non-exhaustive list of which is provided (Table 3). The value of I describes the nucleus' behaviour in NMR in a way that will be explained later. The absolute value of γ gives the nucleus' sensitivity, its sign gives the spinning

direction (trigonometric if positive, clockwise if negative). The natural abundance describes the occurrence of this isotope in nature. Thus, we may note, for example, that a proton (^1H) has a greater sensitivity and is highly abundant compared to ^{15}N , which is much less sensitive and represents only a third of a hundredth of all nitrogens. As we discussed for EM, biological matter, particularly proteins and lipids, is mainly made of hydrogens, carbons, nitrogens, oxygens, sulfurs and phosphorus along with a couple of heavier elements. Aside from ^1H , performing ^{13}C -, ^{15}N - or ^2H -NMR will require isotopic enrichment. We will make use of ^{13}C -, ^{15}N -labelled proteins produced by *Escherichia coli* BL21-DE3 on a minimal medium enriched in isotopically labelled metabolites, such as ^{13}C -glucose and $^{15}\text{NH}_4\text{Cl}$, although more complex labelling schemes can be achieved by replacing these fully labelled metabolites with specifically labelled ones and labelled or unlabelled aminoacids (Habenstein and Loquet, 2016). Deuterated lipids, here PC with at least one deuterated acyl chain, are synthesised by means of organic chemistry (Bragina and Chupin, 1997).

Nucleus	^1H	^{13}C	^{15}N	^2H	^{31}P
I	1/2	1/2	1/2	1	1/2
γ ($10^7 \cdot \text{rad} \cdot \text{s}^{-1} \cdot \text{T}^{-1}$)	26.75	6.73	-2.71	4.11	10.84
Natural abundance (%)	99.99	1.07	0.364	0.0115	100

Table 3

Nuclei of interest in biological NMR. I is the spin number and γ is the gyromagnetic ratio (or sensitivity). Values from Bruker.

2. NMR spectrometer

To perform an NMR experiment, the sample must be placed in a strong magnetic field called \mathbf{B}_0 , whose value is expressed in tesla T (or $\text{N} \cdot \text{m}^{-1} \cdot \text{A}^{-1}$ or $\text{kg} \cdot \text{s}^{-2} \cdot \text{A}^{-1}$) (Bureau International des Poids et Mesures, 2006), typically produced by a superconducting magnet. It is held in place by a probe, whose main function is to send radiofrequency photons and record an electromagnetic induction of an electric current, all via a small coil surrounding the sample. This signal will be amplified, converted to lower frequencies to be digitalised then sent to the desk computer from which the experiment is controlled (Figure 45).

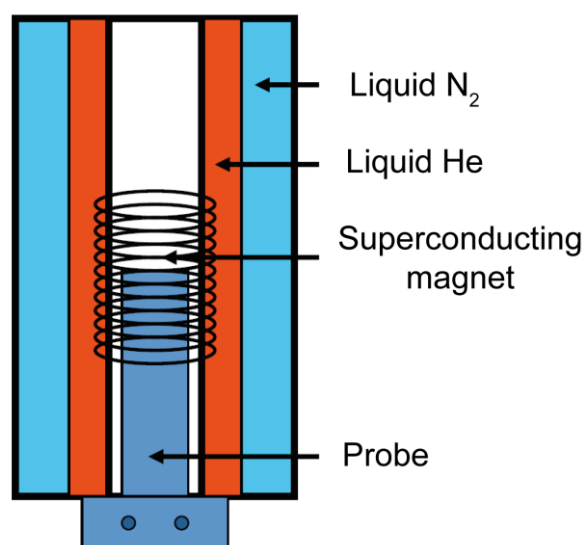


Figure 45

Simplistic schematic of an NMR spectrometer. It has two main components: a superconducting magnet cooled with liquid helium then liquid nitrogen and a probe, to hold the sample, send radiofrequency photons and record an electromagnetic induction of an electric current. From Dr Erick Dufourc's lecture on NMR.

3. Energy levels

Outside of the NMR spectrometer, with the approximation that the Earth's magnetic field is negligible, there is no significant magnetic field and magnetic momenta μ are randomly oriented, so the sum of all μ that is the net magnetisation \mathbf{M} is null. Once inserted in the NMR spectrometer, the sample is submitted to a strong magnetic field \mathbf{B}_0 along z from the superconducting magnet. Then, magnetic momenta μ will rearrange so $M_x = M_y = 0$ but $M_z \neq 0$. It is important to emphasise that all μ are not necessarily parallel to \mathbf{B}_0 and z but their sum is null along both x and y (Figure 46).

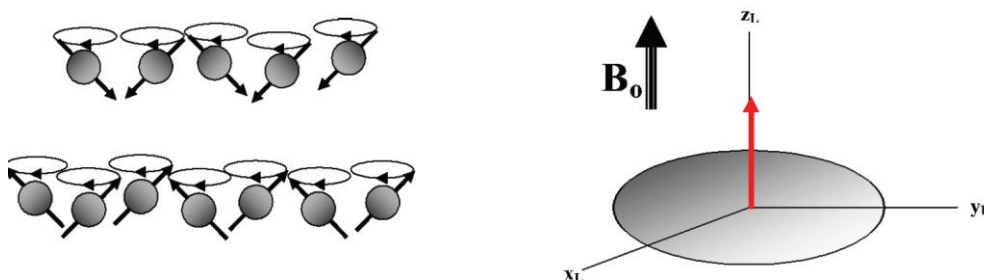


Figure 46

Behaviour of 12 nuclei of spin $I = 1/2$ exposed to a magnetic field \mathbf{B}_0 .

Individual magnetic momenta μ will cancel each other along x and y but not along z :

7 μ_z are aligned with \mathbf{B}_0 while 5 μ_z are aligned against it. This small discrepancy creates a net magnetisation \mathbf{M} (red arrow) such that, at equilibrium, $\mathbf{M} = \mathbf{M}_z$. From Dr Erick Dufourc's lecture on NMR.

An energy diagram may be drawn with a number of energy levels $2I+1$ (Figure 47): it is called a Zeeman splitting. States of lower energies are slightly more populated, giving rise to a non-zero net magnetisation along **z**. In NMR, the populations of each energy level are immovable: do not try to make an analogy with fluorescence! NMR spectroscopy is about manipulating **M**, not modifying energy state populations *per se*.

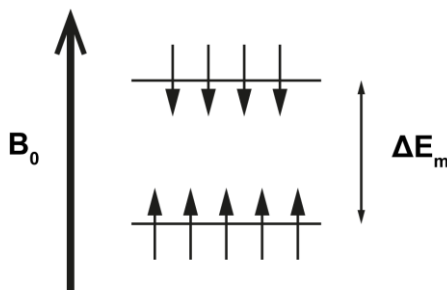


Figure 47

Energy levels for a population of spins $I = 1/2$. Two states are possible: the α state, in which μ_z are aligned with B_0 , and the β state, in which μ_z are aligned against B_0 . As the α state has the lowest energy, it is more populated than β so $N_\alpha > N_\beta$. The energy gap is ΔE_m . For $I > 1/2$, there is no general rule to determine which state has the lowest energy: consider it a property of the nuclei of interest.

4. The simplest NMR experiment

We will consider the case of a population of nuclei whose spin $I = 1/2$, as this is the simplest case. Let us perform the simplest NMR experiment (also called a pulse sequence) possible: to move **M** away from **z** into the **xy** plane and to record an NMR signal (Figure 48).

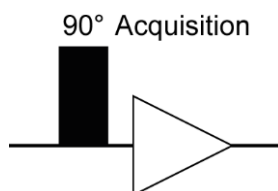


Figure 48

The simplest NMR experiment: 90° - pulse acquisition. The probe sends a radiofrequency wave tuned at the nucleus' NMR frequency, with a power and for a duration required to flip **M** by 90° from **z** to **xy**. The pulse is a few microseconds long. Then, the probe switches, in a few microseconds, to receiver mode and acquires the electromagnetic induction of an electric current: the NMR signal. After a period of time T_1 (a few seconds), **M** is considered to have relaxed and is back along **z**, so another scan can begin.

This requires to move **M** by exactly 90°. We are confronted to a matter of size: how can we apply a magnetic field strong enough to compete and win over B_0 with the probe's tiny coil? Cranking up the power is bound to burn the probe long before it reaches the necessary power to do so. Instead, we will use a geometrical trick. Our nuclei are at equilibrium and are submitted to B_0 thanks to a superconducting magnet

that cannot be turned off, so they rotate on themselves at the exact Larmor frequency ω_0 :

$$\omega_0 = \gamma B_0 \quad (\text{Eq.9})$$

In practice, not all nuclei may rotate at ω_0 exactly for reasons we will discuss soon. Until now, we were thinking in the fixed laboratory frame. We shall switch to a rotating frame of frequency ω_0 . Here, nuclei are immobile and the apparent magnetic field will be null, so we only need to apply a radiofrequency field of ΔE on the sample. Translated back into the fixed frame, this means applying an oscillating radiofrequency field of frequency ω_0 and energy ΔE :

$$\Delta E = \gamma \frac{h}{2\pi} B_0 = \frac{h}{2\pi} \omega_0 \quad (\text{Eq.10})$$

Applying a radiofrequency field is called a pulse: it is generally short enough so nothing of interest happens in that period (generally a few μs). The power, in watts, and the length of the pulse must be tweaked so \mathbf{M} is flipped by exactly 90° . Once in the \mathbf{xy} plane, \mathbf{M} will rotate around and slowly flip back to \mathbf{z} . After a period of time T_1 , equilibrium is reached again: it is said that the spins have relaxed (Figure 49A). The precession of \mathbf{M} is recorded by the probe as the electromagnetic induction of a current: it is the free induction decay (FID), the NMR signal.

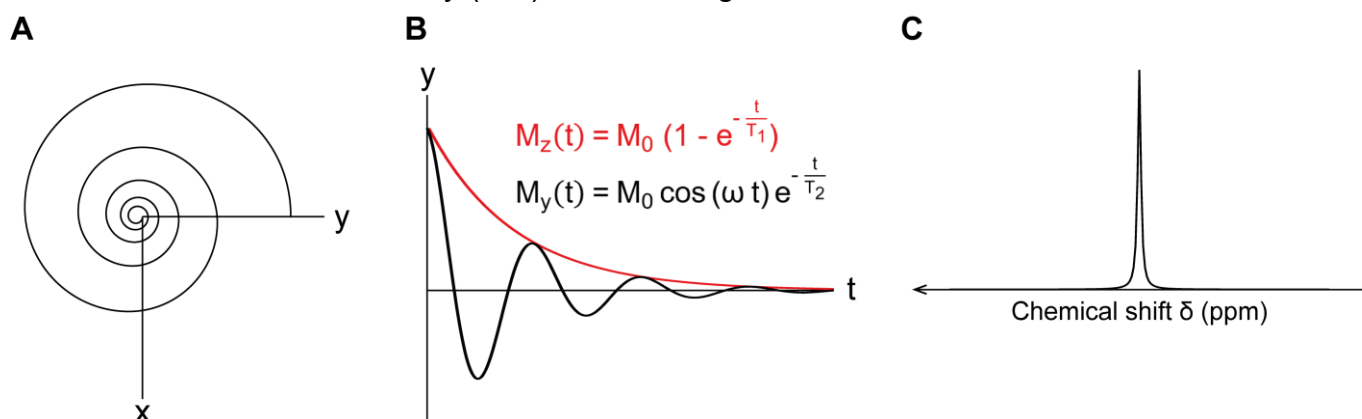


Figure 49

From signal collection to the NMR spectrum. (A) Trajectory of \mathbf{M} in the \mathbf{xy} plane. After a 90° pulse, \mathbf{M} is flipped from \mathbf{z} to \mathbf{xy} and starts precessing around and slowly flip back to \mathbf{z} after a period of time T_1 . (B) Recorded signal in \mathbf{y} (black). Note the exponential decrease in signal (red) as \mathbf{M} flips back to \mathbf{z} . (C) A Fourier transform of (B) with subsequent phase correction yields an NMR spectrum with a single peak of frequency ω .

Nuclei have slightly different Larmor frequencies ω . This implies that every magnetisation of every nucleus with a particular ω will, in time, drift away from the others. The result is a rapid collapse of the NMR signal after a period of time T_2 . The reason for such discrepancies in ω is chemical shielding σ (sometimes abbreviated CS):

$$\sigma = \gamma B_{\text{eff}} = \gamma (B_0 - \sigma B_0) = \omega_0 (1 - \sigma) \quad (\text{Eq.11})$$

σ arises from the influence of the atom's electrons on the nucleus' magnetic behaviour, which depend on the atom's chemical environment (e.g. nearby presence

of an electronegative atom, hybridisation states, aromaticity...). It follows that if $\sigma = 0$ then $\omega = \omega_0$.

We already discussed that a small difference in spin populations yields a non-trivial **M** that is responsible for the NMR signal. Consequently, the signal-to-noise ratio (SNR) is small too. Thus, most NMR experiments must be repeated enough, up to tens of thousands of scans for some of them, to yield an NMR spectrum with acceptable SNR.

5. NMR spectrum

We are interested in the relative abundance of each nuclei with a given Larmor frequency ω . However, the FID gives an amplitude as a function of time (Figure 49B). Fitting the FID with a decreasing exponential (which is the overall shape of any FID) and applying a Fourier transform (to switch from a time-domain to a frequency domain) with phase correction (the Fourier transform does not give phase values, it is computed by the software or found manually based on spectral line shapes) will yield an NMR spectrum: NMR intensity as a function of frequency. (Figure 49C) NMR intensities are defined such as the integral of a peak gives the relative amount of nuclei with a given ω . Most spectra employ normalised frequencies in parts per million (ppm):

$$\delta = \frac{\omega_{\text{sample}} - \omega_0}{\omega_0} \cdot 10^6 \quad (\text{Eq.12})$$

This choice of unit makes comparison between spectra easier (e.g. ^1H resonates between 0 and 10 ppm no matter the spectrometer and its exact **B**₀). It is because ω may deviate from ω_0 due to σ that we can have peaks at δ values other than 0.

We just discussed the simplest NMR experiment: 90° pulse – acquisition. Most NMR spectroscopy requires pulse sequences significantly more complex than this, whose derivations require a basic knowledge of quantum mechanics that we successfully avoided above by making use of the simpler vector model, its classical analogue. Derivations of such experiments is not the subject of this chapter: the interested reader is redirected to (Keeler, 2016). However, we will discuss what these NMR experiments may teach us.

6. Liquid-state vs. solid-state NMR

A liquid sample has all molecules rotating rapidly and no preferential orientation: the sample is said to be isotropic and this results in sharp NMR peaks. In a solid sample, molecules do have preferential orientations and rotate slowly, if at all: the sample is said to be anisotropic and yields a poorly resolved spectrum with an important full width at half-height. If one is interested in orientation parameters, as in the case of ^2H static ssNMR, such spectra can be satisfactory. If not, one needs to “remove” this anisotropy. Some light quantum mechanics are required.

Let **H** be the Hamiltonian operator (the quantum mechanical equivalent of the total energy function in classical mechanics) and let us consider some nuclei of spin $I = 1/2$. We are concerned only with spin states so any other contribution can be neglected (Levitt, 2008):

$$H = H_Z + H_{CS} + H_D^{IS} + H_D^{II} + H_Q \quad (\text{Eq.13})$$

where H_Z is the Zeeman contribution (from spin populations being split between energy levels), H_{CS} is the chemical shielding contribution (arising from chemical shielding), H_D^{IS} and H_D^I are the heteronuclear and homonuclear dipolar coupling contributions (accounting for the magnetic fields induced by the nuclei themselves) and H_Q is the quadrupolar coupling (due to the non-sphericity of the nucleus; it is null for non-quadrupolar nuclei, i.e. all those whose $I = 1/2$). The anisotropic contributions of each component are (Alia et al., 2009; Smith et al., 1992a, 1992b):

$$\begin{aligned} H_{CS} &= \frac{h}{2\pi} \gamma B_0 I_z \sigma_{zz} \left(\frac{3 \cos^2 \beta - 1}{2} + \frac{\eta}{2} \cos(2\alpha) \sin^2 \beta \right) \\ H_D^{IS} &= \frac{h}{4\pi} \frac{\gamma_A \gamma_B}{r_{AB}^3} I_z^A I_z^B D_{zz} \left(\frac{3 \cos^2 \beta - 1}{2} \right) \\ H_D^I &= \frac{h}{4\pi} \frac{\gamma^2}{r^3} (3 I_z^A I_z^B - I^A I^B) D_{zz} \left(\frac{3 \cos^2 \beta - 1}{2} \right) \\ H_Q &= \frac{eQ}{4I(2I-1)} (3 I_z^2 - I^2) V_{zz} \left(\frac{3 \cos^2 \beta - 1}{2} + \frac{\eta}{2} \cos(2\alpha) \sin^2 \beta \right) \end{aligned} \quad (\text{Eq.14})$$

where α is a rotation along \mathbf{z} (in the \mathbf{xy} plane), β is a rotation along \mathbf{y} (in the \mathbf{zx} plane), η is the asymmetry parameter for a given parameter A such as $\eta = \frac{A_y - A_x}{A_z}$, I , σ , D and V are the spin, chemical shielding, dipolar coupling and quadrupolar coupling tensors, respectively, and eQ is the quadrupolar constant. H_Z has no anisotropic contribution.

We wish that all the terms in (Eq.13) equal 0. In practice, we assume $\eta = 0$, so the sample's anisotropy depends on $3 \cos^2 \beta - 1$:

$$\begin{aligned} 3 \cos^2 \beta - 1 &= 0 \\ \beta &= 54.7^\circ = \text{magic angle} \end{aligned} \quad (\text{Eq.15})$$

The value of this magic angle happens to be the same than between a cube's diagonal and one of its consecutive edges. By tilting the sample at 54.7° from \mathbf{z} , and therefore \mathbf{B}_0 , and spinning it, to average the orientations of all molecules within the sample, one can remove anisotropic contributions: this is magic angle spinning (MAS) ssNMR. The spinning rate remains an instrumental limitation: it must surpass the value, in hertz, of the contributions it means to suppress. Thus, NMR rotors (Figure 50), in which samples are held, and their associated probes are designed for spinning at a dozen of kHz at least, over 100 kHz for a 0.7 mm (outer diameter) rotor.

7. ssNMR to study membrane nanodomains

As we saw in section I.E, membrane nanodomains are big, insoluble and non-crystalline objects. Therefore, X-ray crystallography and liquid-state NMR are disqualified. Remorins being rather small, about 23 kDa, cryoEM will have difficulties to analyse anything smaller than high-order stable oligomeric complexes. ssNMR is limited by spectral overlap, i.e. the presence of too many peaks in a small spectral region hindering or even prohibiting analysis. Overcrowded spectra may result from sample heterogeneity, i.e. more than one possible structural conformation of the protein under investigation, increasing the number of peaks or broadening them until

analysis becomes difficult if not impossible. ssNMR can provide unique data on lipid dynamics using the lineshapes of ^2H and ^{31}P static ssNMR spectra – on a sample using ^2H -doped lipids, and protein structure, using ^{13}C - and ^{15}N - MAS ssNMR on isotopically labelled proteins, where each peak will represent the protein's local structure at a given nucleus whose magnetic behaviour is modulated by its chemical environment, namely solvent and surrounding residues. Thus, a great part of our study will rely on ssNMR.

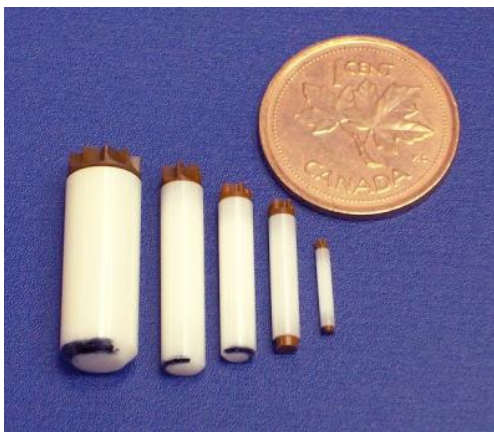


Figure 50

Image of ssNMR rotors. From left to right: 7 mm, 4 mm, 3.2 mm, 2.5 mm and 1.3 mm (of outer diameter) MAS ssNMR rotors from Bruker. These are zirconium oxide cylinders, closed at the top by a plastic cap with small wings. To achieve MAS, air is blown onto them. 2.5 mm rotors and below must also be closed at the bottom with a specific cap. A dark semi-circle is drawn to ensure a correct optical measurement of MAS frequency. A Canadian cent is given for size reference (19.05 mm in diameter, according to the Royal Canadian Mint, <https://www.mint.ca>). From Glenn Facey's blog on NMR, University of Ottawa, Canada (<https://u-of-o-nmr-facility.blogspot.com/2008/04/how-much-sample-do-i-need-to-get-solid.html>).

8. ssNMR to elucidate protein structures

Unlike liquid state NMR, which relies mostly on ^1H detection, ssNMR is mainly limited by dipolar coupling anisotropy (Thureau et al., 2014). As a result, ^1H detection is very tasking and requires very specific and expensive gear. Instead, we used simpler methodologies, where the loss of ^1H detection is compensated by ^{13}C -detected experiments – the nucleus with the second highest sensitivity γ between ^1H and ^{15}N .

a. Cross polarisation (CP)

To enhance the signal-to-noise ratio (SNR), the higher gyromagnetic ratio γ of ^1H is used by transferring the magnetisation \mathbf{M} to ^{13}C via a technique called cross polarisation (CP). While ^{13}C is on \mathbf{z} , ^1H is brought into \mathbf{xy} , then both nuclei are irradiated: ^{13}C with a hard pulse and ^1H with a shaped pulse of increasing power and whose duration is termed “contact time”. At a given power of the shaped pulse, the effective magnetic fields on both nuclei are equal, and magnetisation \mathbf{M} is transferred from ^1H to nearby ^{13}C . Acquisition is performed on the ^{13}C channel while decoupling, i.e. a rapid succession of pulses, occurs on ^1H , to destroy dipolar couplings between

both nuclei. Note that CP works for any two nuclei, granted one is significantly more sensitive than the other.

It follows that a typical ssNMR analysis of a protein starts by recording a one-dimensional ^1H MAS spectrum, which is not very informative besides determining the sample's temperature from the water's chemical shift (Wishart et al., 1995), defining the "0 ppm" using the peak provided by a molecule containing a single ^1H , such as DSS (sodium trimethylsilylpropanesulfonate), and detecting contaminants. Then, a ^1H - ^{13}C CP gives a one-dimensional ^{13}C spectrum (Figure 51). Chemical shift references for all nuclei of all residues can be found in the literature (Merutka et al., 1995; Wang, 2002; Wishart et al., 1992; chemical shifts statistics of the Biological Magnetic Resonance Bank (BMRB)). One can discern $\text{C}\alpha$ (50-75 ppm) and aliphatic carbons (10-50 ppm), aromatic moieties (100-160 ppm) and amide carbons (Co , 160-180 ppm). When dealing with proteins, such a spectrum is often very crowded, and gives only little structural information: peak overlap hinders spectral assignment, i.e. matching peaks with their corresponding nuclei.

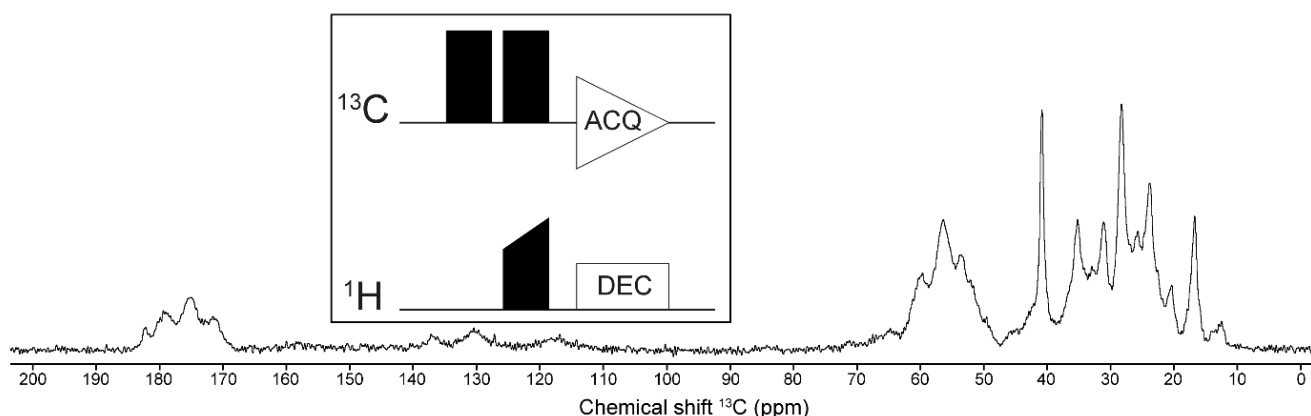


Figure 51

A typical ^1H - ^{13}C CP spectrum of a ^{13}C -labelled protein sample. *Inlet:* pulse sequence. ACQ: acquisition, DEC: decoupling.

b. Proton Driven Spin Diffusion (PDSD)

We will perform a ^{13}C - ^{13}C proton driven spin diffusion (PDSD) experiment to spread all peaks in a two-dimensional (2D) spectrum. This experiment also starts with a ^1H - ^{13}C CP. To get a second axis, the delay labelled as t_1 in the pulse sequence (Figure 52A) is incremented and transformed into a frequency by Fourier transform, thus providing another spectral dimension. It follows that a 2D spectrum is a stack of 1D spectra with an incremented delay. The chemical shift coming from this incremented delay is F_1 (vertical axis) and the one coming from the FID is F_2 (horizontal axis). Since peaks are spread along one additional axis, peak overlap is reduced. Moreover, the intensity of cross-peaks (off-diagonal peaks) is positively correlated to the proximity of the nuclei they are assigned to, the rigidity of the protein and the length of the mixing time t_m : increasing t_m allows obtaining cross-peaks between nuclei that are further apart, at the cost of SNR. As an example (Figure 52B): let us consider an anisotropic sample composed of one hypothetical kind of molecule with three ^{13}C . We are studying

it using ssNMR. Here is its fictional ^{13}C - ^{13}C PDSD spectrum. We can neglect diagonal peaks, as they correspond to those of a ^1H - ^{13}C CP spectrum. Ideally, the spectrum is symmetric along its diagonal, so any peak on one side should also be on the other side (dashed lines). As a rule of thumb, if cross-peaks appear at chemical shifts corresponding to two different nuclei, then these nuclei are close in space, and the bigger the peaks, the closer they are. Here, 1 and 2 seem close from each other while 3 seems further away from 1 and 2. Thus, this experiment offers the possibility to derive distance constraints, which will prove useful in protein structure determination. The ^{13}C - ^{13}C PDSD experiment has one drawback: peaks will only appear if the sample is rigid enough. This is not an issue for an amyloid protein core or a bacterial needle (Daskalov et al., 2015, 2016; Demers et al., 2014; Habenstein et al., 2012). However, flexible regions of a protein may disappear and proteins in a less rigid structural regime may lead to weak SNR, or lack thereof.

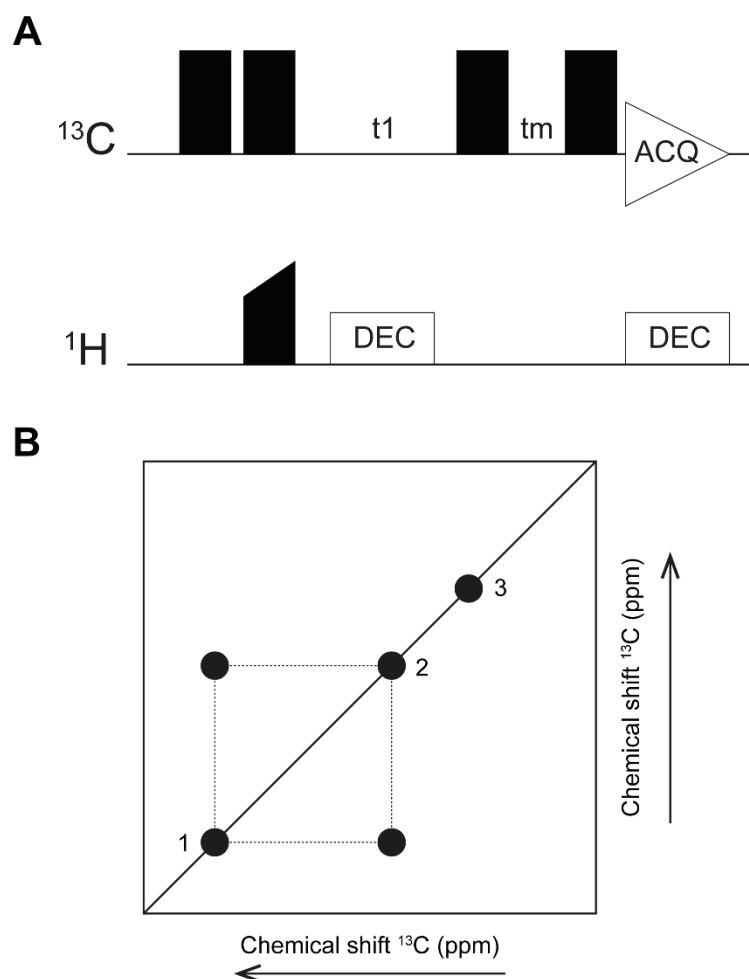


Figure 52

On how to read a ^{13}C - ^{13}C PDSD spectrum. (A) Pulse sequence. t_1 is an incremented delay: the experiment will be repeated at various t_1 values, turned into frequencies reported on the vertical axis in (B). t_m is the mixing time: increasing it allows to collect longer distance restraints between two nuclei, however it decreases SNR. (B) Schematic example of a ^{13}C - ^{13}C PDSD spectrum of a molecule with three

^{13}C , numbered from 1 to 3. In this experiment, cross-peaks (off-diagonal peaks) will appear if nuclei are close in space. Here, 1 and 2 seem close from one another while 3 seems far away from both. Ideally, the spectrum is symmetrical to its diagonal, as indicated by the dashed lines: “if 1 sees 2 then 2 sees 1”.

c. Secondary chemical shifts

By calculating the difference between a measured chemical shift and the expected value for a random coil conformation, one can assess whether a given part of a protein is in a helical (α), if positive, or strand (β) conformation, if negative: this is called the secondary chemical shift or the chemical shift index (Wang, 2002; Wishart et al., 1992). Even if spectral assignment happens to be very tedious, this method can potentially already yield robust structural data.

9. IsNMR to study soluble intrinsically disordered proteins

a. Generalities

Thanks to its high gyromagnetic ratio and abundance, IsNMR makes an extensive use of ^1H . Unlike ssNMR, a protein’s structural fingerprint will not be a ^{13}C - ^{13}C correlated spectrum but a ^1H - ^{15}N Heteronuclear Multiple Quantum Coherence (HMQC). Here, one peak will appear for every amide function. In practice, that is: one peak for every residue’s backbone amide with the exceptions of prolines and the N-terminal residue (they have none), one peak per amide of a tryptophan sidechain and one doublet (two peaks in ^1H , one peak in ^{15}N) per amide of an asparagine or a glutamine sidechain (Merutka et al., 1995) (chemical shift statistics of the BMRB).

b. On intrinsically disordered proteins (IDPs)

StREM1.3 has an N-terminal intrinsically disordered domain, which we will study here: the freshly purified protein will have no particular structure, making nuclei of identical residues appear in the same crowded spectral region, with severe spectral overlap as a consequence. Thus, spreading the peaks with 3D spectra is imperative. A plethora of NMR experiments exist to establish connectivities between residues, i.e. to identify a residue i by assessing which residues could be $i-1$ and $i+1$ (Figure 53).

A disordered protein is in exchange between a variety of conformations (Uversky, 2013). It can be said to “scan a conformational space”. Upon interaction with a ligand or post-translational modifications, such as phosphorylation, this conformational space is modified. Thus, an otherwise disordered protein may fold, at least partially, upon such events. Mapping of phosphorylated residues or interaction surfaces can therefore be achieved by following the evolution of a protein’s ^1H - ^{15}N HMQC spectrum over the course of phosphorylation or interaction with a ligand (Theillet et al., 2013; Kragelund and Skriver, 2020).

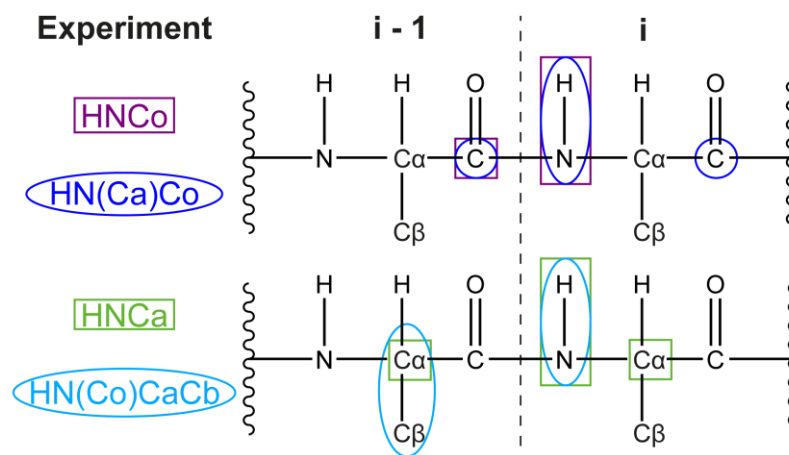


Figure 53

Some experiments to establish connectivities between residues in lsNMR.

The ^1H and ^{15}N chemical shifts (δ) for a backbone amide of a residue i are generally obtained by a ^1H - ^{15}N HMQC spectrum. The first set of 3D experiments (*top*) links i to $i-1$ by their carbonyls: e.g. the Co of $i-1$ yields a blue peak and a purple peak at the δ of ^1H and ^{15}N for i , but it yields only a blue peak at the chemical shifts of ^1H and ^{15}N for $i-1$. The second set of 3D experiments (*bottom*) links i to $i-1$ by their $\text{C}\alpha$: e.g. the $\text{C}\alpha$ of $i-1$ yields a cyan peak and a green peak at the δ of ^1H and ^{15}N for i , but it yields only a green peak at the δ of ^1H and ^{15}N for $i-1$. In addition, the $\text{HN}(\text{Co})\text{CaCb}$ gives the δ of the $\text{C}\beta$ of $i-1$, allowing residue identification based on their chemical shifts.

c. On folded proteins

If our previously disordered protein is now folded, how do we determine its structure? Where ssNMR makes use of ^{13}C - ^{13}C distance constraints obtained from ^{13}C - ^{13}C PDSD spectra, lsNMR will employ ^1H - ^1H Nuclear Overhauser Effect Spectroscopy (NOESY) to obtain distance constraints between neighbouring protons. Software such as ARIA2 and the CCPNMR Grid interface (Nilges et al., 2008; Rieping et al., 2005, 2007; Vranken et al., 2005) can perform computational modelling based on distance restraints obtained by lsNMR and ssNMR as well as secondary chemical shifts (section V.E.9).

10. ssNMR to monitor lipid dynamics: ^2H ssNMR

ssNMR permits the study of membrane biophysics under native conditions. The nuclei of interest are ^{31}P (section V.F.11), which allows easy characterisation of a sample's phase behaviour (Huster, 2014) and shape of liposomes (Pott and Dufourc, 1995), and ^2H which, which informs us about lipid order (Seelig, 1977) and membrane thickness (Grélard et al., 2013). ^2H , unlike ^{31}P , is a poorly abundant isotope. To perform ^2H NMR, one must use a deuterated reporter lipid, whose physical properties may vary slightly from its naturally abundant counterpart (e.g. DMPC has a phase transition temperature of 295K while DMPC-d₅₄'s, a DMPC deuterated on both acyl chains, is 293K).

Liposomes, bearing a deuterated reporter lipid, must be big enough to be anisotropic (>100 nm at least). We commonly employ multilamellar vesicles for their ease of production: hydration of a lipid film or a lipid powder followed by a few freeze-thaw-vortex cycles to ensure homogeneity in size and composition. The sample is then fitted into an ssNMR rotor.

Experiments are performed under static conditions. To enhance the signal-to-noise ratio (SNR), the quadrupolar interaction of ^2H must be refocused by employing a quadrupolar spin echo pulse sequence (90° - τ - 90° - τ -acquisition) *in lieu* of the classical Hahn echo pulse sequence (90° - τ - 180° - τ -acquisition). This interaction will dominate the spectrum (Seelig, 1977). Spectral lineshapes being capital for data analysis, signal acquisition must be started slightly before the top of the echo so signal processing can be performed exactly at the top of it. Powder spectra thus obtained can rapidly give us a global order parameter $\langle S_{\text{CD}} \rangle_{\text{chain}}$ for C-D bonds of aliphatic chains by computing first order spectral moments M_1 :

$$M_1 = \frac{\int_{-\infty}^{+\infty} (\omega - \omega_0) g(\omega - \omega_0) d\omega}{\int_{-\infty}^{+\infty} g(\omega - \omega_0) d\omega} \quad (\text{Eq.16})$$

$$\langle S_{\text{CD}} \rangle_{\text{chain}} = \frac{\sqrt{3}}{\pi A_Q} M_1 \quad (\text{Eq.17})$$

where ω is the NMR frequency, ω_0 is the Larmor frequency, $g(\omega - \omega_0)$ is the spectral lineshape and $A_Q = 167\text{kHz}$ (Burnett and Muller, 1971).

Plotting M_1 or $\langle S_{\text{CD}} \rangle_{\text{chain}}$ as a function of temperature is a powerful mean to assess the phase transition temperature of a sample or to detect any major difference in global order between samples. However, a finer spectral analysis is possible. Powder spectra are a sum of Pake doublets: one per kind of ^2H in a sample; and an optional isotropic peak centred around 0 ppm originating from small liposomes (about < 100 nm in diameter) and deuteriums from water (one usually uses deuterium-depleted water to avoid this unwanted signal). In a DMPC-d54 sample, there are as many Pake doublets as carbon positions along the acyl chains. As the sample is anisotropic, if θ is the angle between the local membrane plane and B_0 , a ^2H NMR spectrum is a sum of ^2H NMR subspectra for each value of θ . This forbids direct measurement of quadrupolar splittings. One must construct a ^2H NMR spectrum for only one value of θ : a de-pake-d spectrum. De-Pake-ing (McCabe and Wassail, 1997) is a calculation routine made specifically to compute such a depaked spectrum. Quadrupolar splittings $\Delta\nu_Q$ measured herein can be translated into local order parameters:

$$\Delta\nu_Q(\theta) = \frac{3}{2} A_Q \left| \frac{3\cos^2(\theta) - 1}{2} \right| S_{\text{CD}} \quad (\text{Eq.18})$$

Measurements of $\Delta\nu_Q$ are refined by spectral simulation, along with half-height widths, interpreted as $1/T_2$, and magnetically induced liposome deformation (Pott and Dufourc, 1995; Seelig, 1977). In our case, we are simply interested in getting S_{CD} values. The general procedure of ^2H static ssNMR analysis is described in (Figure 54).

Plotting $|2 \cdot S_{\text{CD}}|$ as a function of carbon positions along deuterated acyl chains informs us about lipid dynamics at the atomic level. (Grélard et al., 2013) describes a convenient way to compute membrane thicknesses from S_{CD} .

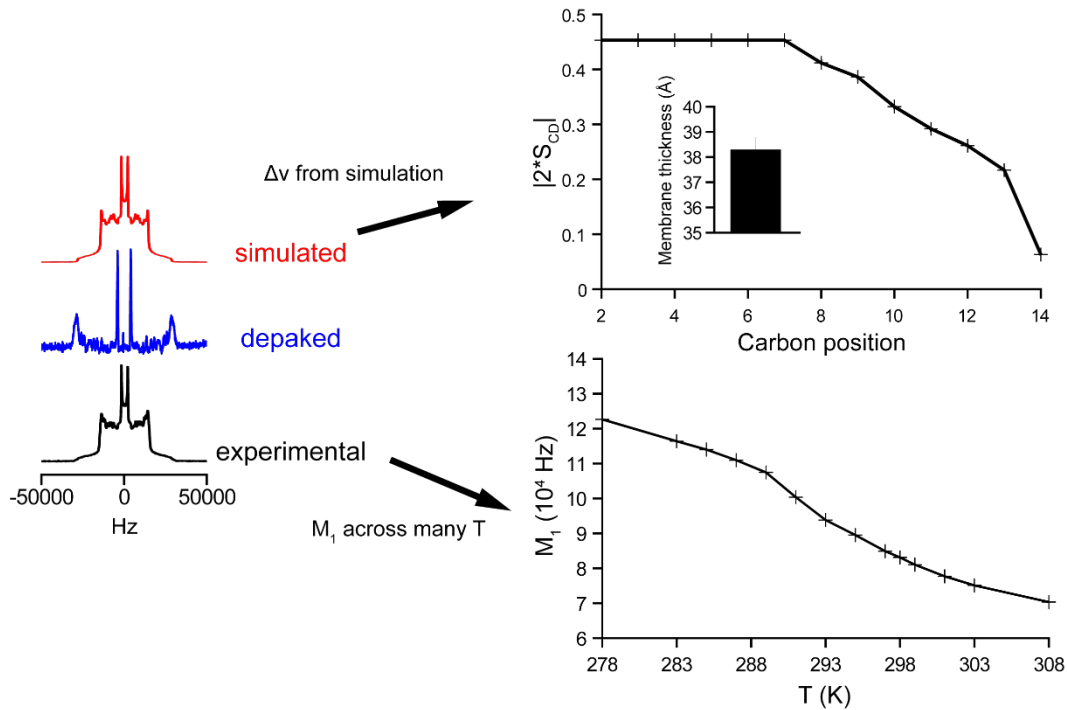


Figure 54

On data analysis of a ^2H static ssNMR experiment. *Left:* the experimental spectrum (black) is recorded. A depaked spectrum at angle θ is calculated (blue), allowing the measurement of quadrupolar splittings $\Delta\nu_Q$ as the difference, in Hz, between both peaks of a given Pake doublet. These $\Delta\nu_Q$ are refined by spectrum simulation (red). *Top right:* $\Delta\nu_Q$ are translated into local order parameters of C-D bonds S_{CD} as a function of carbon position along a deuterated acyl chain. From the here-obtained S_{CD} , a membrane thickness can be computed. *Bottom right:* computation of first spectral moments M_1 from experimental spectra over a range of temperatures T allows the monitoring of phase behaviour and thermotropism.

11. ssNMR to monitor lipid dynamics: ^{31}P ssNMR

^2H static ssNMR unlocks a wealth of structural information about the behaviour of lipids in membranes. Yet, another nucleus is also of interest: ^{31}P , for which data interpretation is significantly easier. The experiment consists of a Hahn echo on ^{31}P with ^1H decoupling. The resulting spectrum can be described by (Huster, 2014):

$$\omega = \omega_{\text{iso}} + \omega_{\text{aniso}} = \sigma_{\text{iso}} \gamma B_0 + \frac{\Delta}{2} (3\cos^2\theta - 1 - \eta \cos(2\alpha) \sin^2\beta) \quad (\text{Eq.19})$$

where α is a rotation along z (in the xy plane), β is a rotation along y (in the zx plane), η is the asymmetry parameter for a given parameter A such as $\eta = \frac{A_y - A_x}{A_z}$ and Δ is the anisotropy parameter. In practice, $\eta = 0$. The spectral lineshape informs on the orientation and the phase behaviour of the lipid bilayers (Figure 55). Spectral simulation allows to compute Δ , half-height widths, and magnetically-induced liposome deformation as described in (Pott and Dufourc, 1995).

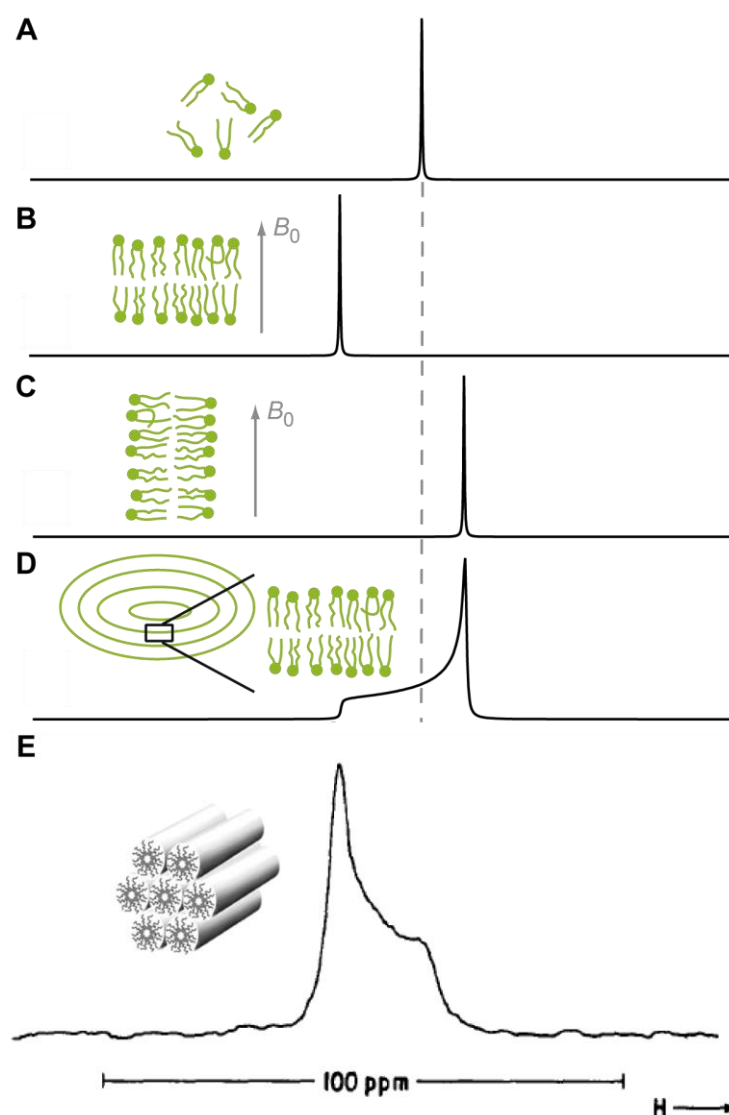


Figure 55

On the different lineshapes of a phospholipid by ^{31}P NMR. (A) In solution, there will be one single peak at $\delta_{\text{isotropic}}$. (B, C) In oriented bilayers, due to the sample's anisotropy, this peak will shift to higher values if the normal \mathbf{n} is parallel to \mathbf{B}_0 (B) or to lower values if \mathbf{n} is perpendicular to \mathbf{B}_0 (C). (D) In large vesicles, the angle θ between \mathbf{n} and \mathbf{B}_0 may take any value. The probability for θ to take a given value defines the line shape (Pott and Dufourc, 1995), which is characteristic of a lamellar phase: with some imagination, one could picture a chair with its back to the right side. (E) For hexagonal phases (here an inverted hexagonal lipid phase made of POPE at 20°C), a mirrored line shape is obtained: a chair with its back to the left side. The width of this line shape is halved compared to its lamellar counterpart (obtained at 5°C) (Cullis and de Kruffy, 1976). *Inlet:* phospholipids in an inverted hexagonal phase H_{II} (Koyanova and Tenchov, 2013). See figure lipid_phases for more details. (A-D) is modified from (Huster, 2014) and E is modified from (Cullis and de Kruffy, 1976).

In our case, we want to confirm that our samples are indeed in a lamellar phase: that we are indeed studying lipid bilayers. A minor isotropic contribution is also expected from small liposomes (roughly < 100 nm in diameter).

Article I

Coiled-coil oligomerization controls localization of the plasma membrane REMORINs

Denis Martinez, **Anthony Legrand**, Julien Gronnier, Marion Decossas, Paul Gouguet, Olivier Lambert, Mélanie Berbon, Loris Verron, Axelle Grélard, Véronique Germain, Antoine Loquet, Sébastien Mongrand, Birgit Habenstein

Journal of Structural Biology
2018
206:1, p12-19

This first article reports on a work that began before my master 2 internship. One of the main focus of this internship was to set up the production and purification of WT and truncated StREM1.3. The work of (Gronnier et al., 2017) had just been published, consecrating the first biophysical analysis of RemCA, and we wondered how the, then putative, coiled-coil oligomerisation (Raffaele et al., 2007a) would come into play regarding membrane interactions. Initial protein constructs had very low production yield: a few milligrams at best. We focused our efforts on the best candidate of all, REM₈₆₋₁₉₈, and, after a few optimisations, managed to produce and purify about 20 mg per litre of LB medium – which became 40 mg per litre later on. When we dialysed the eluted REM₈₆₋₁₉₈ to remove imidazole, we noticed the sample had turned turbid. Negative staining electron microscopy revealed a branched filament architecture. If such ordered structures were made possible by joined assembly of oligomerisation domains, we expected to observe a strong ¹³C-CP ssNMR signal originating from it. Therefore, we undertook a structural analysis of these filaments using ssNMR, cryoEM and molecular modelling. Taking into account previous data on StREM1.3's oligomeric state, we built a structural model of homotrimeric coiled-coil domains of REM₈₆₋₁₉₈ in filaments, in which the oligomerisation's driving force seemed to be hydrophobic contacts between conserved residues. Disruption of the coiled-coil in vivo yielded proteins with diminished PM targeting.

With the help of Mélanie Berbon and Dr Denis Martinez, and the participation of Loris Verron, I set up and performed the production and purification of REM₈₆₋₁₉₈, as well as the sample preparation and observation for electron microscopy. I also participated to the writing of the revised article.



Coiled-coil oligomerization controls localization of the plasma membrane REMORINs

Denis Martinez^a, Anthony Legrand^a, Julien Gronnier^{b,1}, Marion Decossas^c, Paul Gouguet^b, Olivier Lambert^c, Mélanie Berbon^a, Loris Verron^a, Axelle Grélard^a, Veronique Germain^b, Antoine Loquet^{a,*}, Sébastien Mongrand^{b,*}, Birgit Habenstein^{a,*}

^a Institute of Chemistry & Biology of Membranes & Nanoobjects (UMR5248 CBMN), IECB, CNRS, Université Bordeaux, Institut Polytechnique Bordeaux, All. Geoffroy Saint-Hilaire, 33600 Pessac, France

^b Laboratoire de Biogénèse Membranaire – UMR 5200 – CNRS, Université de Bordeaux, 71 Avenue Edouard Bourlaux, 33883 Villenave d'Ornon Cédex, France

^c Institute of Chemistry & Biology of Membranes & Nanoobjects (UMR5248 CBMN), CNRS, Université Bordeaux, Institut Polytechnique Bordeaux, 14 All. Geoffroy Saint-Hilaire, 33600 Pessac, France

ARTICLE INFO

Keywords:

REMORIN
Nanodomain
Membrane protein
Solid-state NMR
Protein filament

ABSTRACT

REMORINs are nanodomain-organized proteins located in the plasma membrane and involved in cellular responses in plants. The dynamic assembly of the membrane nanodomains represents an essential tool of the versatile membrane barriers to control and modulate cellular functions. Nevertheless, the assembly mechanisms and protein organization strategies of nanodomains are poorly understood and many structural aspects are difficult to visualize. Using an ensemble of biophysical approaches, including solid-state nuclear magnetic resonance, cryo-electron microscopy and *in vivo* confocal imaging, we provide first insights on the role and the structural mechanisms of REMORIN trimerization. Our results suggest that the formation of REMORIN coiled-coil trimers is essential for membrane recruitment and promotes REMORIN assembly *in vitro* into long filaments by trimer-trimer interactions that might participate in nanoclustering into membrane domains *in vivo*.

1. Introduction

Membrane nanodomains are dynamic cellular signalling platforms in the plasma membrane of a size of up to a several hundred nanometers that execute essential messaging events between cells and their surroundings (Lingwood and Simons, 2010). Selective dynamic recruitment of specific proteins mediates the formation of functional membrane sub-compartments, related to signal transduction (Grecco et al., 2011) and membrane trafficking (Simons and Sampaio, 2011). Clustering of proteins into membrane compartments is notably driven by protein-lipid and protein-protein interactions (Lingwood and Simons, 2010). A significant number of membrane proteins are involved in protein-protein interactions leading to homo- or hetero-oligomers (McBride et al., 2017). Protein homo- or hetero-oligomerization has been proposed to mediate protein clustering (Kasai and Kusumi, 2014; Suzuki et al., 2012). Moreover, specific nanoclustering of proteins can drive functional compartmentalization, i.e. distinct nanodomains can be enriched in distinct nanodomain-associated proteins (Bucherl et al., 2017; Jarsch et al., 2014). As a consequence of the

complexity of the system, i.e. proteins associated to membrane domains, insights into the structural and mechanistic organization of these proteins are sparse.

The REMORIN family consists of six phylogenetically distinguishable groups (Raffaele et al., 2007) of plant-specific nanodomain-organized proteins of the inner-leaflet of the plasma membrane (PM). Members of the REMORIN family carry out multiple functions related to biotic and abiotic stimuli (Jarsch and Ott, 2011; Lefebvre et al., 2010; Raffaele et al., 2009; Gui et al., 2014). In contrast to a highly variable N-terminal region, putatively implicated in protein-protein interactions (Marin et al., 2012; Toth et al., 2012), all REMORINs contain a conserved C-terminal region that encompasses a predicted coiled-coil domain (Bariola et al., 2004; Raffaele et al., 2007; Raymond et al., 1996), as well as a short membrane anchor domain (Gronnier et al., 2017; Perraki et al., 2012).

Coiled-coil domains are frequent motifs observed in proteins promoting multimerization towards homo- and also hetero-oligomers (Crick, 1953; Kohn et al., 1997; Lupas and Bassler, 2017). Proteins of the REMORIN family can oligomerize *in vivo* and *in vitro* into a

* Corresponding authors.

E-mail addresses: a.loquet@iecb.u-bordeaux.fr (A. Loquet), sebastien.mongrand@u-bordeaux.fr (S. Mongrand), b.habenstein@iecb.u-bordeaux.fr (B. Habenstein).

¹ Present address: Cyril Zipfel's Laboratory, The Sainsbury Laboratory, Norwich Research Park, Colney, Norwich NR4 7UH, United Kingdom.

filamentous state, possibly mediated by the coiled-coil domain (Bariola et al., 2004; Perraki et al., 2012). The *in vivo* functions of REMORIN oligomerization are not understood but they might include protein clustering to assure the nanodomain-mediated tasks. Nanoclustering of proteins is proposed to play an essential role in the segregation and functionalization of membrane rafts (Simons and Sampaio, 2011). Subtype Group 1 REMORINs form trimeric coiled-coil superstructures *in vitro* (Perraki et al., 2012) that lead to the formation of filamentous complexes (Bariola et al., 2004).

Our studies on the membrane anchoring mechanism and nanodomain targeting have recently revealed unconventional protein-membrane interactions mediated by the last 28 residues of the C-terminal region (REMORIN C-terminal anchor, REMCA) (Gronnier et al., 2017) that anchors to the surface of the plasma membrane without providing any transmembrane segment. The role of REMORIN oligomerization during this process remains obscure.

Magic-angle-spinning (MAS) solid-state nuclear magnetic resonance (ssNMR) and cryo-electron microscopy (cryo-EM) are both powerful emerging techniques useful to investigate assembled biomolecules in their native states. These techniques have the complementary characteristics of providing atomic data (reviewed for example in (Habenstein and Loquet, 2015; Loquet et al., 2013; Meier and Bockmann, 2015; Tycko and Wickner, 2013; Weingarth and Baldus, 2013)) and detailed shape/symmetry information (reviewed for example in (Bai et al., 2015; Earl et al., 2017; Jiang and Tang, 2017; Vonck and Mills, 2017)), respectively.

We have here taken advantage of several biochemical, biophysical and bioinformatic tools to decipher the role and the structure of REMORINs' assembly. We report that multimerization of REMORINs into trimers confers their membrane affinity and could participate in the nanoclustering into membrane domains. Establishing homogeneous filament formation of the protein core involved in oligomerization allowed us to combine ssNMR and cryo-EM to gain insights into the supramolecular architecture of oligomerized REMORIN filaments.

We can thus add another piece to the puzzle of the unconventional mechanism of membrane binding and nanodomain recruitment of the REMORIN family. The coiled-coil superstructures of the REMORINs hold functions resulting from the assembled complexes rather than from their monomeric subunits.

2. Material and methods

2.1. Expression, purification and filament formation of recombinant StREM1.3₈₆₋₁₉₈

E. coli BL21 (DE3) strains were transformed with a pET24-StREM1.3(86-198)-His₆ vector, containing the DNA encoding for residues 86–198 of REMORIN1.3 of *Solanum tuberosum*, and plated onto LB agar plates containing 30 g/mL kanamycin. A flask containing 10 mL of LB medium was inoculated with a single colony and incubated overnight at 37 °C under shaking at 200 rpm. The culture and expression of uniformly labelled ¹⁵N, ¹³C StREM1.3(86-198)-His₆ (hereafter called REM_{H6(86-198)}) was performed in M9 medium supplemented in ¹⁵NH₄Cl and ¹³C₆-D-glucose as nitrogen and carbon sources. The labelled M9 medium was inoculated with 2% (v/v) of the unlabelled LB preculture and incubated at 37 °C under shaking until the OD₆₀₀ reaches 0.7–0.8. At this stage, 1 mM IPTG was added to the culture for 20 h protein expression at 18 °C. Cells are then harvested by centrifugation (6000g, 10 min, 4 °C) and resuspended in the lysis buffer (20 mM HEPES, 150 mM NaCl, 20 mM imidazole, 1 mM PMSF, 1 tablet of Complete (Roche), 0.02% NaN₃, pH 7.4). Cells were lysed by sonication on ice for 3 min, 30% magnitude (30 s pulses, 30 s intervals). The suspension was centrifuged at 15 000g for 15 min at 4 °C to recover the supernatant. The affinity purification was realised with the Äkta Pure 25 HPLC system (GE Healthcare Life Sciences) using a His-trap HP affinity column equilibrated with 5 column volumes of washing buffer

(20 mM HEPES, 150 mM NaCl, 20 mM imidazole, 0.02% NaN₃, pH 7.4). The protein was eluted with a linear gradient from 0 to 100% of elution buffer (20 mM HEPES, 150 mM NaCl, 500 mM imidazole, 0.02% NaN₃, pH 7.4) which led to a final yield of 10 mg of pure ¹⁵N, ¹³C labelled protein per liter of culture (Fig. S1). Protein filaments were obtained by dialyzing overnight at room temperature the eluted sample against the assembly buffer (10 mM HEPES, 50 mM NaCl, 0.02% NaN₃, pH 7.4). Protein filaments of REM₍₈₆₋₁₉₈₎, i.e. REM_{H6(86-198)} lacking the N-terminal His₆-tag, were prepared as follows. Affinity purification was performed as described above using a different washing buffer (50 mM Tris, 100 mM NaCl, 0.5 mM EDTA, 1 mM DTT, 0.5 mM PMSF, 0.02% NaN₃, pH = 8.1) and elution buffer (50 mM Tris, 100 mM NaCl, 0.5 mM EDTA, 1 mM DTT, 0.5 mM PMSF, 500 mM imidazole, 0.02% NaN₃, pH = 8.1). REM_{H6(86-198)} contains a TEV cleavable His₆-tag at its N-terminus. Eluted proteins and the TEV protease were mixed in a 100:1 (w/w) ratio, incubated at 4 °C overnight under shaking and dialyzed against 1L of assembly buffer as described above to obtain REM₍₈₆₋₁₉₈₎ filaments.

For ssNMR studies, filaments of REM₍₈₆₋₁₉₈₎ lacking the N-terminal His₆-tag were prepared with a different protocol to enhance purity / yield of the sample. Expression and affinity purification was performed as described for filaments of uniformly ¹⁵N, ¹³C-labelled REM_{H6(86-198)}. Eluted protein fractions were pooled and adjusted to 0.5 mM EDTA and 1 mM DTT. Eluted proteins and TEV protease were mixed in a 100:1 (w/w) ratio, incubated at room temperature for 3 h under shaking and dialyzed overnight at 4 °C against the following buffer: 20 mM HEPES, 150 mM NaCl, 0.02% NaN₃, pH = 7.4. After dialysis, urea was added to the proteins up to 7 M urea and REM₍₈₆₋₁₉₈₎ was retrieved on a His-trap HP column with the following washing buffer: 20 mM HEPES 150 mM NaCl 7 M urea pH = 7.4; and elution buffer: 20 mM HEPES, 150 mM NaCl, 7 M urea, 500 mM imidazole, pH = 7.4. REM₍₈₆₋₁₉₈₎ was enriched in the flowthrough. Uncleaved REM_{H6(86-198)} and TEV protease, containing a His₆-tag, bound to the column and were then eluted. Fractions containing REM₍₈₆₋₁₉₈₎ were pooled and concentrated in an Amicon Ultra-15 centrifugal filter unit with MWCO = 3 kDa up to 0.8 mM, then dialyzed at room temperature against the assembly buffer (10 mM HEPES, 50 mM NaCl, 0.02% NaN₃, pH = 7.4). The sample was then incubated at 37 °C for 3 h under shaking then at room temperature for 7 days.

2.2. Coiled-coil prediction and sequence alignment

StREM1.3₍₈₆₋₁₉₈₎ coiled-coil domain was identified using the software COILS (Lupas et al., 1991) and helical wheel diagrams for coiled-coils were built with DrawCoil 1.0 (<http://www.grigoryanlab.org/drawcoil/>).

Arabidopsis REMORINs were retrieved from (Raffaele et al., 2007). Protein alignment was computed using Multiple Sequence Comparison by Log-Expectation (MUSCLE; (Edgar, 2004)) using BLOSUM62 matrix, an –sv profile scoring method with following parameters; Anchor spacing:32, diagonal break:1, diagonal length:24, diagonal margin:5, gap extension penalty:-1, gap open penalty:-12, hydro:5 and hydro factor1.2) through the JABAWS server (Troshin et al., 2011). Sequence alignments were rendered via the Jalview plugin (Waterhouse et al., 2009) (Fig. S2).

2.3. Microsomal purification and Western blot analyses

Microsomal and soluble fractions from *Nicotiana benthamiana* leaves expressing GFP-StREM1.3 constructs were prepared as described in Perraki et al., 2012. Each fraction was analyzed by western blot using antibodies against StREM1.3 (Raffaele et al., 2009).

2.4. In vivo confocal imaging

Live cell imaging was performed using a Leica SP5 confocal laser

scanning microscopy system (Leica, Wetzlar, Germany) equipped with Argon, DPSS and He-Ne lasers and hybrid detectors. Two days after agro-infiltration *N. benthamiana* leaves samples were transferred between a glass slide and a cover slip in a drop of water. GFP fluorescence was observed with excitation wavelengths of 488 nm and emission wavelengths of 490 to 550 nm. Experiments were performed using strictly identical confocal acquisition parameters (e.g. laser power, gain, zoom factor, resolution, and emission wavelengths reception), with detector settings optimized for low background and no pixel saturation. Pseudo-colored images were obtained using the “Red hot” look-up-table (LUT) of Fiji software (<http://www.fiji.sc/>).

2.5. TEM and cryo-EM

REM_{H6(86-198)} filaments were applied to previously glow-discharged carbon-coated copper 300 mesh grids and stained with a 2% uranyl acetate (w/v) solution. REM_{H6(86-198)} filaments were also prepared for cryo-EM. For the latter, lacey carbon copper grid were submitted to a standard glow discharge procedure and flash-frozen into a liquid ethane bath using EM GP (Leica). Specimens were observed under low-dose conditions using a cryo holder (Gatan, USA). Observations were performed with a FEI Tecnai F20 electron microscope operating at 200 kV and images were acquired using a digital 2 k x 2 k USC1000 camera (GATAN). Measurements of the repetitive patterns were calculated on FFT images of 10 selected areas. REM₍₈₆₋₁₉₈₎ filaments lacking the N-terminal His₆-tag were stained and applied to carbon-coated copper grids as described above. TEM images were recorded under low-dose conditions on a FEI CM120 120 kV FEI electron microscope using a Gatan USC1000 2 k X 2 k camera.

3. 3D modelling

The 3D model of StREM1.3₍₁₁₇₋₁₆₆₎ was constructed by homology using the server I-TASSER (<https://zhanglab.ccmb.med.umich.edu/I-TASSER/>) (Zhang, 2008). Coiled-coil trimers were assembled using the SymmDock server (Schneidman-Duhovny et al., 2005) and a supplementary energy minimization step was performed with Yasara (<http://www.yasara.org/minimizationserver.htm>) (Krieger et al., 2009).

3.1. Solution NMR spectroscopy

¹H, ¹⁵N SOFAST-HMQC (band-Selective Optimized-Flip-Angle Short-Transient Heteronuclear Multiple-Quantum Correlation (Schanda et al., 2005)) experiment was carried out at 313 K on a protein sample containing 200 μM REM₍₈₆₋₁₉₈₎, 20 mM HEPES, 150 mM NaCl, 0.02% Na₃N, pH 7.4. Spectra were recorded on a Bruker Avance Neo 700 MHz spectrometer equipped with a 5 mm TXI 1H/13C/15N/2H probe. The spectrum was acquired with 512 scans, 128 and 2048 complex points in F1 and F2 dimensions, respectively. Frequencies were calibrated according to DSS signal. The NMR data were processed using the TOPSPIN 4 software (Bruker Biospin).

3.2. Solid-state NMR spectroscopy

MAS solid-state NMR experiments were performed on a 600 MHz (REM_{H6(86-198)}) and 800 MHz (REM₍₈₆₋₁₉₈₎) ¹H Larmor frequency spectrometer (Bruker Biospin) using 3.2 mm MAS probes. Solid-state NMR rotors were filled with 10 mg of REM_{H6(86-198)} or (REM₍₈₆₋₁₉₈₎) filaments and span at 11 kHz for spectra acquisition. Sample temperature was set between 0 and 5 °C according to DSS signal used as an internal reference (Bockmann et al., 2009). A ramped CP with a 1 ms (REM_{H6(86-198)}) and 0.7 ms (REM₍₈₆₋₁₉₈₎) contact time was used for the ¹H-¹³C cross-polarization (CP) transfer. An acquisition time of 20 ms and 2 k scans were used for 1D ¹H-¹³C CP. For the 2D spectrum, the ¹³C-¹³C polarization transfer was performed with proton-driven spin diffusion (PDSF) applied for a mixing time of 50 ms to detect intra-residue

correlations. Proton decoupling during the acquisition was achieved using a SPINAL-64 decoupling sequence (Fung et al., 2000). Acquisition times of 20 ms and 6.5 ms (REM_{H6(86-198)}), 20 ms and 7.5 ms (REM₍₈₆₋₁₉₈₎) were chosen for the direct and indirect dimensions, respectively. The total number of scans was 960 and 640 for a total experiment time of 6 and 7 days approximately, for REM_{H6(86-198)} and REM₍₈₆₋₁₉₈₎ respectively. Secondary chemical shifts were calculated using random coil chemical shifts described by Wang and Jardetzky (Wang and Jardetzky, 2002). All data were processed using Topspin 3.2 (Bruker Biospin) and analyzed with CCPNMR Analysis software (Skinner et al., 2016). Backbone and sidechains ¹³C chemical shifts were predicted from the protein 3D coordinates of the coiled-coil model spanning residues 117–166 using the software ShiftX2 (Han et al., 2011).

4. Results

4.1. REMORIN coiled-coil trimerization promoted by the highly-conserved C-terminal is essential for membrane targeting

REMORINs share a highly variable N-terminal domain in terms of length and conservation of the primary sequence and a highly conserved C-terminal region (Bariola et al., 2004; Raffaele et al., 2007; Reymond et al., 1996). Previous work on a *Solanum tuberosum* REMORIN of group 1 isoform 3 (StREM1.3) showed that the C-terminal region encompasses two distinct domains (Fig. 1A): the short C-terminal anchor [171–198] (Perraki et al., 2012) specifically binds plasma membrane phosphatidylinositol 4-phosphate (PI4P) and mediates StREM1.3 PM nanodomain organization (Gronnier et al., 2017), while the region [86–170] contains a segment predicted to be implicated in the oligomerization of the protein (Bariola et al., 2004; Perraki et al., 2012). The latter domain displays a strong propensity to form a coiled-coil super helix (Fig. 1B). In such structures, alpha helical monomers wind around each other to optimize protein-protein contacts and stabilize the multimer assembly (Crick, 1953; Kohn et al., 1997). All the members of the REMORIN family share these predicted structural properties and have strong sequence similarities between their C-terminal regions (Raffaele et al., 2007). We compared and analyzed the sequences of StREM1.3 with 5 *Arabidopsis thaliana* REMORINs from different groups (Groups 1, 3, 4, 5 and 6) to identify conserved elements that might be essential to the formation of coiled-coil super-helices (Figs. 1B and S2). This comparison revealed a sequence similarity of 59% with the most divergent, i.e. AtREM3.1, and 94% sequence similarity with AtREM1.3. Based on the chemical properties of the amino acids, we identified three candidates that could potentially be involved in the helix-helix interfaces within the coiled-coil domain (L126, L137 and L155). The hydrophobic character of the residues at these three positions is highly conserved between the different members of the REMORIN family. Fig. 1C shows the coiled-coil helical wheel at position L155 for the StREM1.3 trimer. L152 and L155 form a hydrophobic patch, which stabilizes the coiled-coil structure. Polar and charged residues (H156, K157 and E158) are exposed either to the solvent or to an opposite charge residue, again potentially stabilizing the structure.

We have recently reported structural insights into the role of the C-terminal peptide REM-CA during PM anchoring and nanodomain organization (Gronnier et al., 2017) and we here aimed at testing the impact of StREM1.3 trimerization on its membrane-binding properties. Based on the sequence analyses, we introduced Prolines, in order to destabilize the coiled-coil superstructure (Chang et al., 1999), at positions L126, L137 and L155. *In vivo* confocal imaging visualized the subcellular localization of GFP-StREM1.3, GFP-StREM1.3^{L126P}, GFP-StREM1.3^{L137P} and GFP-StREM1.3^{L155P} (Fig. 1D). As expected, the wild-type protein localized exclusively at the plasma membrane. However, for all mutants, fluorescence was detected in the cytosol, which indicates that the protein is no longer strictly associated with the plasma membrane. To further confirm this observation we performed cell fractionation of tissues expressing either GFP-StREM1.3, GFP-

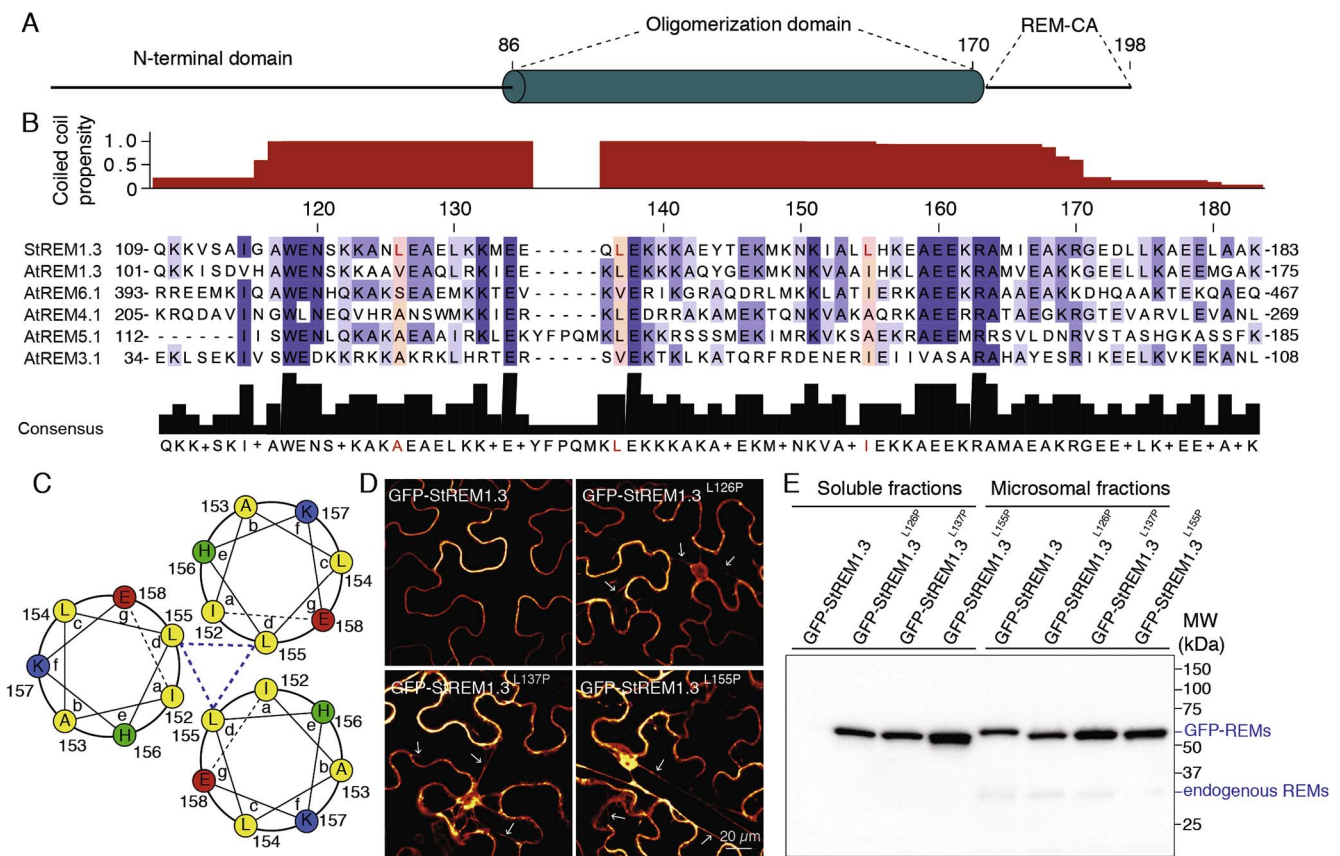


Fig. 1. Mutations of conserved amino acid motifs in the coiled coil impairs PM targeting. (A) Domain organization in StRem1.3. (B) Coiled-coil propensity of StRem1.3C-terminal region (109–183) realised with COILS. Sequence alignment of REMORIN homologs in *S. tuberosum* and *A. thaliana*. Protein sequences are ranked according to the conservation score. Hydrophobic residues potentially involved in helix contacts are highlighted in red. Conserved amino acids between the different REMORINs are shown in blue (dark blue for the most conserved to light blue for the less conserved). (C) Helical wheel corresponding to a coiled-coil trimer centred to the 152–158 region. Residues type are colored as follows: yellow, hydrophobic; blue, basic; red, acid; green, polar. Wheels were drawn using DrawCoil 1.0. (D) Confocal images presenting secant views of *N. benthamiana* epidermal cells expressing GFP-StREM1.3, GFP-StREM1.3^{L126P}, GFP-StREM1.3^{L137P}, GFP-StREM1.3^{L155P}, transiently expressed in tobacco epidermal cells. Scale bars: 20 μm. (E) Tobacco leaf cells expressing each construct were fractionated into soluble (sol.) and microsomal (m) compartments by centrifugation. Proteins were analyzed by Western blot with antibodies against StREM1.3. The protein loading control is presented in Fig. S8.

StREM1.3^{L126P}, GFP-StREM1.3^{L137P}, or GFP-StREM1.3^{L155P} (Fig. 1E). Western blotting with anti-REM antibody (Raffaele et al., 2009) clearly confirmed that StREM1.3 is only found in the microsomal fraction whereas the three mutants are visible in both microsomal and soluble fractions. Altogether, these observations suggest that oligomerization might be required for REMORINs' PM localization.

4.2. Building blocks of assembled REM_{H6(86-198)} form organized fibers as revealed by TEM and cryo-EM

To investigate the assembly features and the structure of REMORIN oligomers, we focused on the conserved C-terminal region (residues 86 to 198), including the coiled-coil domain that most likely is responsible for the assembly (Bariola et al., 2004), and REMCA. We expressed and purified StREM1.3C-terminal moiety (REM_{H6(86-198)}) in *E. coli*. After the purification, we recovered different fractions containing REM_{H6(86-198)} protein and analyzed them with gel-electrophoresis under denaturing conditions (Fig. S1). The fractions containing pure REM_{H6(86-198)} were pooled and the self-assembly was triggered by dialysis. In order to provide an in-depth analysis of the mesoscopic shape as well as structural features of the assembly, we chose several biophysical techniques including negative staining transmission EM (TEM), cryo-EM and SSNMR. TEM and cryo-EM gave us first insights into the morphology of REM_{H6(86-198)} assemblies (Fig. 2A and B, respectively), revealing ordered REMORIN fibers with a repetitive pattern. The repeating elements are propagated both horizontally and vertically. The periodicities

correspond to 13 nm along and approximately 5 nm perpendicular to the fiber axis. Interestingly, along the fibers, their width can vary (Fig. S3) and their endings are irregular. The variable width engendering irregular endings of the fibers suggests an association and juxtaposition of thin filaments (arrow Fig. 2C). This implies that the thin filaments self-assemble into large fibers in a constructive manner leading to the repetitive patterns.

Importantly, filaments of REM₍₈₆₋₁₉₈₎ without the N-terminal His₆-tag do not show specific lateral association (Fig. 2D). However, the SSNMR data on REM₍₈₆₋₁₉₈₎ lacking the His₆-tag clearly confirm that the molecular structure of REM₍₈₆₋₁₉₈₎ in laterally associated (REM_{H6(86-198)}) and single filaments (REM₍₈₆₋₁₉₈₎) does not vary essentially, because the spectral fingerprint is conserved between both filaments (Fig. S4). The lateral association of REM_{H6(86-198)} filaments allows for the analysis of the repetitive patterns promoted by the His₆-tag, indicative of the assembly features.

4.3. The REMORIN coiled-coil domain gains a partially well-organized structure upon trimerization

To decipher the molecular basis underlying the filament formation, we performed a 3D modelling of the StREM1.3 coiled-coil domain based on sequence homology using the I-TASSER server (Zhang, 2008). The modelling was restrained to the region with the higher coiled-coil propensity [117–166] defined by the software COILS (Lupas et al., 1991). The 3D model converged to a regular alpha helix composed of

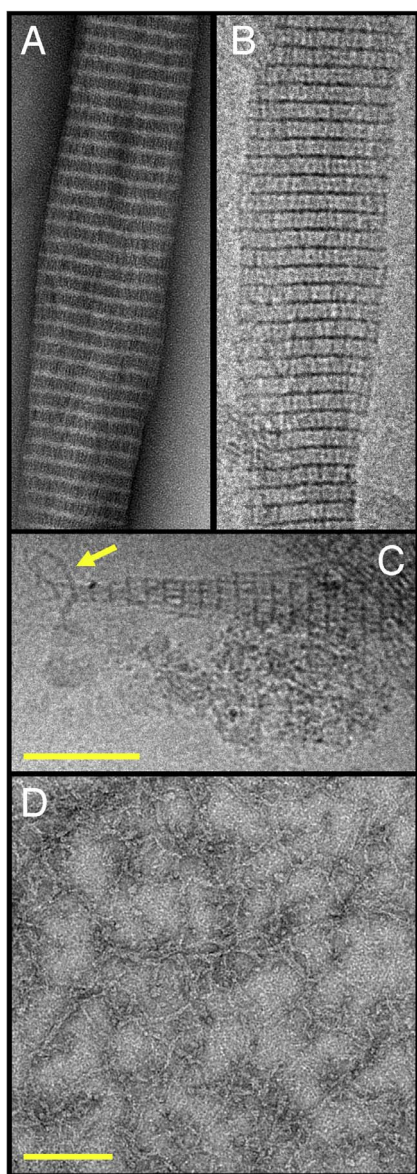


Fig. 2. Electron micrographs of REM_{H6(86-198)} and REM₍₈₆₋₁₉₈₎ filaments. (A) Negative staining TEM and (B) cryo-EM show filaments of REM_{H6(86-198)} with two repetitive patterns perpendicular to each other. Width and thickness of fibers vary over the length of the filaments. (C) CryoEM of the sharp extremity of a REM_{H6(86-198)} fiber shows similar repetitive motifs. Scale Bar of (A), (B) and (C) is the same: 100 nm (D) Negative-staining TEM micrograph of thin filaments of REM₍₈₆₋₁₉₈₎, lacking the N-terminal His6-tag. Scale Bar: 100 nm.

residues 133 to 166. REM₍₁₁₇₋₁₆₆₎ monomers were assembled into a trimer by geometry based docking using the SymmDock server (Schneidman-Duhovny et al., 2005). Fig. 3A shows the trimeric coiled-coil structure of the REMORIN obtained *in silico*. A patch composed of hydrophobic residues, which point towards the trimer core, defines the interface between the three monomers and electrostatic interactions stabilize the architecture.

4.4. SSNMR data on REM_{H6(86-198)} filaments support the 3D model of the coiled-coil domain and identify a short segment in β -strand conformation

To determine whether the 3D model obtained *in silico* reflects the structure adopted by REM_{H6(86-198)} in the filaments, we analyzed ¹⁵N, ¹³C-labelled filaments using liquid and solid-state NMR. Solution NMR analysis revealed that REM_{H6(86-198)} is unstructured in solution and adopts a 3D fold only upon assembly into multimeric complexes

(Fig. S5). SSNMR is an emerging technique providing atomic structural information on molecular assemblies in their native states. We conceived a protocol to successfully produce, purify and assemble suitable quantities (~10 mg) of ¹⁵N- and ¹³C-labelled REM_{H6(86-198)} *in vitro* to conduct multidimensional MAS SSNMR on the REMORIN in its filamentous state. The very intense signal observed in a one-dimensional ¹H-¹³C cross-polarization spectrum revealed the presence of a rigid core in the structure of the assembled proteins (Fig. S6). A two-dimensional ¹³C-¹³C PDS (proton-driven spin diffusion), Fig. 3B, acquired with a short mixing time (50 ms) set up to detect intra-residues ¹³C-¹³C correlations, reveals the SSNMR fingerprint of the REM_{H6(86-198)} structure in filaments. The intense signals again indicate that the filaments contain a rigid protein core and the appearance of well-resolved individual peaks points to a well-defined atomic structure adopted by the monomers composing the assembly. Our *in silico* 3D model of REM₍₁₁₇₋₁₆₆₎ suggests that the REMORIN monomers oligomerize into α -helical coiled-coil trimers promoted by the coiled-coil domain. Based on the 3D model, we used the ShiftX2 software (Han et al., 2011) to predict the expected protein ¹³C chemical shifts for the coiled-coil domain REM₍₁₁₇₋₁₆₆₎ and reported them on the 2D ¹³C-¹³C SSNMR spectrum recorded on REM_{H6(86-198)} filaments (Fig. 3B, red crosses, left spectrum). The majority of the predicted chemical shifts match well with the experimentally observed signals. This strongly supports the model of a α -helical tertiary fold in the filament core, reflecting the coiled-coil domain. However, a non-negligible part of the signals in the 2D spectrum remain unassigned and do not appear in spectral regions where signals from α -helical structural segments are located (Fig. 3B, blue crosses, right spectrum). Among them, a detailed analysis was possible for Thr, Glu, Lys, Val, Ser, Leu, Ile, and Ala amino acids for which the resonances reflecting β -strand secondary structures are isolated in the spectrum. By comparing these residue-specifically assigned amino acids with the primary sequence of REM_{H6(86-198)} we identified the unique motif in the REM_{H6(86-198)} primary sequence (T₈₆-EKRVSLIKA-A₉₅) adjacent to the coiled-coil region. The theoretical sequential peaks are all visible even if their assignments remain ambiguous. The local conformation of these residues was identified via their secondary chemical shifts that reflect a β -strand conformation where negative values were obtained. The unique amino acid composition of T₈₆-EKRVSLIKA-A₉₅ and the clear β -strand conformation of the identified residues indicate the occurrence of a short β -segment at this location (Fig. 3D). The assignment of the R89 spin system remained ambiguous because of the important peak overlap in this spectral region. Likewise, the region around T₈₆-A₉₅ region might be extended but the chemical shifts of these residues could not be identified due to spectral overlap.

4.5. Cryo-EM data suggest that trimeric coiled-coil REM_{H6(86-198)} arranges itself as aligned building blocks into filaments

Cryo-EM micrographs revealed the repetitive motifs in the REM_{H6(86-198)} filaments and the spectral resolution we obtained on the filaments allowed for the detailed measurement of their dimensions (Fig. 4A). The longitudinal repetitions are characterized by 13 nm in length with a width of approximately 5 nm. The dimensions of the 3D model of the REM₍₁₁₇₋₁₆₆₎ coiled-coil trimer, with 8 nm in length and a width of ~1.5 nm without side-chains (Fig. 4A), tie in the distances obtained on the electron micrograph of the REM_{H6(86-198)} fibers. The 3D model of the coiled-coil domain illustrates the tertiary fold of the REM₍₁₁₇₋₁₆₆₎ with the region spanning 132–166 showing well-defined α -helices, slightly twisted to allow protein-protein contacts at positions 155 and 137 (Fig. 4A, B). The segment 117–131 is less ordered than expected for the coiled-coil domain but displays lower structure accuracy for the generated model (Fig. S7). Fig. 4B shows an example of close hydrophobic contacts between Leucine residues in the trimer at the position 155, essential for trimer stability.

Based on the ensemble of our results we propose a cartoon model of the REM_{H6(86-198)} building block in filaments, encompassing a coiled-

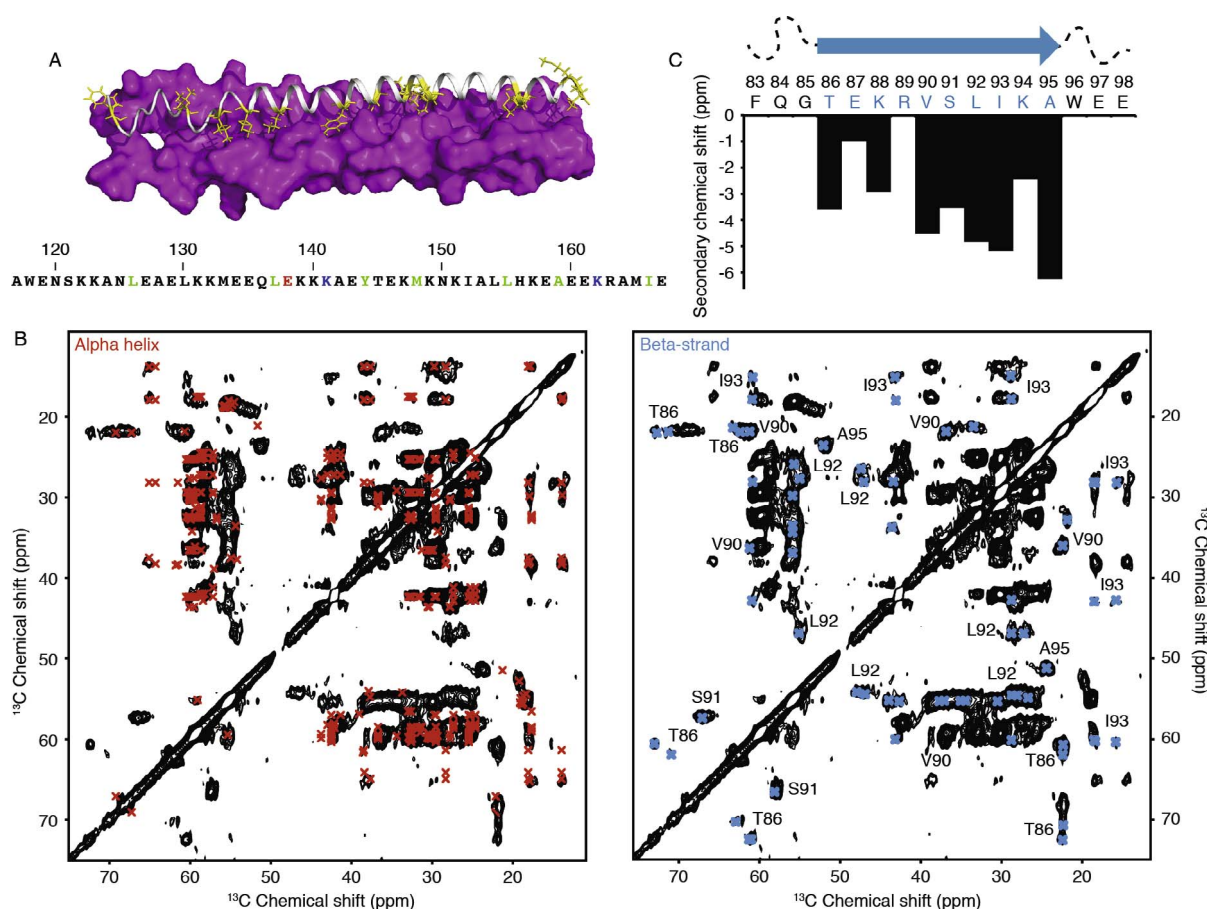


Fig. 3. 3D model and solid-state NMR of REM_{H6(86-198)} filaments. (A) 3D model of StREM1.3 coiled-coil domain predicted with I-TASSER server (Zhang, 2008). Two monomers in magenta are represented in surface mode and the third monomer with cartoon. All the hydrophobic side chains in the monomer are colored in yellow. Residue contacts identified between in StREM1.3 coiled-coil domain are highlighted on the primary sequence (green, hydrophobic contacts; red and blue, electrostatic contacts). (B) 2D PDSD ^{13}C - ^{13}C spectrum of REM_{H6(86-198)} filaments (50 ms mixing time) showing back-calculated ^{13}C chemical shifts with ShiftX2 from the 3D model (left spectrum, red crosses) and assigned chemical shift from β -strands (right spectrum, blue crosses). (C) Secondary chemical shift $\Delta\delta\text{C}\alpha$ - $\Delta\delta\text{C}\beta$ the T86-E87-K88-R89-V90-S91-L92-I93-K94-A95 amino acid segment in REM_{H6(86-198)}, revealing the presence of a β -strand segment.

coil domain, in which the three membrane-affinity impairing mutations are localized, flanked by a short β -strand and supposedly two segments with less well-defined structures on both sides (Fig. 4A). The N-terminal ending of the coiled-coil domain contains a region of less defined structure and a stretch of 10 amino acids, mainly composed of hydrophobic residues constituting a regular β -strand, whereas the C-terminal REM-CA seems to adopt a condensed, unstructured form. The two endings account for the regions of dense protein concentration in the EM micrographs. The proximity of the β -strands could stabilize the trimer through an inter-strand hydrogen-bonding network.

5. Discussion

Our results have demonstrated an unexpected impact of REMORIN oligomerization via the coiled-coil domain on membrane affinity and we therefore decided to tackle the structure of this best-characterized nanodomain-associated plant protein supramolecular assembly.

By using a coiled-coil prediction server, we identified the region with the highest propensity of forming a coiled-coil and we singled out three hydrophobic residues that could stabilize the trimeric architecture, L126, L137 and L155. *In vivo* monitoring of the localization of REMORIN and of the three substitution mutants by confocal microscopy showed that all three mutations strongly impair membrane affinity suggesting that trimer formation is correlated with REMORIN-membrane interactions and that a cooperative effect between REMORINs plays an important role in membrane binding.

Full-length REMORINs form filaments, which were proposed to arise from interactions between coiled-coil trimers of the conserved C-terminal region (Bariola et al., 2004). We show that REM₍₈₆₋₁₉₈₎, lacking the highly variable N-terminal region, also assembles into well-organized filaments. When the N-terminal His₆-tag of REM₍₈₆₋₁₉₈₎ is conserved, i.e. REM_{H6(86-198)}, the filaments arrange into fibers that vary in width over the filament length and end in a thin architecture. This behaviour is consistent with the association or dissociation of trimeric building blocks that build a strong intermolecular network of weak interactions. Importantly, these fibers show very homogeneous repetitive patterns in electron micrographs that enable the analysis of the molecular building blocks in the filaments.

Creating an *in silico* 3D model of the coiled-coil domain allowed us to visualize the underlying 3D structures, to identify stabilizing hydrophobic and electrostatic contacts and to estimate the dimensions of such coiled-coil trimer. In this model, the three Leucines are located in essential positions, explaining the destabilizing effect and membrane-affinity loss of Proline mutations, L126P, L137P and L155P.

To corroborate our working model of trimeric coiled-coil building units, we performed SSNMR on REM_{H6(86-198)} and REM₍₈₆₋₁₉₈₎ filaments, obtaining atomic structural data on the intact filaments. Based on the 3D trimeric model, we compared predicted with observed SSNMR chemical shifts, validating the hypothesis of trimeric coiled-coil units that associate laterally and, furthermore, residue-type and sequential assignments revealed longitudinal interactions between the trimers involving a short β -strand and less well-ordered condensed

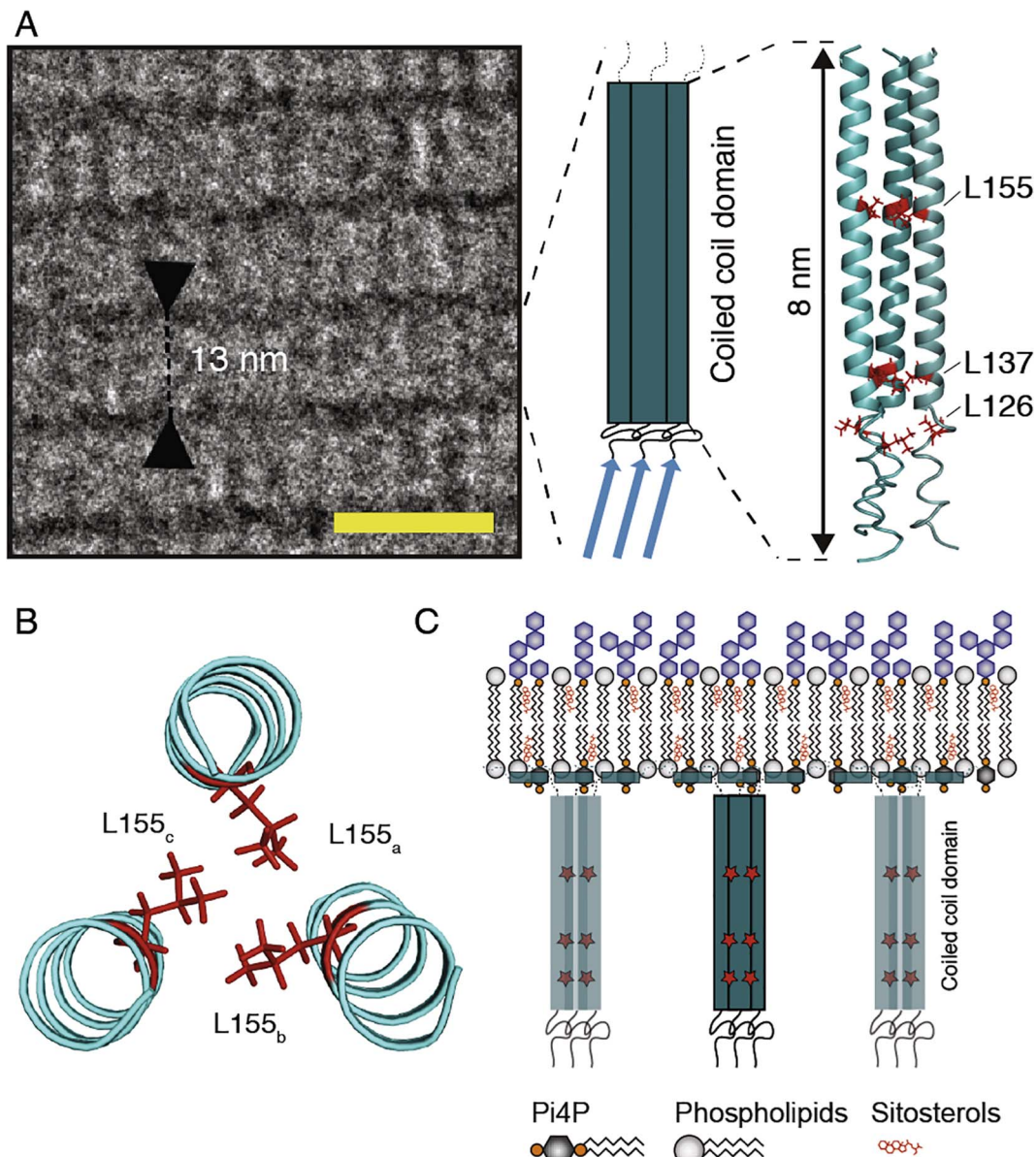


Fig. 4. 3D architecture of REM₍₈₆₋₁₉₈₎ inside the filaments and associated to PM nanodomains. (A) Cryo-EM micrograph of REM_{H6(86-198)} fibers depicts 13 nm horizontal repetitive patterns corresponding to a regular assembly of REM_{H6(86-198)}. Scale bar: 20 nm. Schematic representation of REM_{H6(86-198)} structure inside the filament (β -strands are represented as blue arrows and α -helices as rectangles) and 3D structural model of REM₍₈₆₋₁₉₈₎ coiled-coil domain. (B) Example of protein contacts inside the coiled coil domain. α -helices are represented in cartoon and Leucine sidechains in sticks. (C) Schematic representation of REM₍₈₆₋₁₉₈₎ structure when associated to the PM nanodomains. Red stars represent point mutations, which impair the membrane localization of StREM1.3. α -helices are represented as rectangles. The C-terminal membrane anchor REM-CA contains a short α -helix. Point mutations for *in vivo* confocal imaging experiments are highlighted in red.

segments. The dimensions of the building blocks obtained from cryo-EM micrographs are compatible with the trimeric REM_{H6(86-198)} coiled-coil units, derived from the 3D model. Combining the structural data from SSNMR, the *in silico* model, and cryo-EM, we propose a cartoon model that reflects the architecture in REM_{H6(86-198)} and REM₍₈₆₋₁₉₈₎ filaments (Fig. 4A). Furthermore, incorporating the recently proposed model of the REM-CA peptide structure during nanodomain formation and the data obtained on the role and structure of coiled-coil trimers, we propose a cartoon model for the nanodomain-associated REM₍₈₆₋₁₉₈₎ (Fig. 4C). The coiled-coil trimers are stabilized by intermolecular protein-protein interactions including the three Leucine-Leucine contacts of residues 126, 137 and 155 (Fig. 4C, red stars).

6. Conclusions

Protein organization into membrane domains relies on complex and

scarcely in-detail explored structural mechanisms, involving lipid-protein and protein-protein interactions (Simons and Sampaio, 2011). Considered as genuine PM nanodomain-organized proteins in plants, REMORINs attach to the PM and concentrate in nanodomains by an original mechanism via the C-terminal anchor, REM-CA (Gronnier et al., 2017). We here report that REM-CA alone is not sufficient and responsible for membrane targeting. We show that the conserved trimerization region plays a central role and we investigated the structure of this region by conceiving a protocol to obtain filaments of mesoscopic scale that we analyzed by various techniques. The obtained data and proposed cartoon model might also reveal other modes of interaction of REMORINs during oligomerization such as β -strand hydrogen bonding. However, the interactions between trimer coiled-coil domains promoting the filament assembly might reflect interactions that favour the highly specific nanoclustering occurring between REMORINs of the same family (Jarsch et al., 2014). Our findings open an avenue to

understanding the complex nanodomain-targeting mechanisms of REMORIN proteins based on the combination of SSNMR and cryo-EM and aim at contributing to the comprehension of molecular strategies employed by membrane-domain proteins to perform their cellular functions.

Acknowledgments

We acknowledge the financial support by the ANR (ANR-13-PDOC-0017-01 to B.H. and ANR-14-CE09-0020-01 to A.L.), the IdEx Bordeaux “Investments for the future” (ANR-10-IDEX-03-02 to B.H.) and PEPS to B.H. and S.M., the European Research Council (ERC-2015-StG GA no. 639020 to A.L.) and the CNRS (IR-RMN FR3050). A.L. is supported by the Ministère de l'Enseignement Supérieur et de la Recherche, France (MERS, doctoral grants). TEV protease was a gift from Lionel Beaurepaire and the work has benefited from the facilities and expertise of the Biophysical and Structural Chemistry platform (BPCS) at IECB, CNRS UMS3033, Inserm US001, Bordeaux University <http://www.iecb.u-bordeaux.fr/index.php/fr/plateformestecnologiques>.

Appendix A. Supplementary data

Supplementary data associated with this article can be found, in the online version, at <http://dx.doi.org/10.1016/j.jsb.2018.02.003>.

References

- Bai, X.C., McMullan, G., Scheres, S.H., 2015. How cryo-EM is revolutionizing structural biology. *Trends Biochem. Sci.* 40, 49–57.
- Bariola, P.A., Retelska, D., Stasiak, A., Kammerer, R.A., Fleming, A., Hijri, M., Frank, S., Farmer, E.E., 2004. Remorins form a novel family of coiled coil-forming oligomeric and filamentous proteins associated with apical, vascular and embryonic tissues in plants. *Plant Mol. Biol.* 55, 579–594.
- Bockmann, A., Gardiennet, C., Verel, R., Hunkeler, A., Loquet, A., Pintacuda, G., Emsley, L., Meier, B.H., Lesage, A., 2009. Characterization of different water pools in solid-state NMR protein samples. *J. Biomol. NMR* 45, 319–327.
- Bucherl, C.A., Jarsch, I.K., Schudoma, C., Segonzac, C., Mbengue, M., Robatzek, S., MacLean, D., Ott, T., Zipfel, C., 2017. Plant immune and growth receptors share common signalling components but localise to distinct plasma membrane nanodomains. *Elife* 6.
- Chang, D.K., Cheng, S.F., Trivedi, V.D., Lin, K.L., 1999. Proline affects oligomerization of a coiled coil by inducing a kink in a long helix. *J. Struct. Biol.* 128, 270–279.
- Crick, F.H., 1953. The packing of [alpha]-helices: simple coiled-coils. *Acta Cryst.* 6, 689–697.
- Earl, L.A., Falconieri, V., Milne, J.L., Subramaniam, S., 2017. Cryo-EM: beyond the microscope. *Curr. Opin. Struct. Biol.* 46, 71–78.
- Edgar, R.C., 2004. MUSCLE: multiple sequence alignment with high accuracy and high throughput. *Nucleic Acids Res.* 32, 1792–1797.
- Fung, B.M., Khitrin, A.K., Ermolaev, K., 2000. An improved broadband decoupling sequence for liquid crystals and solids. *J. Magn. Reson.* 142, 97–101.
- Grecco, H.E., Schmick, M., Bastiaens, P.I., 2011. Signaling from the living plasma membrane. *Cell* 144, 897–909.
- Gronnier, J., Crowet, J.M., Habenstein, B., Nasir, M.N., Bayle, V., Hosy, E., Platré, M.P., Gouguet, P., Raffaele, S., Martinez, D., Grelard, A., Loquet, A., Simon-Plas, F., Gerbeau-Pissot, P., Der, C., Bayer, E.M., Jaillais, Y., Deleu, M., Germain, V., Lins, L., Mongrand, S., 2017. Structural basis for plant plasma membrane protein dynamics and organization into functional nanodomains. *Elife* 6.
- Gui, J., Liu, C., Shen, J., Li, L., 2014. Grain setting defect1, encoding a remorin protein, affects the grain setting in rice through regulating plasmodesmatal conductance. *Plant Physiol.* 166, 1463–1478.
- Habenstein, B., Loquet, A., 2015. Solid-state NMR: An emerging technique in structural biology of self-assemblies. *Biophys. Chem.*
- Han, B., Liu, Y., Ginzinger, S.W., Wishart, D.S., 2011. SHIFTX2: significantly improved protein chemical shift prediction. *J. Biomol. NMR* 50, 43–57.
- Jarsch, I.K., Ott, T., 2011. Perspectives on remorin proteins, membrane rafts, and their role during plant-microbe interactions. *Mol. Plant Microbe Interact* 24, 7–12.
- Jarsch, I.K., Konrad, S.S., Stratil, T.F., Urbanus, S.L., Szymanski, W., Braun, P., Braun, K.H., Ott, T., 2014. Plasma membranes are subcompartmentalized into a plethora of coexisting and diverse microdomains in arabidopsis and nicotiana benthamiana. *Plant Cell* 26, 1698–1711.
- Jiang, W., Tang, L., 2017. Atomic cryo-EM structures of viruses. *Curr. Opin. Struct. Biol.* 46, 122–129.
- Kasai, R.S., Kusumi, A., 2014. Single-molecule imaging revealed dynamic GPCR dimerization. *Curr. Opin. Cell Biol.* 27, 78–86.
- Kohn, W.D., Mant, C.T., Hodges, R.S., 1997. Alpha-helical protein assembly motifs. *J. Biol. Chem.* 272, 2583–2586.
- Krieger, E., Joo, K., Lee, J., Raman, S., Thompson, J., Tyka, M., Baker, D., Karplus, K., 2009. Improving physical realism, stereochemistry, and side-chain accuracy in homology modeling: four approaches that performed well in CASP8. *Proteins* 77 (Suppl 9), 114–122.
- Lefebvre, B., Timmers, T., Mbengue, M., Moreau, S., Herve, C., Toth, K., Bittencourt-Silvestre, J., Klaus, D., Deslandes, L., Godiard, L., Murray, J.D., Udvardi, M.K., Raffaele, S., Mongrand, S., Cullimore, J., Gamas, P., Niebel, A., Ott, T., 2010. A remorin protein interacts with symbiotic receptors and regulates bacterial infection. *PNAS* 107, 2343–2348.
- Lingwood, D., Simons, K., 2010. Lipid rafts as a membrane-organizing principle. *Science* 327, 46–50.
- Loquet, A., Habenstein, B., Lange, A., 2013. Structural investigations of molecular machines by solid-state NMR. *Acc. Chem. Res.* 46, 2070–2079.
- Lupas, A., Van Dyke, M., Stock, J., 1991. Predicting coiled coils from protein sequences. *Science* 252, 1162–1164.
- Lupas, A.N., Bassler, J., 2017. Coiled coils – a model system for the 21st Century. *Trends Biochem. Sci.* 42, 130–140.
- Marin, M., Thallmair, V., Ott, T., 2012. The intrinsically disordered N-terminal region of AtREM1.3 remorin protein mediates protein-protein interactions. *J. Biol. Chem.* 287, 39982–39991.
- McBride, Z., Chen, D., Reick, C., Xie, J., Szymanski, D.B., 2017. Global analysis of membrane-associated protein oligomerization using protein correlation profiling. *Mol. Cell Proteomics.*
- Meier, B.H., Bockmann, A., 2015. The structure of fibrils from 'misfolded' proteins. *Curr. Opin. Struct. Biol.* 30, 43–49.
- Perraki, A., Cacas, J.L., Crowet, J.M., Lins, L., Castroviejo, M., German-Retana, S., Mongrand, S., Raffaele, S., 2012. Plasma membrane localization of Solanum tuberosum remorin from group 1, homolog 3 is mediated by conformational changes in a novel C-terminal anchor and required for the restriction of potato virus X movement]. *Plant Physiol.* 160, 624–637.
- Raffaele, S., Mongrand, S., Gamas, P., Niebel, A., Ott, T., 2007. Genome-wide annotation of remorins, a plant-specific protein family: evolutionary and functional perspectives. *Plant Physiol.* 145, 593–600.
- Raffaele, S., Bayer, E., Lafarge, D., Cluzet, S., German Retana, S., Boubekur, T., Leborgne-Castel, N., Carde, J.P., Lherminier, J., Noirot, E., Satiat-Jeunemaitre, B., Laroche-Traineau, J., Moreau, P., Ott, T., Maule, A.J., Reymond, P., Simon-Plas, F., Farmer, E.E., Bessoule, J.J., Mongrand, S., 2009. Remorin, a solanaceae protein resident in membrane rafts and plasmodesmata, impairs potato virus X movement. *Plant Cell* 21, 1541–1555.
- Reymond, P., Kunz, B., Paul-Pletzer, K., Grimm, R., Eckerskorn, C., Farmer, E.E., 1996. Cloning of a cDNA encoding a plasma membrane-associated, uronide binding phosphoprotein with physical properties similar to viral movement proteins. *Plant Cell* 8, 2265–2276.
- Schanda, P., Kupce, E., Brutscher, B., 2005. SOFAST-HMQC experiments for recording two-dimensional heteronuclear correlation spectra of proteins within a few seconds. *J. Biomol. NMR* 33, 199–211.
- Schneidman-Duhovny, D., Inbar, Y., Nussinov, R., Wolfson, H.J., 2005. PatchDock and SymmDock: servers for rigid and symmetric docking. *Nucleic Acids Res.* 33, W363–367.
- Simons, K., Sampaio, J.L., 2011. Membrane organization and lipid rafts. *Cold Spring Harb Perspect. Biol.* 3, a004697.
- Skinner, S.P., Fogh, R.H., Boucher, W., Ragan, T.J., Mureddu, L.G., Vuister, G.W., 2016. CcpNmr AnalysisAssign: a flexible platform for integrated NMR analysis. *J. Biomol. NMR* 66, 111–124.
- Suzuki, K.G., Kasai, R.S., Hirosawa, K.M., Nemoto, Y.L., Ishibashi, M., Miwa, Y., Fujiwara, T.K., Kusumi, A., 2012. Transient GPI-anchored protein homodimers are units for raft organization and function. *Nat. Chem. Biol.* 8, 774–783.
- Toth, K., Stratil, T.F., Madsen, E.B., Ye, J., Popp, C., Antolin-Llovera, M., Grossmann, C., Jensen, O.N., Schussler, A., Parniske, M., Ott, T., 2012. Functional domain analysis of the Remorin protein LjSYMREM1 in Lotus japonicus. *PLoS one* 7, e30817.
- Troshin, P.V., Procter, J.B., Barton, G.J., 2011. Java bioinformatics analysis web services for multiple sequence alignment-JABAWS:MSA. *Bioinformatics* 27, 2001–2002.
- Tycko, R., Wickner, R.B., 2013. Molecular structures of amyloid and prion fibrils: consensus versus controversy. *Acc. Chem. Res.* 46, 1487–1496.
- Vonck, J., Mills, D.J., 2017. Advances in high-resolution cryo-EM of oligomeric enzymes. *Curr. Opin. Struct. Biol.* 46, 48–54.
- Wang, Y., Jardetzky, O., 2002. Probability-based protein secondary structure identification using combined NMR chemical-shift data. *Protein Sci.: Publ. Protein Soc.* 11, 852–861.
- Waterhouse, A.M., Procter, J.B., Martin, D.M., Clamp, M., Barton, G.J., 2009. Jalview Version 2—a multiple sequence alignment editor and analysis workbench. *Bioinformatics* 25, 1189–1191.
- Weingarth, M., Baldus, M., 2013. Solid-state NMR-based approaches for supramolecular structure elucidation. *Acc. Chem. Res.* 46, 2037–2046.
- Zhang, Y., 2008. I-TASSER server for protein 3D structure prediction. *BMC Bioinf.* 9, 40.

Coiled-coil oligomerization controls nanodomain organization of the plasma membrane REMORINs.

Supplementary Information

Denis Martinez^a, Anthony Legrand^a, Julien Gronnier^{b#}, Marion Decossas^c, Paul Gouguet^b, Olivier Lambert^c, Mélanie Berbon^a, Loris Verron^a, Axelle Grélard^a, Veronique Germain^b, Antoine Loquet^{a*}, Sébastien Mongrand^{b*}, Birgit Habenstein^{a*}

^a Institute of Chemistry & Biology of Membranes & Nanoobjects (UMR5248 CBMN), IECB, CNRS, Université Bordeaux, Institut Polytechnique Bordeaux, All. Geoffroy Saint-Hilaire, 33600 Pessac, France.

^b Laboratoire de Biogénèse Membranaire - UMR 5200 - CNRS, Université de Bordeaux, 71 Avenue Edouard Bourlaux, 33883 Villenave d'Ornon Cédex

^c Institute of Chemistry & Biology of Membranes & Nanoobjects (UMR5248 CBMN), CNRS, Université Bordeaux, Institut Polytechnique Bordeaux, 14 All. Geoffroy Saint-Hilaire, 33600 Pessac, France.

[#] present address: Cyril Zipfel's laboratory. The Sainsbury Laboratory, Norwich Research Park, Colney, Norwich, NR4 7UH

Corresponding authors: a.loquet@iecb.u-bordeaux.fr (A. Loquet), sebastien.mongrand@u-bordeaux.fr (S. Mongrand) and b.habenstein@iecb.u-bordeaux.fr (B. Habenstein)

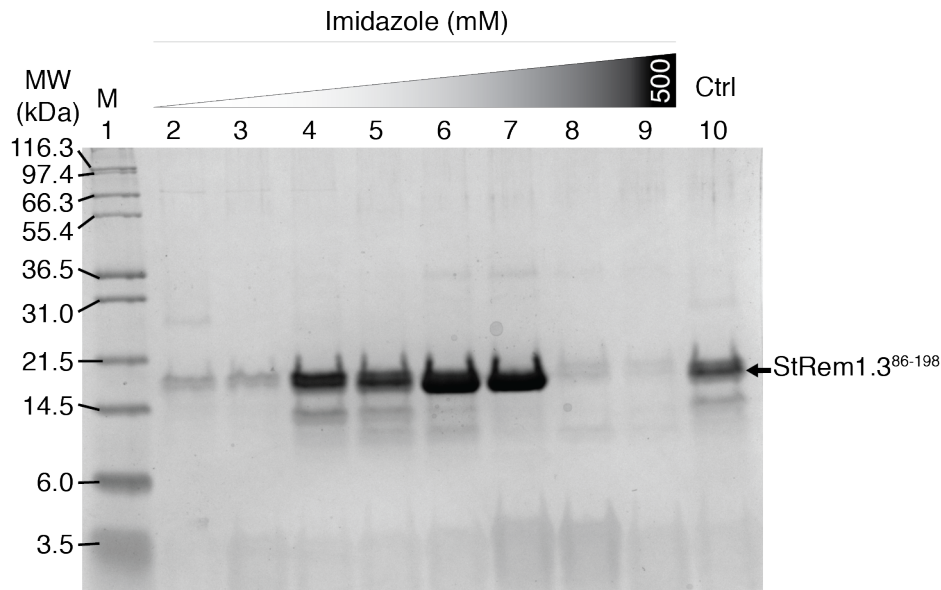


Figure S1. SDS-PAGE (12 % acrylamide gel) of REM_{H6(86-198)} at different stages of His-trap chromatography purification. Molecular weight marker in lane 1; Washing fraction at 25 mM imidazole – lanes 2 and 3; Elution with 400 mM imidazole – lanes 4 to 7; Elution with 500 mM imidazole – lanes 8 and 9; Purified fraction after HPLC as a control – lane 10; the arrow indicates the position of the recombinant REM_{H6(86-198)}.

Figure S2. Residues conservation in REMORINs. MUSCLE multiple alignments of full length StREM1.3 and Arabidopsis REMORINs proteins were visualized using JalView v2.10.2b2. The alignment is colour-coded by percentage identity.

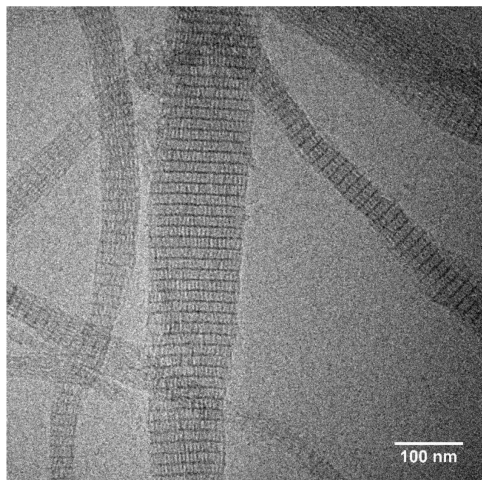


Figure S3. Cryo TEM micrograph of REM_{H6(86-198)} illustrating the varying filament thickness. Scale bar : 100 nm.

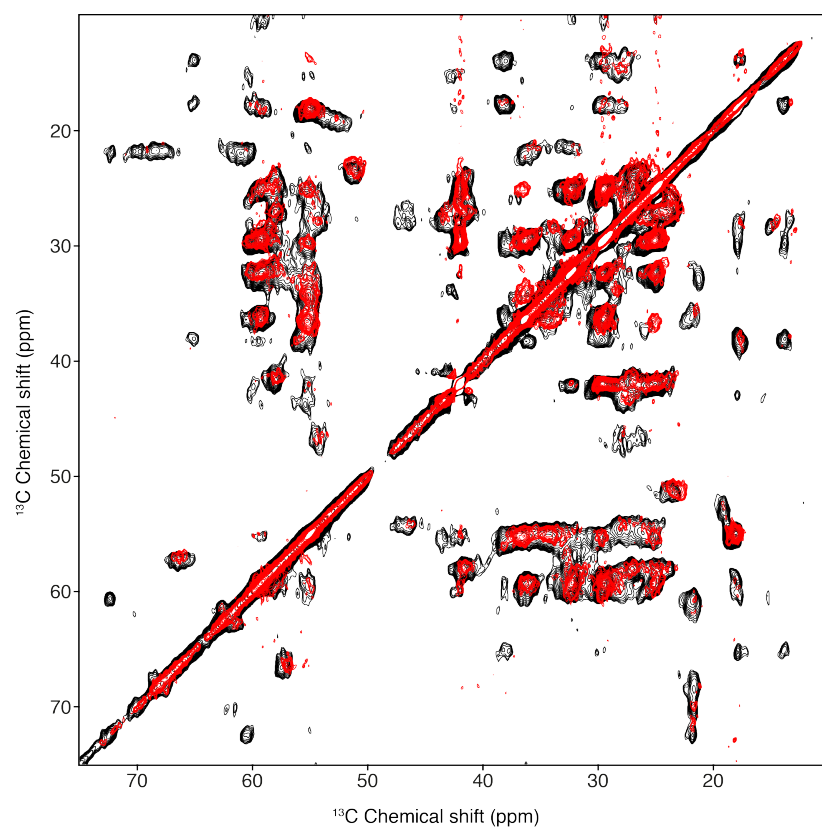


Figure S4. 2D SSNMR on $\text{REM}_{\text{H6}(86-198)}$ and $\text{REM}_{(86-198)}$ filaments. Overlay of 2D PDSD ^{13}C - ^{13}C spectra of $\text{REM}_{\text{H6}(86-198)}$ (black, recorded on a 600MHz spectrometer) and $\text{REM}_{(86-198)}$ (red, recorded on a 800MHz spectrometer) filaments (50 ms mixing time).

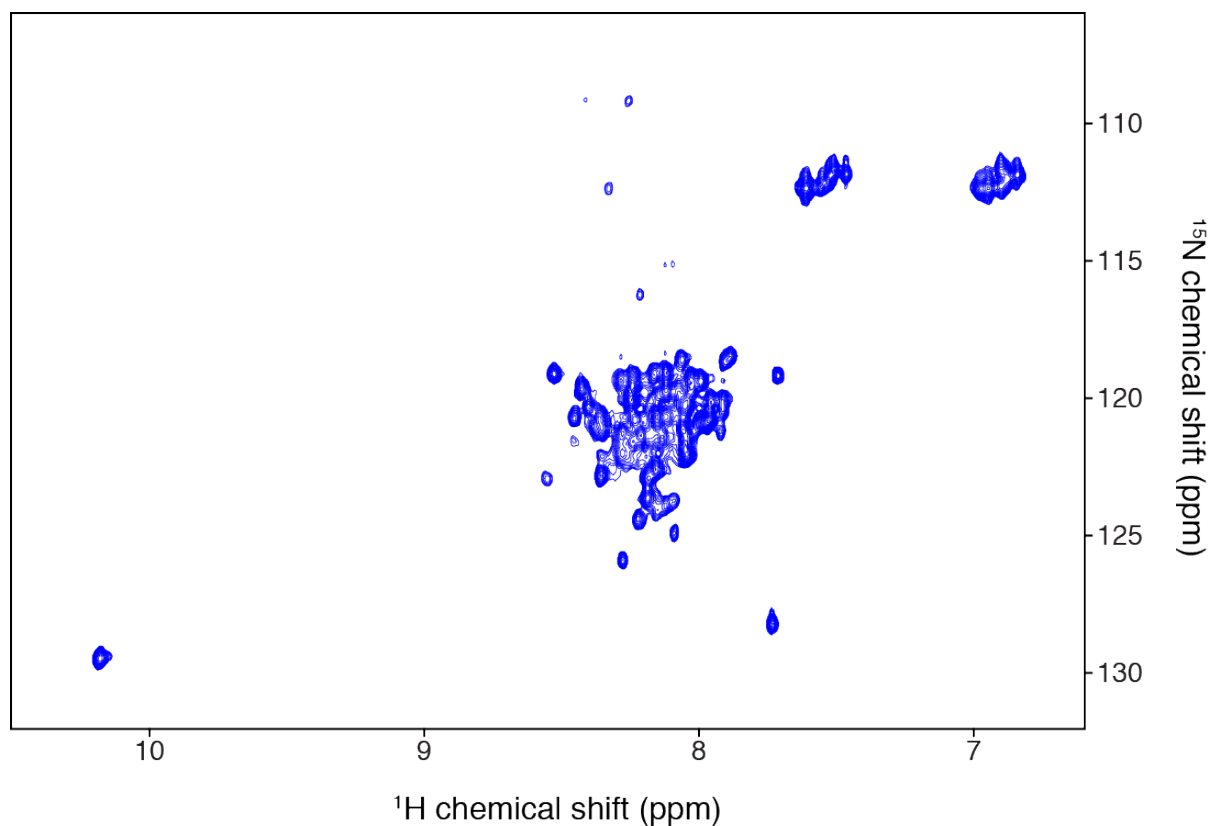


Figure S5. ^1H , ^{15}N SOFAST-HMQC liquid-state NMR spectrum of the unfolded $\text{REM}_{\text{H6}(86-198)}$ in solution. The spectrum was acquired at 313K on a ^{15}N , ^{13}C labelled protein sample at a concentration of 200 μM in 20 mM HEPES, 150 mM NaCl, 0.02% NaN_3 , pH 7.4 in a mixture of 90% H_2O , 10 % D_2O . The spectrum was referenced according to the DSS signal added in the sample.

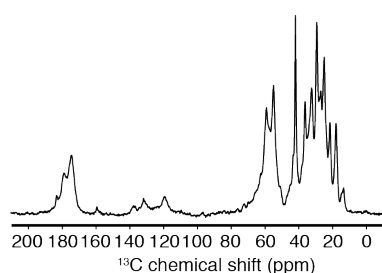


Figure S6. 1D ^{13}C solid-state NMR spectrum of $\text{REM}_{\text{H6}(86-198)}$ filaments recorded using a ^1H - ^{13}C cross-polarization transfer. The spectrum was referenced according to DSS signal added in the sample.

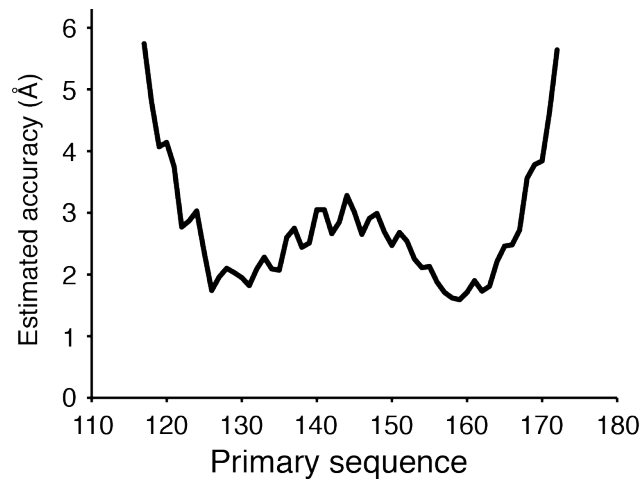


Figure S7. Accuracy graph of the generated 3D model. Residue-level quality of the protein structure prediction has been evaluated by the program ResQ (Yang et al., 2016)

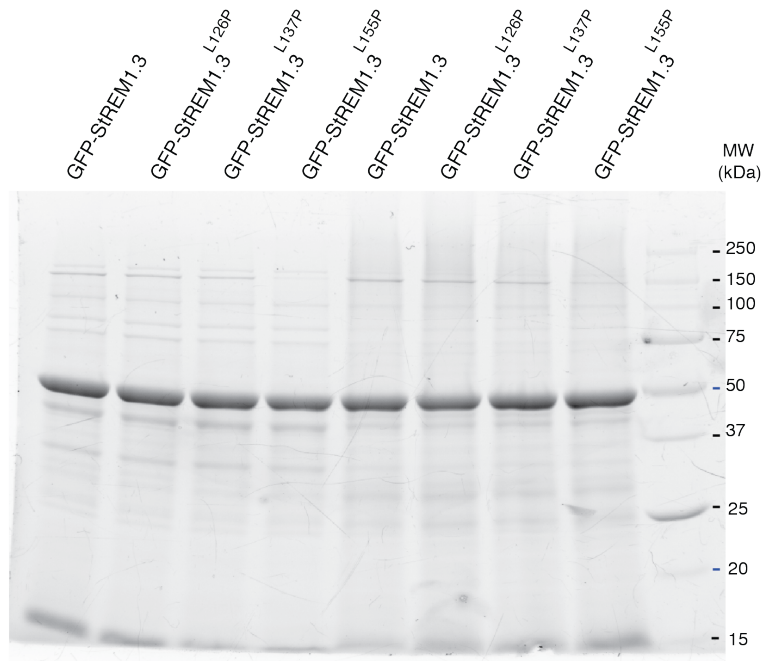


Figure S8. Stain-free of SDS_PAGE showing the loading of proteins for the western blot presented Figure 1.

Yang, J., Wang, Y., Zhang, Y., 2016. ResQ: An Approach to Unified Estimation of B-Factor and Residue-Specific Error in Protein Structure Prediction. *Journal of molecular biology* 428, 693-701.

Article I: addendum

After working on filaments of REM₈₆₋₁₉₈ to gather structural insights into its coiled-coil oligomerisation domain, we focused on inserting the protein in membranes. Would the structural fingerprint be modified? Would RemCA's structural fingerprint appear as it was first observed (Gronnier et al., 2017)?

I. REM₈₆₋₁₉₈ in liposomes by ssNMR

¹⁵N-, ¹³C- labelled REM₈₆₋₁₉₈ was reconstituted in DMPC/sitosterol/PIPMix (70/15/15 molar ratio) liposomes as described in Article IV. The sample was analysed on a Bruker Avance NEO Solids operating at 600 MHz for proton with a CPMAS 4 mm probe. MAS frequency was 11 kHz. ¹³C-¹³C PDSD spectra were recorded using 20 ms and 7 ms acquisition times in direct and indirect dimensions, respectively. ¹H decoupling during acquisition was performed using a SPINAL-64 decoupling sequence (Fung et al., 2000). All experiments are carried out at 4°C according to water's chemical shift (Wishart et al., 1995).

In the presence of membranes, the N-terminal β-region of REM₈₆₋₁₉₈ disappears while the helical region remains mostly unchanged (Figure 56). Superimposing RemCA's structural fingerprint (Gronnier et al., 2017), we could not match any peaks. In addition, no new peaks were detected. This may imply that: (1) RemCA's conformation in the protein differs from the lone anchor or (2) most of it is too flexible to be detected by ¹³C-¹³C PDSD. Nonetheless, the proteoliposomes preparation was contaminated with filaments of REM₈₆₋₁₉₈ (Figure 57).

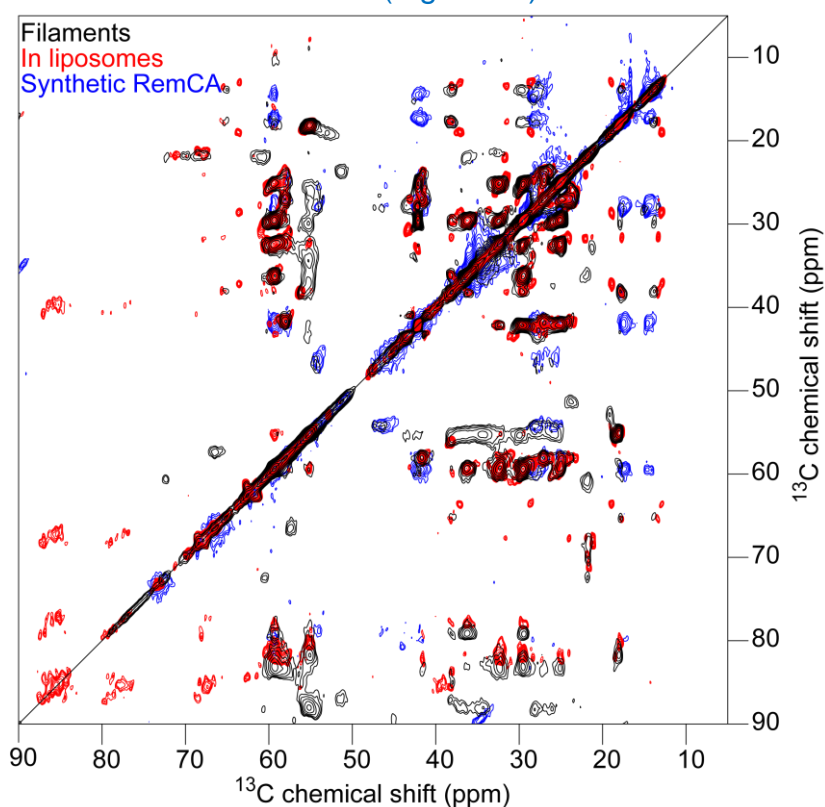


Figure 56

^{13}C - ^{13}C PDSD spectra of REM₈₆₋₁₉₈ in liposomes of PC/sitosterol/PIPmix 75/10/15 (molar ratio) with mixing times of 50 ms (black) and 150 ms (red). ^{13}C - ^{13}C PDSD of RemCA (blue) in liposomes containing PIPmix with a 50 ms mixing time from (Gronnier et al., 2017).

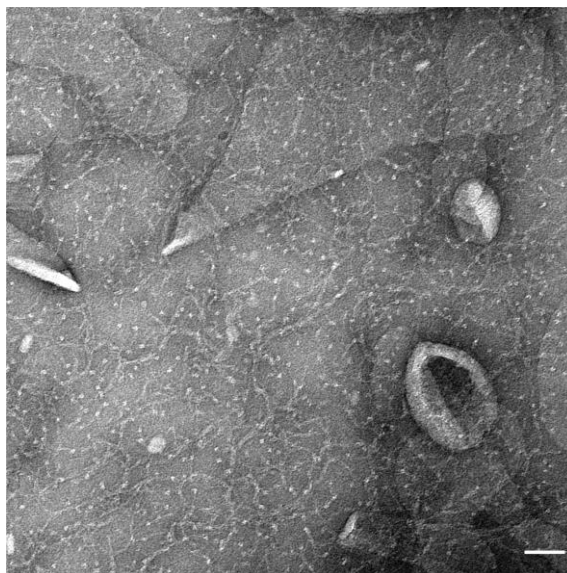


Figure 57

Negative staining electron microscopy on ^{15}N -, ^{13}C -labelled REM₈₆₋₁₉₈ in liposomes (Figure 56). Due to the staining protocol, liposomes are deformed and adopt a flat balloon shape. Scale bar: 50nm.

II. Structure of RemCA in micelles

We decided to work on RemCA alone. IsNMR already showed that it was disordered in H_2O and that it would fold differently whether it was in trifluoroethane or in deuterated dodecyl phosphatidylcholine (DPC-d38) micelles (Gronnier et al., 2017). The latter being more relevant in mimicking a biological membrane, we pursued a full structural investigation of RemCA by IsNMR. The following is a revised translation of my master 2 internship report. This work was done under the direct supervision of Dr Denis Martinez, who performed IsNMR experiments and structure calculations.

A. Material and methods

1 mM of synthetic N-acetylated RemCA peptide is mixed with 20 mM of DPC-d38 in 9/1 $\text{H}_2\text{O}/\text{D}_2\text{O}$ (V/V). The sample was analysed on a Bruker Avance III spectrometer operating at 800 MHz for proton with a 5 mm TCI cryoprobe controlled by TopSpin 3.1 (Bruker). Pulse sequences used were: ^1H - ^{15}N HMQC, ^1H - ^{13}C HMQC, ^1H - ^1H TOCSY (150 ms mixing time) and ^1H - ^1H NOESY (300 ms mixing time) (Levitt, 2008). Spectra were analysed with CCPNMR Analysis (<http://www.ccpn.ac.uk>) and chemical shift statistics from the BMRB. Structure calculation were handled through the CCPNMR Grid interface (Fogh et al., 2005; Nilges et al., 2008; Rieping et al., 2007; Vranken et al., 2005).

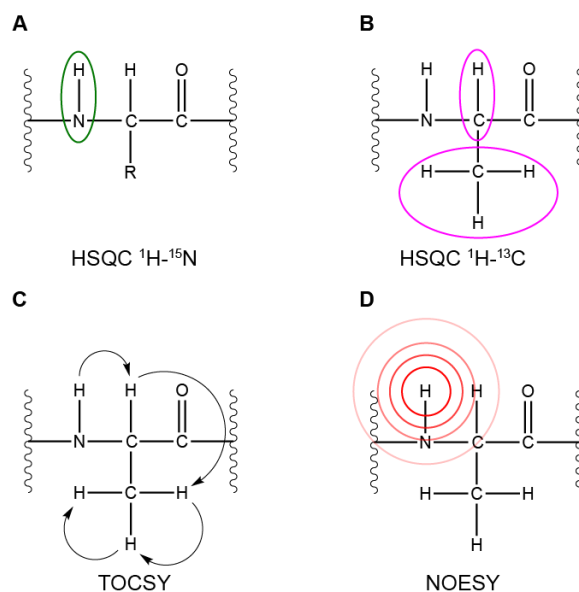


Figure 58

Information provided by the different NMR pulse sequences employed. R is a lateral chain of a residue. In B, C and D, the case of an alanine is illustrated. (A) ^1H - ^{15}N HMQC informs on the chemical shifts of the highlighted ^1H and ^{15}N of the amide backbone. (B) ^1H - ^{13}C HMQC informs us on the chemical shifts of a given ^{13}C and the ^1H bound to it. (C) ^1H - ^1H TOCSY allows to obtain all the ^1H chemical shifts of a given spin system, i.e. a residue. (D) ^1H - ^1H NOESY provides distance constraints between neighbouring ^1H : the intensity of a cross-peaks is correlated to their distance from one another (Nilges et al., 2008).

B. Results

To access RemCA's structure, it was reconstituted in DPC-d38 micelles and analysed by lsNMR. Peak assignment was performed manually with the following methodology: (1) chemical shifts of ^1H bound to backbone nitrogens were determined using the ^1H - ^{15}N HMQC; (2) ^1H - ^1H NOESY cross-peaks in the amide region were used to assess connectivities between neighbouring residues; (3) using both the ^1H - ^1H NOESY and the ^1H - ^1H TOCSY, each residue was identified by its expected chemical shifts (according to the BMRB) and, finally, (4) weak ^1H - ^1H NOESY peaks are assigned to more distant connectivities between residues (Figure 58). Figure 59 gives an example of the assignment process for residues 171 to 175. Figure 60 shows the assigned ^1H - ^{15}N HMQC spectrum.

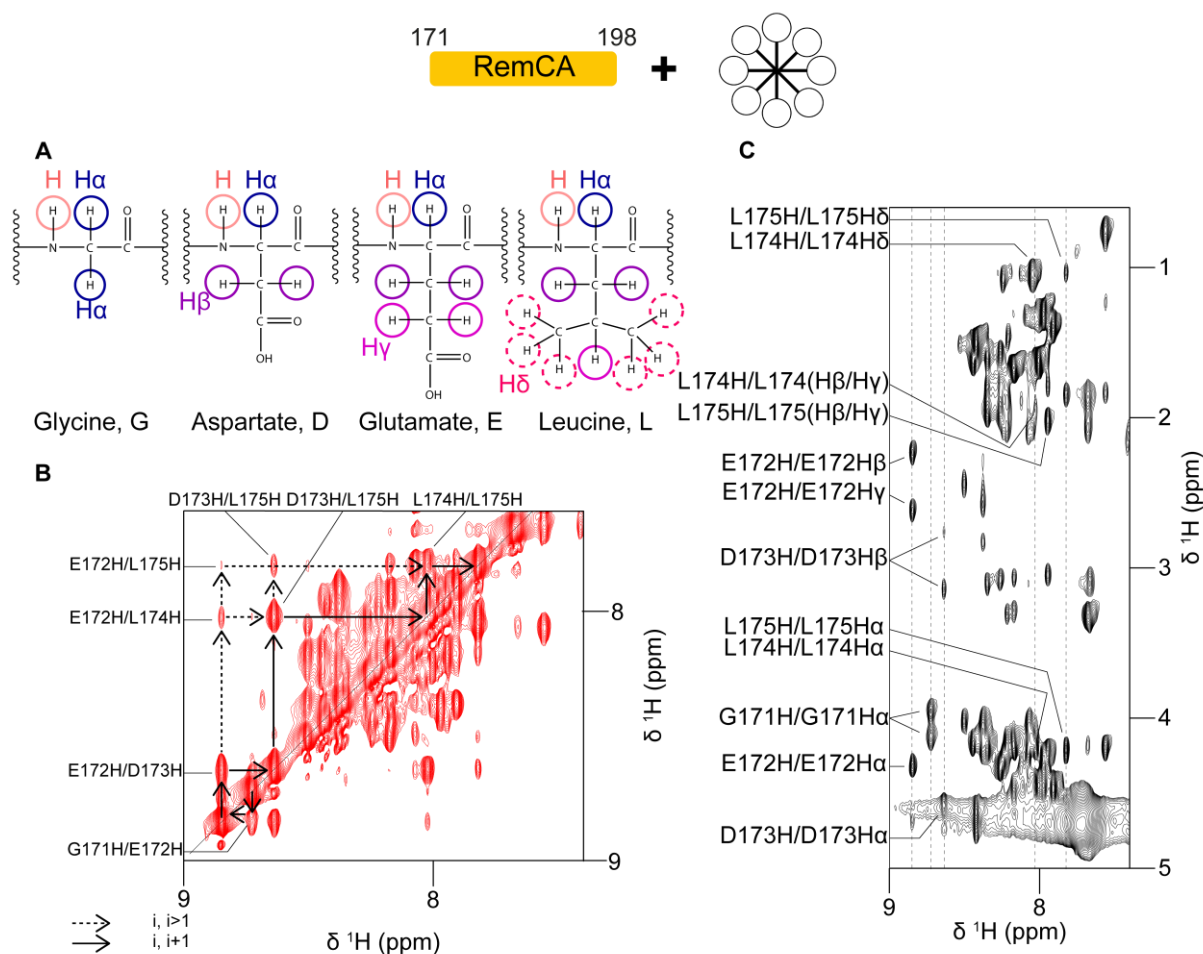


Figure 59

Assignment of residues 171 to 175. (A) Abbreviations used to designate ^1H . (B) Connectivities between residues are defined using ^1H - ^1H NOESY cross-peaks in the H region. Full arrows: $i, i + 1$ connectivities. Dashed arrows: $i, i + n > i + 1$ connectivities (longer range connectivities). (C) Each residue is identified using the ^1H - ^1H TOCSY and the expected chemical shifts from the BMRB.

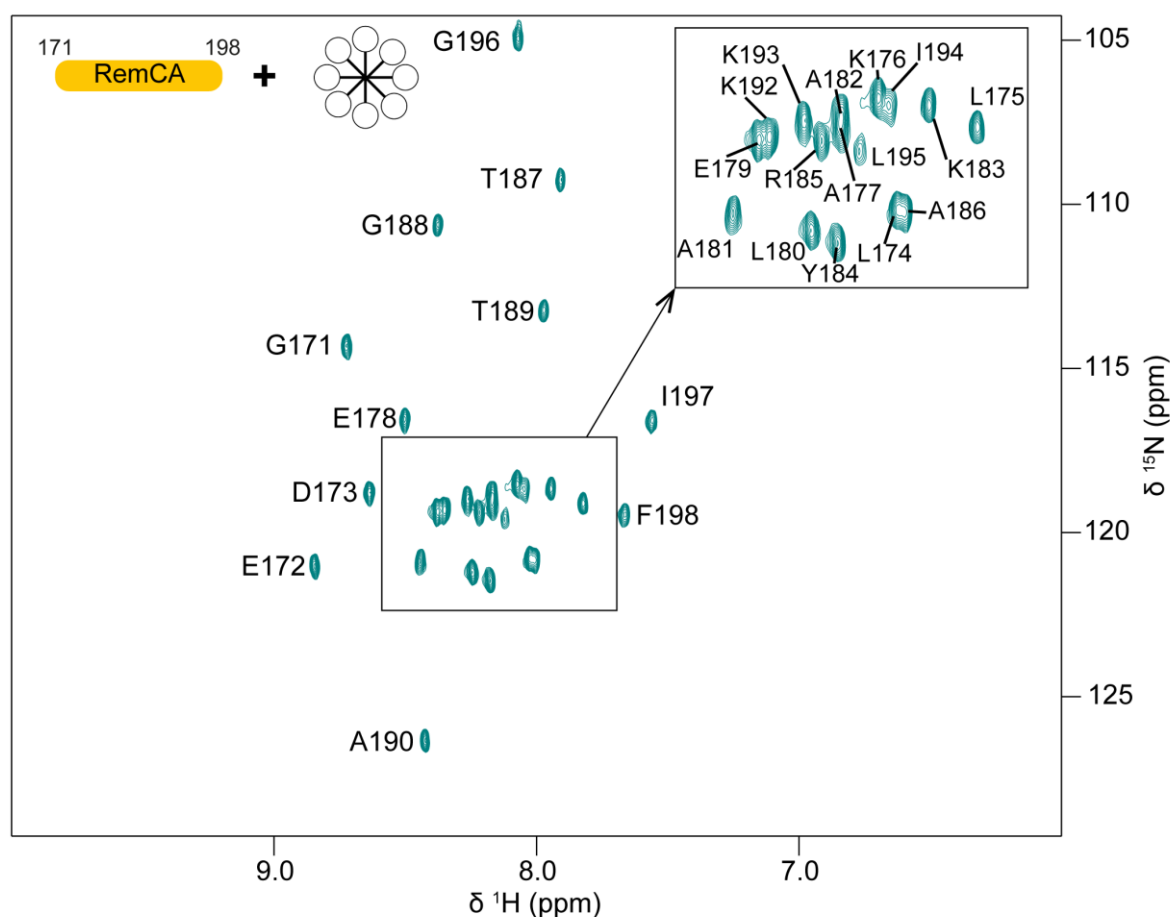


Figure 60

Assigned ^1H - ^{15}N HMQC for RemCA in micelles of DPC-d38. Due to the RemCA's N-terminal being acetylated, G171 has a backbone amide and thus can be detected.

990 peaks were assigned on the ^1H - ^1H NOESY, among which 359 ambiguous assignments (Table 4). Preliminary structure calculations converge to a structure bearing, in N-terminal, one α -helix of 4 residues then a second α -helix of 9 residues, kinked by an angle of 96° , followed by a loop and a flexible C-terminal region (Figure 61). The helix break in N-terminal could be an artefact due to the non-physiological micellar environment: it is the major difference with the model from (Gronnier et al., 2017), in which there was only a single N-terminal helix. As a reminder, in the full length protein, a long helix is attached at the N-terminal of RemCA. It is unlikely that both would be connected by a loop partially embedded in the membrane.

Connectivities	i, i	i, i+1	i, i+2	i, i+3	i, i+4	i, i>4
Number of peaks	215	216	88	113	81	277
Ambiguities	40	52	23	30	20	194

Table 4

Number of assigned cross-peaks of the ^1H - ^1H NOESY spectrum and amount of ambiguous assignments, sorted by connectivity types, where i is a given residue.

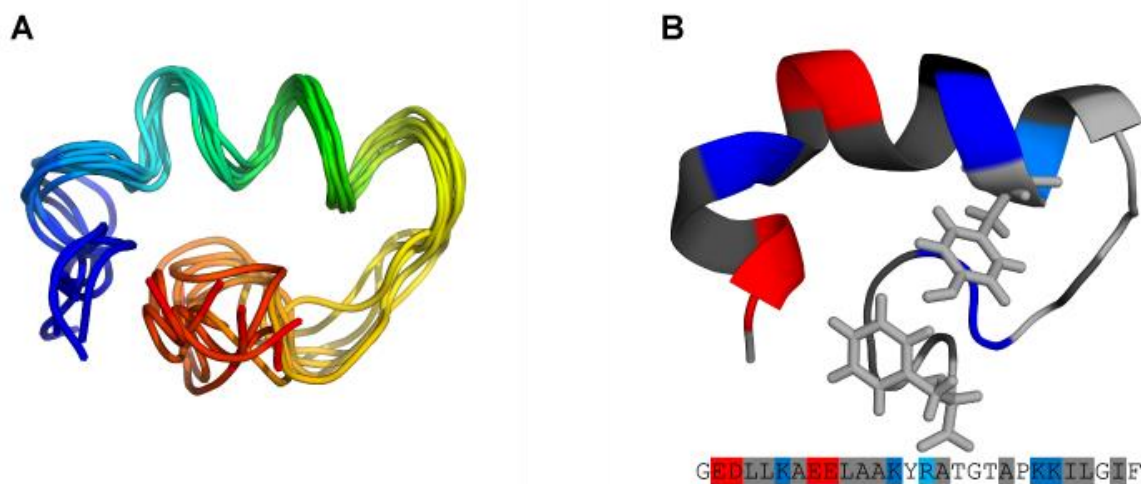


Figure 61

Preliminary structure of RemCA in micelles of DPC-d38. (A) 7 structures were calculated from the same dataset then superimposed. Blue end: N-terminal. Red end: C-terminal. (B) Structure of lowest energy from (A). Dark blue: lysines. Light blue: arginine. Red: aspartate and glutamates. Grey: hydrophobic residues. Aromatic sidechains are represented as sticks. Hydrophobicity and hydrophilicity labelled according to the Kyte-Doolittle scale (Perraki et al., 2012).

III. Structural analysis of RemCA in native-like conditions by ssNMR

We decided to change the membrane mimetic for something more physiologically relevant i.e. multilamellar vesicles (MLVs).

Ordering synthetic RemCA peptides that are fully labelled with ^{13}C and ^{15}N is too expensive, so we decided to produce a fusion protein GFP-(TEV cleavage site)-RemCA in *E. coli* BL21-DE3. The production of GFP-RemCA in BL21-DE3 cells was induced by the addition of 1 mM IPTG followed by overnight incubation at 18°C under stirring. Cells were lysed and the supernatant was loaded onto a HisTrap column controlled with an Atka Pure 25 HPLC system (GE Healthcare) equilibrated with 20 mM HEPES 150 mM NaCl 20 mM imidazole 0.02% NaN_3 pH=7.4 and eluted with 20 mM HEPES 150 mM NaCl 500 mM imidazole 0.02% NaN_3 pH=7.4. GFP-RemCA was adjusted to 0.5 mM EDTA and 1 mM DTT then TEV protease was added in a ~ 1/200 TEV/GFP-RemCA weight ratio. The mixture was incubated for 2-3h at room temperature then dialysed at 4°C overnight in a MWCO = 1 kDa dialysis tubing made of regenerated cellulose (Spectra Labs). It was adjusted to 7M urea and incubated for 1h at room temperature before being loaded onto a HisTrap column equilibrated with 20 mM HEPES 150 mM NaCl 7 M urea pH=7.4 and with 20 mM HEPES 150 mM NaCl 7 M urea 500 mM imidazole pH=7.4 as elution buffer. Free RemCA flowed through the column without binding to the resin. It was dialysed three times against water.

We were able to produce 3 mg of fully ^{15}N -, ^{13}C -labelled RemCA per litre of labelled culture medium. The peptide was lyophilised, co-solubilised in $\text{CHCl}_3/\text{MeOH}$ 2/1 (v/v) with DMPC/sitosterol/PIPmix 75/15/10 (molar ratio) (PIPmix is PS/PI/PI4P/PI4,5P₂ 50/20/15/15 (Gronnier et al., 2017)), lyophilised and re-hydrated. The final sample was fitted into a 3.2 mm rotor and analysed by ssNMR on a Bruker Avance NEO operating

at 800 MHz for proton with a CPMAS 3.2 mm probe. Acquisition times were 20 ms and 8 ms in the direct and indirect dimensions, respectively. ^1H decoupling during acquisition was performed using a SPINAL-64 decoupling sequence (Fung et al., 2000).

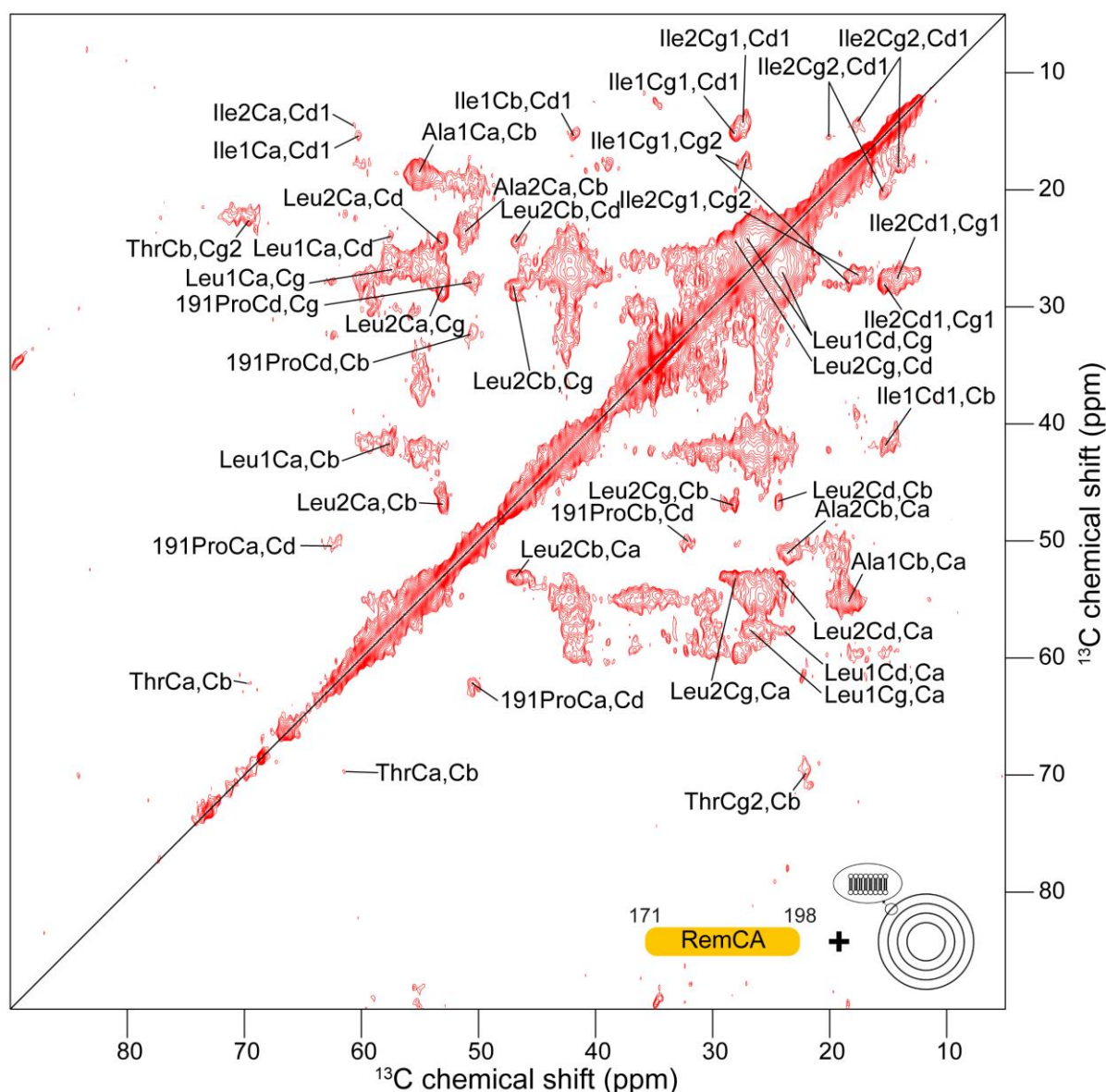


Figure 62

^{13}C - ^{13}C PDSD (50 ms mixing time) spectrum of RemCA co-solubilised in PC/sitosterol/PIPMix liposomes. Unambiguously assigned spin systems are highlighted. Due to spectral overlap and possible sample aggregation, the assignment of some peaks is deemed too ambiguous and is not shown here.

The residue types of a few spin systems could be identified without ambiguity (Figure 62): two alanines (at least), two isoleucines, two leucines (at least), 191Pro and a threonine. The SNR is quite poor and obtaining unambiguous inter-residue cross-peaks to perform structure calculations will prove difficult. Instead, we will use the simpler but nonetheless robust secondary chemical shift index: by computing the

difference in chemical shift between an assigned C α or C β and the value for such a nucleus in a residue of random coil conformation, we can determine if the residue in a helical conformation or a strand conformation (Figure 63) (Wang, 2002). A positive value in C α is characteristic of helical conformation while a negative one indicates a strand conformation. This reasoning is inverted for C β : strands yield positive values, helices yield negative ones.

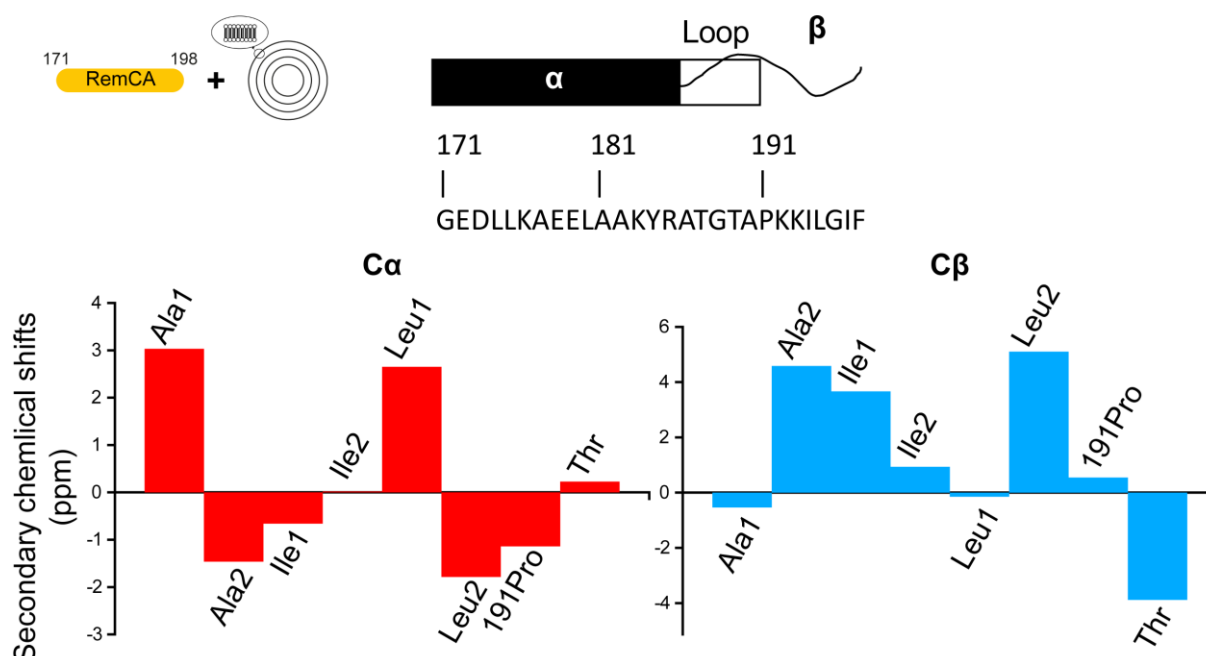


Figure 63

Secondary chemical shifts for spin systems identified in Figure 7, based on (Wang, 2002). Top: sequence and fold of RemCA according to (Gronnier et al., 2017). Bottom: secondary chemical shifts of assigned spin systems in C α and C β . Positive secondary chemical shift in C α indicates a helical fold while a negative value indicate a strand conformation. It is the opposite for secondary chemical shifts in C β . Notice the change of scale between both plots.

There are five alanines in RemCA. At least of them are assignable as Ala1 and Ala2. Furthermore, there are some less intense signals in the Ala region, indicating sample heterogeneity, multiple conformations or alanines in less rigid conformation. Ala1 is in a blatant helical conformation while Ala2 adopts a strand conformation. According to our model (Gronnier et al., 2017), alanines are either in the N-terminal helix, which could correspond to Ala1's, or in the loop, close to the extended β -strand, which could fit Ala2's secondary chemical shifts. Both isoleucines are in a strand conformation, which is consistent with our model (Gronnier et al., 2017). Similarly, proline 191, which is supposed to be at the junction between the loop and the β segment, displays a strand conformation. There are two identified leucines, with cross-peaks of similar identities but opposite conformations: one is a helical conformation, the other in a strand conformation. Since there are three leucines in the putative N-terminal helix and two in the C-terminal region, these secondary chemical shifts confirm that one part of RemCA is helical and that another part contains an extended β -strand. Overall, this

structural analysis of RemCA by ssNMR does not contradict, and might confirm, the model of (Gronnier et al., 2017).

IV. On a putative role of the N-terminal IDD of StREM1.3 on the structure of its filaments

We wished to compare REM₈₆₋₁₉₈ to full length StREM1.3 filaments (figure 64). Using the same methodology, with the exception that StREM1.3's histag is not cleavable, we compared the fingerprint of both samples (Figure 65).

Most peaks of the β -region in REM₈₆₋₁₉₈ vanish when switching to the full length StREM1.3, indicating that the presence of this β -segment was artifactual. Otherwise, the structural fingerprints of both constructs are identical, proving that depletion of the first 85 aminoacids of StREM1.3 does not disrupt its propensity to form coiled-coil domains with a wild-type fold. Reciprocally, it implies that this region is not involved in the formation of the coiled-coil structure nor the assembly of the filaments.

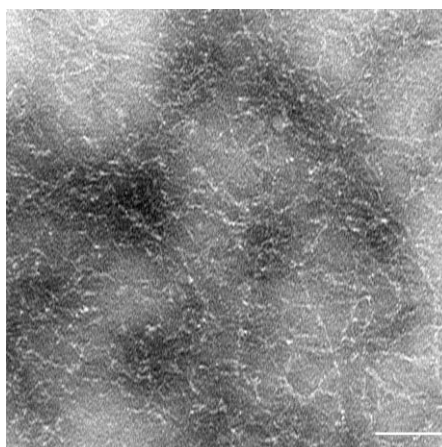


Figure 64

Negative staining electron microscopy on ^{15}N -, ^{13}C -labelled StREM1.3 filaments (NMR spectrum is given on Figure 65). Scale bar: 50 nm.

V. Conclusion

As a general conclusion, the short N-terminal β -segment of REM₈₆₋₁₉₈ spotted in (Martinez et al., 2018) in filaments is artifactual: it disappears if the protein is in membranes as well as in filaments of the full length StREM1.3. Also, the coiled-coil signature is retained between filaments of both constructs, StREM1.3 and REM₈₆₋₁₉₈, and between REM₈₆₋₁₉₈ in filaments and in liposomes. Reconstitution of RemCA peptides in lipid bilayers and structural analysis by ssNMR strengthened the validity of our structural model of RemCA in membranes. In addition, preliminary data obtained in micelles provided by lsNMR, although tainted by a micelle-induced artefact, corroborated some of the findings of (Gronnier et al., 2017): an N-terminal helix followed by a loop then a flexible and extended β -strand C-terminal.

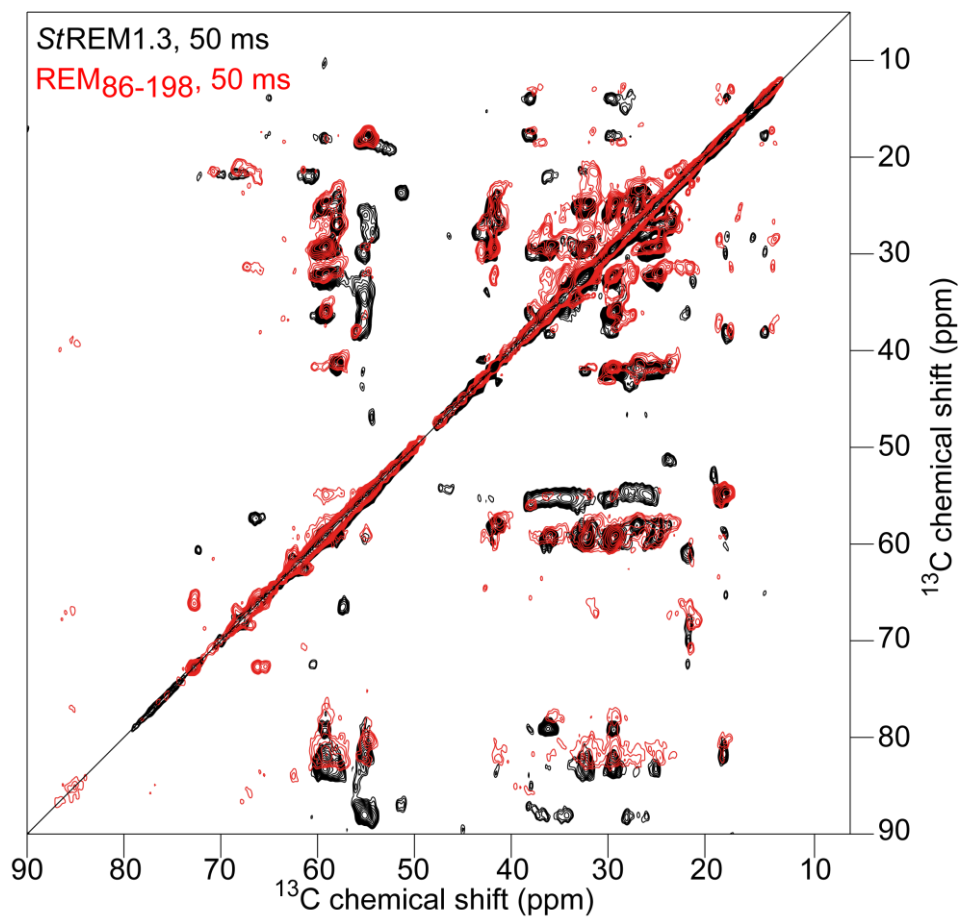


Figure 65

^{13}C - ^{13}C PDSD of REM₈₆₋₁₉₈ filaments (black) (Martinez et al., 2018) and StREM1.3 filaments (red) at 50 ms mixing time.

Article II

REM1.3's phospho-status defines its plasma membrane nanodomain organization and activity in restricting PVX cell-to-cell movement

Artemis Perraki, Julien Gronnier, Paul Gouguet, Marie Boudsocq,
Anne-Flore Deroubaix, Vincent Simon, Sylvie Germain-Retana,
Anthony Legrand, Birgit Habenstein, Cyril Zipfel, Emmanuelle Bayer,
Sébastien Mongrand, Véronique Germain

PLOS Pathogens

2018

14, e1007378

This second article was much more focused on biology, and much less on biophysics. The thematic was *StREM1.3*'s phosphocode and interactome, and how it relates to remorin-mediated PD closure and slowing down of PVX cell-to-cell propagation. *StREM1.3* was phosphorylated *in vitro* using *N. benthamiana* extracts, including purified PMs and [γ - ^{33}P]-ATP further detected by autoradiography. Inhibition by EGTA, a Ca^{2+} chelator, narrowed our field of research to the *Arabidopsis thaliana* calcium-dependent protein kinase 3 *AtCPK3*, which is indeed able to phosphorylate *StREM1.3* *in vitro*. Mass spectrometry-based phospho-mapping failed, so we resorted to systematic mutations of the three most putative phosphorylation sites S74, T86 and S91 (Marin et al., 2012) to Alanine (A), phosphodead, or Aspartic acid (D), phosphomimetic. High resolution microscopy Spt-PALM showed *StREM1.3*^{AAA} mutant was less mobile than *StREM1.3*^{DDD}, with *StREM1.3*^{WT} in between. We assessed these mutants' biological activity by measuring PVX infection foci area in leaves of *N. benthamiana*.

I got involved after the article's first submission, when reviewers asked to perform a finer mutant analysis by testing single-residue mutations (single mutants). Under the supervision and training of Paul Gouguet (PhD student then), who taught me how to use an epifluorescence microscope, we undertook the cloning and analysis of single phosphomutants shown in Figure 3D, from agroinfiltration to observation of viral propagation and data analysis. We were able to show that single phosphodead-mutants (particularly S74) had a WT-like phenotype, hinting at a functional redundancy between these three phospho-residues. I was briefly involved in the re-writing process, mostly for grammar corrections.

RESEARCH ARTICLE

REM1.3's phospho-status defines its plasma membrane nanodomain organization and activity in restricting PVX cell-to-cell movement

Artemis Perraki¹[✉], Julien Gronnier¹[✉], Paul Gouguet¹, Marie Boudsocq²[✉], Anne-Flore Deroubaix¹, Vincent Simon³, Sylvie German-Retana³, Anthony Legrand^{1,4}[✉], Birgit Habenstein⁴[✉], Cyril Zipfel^{5,6}[✉], Emmanuelle Bayer¹[✉], Sébastien Mongrand^{1*}[✉], Véronique Germain¹

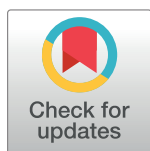
1 Laboratoire de Biogenèse Membranaire (LBM), UMR 5200, CNRS/Université de Bordeaux, Bordeaux, France, **2** Institute of Plant Sciences Paris Saclay (IPS2), CNRS, INRA, Université Paris-Sud, Université d'Evry, Université Paris-Saclay, Université Paris-Diderot, Sorbonne Paris-Cité, Plateau du Moulon, France, **3** Equipe de Virologie UMR BFP 1332 INRA, Villenave d'Ornon, France, **4** Institute of Chemistry & Biology of Membranes & Nanoobjects (UMR5248 CBMN), IECB, CNRS, Université de Bordeaux, Institut Polytechnique de Bordeaux, All. Geoffroy Saint-Hilaire, Pessac, France, **5** The Sainsbury Laboratory, Norwich Research Park, Norwich, United Kingdom, **6** Institute of Plant and Microbial Biology and Zürich-Basel Plant Science Center, University of Zürich, Zürich, Switzerland

 These authors contributed equally to this work.

[✉] Current address: Department of Plant Sciences, University of Cambridge, Cambridge, United Kingdom

[✉] Current address: Institute of Plant and Microbial Biology and Zürich-Basel Plant Science Center, University of Zürich, Zürich, Switzerland.

* sebastien.mongrand@u-bordeaux.fr



OPEN ACCESS

Citation: Perraki A, Gronnier J, Gouguet P, Boudsocq M, Deroubaix A-F, Simon V, et al. (2018) REM1.3's phospho-status defines its plasma membrane nanodomain organization and activity in restricting PVX cell-to-cell movement. PLoS Pathog 14(11): e1007378. <https://doi.org/10.1371/journal.ppat.1007378>

Editor: Aiming Wang, Agriculture and Agri-Food Canada, CANADA

Received: July 5, 2018

Accepted: October 3, 2018

Published: November 12, 2018

Copyright: © 2018 Perraki et al. This is an open access article distributed under the terms of the [Creative Commons Attribution License](https://creativecommons.org/licenses/by/4.0/), which permits unrestricted use, distribution, and reproduction in any medium, provided the original author and source are credited.

Data Availability Statement: All relevant data are within the paper and its Supporting Information files are available from Arabidopsis Genome Initiative (<https://www.arabidopsis.org/index.jsp>), and GenBank/EMBL (<https://www.ncbi.nlm.nih.gov/genbank/>) databases under the accession numbers: StREM1.3 (NP_001274989), AtREM1.2 (At3g61260), AtREM1.3 (At2g45820), AtCPK3 (At4g23650).

Abstract

Plants respond to pathogens through dynamic regulation of plasma membrane-bound signaling pathways. To date, how the plant plasma membrane is involved in responses to viruses is mostly unknown. Here, we show that plant cells sense the Potato virus X (PVX) COAT PROTEIN and TRIPLE GENE BLOCK 1 proteins and subsequently trigger the activation of a membrane-bound calcium-dependent kinase. We show that the *Arabidopsis thaliana* CALCIUM-DEPENDENT PROTEIN KINASE 3-interacts with group 1 REMORINS *in vivo*, phosphorylates the intrinsically disordered N-terminal domain of the Group 1 REMORIN REM1.3, and restricts PVX cell-to-cell movement. REM1.3's phospho-status defines its plasma membrane nanodomain organization and is crucial for REM1.3-dependent restriction of PVX cell-to-cell movement by regulation of callose deposition at plasmodesmata. This study unveils plasma membrane nanodomain-associated molecular events underlying the plant immune response to viruses.

Author summary

Viruses propagate in plants through membranous channels, called plasmodesmata, linking each cell to its neighboring cell. In this work, we challenge the role of the plasma

Funding: AP was supported by the Greek fellowship program IKY, <https://www.iky.gr/en/>. JG, PG and AFD were supported by the Ministère de l'Enseignement Supérieur et de la Recherche, France (doctoral grants), <http://www.enseignementsup-recherche.gouv.fr/cid76053/le-financement-doctoral.html>. MB was supported by LabEx Saclay Plant Sciences-SPS (ANR-10-LABX-0040-SPS), <https://www6.inra.fr/saclay-plant-sciences>. VG, SM, EB, VS VG were supported by the French ANR project "Potymove" (ANR-16-CE20-008-01), <http://www.agence-nationale-recherche.fr/en/>. EB, VG and SM were supported by ANR project (CE19_2014_CONNECT) <http://www.agence-nationale-recherche.fr/en/>. CZ was supported by Gatsby Charitable Foundation, <http://www.gatsby.org.uk> and the European Research Council (grant "PHOSPHinnATE"), <https://erc.europa.eu>. The funders had no role in study design, data collection and analysis, decision to publish, or preparation of the manuscript.

Competing interests: The authors have declared that no competing interests exist.

membrane in the regulation of virus propagation. By studying the dynamics and the activation of a plant-specific protein called REMORIN, we found that the way this protein is organized inside the membrane is crucial to fulfill its function in the immunity of plants against viruses.

Introduction

The cell plasma membrane (PM) constitutes a regulatory hub for information processing [1]. Current knowledge suggests that PM proteins and lipids dynamically associate with each other to create specialized sub-compartments or nanodomains [2], that regulate the cellular responses in space and time [3–5]. For instance, modeling of the localization behavior of a PM-bound receptor and its downstream interactor before and after ligand perception in animal cells suggests that PM-partitioning into nanodomains improves the reliability of cell signaling [6]. In plants a recent example of PM partitioning shows that despite sharing several signaling components, the immune and growth receptors FLS2 and BRI1 are divided into context-specific nanodomains to confer signaling specificity [7]. The REMORIN (REM) family is one of the best-characterized PM nanodomain-associated proteins in plants [7–12]. The association of REMs to the PM is mediated by a short sequence at the extremity of the C-terminus of the protein, called REM-CA (REMORIN C-terminal Anchor) [13, 14]. The REM C-terminal domain contains a coiled-coil (residues 117–152, [15]) which is thought to regulate REM oligomerization [11, 14, 16] and may be involved in regulating REM spatial organization at the PM [15]. Members of the REM family have been associated with plant responses to biotic [9, 17, 18], abiotic stress [19, 20] and developmental clues [12] and current view suggests they could regulate signaling events through nanodomain association [21]. However, the molecular mechanisms leading to REM-associated downstream events remain elusive.

Several REM proteins have been identified as components of the plasmodesmata-plasma membrane subcompartment (PD-PM) [8, 22, 23]. PD are membranous nanopores, crossing the plant cell wall and enabling cytoplasmic, endoplasmic reticulum and PM continuity between adjacent cells. They regulate the intercellular transport of proteins and small molecules during development and defense [24, 25]. The PD-PM is a particular subcompartment of the PM, which displays a unique molecular composition, notably enriched in sterols [26]. The movement of macromolecules through PD can be tightly controlled through modulation of the PD size-exclusion limit (SEL) *via* hypo- or hyper-accumulation of callose at the PD neck region [27–29]. Overexpression of GRAIN SETTING DEFECT 1 (GSD1) encoding a phylogenetic-group 6 REM protein from rice, restricts PD aperture and transport of photo-assimilates [23].

PDs are also the only route available for plant viruses to spread from cell-to-cell. *Potato virus X* (PVX) promotes its cell-to-cell movement *via* modification of PD permeability [30] through the action of TRIPLE GENE BLOCK PROTEIN 1 (TGBp1) [31]. Overexpression of *StREM1.3* (*Solanum tuberosum* REM from group 1b, homolog 3 [32], further referred as REM1.3) hampers TGBp1's ability to increase PD permeability [33]. How REM1.3 obstructs TGBp1 action is still unknown. Here, we used REM1.3 and PVX pathosystem in the solanaceae *Nicotiana benthamiana*, because PVX cannot infect *Arabidopsis* [34] and *N. benthamiana* is a widely used model for research on plant-virus interaction [35]. We previously showed that REM1.3 lateral organization into nanodomains at the PM is directly linked with its ability to restrict PVX movement and regulate PD conductance [36].

REM1.3 was the first REM family member discovered and initially described as a protein phosphorylated upon treatment with oligogalacturonides, which are plant cell wall components and elicitors of plant defense [37, 38]. The biological relevance of REM phosphorylation is not known of different REM phospho-statuses suggest that the activity of these proteins could be regulated by phosphorylation during plant-microbe interactions [16, 17, 39, 40].

In the present paper, we show that phosphorylation of REM dictates its membrane dynamics and antiviral defense by the reduction of PD permeability. Our data point towards a model in which viral proteins such as the Coat Protein (CP), TGBp1 from PVX and 30K proteins from *Tobacco mosaic virus* (TMV) elicit the activation of protein kinase(s), which in turn phosphorylate(s) REM1.3 at its N-terminal domain. In turn, REM1.3's phospho-status regulates its spatial-temporal organization at the PM and association with PD. The latter is associated with PD closure by induction of callose deposition at PD pit fields and restriction of viral cell-to-cell movement. Last, we further provide evidence that the membrane bound *Arabidopsis* CALCIUM-DEPENDENT PROTEIN KINASE 3 (CPK3) interacts with the taxonomic group 1b REMs *in vivo*, phosphorylates REM1.3 *in vitro* and restricts PVX propagation in a REM-dependent manner. Collectively, this study brings valuable information about the involvement of PM nanodomains dynamics during the establishment of membrane-bound signaling processes.

Results

PVX triggers changes in REM1.3's membrane dynamic behavior and REM1.3 association with plasmodesmata

Group 1 and group 6 REM have been described as proteins regulating PD size-exclusion limit [8, 23, 33]. REM1.3 plays a role in restricting PVX passage through PD channels [8], [33] counteracting PVX movement proteins which promote PD opening [41]. To study the potential function of REM1.3 at PD in response to PVX infection, we surveyed simultaneously PD callose content and REM1.3 PD localization in healthy or PVX-infected *N. benthamiana* transiently expressing YFP-REM1.3 [42] (S1 Fig). Our analysis showed a significant increase in callose deposition in PVX-infected cells compared to mock conditions (Fig 1A and 1B). This finding suggests the recognition of PVX-encoded elicitors and the mobilization of a plant defense response leading to an increase of callose accumulation at PD pit fields.

Since protein activation is often linked to changes in subcellular localization [3, 44], we next examined whether PVX infection triggers changes in REM1.3 association with PD. Calculation of the PD index (ratio between fluorescence intensity of YFP-REM1.3 at the aniline-labeled PD pit fields and fluorescence at the PM around the pit fields [28], S1 Fig). Fig 1A and 1B showed that despite its role on PD regulation, YFP-REM1.3 is not enriched in the PD region of healthy *N. benthamiana* epidermal cells. We however reproducibly observed a slight increase of YFP-REM1.3 PD index upon PVX infection suggesting that PVX perception modulates REM1.3 localization and association with the PD pitfields (Fig 1A and 1B).

To gain further insights into REM1.3 dynamic localization at the PM upon PVX infection, we applied single-particle tracking Photoactivated Localization Microscopy in Variable Angle Epifluorescence Microscopy mode (spt-PALM VAEM) in living *N. benthamiana* epidermal cells [45] in absence or presence of PVX. We used the photoconvertible fluorescent protein EOS [46, 47] fused to REM1.3 to visualize, track, and characterize mobility behavior of single REM1.3 molecules. In addition, nanoscale localizations of single molecules observed overtime were computed to obtain super-resolution images and analyze REM1.3 organization at a molecular level. By this approach, we recently studied the protein organization and mobility parameters of single EOS-REM1.3 molecules in non-infected conditions and found that

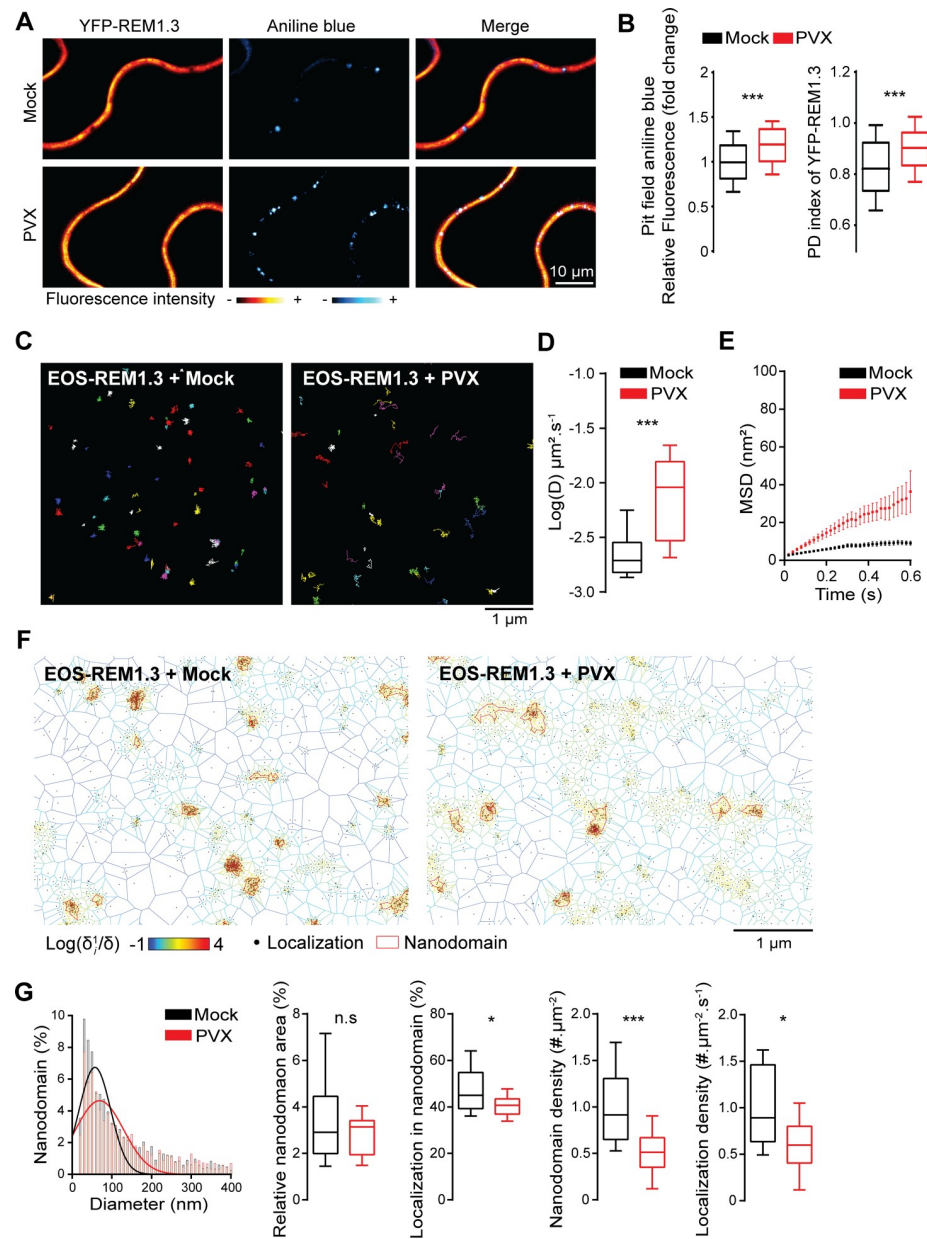


Fig 1. REM1.3 modulates plasmodesmata callose accumulation and displays altered PM organization and dynamic following PVX infection. (A) Representative confocal images of aniline blue stained *N. benthamiana* leaf epidermal cells transiently expressing YFP-REM1.3 in the absence (mock is infiltration with empty *A. tumefaciens*) or the presence of PVX at 2 days after infiltration (DAI). Color-coding indicates fluorescence intensity. (B) *Left*, Pit field aniline blue fluorescence intensity was quantified by ImageJ as described in S1 Fig and expressed as the percentage of the mock control. *Right*, Quantification of the PD residency of YFP-REM1.3 in the absence (mock) and in the presence of PVX using the PD index [28] as described in S1 Fig. Graphs represent quantifications from 3 independent biological experiments. At least 15 cells per condition were analysed per experiment. Significant differences were determined by Mann-Whitney comparisons test *** $p < 0.001$. (C) Super-resolved trajectories of EOS-REM1.3 molecules (illustrated by different colours) in the PM plane in the absence (Mock) and presence of PVX obtained by high-resolution microscopy spt-PALM. EOS-REM1.3 was transiently expressed in *N. benthamiana* (D) Diffusion coefficients (D) of EOS-REM1.3 expressed as log(D) in the absence (Mock) and presence of PVX. Statistical significances were assessed by Mann-Whitney test *** $p < 0.001$ using data collected over two independent experiments. (E) Mean Square Displacement (MSD) over time for the global trajectories of EOS-REM1.3 followed during at least 600 ms reflecting two independent experiments. (F) Live PALM analysis of EOS-REM1.3 localization in the absence (mock) and presence of PVX by tessellation-based automatic segmentation of super-resolution images. (G) Computation of EOS-REM1.3 single molecule organization features based on tessellation-based automatic segmentation images. For

REM1.3 nanodomain size distribution for the indicated conditions, the Gaussian fits in absence (mock) and presence of PVX are indicated by lines. Total nanodomain area is expressed as percentage of the total PM surface. Percentage of EOS-REM1.3 molecules localizing into nanodomains, relative to all molecules observed. Localization density refers to the number of molecules observed per μm^2 per second. Statistics were performed on at least 10 data sets per condition, from two independent experiments. Significant differences were determined by Mann-Whitney test * $p < 0.05$, *** $p < 0.001$.

<https://doi.org/10.1371/journal.ppat.1007378.g001>

EOS-REM1.3 displays an immobile and confined PM localization pattern, as commonly observed for plant membrane-associated proteins (Fig 1C–1E) [48], [36]. Reminiscent of these data, previous studies using different techniques described REM-associated PM domains to be predominantly laterally static [36, 48, 49]. Analysis of PVX-infected cells demonstrated an increase of EOS-REM1.3 diffusion coefficient (D) and mean square displacement (MSD), reflecting an increase of REM1.3 mobility (Fig 1C–1E). We next apply mathematical computation (Voronoi tessellation method [36, 50]) to compare the supra-molecular organization of EOS-REM1.3 of live PALM data in mock- and PVX-infected conditions (Fig 1F and 1G). Computation of EOS-REM1.3 single molecule organization features demonstrated a modulation of REM1.3 nanodomain-organization upon PVX infection (Fig 1G). Following PVX infection, the EOS-REM1.3-formed nanodomains are bigger in size, and there is a slight decrease of the proportion of molecules that localized into nanodomains as well as a decrease in the number of nanodomains formed. Overall, in both conditions, EOS-REM1.3 nanodomains represented similar proportions of the total PM surface. Additionally, a decrease in the localization density (number of molecules observed per μm^2 per s) showed that upon PVX infection, there was less REM1.3 protein at the PM level. Overall, the changes of REM1.3 distribution under PVX infection *i.e.* enrichment of YFP-REM1.3 in the PD pit field regions, the increase of REM1.3's mobility and the modulation of REM1.3 nanodomain organization, suggest that the plant cell modulates PD-PM and PM nanodomain dynamics to circumvent PVX infection.

Perception of PVX proteins by plant cells leads to the activation of kinase(s) phosphorylating REM1.3

REM1.3 overexpression restricts PVX local and systemic spreading in both *Solanum lycopersicum* [8] and *Nicotiana benthamiana* [33, 36] (S2A and S2B Fig). Because REM1.3 protein level is not affected by PVX infection (S2C and S2D Fig), we assumed that neither synthesis nor degradation of the protein is modified by PVX, but perhaps post-translational modifications. As REM1.3 was originally discovered as a PM-associated phosphorylated protein [38], we first asked whether REM1.3 could be phosphorylated by leaf protein extracts. Equal protein amounts of microsomal and soluble extracts from *N. benthamiana* leaves were used as a potential kinase source to phosphorylate affinity-purified full-length 6His-REM1.3 in an *in vitro* kinase assay in the presence of ATP [γ - ^{33}P]. Autoradiography revealed the presence of a clear band corresponding to a phosphorylated form of 6His-REM1.3 by kinase(s) present in the microsomal fraction (Fig 2A). The intensity of this band was completely abolished by competition with cold ATP, but not cold AMP, indicating a valid experimental set-up to study a genuine transphosphorylation event (S3A Fig). Phosphorylation of 6His-REM1.3 was almost undetectable in soluble fractions, representing cytosolic kinases (Fig 2A). *In silico* analysis predicted phosphorylation sites throughout REM1.3 sequence (Diphos, DEPP and NETPHOS prediction softwares). In agreement with the location of the sites presenting the highest phosphorylation potential, we experimentally found that REM1.3 was phosphorylated in its N-terminal domain (residues 1–116, hereafter 6His:REM1.3^N) whereas the C-terminal domain

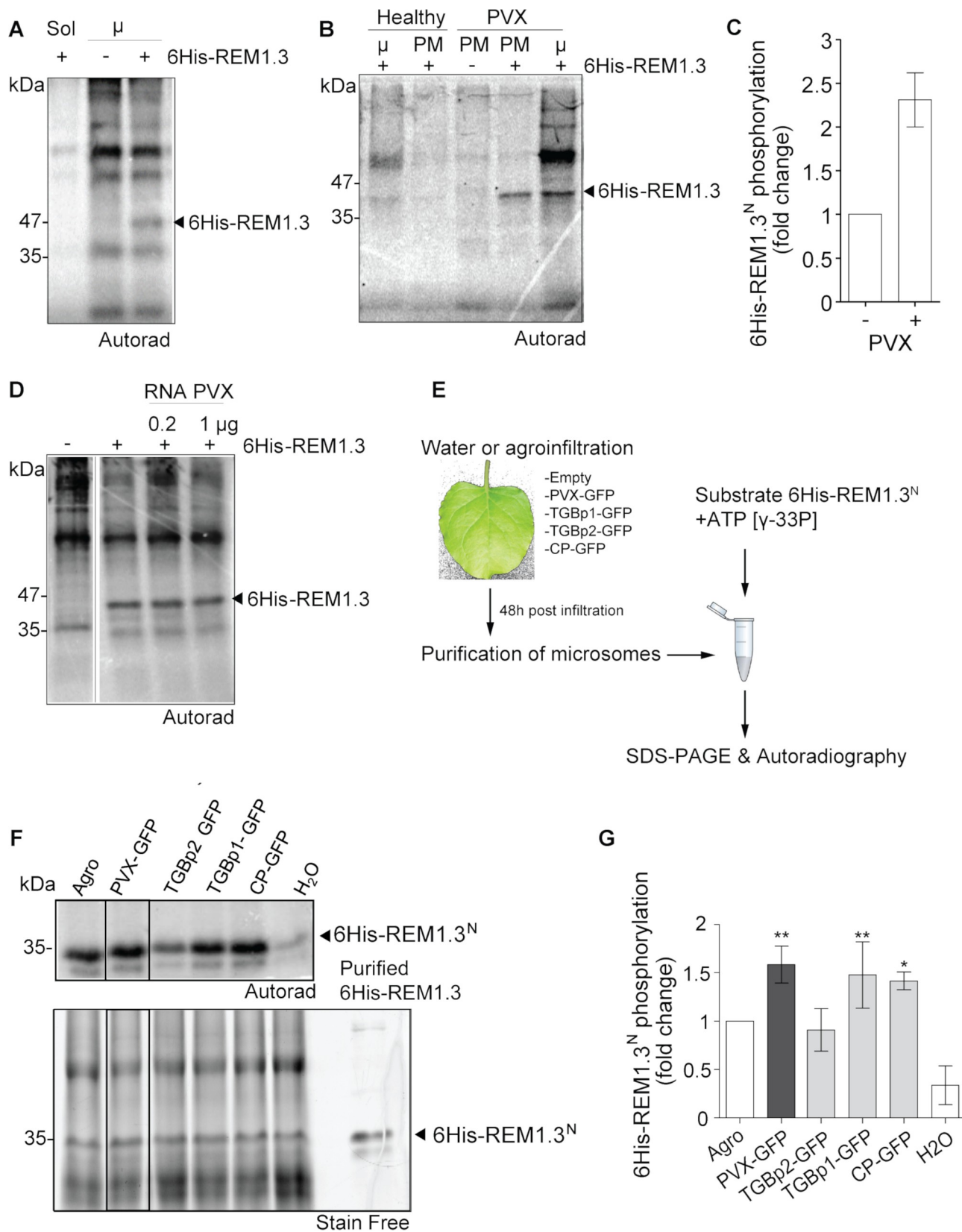


Fig 2. PVX and viral proteins induce REM1.3 phosphorylation in its N-terminal domain. (A, B) *In vitro* protein phosphorylation assays were performed by incubation of recombinant affinity-purified 6His-REM1.3 and *N. benthamiana* extracts with [γ - 33 P]-ATP. The samples were run on SDS-PAGE gels and developed by autoradiography. Soluble (Sol) or microsomal (μ) extracts of healthy leaves in (A), or microsomal and PM extracts from healthy and PVX-infected plants in (B) were used. (C) *In vitro* phosphorylation of 6His-REM1.3^N by leaf microsomal extracts of healthy or PVX-infected *N. benthamiana* leaves. Bars show the quantification of phosphorylated 6His-REM1.3N bands from 5 independent repeats. (D) *In vitro* phosphorylation of 6His-REM1.3 by leaf microsomal extracts in the presence of total RNA extracts from PVX-infected leaves. (E) Experimental flow-chart to study the role virus protein in membrane-bound kinase activation. (F) 6His-REM1.3N phosphorylation by microsomal extracts infected with PVX-GFP or expressing the indicated viral proteins at 4 DAI. Leaves expressing GFP alone, infiltrated with water or with *A. tumefaciens* strain GV3101 alone served as controls. Expression of the viral proteins is presented in S3 Fig. (G) Graph represents the quantification of 6His-REM1.3N bands from three independent repeats (n = 3), as a percentage of the activity induced by *A. tumefaciens* strain GV3101 alone. Error bars show SE, and significance is assessed by Dunnett's multiple comparison test to water control (*, P < 0.1; **, P < 0.05; ***, P < 0.001). Phosphorylated proteins were detected by autoradiography and total proteins by stain free procedure. In all experiments 10 μ g of total protein extracts and 1 μ g of affinity purified 6His-REM1.3 or 6His-REM1.3^N were loaded per lane.

<https://doi.org/10.1371/journal.ppat.1007378.g002>

(residues 117–198, hereafter 6His:REM1.3^C) did not present any detectable phosphorylation (S3B and S3C Fig).

We next tested whether PVX activates the kinase(s) that phosphorylate(s) REM1.3. Our results unveiled that microsomal and PM fractions extracted from symptomatic PVX-infected leaves promoted higher levels of 6His-REM1.3 phosphorylation compared to non-infected plants (Fig 2B and 2C). Studies have shown that functionally different viral components, such as virus-encoded proteins and double-stranded RNA, can trigger plant defense responses [51–56]. We therefore examined whether the PVX genome in its free form was an eliciting signal for kinase activation. We found that the addition of total RNAs extracted from PVX-infected plants in the kinase reaction mix did not alter the levels of 6His-REM1.3 phosphorylation (Fig 2D). We then examined whether the sole expression of individual viral movement proteins was sufficient to trigger REM1.3 phosphorylation (Fig 2E). Importantly, our results demonstrated that the expression of TGBp1 and Coat Protein (CP) fused to GFP triggered the strongest levels of 6His-REM1.3^N phosphorylation to the same extent as the full PVX-GFP construct (Fig 2F and 2G and S3E Fig for controls of viral fluorescent-tagged protein expression as described in [41]). In good agreement, expression of a TGBp1-deleted version of PVX (PVX Δ TGBp1) decreased 6His-REM1.3 phosphorylation levels compared to wild-type PVX extracts (S3D Fig). Expression of TGBp2 and infiltration of the empty *Agrobacterium* strain alone protein also induced 6His-REM1.3^N phosphorylation, albeit less effective than TGBp1 and CP proteins (Fig 2F and 2G). In accordance with previous reports suggesting REM phosphorylation during plant-microbe interactions [9], *Agrobacterium* infected *N. benthamiana* extracts induced much stronger REM1.3 phosphorylation than the water control condition (Fig 2F and 2G). Furthermore, we found that the 30K-RFP protein from Tobacco mosaic virus (TMV) also induces REM phosphorylation (S3D Fig). Similar to PVX-TGBp1, REM1.3 interferes with the ability of TMV-30K to increase PD permeability [33] and overexpression of REM1.3 restricts TMV-GFP cell-to-cell movement in *N. benthamiana* epidermal cells (S4A Fig).

Altogether our data suggest an additional role of REM-mediated plant response against TMV and possibly to bacteria. Our results also indicate that REM1.3 phosphorylation status is modulated by the perception of viral proteins by plant cells.

Phosphorylation of REM1.3 regulates its function in restricting PVX spreading via PD aperture modulation

Since phosphorylation of REM occurs upon PVX infection, we next aimed to functionally characterize the importance of REM1.3 phosphorylation for the regulation of PVX cell-to-cell movement. Despite our efforts, the identification of *in vivo* phosphorylation sites of REM1.3 appeared technically challenging and remained unsuccessful. *In silico* predictions and *in vitro*

kinase assays however showed that REM1.3^N displays regions of intrinsic disorder and presents the highest potential of phosphorylation (Fig 2C–2F and Fig 3A). For functional characterization, we selected the three putative phosphorylation Serine(S) /Threonine(T) sites present in REM1.3^N, namely S74, T86 and S91, that presented high scores of phosphorylation prediction in intrinsic disorder regions (Fig 3A). S74 and S91 are conserved across the phylogenetic group 1b of REM proteins, suggesting functional redundancy (S5A Fig) [32, 57]. S74 and S91 were the analogous residues identified as phosphorylated *in vivo* in the group 1b REM *AtREM1.3* (At2g45820) of *Arabidopsis thaliana* (hereafter *Arabidopsis*) in a stimuli-dependent manner [39, 40, 57]. Biochemical analysis showed that α -1,4-poly-D-galacturonic acid (PGA)-induced phosphorylation of *StREM1.3* occurs on T32, S74 and T86 [58]. T86 is not conserved in *Arabidopsis* but it is conserved in Solanaceae REM proteins, such as in *N. benthamiana* (S5A Fig). By an *in vitro* kinase assay, we show that phosphorylation occurs within three potential phosphor-residues, since mutation of S74, T86 and S91 to the non-phosphorylatable Aspartic acid (D), generating the 6His-REM1.3^{DDD} mutant abolished REM phosphorylation by the PVX-activated kinase(s) (Fig 3B and 3C).

To discriminate which residues are functionally relevant in the context of PVX-GFP propagation, we generated RFP-tagged REM1.3 phosphomutants, individually mutated at those sites to the non-phosphorylatable Alanine. Transient expression in *N. benthamiana* coupled with PVX-GFP infection assays demonstrated that individual phospho-null mutations at those sites induce a loss of function of REM1.3 in restricting PVX-GFP spreading (Fig 3D). This result suggests that phosphorylation of either S74, T86 and S91 is important for REM1.3 function.

To further characterize the relevance of different REM1.3 phospho-statuses in the context of PVX-GFP propagation and PD-aperture regulation, we analysed RFP-tagged REM1.3^{DDD} to mimic constitutive phosphorylation hereafter termed phosphomimetic mutant, or to Alanine (REM1.3^{AAA}) hereafter termed phosphodead mutant. Infection assays in *N. benthamiana* confirmed that the phosphodead mutant completely lost REM1.3 ability to restrict PVX-GFP cell-to-cell movement, while the phosphomimetic mutant maintained this ability (Fig 3D). TMV-GFP propagation was similarly affected by the phospho-status of REM1.3 (S4A Fig). We then analyzed the capacity of REM1.3 phosphomutants to regulate PD aperture in the absence of viral infection. As previously described [33, 36], RFP-REM1.3 reduces the PD size-exclusion limit as measured by free-GFP cell-to-cell diffusion (Fig 3E). Detailed analysis of REM1.3 phosphorylation mutants demonstrated that the phosphomimetic mutant recapitulated REM1.3 activity towards PD-aperture regulation, while the phosphodead mutant did not (Fig 3E).

Altogether, these results provide strong evidence that REM1.3's phosphorylation state at the evolutionarily conserved positions of S74, T86 and S91 is linked to its function in controlling viral infection and PD conductance.

REM1.3 phospho-status modulates its dynamic lateral segregation in the PM and PD sub-compartments

Both REM1.3 phosphomimetic and phosphodead mutants maintained PM localization, similarly to wild-type REM1.3, when transiently expressed in fusion with YFP in *N. benthamiana* (S4B Fig). Upon PVX infection we observed a modulation of REM1.3 PD-association and PM dynamics (Fig 1), linked to REM1.3 phosphorylation (Fig 2) that is required for REM1.3 function against PVX infection (Fig 3). We then asked whether different REM1.3 phospho-statuses might regulate its lateral organization at the PM and PD compartments in the absence of PVX. We examined the enrichment of REM1.3 YFP-tagged phosphomutants at the PD pit fields, previously calculated by the PD index (S1 Fig) and found that similarly to YFP-REM1.3, none

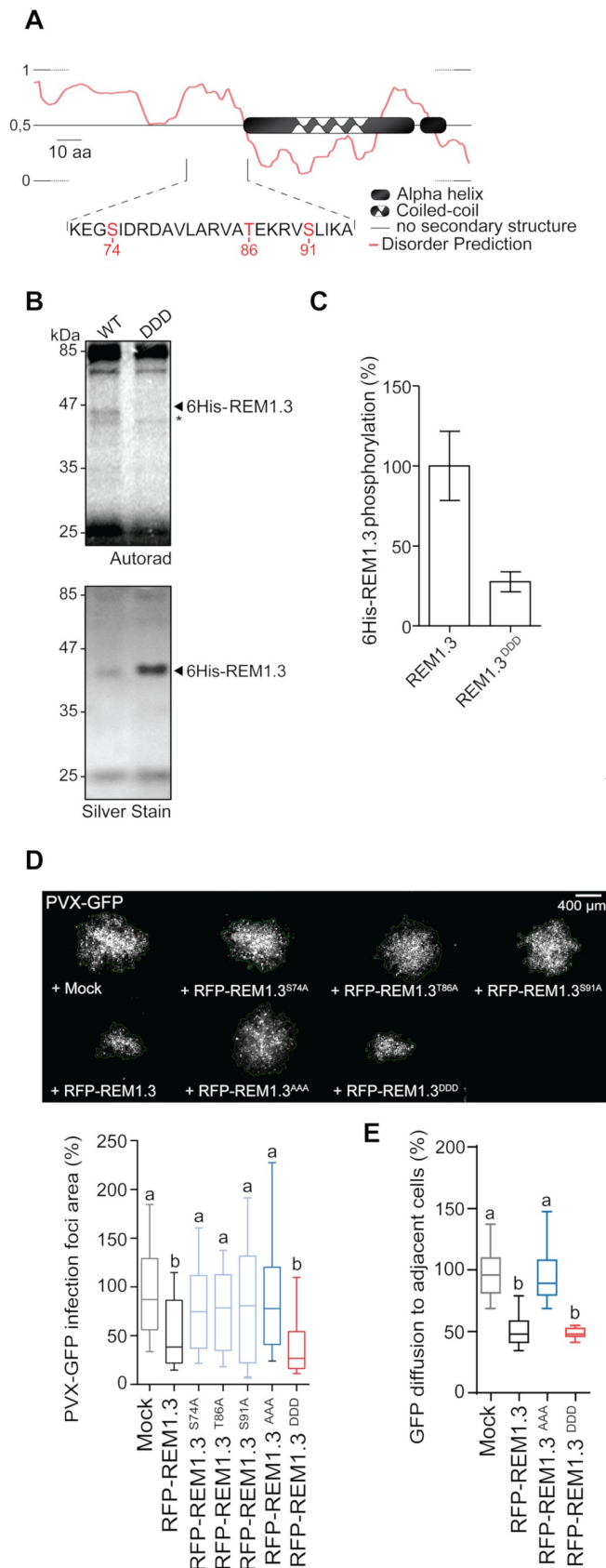


Fig 3. Mutational analysis reveals three critical phospho-residues required for REM1.3 regulation of PVX-GFP propagation and PD conductance. (A) *In silico* analysis of REM1.3 protein sequence. Prediction of putative phosphorylation sites was performed by Diphos, DEPP and NETPHOS coupled with published MS data. Predictions highlight three residues S74, T86 and S91 with high probability to be phosphorylated. Disordered prediction was performed by pDONR VL XT. Numbers indicate amino acid position. (B) *In vitro* kinase assay on recombinant affinity purified 6His-REM1.3 or 6His-REM1.3DDD by incubation with [γ - 32 P]-ATP and microsomal extracts of PVX-infected *N. benthamiana* leaves, as described in Fig 2. Phosphorylated proteins were detected by autoradiography and total proteins by silver staining. Asterisk * indicates phosphorylation of a *N. benthamiana* protein of close molecular weight not detected by silver staining. (C) Graph represents the relative quantifications from 4 independent reactions, using WT signal as a reference. (D) *Left*, Representative epifluorescence microscopy images of PVX-GFP infection foci on *N. benthamiana* leaf epidermal cells at 5 DAI. Graph represents the mean relative PVX-GFP foci area in cells transiently expressing RFP alone, wild-type RFP-REM1.3 or carrying single serine /threonine mutations to alanine. Co-infiltration of PVX-GFP with an empty *A. tumefaciens* strain served as mock control. Approximately 160 foci per condition from 3 independent biological repeats were measured. Letters indicate significant differences revealed by Dunn's multiple comparisons test $p < 0.001$. *Right*, Graph represents the mean relative PVX-GFP foci area in cells transiently expressing wild-type RFP-REM1.3 or triple RFP-REM1.3 phosphodead and phosphomimetic mutants compared to mock control (co-infiltration of PVX-GFP with an empty *A. tumefaciens* strain). Approximately 250 foci per condition from 5 independent biological repeats were measured. Letters indicate significant differences revealed by Dunn's multiple comparisons test $p < 0.001$. Epifluorescence microscopy images show representative PVX-GFP infection foci on *N. benthamiana* leaf epidermal cells at 5 DAI. (E) GFP diffusion to neighbor cells was estimated by epifluorescence microscopy at 5 DAI in *N. benthamiana* cells transiently expressing RFP-REM1.3 or phosphomutants. Measurements from 3 independent biological repeats were normalized to mock control (co-infiltration with an empty *A. tumefaciens* strain). Letters indicate significant differences determined by Dunn's multiple comparisons test $p < 0.001$.

<https://doi.org/10.1371/journal.ppat.1007378.g003>

of the phosphomutants appeared enriched at the pit field level (Fig 4A and 4C). The phosphodead mutant appeared statistically more excluded than YFP-REM1.3, whereas the phosphomimetic mutant displayed an increase of its PD index (Fig 4C), reminiscent of the REM1.3 localization phenotype under PVX infection (Fig 1A and 1B). Importantly, REM1.3 phosphomutants' association with PD was directly correlated with callose content at PD (Fig 4B). These observations reinforced the hypothesis that REM1.3-mediated increase of callose levels at PD is associated with a dynamic and phosphorylation-dependent redistribution of REM1.3 to the PD surroundings.

We next used spt-PALM VAEM to characterize the localization and mobility behaviour of the EOS-REM1.3 phosphomutants in the PM plane. The analysis of reconstructed trajectories and corresponding super-resolved localization maps indicated slight modifications of lateral mobility behavior between the phosphomutants (Fig 4D and 4E). Quantification of the diffusion coefficient values (D) extracted for each individual molecule revealed that EOS-REM1.3^{AAA} displayed a more immobile behavior than EOS-REM1.3^{DDD} and EOS-REM1.3. Consistently, EOS-REM1.3^{DDD} exhibited a higher mobility illustrated by higher diffusion coefficient and mean square displacement values (Fig 4D and 4E). Analysis of the supra-molecular organization of the phosphomutants by Voronoï tessellation (Fig 4F) firstly showed that all mutants displayed similar nanodomain size and localization density compared to EOS-REM1.3WT. Compared to EOS-REM1.3^{AAA}, the EOS-REM1.3^{DDD} nanodomains occupied a smaller area of the total PM and their density in the PM plane appeared slightly reduced (Fig 4F and 4G). A higher number of nanodomains were formed with the EOS-REM1.3^{AAA} mutant. Hence, the phosphomimetic mutations favor a less confined and a more dynamic localization pattern of REM1.3 at the PM, reminiscent to the phenotype of EOS-REM1.3WT in the context of PVX infection (Fig 1C and 1D).

These results suggest that differential REM1.3 phosphorylation is involved in regulating REM1.3 mobility and PM domain organization and support the hypothesis that REM1.3 phosphorylation on S74, T86 and S91 reflects an 'active form' of the protein necessary for REM1.3-mediated defense signaling.

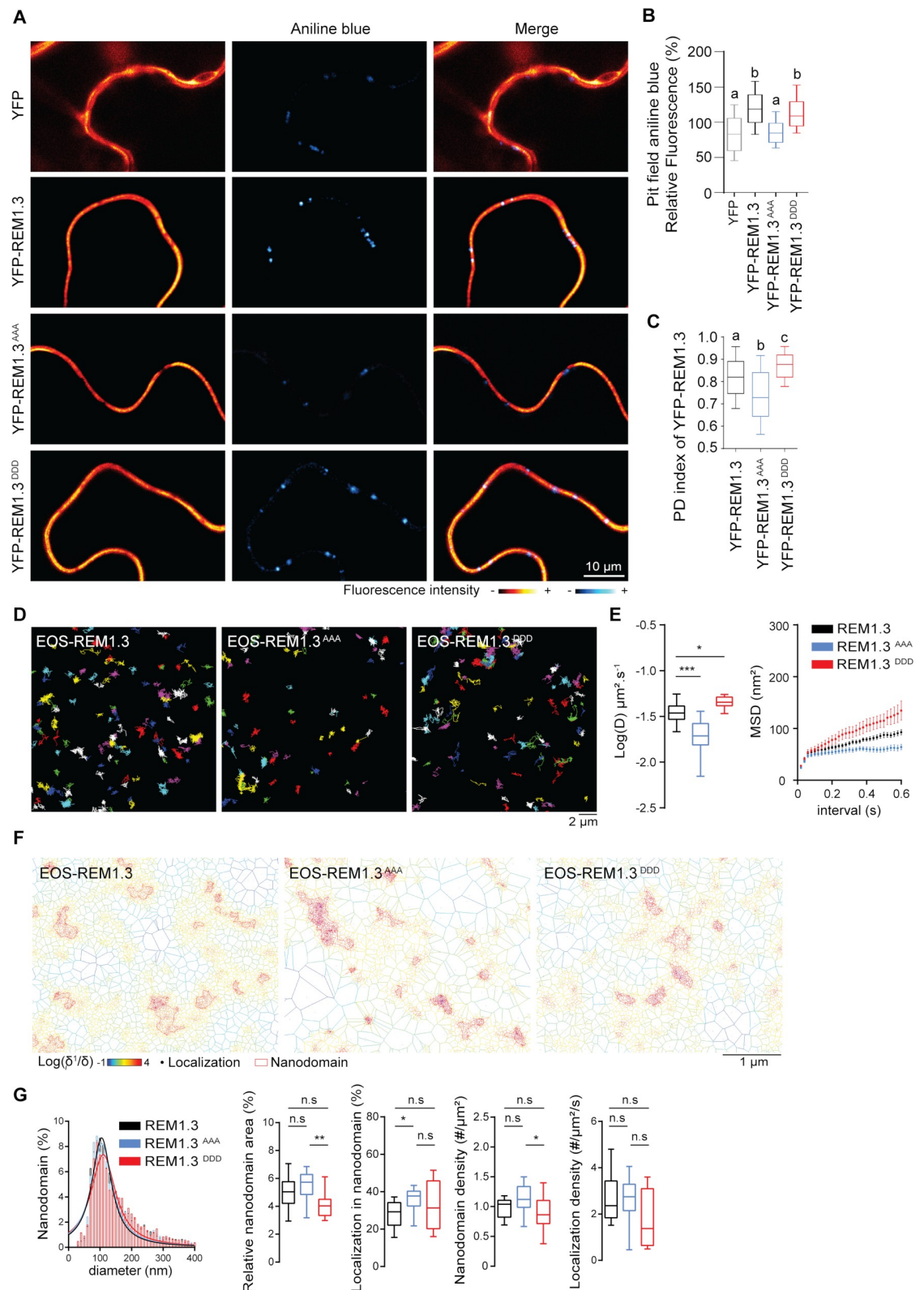


Fig 4. REM1.3's dynamic localization in PD and PM nanodomains is regulated by its phospho-status. (A) Representative confocal images showing aniline blue staining of callose deposition at the PD pitfields in *N. benthamiana* leaf epidermal cells transiently expressing YFP-REM1.3 or phosphomutants. Color-coding indicates fluorescence intensity. (B) Graphs show aniline

blue fluorescence intensities in cells transiently expressing YFP-REM1.3 and phosphomutants relative to control cells expressing YFP alone. Three independent biological experiments were performed and at least 15 cells per condition and per experiment were analyzed. Letter indicate significant differences revealed by Dunn's multiple comparisons test $p < 0.001$. (C) PD index of YFP-REM1.3 phosphomutants was calculated as described in S1 Fig. Graphs present quantifications from 3 independent biological experiments. Letter indicate significant differences revealed by Dunn's multiple comparisons test $p < 0.002$. (D) Super-resolved trajectories (illustrated by different colours) of transiently expressed EOS-REM1.3, and phosphomutants, transiently expressed in *N. benthamiana* cells, observed by spt-PALM. Scale bars, 2 μm . (E) Distribution of diffusion coefficients (D) represented as $\log(D)$ of the different fusion proteins. Mean Square Displacement (MSD) over time for the global trajectories of each EOS-REM1.3 construct followed during at least 600ms. 27 cells for EOS-REM1.3, 15 cells for EOS-REM1.3AAA and 17 cells for EOS-REM1.3DDD were analyzed in 3 independent experiments. Statistical analysis was performed by Mann-Whitney test * $p < 0.05$ ** $p < 0.01$. (F) Live PALM analysis of EOS-REM1.3 phosphomutants by tessellation-based automatic segmentation of super-resolution images. (G) Computation of EOS-REM1.3 and phosphomutants single molecule organization features based on tessellation-based automatic segmentation images. For REM1.3 and phosphomutants nanodomain size distribution and the Gaussian fits are indicated. Total nanodomain area is expressed as percentage of the total PM surface. Percentage of EOS-REM1.3 molecules localizing into nanodomains, relative to all molecules observed. Localization density refers to the number of molecules observed per μm^2 per second. Statistics were performed on at least 13 data sets per condition extracted from 3 independent experiments. Statistical differences determined by Mann-Whitney test * $p < 0.05$, ** $p < 0.01$.

<https://doi.org/10.1371/journal.ppat.1007378.g004>

AtCPK3 phosphorylates REM1.3

To gain more insights into the signaling processes leading to REM1.3 phosphorylation, we aimed to biochemically characterize the kinase(s) involved in the phosphorylation of REM1.3. Previous evidence suggested that the kinase(s) phosphorylating REM1.3 are membrane-associated (Fig 2) [38]. We therefore biochemically analyzed the localization of the kinase(s) phosphorylating REM1.3. Plant material from healthy and PVX-GFP-infected leaves was cell-fractionated to obtain crude extracts, soluble and microsomal fractions [59] to perform *in vitro* kinase assays on REM1.3N. Analysis confirmed a maximal kinase activity in purified microsomes (Figs 5A and 2A). Since a kinase in close proximity with its substrate would enhance reaction kinetics [60] and signal fidelity [61], and given that REM1.3 is enriched in detergent-resistant membranes (DRM) [8], we investigated whether the kinase activity towards 6His-REM1.3 is enriched in this biochemical fraction. We included "control PM" (C-PM) preparations, submitted to discontinuous sucrose gradients but in the absence of Triton-X100 treatments [62]. *In vitro* kinase assays on 6His-REM1.3N showed that the kinase activity in C-PM was 5 times inferior than in freshly purified PM not submitted to the sucrose gradient, suggesting that the kinase is not stable during the overnight purification procedure. Only half of the specific activity of the kinase was found in DRMs compared to the C-PM fraction, indicating that the kinase(s) phosphorylating REM1.3 is (are) only partially located in the DRM fraction (Fig 5B).

To gain more information concerning the biochemical characteristics of the kinase phosphorylating REM1.3, we analyzed its activity in the presence of known inhibitors. We firstly tested staurosporine, [63, 64] a general inhibitor that prevents ATP binding to kinases. We found an inhibition of REM1.3 phosphorylation starting at very low concentrations (30 nM) (S6A Fig). We further tested the effect of poly-L-lysine, described to stimulate the activity of the CK2 kinases and inhibit several CDPK kinases [65, 66]. No significant differences on REM1.3 phosphorylation levels were observed under increasing concentrations of poly-L-lysine (S6B Fig). The addition of the wide range of Ser/Thr phosphatases inhibitor β -glycerophosphate (BGP) [66] to the reaction mix did not alter the levels of phosphorylated 6His-REM1.3, indicating that the observed data was due to the activation of kinase activity by PVX rather than by inhibition of phosphatases (S6B Fig). Competition assays in the presence of cold AMP and GTP showed that only cold ATP even at 2 mM caused 20-fold depletion in [γ - ^{33}P] incorporation, suggesting that ATP is the major phosphoryl-donor for the kinase (S6B Fig). Addition in the reaction mix of 0,2 mM of EGTA, a chelator of Ca^{2+} , strongly inhibited the kinase activity suggesting that the kinase(s) phosphorylating REM1.3 in healthy leaves is

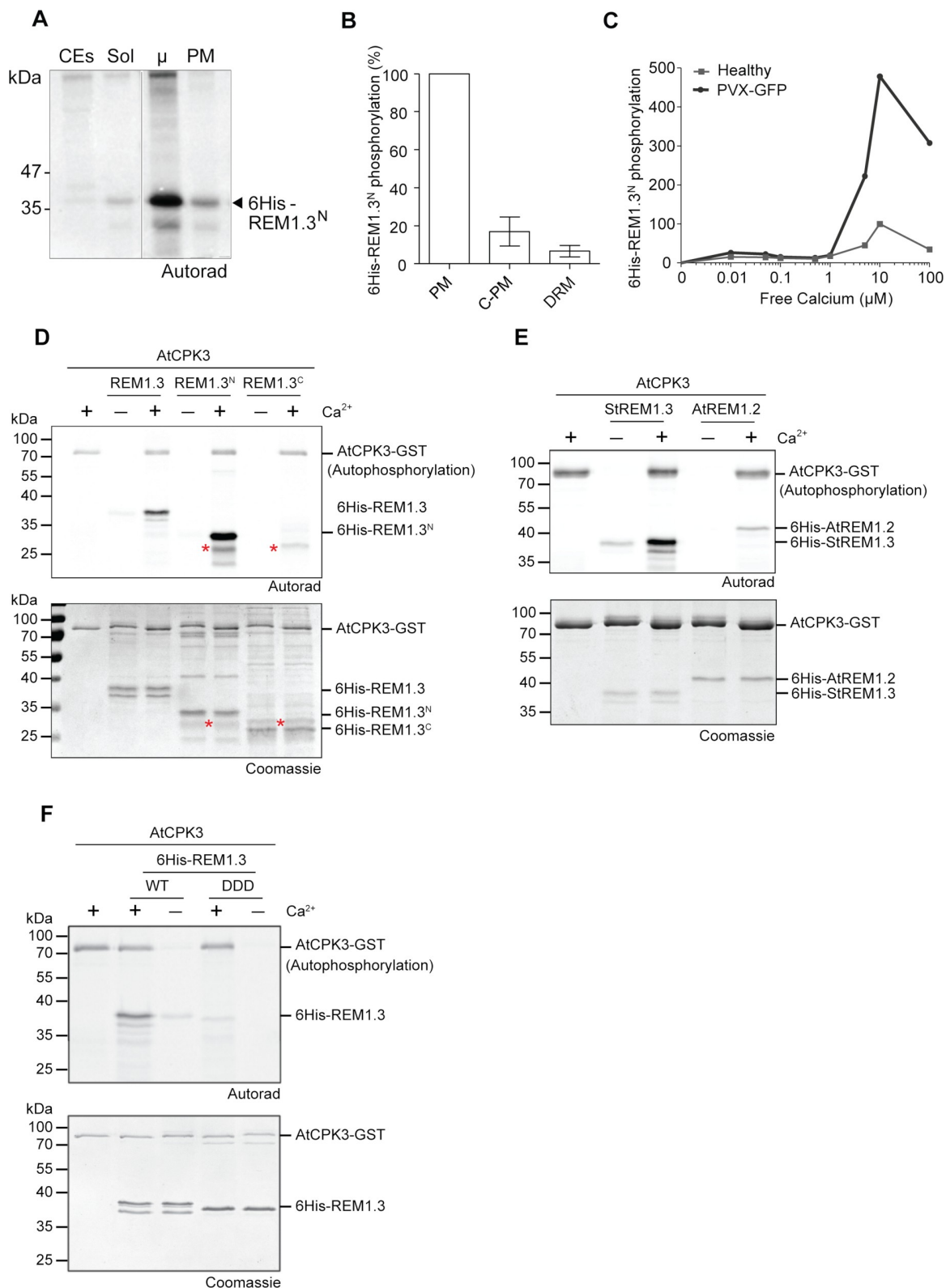


Fig 5. AtCPK3 phosphorylates REM1.3 in a calcium-dependent manner. (A, B) *In vitro* phosphorylation of purified 6His:REM1.3^N by kinase(s) from different cellular fractions of *N. benthamiana* leaves, CEs, leaf crude extracts; Sol, Soluble fraction; μ , microsomal fraction; PM, Plasma Membrane; C-PM: "Control-PM" is PM fraction not treated by TX100, but submitted to sucrose gradient; DRM, Detergent

resistant membranes [62]. The graph represents the relative quantification of 3 independent experiments normalized to the activity in the PM fraction +/- SEM. (C) Quantification of the calcium dose response of kinase activity on 6His-REM1.3^N phosphorylation by *N. benthamiana* microsomal extracts from healthy and PVX infected leaves. (D, E, F) Autoradiography gels show *in vitro* phosphorylation of 6His-REM1.3, 6His-REM1.3^N and 6His-REM1.3^C, 6His-REM1.3^{DD} or 6His-AtREM1.2 by affinity purified GST-AtCPK3 in the presence or the absence of Ca²⁺. Bands corresponding to autophosphorylation of AtCPK3-GST and transphosphorylation of 6His-tagged group 1 REM variants are indicated. Gels were stained by coomassie blue to visualize protein loading. Asterisk* indicates a non-specific band present in both 6His-REM1.3^C and 6His-REM1.3^N preparation.

<https://doi.org/10.1371/journal.ppat.1007378.g005>

calcium sensitive (S6C Fig). Calcium is a conserved second messenger in signal transduction during biotic and abiotic stress. In plants, kinases harboring different calcium sensitivities can perceive calcium variations and translate them into downstream signaling activation [67, 68]. To determine whether the PVX-activated kinase phosphorylating REM1.3 is sensitive to calcium regulation, *in vitro* kinase assays from microsomes of healthy and PVX-infected *N. benthamiana* leaves were assayed in the presence of free calcium (Ca²⁺) concentrations ranging from 10 nM to 0,1 mM. Fig 5C shows that the kinase(s) displays a high sensitivity to calcium with an optimal activity in the presence of 10 μM of free Ca²⁺. At this concentration, a 5-fold increase of 6His-REM1.3^N phosphorylation was observed in PVX-infected leaves (Fig 5C). These experiments allowed us to narrow-down the kinase(s) phosphorylating REM1.3 after PVX infection to the group of membrane-bound Ca²⁺-dependent protein kinases [67].

Plants possess three main families of calcium-regulated kinases: calmodulin-binding kinases (CBKs), calcineurin B-like-interacting protein kinases (CIPKs) and calcium-dependent protein kinases (CPKs) [67]. CPKs have the unique feature of calcium sensing and responding activities in one single polypeptide, best characterized in the model plant *Arabidopsis* [67]. Based on the measured calcium dose response (Fig 5C), we correlated the kinase phosphorylating REM1.3 in *N. benthamiana* with homologs of *Arabidopsis* subgroup II AtCPKs [69], and we aimed to capitalize on the knowledge of *Arabidopsis* CPKs to test REM1.3 phosphorylation. Among the characterized members of subgroup II AtCPKs, we selected the *Arabidopsis* AtCPK3 as a good candidate to test its putative role in REM1.3 phosphorylation, since previous proteomics studies in *Arabidopsis* have identified both AtCPK3 and AtREM1.3 as being enriched in PM, PD and DRM fractions [22, 70]. In addition, one study showed that AtREM1.3 from microsomal fractions is phosphorylated *in vitro* by AtCPK3 [71]. We therefore predicted that REM1.3 might share common functions with the evolutionarily conserved group 1b *Arabidopsis* REMs [32]. AtREM1.2 and AtREM1.3 are close homologs to REM1.3 and group 1 *N. benthamiana* REMs (NbREMs) in term of protein sequence [32, 36] and they conserved at least the S74 and S91 phosphorylation sites [39], [40, 57] (S5A Fig). Using super-resolution microscopy, Demir *et al.* showed that, when co-expressed in *Arabidopsis* leaves, REM1.3 and AtREM1.3 co-localized in the same PM-nanodomains [72]. Importantly, transient expression of AtREM1.2 and AtREM1.3 in *N. benthamiana* epidermal cells impaired PVX-GFP cell-to-cell movement, as REM1.3 does (S5B Fig), strengthening the hypothesis that the function of group 1 REMs might be conserved between homologs in different plant species [36].

We assayed the *in vitro* phosphorylation activity of the affinity-purified AtCPK3-GST towards the 6His-REM1.3, the 6His-REM1.3^N and the 6His-REM1.3^C, as well as the homologous substrate 6His-AtREM1.2. Similar to our previous results (S3B and S3C Fig), AtCPK3-GST could phosphorylate strongly both 6His-REM1.3 and 6His-REM1.3^N, but not 6His-REM1.3^C (Fig 5D). In accordance with the effect of AtREM1.2 in PVX-GFP propagation (S5B Fig), AtCPK3-GST can also phosphorylate 6His-AtREM1.2 (Fig 5E). Addition of Ca²⁺ is essential for a strong kinase activity as shown by both kinase auto-phosphorylation and transphosphorylation (Fig 5D and 5E). AtCPK3-GST specifically phosphorylated S74, T86 and S91

residues of REM1.3, since the phosphorylation was abolished in the phosphomimetic mutant 6His-REM1.3^{DDD} (Fig 5F).

These results suggest that AtCPK3 is a good candidate for group 1b REM phosphorylation and further support that the S74, T86, and S91 are the phosphorylation sites of REM1.3 (Figs 3A and 5E).

AtCPK3 interacts with group 1b REMs and restricts PVX propagation in a REM-dependent manner

CPKs harbor a variable N-terminal domain, a Ser/Thr kinase domain, an auto-inhibitory junction region and a regulatory calmodulin-like domain. The calmodulin-like domain contains four EF-hand binding motifs that determine the sensitivity of each kinase to calcium [73, 74]. To investigate the role of AtCPK3 in REM-dependent signalling, we generated AtCPK3 mutants presenting altered kinase activities. Deletion of the inhibitory junction region and the regulatory calmodulin-like domain in CPKs creates a constitutive active kinase while mutation of the aspartic acid residue in the catalytic center 'DLK' motif of the kinase domain to an alanine (D202A) creates a catalytically inactive or 'dead' kinase [67] (Fig 6A). We generated AtCPK3 full-length (AtCPK3), constitutive active (AtCPK3CA, residues 1–342) and kinase-dead (AtCPK3CAD202A) constructs for transient protein expression (Fig 6A). We evaluated their catalytic activities by expressing them transiently in *Arabidopsis* mesophyll protoplasts and performing immunoprecipitation coupled to kinase assays using 6His-REM1.3 and histone as a generic substrate [67]. Autoradiography confirmed that *in vivo* purified AtCPK3-CA-HA could trans-phosphorylate both 6His-REM1.3 and histone without the addition of calcium, while the point mutation D202A drastically abolished kinase activity (S7 Fig).

We next examined the sub-cellular localization of both AtCPK3 and AtCPK3CA fused to YFP and found that both proteins disclosed a partial association with the PM, which was further confirmed by their presence, after cell fractionation, in the microsomal fraction at the expected molecular weight (Fig 6B) in good agreement with [71]. We further used AtCPK3CA to test the interaction with group 1b REMs. Bimolecular Fluorescence Complementation (BiFC) experiments showed that AtCPK3CA and REM1.3, REM1.3^{AAA} and REM1.3^{DDD} interact together at the level of the PM *in planta*. Importantly, we also confirmed the interaction of AtCPK3CA with homologous AtREM1.2 and AtREM1.3 (Fig 6C). REM1.3/REM1.3 interaction was used as a positive control, and AtCPK3CA /AtCPK3CA as a negative control.

We finally aimed to functionally characterize the AtCPK3- and REM1.3-mediated signaling in the context of PVX infection. Transient over-expression of AtCPK3-RFP alone induces a reduction of PVX-GFP infection foci suggesting that AtCPK3 is indeed important for antiviral responses in plant cells (Fig 6D). Expression of the constitutively-active AtCPK3CA-RFP had a stronger effect on PVX-GFP spreading and to a similar degree with the over-expression of REM1.3 alone (Fig 6D). AtCPK3's function towards PVX movement was observed to be mediated by its kinase activity, as the expression of the catalytically inactive mutant AtCPK3-CA^{D202A} had no effect on PVX-GFP propagation (Fig 6D).

This raised the question whether the effect of AtCPK3CA on PVX propagation was REM-dependent. To tackle this question, we stably transformed *N. benthamiana* plants with a hairpin construct, to induce post-transcriptional gene silencing, which resulted in lowering RNA and protein expression of group 1 endogenous NbREMs (S8A and S8B Fig). Consistent with previous studies [8], silencing of group 1 REM correlates with an increase of PVX-GFP cell-to-cell movement in inoculated leaves (S8C Fig). No difference was observed by ELISA when measuring PVX accumulation in systemic leaves (S8D Fig). Importantly, PVX assays demonstrated that AtCPK3CA ability to restrict PVX movement was impaired in two independent *N.*

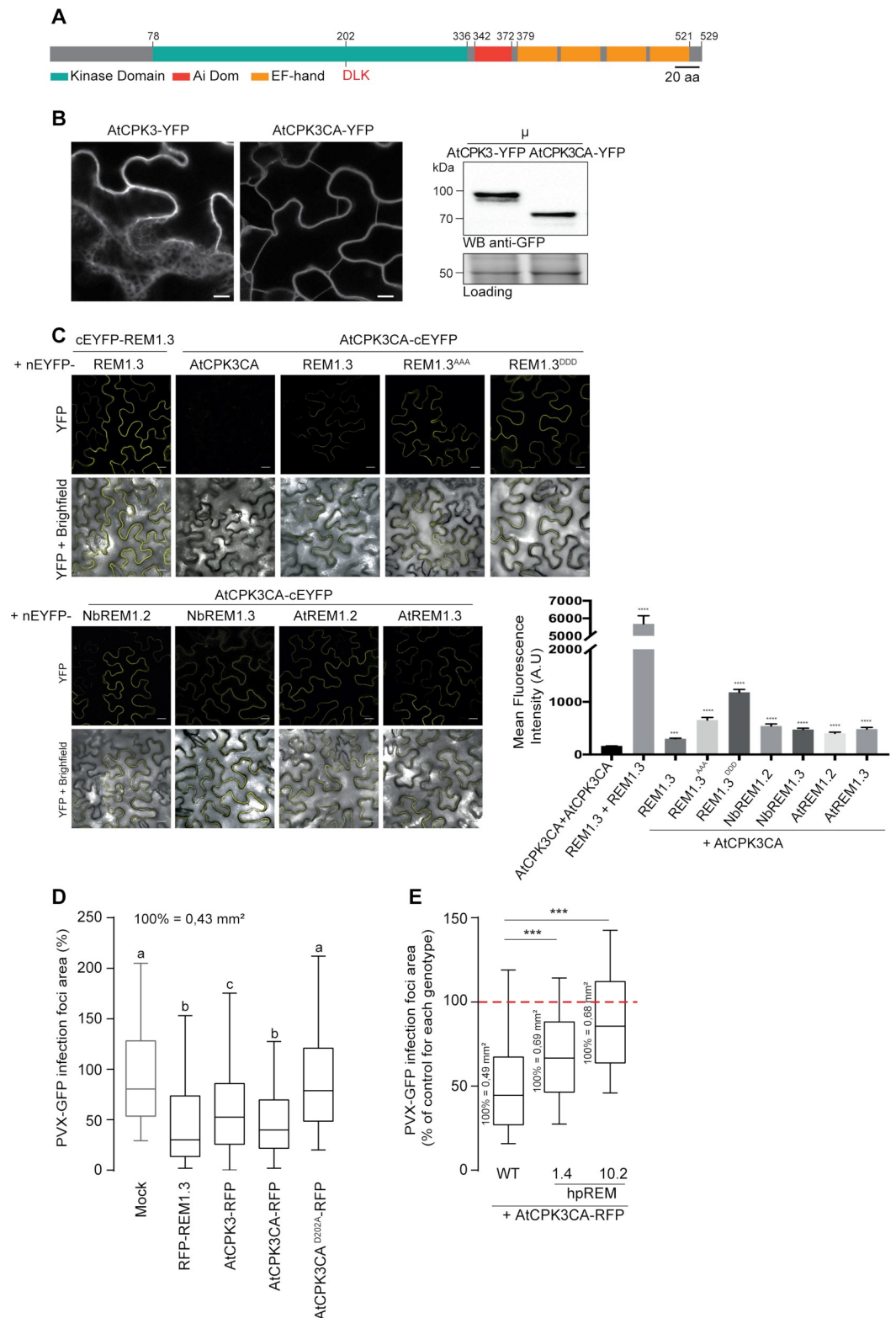


Fig 6. AtCPK3 physically interacts *in vivo* with group 1b REMs and impairs PVX cell-to-cell movement in a REM-dependent manner. (A) Primary sequence of AtCPK3. EF-hands are helix E-loop-helix F structural domains able to bind calcium. Ai: Autoinhibitory domain. The position of the DLK motif (Aspartic acid-Leucine-Lysine) at the catalytic domain conserved in all CPKs is indicated. (B) Confocal images showing AtCPK3-YFP and AtCPK3CA-YFP localization in *N. benthamiana*. (C) Fluorescence microscopy images and a bar graph showing the interaction of AtCPK3CA with various REM proteins. (D) Box plot showing the percentage of PVX-GFP infection foci area for different genotypes. (E) Box plot showing the percentage of PVX-GFP infection foci area for WT, 1.4, and 10.2 hpREM genotypes.

benthamiana epidermal cells. Scale bar shows 10 μ m. Western blot against GFP showing AtCPK3-YFP and AtCPK3CA-YFP expression in the microsomal fraction (μ) of *N. benthamiana* leaves. (C) *In planta* Bimolecular Fluorescence Complementation (BiFC) analysis showing interaction of AtCPK3 with Group 1 REMs. REM1.3-YFPN/REM1.3-YFPC was used as a positive control, and AtCPK3CA-nYFP/AtCPK3CA-cYFP as a negative control. Mean fluorescence intensity at the cell boundary level was recorded using ImageJ. Statistical differences were determined by Mann-Whitney test compared to AtCPK3CA + AtCPK3CA.*** $p = 0.0002$, **** $p < 0.0001$. All scale bars indicate 20 μ m. (D) PVX-GFP spreading in *N. benthamiana* cells expressing RFP-REM1.3 or AtCPK3FL-RFP, AtCPK3CA-RFP, AtCPK3CAD202A-RFP. Graph represents the area of PVX-GFP infection foci relative to the mock control (co-infiltration of PVX-GFP with empty *A. tumefaciens*). At least 200 PVX-GFP infection foci from at least 3 independent repeats were imaged at 5DAI. Letters indicate significant differences revealed by Dunn's multiple comparisons test $p < 0.001$. (E) Effect of AtCPK3CA on PVX-GFP cell-to-cell movement in WT *N. benthamiana* or in transgenic lines constitutively expressing hairpin REM (hpREM) constructs. At least 200 PVX-GFP infection foci from at least 3 independent repeats were imaged at 5DAI. For each *N. benthamiana* line the effect of AtCPK3CA is expressed as a percentage of the corresponding mock control (empty *Agrobacteria*). Absolute values of the average foci area for each mock control are indicated.

<https://doi.org/10.1371/journal.ppat.1007378.g006>

benthamiana lines underexpressing group 1 REM levels, (namely lines 1.4 and 10.2 with expression levels decreased respectively by 2 and 20 times) (Fig 6E), indicating that REMs might be the direct substrate of CPK3 *in vivo*.

Altogether, these data suggest that CPK3 and group 1 REMs are major regulators involved in signaling and antiviral defense at the PM level.

Discussion

Protein phosphorylation is a ubiquitous and specific mechanism of cell communication [75]. The addition of a phosphate group on one or more critical residues of a given protein can induce important conformational changes that affect energetically favorable interactions and may lead to changes in its interacting network, localization, abundance and may influence the activity of protein signaling pools [76]. Although, since the initial discovery of REM1.3 in 1989, accumulating evidence suggests that the functions of REM proteins are regulated by protein phosphorylation [38–40]. The biological significance of this phosphorylation remained unclear to this date. REM proteins were among the first plant proteins described which supported the notion of PM sub-compartmentalization to functional protein-lipid nanodomains [8, 11, 77], also named membrane rafts [3, 4, 21]. In the present paper, we used REM1.3 and PVX as an experimental system to study the role of protein phosphorylation and membrane dynamics in the context of stress response.

REM1.3 functions likely involve distinct PM compartments during plant PVX-sensing

Understanding how plants defend themselves against viruses remains a challenging field. The canonical plant immune response against viruses is mainly represented by the mechanism of RNA silencing [78, 79], while additional mechanisms of plant antiviral defense involve hormonal signaling, protein degradation, suppression of protein synthesis and metabolic regulation [51, 78, 80]. Antiviral defense presents similarities to the immune response against microbes [81–83]. Compelling evidence suggests that cell-surface as well as intracellular plant immune receptors recognize viral elicitors [55, 84–89]. An additional number of host cell components have been shown genetically to affect viral replication or cell-to-cell movement [8, 90], indicating that more sophisticated plant defense mechanisms against viruses may exist.

For instance, manipulation of REM levels in transgenic *Solanaceae* suggested that REM is as a positive regulator of defense against the PVX by affecting viral cell-to-cell movement [8, 14, 36]. We recently showed that REM1.3 does not interfere with the suppressor ability of PVX movement protein TGBp1, but specifically affects its gating ability [33]. Group 1 REMs could

be a target for viruses (and other pathogens) to circumvent infection as illustrated by the case of *Rice Stripe Virus* that targets NbREM1 for degradation by 26S proteasome [91]. Nevertheless, in this study we show that REM1.3 protein levels are not altered during PVX infection (S2C and S2D Fig).

In this paper, we provide supporting mechanistic evidence that REM1.3 regulates the levels of callose accumulation at PD pit fields during PVX infection (Fig 1). Whether this function is mediated by a direct interaction with callose synthase/glucanase complexes remains however still unknown. Surprisingly, we found that REM1.3 is not dramatically recruited to PD pit fields, although its PD index is slightly increased after PVX infection (Fig 1). This suggests that association of a sub-fraction of the REM1.3 to the PD-PM region may be sufficient to increase callose accumulation, although we cannot rule out the possibility that REM1.3 may regulate PD permeability *via* a more indirect mechanism. The spt-PALM VAEM microscopy data supports an increase of protein mobility and redistribution to distinct domains during PVX infection (Fig 1). These findings indicate the existence of a mechanism that operates at specific REM1.3-associated PM nanodomains, capable of regulating PD permeability (Fig 1). The dynamic partitioning between PM nanodomains and PD pit fields needs to be further studied.

Plant PVX-sensing induces the activation of a calcium-dependent protein kinase

Since various studies have reported REM phosphorylation during plant-microbe interactions [16, 17, 39, 40], we set out to address which kinase phosphorylates REM and whether REM1.3 phosphorylation plays a role in REM-mediated anti-viral defense. Indeed, our experimental findings show that plant PVX sensing induces the activation of a membrane-bound calcium-dependent protein kinase that in turn phosphorylates REM1.3 (Fig 2, Fig 5). Importantly, we show that the kinase able to phosphorylate REM1.3 is activated specifically by the expression of two PVX proteins, namely CP and TGBp1. Deciphering the exact mechanisms allowing the molecular recognition of those PVX components will be a crucial step toward understanding REM-mediated anti-viral defense. Intriguingly, the finding that the presence of *Agrobacterium* also induces REM1.3 phosphorylation (Fig 2G) is in agreement with previous reports suggesting phosphorylation of REMs under bacterial infection [39, 40] and suggests that phosphorylation should be also a way to regulate -yet unknown functions- of REM1.3 in bacterial defense.

Genetic studies have established that different CPKs comprise critical plant signaling hubs by sensing and translating pathogen-induced changes of calcium concentrations [67, 68]. Biochemical characterization of the kinase phosphorylating 6His-REM1.3 showed that its strong sensitivity to calcium (Fig 5C) corresponds to homologs of phylogenetic subgroup II CPKs from *Arabidopsis* [67]. CPK3 is a prominent member of subgroup II, shown to function in stomatal ABA signaling [92], in salt stress response [71, 93] and in a defense response against an herbivore [94]. Interestingly, it was suggested that *AtREM1.3* from taxonomical group 1 of REMs could be a substrate for *AtCPK3* in response to salt stress [71]. Here we show that *AtCPK3* can interact *in vivo* with group 1 REM (Fig 6C) and that *AtCPK3* phosphorylates group 1 REM in an *in vitro* kinase assay (Fig 5D). Transient overexpression of *AtCPK3* in *N. benthamiana* resulted in a reduction of PVX propagation in a REM-dependent manner, providing compelling evidence that CPK3 together with REM contribute to the plant antiviral immunity. This is the first report demonstrating the participation of CPKs in plant basal immunity against viruses.

Although [95] reports that there is no calcium signal during early recognition of PVX, the activation of CPKs by PVX supports the notion that calcium might be involved in some other late steps of plant-virus interaction like the control of intercellular connectivity. These changes

in calcium concentrations in the cell are sensed by the CPKs and translated via the phosphorylation of REM and/or other unknown downstream components. In *Nicotiana tabacum* calmodulin isoforms are critical for the plant resistance against Tobacco Mosaic Virus and Cucumber Mosaic Virus, further illustrating the existence of virus-specific patterns of calcium signals [96, 97]. More work is needed to identify the CPK family members participating to the response and also the nature and specificity of those PVX-induced calcium changes.

Phosphorylation regulates group 1 REM's function during PVX cell-to-cell movement

AtCPK3 specifically phosphorylated REM1.3 at its N-terminal domain (residues 1–116), a domain displaying a mostly intrinsically disordered secondary structure (Figs 3A and 5). *In silico* analysis followed by a mutagenesis approach coupled with *in vitro* kinase assays revealed three major putative phosphorylation sites for REM1.3, namely S74, T86 and S91 on REM1.3. The *in vitro* phosphorylation of REM1.3 (Figs 3A and 5E) is almost totally lost when S74, T86 and S91 are mutated to non-phosphorylatable residues, confirming these residues as major REM1.3 phosphorylation sites. Individual phospho-null mutations at those sites impaired REM1.3 ability to restrict PVX cell-to-cell movement to various extent (Fig 3D). The triple phospho-null mutant, YFP-REM1.3^{AAA} totally obliterated REM1.3's capability to restrict PVX cell-to-cell movement (Fig 3D) and to regulate PD permeability (Fig 3E). Reciprocally, REM1.3 triple phosphomimetic mutant, RFP-REM1.3^{DDD} appeared fully functional (Fig 3E and 3F). These results strongly support the functional involvement of single or combined phosphorylation in the N-terminal domain of S74, T86 and S91 to establish REM's function in the context of PVX infection. This is in contrast with LjSYMREM1 from *Lotus japonicus* which was shown to be phosphorylated at its C-terminal domain *in vitro* by SYMRK [16]. Despite the fact that phosphorylation of REM proteins has been widely reported [16, 17, 39, 40, 57], this work firstly describes an associated role of REM-induced phosphorylation with its function.

Toward the understanding of REMORIN function

Our finding that overexpression of *AtREM1.2* and *AtREM1.3* also restricts PVX-GFP cell-to-cell movement (S5B Fig) suggests that REM phosphorylation and its associated functions might be conserved for some REMs of taxonomic group 1b. In good agreement, *AtREM1.2* and *AtREM1.3* localize to the same PM nanodomains [72] and maintain conserved phosphorylation sites with REM1.3 (S5A Fig). By contrast, *AtREM4.1* from subgroup 4, presenting a different N-terminal domain and different expected phosphorylation profile has an opposite effect against geminiviral propagation by promoting susceptibility to *Beet curly top virus* and *Beet severe curly top virus* [17, 57]. This further argues that REMs might be phosphorylated by diverse families of kinases in order to respond to different stimuli [57].

Overexpression of REM1.3 restricts TMV propagation (S4A Fig), and additionally modulates the movement proteins from different virus genera [33, 91]. These findings suggest that the initial hypothesis that REM1.3 causes the sequestration of the PVX virions at the PD [8] might not hold true, but rather that REM1.3 might have a more general role in plant stress and PD regulation (Figs 1 and 3). Interestingly, REM1.3 promotes susceptibility to *Phytophthora infestans* in *N. benthamiana* and localizes exclusively to the PM and the extrahaustorial membrane around non-callosic haustoria [42]. The exact role of REM1.3 as a common regulator of different signaling pathways and its role in PD permeability regulation remains to be determined.

It has been speculated that phosphorylation in intrinsically disorder regions of proteins may act as a molecular switch and confer potential protein-protein interaction plasticity [76, 98]. The intrinsically disordered REM1.3 N-terminal domain exhibits the most sequence variability in REM proteins, presumably conferring signaling specificity [32, 57]. Phosphorylation of *AtREM1.3*'s N-terminal domain could stabilize coil-coiled-associated protein trimerization and protein-protein interactions [57]. Phosphorylated REM1.3 seems to be further targeted to PD-PM to trigger callose deposition. In good agreement, we found that the mobility in the PM of REM1.3 changed depending on its phospho-status (Fig 4). The triple phosphomimetic mutant exhibited a less confined and more mobile behavior at the PM, reminiscent of the WT protein in the context of PVX infection (Fig 4D). Similarly to the role of 14.3.3 proteins in plants [99], REM1.3 could act as a scaffolding protein, interacting with multiple members of a signaling pathway and tethering them into complexes to specific areas of the membrane. Hence, REM1.3 phosphorylation could act as a regulatory switch of protein conformations that would modulate REM1.3 specific interaction patterns and transient signalosomes at the PM. The triple phosphomimetic REM mutant might reflect a 'functionally active' form that constitutes REM-guided signalosomes against PVX-infection at the PM and should be exploited in future studies. The study of the phosphorylation-dependent interactions of REM1.3 (and related phosphocode) in regard to the modulation of REM1.3 PM dynamics and molecular function is the topic for future studies.

Materials and methods

Plant material

Nicotiana benthamiana plants were cultivated in controlled conditions (16 h photoperiod, 25 °C). Proteins were transiently expressed via *Agrobacterium tumefaciens*-mediated transformation for virus and PD functional assays as in [14, 33] or for the localization experiments as described in the appendix. For subcellular localization studies and protein extractions, plants were analyzed 2 or at 4 days after inoculation (DAI) in the phosphorylation assays. Imaging for PVX-GFP spreading assays and plasmodesmata GFP-diffusion experiments were done at 5 DAI. PVX inoculation for test ELISA was performed at 4-week-old *N. benthamiana* plants. Details on molecular cloning and protein work, transgenic lines generation are described in the Appendix.

Cloning and molecular constructs

All vectors constructs were generated using classical Gateway cloning strategies (www.lifetechnologies.com), pDONR211 and pDONR207 as entry vectors, and pK7WGY2, pK7YWG2, pK7WGR2, pK7RWG2, and pGWB14 and pGWB15 as destination vectors [100]. The REM1.31–116, REM1.3117–198 and REM1.3 single S74A, T86A and S91A and triple S74/T86/S91AAA and S74/T86/S91DDD mutants were synthesized in a pUC57 vector (including the AttB sites) by Genscript (<http://www.genscript.com/>) or GENEWIZ (<http://www.genewiz.com/>) and next cloned to Gateway destination vectors. AtCPK3D202A mutant was generated by site-directed mutagenesis as previously described [101] with minor modifications. For BiFC experiments, the genes of interest were cloned into pSITE-BIFC- C1nec, -C1cec, -N1nen, and -N1cen destination vectors [102]. To map the dynamics of single molecules with sptPALM, REM1.3 and phosphomutants were cloned in fusion with EOS in the gateway compatible vector pUBN-Dest::EOS [103]. EOS protein has been widely use for single molecule localization microscopy in mammals, bacteria, and plant cells. It corresponds to the name of a fluorescent protein from the stony coral *Lobophyllia hemprichii* which peculiarity resides in its photoconvertability. The energy of UV light can break the core polypeptidic

chain of EOS fluorescent protein inducing changes in EOS spectral fluorescence properties. Due to the stochasticity of EOS photoconversion at low UV radiation (space and number of events/sec can be controlled by modulating UV laser power), single molecules can be converted, localized and tracked.

Generation of transgenic stable hairpin REM and 35S::GFP-REM1.3 *N. benthamiana* lines

Leaf discs were cut from *N. benthamiana* leaves, transferred on petri plates containing culture medium (complete Murashige and Skoog medium (MS) supplemented with 30g/L saccharose, pH 5.8; phytoagar HP696 (Kalys) 5.5 g/L and the hormones: AIA 0.1 mg/L, BAP 2 mg/L) and incubated for 48 h in the growth room (16 h photoperiod, 30 μ mol photons.m⁻².s⁻¹, 23 °C). For the transformation, the *N. benthamiana* plants disk leaves were incubated with the *Agrobacterium* cultures (GV3101 strain) carrying the plasmid of interest for 20 min. The leaf samples were next placed on plates with the complete medium previously described. 48 hours later, the leaf fragments were washed 3 times with sterile water (with 0.1% Tween20). The leaf fragments were next washed with MS complete medium supplemented with Timentin (300 μ g/mL). The leaves were next placed on plates with regeneration medium (MS culture medium, as previously described, supplemented with 300 mg/L of timentin and 150 mg/L of kanamycin). The plates were next incubated in the growth room. The explants were transferred to fresh regeneration medium with a maximum periodicity of 7 days until the development of callus. The regenerated seedlings were transferred to a rooting medium (MS, sucrose 30 g/L, phytoagar 5.5 g/L, timentin 200 mg/L, kanamycin 150 mg/L). The regenerated plants (T0) were transferred to the greenhouse for growth and self-fertilization. Homozygous T2 lines carrying a single transgene insertion were selected by segregation analysis on selective Kanamycin media and used for physiological studies and phenotypic characterization. The expression of the GFP-REM1.3 or silencing levels of endogenous NbREMs was controlled by cytological, biochemical and expression analysis. Cytological analysis of the GFP-REM1.3 expression in all leaf cells was performed to avoid chimeric expression, see [S2A and S2B Fig](#).

Transient expression in *N. benthamiana*

Four-week-old *N. benthamiana* greenhouse plants grown at 22–24 °C were used for *Agrobacterium tumefaciens*-mediated transient expression. *A. tumefaciens* were pre-cultured at 28 °C overnight and used as inoculum for culture at initial OD_{600nm} of 0.15 in pre-warmed media. Cultures were grown until OD_{600nm} reached 0.6 to 0.8 values (3–5 h). Cultures were then centrifuged at 3,200 g for 5 min, pellet were washed twice, using water to the desired OD_{600nm}. Bacterial suspensions at OD_{600nm} of 0.2 and 0.1 were used for subcellular localization and Spt-PALM experiments, respectively. The bacterial suspensions were inoculated using a 1-mL syringe without a needle by gentle pressure through a <1mm-hole punched on the lower epidermal surface [104]. Transformed plants were incubated under normal growth conditions for 2 days at 22–24 °C. Transformed *N. benthamiana* leaves were analyzed 2–5 DAI depending on the experiment.

Viral spreading, GFP diffusion assays

PVX-GFP cell-to-cell movement experiments were performed as previously described [14, 36], with minor modifications. Briefly, *A. tumefaciens* strain GV3101 carrying the constructs tested were infiltrated at a final optical density at 600 nm (OD_{600nm}) = 0.2 together with the same strain carrying the plasmid pGr208, which expresses the PVX-GFP complementary DNA harboring GFP placed under the control of a Coat protein promoter, as well as the helper

plasmid pSoup [105] at final OD_{600nm} of 0.001. Viral spreading of PVX-GFP was visualized by epifluorescence microscopy (using GFP long pass filter on a Nikon Eclipse E800 with x4 objective coupled to a Coolsnap HQ2 camera) at 5 DAI and the area of at least 30 of PVX-GFP infection foci was measured using Fiji software (<http://www.fiji.sc/>) via a homemade macro or ImageJ. The expression levels of transiently expressed constructs were confirmed by Western blot. ELISA tests in systemic *N. benthamiana* leaves were performed similarly to [8] to follow the global virus accumulation. Briefly, GFP-REM1.3 or hpREM plants were mechanically inoculated with PVX, and viral accumulation in systemically invaded leaves (at 3 nodes above the inoculated leaf) was evaluated at 10 or 14 DAI with a specific anti-PVX coat protein antibody (Sediag). Five plants per line for GFP-REM1.3 and 8 for hpREM plants were tested per experiment. GFP diffusion at PD experiments was performed as previously described [33]. All the experiments were repeated at least three times.

Epidermal cells live imaging and quantification. Bimolecular Fluorescence Complementation

Live imaging was performed using a Leica SP5 confocal laser scanning microscopy system (Leica, Wetzlar, Germany) equipped with Argon, DPSS and He-Ne lasers and hybrid detectors. *N. benthamiana* leaf samples were gently transferred between a glass slide and a cover slip in a drop of water. YFP and mCitrine (cYFP) fluorescence were observed with similar settings (*i.e.*, excitation wavelengths of 488 nm and emission wavelengths of 490 to 550 nm). In order to obtain quantitative data, experiments were performed using strictly identical confocal acquisition parameters (*e.g.* laser power, gain, zoom factor, resolution, and emission wavelengths reception), with detector settings optimized for low background and no pixel saturation. Pseudo-colored images were obtained using the “Red hot” look-up-table (LUT) of Fiji software (<http://www.fiji.sc/>). All quantifications were performed for at least 10 cells, at least two plants by condition with at least 3 independent replicates. BiFC images were taken 2 DAI by confocal microscopy (Zeiss LSM 880). Quantification of fluorescent intensities was performed by ImageJ, as described in [36].

Spt-PALM, single molecule localization and tracking

N. benthamiana epidermal cells were imaged at room temperature (RT). Samples of leaves of 2-week-old plants expressing EOS constructs were mounted between a glass slide and a cover slip in a drop of water to avoid dehydration. Acquisitions were done on an inverted motorized microscope Nikon Ti Eclipse (Nikon France S.A.S., Champigny-sur-Marne, France) equipped with a 100× oil-immersion PL-APO objective (NA = 1.49), a TIRF arm, a Perfect Focus System (PFS), allowing long acquisition in oblique illumination mode, and a sensitive Evolve EMCCD camera (Photometrics, Tucson, USA). Images acquisitions and processing were done as previously described [45].

Single molecule fluorescent spots were localized in each image frame and tracked over time using image processing techniques such as a combination of wavelet segmentation [106] and simulated annealing algorithms [107]. The software package used to extract quantitative data on protein localization and dynamics is custom written as a plug-in running within the MetaMorph software environment. This plugin is now property of Molecular devices company (<https://www.moleculardevices.com/sites/default/files/en/assets/product-brochures/dd/img/metamorph-super-resolution-software.pdf>).

Single molecule localization organization analysis, $\text{Log}(\delta 1/\delta)$ correspond to the ratio between the local molecule density to overall molecule density at the PM. After correction for artefacts due to multiple single-molecule localization (described in [36] and now presented in

material and methods section), we computed potential nanodomain by applying a threshold $\delta l_i > 2\delta N$, where δN is the average localization density at PM level and δl_i is the density in presumed protein-forming nanodomain, with a minimal area of 32 nm² and with at least 5 localizations per nanodomain.

SR-Tesseler software was used to produce Voronoï diagrams, and subsequently quantify molecule organization parameters as previously recommended [50]. Taking in account fluorophore photophysical parameters, localization accuracy and the first rank of local density of fluorescent molecules, correction for multiple detections occurring in a vicinity of space (w) and blinking tolerance time interval (t) are identified as the same molecule, merged together and replaced by a new detection at a location corresponding to their barycentre. Because first rank of local density of fluorescent molecules was below 0.5 mol/mm² (c.a ranking from 0.1 to 0.3 mol/mm²), we used a fixed search radius w of 48 nm as recommended [50]. To determine the correct time interval t, the photophysics of the fluorophore namely the off-time, number of blinks per molecule and on-time distributions are computed for each cell. For example, for a dataset composed of 618,502 localizations, the average number of blinks per molecule was 1.42, and the number of molecules after cleaning was 315,929. As a control, the number of emission bursts (439,331), counted with t = 0, divided by the average number of blinks per molecule (1.42) was only 2.15% different. After correction for artefacts due to multiple single-molecule localization, we computed potential cluster using a threshold $d l_i > 2d N$, where $d N$ is the average localization density at PM level and $d l_i$ is the density in presumed protein-forming nanocluster, with a minimal area of 32 nm² and with at least five localization by cluster.

Over the two independent experiments 54 446 single molecule trajectories have been observed (34 740 Mock / 19 706 PVX). We then computed single molecule mobility behavior (Diffusion coefficient and Mean square displacement) using trajectories of at least 8 time points (tracked for at least 0.16 s; representing 19495 trajectories in total, 12073 for Mock condition and 7422 for PVX condition).

***In silico* analysis of REM1.3 protein sequence**

Prediction of putative phosphorylation sites was performed by Diphos, DEPP and NETPHOS coupled with published data. Disordered domains were performed by pDONR VL XT.

***In vitro* REM1.3 phosphorylation assays**

6His-REM1.3 and mutant recombinant proteins were purified from bacteria using fast flow chelating sepharose resin (Amersham) according to manufacturer's instructions and as in [14]. For the *in vitro* REM1.3 phosphorylation assays about 2 µg of total plant extracts were incubated with 1 µg of affinity-purified 6His:REM1.3 protein variants for 10 minutes at room temperature and in a phosphorylation buffer (Tris-HCl 30mM, EDTA 5mM, MgCl₂ 15mM, DTT 1mM, Na₃VO₄ 2,5 mM, NaF 10 mM and 10 µCi/reaction ATP [γ -³³P]- (3000Ci/mmol, Perkinelmer). The buffer contained also 10–5 M of free Ca²⁺ which allows the detection of 6His-REM1.3 phosphorylation also in mock conditions. Gradual concentrations of free Ca²⁺ as in [108] were added for Fig 5C. Reactions were performed for 15 minutes in a volume of 25 µl. The reactions were stopped by the addition of 15 µl of 6x loading buffer. Proteins were separated by SDS-PAGE and phosphorylation status of REM1.3 was analysed by autoradiography using a phosphor-Imager and quantified by ImageQuant TL program.

***In vitro* CPK3 kinase assays**

CPK3-HA was transiently expressed in mesophyll protoplasts and immunopurified with anti-HA antibodies as performed in [109] while CPK3-GST recombinant protein was purified

from bacterial extracts as reported in [69]. For *in vitro* kinase assays, the tagged CPK was incubated with 0.5–1 µg histone or 6His-REM1.3 proteins in the following kinase reaction buffer (20 mM Tris HCl pH 7.5, 10 mM MgCl₂, 1 mM DTT, 50 µM cold ATP, ATP [γ -³³P] 2 µCi per reaction, 1 mM CaCl₂ or 5 mM EGTA) in a volume of 15 µL for 30 min at RT. The reaction was stopped with 5 µL 4X Laemmli buffer, then samples were heated at 95 °C for 3 min. Proteins samples were separated by SDS-PAGE on 12% acrylamide gel. After migration, the gel was dried before exposing against a phosphorScreen to reveal radioactivity on a Storm Imaging system (GE Healthcare). The gel was then rehydrated for Coomassie staining.

Protein work

SDS-PAGE, Western Blot analysis, protein extractions and recombinant protein purification were performed in *E. coli* as in [14]. Cell fractionation and extractions followed the established protocol from [59] and [62]. Anti-REM antibodies were previously described in [8].

Accession numbers

All relevant data are within the paper and its Supporting Information files are available from Arabidopsis Genome Initiative (<https://www.arabidopsis.org/index.jsp>), and GenBank/EMBL (<https://www.ncbi.nlm.nih.gov/genbank/>) databases under the accession numbers: *StREM1.3* (NP_001274989), *AtREM1.2* (At3g61260), *AtREM1.3* (At2g45820), *AtCPK3* (At4g23650).

Supporting information

S1 Fig. Callose quantification by aniline blue staining and PD index calculation. (A) Original sample image is an 8-bit, single-channel image. (B) Masks of total Region Of Interest (ROI) objects before particle analysis were created using the following filters; background subtraction with a rolling ball radius as in [43]; “smooth” twice and an auto-local threshold Max Entropy dark, creating a black and white mask, used for particle detection. (C) Overlay of outlines of the analyzed ROI (green; after particle analysis with particle size 3–100 pixel² circularity (0.3–1) exclude on edge) with the original image. Scale bar indicates 10 µm. (D) Quantification of PD Index; after aniline blue labeled pit-field detection, YFP-REM1.3 fluorescence intensity was manually measured at pit-field level (ROI2) and surrounding PM (ROI1 and ROI3) using a circle of fixed area (0.18 µm²). The PD index was then calculated as the ratio between YFP-REM1.3 pit-field fluorescence (ROI2) and the mean of YFP-REM1.3 fluorescence intensity at surrounding PM (ROI1+ROI3). (TIF)

S2 Fig. Overexpression of GFP-REM1.3 results in reduced PVX accumulation in *N. benthamiana* and REM1.3 protein levels are not affected by PVX infection. A. Top, Confocal image showing GFP-REM1.3 localisation in the PM in *N. benthamiana* lines Bottom, The GFP:REM1.3 expression in three independent transgenic lines #6, 7 and 16 was tested by Western blot against REM and showed that it contains at least three times the amount of endogenous *N. benthamiana* REM. B. PVX infection assays in independent stably expressing GFP-REM1.3 and wild-type control *N. benthamiana* lines. Viral charge was assayed by test DAS-ELISA using antibodies to PVX coat protein on distal (3 nodes above inoculation) leaves at 14 DAI. Three independent experiments were performed with five plants for each transgenic line and non-transgenic (WT). Error bars show SE, and significance is assessed by Dunnett’s multiple comparison test against

WT (*, $P < 0.1$; **, $P < 0.05$; ***, $P < 0.001$).

C, Western blot against REM1.3 was performed on total protein extracts from wild type *N. benthamiana* leaves infected by PVX-GFP at 0, 3, 5 and 7 DAI. Stain free loading is indicated below.

D, Confocal images showing PVX-GFP foci at the indicated DAI, tested in C. (TIF)

S3 Fig. Analysis of *in vitro* 6His-REM1.3 phosphorylation and viral proteins expression.

(A) Effect of the addition of ATP or AMP in *in vitro* phosphorylation assays of 6His-REM1.3 by kinase(s) in microsomal (μ) or PM extracts of *N. benthamiana* leaves developed by autoradiography.

(B) 6His-REM1.3^N and 6His-REM1.3 phosphorylation by healthy *N. benthamiana* leaf microsomal (μ) and plasma membrane (PM) extracts.

(C) 6His-REM1.3^N and 6His-REM1.3^C phosphorylation by kinase(s) in microsomal (μ) and soluble extracts.

(D) 6His-REM1.3 was differentially phosphorylated by leaf microsomal extracts expressing the indicated constructs *i.e.* PVX alone, PVX deleted for TGBp1 (PVX Δ TGBp1), 30K protein from Tobacco Mosaic Virus (TMV), PVX fused to GFP, and GFP alone at 4 DAI. See the rationale Fig 2E. Control of loading is shown after stain free procedure. In all phosphorylation experiments about 10 μ g of total protein extracts and 1 μ g of affinity purified 6His-REM1.3, REM1.3^N or REM1.3^C were loaded per lane.

(E) Controls of expression of fluorescently-tagged viral proteins, namely CP, TGBp1, TGBp2 used in Fig 2. (TIF)

S4 Fig. REM1.3 S74 T86 S91 phosphorylation is important to regulate Tobacco mosaic virus movement and REM1.3 phosphorylation mutants maintain PM localization.

(A) Representative epifluorescence microscopy images of Tobacco Mosaic Virus (TMV-GFP) infection foci in *N. benthamiana* leaf epidermal cells at 5 DAI. Graph represents the relative foci area of REM1.3 or phosphomutants (S74, T86 and S91 into Alanine, AAA or Aspartic Acid, DDD) compared to mock control (co-infiltration of PVX-GFP with an empty *A. tumefaciens* strain). About 78–128 foci per condition were measured in 2 independent biological repeats. Dunn's multiple comparison tests were applied for statistical analysis, $p < 0.001$.

(B) Confocal microscopy images of secant views of *N. benthamiana* epidermal cells expressing YFP-REM1.3, YFP-REM1.3AAA and YFP-REM1.3DDD at 2 DAI. Scale bar indicates 10 μ m. (TIF)

S5 Fig. Group 1b AtREMs and REM1.3 have similar behavior against PVX cell-to-cell movement in *N. benthamiana* epidermal cells.

(A) Clustal alignments of protein sequences of group 1b REMORINs: AtREM1.2, AtREM1.3, NbREM1.2, NbREM1.3 and REM1.3 (StREM1.3). Blue color-coding shows percentage of identity. The REM1.3 S74, T81 and S91 sites are highlighted.

(B) *Left*, Representative epifluorescence microscopy images of PVX-GFP infection foci on *N. benthamiana* leaf epidermal cells transiently expressing RFP-REM1.3, RFP-AtREM1.2 or RFP-AtREM1.3 at 5 DAI. Scale bar indicate 400 μ m. *Right*, Graph represents the relative PVX-GFP infection foci area in the presence of RFP-REM1.3 or Arabidopsis homologs compared to mock control (co-infiltration of PVX-GFP with empty *A. tumefaciens* strain). At least 184 foci per condition in 4 independent biological repeats were measured. Statistical differences are indicated by letters as revealed by Dunn's multiple comparisons test $p < 0.001$. (TIF)

S6 Fig. *In vitro* characterization of REM1.3 phosphorylation conditions. Autoradiography reveals *in vitro* phosphorylated 6His-REM1.3N (A) or 6His-REM1.3 (B) by microsomal extracts of healthy *N. benthamiana* leaves in the presence of increasing concentrations of staurosporine (A) or Polylysine, β -glycerophosphate (BGP), GTP, AMP and ATP (B). (C) Effect of Ca^{2+} and EGTA on 6His-REM1.3^N phosphorylation by kinase(s) in microsomal extracts.

(TIF)

S7 Fig. AtCPK3CAD202A dead mutant does not phosphorylate REM1.3 *in vitro*. AtCPK3-CA-HA and AtCPK3CAD202A-HA were expressed in *Arabidopsis thaliana* mesophyll protoplasts. Immunoprecipitated proteins were incubated with ATP [γ -³³P] and submitted to an *in vitro* kinase assay using 6His-REM1.3 or histone as substrates. *In vitro* kinase assays were revealed by autoradiography. Trans-phosphorylation of the substrates 6His-REM1.3 or histone is indicated. Western blot against HA shows the expression levels of the expressed proteins.

(TIF)

S8 Fig. Stable transgenic lines *N. benthamiana* under-expressing group 1 REMORINs. (A) Protein expression levels of endogenous NbREMs in the hpREM lines, determined by Western Blot analysis using anti-REM1.3 antibodies. Protein extracts from three independent plants per line were used, namely lines 1.4, 2.1, 10.2.

(B) Expression of endogenous NbREMs in the hpREM lines determined by RT-qPCR analysis. Results are expressed relative to the NbREMs expression levels in the WT background. RT-qPCR signals were normalized to actin levels.

(C) PVX-GFP spreading is accelerated in the hpREM lines. Graph represents the PVX-GFP infection foci area in the different hpREM lines compared to WT. At least three independent experiments were performed. Error bars show \pm SEM. Statistical differences compared to WT were determined by Mann-Whitney test *** $p < 0.001$.

(D) PVX systemic propagation is inversely correlated with REM levels in 4-week-old transgenic *N. benthamiana* leaves. Viral charges were assayed by DAS ELISA using antibodies to PVX coat protein (diluted on 1/100) on distal leaves (at 3 nodes above the inoculated leaves) at 10 DAI. 3 independent experiments were performed with eight plants for each hpREM transgenic line and WT or empty vector control (mock). Error bars show SE, and significance is assessed by Mann-Whitney non-parametric test (*, $P < 0.1$; **, $P < 0.05$; ***, $P < 0.001$).

(TIF)

Acknowledgments

Imaging was performed at the Bordeaux Imaging Center, member of the national infrastructure France BioImaging. We acknowledge Dr S. P. Dinesh-Kumar for the gift of TMV-GFP clone, Dr Alicia Zelada for the gift of PVX Δ TGBp1 and viral protein constructs and Ms Coralie Chesseron for greenhouse facilities.

Author Contributions

Conceptualization: Artemis Perraki, Julien Gronnier, Paul Gouguet, Marie Boudsocq, Cyril Zipfel, Emmanuelle Bayer, Sébastien Mongrand, Véronique Germain.

Data curation: Artemis Perraki, Paul Gouguet, Marie Boudsocq, Sébastien Mongrand.

Formal analysis: Artemis Perraki, Julien Gronnier, Paul Gouguet, Marie Boudsocq, Anne-Flore Deroubaix, Sébastien Mongrand.

Funding acquisition: Artemis Perraki, Cyril Zipfel, Sébastien Mongrand.

Investigation: Artemis Perraki, Julien Gronnier, Paul Gouguet, Marie Boudsocq, Anne-Flore Deroubaix, Vincent Simon, Sylvie German-Retana, Anthony Legrand, Sébastien Mongrand, Véronique Germain.

Methodology: Artemis Perraki, Julien Gronnier, Paul Gouguet, Marie Boudsocq, Vincent Simon, Sylvie German-Retana, Birgit Habenstein, Emmanuelle Bayer, Sébastien Mongrand, Véronique Germain.

Project administration: Sébastien Mongrand.

Resources: Artemis Perraki, Julien Gronnier, Marie Boudsocq, Vincent Simon, Sylvie German-Retana, Birgit Habenstein, Cyril Zipfel, Emmanuelle Bayer, Sébastien Mongrand, Véronique Germain.

Software: Julien Gronnier.

Supervision: Birgit Habenstein, Sébastien Mongrand, Véronique Germain.

Validation: Artemis Perraki, Julien Gronnier, Sébastien Mongrand.

Visualization: Artemis Perraki, Julien Gronnier, Paul Gouguet, Anne-Flore Deroubaix, Anthony Legrand, Sébastien Mongrand.

Writing – original draft: Artemis Perraki, Julien Gronnier, Paul Gouguet, Sébastien Mongrand, Véronique Germain.

Writing – review & editing: Artemis Perraki, Julien Gronnier, Paul Gouguet, Marie Boudsocq, Emmanuelle Bayer, Sébastien Mongrand, Véronique Germain.

References

1. Nicolson GL. The Fluid-Mosaic Model of Membrane Structure: still relevant to understanding the structure, function and dynamics of biological membranes after more than 40 years. *Biochimica et biophysica acta*. 2014; 1838(6):1451–66. <https://doi.org/10.1016/j.bbamem.2013.10.019> PMID: 24189436.
2. Sezgin E, Levental I, Mayor S, Eggeling C. The mystery of membrane organization: composition, regulation and roles of lipid rafts. *Nature reviews Molecular cell biology*. 2017; 18(6):361–74. <https://doi.org/10.1038/nrm.2017.16> PMID: 28356571; PubMed Central PMCID: PMC5500228.
3. Lingwood D, Simons K. Lipid rafts as a membrane-organizing principle. *Science*. 2010; 327(5961):46–50. <https://doi.org/10.1126/science.1174621> PMID: 20044567.
4. Simons K, Gerl MJ. Revitalizing membrane rafts: new tools and insights. *Nature reviews Molecular cell biology*. 2010; 11(10):688–99. Epub 2010/09/24. doi: nrm2977 [pii] <https://doi.org/10.1038/nrm2977> PMID: 20861879.
5. Kusumi A, Fujiwara TK, Chadda R, Xie M, Tsunoyama TA, Kalay Z, et al. Dynamic organizing principles of the plasma membrane that regulate signal transduction: commemorating the fortieth anniversary of Singer and Nicolson's fluid-mosaic model. *Annu Rev Cell Dev Biol*. 2012; 28:215–50. <https://doi.org/10.1146/annurev-cellbio-100809-151736> PMID: 22905956.
6. Mugler A, Tostevin F, ten Wolde PR. Spatial partitioning improves the reliability of biochemical signaling. *Proceedings of the National Academy of Sciences of the United States of America*. 2013; 110(15):5927–32. <https://doi.org/10.1073/pnas.1218301110> PMID: 23530194; PubMed Central PMCID: PMC3625283.
7. Bucherl CA, Jarsch IK, Schudoma C, Segonzac C, Mbengue M, Robatzek S, et al. Plant immune and growth receptors share common signalling components but localise to distinct plasma membrane nanodomains. *Elife*. 2017; 6. <https://doi.org/10.7554/eLife.25114> PMID: 28262094; PubMed Central PMCID: PMC5383397.
8. Raffaele S, Bayer E, Lafarge D, Cluzet S, German Retana S, Boubekeur T, et al. Remorin, a solanaceae protein resident in membrane rafts and plasmodesmata, impairs potato virus X movement. *The Plant cell*. 2009; 21(5):1541–55. Epub 2009/05/28. doi: tpc.108.064279 [pii] <https://doi.org/10.1105/tpc.108.064279> PMID: 19470590; PubMed Central PMCID: PMC2700541.

9. Jarsch IK, Ott T. Perspectives on remorin proteins, membrane rafts, and their role during plant-microbe interactions. *Molecular plant-microbe interactions: MPMI*. 2011; 24(1):7–12. <https://doi.org/10.1094/MPMI-07-10-0166> PMID: 21138374.
10. Jarsch IK, Konrad SS, Stratil TF, Urbanus SL, Szymanski W, Braun P, et al. Plasma Membranes Are Subcompartmentalized into a Plethora of Coexisting and Diverse Microdomains in Arabidopsis and *Nicotiana benthamiana*. *The Plant cell*. 2014; 26(4):1698–711. <https://doi.org/10.1105/tpc.114.124446> PMID: 24714763; PubMed Central PMCID: PMC4036580.
11. Lefebvre B, Timmers T, Mbengue M, Moreau S, Herve C, Toth K, et al. A remorin protein interacts with symbiotic receptors and regulates bacterial infection. *Proceedings of the National Academy of Sciences of the United States of America*. 2010; 107(5):2343–8. <https://doi.org/10.1073/pnas.0913320107> PMID: 20133878; PubMed Central PMCID: PMC2836688.
12. Gui J, Zheng S, Liu C, Shen J, Li J, Li L. OsREM4.1 Interacts with OsSERK1 to Coordinate the Interlinking between Absciscic Acid and Brassinosteroid Signaling in Rice. *Dev Cell*. 2016; 38(2):201–13. <https://doi.org/10.1016/j.devcel.2016.06.011> PMID: 27424498.
13. Raffaele S, Perraki A, Mongrand S. The Remorin C-terminal Anchor was shaped by convergent evolution among membrane binding domains. *Plant signaling & behavior*. 2013; 8(3). Epub 2013/01/10. <https://doi.org/10.4161/psb.23207> PMID: 23299327; PubMed Central PMCID: PMC3676492.
14. Perraki A, Cacas JL, Crowet JM, Lins L, Castroviejo M, German-Retana S, et al. Plasma membrane localization of *Solanum tuberosum* remorin from group 1, homolog 3 is mediated by conformational changes in a novel C-terminal anchor and required for the restriction of potato virus X movement]. *Plant physiology*. 2012; 160(2):624–37. Epub 2012/08/03. <https://doi.org/10.1104/pp.112.200519> PMID: 22855937; PubMed Central PMCID: PMC3461544.
15. Martinez D, Legrand A, Gronnier J, Decossas M, Gouguet P, Lambert O, et al. Coiled-coil oligomerization controls localization of the plasma membrane REMORINs. *J Struct Biol*. 2018. <https://doi.org/10.1016/j.jsb.2018.02.003> PMID: 29481850.
16. Toth K, Stratil TF, Madsen EB, Ye J, Popp C, Antolin-Llovera M, et al. Functional domain analysis of the Remorin protein LjSYMREM1 in *Lotus japonicus*. *PloS one*. 2012; 7(1):e30817. <https://doi.org/10.1371/journal.pone.0030817> PMID: 22292047; PubMed Central PMCID: PMC3264624.
17. Son S, Oh CJ, An CS. Arabidopsis thaliana Remorins Interact with SnRK1 and Play a Role in Susceptibility to Beet Curly Top Virus and Beet Severe Curly Top Virus. *The plant pathology journal*. 2014; 30(3):269–78. <https://doi.org/10.5423/PPJ.OA.06.2014.0061> PMID: 25289013; PubMed Central PMCID: PMC4181108.
18. Jamann TM, Luo X, Morales L, Kolkman JM, Chung CL, Nelson RJ. A remorin gene is implicated in quantitative disease resistance in maize. *Theor Appl Genet*. 2016; 129(3):591–602. <https://doi.org/10.1007/s00122-015-2650-6> PMID: 26849237.
19. Checker VG, Khurana P. Molecular and functional characterization of mulberry EST encoding remorin (MiREM) involved in abiotic stress. *Plant Cell Rep*. 2013; 32(11):1729–41. <https://doi.org/10.1007/s00299-013-1483-5> PMID: 23942844.
20. Yue J, Li C, Liu Y, Yu J. A remorin gene SiREM6, the target gene of SiARDP, from foxtail millet (*Setaria italica*) promotes high salt tolerance in transgenic Arabidopsis. *PloS one*. 2014; 9(6):e100772. <https://doi.org/10.1371/journal.pone.0100772> PMID: 24967625; PubMed Central PMCID: PMC4072699.
21. Gronnier J, Gerbeau-Pissot P, Germain V, Mongrand S, Simon-Plas F. Divide and Rule: Plant Plasma Membrane Organization. *Trends in plant science*. 2018. <https://doi.org/10.1016/j.tplants.2018.07.007> PMID: 30174194.
22. Fernandez-Calvino L, Faulkner C, Walshaw J, Saalbach G, Bayer E, Benitez-Alfonso Y, et al. Arabidopsis plasmodesmal proteome. *PloS one*. 2011; 6(4):e18880. Epub 2011/05/03. <https://doi.org/10.1371/journal.pone.0018880> PMID: 21533090; PubMed Central PMCID: PMC3080382.
23. Gui J, Zheng S, Shen J, Li L. Grain setting defect1 (GSD1) function in rice depends on S-acylation and interacts with actin 1 (OsACT1) at its C-terminal. *Frontiers in plant science*. 2015; 6:804. <https://doi.org/10.3389/fpls.2015.00804> PMID: 26483819; PubMed Central PMCID: PMC4590517.
24. Tilsner J, Nicolas W, Rosado A, Bayer EM. Staying Tight: Plasmodesmal Membrane Contact Sites and the Control of Cell-to-Cell Connectivity in Plants. *Annu Rev Plant Biol*. 2016; 67:337–64. <https://doi.org/10.1146/annurev-arplant-043015-111840> PMID: 26905652.
25. Nicolas WJ, Grison MS, Trepout S, Gaston A, Fouche M, Cordelieres FP, et al. Architecture and permeability of post-cytokinesis plasmodesmata lacking cytoplasmic sleeves. *Nat Plants*. 2017; 3:17082. <https://doi.org/10.1038/nplants.2017.82> PMID: 28604682.
26. Grison MS, Brocard L, Fouillen L, Nicolas W, Wewer V, Dormann P, et al. Specific membrane lipid composition is important for plasmodesmata function in Arabidopsis. *The Plant cell*. 2015; 27

- (4):1228–50. <https://doi.org/10.1105/tpc.114.135731> PMID: 25818623; PubMed Central PMCID: PMC4558693.
27. Lee JY, Wang X, Cui W, Sager R, Modla S, Czymmek K, et al. A plasmodesmata-localized protein mediates crosstalk between cell-to-cell communication and innate immunity in Arabidopsis. *The Plant cell*. 2011; 23(9):3353–73. <https://doi.org/10.1105/tpc.111.087742> PMID: 21934146; PubMed Central PMCID: PMC4558693.
28. Zavaliev R, Dong X, Epel BL. Glycosylphosphatidylinositol (GPI) Modification Serves as a Primary Plasmodesmal Sorting Signal. *Plant physiology*. 2016; 172(2):1061–73. <https://doi.org/10.1104/pp.16.01026> PMID: 27559035; PubMed Central PMCID: PMC4558693.
29. Chen XY, Kim JY. Callose synthesis in higher plants. *Plant signaling & behavior*. 2009; 4(6):489–92. <https://doi.org/10.4161/psb.4.6.8359> PMID: 19816126; PubMed Central PMCID: PMC4558693.
30. Angell SM, Davies C, Baulcombe DC. Cell-to-cell movement of potato virus X is associated with a change in the size-exclusion limit of plasmodesmata in trichome cells of *Nicotiana glauca*. *Virology*. 1996; 216(1):197–201. Epub 1996/02/01. doi: S0042-6822(96)90046-X [pii] <https://doi.org/10.1006/viro.1996.0046> PMID: 8614986.
31. Howard AR, Heppler ML, Ju HJ, Krishnamurthy K, Payton ME, Verchot-Lubicz J. Potato virus X TGBp1 induces plasmodesmata gating and moves between cells in several host species whereas CP moves only in *N. benthamiana* leaves. *Virology*. 2004; 328(2):185–97. Epub 2004/10/07. doi: S0042-6822(04)00399-X [pii] <https://doi.org/10.1016/j.virol.2004.06.039> PMID: 15464839.
32. Raffaele S, Mongrand S, Gamas P, Niebel A, Ott T. Genome-wide annotation of remorins, a plant-specific protein family: evolutionary and functional perspectives. *Plant physiology*. 2007; 145(3):593–600. Epub 2007/11/07. <https://doi.org/10.1104/pp.107.108639> PMID: 17984200; PubMed Central PMCID: PMC2048807.
33. Perraki A, Binaghi M, Mecchia MA, Gronnier J, German-Retana S, Mongrand S, et al. StRemorin1.3 hampers Potato virus X TGBp1 ability to increase plasmodesmata permeability, but does not interfere with its silencing suppressor activity. *FEBS letters*. 2014; 588(9):1699–705. <https://doi.org/10.1016/j.febslet.2014.03.014> PMID: 24657438.
34. Jaubert M, Bhattacharjee S, Mello AF, Perry KL, Moffett P. ARGONAUTE2 mediates RNA-silencing antiviral defenses against Potato virus X in Arabidopsis. *Plant physiology*. 2011; 156(3):1556–64. <https://doi.org/10.1104/pp.111.178012> PMID: 21576511; PubMed Central PMCID: PMC3135937.
35. Goodin MM, Zaitlin D, Naidu RA, Lommel SA. *Nicotiana benthamiana*: Its History and Future as a Model for Plant-Pathogen Interactions. *Molecular plant-microbe interactions: MPMI*. 2015; 2015(1):28–39. <https://doi.org/10.1094/MPMI-00-00-1015-REV.testissue> PMID: 27839076.
36. Gronnier J, Crowet JM, Habenstein B, Nasir MN, Bayle V, Hosy E, et al. Structural basis for plant plasma membrane protein dynamics and organization into functional nanodomains. *Elife*. 2017; 6. <https://doi.org/10.7554/eLife.26404> PMID: 28758890; PubMed Central PMCID: PMC5536944.
37. Farmer EE, Moloshok TD, Saxton MJ, Ryan CA. Oligosaccharide signaling in plants. Specificity of oliguronide-enhanced plasma membrane protein phosphorylation. *The Journal of biological chemistry*. 1991; 266(5):3140–5. PMID: 1993685.
38. Reymond P, Kunz B, Paul-Pletzer K, Grimm R, Eckerskorn C, Farmer EE. Cloning of a cDNA encoding a plasma membrane-associated, uronide binding phosphoprotein with physical properties similar to viral movement proteins. *The Plant cell*. 1996; 8(12):2265–76. <https://doi.org/10.1105/tpc.8.12.2265> PMID: 8989883; PubMed Central PMCID: PMC161351.
39. Benschop JJ, Mohammed S, O'Flaherty M, Heck AJ, Slijper M, Menke FL. Quantitative phosphoproteomics of early elicitor signaling in Arabidopsis. *Molecular & cellular proteomics: MCP*. 2007; 6(7):1198–214. <https://doi.org/10.1074/mcp.M600429-MCP200> PMID: 17317660.
40. Widjaja I, Naumann K, Roth U, Wolf N, Mackey D, Dangl JL, et al. Combining subproteome enrichment and Rubisco depletion enables identification of low abundance proteins differentially regulated during plant defense. *Proteomics*. 2009; 9(1):138–47. <https://doi.org/10.1002/pmic.200800293> PMID: 19053141.
41. Tilsner J, Linnik O, Louveaux M, Roberts IM, Chapman SN, Oparka KJ. Replication and trafficking of a plant virus are coupled at the entrances of plasmodesmata. *J Cell Biol*. 2013; 201(7):981–95. <https://doi.org/10.1083/jcb.201304003> PMID: 23798728; PubMed Central PMCID: PMC3691464.
42. Bozkurt TO, Richardson A, Dagdas YF, Mongrand S, Kamoun S, Raffaele S. The Plant Membrane-Associated REMORIN1.3 Accumulates in Discrete Periaxial Domains and Enhances Susceptibility to *Phytophthora infestans*. *Plant physiology*. 2014; 165(3):1005–18. <https://doi.org/10.1104/pp.114.235804> PMID: 24808104; PubMed Central PMCID: PMC4081318.

43. Scholthof KB, Adkins S, Czosnek H, Palukaitis P, Jacquot E, Hohn T, et al. Top 10 plant viruses in molecular plant pathology. *Molecular plant pathology*. 2011; 12(9):938–54. <https://doi.org/10.1111/j.1364-3703.2011.00752.x> PMID: 22017770.
44. Kusumi A, Suzuki K. Toward understanding the dynamics of membrane-raft-based molecular interactions. *Biochimica et biophysica acta*. 2005; 1746(3):234–51. Epub 2005/12/22. <https://doi.org/10.1016/j.bbamcr.2005.10.001> PMID: 16368465.
45. Hosy E, Martiniere A, Choquet D, Maurel C, Luu DT. Super-resolved and dynamic imaging of membrane proteins in plant cells reveal contrasting kinetic profiles and multiple confinement mechanisms. *Molecular plant*. 2015; 8(2):339–42. <https://doi.org/10.1016/j.molp.2014.10.006> PMID: 25680779.
46. Manley S, Gillette JM, Patterson GH, Shroff H, Hess HF, Betzig E, et al. High-density mapping of single-molecule trajectories with photoactivated localization microscopy. *Nat Methods*. 2008; 5(2):155–7. <https://doi.org/10.1038/nmeth.1176> PMID: 18193054.
47. Wiedenmann J, Ivanchenko S, Oswald F, Schmitt F, Rocker C, Salih A, et al. EosFP, a fluorescent marker protein with UV-inducible green-to-red fluorescence conversion. *Proceedings of the National Academy of Sciences of the United States of America*. 2004; 101(45):15905–10. <https://doi.org/10.1073/pnas.0403668101> PMID: 15505211; PubMed Central PMCID: PMC528746.
48. Martiniere A, Lavagi I, Nageswaran G, Rolfe DJ, Maneta-Peyret L, Luu DT, et al. Cell wall constrains lateral diffusion of plant plasma-membrane proteins. *Proceedings of the National Academy of Sciences of the United States of America*. 2012; 109(31):12805–10. Epub 2012/06/13. <https://doi.org/10.1073/pnas.1202040109> PMID: 22689944; PubMed Central PMCID: PMC3411962.
49. Konrad SS, Popp C, Stratil TF, Jarsch IK, Thallmair V, Folgmann J, et al. S-acylation anchors remorin proteins to the plasma membrane but does not primarily determine their localization in membrane microdomains. *The New phytologist*. 2014; 203(3):758–69. <https://doi.org/10.1111/nph.12867> PMID: 24897938.
50. Levet F, Hosy E, Kechkar A, Butler C, Beghin A, Choquet D, et al. SR-Tesseler: a method to segment and quantify localization-based super-resolution microscopy data. *Nat Methods*. 2015; 12(11):1065–71. <https://doi.org/10.1038/nmeth.3579> PMID: 26344046.
51. Calil IP, Fontes EPB. Plant immunity against viruses: antiviral immune receptors in focus. *Ann Bot*. 2017; 119(5):711–23. <https://doi.org/10.1093/aob/mcw200> PMID: 27780814.
52. Nicaise V, Candresse T. Plum pox virus capsid protein suppresses plant pathogen-associated molecular pattern (PAMP)-triggered immunity. *Molecular plant pathology*. 2017; 18(6):878–86. <https://doi.org/10.1111/mpp.12447> PMID: 27301551.
53. de Ronde D, Butterbach P, Kormelink R. Dominant resistance against plant viruses. *Frontiers in plant science*. 2014; 5:307. <https://doi.org/10.3389/fpls.2014.00307> PMID: 25018765; PubMed Central PMCID: PMC4073217.
54. de Ronde D, Pasquier A, Ying S, Butterbach P, Lohuis D, Kormelink R. Analysis of Tomato spotted wilt virus NSs protein indicates the importance of the N-terminal domain for avirulence and RNA silencing suppression. *Molecular plant pathology*. 2014; 15(2):185–95. <https://doi.org/10.1111/mpp.12082> PMID: 24103150.
55. Gouveia BC, Calil IP, Machado JP, Santos AA, Fontes EP. Immune Receptors and Co-receptors in Antiviral Innate Immunity in Plants. *Front Microbiol*. 2016; 7:2139. <https://doi.org/10.3389/fmicb.2016.02139> PMID: 28105028; PubMed Central PMCID: PMC4521445.
56. Niehl A, Appaix F, Bosca S, van der Sanden B, Nicoud JF, Bolze F, et al. Fluorescent Tobacco mosaic virus-Derived Bio-Nanoparticles for Intravital Two-Photon Imaging. *Frontiers in plant science*. 2015; 6:1244. <https://doi.org/10.3389/fpls.2015.01244> PMID: 26793221; PubMed Central PMCID: PMC4710741.
57. Marin M, Ott T. Phosphorylation of intrinsically disordered regions in remorin proteins. *Frontiers in plant science*. 2012; 3:86. <https://doi.org/10.3389/fpls.2012.00086> PMID: 22639670; PubMed Central PMCID: PMC3355724.
58. Cluzet S. Etude du rôle de la rémorine dans la défense végétale. Thèse de doctorat, Université de Lausanne. 2001.
59. Mongrand S, Morel J, Laroche J, Claverol S, Carde JP, Hartmann MA, et al. Lipid rafts in higher plant cells: purification and characterization of Triton X-100-insoluble microdomains from tobacco plasma membrane. *The Journal of biological chemistry*. 2004; 279(35):36277–86. Epub 2004/06/11. <https://doi.org/10.1074/jbc.M403440200> PMID: 15190066.
60. Kalay Z. Reaction kinetics in the plasma membrane. *Biotechnol J*. 2012; 7(6):745–52. <https://doi.org/10.1002/biot.201100362> PMID: 22378739.
61. Tian T, Harding A, Inder K, Plowman S, Parton RG, Hancock JF. Plasma membrane nanoswitches generate high-fidelity Ras signal transduction. *Nature cell biology*. 2007; 9(8):905–14. <https://doi.org/10.1038/ncb1615> PMID: 17618274.

62. Furt F, Konig S, Bessoule JJ, Sargueil F, Zallot R, Stanislas T, et al. Polyphosphoinositides are enriched in plant membrane rafts and form microdomains in the plasma membrane. *Plant physiology*. 2010; 152(4):2173–87. Epub 2010/02/26. doi: pp.109.149823 [pii] <https://doi.org/10.1104/pp.109.149823> PMID: 20181756; PubMed Central PMCID: PMC2850013.
63. Meggio F, Donella Deana A, Ruzzene M, Brunati AM, Cesaro L, Guerra B, et al. Different susceptibility of protein kinases to staurosporine inhibition. Kinetic studies and molecular bases for the resistance of protein kinase CK2. *European journal of biochemistry / FEBS*. 1995; 234(1):317–22. PMID: 8529658.
64. Ruegg UT, Burgess GM. Staurosporine, K-252 and UCN-01: potent but nonspecific inhibitors of protein kinases. *Trends Pharmacol Sci*. 1989; 10(6):218–20. PMID: 2672462.
65. Meggio F, Pinna LA. One-thousand-and-one substrates of protein kinase CK2? *FASEB journal: official publication of the Federation of American Societies for Experimental Biology*. 2003; 17(3):349–68. <https://doi.org/10.1096/fj.02-0473rev> PMID: 12631575.
66. Binder BM, Harper JF, Sussman MR. Characterization of an Arabidopsis calmodulin-like domain protein kinase purified from *Escherichia coli* using an affinity sandwich technique. *Biochemistry*. 1994; 33(8):2033–41. PMID: 8117660.
67. Boudsocq M, Sheen J. CDPKs in immune and stress signaling. *Trends in plant science*. 2013; 18(1):30–40. <https://doi.org/10.1016/j.tplants.2012.08.008> PMID: 22974587; PubMed Central PMCID: PMC3534830.
68. Schulz P, Herde M, Romeis T. Calcium-dependent protein kinases: hubs in plant stress signaling and development. *Plant physiology*. 2013; 163(2):523–30. <https://doi.org/10.1104/pp.113.222539> PMID: 24014579; PubMed Central PMCID: PMC3793034.
69. Boudsocq M, Droillard MJ, Regad L, Lauriere C. Characterization of Arabidopsis calcium-dependent protein kinases: activated or not by calcium? *The Biochemical journal*. 2012; 447(2):291–9. <https://doi.org/10.1042/BJ20112072> PMID: 22827269.
70. Kierszniowska S, Seiwert B, Schulze WX. Definition of Arabidopsis sterol-rich membrane microdomains by differential treatment with methyl-beta-cyclodextrin and quantitative proteomics. *Molecular & cellular proteomics: MCP*. 2009; 8(4):612–23. Epub 2008/11/28. doi: M800346-MCP200 [pii] <https://doi.org/10.1074/mcp.M800346-MCP200> PMID: 19036721; PubMed Central PMCID: PMC2667346.
71. Mehlmer N, Wurzinger B, Stael S, Hofmann-Rodrigues D, Csaszar E, Pfister B, et al. The Ca(2+)-dependent protein kinase CPK3 is required for MAPK-independent salt-stress acclimation in Arabidopsis. *The Plant journal: for cell and molecular biology*. 2010; 63(3):484–98. <https://doi.org/10.1111/j.1365-3113.2010.04257.x> PMID: 20497378; PubMed Central PMCID: PMC2988408.
72. Demir F, Horntrich C, Blachutzik JO, Scherzer S, Reinders Y, Kierszniowska S, et al. Arabidopsis nanodomain-delimited ABA signaling pathway regulates the anion channel SLAH3. *Proceedings of the National Academy of Sciences of the United States of America*. 2013; 110(20):8296–301. <https://doi.org/10.1073/pnas.1211667110> PMID: 23630285; PubMed Central PMCID: PMC3657796.
73. Harmon AC, Gribskov M, Harper JF. CDPKs—a kinase for every Ca2+ signal? *Trends in plant science*. 2000; 5(4):154–9. PMID: 10740296.
74. Harper JF, Breton G, Harmon A. Decoding Ca(2+) signals through plant protein kinases. *Annu Rev Plant Biol*. 2004; 55:263–88. <https://doi.org/10.1146/annurev.arplant.55.031903.141627> PMID: 15377221.
75. Ubersax JA, Ferrell JE Jr., Mechanisms of specificity in protein phosphorylation. *Nature reviews Molecular cell biology*. 2007; 8(7):530–41. <https://doi.org/10.1038/nrm2203> PMID: 17585314.
76. Bah A, Vernon RM, Siddiqui Z, Krzeminski M, Muhandiram R, Zhao C, et al. Folding of an intrinsically disordered protein by phosphorylation as a regulatory switch. *Nature*. 2015; 519(7541):106–9. <https://doi.org/10.1038/nature13999> PMID: 25533957.
77. Gui J, Liu C, Shen J, Li L. Grain setting defect1, encoding a remorin protein, affects the grain setting in rice through regulating plasmodesmatal conductance. *Plant physiology*. 2014; 166(3):1463–78. <https://doi.org/10.1104/pp.114.246769> PMID: 25253885; PubMed Central PMCID: PMC4226345.
78. Incarbone M, Dunoyer P. RNA silencing and its suppression: novel insights from in planta analyses. *Trends in plant science*. 2013; 18(7):382–92. <https://doi.org/10.1016/j.tplants.2013.04.001> PMID: 23684690.
79. Carr JP, Loebenstein G. Natural and engineered resistance to plant viruses, part II. Preface. *Adv Virus Res*. 2010; 76:vii. [https://doi.org/10.1016/S0065-3527\(10\)76011-5](https://doi.org/10.1016/S0065-3527(10)76011-5) PMID: 20362221.
80. Zorzatto C, Machado JP, Lopes KV, Nascimento KJ, Pereira WA, Brustolini OJ, et al. NIK1-mediated translation suppression functions as a plant antiviral immunity mechanism. *Nature*. 2015; 520(7549):679–82. <https://doi.org/10.1038/nature14171> PMID: 25707794; PubMed Central PMCID: PMC4779052.

81. Zipfel C. Plant pattern-recognition receptors. *Trends Immunol.* 2014; 35(7):345–51. <https://doi.org/10.1016/j.it.2014.05.004> PMID: 24946686.
82. Dodds PN, Rathjen JP. Plant immunity: towards an integrated view of plant-pathogen interactions. *Nat Rev Genet.* 2010; 11(8):539–48. <https://doi.org/10.1038/nrg2812> PMID: 20585331.
83. Dangl JL, Horvath DM, Staskawicz BJ. Pivoting the plant immune system from dissection to deployment. *Science.* 2013; 341(6147):746–51. <https://doi.org/10.1126/science.1236011> PMID: 23950531; PubMed Central PMCID: PMC3869199.
84. Kroner A, Hamelin G, Andrion D, Val F. Quantitative resistance of potato to *Pectobacterium atrosepticum* and *Phytophthora infestans*: integrating PAMP-triggered response and pathogen growth. *PLoS one.* 2011; 6(8):e23331. <https://doi.org/10.1371/journal.pone.0023331> PMID: 21853112; PubMed Central PMCID: PMC3154927.
85. Hanssen IM, van Esse HP, Ballester AR, Hogewoning SW, Parra NO, Paeleman A, et al. Differential tomato transcriptomic responses induced by pepino mosaic virus isolates with differential aggressiveness. *Plant physiology.* 2011; 156(1):301–18. <https://doi.org/10.1104/pp.111.173906> PMID: 21427280; PubMed Central PMCID: PMC3091055.
86. Love AJ, Yun BW, Laval V, Loake GJ, Milner JJ. Cauliflower mosaic virus, a compatible pathogen of *Arabidopsis*, engages three distinct defense-signaling pathways and activates rapid systemic generation of reactive oxygen species. *Plant physiology.* 2005; 139(2):935–48. <https://doi.org/10.1104/pp.105.066803> PMID: 16169957; PubMed Central PMCID: PMC31256007.
87. Whitham SA, Quan S, Chang HS, Cooper B, Estes B, Zhu T, et al. Diverse RNA viruses elicit the expression of common sets of genes in susceptible *Arabidopsis thaliana* plants. *The Plant journal: for cell and molecular biology.* 2003; 33(2):271–83. PMID: 12535341.
88. Jones JD, Dangl JL. The plant immune system. *Nature.* 2006; 444(7117):323–9. <https://doi.org/10.1038/nature05286> PMID: 17108957.
89. Mandadi KK, Scholthof KB. Plant immune responses against viruses: how does a virus cause disease? *The Plant cell.* 2013; 25(5):1489–505. <https://doi.org/10.1105/tpc.113.111658> PMID: 23709626; PubMed Central PMCID: PMC3694688.
90. Levy A, Zheng JY, Lazarowitz SG. Synaptotagmin SYTA forms ER-plasma membrane junctions that are recruited to plasmodesmata for plant virus movement. *Current biology: CB.* 2015; 25(15):2018–25. <https://doi.org/10.1016/j.cub.2015.06.015> PMID: 26166780; PubMed Central PMCID: PMC4526382.
91. Fu S, Xu Y, Li C, Li Y, Wu J, Zhou X. Rice Stripe Virus Interferes with S-acylation of Remorin and Induces Its Autophagic Degradation to Facilitate Virus Infection. *Molecular plant.* 2018; 11(2):269–87. <https://doi.org/10.1016/j.molp.2017.11.011> PMID: 29229567.
92. Mori IC, Murata Y, Yang Y, Munemasa S, Wang YF, Andreoli S, et al. CDPKs CPK6 and CPK3 function in ABA regulation of guard cell S-type anion- and Ca(2+)-permeable channels and stomatal closure. *PLoS Biol.* 2006; 4(10):e327. <https://doi.org/10.1371/journal.pbio.0040327> PMID: 17032064; PubMed Central PMCID: PMC1592316.
93. Latz A, Mehler N, Zapf S, Mueller TD, Wurzing B, Pfister B, et al. Salt stress triggers phosphorylation of the *Arabidopsis* vacuolar K⁺ channel TPK1 by calcium-dependent protein kinases (CDPKs). *Molecular plant.* 2013; 6(4):1274–89. <https://doi.org/10.1093/mp/sss158> PMID: 23253603; PubMed Central PMCID: PMC3971370.
94. Kanchiswamy CN, Takahashi H, Quadro S, Maffei ME, Bossi S, Berteaux C, et al. Regulation of *Arabidopsis* defense responses against *Spodoptera littoralis* by CPK-mediated calcium signaling. *BMC plant biology.* 2010; 10:97. <https://doi.org/10.1186/1471-2229-10-97> PMID: 20504319; PubMed Central PMCID: PMC3095362.
95. Shabala S, Babourina O, Rengel Z, Nemchinov LG. Non-invasive microelectrode potassium flux measurements as a potential tool for early recognition of virus-host compatibility in plants. *Planta.* 2010; 232(4):807–15. <https://doi.org/10.1007/s00425-010-1213-y> PMID: 20623138.
96. Takabatake R, Karita E, Seo S, Mitsuhara I, Kuchitsu K, Ohashi Y. Pathogen-induced calmodulin isoforms in basal resistance against bacterial and fungal pathogens in tobacco. *Plant Cell Physiol.* 2007; 48(3):414–23. <https://doi.org/10.1093/pcp/pcm011> PMID: 17251204.
97. Nakahara KS, Masuta C, Yamada S, Shimura H, Kashiwara Y, Wada TS, et al. Tobacco calmodulin-like protein provides secondary defense by binding to and directing degradation of virus RNA silencing suppressors. *Proceedings of the National Academy of Sciences of the United States of America.* 2012; 109(25):10113–8. <https://doi.org/10.1073/pnas.1201628109> PMID: 22665793; PubMed Central PMCID: PMC3382489.
98. Iakoucheva LM, Radivojac P, Brown CJ, O'Connor TR, Sikes JG, Obradovic Z, et al. The importance of intrinsic disorder for protein phosphorylation. *Nucleic acids research.* 2004; 32(3):1037–49. <https://doi.org/10.1093/nar/gkh253> PMID: 14960716; PubMed Central PMCID: PMC373391.

99. Cotellet V, Leonhardt N. 14-3-3 Proteins in Guard Cell Signaling. *Frontiers in plant science*. 2015; 6:1210. <https://doi.org/10.3389/fpls.2015.01210> PMID: 26858725; PubMed Central PMCID: PMC4729941.
100. Karimi M, Inze D, Depicker A. GATEWAY vectors for Agrobacterium-mediated plant transformation. *Trends in plant science*. 2002; 7(5):193–5. PMID: 11992820.
101. Taton M, Husselstein T, Benveniste P, Rahier A. Role of highly conserved residues in the reaction catalyzed by recombinant Delta7-sterol-C5(6)-desaturase studied by site-directed mutagenesis. *Biochemistry*. 2000; 39(4):701–11. PMID: 10651635.
102. Martin K, Kopperud K, Chakrabarty R, Banerjee R, Brooks R, Goodin MM. Transient expression in *Nicotiana benthamiana* fluorescent marker lines provides enhanced definition of protein localization, movement and interactions in planta. *The Plant journal: for cell and molecular biology*. 2009; 59(1):150–62. <https://doi.org/10.1111/j.1365-313X.2009.03850.x> PMID: 19309457.
103. Grefen C, Donald N, Hashimoto K, Kudla J, Schumacher K, Blatt MR. A ubiquitin-10 promoter-based vector set for fluorescent protein tagging facilitates temporal stability and native protein distribution in transient and stable expression studies. *The Plant journal: for cell and molecular biology*. 2010; 64(2):355–65. <https://doi.org/10.1111/j.1365-313X.2010.04322.x> PMID: 20735773.
104. Sparkes IA, Runions J, Kearns A, Hawes C. Rapid, transient expression of fluorescent fusion proteins in tobacco plants and generation of stably transformed plants. *Nat Protoc*. 2006; 1(4):2019–25. <https://doi.org/10.1038/nprot.2006.286> PMID: 17487191.
105. Peart JR, Lu R, Sadanandom A, Malcuit I, Moffett P, Brice DC, et al. Ubiquitin ligase-associated protein SGT1 is required for host and nonhost disease resistance in plants. *Proceedings of the National Academy of Sciences of the United States of America*. 2002; 99(16):10865–9. <https://doi.org/10.1073/pnas.152330599> PMID: 12119413; PubMed Central PMCID: PMC125064.
106. Izeddin I, Boulanger J, Racine V, Specht CG, Kechkar A, Nair D, et al. Wavelet analysis for single molecule localization microscopy. *Opt Express*. 2012; 20(3):2081–95. <https://doi.org/10.1364/OE.20.002081> PMID: 22330449.
107. Racine VH, A. Jouanneau, J. Salamero, J. Kervrann C., Sibarita., JP. MULTIPLE-TARGET TRACKING OF 3D FLUORESCENT OBJECTS BASED ON SIMULATED ANNEALING. *Conference Paper*. 2006. <https://doi.org/10.1109/ISBI.2006.1625094>
108. Claro E, Sarri E, Picatoste F. Measurement of phospholipase C activity in brain membranes. *Methods in molecular biology*. 1995; 41:177–88. <https://doi.org/10.1385/0-89603-298-1:177> PMID: 7655555.
109. Boudsocq M, Willmann MR, McCormack M, Lee H, Shan L, He P, et al. Differential innate immune signalling via Ca(2+) sensor protein kinases. *Nature*. 2010; 464(7287):418–22. <https://doi.org/10.1038/nature08794> PMID: 20164835; PubMed Central PMCID: PMC2841715.

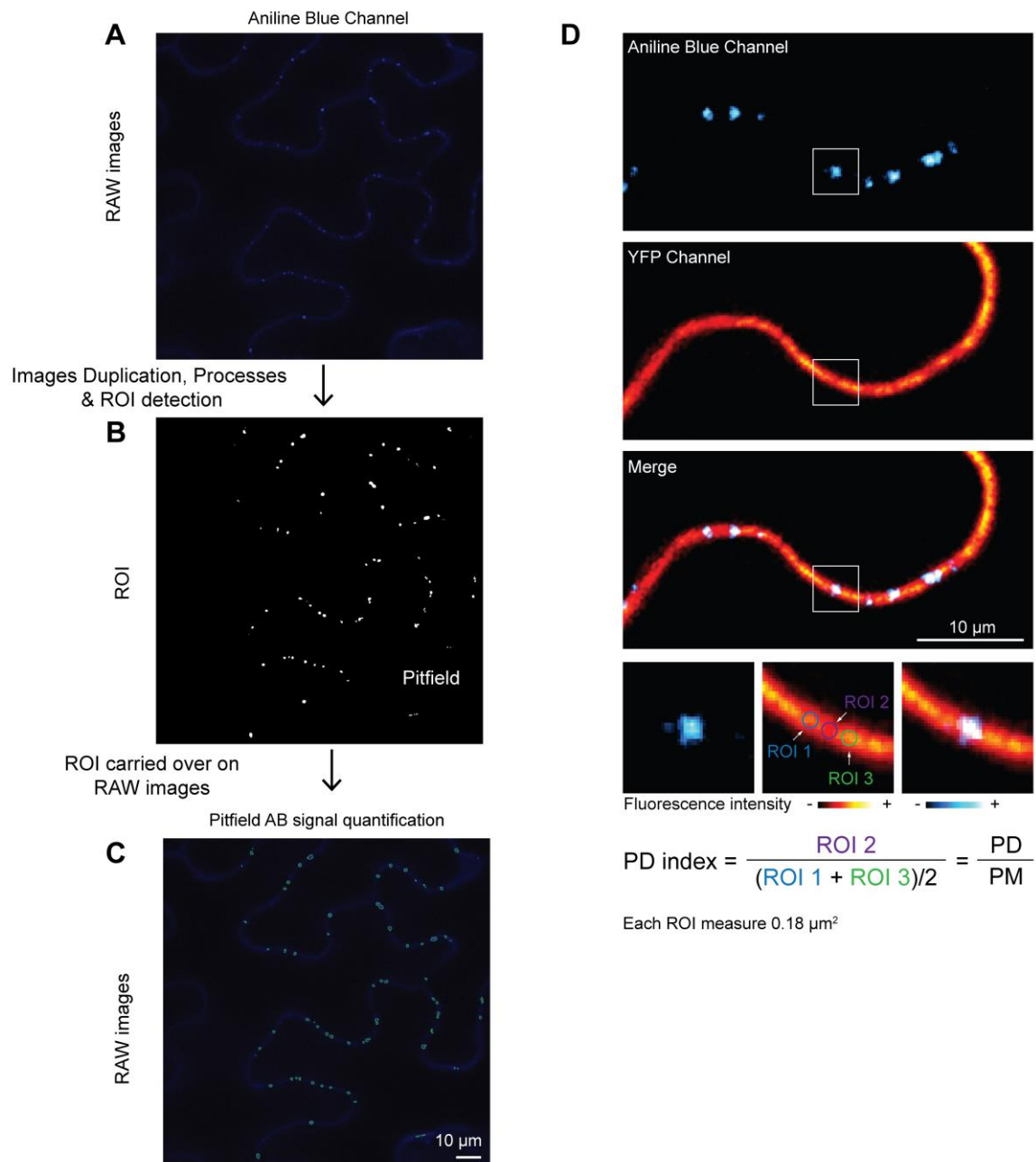


Figure S1

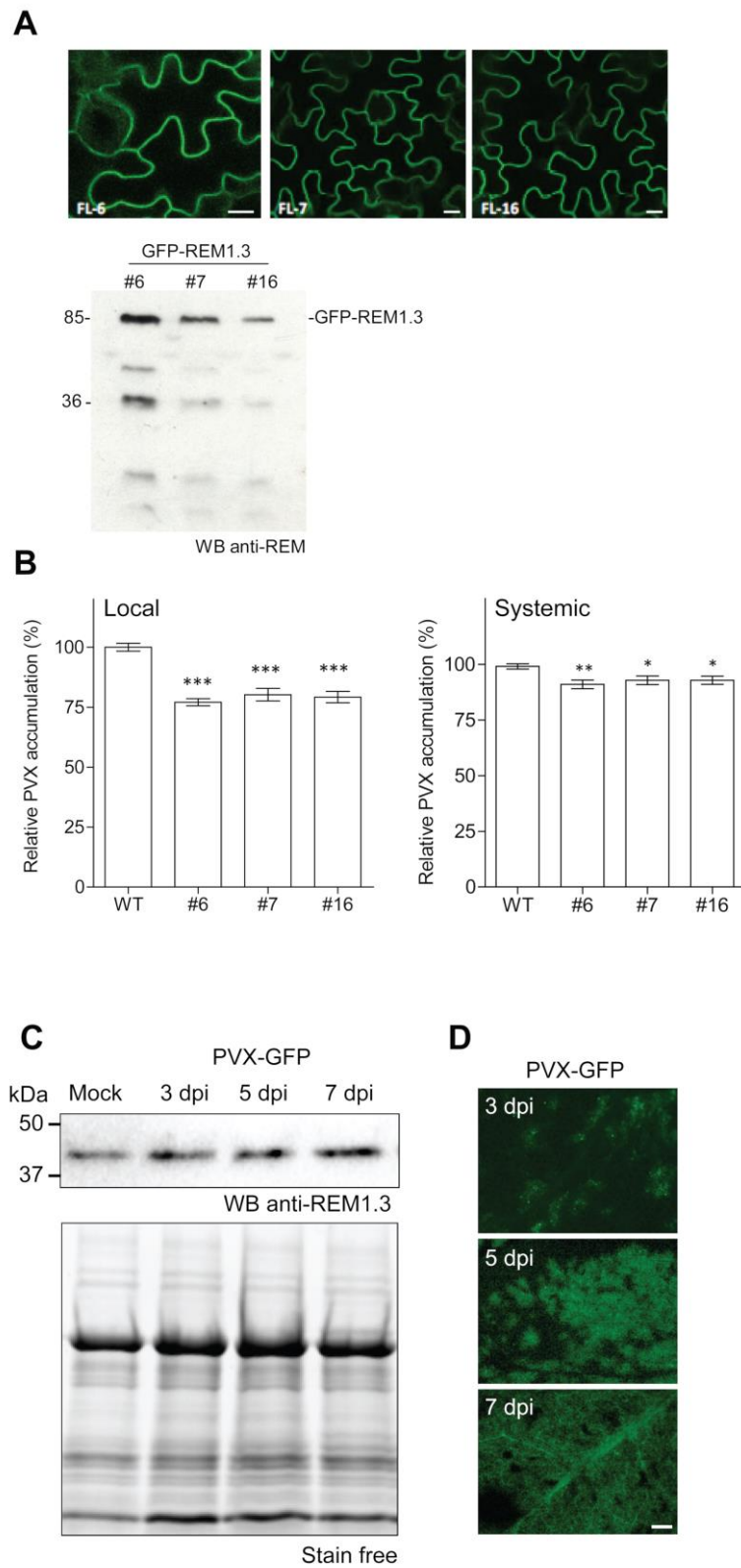


Figure S2

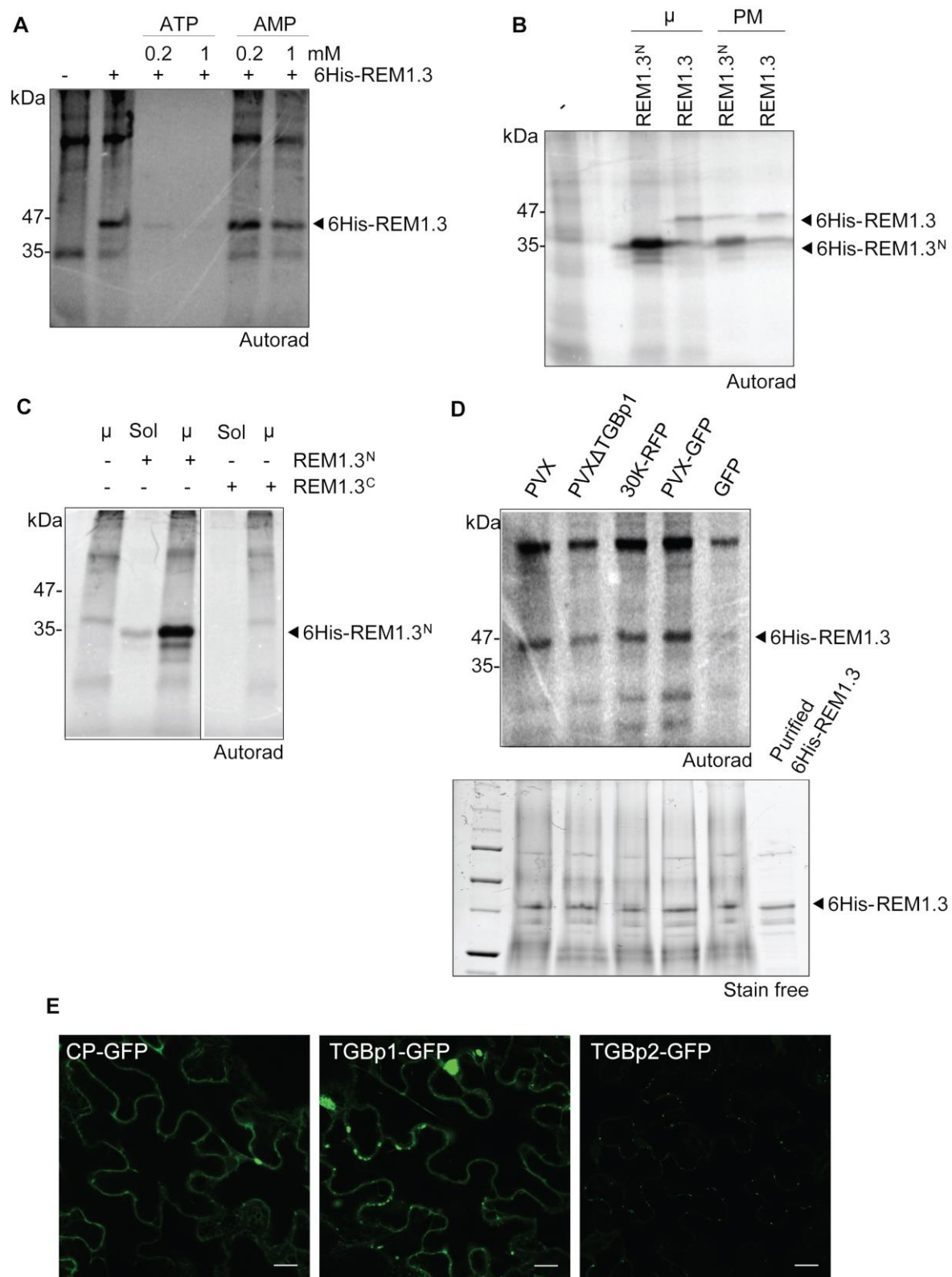


Figure S3

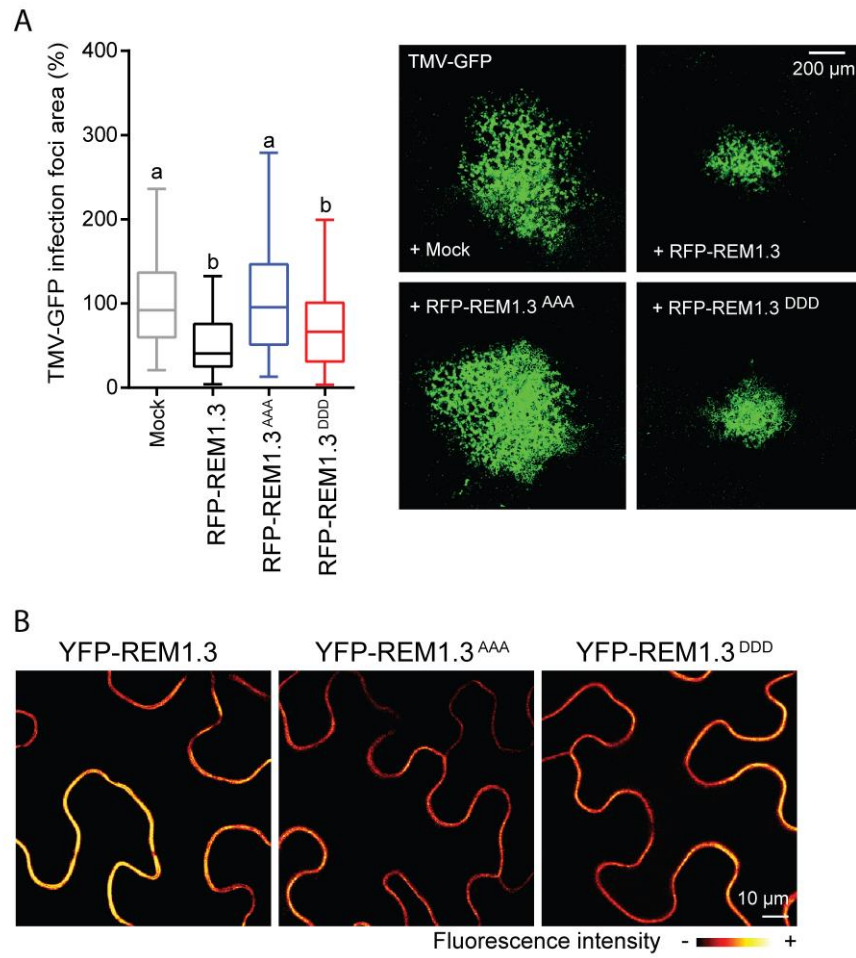


Figure S4

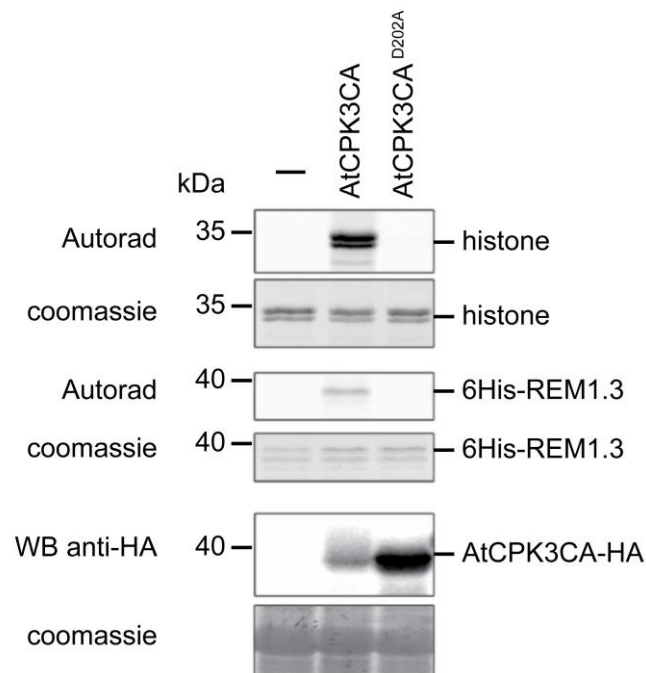


Figure S7

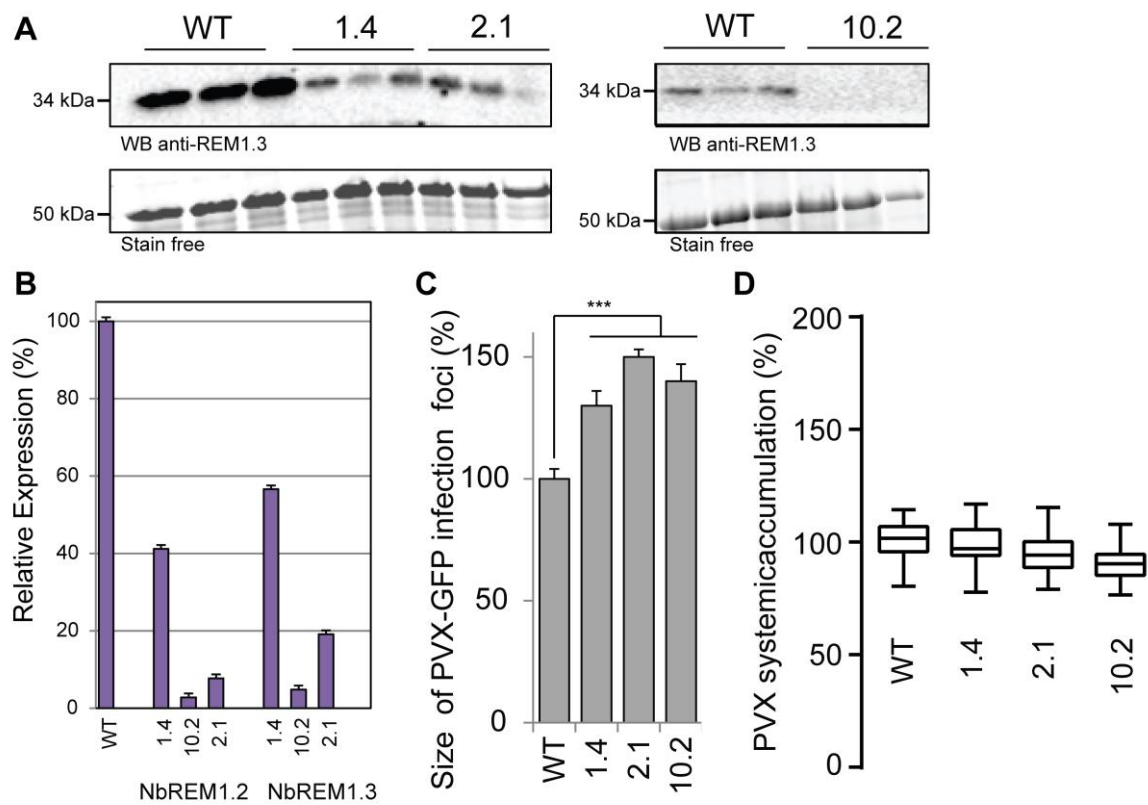


Figure S8

Article II: addendum

We pursued our quest to discover more about StREM1.3's interactome and to map, by biophysical means, its phosphorylation sites. Its N-terminal is predicted to be intrinsically disordered (Perraki et al., 2018), however this has never been proven experimentally. If it truly is an IDD, it is tempting to envision it as a domain responsible for many interactions (Uversky, 2013), such as those we have already discussed in Article II, namely kinase AtCPK3 and, directly or through an uncharacterised signalling pathway, callose synthase. We decided to work solely on this IDD. Thus, the protein of interest here will be a truncated StREM1.3: REM₁₋₁₁₆.

REM₁₋₁₁₆ was produced in BL21-DE3 cells in minimal medium with ¹³C-labelled glucose and ¹⁵NH₄Cl, by addition of 1 mM IPTG at OD₆₀₀ = 0.6-0.8 and incubation at 37°C for 3h. Cells were lysed by sonication and the supernatant was loaded onto a HisTrap column (GE Healthcare) equilibrated in 20 mM HEPES 150 mM NaCl 20 mM imidazole 0.02% NaN₃ pH=7.4 and eluted with 20 mM HEPES 150 mM NaCl 500 mM imidazole 0.02% NaN₃ pH=7.4. Eluted REM₁₋₁₁₆ was adjusted to 1 mM DTT and 0.5 mM EDTA then TEV protease was added in a ~1/200 TEV/REM₁₋₁₁₆ mass ratio. The mixture is incubated for 3h at room temperature then desalted against 10 mM HEPES 50 mM NaCl 0.02% NaN₃ pH=7.5 with a HiPrep column (GE Healthcare). Under native conditions, REM₁₋₁₁₆ was loaded onto a HisTrap column equilibrated with 20 mM HEPES 150 mM NaCl 0.02% NaN₃ pH=7.4 and eluted with the same elution buffer as above. Under denaturing conditions, this step was performed in buffers containing 7M urea. Finally, REM₁₋₁₁₆ was desalted again against 10 mM HEPES 50 mM NaCl 0.02% NaN₃ pH=7.5.

In vitro phosphorylation of 0.5 mM of REM₁₋₁₁₆ by AtCPK3 required adjusting the sample to 10 mM MgCl₂, 1 mM CaCl₂, 1 mM DTT and 3 mM ATP. The reaction was initiated by the addition of 88 µM of AtCPK3 and incubation at 20°C.

IsNMR was performed on a Bruker Avance NEO spectrometer operating at 700 MHz for proton with a TXI 5 mm probe. The sample was adjusted to 9/1 H₂O/D₂O to lock the magnetic field. ¹H-¹⁵N HMQC spectra were recorded at 283 K (10°C).

I performed the cloning, production and purification of labelled ¹⁵N-, ¹³C-labelled REM₁₋₁₁₆. Axelle Grélard and Estelle Morvan, engineers of the NMR platform, trained me to perform all the IsNMR experiments and data analysis. The *in vitro* phosphorylation assay by AtCPK3 was designed and optimised by Dr Marie Boudsocq, who confirmed the phosphorylation of REM₁₋₁₁₆ by biochemical means.

The structural fingerprint of REM₁₋₁₁₆ is characteristic of an IDP (Figure 66). In addition, using either native or denaturing conditions during purification had no impact its fingerprint. Next, we performed the *in vitro* phosphorylation of REM₁₋₁₁₆ by AtCPK3 with cold ATP in the NMR tube and monitored the evolution of its structural fingerprint. In addition to many chemical shifts being slightly perturbed, three peaks (3 and 4) disappeared and two new peaks appeared (1 and 2) (Figure 67). Even so, the structural fingerprint remains that of an IDP: most peaks are still clogged in the same spectral region. Plotting NMR intensities as a function of time, maximal intensities for

1 and 2 and minimal intensities for 3 and 4 are reached after ~ 4h, meaning that the phosphorylation reaction is complete at that time (Figure 68).

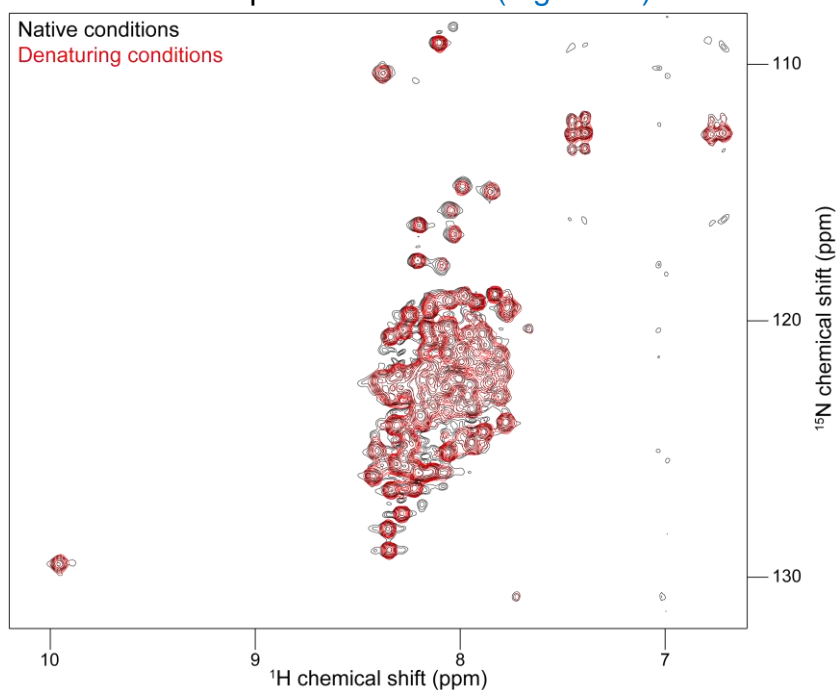


Figure 66

^1H - ^{15}N HMQC spectra of REM₁₋₁₁₆ purified under native (black) or denaturing conditions using 7M of urea (red).

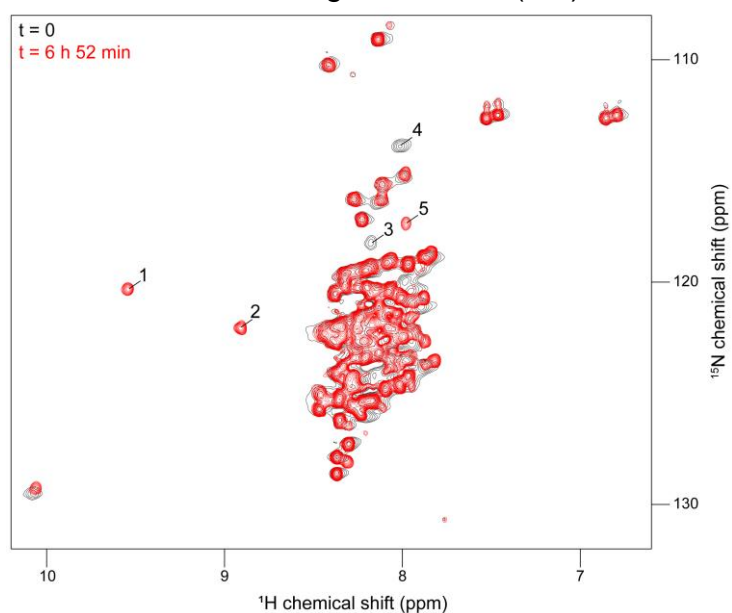


Figure 67

^1H - ^{15}N HMQC spectra of REM₁₋₁₁₆ in AtCPK3's reaction buffer before addition (black) or 14 h 13 min after addition (red) of AtCPK3. Notice how the peaks labelled 1,2 and 5 appeared over time while 3 and 4 disappeared. Each spectrum was acquired using 2 scans for an experimental time of 1 min 42 s each.

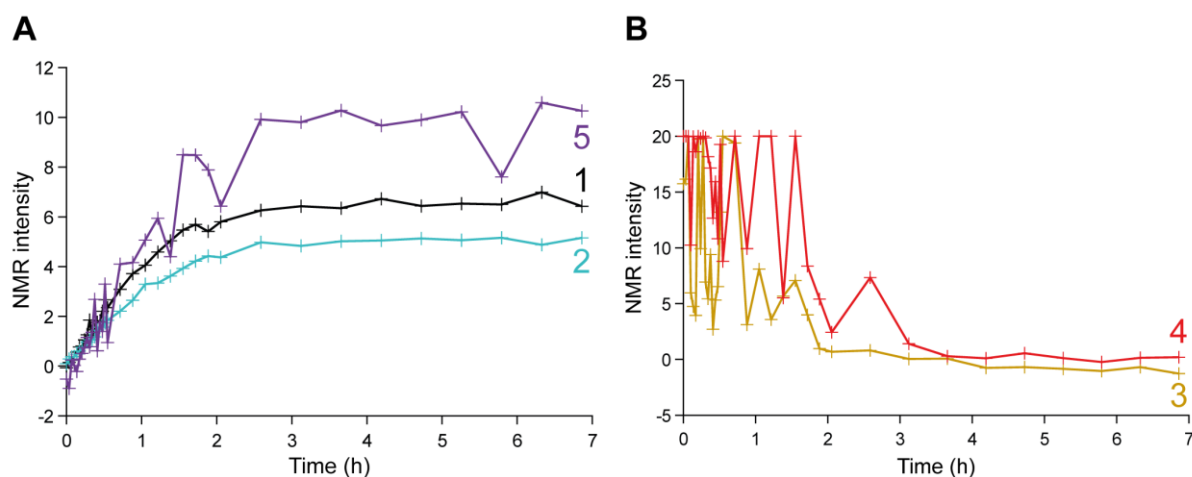


Figure 68

Kinetics of phosphorylation of REM₁₋₁₁₆ by AtCPK3. NMR intensities are plotted as a function of time for peaks 1 to 5 according to (Figure 67). Each data point was obtained from a ¹H-¹⁵N HMQC spectrum acquired using 2 scans for an experimental time of 1 min 42 s. Notice the difference of scale in NMR intensity between (A) and (B).

Recording 3D NMR spectra, namely HNCa and HN(Co)CaCb, will prove capital to establish connectivities between residues and to identify them, thus mapping, for the first time, the phosphorylated residues of StREM1.3 through biophysical means. Then, having both phosphorylated and non-phosphorylated REM₁₋₁₁₆, we shall be able to monitor interactions between putative ligands and both forms of the protein. By looking for changes in its structural fingerprint, we could identify their interaction sites on REM₁₋₁₁₆ (to be done).

Article III

Mechanisms governing subcompartmentalization of biological membranes

Julien Gronnier, **Anthony Legrand**, Antoine Loquet, Birgit Habenstein,
Véronique Germain, Sébastien Mongrand

Current Opinion in Plant Biology

2019

52, p114–123

This first review was aimed at showcasing some known cases of plant membrane subcompartmentalisation and how they could be studied. Examples given included remorins, thylakoids, chloroplast envelope and mitochondria cristae. Biophysical tools to study domains are given, with a special focus on ssNMR.

My major contribution was to design Figure 2 and write its caption. I reviewed the main text for grammar corrections and general organisation of ideas. I also offered some technical assistance with Illustrator to make Figure 1.



Mechanisms governing subcompartmentalization of biological membranes

Julien Gronnier², Anthony Legrand^{1,3}, Antoine Loquet³,
 Birgit Habenstein³, Véronique Germain¹ and
 Sébastien Mongrand¹

Membranes show a tremendous variety of lipids and proteins operating biochemistry, transport and signalling. The dynamics and the organization of membrane constituents are regulated in space and time to execute precise functions. Our understanding of the molecular mechanisms that shape and govern membrane subcompartmentalization and inter-organelle contact sites still remains limited. Here, we review some reported mechanisms implicated in regulating plant membrane domains including those of plasma membrane, plastids, mitochondria and endoplasmic reticulum. Finally, we discuss several state-of-the-art methods that allow nowadays researchers to decipher the architecture of these structures at the molecular and atomic level.

Addresses

¹ Univ. Bordeaux, CNRS, Laboratoire de Biogenèse Membranaire (LBM), UMR 5200, 33140 Villenave d'Ornon, France

² Department of Plant and Microbial Biology, Zurich-Basel Plant Science Center, University of Zürich, Zürich, Switzerland

³ Institute of Chemistry & Biology of Membranes & Nanoobjects (UMR5248 CBMN), IECB, CNRS, Université de Bordeaux, Institut Polytechnique de Bordeaux, All. Geoffroy Saint-Hilaire, Pessac, France

Corresponding author:

Mongrand, Sébastien (sebastien.mongrand@u-bordeaux.fr)

Current Opinion in Plant Biology 2019, **52**:114–123

This review comes from a themed issue on **Cell biology**

Edited by **Eva Benkova** and **Yasin Dagdas**

<https://doi.org/10.1016/j.pbi.2019.08.003>

1369-5266/© 2019 Elsevier Ltd. All rights reserved.

Introduction

Spatiotemporal organization of the cellular biomolecules is critical to coordinate the numerous activities simultaneously carried out by cells. Biological membranes delimit cells and organelles and constitute specialized subunits that are constantly reshaped to adapt to ever-changing environmental conditions and to operate cell functions effectively (Special issue on cell biology edited by Ref. [1]). Cell membranes are composed of a specific

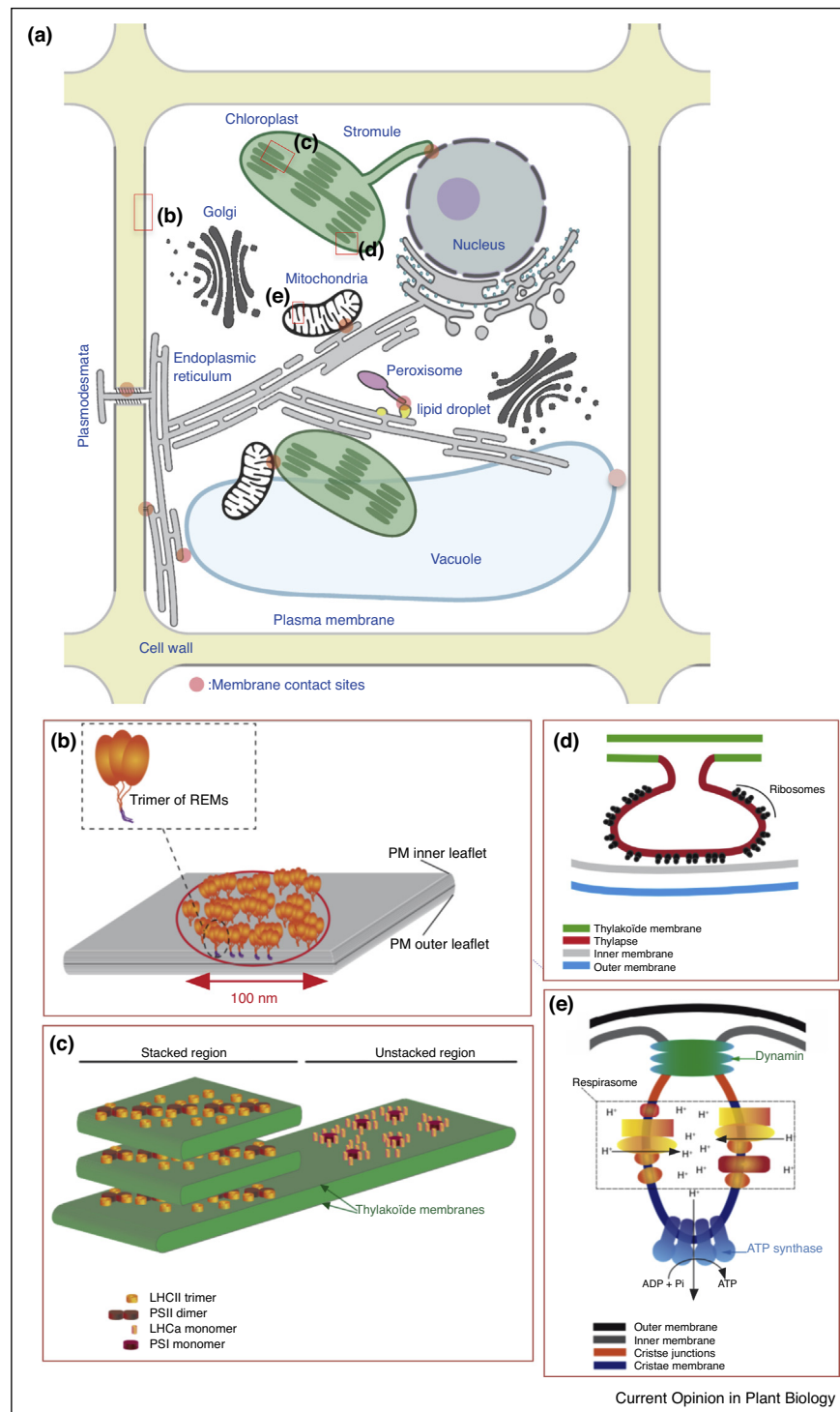
set of biomolecules defining their identity. For example, phosphoinositide lipids and small GTPases proteins are major contributors to endosome identity [2,3]. A tremendous body of evidence shows that the motion and the organization of membrane constituents are dynamically regulated on the level of the membrane to form functional domains and this conversely throughout the tree of life [4^{**},5,6]. Thus, it appears that membrane subcompartmentalization into domains is universal and may represent an essential characteristic. Taking into account the knowledge acquired in various model organisms and model systems over the past decades, membrane domains can be defined as membrane regions in which the local composition, lateral organization, and/or dynamics differ in some way from the average membrane properties [7–9]. Such local specificity is dictated by preferential intermolecular interactions, including intra-membrane interactions (i.e lipid–protein, lipid–lipid and protein–protein) and associations with structures peripheral to the membrane for example cortical cytoskeleton and the cell wall in the case of plasma membrane. This also leads to the formation of inter-membrane interaction through Membrane Contact Sites (MCS), important functional platforms for the exchange of lipids and signalling proteins [10,11], see **Figure 1**. Yet, membranes being constituted of several thousands of molecules surrounded by variable and complex environments, a tremendous mechanistic complexity remains to be uncovered. Here, we review some described mechanisms regulating membrane architecture in plants and discuss recent technological advancements allowing researchers to study membrane organization with molecular and atomic resolution.

Examples of subcompartmentalization of plant membranes

Plasma membrane domains

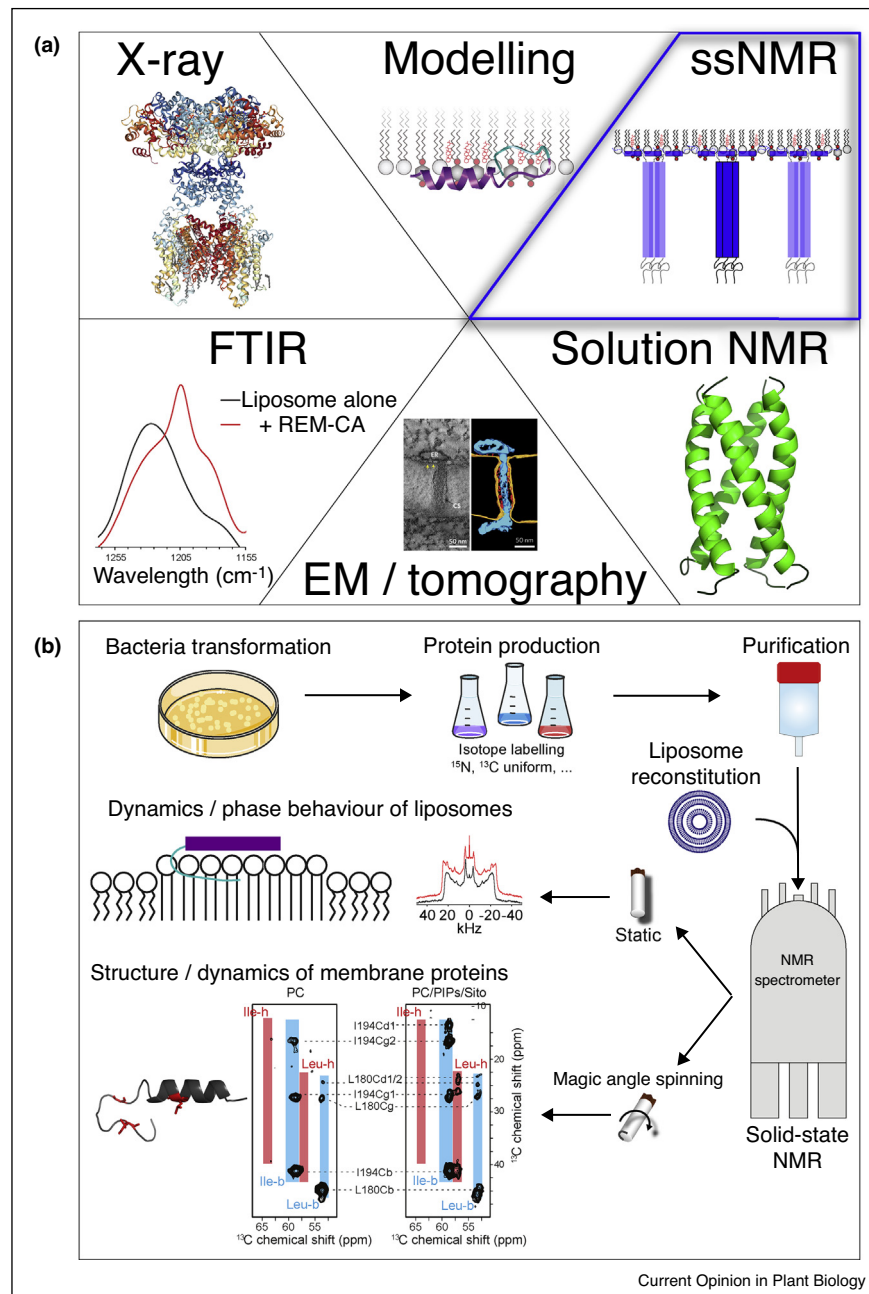
The plasma membrane (PM) is the outermost boundary of the cell, acting as a communication headquarter integrating signal from the environment to the cell interior and *vice-versa*. The PM is asymmetric, as exemplified by the enrichment of sphingolipids in the outer leaflet and phospholipids in the inner leaflet [12,13]. The PM associates with the cortical cytoskeleton network and the cell wall creating a continuum at the cell surface [14]. PM establishes MCS with organelles, notably with ER at the level of PD, see **Figures 1a** and **2**. The lipid and protein composition of the domains formed at these MCS is very

Figure 1



Examples of subcompartmentalization of membranes and membrane contact sites (MCS) in different organelles of plant cells. **(a)** Scheme of a plant cell showing the membrane contact sites (MCS) between organelles shown by a red dot. Few examples of subcompartmentalization of biological membranes are emphasized in the plasma membrane **(b)**, thylakoids **(c)**, chloroplast envelope **(d)**, mitochondria cristae **(e)**.

Figure 2



Biophysical techniques to study membrane domains.

(a) Examples of major biophysical tools to analyse membrane domains and membrane-associated proteins, subsequently deciphering the molecular mechanisms at play in nanodomain organization. X-ray: shaker family voltage-dependent potassium channel Kv represented in the cartoon, lipids in stick (PDB: 2R9R, [111]). Modelling: C-terminal anchor of StREM1.3 interacting with membranes enriched in phosphoinositol-4-phosphate and sitosterol. ssNMR: model of StREM1.3 nanodomains. FTIR: insertion of C-terminal anchor of StREM1.3 in nanodomain-like membranes [16^{**}]. EM/tomography: observation of ER-PM membrane contact sites at plasmodesmata [89^{**}]. Solution NMR: membrane-embedded domain of the Influenza B BM2 integral protein (PDB: 2KIX, [112]). **(b)** ssNMR workflow to study membrane domain-associated proteins. Bacterial expression cells (e.g. *E. coli* BL21-DE3) are transformed with a high expression level plasmid coding for the protein of interest. Protein production is achieved in minimal culture media supplemented with isotope labelled metabolites depending on the desired isotopic labelling scheme of the protein (e.g. ^{13}C -glucose, 1,3- ^{13}C -glycerol, 2- ^{13}C -glycerol . . .). Proteins are purified and reconstituted into liposomes of a chosen lipid composition. ssNMR allows obtaining two types of structural data: magic angle spinning (MAS) ssNMR is used to analyze the structure and dynamics of the membrane protein [16^{**}], and ^2H (unpublished typical data) and ^{31}P (not shown) ssNMR to decipher the dynamics and phase behavior of the membranes of interest comprising deuterated lipids.

specific [11]. Organization of the PM can be rationalized into two types: microdomains and nanodomains. Microdomains are site-specific enrichment of membrane compounds at the cellular level usually referred to as polar domains that control localized cell activities. Nanodomains represent submicrometric heterogeneity of the PM whose visualization often requires the use of high or superresolution microscopy techniques [15,9]. Nanodomains have been proposed to act as dedicated platforms regulating cell signalling notably [4[•],16^{••},9,17[•],15]. Mechanisms regulating the organization of PM domains being recently reviewed [9,15,13,18–22], we present here only three case studies to illustrate the molecular mechanisms at play in the organization and dynamics of PM domains.

REMORINs are plant-specific proteins regulating notably immunity [23–26], symbiosis [27,28,29[•]] and development [30] possibly by modulating nanodomain-associated complexes [16^{••},31,32,17[•],29[•]]. REMORINs predominantly associate with the PM [33,23,31,34,35]. In addition, isoforms from group 1 and group 6 REMORINs have been shown to be associated with plasmodesmata (PD) in Rice and in *Solanaceae* [23,36,30,31]. Electron microscopy immunolocalization, stimulated emission depletion microscopy (STED) and photoactivated localization microscopy (PALM) studies showed group 1 REMORINs are organized into nanodomains of about 70–90 nm in diameter that are sensitive to sterol composition [23,37,16^{••}] and cytoskeleton integrity [38]. Molecular mechanisms at the basis of REMORIN domain organization are being discovered: REMORINs are targeted from the cytosol to the cytosolic leaflet of the PM *via* a short unconventional sequence at the extremity of the C-terminus of the protein, called REM-CA (REMORIN C-terminal Anchor) [39,34,40], see Figures 1b and 2; REM-CA undergoes conformational changes upon binding of conserved positively charged residues to phosphoinositides and provides to REMORINs biochemical properties indistinguishable from integral proteins [23,39,16^{••}]; REM-CA-sterol-phosphoinositide interactions are required for Group 1 REMORINs supra-molecular organization into functional domains involved in plant response to the *Potato Virus X* (PVX). Numerous REMORINs present cysteine residues that can be S-acylated [41,34,42,43]. While S-acylation of *Arabidopsis* REMORINs seems to regulate PM affinity but not primarily nanodomain organization [34], the substitution of an S-acylated cysteine of *Nicotiana benthamiana* REM alters nanodomain organization [43], suggesting functional divergence of REMORIN S-acylation. Oligomerization of group 1 REMORINs into homotrimers is required for PM localization [39,44], suggesting that REMORINs' self-assembly constitute an early step of PM targeting. Furthermore, REMORIN organization seems regulated by intermolecular protein association. Indeed, in *Medicago*, FLOT4 scaffolds SYMBIOTIC REM1 to recruit the Nod factor co-receptor LYSINE MOTIF KINASE 3 (LYK3) to specific nanodomains

controlling root hair infection by *Sinorhizobium meliloti* and the establishment of symbiosis [29[•]]. Interaction of AtREM1.3 with AtHIR1 in *Arabidopsis* suggests that association of SPFH (Stomatin, Prohibitin, Flotillin, HflK/C) proteins with REMORINs may represent a conserved core module shaping PM organization [45]. Finally, phosphorylation of group 1 REMORINs upon infection of *N. benthamiana* by the PVX modulates REM1.3 organization and function [31], probably through the modulation of protein–protein interactions. Thus the genesis and regulation of REMORIN nanodomains appear to rely on several molecular mechanisms such as post-translational modifications, and protein–lipid and protein–protein interactions.

Rho of Plants (ROPs) are the plant-specific subfamily of Rho/Rac small GTP binding proteins, regulating numerous cellular processes such as signalling, trafficking and cytoskeleton dynamics [46,47]. Reversible switch from a GDP-bound state to a GTP-bound state mediated by ROP-GEFs and ROP-GAPs regulates ROPs activity [48]. Polarization of the growth machinery to a predefined root hair initiation domain (RHID) pledges root hair formation in trichoblast cells. ROP2, 4 and 6, are recruited to the RHID before any detectable cell bulging and serve as a landmark for the recruitment of downstream effectors [49,50[•]]. Strikingly, guanine nucleotide exchange factor 3 (GEF3) defines the RHID by guiding ROPs polarization *via* direct protein–protein binding [50[•]]. At the bulging stage, phosphatidylinositol-4-phosphate 5-kinase 3 (PIP5K3), the AGCVIII kinase D6 PROTEIN KINASE (D6PK) and sterol composition modulate ROPs association to the RHID [51,52]. Here, co-regulation of ROP, phosphoinositides and phosphoinositide kinases has been proposed to form a self-organizing system amplifying ROP recruitment and activation [3]. In addition, ROPs associate with the PM *via* post-translational lipid modifications and direct interaction with membrane lipids mediated by the carboxy-terminal tail [53,47,4^{••}]. For example, ROP6 interacts with phosphatidylserine (PS) *via* its polybasic tail, a process likely at the basis of nanodomain organization. Recently, using live superresolution microscopy, Platre *et al.* elegantly showed that variation in PS level during root development stabilized ROP6 into nanodomains to regulate auxin signaling [4^{••}]. In metaxylem vessel cells, ROP-GEF4 locally activate ROP11 to recruit MICROTUBULE DEPLETION DOMAIN 1 scaffold protein which in turn recruits microtubule-depolymerizing kinesin-13A enabling the formation of pits in secondary cell walls [54,55]. IQD13 associates with cortical microtubules (cMTs) and the PM to laterally restrict the localization of ROP GTPase domains, establishing a lateral fence for ROP GTPase [56]. In contrary, CORTICAL MICROTUBULE DISORDERING1-induced disorganization of cortical microtubules impairs the boundaries of PM domains of active ROP11 GTPase [57].

Cellulose microfibrils are synthesized by the PM-embedded cellulose synthase (CESA) complexes (CSCs) which are composed of 18–36 cellulose synthase subunits [58]. Cortical microtubules recruit CESA-containing vesicles and guide the trajectory of CSCs at the PM [59–61]. In addition, S-acylation of CESAs influences its immediate membrane environment and conditions their location to the PM [62]. CSCs are tethered to cortical microtubules via two integral components, CELLULOSE SYNTHASE INTERACTING 1 [63–65] which determines the trajectory of CSCs along the cMTs [59] and COMPANION OF CELLULOSE SYNTHASE 1 (CC1), which sustains cellulose synthesis by promoting the formation of a stress-tolerant microtubule array during salt stress [66**].

These examples emphasized that regulation of plasma membrane subcompartmentalization is regulated as part of developmental program, is modulated to respond to environmental clues, relies on the cooperation of multiple factors and is fundamental for function.

Chloroplastic membrane domains

Chloroplasts are organelles composed of a double membrane envelope and thylakoids found in plant cells and algae that conduct photosynthesis. Little is known about how the photosynthetic membrane machinery is arranged in time and space. Microscopy and biophysical shreds of evidence showed the coexistence of domains where lipids are organized in lamellar or hexagonal phases. For example, hexagonal phases have been described in etioplasts of prolamellar bodies or during the transfer of lipids between the envelope and thylakoids, such hexagonal phase domains may be of importance for localizing metabolic activities, for example the violaxanthine-epoxidase in thylakoid domains [67].

Biochemical, 3D reconstruction, *in vivo* spectroscopy and immunolocalization data, reveal that thylakoids display a heterogeneous subcompartmentalization of photosynthetic complexes in domains which redistribute during state transitions in *Chlamydomonas* [68] and diatoms [69], see Figure 1c. These domains are interconnected, ensuring fast equilibration of electron carriers for efficient and optimal photosynthesis. Underlying molecular events at the basis of thylakoid subcompartmentalization remain unclear. Thylakoids possess a special fatty acid namely trans- Δ^3 -hexadecenoic acid (trans-16:1) esterified in phosphatidylglycerol (PG) which may play a role in cementing thylakoids during granum formation and control of light reactions of photosynthesis [70]. Recent 3D cryo-electron tomography showed the thylakoid network of cyanobacteria is organized in domains and forms a synapse-like MCS decorated by ribosomes (but not by phycobilisomes) in tight association with the PM of cyanobacteria. This MCS was named the ‘thylapse’, for ‘thyl(akoid syn)apse’, and likely serves for compartmentalization of the different functions of the thylakoids that is photosynthesis or protein

synthesis [71**], see Figure 1d. Because PM of cyanobacteria represents the inner membrane of eukaryotic plastids, thylapses most likely also exist in higher plants.

Chloroplast envelope establishes numerous MCS with other organelles [10]. For example, plastid and mitochondrion envelopes establish membrane connection during phosphate deprivation. The molecular content of this MCS has been recently identified by biochemical and proteomic approaches and showed a big complex of hundred proteins enriched in specific lipids. AtMic60, a conserved protein of the mitochondria inner membrane, plays a crucial role in the lipid transport process by regulating the proximity between mitochondrial membranes via its interaction with the outer membrane protein Tom40 and by destabilizing membranes, likely to promote lipid desorption [72**]. Plastids can also undergo drastic changes in shape under stress, through specialized protrusive membrane domains called stromules (stroma-filled tubules, see Figure 1a) which link plastid envelope with other organelles such as ER, Golgi and nucleus [73,74]. The molecular mechanisms governing stromule formation are not established, but the involvement of cytoskeleton motors has been proposed [75]. Similarly, peroxules, peroxisomal protrusions tethering chloroplasts or mitochondria through specialized membrane microdomains have been evidenced [76,77]. Peroxules also for example link with lipid droplets, see section ‘Endoplasmic reticulum domains’. These studies reveal the importance of physical connections through plant membrane domains for establishing complex metabolic pathways.

Mitochondrial membrane domains

Mitochondria are double-membrane-bound organelles. The outer mitochondrial membrane encloses the entire organelle and can be in contact with other organelles for example during phosphate starvation, see above [10]. The inner membrane separates the mitochondrial matrix from the intermembrane space. The structure of the inner mitochondrial membrane is extensively folded. These invaginations are separated from the inner membrane by dynamin proteins to form three domains namely, the inner boundary membrane, the cristae junctions and the cristae membranes [78], see Figure 1e. The latter contains enzymes of the mitochondrial respiratory chain that, instead of being dispersed in the membrane, are organized into a functional supramolecular respiratory domain called respirasome, see Figure 1. ATP synthase dimers sit at the edge of the cristae. Mitochondria inner membrane is rich in cardiolipin (CL), a key phospholipid playing important roles in maintaining the functional integrity and dynamics of mitochondria. Arabidopsis CL localizes to mitochondria and is enriched at specific domains and CARDIOLIPIN SYNTHASE targets to the inner membrane of mitochondria with its C-terminus in the intermembrane space [79]. Mitochondria of *cls* mutants exhibit altered structural integrity and morphogenesis. In contrast to animal and yeast, plant CL

plays a dominant role in mitochondrial fission and exerts this function through stabilizing the protein complex of DYNAMIN-RELATED PROTEIN3 [79]. In addition, CL induces membrane invaginations which are stabilized by dimers of ATP synthase. In reconstituted systems, bovine ATP synthase is sufficient to deform a lipid bilayer, which is likely the driving force triggering cristae curvature [80]. Recently, dimers of mitochondrial ATP synthase from the green algae *Polytomella* were shown to be required for cristae formation and constitute the main factor in mitochondrial morphogenesis to induce membrane curvature and self-assembly into rows [81[•]]. Finally, mitochondria-associated ER membrane (MAM) is another structural element that is increasingly recognized for its critical role in cellular physiology and homeostasis of mitochondria [10].

Endoplasmic reticulum domains

The endoplasmic reticulum forms a membrane network virtually in contact with all cell organelles, see Figure 1a. Thus, the ER is actively engaged in organizing membrane domains to perform various functions. For example, ER is known to be organized into smooth and rough domains, the latter being enriched in ribosomes involved in protein production, protein folding, quality control and dispatch. Formation of these domains is regulated by syntaxin proteins [82]. Lipid droplets (LD) are lipid-rich cellular organelles regulating storage and hydrolysis of neutral lipids. LD biogenesis takes place at ER subdomains which are regulated by lipodystrophy proteins called SEIPINs in human, yeast, and plants. SEIPINs reorganize the normal, reticulated ER structure into discrete ER domains that colocalize with LD. In plants, SEIPINs modulate the number and sizes of LD [83[•],84]. Recent work in plants showed that peroxisome extensions deliver the major TAG lipase Sugar-Dependent 1 (SDP1) to the LD. At early stages of seedling development, SDP1 localizes to a peroxisome membrane domain and then possibly moves to the LD surface through peroxisome tubulations [85]. This constitutes an interesting case of inter-organelle communication and protein transport that is reminiscent of stromule.

In the next chapter, we will briefly describe state-of-the-art biophysical methods that have provided access to the structural basis membrane domain organization.

How to study the molecular mechanisms shaping biological membrane domains in plants?

Membrane subcompartmentalization is intimately linked to the preferential association of membrane constituents. Therefore, establishing the structure-function relationship between the membrane subcompartment components is an essential piece of the puzzle towards understanding the complex interplay of the cells with the extracellular environment. Yet, the intrinsic soft matter state of membrane-related systems in their native environment, such as

peripheral or membrane-embedded proteins, hampers the application of numerous techniques in structural biology to visualize molecular association at the atomic level. To provide an overview on a promising route towards understanding the molecular basis underlying membrane subcompartmentalization, we can list tools such as X-ray, crystallography and solution NMR [86–88]. The recent developments of superresolution microscopy (eg. STED, PALM), cryo-electron microscopy (EM) and tomography methods allowed the study of the organization of proteins and lipids and the characterization of membrane subcompartmentalization and MCS [89^{••},16^{••},90[•]] with unprecedented resolution. The complementary biophysical tools to investigate lipid/protein interactions such as Langmuir monolayer, Fourier-Transform InfraRed spectroscopy (FTIR), NMR or modelling are reviewed in [91,11,13]. Figure 2a shows several examples of diverse contributions, including solid-state nuclear magnetic resonance (ssNMR), X-ray crystallography, modelling, FTIR, tomography by EM and solution NMR. The development of lipid and protein imagery by isotope-labeled high-resolution secondary ion mass spectrometry (nano-SIMS) would allow the study of molecular events at play in domain formation and dynamics [92,93]. In plants, nano-SIMS was used to localize elements such as manganese, arsenic, iron, zinc, and cadmium at the nanoscale level [94], but this approach could also be used for lipids and proteins in internal organelles.

Here, we further describe the powerful technique ssNMR that emerges as a tool to understand domain assembly. SsNMR is a versatile technology reporting on membrane and protein structure, sensitive to dynamics and protein–lipid interactions. A major advantage relies in its application on systems in the native bilayer environment, that is reconstituted liposomes that can represent membranes of a chosen lipid composition. The flowchart in Figure 2b illustrates the overall procedure applied to inquire on the previously mentioned aspects of membrane-associated proteins. Reporting membrane biophysical and structural parameters are achieved by well-established membrane-focused ssNMR, mainly recorded on ²H and ³¹P nuclei [95,96]. The quadrupolar ²H signal in static ssNMR encodes for the overall lipid mobility and, importantly, the local dynamics along the acyl chain. Upon varying the membrane components (lipid composition, presence or absence of protein) and environment (temperature, pH), ²H ssNMR reveals detailed insights on phase, phase transitions, acyl chain dynamics and membrane thickness and curvature depending on the precise lipid composition and on the presence of a potential interaction partner. The chemical shift of ³¹P nuclei complements and corroborates the data reporting on phase behavior and the impact of potential partner molecules on the lipid head groups. Tackling membrane proteins is based on Magic-Angle spinning (MAS) ssNMR, a method which has seen tremendous advances in elucidating insoluble protein structures, dynamics and interactions in soft matter states such as

assemblies, aggregates [97*,98,99] or membrane-association [100**,101,102]. Since 2002, when the first structure of a microcrystalline protein has been solved by MAS ssNMR [103], the technology has proven very powerful to elucidate protein assemblies such as the first amyloid protein structure [104], bacterial filaments [105,106] and protein–membrane complexes [107*]. A considerable knowledge has already been derived from ssNMR on protein–lipid, lipid–lipid interactions and membrane dynamics and functioning [108–110,96,102]. Most recent technological developments achieving ultra-fast MAS frequencies (≥ 100 kHz) MAS ssNMR allow for observing proton nuclei in protonated protein samples (~ 500 μ g) and should facilitate ssNMR to serve as a common tool for structural biology on membrane/protein related questions. Because of its striking technological evolution, MAS ssNMR has recently been applied in few cases to shed light on protein structures, dynamics and protein–lipid interactions promoted by lipid-dependent membrane features [100**]. Membrane domain formation in plants, relying on the plant protein and lipid interplay (see below the example of REMORIN in PM [16**,44]) remains a field to explore by MAS ssNMR.

Conclusions

Virtually all membranes are organized in functional domains that coordinate cell functions. Recent breakthrough in biochemistry, biophysics and microscopy approaches allow nowadays the study of the mechanisms regulating the formation of membrane domains, particularly the interplay between lipids and proteins. The next decade will likely open a vast area of research to understand the roles of membrane organization during plant development and adaptation.

Conflict of interest statement

Nothing declared.

Acknowledgements

This work was sustained by CNRS (Centre National de la Recherche Scientifique) and the University of Bordeaux. We thank the European Molecular Biology Organization (EMBO Long-Term Fellowship 438-2018) for financial support to J.G. This work has benefited from the facilities of the Bordeaux Metabolome/lipidome Facility-MetaboHUB to SM, VG (grant no. ANR-11-INBS-0010), a CNRS Momentum project to BH, and an ERC Starting Grantproject “WEAKINTERACT” to AL. We thank Christophe Rocher (LBM, Bordeaux) and Juliette Jouhet (LPCV, Grenoble) for fruitful discussions.

References and recommended reading

Papers of particular interest, published within the period of review, have been highlighted as:

- of special interest
- of outstanding interest

1. Russinova E, Schumacher K: **Editorial overview: cell biology: membrane dynamics - being at the right place at the right time.** *Curr Opin Plant Biol* 2017, **40**:iii-iv.
 2. Jean S, Kiger AA: **Coordination between RAB GTPase and phosphoinositide regulation and functions.** *Nat Rev Mol Cell Biol* 2012, **13**:463-470.
 3. Noack LC, Jaillais Y: **Precision targeting by phosphoinositides: how PIs direct endomembrane trafficking in plants.** *Curr Opin Plant Biol* 2017, **40**:22-33.
 4. Platre MP, Bayle V, Armengot L, Bareille J, Marques-Bueno MDM, •• Creff A, Maneta-Peyret L, Fiche JB, Nollmann M, Mieg C *et al.*: **Developmental control of plant Rho GTPase nano-organization by the lipid phosphatidylserine.** *Science* 2019, **364**:57-62.
- In this study, the authors elegantly showed that variation in phosphatidylserine during root development stabilized Rho protein ROP6 into nanodomains to regulate auxin signaling.
5. Garcia-Fernandez E, Koch G, Wagner RM, Fekete A, Stengel ST, Schneider J, Mielich-Suss B, Geibel S, Markert SM, Stigloher C *et al.*: **Membrane microdomain disassembly inhibits MRSA antibiotic resistance.** *Cell* 2017, **171**:1354-1367 e1320.
 6. Zhou Y, Prakash P, Liang H, Cho KJ, Gorfe AA, Hancock JF: **Lipid-sorting specificity encoded in K-ras membrane anchor regulates signal output.** *Cell* 2017, **168**:239-251 e216.
 7. Jacobson K, Liu P, Lagerholm BC: **The lateral organization and mobility of plasma membrane components.** *Cell* 2019, **177**:806-819.
 8. Sezgin E, Levental I, Mayor S, Eggeling C: **The mystery of membrane organization: composition, regulation and roles of lipid rafts.** *Nat Rev Mol Cell Biol* 2017, **18**:361-374.
 9. Gronnier J, Gerbeau-Pissot P, Germain V, Mongrand S, Simon-Plas F: **Divide and rule: plant plasma membrane organization.** *Trends Plant Sci* 2018, **23**:899-917.
 10. Michaud M, Jouhet J: **Lipid trafficking at membrane contact sites during plant development and stress response.** *Front Plant Sci* 2019, **10**:2.
 11. Petit JD, Immler F, Lins L, Bayer EM: **Lipids or proteins: who is leading the dance at membrane contact sites?** *Front Plant Sci* 2019, **10**:198.
 12. Cacas JL, Bure C, Grosjean K, Gerbeau-Pissot P, Lherminier J, Rombouts Y, Maes E, Bossard C, Gronnier J, Furt F *et al.*: **Re-visiting plant plasma membrane lipids in tobacco: a focus on sphingolipids.** *Plant Physiol* 2015, **170**:367-384.
 13. Mamode Cassim A, Gougnet P, Gronnier J, Laurent N, Germain V, Grison M, Boutte Y, Gerbeau-Pissot P, Simon-Plas F, Mongrand S: **Plant lipids: key players of plasma membrane organization and function.** *Prog Lipid Res* 2019, **73**:1-27.
 14. McKenna JF, Tolmie AF, Runions J: **Across the great divide: the plant cell surface continuum.** *Curr Opin Plant Biol* 2014, **22**:132-140.
 15. Ott T: **Membrane nanodomains and microdomains in plant-microbe interactions.** *Curr Opin Plant Biol* 2017, **40**:82-88.
 16. Gronnier J, Crowet JM, Habenstein B, Nasir MN, Bayle V, Hosy E, •• Platre MP, Gougnet P, Raffaele S, Martinez D *et al.*: **Structural basis for plant plasma membrane protein dynamics and organization into functional nanodomains.** *eLife* 2017, **6**.
- Combining super resolution microscopy, modelling and biophysical experiments, the authors decipher a molecular mechanism regulating the formation of functional nanodomains involved in plant immunity against a virus.
17. Bucherl CA, Jarsch IK, Schudoma C, Segonzac C, Mbengue M, Robatzek S, MacLean D, Ott T, Zipfel C: **Plant immune and growth receptors share common signalling components but localise to distinct plasma membrane nanodomains.** *eLife* 2017, **6**.
- Using quantitative image analysis the authors propose that spatial separation support functional specification of immune and growth receptors kinase.
18. Faulkner C: **A cellular backline: specialization of host membranes for defence.** *J Exp Bot* 2015, **66**:1565-1571.
 19. Burkart RC, Stahl Y: **Dynamic complexity: plant receptor complexes at the plasma membrane.** *Curr Opin Plant Biol* 2017, **40**:15-21.
 20. Tilsner J, Nicolas W, Rosado A, Bayer EM: **Staying tight: plasmodesmal membrane contact sites and the control of cell-to-cell connectivity in plants.** *Annu Rev Plant Biol* 2016, **67**:337-364.

21. Naramoto S: **Polar transport in plants mediated by membrane transporters: focus on mechanisms of polar auxin transport.** *Curr Opin Plant Biol* 2017, **40**:8-14.
22. Nakamura M, Grebe M: **Outer, inner and planar polarity in the Arabidopsis root.** *Curr Opin Plant Biol* 2018, **41**:46-53.
23. Raffaele S, Bayer E, Lafarge D, Cluzet S, German Retana S, Boubekeur T, Leborgne-Castel N, Carde JP, Lherminier J, Noirot E *et al.*: **Remorin, a solanaceae protein resident in membrane rafts and plasmodesmata, impairs potato virus X movement.** *Plant Cell* 2009, **21**:1541-1555.
24. Bozkurt TO, Richardson A, Dagdas YF, Mongrand S, Kamoun S, Raffaele S: **The plant membrane-associated REMORIN1.3 accumulates in discrete periaustorial domains and enhances susceptibility to phytophthora infestans.** *Plant Physiol* 2014, **165**:1005-1018.
25. Son S, Oh CJ, An CS: **Arabidopsis thaliana remorins interact with SnRK1 and Play a role in susceptibility to beet curly top virus and beet severe curly top virus.** *Plant Pathol J* 2014, **30**:269-278.
26. Jamann TM, Luo X, Morales L, Kolkman JM, Chung CL, Nelson RJ: **A remorin gene is implicated in quantitative disease resistance in maize.** *Theor Appl Genet* 2016, **129**:591-602.
27. Lefebvre B, Timmers T, Mbengue M, Moreau S, Herve C, Toth K, Bittencourt-Silvestre J, Klaus D, Deslandes L, Godiard L *et al.*: **A remorin protein interacts with symbiotic receptors and regulates bacterial infection.** *Proc Natl Acad Sci U S A* 2010, **107**:2343-2348.
28. Toth K, Stratil TF, Madsen EB, Ye J, Popp C, Antolin-Llovera M, Grossmann C, Jensen ON, Schussler A, Parniske M *et al.*: **Functional domain analysis of the Remorin protein LjSYMREM1 in Lotus japonicas.** *PLoS One* 2012, **7**:e30817.
29. Liang P, Stratil TF, Popp C, Marin M, Folgmann J, Mysore KS, Wen J, Ott T: **Symbiotic root infections in Medicago truncatula require remorin-mediated receptor stabilization in membrane nanodomains.** *Proc Natl Acad Sci U S A* 2018, **115**:5289-5294.
- The authors proposed that immobilization of symbiotic cell entry receptor LYK3 is mediated by two molecular scaffold proteins, FLOT4 and SYMREM1 and ensures progression of the primary infection thread into root cortical cells.
30. Gui J, Liu C, Shen J, Li L: **Grain setting defect1, encoding a remorin protein, affects the grain setting in rice through regulating plasmodesmatal conductance.** *Plant Physiol* 2014, **166**:1463-1478.
31. Perraki A, Gronnier J, Gouguet P, Boudsocq M, Deroubaix AF, Simon V, German-Retana S, Legrand A, Habenstein B, Zipfel C *et al.*: **REM1.3's phospho-status defines its plasma membrane nanodomain organization and activity in restricting PVX cell-to-cell movement.** *PLoS Pathog* 2018, **14**:e1007378.
32. Jarsch IK, Ott T: **Perspectives on remorin proteins, membrane rafts, and their role during plant-microbe interactions.** *Mol Plant Microbe Interact* 2011, **24**:7-12.
33. Jarsch IK, Konrad SS, Stratil TF, Urbanus SL, Szymanski W, Braun P, Braun KH, Ott T: **Plasma membranes are subcompartmentalized into a plethora of coexisting and diverse microdomains in arabidopsis and Nicotiana benthamiana.** *Plant Cell* 2014, **26**:1698-1711.
34. Konrad SS, Popp C, Stratil TF, Jarsch IK, Thallmair V, Folgmann J, Marin M, Ott T: **S-acylation anchors remorin proteins to the plasma membrane but does not primarily determine their localization in membrane microdomains.** *New Phytol* 2014, **203**:758-769.
35. Marin M, Thallmair V, Ott T: **The intrinsically disordered N-terminal region of AtREM1.3 remorin protein mediates protein-protein interactions.** *J Biol Chem* 2012, **287**:39982-39991.
36. Fernandez-Calvino L, Faulkner C, Walshaw J, Saalbach G, Bayer E, Benitez-Alfonso Y, Maule A: **Arabidopsis plasmodesmal proteome.** *PLoS One* 2011, **6**:e18880.
37. Demir F, Horntrich C, Blachutsk JO, Scherzer S, Reinders Y, Kierszniowska S, Schulze WX, Harms GS, Hedrich R, Geiger D *et al.*: **Arabidopsis nanodomain-delimited ABA signaling pathway regulates the anion channel SLAH3.** *Proc Natl Acad Sci U S A* 2013, **110**:8296-8301.
38. Szymanski WG, Zauber H, Erban A, Gorka M, Wu XN, Schulze WX: **Cytoskeletal components define protein location to membrane microdomains.** *Mol Cell Proteomics* 2015, **14**:2493-2509.
39. Perraki A, Cacas JL, Crowet JM, Lins L, Castroviejo M, German-Retana S, Mongrand S, Raffaele S: **Plasma membrane localization of Solanum tuberosum remorin from group 1, homolog 3 is mediated by conformational changes in a novel C-terminal anchor and required for the restriction of potato virus X movement.** *Plant Physiol* 2012, **160**:624-637.
40. Raffaele S, Perraki A, Mongrand S: **The remorin C-terminal anchor was shaped by convergent evolution among membrane binding domains.** *Plant Signal Behav* 2013, **8**:e23207.
41. Hemsley PA: **Assaying protein S-acylation in plants.** *Methods Mol Biol* 2013, **1043**:141-146.
42. Gui J, Zheng S, Shen J, Li L: **Grain setting defect1 (GSD1) function in rice depends on S-acylation and interacts with actin 1 (OsACT1) at its C-terminal.** *Front Plant Sci* 2015, **6**:804.
43. Fu S, Xu Y, Li C, Li Y, Wu J, Zhou X: **Rice stripe virus interferes with S-acylation of remorin and induces its autophagic degradation to facilitate virus infection.** *Mol Plant* 2018, **11**:269-287.
44. Martinez D, Legrand A, Gronnier J, Decossas M, Gouguet P, Lambert O, Berbon M, Verron L, Grelard A, Germain V *et al.*: **Coiled-coil oligomerization controls localization of the plasma membrane REMORINS.** *J Struct Biol* 2019, **206**:12-19.
45. Lv X, Jing Y, Xiao J, Zhang Y, Zhu Y, Julian R, Lin J: **Membrane microdomains and the cytoskeleton constrain AtHIR1 dynamics and facilitate the formation of an AtHIR1-associated immune complex.** *Plant J* 2017, **90**:3-16.
46. Christensen TM, Vejrupkova Z, Sharma YK, Arthur KM, Spatafora JW, Albright CA, Meeley RB, Duvick JP, Quatrano RS, Fowler JE: **Conserved subgroups and developmental regulation in the monocot rop gene family.** *Plant Physiol* 2003, **133**:1791-1808.
47. Feiguelman G, Fu Y, Yalovsky S: **ROP GTPases structure-function and signaling pathways.** *Plant Physiol* 2018, **176**:57-79.
48. Berken A, Wittinghofer A: **Structure and function of rho-type molecular switches in plants.** *Plant Physiol Biochem* 2008, **46**:380-393.
49. Molendijk AJ, Bischoff F, Rajendrakumar CS, Friml J, Braun M, Gilroy S, Palme K: **Arabidopsis thaliana Rop GTPases are localized to tips of root hairs and control polar growth.** *EMBO J* 2001, **20**:2779-2788.
50. Denninger P, Reichelt A, Schmidt VAF, Mehlhorn DG, Asseck LY, Stanley CE, Keinath NF, Evers JF, Grefen C, Grossmann G: **Distinct RopGEFs successively drive polarization and outgrowth of root hairs.** *Curr Biol* 2019.
- Using microfluidics and live cell imaging, Denninger *et al.* dissect the timing of the growth machinery assembly in polarizing hair cells and show that GEF3 serves as a membrane landmark recruiting growth machinery to specialized membrane domains.
51. Stanislas T, Huser A, Barbosa IC, Kiefer CS, Brackmann K, Pietra S, Gustavsson A, Zourelidou M, Schwechheimer C, Grebe M: **Arabidopsis D6PK is a lipid domain-dependent mediator of root epidermal planar polarity.** *Nat Plants* 2015, **1**:15162.
52. Barbosa IC, Zourelidou M, Willige BC, Weller B, Schwechheimer C: **D6 PROTEIN KINASE activates auxin transport-dependent growth and PIN-FORMED phosphorylation at the plasma membrane.** *Dev Cell* 2014, **29**:674-685.
53. Bloch D, Yalovsky S: **Cell polarity signaling.** *Curr Opin Plant Biol* 2013, **16**:734-742.
54. Oda Y, Fukuda H: **Initiation of cell wall pattern by a Rho- and microtubule-driven symmetry breaking.** *Science* 2012, **337**:1333-1336.

55. Oda Y, Fukuda H: **Rho of plant GTPase signaling regulates the behavior of Arabidopsis kinesin-13A to establish secondary cell wall patterns.** *Plant Cell* 2013, **25**:4439-4450.
 56. Sugiyama Y, Wakazaki M, Toyooka K, Fukuda H, Oda Y: **A novel plasma membrane-anchored protein regulates xylem cell-wall deposition through microtubule-dependent lateral inhibition of rho GTPase domains.** *Curr Biol* 2017, **27**:2522-2528 e2524.
 57. Sasaki T, Fukuda H, Oda Y: **Cortical microtubule disordering1 is required for secondary cell wall patterning in xylem vessels.** *Plant Cell* 2017, **29**:3123-3139.
 58. McFarlane HE, Doring A, Persson S: **The cell biology of cellulose synthesis.** *Annu Rev Plant Biol* 2014, **65**:69-94.
 59. Paredes AR, Somerville CR, Ehrhardt DW: **Visualization of cellulose synthase demonstrates functional association with microtubules.** *Science* 2006, **312**:1491-1495.
 60. Crowell EF, Bischoff V, Desprez T, Rolland A, Stierhof YD, Schumacher K, Gonneau M, Hofte H, Vernhettes S: **Pausing of Golgi bodies on microtubules regulates secretion of cellulose synthase complexes in Arabidopsis.** *Plant Cell* 2009, **21**:1141-1154.
 61. Gutierrez R, Lindeboom JJ, Paredes AR, Emons AM, Ehrhardt DW: **Arabidopsis cortical microtubules position cellulose synthase delivery to the plasma membrane and interact with cellulose synthase trafficking compartments.** *Nat Cell Biol* 2009, **11**:797-806.
 62. Kumar M, Wightman R, Atanassov I, Gupta A, Hurst CH, Hemsley PA, Turner S: **S-acylation of the cellulose synthase complex is essential for its plasma membrane localization.** *Science* 2016, **353**:166-169.
 63. Bringmann M, Landrein B, Schudoma C, Hamant O, Hauser MT, Persson S: **Cracking the elusive alignment hypothesis: the microtubule-cellulose synthase nexus unraveled.** *Trends Plant Sci* 2012, **17**:666-674.
 64. Gu Y, Somerville C: **Cellulose synthase interacting protein: a new factor in cellulose synthesis.** *Plant Signal Behav* 2010, **5**:1571-1574.
 65. Li S, Lei L, Somerville CR, Gu Y: **Cellulose synthase interactive protein 1 (CSI1) links microtubules and cellulose synthase complexes.** *Proc Natl Acad Sci U S A* 2012, **109**:185-190.
 66. Endler A, Kesten C, Schneider R, Zhang Y, Ivakov A, Froehlich A, Funke N, Persson S: **A mechanism for sustained cellulose synthesis during salt stress.** *Cell* 2015, **162**:1353-1364.
- The authors outline the molecular mechanism by which COMPANION OF CELLULOSE SYNTHASE1 (CC1) controls microtubule bundling and dynamics to sustain plant growth under salt stress.
67. Jouhet J: **Importance of the hexagonal lipid phase in biological membrane organization.** *Front Plant Sci* 2013, **4**:494.
 68. Nawrocki WJ, Santabarbara S, Mosebach L, Wollman FA, Rappaport F: **State transitions redistribute rather than dissipate energy between the two photosystems in chlamydomonas.** *Nat Plants* 2016, **2**:16031.
 69. Flori S, Jouneau PH, Bailleul B, Gallet B, Estrozi LF, Moriscot C, Bastien O, Eicke S, Schober A, Bartulos CR et al.: **Plastid thylakoid architecture optimizes photosynthesis in diatoms.** *Nat Commun* 2017, **8**:15885.
 70. Furse S: **Is phosphatidylglycerol essential for terrestrial life?** *J Chem Biol* 2017, **10**:1-9.
 71. Rast A, Schaffer M, Albert S, Wan W, Pfeffer S, Beck F, Plitzko JM, Nickelsen J, Engel BD: **Biogenic regions of cyanobacterial thylakoids form contact sites with the plasma membrane.** *Nat Plants* 2019, **5**:436-446.
- Cryo-electron tomography was used here to show that thylakoids organized in domains enriched in ribosomes, but deprived in photosynthetic machinery, to allow contact sites with the cyanobacterial plasma membrane.
72. Michaud M, Gros V, Tardif M, Brugiére S, Ferro M, Prinz WA, Toulmay A, Mathur J, Wozny M, Falconet D et al.: **AtMic60 is involved in plant mitochondria lipid trafficking and is part of a large complex.** *Curr Biol* 2016, **26**:627-639.
- Elegant biochemical characterization of the MCS between mitochondria and chloroplasts involved in the exchange of DGDG during phosphate deprivation.
73. Park E, Caplan JL, Dinesh-Kumar SP: **Dynamic coordination of plastid morphological change by cytoskeleton for chloroplast-nucleus communication during plant immune responses.** *Plant Signal Behav* 2018, **13**:e1500064.
 74. Erickson JL, Kanteck M, Schattat MH: **Plastid-nucleus distance alters the behavior of stromules.** *Front Plant Sci* 2017, **8**:1135.
 75. Erickson JL, Schattat MH: **Shaping plastid stromules-principles of in vitro membrane tubulation applied in planta.** *Curr Opin Plant Biol* 2018, **46**:48-54.
 76. Gao H, Metz J, Teanby NA, Ward AD, Botchway SW, Coles B, Pollard MR, Sparkes I: **In vivo quantification of peroxisome tethering to chloroplasts in tobacco epidermal cells using optical tweezers.** *Plant Physiol* 2016, **170**:263-272.
 77. Jaipargas EA, Mathur N, Bou Daher F, Wasteneys GO, Mathur J: **High light intensity leads to increased peroxule-mitochondria interactions in plants.** *Front Cell Dev Biol* 2016, **4**:6.
 78. Quintana-Cabrera R, Mehrotra A, Rigoni G, Soriano ME: **Who and how in the regulation of mitochondrial cristae shape and function.** *Biochem Biophys Res Commun* 2018, **500**:94-101.
 79. Pan R, Jones AD, Hu J: **Cardiolipin-mediated mitochondrial dynamics and stress response in Arabidopsis.** *Plant Cell* 2014, **26**:391-409.
 80. Jiko C, Davies KM, Shinzawa-Itoh K, Tani K, Maeda S, Mills DJ, Tsukihara T, Fujiyoshi Y, Kuhlbrandt W, Gerle C: **Bovine F1Fo ATP synthase monomers bend the lipid bilayer in 2D membrane crystals.** *eLife* 2015, **4**:e06119.
 81. Blum TB, Hahn A, Meier T, Davies KM, Kuhlbrandt W: **Dimers of mitochondrial ATP synthase induce membrane curvature and self-assemble into rows.** *Proc Natl Acad Sci U S A* 2019.
- Use of electron cryotomography provided experimental proof that mitochondrial ATP synthase dimers assemble spontaneously into rows upon membrane reconstitution, likely the first step in the formation of mitochondrial cristae.
82. Iinuma T, Aoki T, Arasaki K, Hirose H, Yamamoto A, Samata R, Hauri HP, Arimitsu N, Tagaya M, Tani K: **Role of syntaxin 18 in the organization of endoplasmic reticulum subdomains.** *J Cell Sci* 2009, **122**:1680-1690.
 83. Cai Y, Goodman JM, Pyc M, Mullen RT, Dyer JM, Chapman KD: **Arabidopsis SEIPIN proteins modulate triacylglycerol accumulation and influence lipid droplet proliferation.** *Plant Cell* 2015, **27**:2616-2636.
- First role of SEIPIN in regulation lipid droplet formation in plants.
84. Taurino M, Costantini S, De Domenico S, Stefanelli F, Ruano G, Delgadillo MO, Sanchez-Serrano JJ, Sanmartin M, Santino A, Rojo E: **SEIPIN proteins mediate lipid droplet biogenesis to promote pollen transmission and reduce seed dormancy.** *Plant Physiol* 2018, **176**:1531-1546.
 85. Thazar-Poulot N, Miquel M, Fobis-Loisy I, Gaude T: **Peroxisome extensions deliver the Arabidopsis SDP1 lipase to oil bodies.** *Proc Natl Acad Sci U S A* 2015, **112**:4158-4163.
 86. Hunte C, Richers S: **Lipids and membrane protein structures.** *Curr Opin Struct Biol* 2008, **18**:406-411.
 87. Maslennikov I, Choe S: **Advances in NMR structures of integral membrane proteins.** *Curr Opin Struct Biol* 2013, **23**:555-562.
 88. Oxenoid K, Chou JJ: **The present and future of solution NMR in investigating the structure and dynamics of channels and transporters.** *Curr Opin Struct Biol* 2013, **23**:547-554.
 89. Nicolas WJ, Grison MS, Trepout S, Gaston A, Fouche M, Cordeliers FP, Oparka K, Tilsner J, Brocard L, Bayer EM: **Architecture and permeability of post-cytokinesis plasmodesmata lacking cytoplasmic sleeves.** *Nat Plants* 2017, **3**:17082.
- Using electron tomography the authors shows that within plasmodesmata ER-PM contact sites undergo substantial remodelling events during cell differentiation to regulate cell-cell communication.
90. Hosy E, Martinieri A, Choquet D, Maurel C, Luu DT: **Super-resolved and dynamic imaging of membrane proteins in plant cells reveal contrasting kinetic profiles and multiple confinement mechanisms.** *Mol Plant* 2015, **8**:339-342.

Proof of concept for the use of spt-PALM in plant PM proteins.

91. Deleu M, Crowet JM, Nasir MN, Lins L: **Complementary biophysical tools to investigate lipid specificity in the interaction between bioactive molecules and the plasma membrane: a review.** *Biochim Biophys Acta* 2014, **1838**:3171-3190.
92. Frisz JF, Klitzing HA, Lou K, Hutcheon ID, Weber PK, Zimmerberg J, Kraft ML: **Sphingolipid domains in the plasma membranes of fibroblasts are not enriched with cholesterol.** *J Biol Chem* 2013, **288**:16855-16861.
93. Frisz JF, Lou K, Klitzing HA, Hanafin WP, Lizunov V, Wilson RL, Carpenter KJ, Kim R, Hutcheon ID, Zimmerberg J *et al.*: **Direct chemical evidence for sphingolipid domains in the plasma membranes of fibroblasts.** *Proc Natl Acad Sci U S A* 2013, **110**: E613-E622.
94. Ondrasek G, Rengel Z, Clode PL, Kilburn MR, Guagliardo P, Romic D: **Zinc and cadmium mapping by NanoSIMS within the root apex after short-term exposure to metal contamination.** *Ecotoxicol Environ Saf* 2019, **171**:571-578.
95. Epand RM, D'Souza K, Berno B, Schlame M: **Membrane curvature modulation of protein activity determined by NMR.** *Biochim Biophys Acta* 2015, **1848**:220-228.
96. Molugu TR, Lee S, Brown MF: **Concepts and methods of solid-state NMR spectroscopy applied to biomembranes.** *Chem Rev* 2017, **117**:12087-12132.
97. Loquet A, El Mammeri N, Stanek J, Berbon M, Bardiaux B, Pintacuda G, Habenstein B: **3D structure determination of amyloid fibrils using solid-state NMR spectroscopy.** *Methods* 2018, **138-139**:26-38.

Structural studies of molecular assemblies such as amyloids are one of the major application of solid-state NMR. This review concisely describes state-of-the-art ssNMR methods to investigate structures of protein assemblies. The explained methods can generally be applied to elucidate structures of molecular assemblies.

98. Habenstein B, Loquet A: **Solid-state NMR: an emerging technique in structural biology of self-assemblies.** *Biophys Chem* 2016, **210**:14-26.
99. Weingarth M, Baldus M: **Solid-state NMR-based approaches for supramolecular structure elucidation.** *Acc Chem Res* 2013, **46**:2037-2046.
100. Mandala VS, Williams JK, Hong M: **Structure and dynamics of membrane proteins from solid-state NMR.** *Annu Rev Biophys* 2018, **47**:201-222.

The authors review ssNMR studies that ingeniously combine different ssNMR approaches to understand membrane protein structure and

functional mechanisms. Protein structures, as well as protein-lipid interactions, are discussed from an ssNMR point of view.

101. Opella SJ, Marassi FM: **Applications of NMR to membrane proteins.** *Arch Biochem Biophys* 2017, **628**:92-101.
 102. Ladizhansky V: **Applications of solid-state NMR to membrane proteins.** *Biochim Biophys Acta Proteins Proteom* 2017, **1865**:1577-1586.
 103. Castellani F, van Rossum B, Diehl A, Schubert M, Rehbein K, Oschkinat H: **Structure of a protein determined by solid-state magic-angle-spinning NMR spectroscopy.** *Nature* 2002, **420**:98-102.
 104. Wasmer C, Soragni A, Sabate R, Lange A, Riek R, Meier BH: **Infectious and noninfectious amyloids of the HET-s(218-289) prion have different NMR spectra.** *Angew Chem Int Ed Engl* 2008, **47**:5839-5841.
 105. Habenstein B, Loquet A, Hwang S, Giller K, Vasa SK, Becker S, Habeck M, Lange A: **Hybrid structure of the type 1 pilus of uropathogenic *Escherichia coli*.** *Angew Chem Int Ed Engl* 2015, **54**:11691-11695.
 106. Loquet A, Sgourakis NG, Gupta R, Giller K, Riedel D, Goosmann C, Griesinger C, Kolbe M, Baker D, Becker S *et al.*: **Atomic model of the type III secretion system needle.** *Nature* 2012, **486**:276-279.
 107. Retel JS, Nieuwkoop AJ, Hiller M, Higman VA, Barbet-Massin E, Stanek J, Andreas LB, Franks WT, van Rossum BJ, Vinothkumar KR *et al.*: **Structure of outer membrane protein G in lipid bilayers.** *Nat Commun* 2017, **8**:2073.
- Recent MAS ssNMR approaches have been used to determine the structure of an integral membrane protein. This study is a well-timed example of the potential of MAS ssNMR in structural investigations on membrane proteins.
108. Huster D: **Solid-state NMR spectroscopy to study protein-lipid interactions.** *Biochim Biophys Acta* 2014, **1841**:1146-1160.
 109. Brown LS, Ladizhansky V: **Membrane proteins in their native habitat as seen by solid-state NMR spectroscopy.** *Protein Sci* 2015, **24**:1333-1346.
 110. Elkins MR, Hong M: **Elucidating ligand-bound structures of membrane proteins using solid-state NMR spectroscopy.** *Curr Opin Struct Biol* 2019, **57**:103-109.
 111. Long SB, Tao X, Campbell EB, MacKinnon R: **Atomic structure of a voltage-dependent K⁺ channel in a lipid membrane-like environment.** *Nature* 2007, **450**:376-382.
 112. Wang J, Pielak RM, McClintock MA, Chou JJ: **Solution structure and functional analysis of the influenza B proton channel.** *Nat Struct Mol Biol* 2009, **16**:1267-1271.

Article IV

Nanodomain Clustering of the Plant Protein Remorin by Solid-State NMR

Anthony Legrand, Denis Martinez, Axelle Grélard, Mélanie Berbon, Estelle Morvan, Arpita Tawani, Antoine Loquet, Sébastien Mongrand, Birgit Habenstein

Frontiers in Molecular Biosciences

2019

6

In this work, my first as a first author, we studied the lipid dynamics of artificial lipid membranes in the presence of whole or mutated *StREM1.3*. We already had a hypothetical model of remorin nanodomain formation: (1) homotrimeric *StREM1.3* binds to and clusters PI4P. These PI4P have mostly saturated acyl chains (Furt et al., 2010). Cholesterol has a higher affinity for saturated than unsaturated phospholipids (Engberg et al., 2016). By analogy, we expect sitosterol to be recruited in this nascent cluster. (2) More PI4P and sitosterol would coalesce into a larger nanodomain. But what are the exact driving forces and molecular determinants in the formation of *StREM1.3* nanodomains? PIPs can cluster on their own (Bilkova et al., 2017; van den Bogaart et al., 2011), and therefore drive nanodomain formation. Does *StREM1.3*'s interaction with lipids change that? What about a *StREM1.3-StREM1.3* driven clustering?

²H static ssNMR allows experimental measurement of lipid dynamics using a deuterated reporter lipid, here DMPC-d₅₄ (fully deuterated on both acyl chains). We employed this methodology to monitor the phase behaviour, thermotropism, lipid dynamics and membrane thickness of liposomes in presence of PC, sitosterol, PIPs and PS as well as RemCA WT or mutated. Next, we reconstructed, domain by domain, the full length *StREM1.3* to assess the impact of each domain on these parameters. Finally, we proposed an updated model for the formation of *StREM1.3* nanodomains.

Under the help of Mélanie Berbon, I produced and purified both protein constructs REM₈₆₋₁₉₈ and *StREM1.3*. Experiments with peptides and liposome formation were taught to me by Denis Martinez. Under the guidance and training of Axelle Grélard and Estelle Morvan, I was trained to and performed all the NMR experiments in this report, with the exception of ³¹P MAS ssNMR that was performed by Estelle Morvan. For data analysis, interpretation and critical reviewing, I was helped by Dr Denis Martinez and Dr Arpita Tawani. The first draft was made by Dr Birgit Habenstein, who conceptualised the study, and myself, then reviewed by all the authors of this manuscript.



Nanodomain Clustering of the Plant Protein Remorin by Solid-State NMR

Anthony Legrand^{1,2}, Denis Martinez¹, Axelle Grélard¹, Melanie Berbon¹, Estelle Morvan³, Arpita Tawani¹, Antoine Loquet¹, Sébastien Mongrand² and Birgit Habenstein^{1*}

¹ Institute of Chemistry & Biology of Membranes & Nanoobjects (UMR5248 CBMN), IECB, CNRS, Université Bordeaux, Institut Polytechnique Bordeaux, Pessac, France, ² Laboratoire de Biogenèse Membranaire - UMR 5200 - CNRS, Université de Bordeaux, Villenave-d'Ornon, France, ³ European Institute of Chemistry and Biology - UMS3033/US001, Pessac, France

OPEN ACCESS

Edited by:

Anja Böckmann,
UMR5086 Microbiologie Moléculaire
et Biochimie Structurale
(MMSB), France

Reviewed by:

Philip T. F. Williamson,
University of Southampton,
United Kingdom
Manuel Etzkorn,
Heinrich Heine University of
Düsseldorf, Germany
Benjamin James Wylie,
Texas Tech University, United States

*Correspondence:

Birgit Habenstein
birgit.habenstein@u-bordeaux.fr

Specialty section:

This article was submitted to
Structural Biology,
a section of the journal
Frontiers in Molecular Biosciences

Received: 01 July 2019

Accepted: 30 September 2019

Published: 15 October 2019

Citation:

Legrand A, Martinez D, Grélard A,
Berbon M, Morvan E, Tawani A,
Loquet A, Mongrand S and
Habenstein B (2019) Nanodomain
Clustering of the Plant Protein
Remorin by Solid-State NMR.
Front. Mol. Biosci. 6:107.
doi: 10.3389/fmolb.2019.00107

Nanodomains are dynamic membrane subcompartments, enriched in specific lipid, and protein components that act as functional platforms to manage an abundance of cellular processes. The remorin protein of plants is a well-established nanodomain marker and widely serves as a paradigm to study nanodomain clustering. Located at the inner leaflet of the plasma membrane, remorins perform essential functions during signaling. Using deuterium and phosphorus solid-state NMR, we inquire on the molecular determinants of the lipid-protein and protein-protein interactions driving nanodomain clustering. By monitoring thermotropic properties, lipid acyl chain order and membrane thickness, we report the effects of phosphoinositides and sterols on the interaction of various remorin peptides and protein constructs with the membrane. We probed several critical residues involved in this interaction and the involvement of the coiled-coil homo-oligomerisation domain into the formation of remorin nanodomains. We trace the essential role of the pH in nanodomain clustering based on anionic lipids such as phosphoinositides. Our results reveal a complex interplay between specific remorin residues and domains, the environmental pH and their resulting effects on the lipid dynamics for phosphoinositide-enriched membranes.

Keywords: nanodomains, lipid raft, solid-state NMR, membrane protein, plant protein, phosphoinositide, sterol, remorin

INTRODUCTION

The fluid mosaic model of Singer and Nicolson (1972) describes a biological membrane as a bilayer of phospholipids, hydrophobic parts buried and hydrophilic parts exposed, with membrane proteins spanning or anchoring to the bilayer. In this model, lipid heterogeneity, and precise lipid-protein interactions that might lead to cooperative local enrichment of specific components, i.e., nanodomain organization becomes conceivable. Due to their eclectic composition, membranes are key players in cell biology, and have a plethora of functions (Grecco et al., 2011; Ott, 2017), thus constituting prime drug design targets.

The lipid raft hypothesis, that is the lateral segregation of membrane components, was first formulated by Simons and Ikonen (1997). Lipid rafts have different characteristics depending on the organism and bore different names throughout past decades, accounting for the variety of techniques allowing their detection. Here, we will commit to the word nanodomain because remorin, isoform StREM1.3, segregates into around 80 nm wide domains (Raffaele et al., 2009). Considering the recent technological advancements in analyzing nanodomains (Sezgin et al., 2017), the description given by Pike (2006), herein named “membrane raft,” is still relevant: a

small (10–200 nm wide) region of a membrane, not necessarily the plasma membrane (PM), enriched in sterols, and specific proteins and lipids, like phosphoinositides (PIPs) (Furt et al., 2010; Brown, 2017). Nanodomain formation thus relies on the diffusion of the membrane components creating detectable membrane heterogeneity. Importantly, the diffusing, internally ordered lipids can separate into liquid-ordered (Lo) and liquid-disordered (Ld) regions in membranes, including PM-mimicking environments (Kaiser et al., 2009). Considering typical nanodomain compositions, these membrane regions should have a tendency of manifesting Lo behavior, usually containing lipids fostering liquid order such as sterols.

Members of the multigenic, aerial plant-specific family of remorins (Raffaele et al., 2007) are well-known protein markers of such nanodomains in plants (Mongrand et al., 2004; Raffaele et al., 2009). This family is made of 6 phylogenetic groups sharing a canonical C-terminal domain, containing a segment with high coiled-coil propensity, and a variable N-terminal domain (Raffaele et al., 2007). Our study will focus on potato (*Solanum tuberosum*) remorin group 1 isoform 3 (*StREM1.3*). It contains an intrinsically disordered N-terminal domain involved in protein-protein interactions (Raffaele et al., 2009) and phosphorylation events (Marín et al., 2012; Perraki et al., 2018), a coiled-coil domain involved in homo-trimerisation (Martinez et al., 2018) and a C-terminal domain called the Remorin C-terminal membrane Anchor (RemCA).

StREM1.3 specifically binds negatively charged liposomes *in vitro*, as we showed in Perraki et al. (2012). Expression of a plasma membrane (PM)-targeted phosphatidylinositol 4-phosphatase MAP-SAC1p in *Nicotiana benthamiana* leaves leads to a strong decrease of a *StREM1.3*'s PM targeting and lateral segregation, implying that it has a specific affinity for PI4P of the PM's inner leaflet (Gronnier et al., 2017). Moreover, PM vesicles of *Nicotiana benthamiana* leaves treated with methyl β -cyclodextrin, a chelator of sterols, showed a complete loss of remorin nanoclustering, indicating phytosterols also play a role in the formation of nanodomains (Raffaele et al., 2009). Similarly, treatment with sterol inhibitor fenpropimorph strongly impaired nanodomain clustering, without affecting PM targeting of *StREM1.3* (Gronnier et al., 2017).

Membrane anchoring of *StREM1.3* proceeds over an unconventional mechanism with a hydrophilic domain tethering to the membrane and organizing into nanodomains (Gronnier et al., 2017). From the latter study, we formulated a hypothetical two-step mechanism for the formation of *StREM1.3* nanodomains: (1) the remorin, likely as a homotrimer (Perraki et al., 2012), binds to PI4P of the PM's inner leaflet with a ratio of 1 PI4P moiety per 1 RemCA, therefore clustering the 3 lipids with the remorin; (2) PI4P moieties, bearing mostly saturated acyl chains (Furt et al., 2010), will preferentially attract plant sterols, of which sitosterol is the main representative, while other PI4P moieties gather around the nascent PI4P nanocluster (Picas et al., 2016). Removal of sterols by m- β -cyclodextrin on PM vesicles disrupts nanodomain clustering but not PM binding (Raffaele et al., 2009), revealing a dependency of nanodomain formation on sterols. Remorins are also known to form filaments *in vitro* though no such structure has yet been unambiguously observed *in vivo* (Bariola et al., 2004; Martinez et al., 2018).

In essence, remorins might bind over a complex mechanism involving electrostatic interactions between the positively charged lysines in the RemCA (**Figure 1A**) with negatively charged PI4P head groups (Gronnier et al., 2017), favoring the formation of sitosterol and PIP enriched clusters (**Figure 1B**).

Structural studies of the mechanisms behind protein-lipid nanodomain formation and assembly at the atomic level remain scarce, mostly relying on molecular dynamics (Ackerman and Feigenson, 2015; Gronnier et al., 2017; Javanainen et al., 2017). Indeed, the size, insolubility, non-crystallinity and required native state of the objects of interest disqualify most biophysical techniques, such as X-ray crystallography and liquid-state NMR, to obtain experimental evidence at the atomic level. We use solid-state NMR spectroscopy (ssNMR), a technique tailored to study such objects, both in terms of protein fold and interactions (Habenstein and Loquet, 2016; Loquet et al., 2017) in the native membrane environment (Cady et al., 2010; Baker et al., 2015; Stanek et al., 2016; Ladizhansky, 2017; Lalli et al., 2017; Mandala et al., 2018) and to determine membrane dynamics and interactions at the atomic level using static deuterium NMR on deuterated liposomes (Dufourc et al., 1992; Beck et al., 2007; Huster, 2014; Yao and Hong, 2014; Molugu et al., 2017).

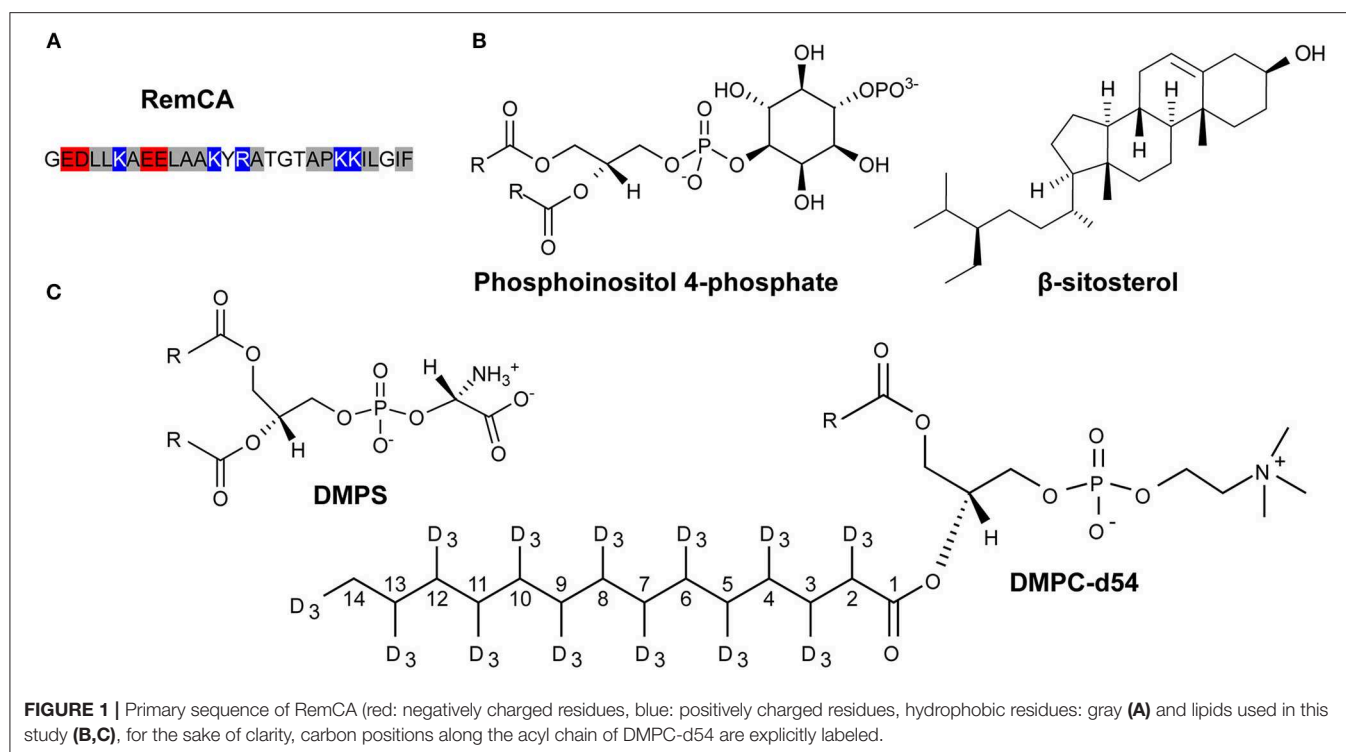
Here, we aim at deciphering the molecular mechanisms by which *StREM1.3* anchors to PM to form nanodomains using deuterated liposomes along with deuterium (^2H) ssNMR as our main tool. To reflect the lipid-protein interactions and dynamic behavior during nanodomain formation, we chose to work with liposomes of nanodomain-mimicking lipid compositions, including PIPs and sitosterol (**Figure 1B**). Using different remorin constructs including the membrane anchor RemCA alone, in the wild-type and several mutated versions, Rem_{86–198}, composed of RemCA and the coiled-coil segment, and the intact *StREM1.3*, we monitored the overall mechanisms and the fine molecular implications of nanodomain assembly guided by remorin. We tested the behavior of RemCA and its critical mutants in various nanodomain-like and unlike lipid environments, assessing the lipid preferences and electrostatic interactions involved in the anchor-membrane association. We then monitored the impact of the coiled-coil trimerisation domain, and its capacity of forming higher-order oligomers, as well as of the intrinsically disordered domain (IDD) of *StREM1.3* on its membrane-binding behavior.

MATERIALS AND METHODS

Protein Production and Purification

Synthetic RemCA peptides were ordered from GenScript HK Limited at >90% purity with N-terminal acetylation.

Escherichia coli BL21-DE3 were transformed with a pET24 vector containing the DNA encoding for *StREM1.3* or REM_{86–198} and plated onto LB-agar plates containing 30 $\mu\text{g}/\text{mL}$ kanamycin. A pre-culture of 100 mL LB medium was inoculated with a single transformed colony and incubated at 37°C overnight (about 20 h). 1L of LB medium is inoculated with the pre-culture at OD₆₀₀ = 0.2 and incubated at 37°C until OD₆₀₀ = 0.7–0.8. Protein production was induced with 1 mM of IPTG at 18°C overnight. Cells were pelleted at 6,000 g for 20 min at 4°C and resuspended in a lysis buffer (20 mM HEPES,



150 mM NaCl, 20 mM imidazole, 1 mM PMSF, 0.02% NaN₃, pH = 7.4) containing protease inhibitors (Complete, Roche). Cells were sonicated on ice at 30% magnitude three times (30s on, 30s off) and centrifuged at 15,000 g for 30 min at 4°C to recover the supernatant.

Purification of StREM1.3 was achieved with an Akta Pure 25 HPLC system (GE Healthcare) on a HisTrap affinity column equilibrated in wash buffer (20 mM HEPES, 150 mM NaCl, 20 mM imidazole, 0.02% NaN₃, pH = 7.4). The protein was eluted with a stepwise gradient of elution buffer (20 mM HEPES, 150 mM NaCl, 500 mM imidazole, 0.02% NaN₃, pH = 7.4): 15, 40, 80, and 100% elution buffer. About 20 mg of pure unlabelled StREM1.3 were obtained from a 1L culture in LB medium. Purification of REM_{86–198} was performed as described previously in Martinez et al. (2018). After purification, proteins were buffer-exchanged against a reconstitution buffer (10 mM HEPES, 10 mM NaCl, 0.02% NaN₃, pH = 7.4) using a HiPrep gel filtration column (GE Healthcare).

Liposome Reconstitution

1,2-dimyristoyl-d54-sn-glycero-3-phosphocholine (DMPC-d54), 1,2-dimyristoyl-sn-glycero-3-phosphocholine (DMPC), 1,2-dimyristoyl-sn-glycero-3-phosphatidylserine (DMPS), β-sitosterol were purchased from Avanti Polar Lipids, Inc. (USA) and phosphoinositides from bovine brain (PIP mix, PS/PI/PI4P/PI(4,5)P₂ 50/20/15/15 (mol/mol) from Sigma-Aldrich.

Synthetic RemCA peptides were co-solubilized in CHCl₃/MeOH 2/1 (V/V) with the appropriate amount of lipids (peptide/lipid molar ratio of 1/20). Organic solvents

were evaporated under an air stream, hydrated, and then lyophilized. Lipid and lipid-peptide powders were rehydrated with deuterium-depleted water or 260 mM Tris buffer. The hydrated samples were submitted to three freeze-thaw-vortex cycles (1 min in liquid N₂, 10 min at ~40°C, 20 s vortexing) for sample homogenization and packed into a ssNMR rotor. This sample preparation has been used for triplicate error assessment on liposomes of the following composition: PC/β-sitosterol/PIP mix 75/15/10 (molar ratio) and RemCA K192A/K193A (lipid/peptide = 20) (Figures S1A,C,E).

For protein reconstitution, pre-formed liposomes were incubated overnight at 30°C with the protein at a protein/lipid molar ratio of 1/20. The milky solution was centrifuged at 100,000 g for 2 h at 4°C to recover the proteoliposomes. To remove filaments, proteins were centrifuged at 12,000 g for 20 min at 4°C before reconstitution and liposomes were then recovered by centrifugation at 12,000 g for 20 min at 4°C. This sample preparation has been used for triplicate error assessment on liposomes of the following composition PC/β-sitosterol/PIP mix 75/15/10 (molar ratio) incubated without protein (Figures S1B,D,F).

NMR

For ²H static ssNMR, we applied a static quadrupolar spin echo sequence (Davis et al., 1976) at the ²H frequency of 76.8 MHz on a 500 MHz (11.7 T) Bruker Avance III NMR spectrometer, with a 90° pulse of 3.8 μs, a delay of 40 μs, a recycle delay of 2 s, a spectral window of 500 kHz and a number of scans of 512 at least. We acquired spectra at different temperatures, ranging from 278 to 308 K. Sample temperature was stabilized

for 20 min prior to data acquisition. All spectra were processed with TopSpin 4.0.6 (Bruker). An exponential window function with a line broadening factor of 300 Hz was applied prior to Fourier transformation. De-Pake-ing procedure (Bloom et al., 1981; McCabe and Wassail, 1997), first order spectral moments M_1 and local order parameters $|2^*S_{CD}|$ along the acyl chains of DMPC-d54 were calculated with NMR Depaker (provided by Dr. Sébastien Buchoux) and refined by spectra simulation with NMR-099 (provided by Arnaud Grélard) as described in Beck et al. (2007). Membrane thickness is calculated as described in Grélard et al. (2013). For DMPC-d54/DMPS 90/10 (molar ratio) liposomes, 2H static ssNMR was performed on a 300 MHz (7.1 T) Bruker Avance III at 121.50 MHz for ^{31}P with a 90° pulse of 3.3 μs , a delay of 30 μs , a recycle delay of 2 s, a spectral window of 500 kHz and a number of scans of 512 at least. Sample temperature was stabilized for 10 min prior to data acquisition. Error bars on M_1 and $|2^*S_{CD}|$ are presented in **Figure S1** and reflect standard deviations of three independent experiments on the two conditions (see sample preparation 2.2). Error bars for membrane thicknesses are 0.5 Å, based on (Grélard et al., 2013) plus the error contributions from the standard deviations of the $|2^*S_{CD}|$ at each position.

For ^{31}P ssNMR, we applied a static Hahn spin echo sequence at the ^{31}P frequency of 162 MHz on a 400 MHz (9.4 T) Bruker Avance III HD spectrometer, with a 90° pulse of 8 μs , a delay of 40 μs , a recycle delay of 5 s, a spectral window of 400 ppm

and a number of scans of 1,024 at least. Spectra were processed with TopSpin 4.0.6 (Bruker). An exponential window function with a line broadening factor of 200 Hz was applied prior to Fourier transformation.

^{31}P magic-angle spinning (MAS) ssNMR was performed on a Bruker Avance III spectrometer with a 4 mm HX probe at the frequency of 121.52 MHz, a MAS rate of 7 kHz and a 2.5 μs 90° pulse-acquisition sequence. Five hundred twelve scans were acquired for both experiments. Pure H_3PO_4 was used as external reference.

Negative Staining Electron Microscopy

Samples were loaded onto previously glow-discharged carbon-coated copper grids and stained with 2% uranyl acetate (w/v) solution. Observations were performed under low-dose conditions on a CM120 120 kV FEI electron microscope using a Gatan USC1000 2k \times 2k camera. Clichés were analyzed with the Fiji distribution of ImageJ2 (Schindelin et al., 2012; Rueden et al., 2017).

RESULTS

Nanodomain Segregation by RemCA Involves Both PIPs and β -Sitosterol

Using 2H ssNMR, we monitored thermotropism, lipid dynamics, and membrane thickness of liposomes containing

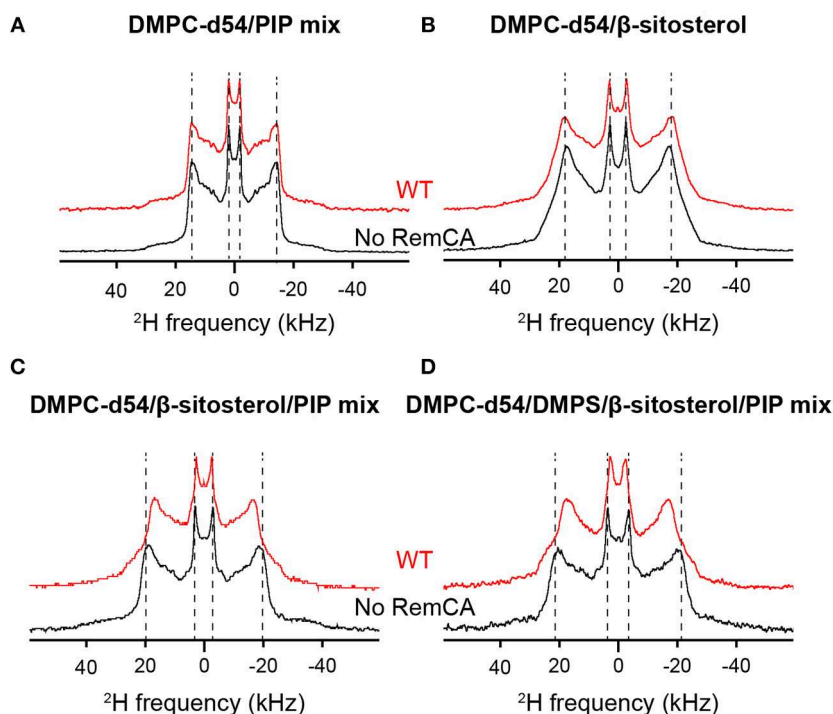


FIGURE 2 | Comparison of 2H quadrupolar spin echo spectra acquired at 298K in absence (black) or in presence (red) of RemCA WT. Inner line pairs indicate the Pake doublet frequency of the terminal CD_3 while outer line pairs indicate the plateau region (usually between positions 2 and 8). Liposome compositions are (A) DMPC-d54/PIP mix 90/10, (B) DMPC-d54/ β -sitosterol 85/15, (C) DMPC-d54/ β -sitosterol/PIP mix 75/15/10, (D) DMPC-d54/DMPS/ β -sitosterol/PIP mix 65/10/15/10 (molar ratio), at pH = 7–8.

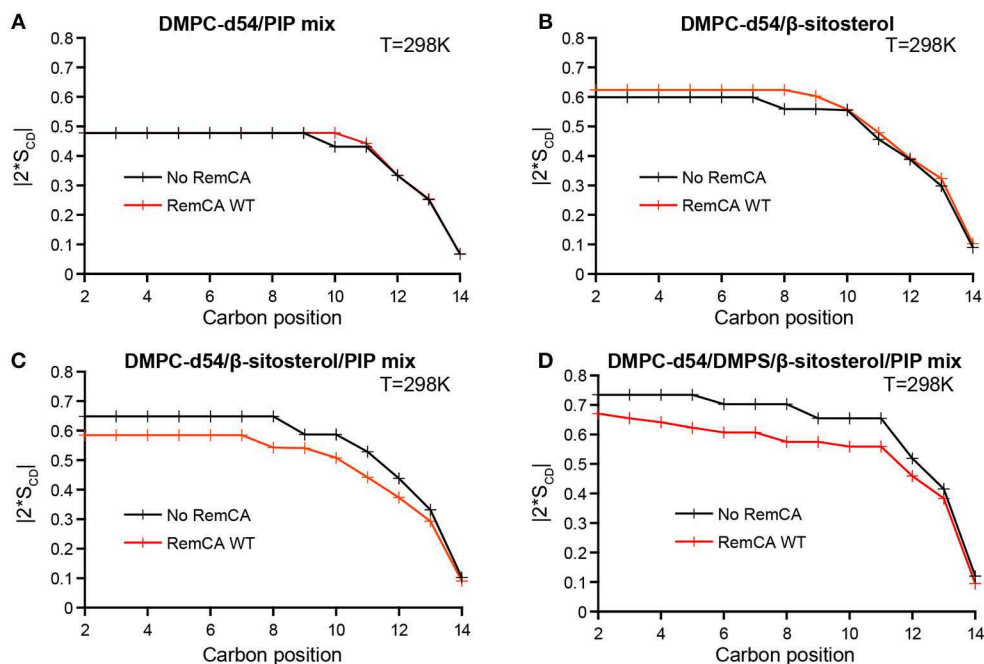


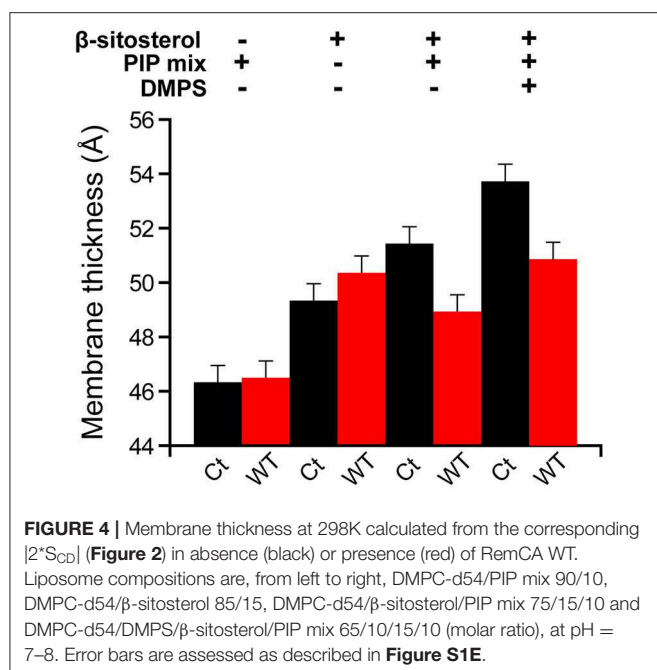
FIGURE 3 | Local order parameters $|2^*S_{CD}|$ as a function of the carbon positions along the acyl chains of DMPC-d54 in absence (black) or presence (red) of RemCA WT. Liposome compositions are **(A)** DMPC-d54/PIP mix 90/10, **(B)** DMPC-d54/ β -sitosterol 85/15, **(C)** DMPC-d54/ β -sitosterol/PIP mix 75/15/10, **(D)** DMPC-d54/DMPS/ β -sitosterol/PIP mix 65/10/15/10 (molar ratio), at pH = 7–8. Representative error bars are shown in **Figure S1C**.

consecutively the different membrane components that might impact on remorin-driven nanodomain assembly. The lipid systems of choice included, consecutively, perdeuterated phosphatidylcholine (PC, here DMPC-d54), phosphoinositolphosphates (PIPs), β -sitosterol and phosphatidylserine (PS, here DMPS), **Figures 1B,C**. Deuterium spectra reveal the quadrupolar splittings that can be assigned to the positions of the ^2H along the acyl chain of the deuterated lipid. The splitting of the so-called Pake doublet depends on the dynamics of the Carbon-Deuterium bond and can be translated into the local order parameters ($|2^*S_{CD}|$) along the acyl chains of DMPC-d54 by de-Pake-ing (Davis, 1983). To accurately measure the impact of RemCA WT peptides on lipid dynamics we detected the quadrupolar splittings and then computed the order parameters $|2^*S_{CD}|$ in presence and in absence of RemCA. We chose the physiologically relevant temperature of 298K (25°C). Addition of RemCA to liposomes containing PC/PIPs and PC/ β -sitosterol did not visually modify the quadrupolar splittings (**Figures 2A,B**) whereas RemCA has a clear impact on membranes containing PC/ β -sitosterol/PIPs and PC/PS/ β -sitosterol/PIPs (**Figures 2C,D**). Membrane-protein interactions generally entail a modification of the lipid dynamic behavior. The selective impact of RemCA points out the importance of β -sitosterol and PIP being simultaneously present to allow for its nanodomain association.

Assessing the order parameters along the acyl chain provides a detailed view on the impact of RemCA on the membrane dynamics (**Figure 3**). No significant change in $|2^*S_{CD}|$ was

observed in PC/PIPs and PC/ β -sitosterol liposomes upon addition of RemCA (**Figures 3A,B**), despite a slight increase of the order parameter in the presence of β -sitosterol. PC/ β -sitosterol/PIPs and PC/PS/ β -sitosterol/PIPs liposomes display lower $|2^*S_{CD}|$ along their acyl chains in the presence of RemCA, indicating a PIP- and sterol-dependent interaction between RemCA and the membrane (**Figures 3C,D**). The chosen lipids display a consecutively rigidifying effect on the membrane (**Figure S2**). RemCA then increases the lipid mobility in the membranes of the complex lipid mixtures PC/ β -sitosterol/PIPs and PC/PS/ β -sitosterol/PIPs. Addition of PS does not significantly enhance the observed effect of RemCA on liposomes containing β -sitosterol/PIPs (**Figure 3D**). To monitor whether the impact of the peptide depends exclusively on the simultaneous presence of PIPs and β -sitosterol, we tested its effect also on PC/PS-containing liposomes and we observe no detectable change of the $|2^*S_{CD}|$ (**Figure S3**). The representative error for this type of sample preparation (**Figure S1C**) is below 0.9% at carbon positions 2–6.

The local order parameter $|2^*S_{CD}|$ can further be translated into the average membrane thickness (Grélaud et al., 2013) at 298K (**Figure 4**). PC/PIPs and PC/ β -sitosterol liposomes without and with RemCA display similar membrane thicknesses (46.3 Å vs. 46.5 Å and 49.3 Å vs. 50.4 Å) whereas the membrane thickness of PC/ β -sitosterol/PIPs and PC/PS/ β -sitosterol/PIPs decreases slightly in the presence of RemCA (51.4 Å–48.9 Å and 52.7 Å–50.9 Å, respectively).



The first order spectral moments M_1 , which can be extracted from the deuterium spectra, report on the bilayer phase behavior and thermotropism (Figure S4). The inflection point between higher M_1 values indicating a gel phase to lower ones pointing to a fluid phase reports on the phase transition. For all lipid compositions, the phase transition temperatures (T_m) seem to remain close to the T_m of DMPC-d54 alone, 293K, but no clear phase transitions were detected in the presence of β-sitosterol. We observe a clear thermotropic transition in the absence of sterols, but only a slow descent of M_1 in their presence. Sterols might broaden the primary transition or it might be below the chosen temperature range (Dufourc, 2008). The presence of RemCA WT peptides does not have a significant effect on M_1 values nor on T_m across the range of temperature considered, 278–308 K. ^{31}P NMR confirms the presence of lamellar phases in liposomes in all samples, as well as small vesicles in presence of PIPs (Figure S5).

Taken together with the $|2^*S_{CD}|$ analysis, our results show that upon interaction with membranes of relevant lipid compositions (PC/β-sitosterol/PIP and PC/PS/β-sitosterol/PIP), RemCA WT binds to the lipid bilayer without disrupting its structural integrity and lipid phase, while exerting a noticeable effect on its internal dynamics, reflected by the variations of the order parameters.

pH Dependency of Protein-Lipid Interactions in Nanodomain Association

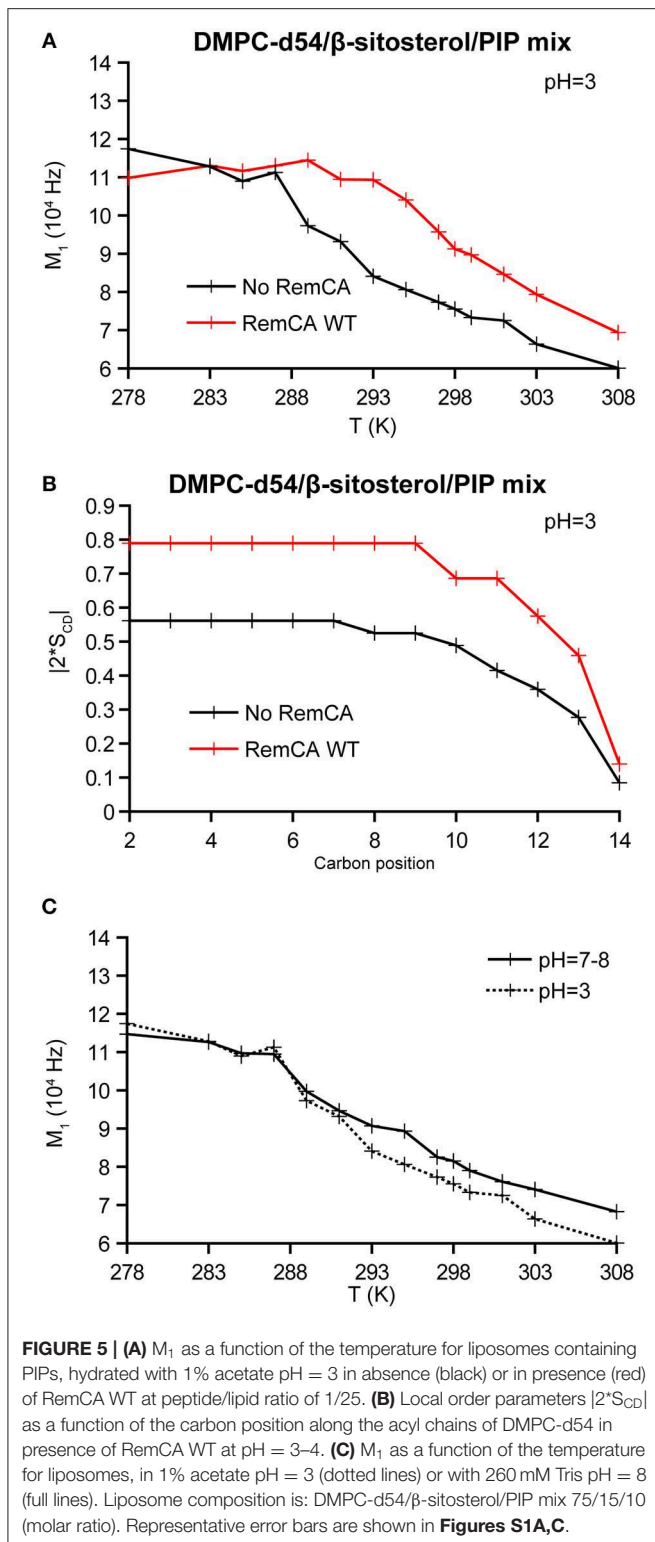
At low pH ($\text{pH} \approx 3\text{--}4$), polyphosphate PIPs lose parts of their negative charges present at $\text{pH} = 7\text{--}8$ (Kooijman et al., 2009). Though, to our knowledge, no values on the pH dependency of the charges for all PIPs of the PIP mix have been documented, in analogy to $\text{PI}(3,5)\text{P}_2$, the PIPs of the PIP mix (including

PI4P) should be neutralized at $\text{pH} \approx 3\text{--}4$. Moreover (Redfern and Gericke, 2004) showed that di-palmitoyl phosphoinositol mono-phosphates were able to segregate into phosphatidylinositol-enriched microdomains at $\text{pH} = 7\text{--}9.5$ but not at $\text{pH} = 4$. To obtain insights into the role of electrostatic interactions during the RemCA-membrane interplay, we decided to test how the pH value influences the impact of RemCA on nanodomain-mimicking membranes. To assess the lipid interactions during RemCA-membrane association, we co-solubilised synthetic RemCA WT peptides in various liposome preparations (%/% molar ratio): DMPC/PIP mix 90/10, DMPC/β-sitosterol 85/15, DMPC/β-sitosterol/PIP mix 75/15/10 and DMPC/DMPS/β-sitosterol/PIP mix 65/10/15/10. Peptides used in our study carried impurities ($<10\%$ w/w), such as TFA, which acidified the samples to $\text{pH} = 3\text{--}4$ during peptide-containing liposome preparation, as judged by pH paper. We therefore chose to buffer our samples to an approximate $\text{pH} = 7\text{--}8$, as judged by pH paper. To reveal the RemCA/membrane interactions at low pH, we also rehydrated our samples in pure 1% acetate $\text{pH} = 3$ during proteoliposome reconstitution (final $\text{pH} = 3$). Monitoring phase behavior (Figure 5A), spectral line shapes (Figure S6), and local order parameters $|2^*S_{CD}|$ (Figure 5B) at low pH revealed the significant effect of the head group charges on RemCA-lipid interactions. RemCA, when in contact with low pH nanodomain-mimicking membranes has the inverse effect on the phase behavior, as observed by an increase of the first spectral moment M_1 (Figure 5A), and local order parameter (Figure 5B) as compared to neutral pH (Figure 3C and Figure S4C). Thus, the impact of the peptide on membrane dynamics is significantly modified because of the lower pH. ^{31}P MAS ssNMR revealed significant chemical shift perturbations as a function of pH (Figure S7). Based on (Kishore and Prestegard, 2003; Müller et al., 2004), we tentatively assigned the four visible signals, from higher to lower chemical shifts: 4-phosphate (4-P)-, 4,5-bisphosphate (4,5- P_2)-monoester, PS and PC. The diester groups might be obscured by the PS and PC signal. Assignment of 4,5- P_2 - remained ambiguous as a second peak was expected. Signals assigned to the monoesters witnessed a heavy shift between spectra at $\text{pH} = 7\text{--}8$ and revealing important modifications of their chemical environment which may be attributed to a change in their protonation state (van Paridon et al., 1986).

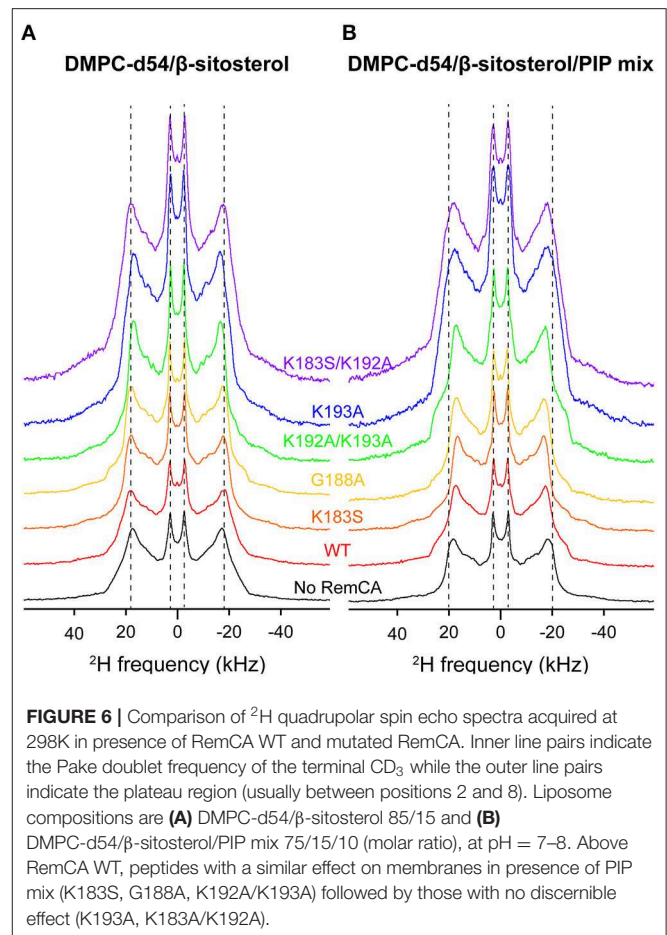
The acidic pH entails a negligible effect on phase behavior (Figure 5C) whereas it significantly modifies the local order parameter at 298K (black curves, Figure 3C vs. Figure 5B).

K192 and K193 Are Critical Residues in the Targeting of PIPs by RemCA WT

Based on a pre-established list of mutants impaired for both PM and nanodomain targeting (Gronnier et al., 2017), we employed mutated RemCA peptides to evidence the concerted role of lipid-amino acid interactions involving the specific targeting of PIPs. According to previous molecular dynamics experiments, residues K192 and K193 play a key role in the targeting of PI4P by StREM1.3 . We limited ourselves to five



mutants (Gronnier et al., 2017): G188A, a negative control that should show no specific difference to the wild-type peptide; K183S, K193A, K183S/K192A, and K192A/K193A, localizing less efficiently into nanodomains. To trace the influence of each



mutation on the peptide-PIP interaction, each mutant and the WT were co-solubilised in liposomes of two different lipid compositions: PC/ β -sitosterol 85/15 and PC/ β -sitosterol/PIP mix 75/15/10 (molar ratio). We then determined the local order parameter $[2^*S_{CD}]$ of DMPC-d54 at 298K for every sample (WT, K183S, G188A, K192A/K193A, K193A, and K183S/K192A) (**Figures 6, 7**). In absence of PIPs, the effect of the peptides on the quadrupolar splitting and the local order parameter $[2^*S_{CD}]$ of the liposomes does not differ between RemCA WT and the mutants (**Figures 6A, 7A,C**); the impact of RemCA WT and the mutants is undetectable or entails a slight increase of the local $[2^*S_{CD}]$. In presence of PIPs, we observe two different behaviors (**Figures 6B, 7B,D**). The wild type peptide (RemCA WT) and a group of mutants (K183S, G188A, and K192A/K193A) have a pronounced effect on the membranes, decreasing $[2^*S_{CD}]$ all along the acyl chains of DMPC-d54. Importantly, this effect is abolished for a second group composed of the mutants K193A and K183S/K192A (**Figures 6B, 7B,D**), exposing an undetectable or a slightly increasing effect on the $[2^*S_{CD}]$. This observation suggests that mutants from the first group, together with RemCA WT, interact with PIP-containing liposomes whereas peptides from the second group do not (**Figures 6, 7**). Unexpectedly, the double mutant K192A/K193A still binds to liposomes containing PIPs, possibly through an alternative mechanism involving K183.

The representative error for this type of sample preparation (**Figure S1C**) is below 0.9% at carbon positions 2–6.

Measurements of the membrane thickness reflect a comparable trend, as expected, since they rely on the ^2H NMR data. The membrane thicknesses without PIPs are all within the same range of ≈ 50 Å. Liposomes containing PIPs are split in the same two groups as described above with RemCA WT, K183S, G188A, or K192A/K193A decreasing membrane thickness more or less significantly (≈ 49 Å) whereas RemCA K193A or K183S/K193A have no effect (≈ 51 Å) (**Figure 8**). Our data corroborate the *in vivo* results that K192 and K193 are critical residues in the targeting of PIPs by RemCA. However, the results reveal that the *in vivo* membrane association of StREM1.3 relies on a more complex behavior of the positively charged residues during the trimerised protein-membrane interaction.

Monitoring M_1 as a function of temperature, we detect no important impact of the different mutants and the WT on the phase behavior (**Figure S8**). Above 293K, M_1 values in presence of PIP mix seem to spread out a little more than without PIP mix. All samples contain large liposomes in lamellar phase along with smaller vesicles in presence of PIP mix (**Figure S9**). Our data point to different effects of the different mutations, larger than the error margins for repetition of the identical conditions. However, considering possible uncertainties introduced by other sources (e.g., varying impurities in different peptide stocks) future interpretation of these results should be handled with care.

Oligomerisation Modifies RemCA Behavior on Nanodomain-Mimicking Membranes

We have previously demonstrated (Martinez et al., 2018) that disrupting the coiled-coil region of StREM1.3 would partially disrupt membrane targeting. While we hypothesize that the intrinsically disordered domain, responsible for protein-protein interactions, and the coiled-coil homo-oligomerisation domain do not directly interact with the nanodomains, they could indirectly influence nanodomain targeting. To monitor the effect of the two domains, we designed two protein constructs for NMR investigation. We expressed and purified the truncated StREM1.3 (REM_{86–198}), bearing only RemCA and the coiled-coil domain (Martinez et al., 2018), and the full length StREM1.3 including also the IDD.

We achieved setting up a protocol to produce high quantities of StREM1.3 in *E. coli* (about 20 mg/L of culture medium) (**Figures S10, S11A**). Both protein constructs, REM_{86–198} and StREM1.3, were purified to high purity (**Figure S11B**). We avoided reconstitution into liposomes by co-solubilisation to mitigate the risk of misfolding and non-native interactions with lipids. Instead, we incubated the proteins with preformed liposomes overnight at 30°C, using two lipid compositions: DMPC-d54/ β -sitosterol 85/15 or DMPC-d54/ β -sitosterol/PIP mix 75/15/10 (molar ratio). For each proteoliposome sample, about 40–50% of the proteins were pelleted by ultracentrifugation, as could be assessed by

absorbance at 280 nm of the supernatant fractions and SDS-PAGE of the pellets (**Figure S12**). We used deuterium NMR to probe the lipid order in presence of the two remorin domains.

Local order parameters $|2^*\text{SCD}|$ of PC-d54/ β -sitosterol membranes are similar whether in absence or presence of both REM_{86–198} and StREM1.3, no protein-membrane interactions seem to occur (**Figure 9A** and **Figure S13A**). In contrast, DMPC-d54/ β -sitosterol/PIP liposomes containing REM_{86–198} or StREM1.3 witnessed a similar increase of the order parameter $|2^*\text{SCD}|$ all along their acyl chains (**Figure 9B** and **Figure S13B**). In accordance, membrane thicknesses were similar in absence of PIPs but increased comparably in presence of PIPs and one of the proteins (**Figure S14**). The representative error for this type of sample preparation (**Figure S1D**) is below 3.7% at carbon positions 2–7. The samples contain large liposomes in lamellar phase with a small isotropic peak in presence of PIPs (**Figure S15**). All samples displayed a T_m around 293K (**Figure 10**, representative error in **Figure S1B**). When compared to the monomeric anchor RemCA, REM_{86–198} and StREM1.3 show an inverse effect on nanodomain-mimicking membranes, revealing the crucial impact of remorin oligomerisation during nanodomain clustering.

In contrast, both constructs, REM_{86–198} and StREM1.3, display a very similar behavior on the membranes, indicating that the non-phosphorylated intrinsically disordered domain does not influence remorin nanodomain targeting. The sample preparation used for measuring the effects of the two longer constructs should lead to reduced detectable readout range since predominantly the outer leaflet of the liposomes will be accessible. In line with this view, our results indeed show smaller effects for all tested conditions. Consequently, the data and interpretation should be handled with care.

Transient Higher-Order Oligomer Formation Could Stabilize Nanodomain Clustering

When incorporating the constructs REM_{86–198} and StREM1.3 into liposomes, negative staining electron microscopy revealed the presence of protein filaments (**Figure S16**). Notably, this observation mostly concerned samples without PIPs (**Figures S16A,B,E,F**) whereas in the presence of PIPs very few filaments were observed (**Figures S16C,D,G,H**). Since there is no significant effect of either protein on liposomes in absence of PIPs and filament formation is significantly reduced in the presence of PIPs, we assume that the filaments do not directly interfere with liposomes. Nevertheless, we attempted to remove filaments by pelleting at lower centrifugal force before reconstitution. Removing the filamentous objects before reconstitution into liposomes caused both proteins to remain mostly in solution when exposed to the preformed liposomes, as assessed by absorbance at 280 nm (2.5 and 1.7 in solution before reconstitution, 2.8 and 1.7 in supernatant after reconstitution and liposome pelleting for REM_{86–198} and StREM1.3, respectively). Absorbance measurement may be biased by remaining small liposomes. However, few proteins were still incorporated into the liposomes, for REM_{86–198} only in the presence of PIPs,

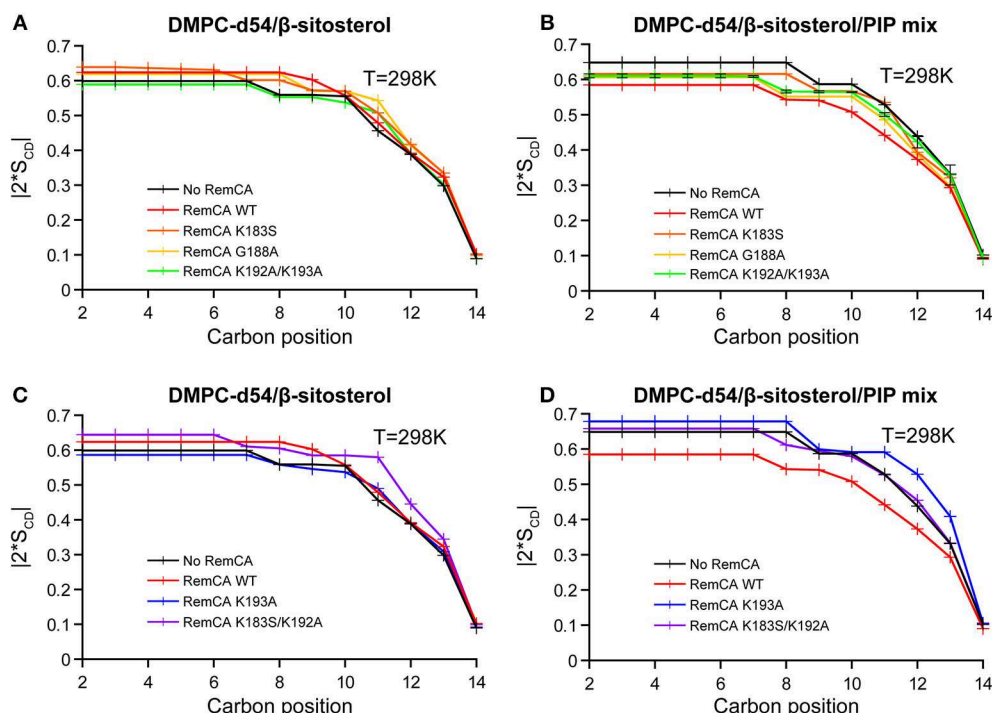


FIGURE 7 | Local order parameters $[2^*S_{CD}]$ as a function of carbon positions along the acyl chains of DMPC-d54 in presence of RemCA WT or mutated RemCA. Liposome compositions are **(A,C)** DMPC-d54/β-sitosterol 85/15 and **(B,D)** DMPC-d54/β-sitosterol/PIP mix 75/15/10 (molar ratio), at pH = 7–8. Representative error bars are shown in **Figure S1C**.

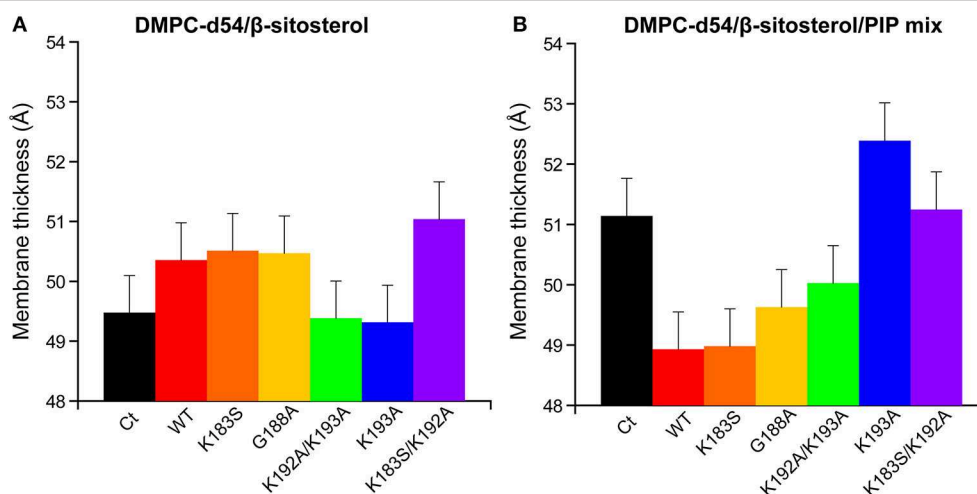


FIGURE 8 | Membrane thickness at 298K calculated from the corresponding $[2^*S_{CD}]$ (**Figure 6**). Liposome compositions are **(A)** DMPC-d54/β-sitosterol 85/15 and **(B)** DMPC-d54/β-sitosterol/PIP mix 75/15/10 (molar ratio), at pH = 7–8. Error bars are assessed as described in **Figure S1E**.

as the band seems to be absent, even though it might be hidden under the liposome smear (**Figure S17**). No filaments were found on the liposomes (example given for REM_{86–198}, **Figure S18**). We could not detect an effect of this low protein amount on the membrane dynamics as reflected in the local

order parameter $[2^*S_{CD}]$ of DMPC-d54 (**Figure S19**). Since filaments do not seem to have a direct impact on liposomes and their formation is reduced in the presence of PIPs, transient higher-order oligomer formation might stabilize protein-lipid interactions during membrane association.

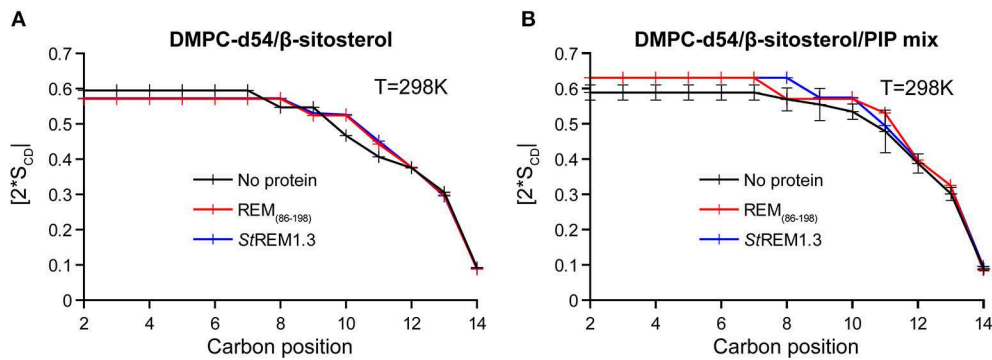


FIGURE 9 | Local order parameters $[2^*S_{CD}]$ as function of the carbon position along the acyl chains of DMPC-d54 in presence of REM₈₆₋₁₉₈ or StREM1.3. Liposome compositions are **(A)** DMPC-d54/β-sitosterol 85/15 and **(B)** DMPC-d54/β-sitosterol/PIP mix 75/15/10 (molar ratio), at pH = 7–8. Representative error bars are shown in **Figure S1D**.

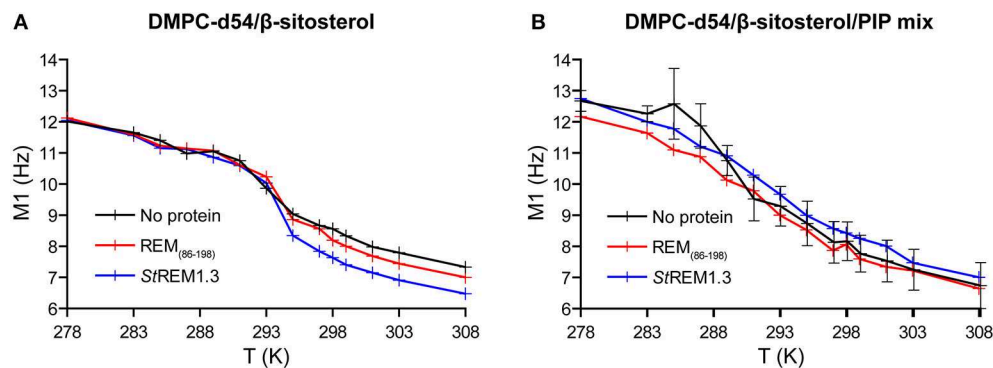


FIGURE 10 | Variation of first order spectral moments M_1 as a function of temperature T in presence of REM₈₆₋₁₉₈ or StREM1.3. Liposome compositions are **(A)** DMPC-d54/β-sitosterol 85/15 and **(B)** DMPC-d54/β-sitosterol/PIP mix 75/15/10 (molar ratio). Error bars are standard deviations of three independent experiments, as shown in **Figure S1B**.

DISCUSSION

Our results shed light on the detailed mechanisms of StREM1.3-driven nanodomain clustering. We dissect the roles of the three StREM1.3 domains, the C-terminal anchor RemCA, the coiled-coil oligomerisation domain and the intrinsically disordered domain (IDD), implicated in protein-protein interactions.

We have monitored a fluidifying effect of RemCA on the membrane, assessed by the decrease of the local carbon-deuterium order parameter all along the acyl chains of DMPC-d54, only in presence of PIPs and β-sitosterol simultaneously. RemCA's membrane interactions therefore depend on the presence of both PIPs and β-sitosterol during nanodomains clustering, as we have suggested earlier (Raffaele et al., 2009; Gronnier et al., 2017). Moreover, addition of DMPS, another negatively charged phospholipid, does not modify this behavior, corroborating RemCA's genuine specificity for PIP and β-sitosterol.

RemCA peptides lacking K192 or K193, namely RemCA K183S/K192A or K193A, do not show any fluidifying effect on nanodomain-mimicking membranes, highlighting the

important role of these two positively charged residues. In the absence of PIPs RemCA and several mutants show a slight increase of the lipid order parameters in the presence of β-sitosterol, which could be attributed to a low overall membrane binding without the formation of lipid clusters. K183S and K192A/K193A mutants still interact with the nanodomain-mimicking membranes such as the wild-type RemCA. These two mutants behave similarly to K183S/K192A or K193A, when considering their segregation into nanodomains in StREM1.3 *in vivo*, detected by Single-Particle Tracking Photoactivated Localization Microscopy, spt-PALM (Gronnier et al., 2017). Their behavior on nanodomain-mimicking membranes *in vitro* therefore suggests a more complex interplay between the different positive charges in the intact StREM1.3 *in vivo* (Gronnier et al., 2017), possibly influenced by the oligomerisation and the subsequent trimeric exhibition of the anchor RemCA. However, our results are coherent with specific electrostatic interactions between K192 and K193 and the polar head of PI4P from the PM's inner leaflet (Gronnier et al., 2017).

In the K192A/K193A mutant, still displaying specificity for PIPs, the replacement of two consecutive positively charged

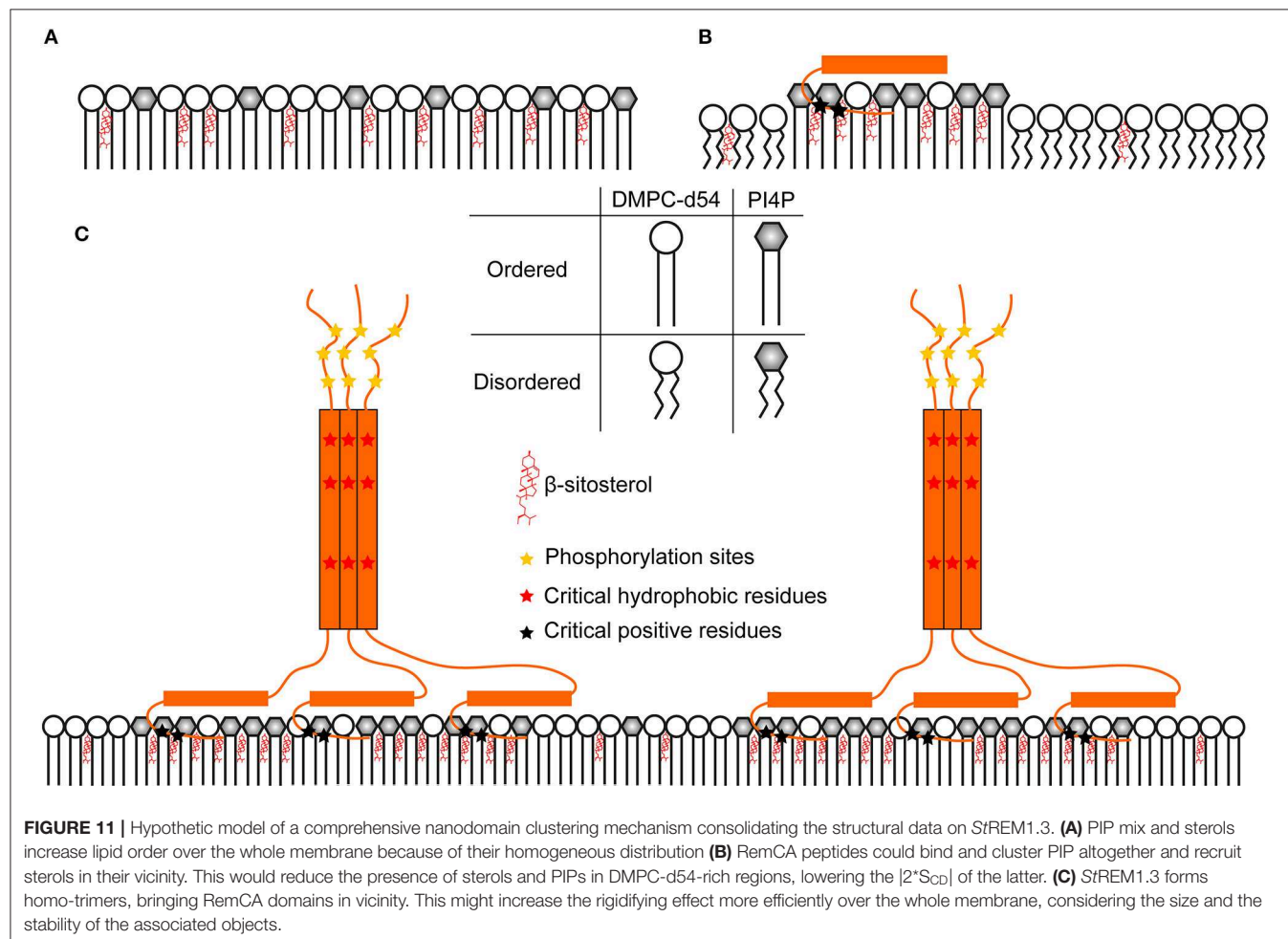
lysines by two consecutive hydrophobic alanines might allow an alternative folding and binding mechanism. However, we cannot exclude the possibility of errors that might not have been monitored by our error assessment, so we suggest treating the data with care.

Our findings show that negative PIP head group charges should foster RemCA nanodomain-mimicking membrane association. We therefore tested the impact of the pH on RemCA-membrane interactions. The impact of RemCA on phase behavior and acyl chain mobility at acidic pH is inverted compared to neutral pH, i.e., RemCA reduces acyl chain mobility in the nanodomain-mimicking membrane in acidic conditions. This might rely on an alternative binding mode of RemCA to the lipid bilayer, potentially reflecting an unspecific overall membrane binding, as is also the case for low binding of the peptide and its mutants in the presence of β -sitosterol. The electrostatic PIP-RemCA interactions present at physiological conditions should therefore represent a crucial actor during remorin nanodomain clustering.

We then examined the membrane- and nanodomain-association of the C-terminal anchor in conjunction with the coiled-coil oligomerisation domain REM_{86–198} and the

full-length StREM1.3, including the intrinsically disordered region. In line with our knowledge on StREM1.3, they only associate to nanodomain-mimicking membranes, i.e., containing PIPs and β -sitosterol responsible for StREM1.3 nanodomain segregation. Their effect on the membrane dynamics is very similar, indicating that the intrinsically disordered domain does not directly influence the nanodomain association. However, use of phosphodead StREM1.3 S74A/T86A/S91A and phosphomimetic StREM1.3 S74D/T86D/S91D mutants revealed a phosphorylation-dependent change in nanodomain organization *in vivo* (Perraki et al., 2018), implying the StREM1.3's intrinsically disordered region indirectly modifies the membrane-associating behavior, possibly by altering the interactions with other proteins or itself.

Both REM_{86–198} and the full-length StREM1.3 have an inverse effect on nanodomain-mimicking membrane dynamics when compared to RemCA WT. The anchoring domain alone is in a monomeric state and therefore represents the lipid specificity of the peptide alone (Figures 11A,B), presumably fostering the formation of lipid clusters. In the absence of RemCA, the lipid dynamics could represent the homogeneous rigidifying effect of intercalated PIP/sitosterol (Figure S1) along the reporter DMPC



acyl chain (**Figure 11A**). When RemCA is present, it might cluster the PIP/sitosterol moieties and therefore have a fluidifying effect on the reporter DMPC acyl chains (**Figure 11B**). Including the coiled-coil domain drastically increases the complexity of the native trimeric StREM1.3 structure, containing three RemCA anchors. REM_{86–198} and StREM1.3 would reflect the rigidifying impact of the clustered protein on the nanodomain-mimicking membranes (**Figure 11C**) with the inner bilayers of the liposomes unaffected and the outer exposed to the trimeric remorin. The protein and lipid clustering might reflect driving mechanisms of nanodomain formation in native membranes. Again, we cannot exclude the possibility of errors that might not have been monitored by our error assessment, in consequence we suggest treating the data with care.

We found that REM_{86–198} and StREM1.3 formed filaments even at low protein concentration, when we proceeded to liposome reconstitution (**Figure S16**). Filament formation observed by EM was much reduced by the presence of PIP (**Figures S16C,D,G,H**) and the pelleted liposomes contained a significantly higher amount of protein in the presence of PIP (**Figure S12**), indicating that the protein is incorporated into membranes. When removing filaments by moderate centrifugation, the relative amount of proteins incorporated into liposomes drastically decreases, indicating that the presence of transient higher-order oligomers might favor the incorporation of trimeric remorins into the nanodomain-mimicking membranes. Although filaments are unlikely to be stable *in vivo*, the underlying ability of StREM1.3 to cluster with its peers into higher-order complexes could be biologically relevant. In line with this results, disrupting the coiled-coil region resulted in a partial loss of membrane targeting, indicating this domain is required to ensure a tight binding to the PM (Martinez et al., 2018).

CONCLUSION

Gaining mechanistic insights into the interactions and protein/membrane structures governing nanodomain formation remains difficult because of the complexity of the native protein-bilayer system. Here, we employed a ²H ssNMR-based methodology to tackle the lipid-protein interactions and mechanisms behind nanodomain clustering driven by StREM1.3. Using a divide-and-conquer approach, we deciphered the roles of the membrane anchor RemCA in isolation, REM_{86–198}, including the coiled-coil domain responsible for trimerisation and the intact StREM1.3. We seek to uncover the essential electrostatic interactions between RemCA's positive residues and the negatively charged PIP head groups involved in nanodomain formation. Our data moreover suggest that nanodomain clustering depends on the evolutionary evolved trimeric structure, which can only be partially represented by the monomeric anchor. The trimers of remorins appear to confer

nanodomain clustering while the pure protein-lipid association relies mostly on the membrane anchor RemCA. Furthermore, we reveal that transient higher-order oligomer formation might stabilize the *in vivo* association of remorins to nanodomains, which is further supported by the structural conservation of the oligomerisation domain in the six phylogenetic groups (Raffaele et al., 2007).

Our results shed new light on the essential role of certain specific electrostatic protein-lipid interactions and protein oligomerisation properties toward understanding the driving forces in the nanoclustering of StREM1.3. We propose a more general picture of the relevance of oligomerisation, a character often present in nanodomain-segregating proteins. To gain more precise notions on the mechanisms behind lipid domain assembly, it will be vital to understand the structural implications of protein oligomerisation and the lipid-protein interactions from a protein structural point of view.

DATA AVAILABILITY STATEMENT

All datasets generated for this study are included in the manuscript/Supplementary Files.

AUTHOR CONTRIBUTIONS

ALe, DM, AG, MB, AT, and EM performed the experiments. ALe, DM, ALo, SM, and BH interpreted the data. ALo, SM, and BH designed the experiments. BH conceptualized the research. All authors revised and edited the manuscript.

FUNDING

We acknowledge funding from the Centre National de la Recherche Scientifique CNRS Momentum (BH), IdEx Bordeaux-Chaire d'installation (BH), the region Nouvelle Aquitaine (BH, grant convention N° 2017-1R10305-00013031), the CNRS (BH and SM, PEPS project Idex Bordeaux-PEPS 2316), ALe was supported by a French doctoral fellowship MESRI. Research was supported by European Research Council (ERC-2015-StG GA no. 639020 to ALo), and by the French ANR project Potymove (ANR-16-CE20-008-01 to SM), <https://anr.fr/en/>.

ACKNOWLEDGMENTS

We thank Marion Decossas and Olivier Lambert for technical assistance and advice for acquisition of EM images.

SUPPLEMENTARY MATERIAL

The Supplementary Material for this article can be found online at: <https://www.frontiersin.org/articles/10.3389/fmolb.2019.00107/full#supplementary-material>

REFERENCES

- Ackerman, D. G., and Feigenson, G. W. (2015). Multiscale modeling of four-component lipid mixtures: domain composition, size, alignment, and properties of the phase interface. *J. Phys. Chem.* 119, 4240–4250. doi: 10.1021/jp511083z
- Baker, L. A., Folkers, G. E., Sinnige, T., Houben, K., Kaplan, M., van der Cruysen, E. A. W., et al. (2015). “Magic-angle-spinning solid-state NMR of membrane proteins,” in *Methods in Enzymology*, ed K. S. Arun (Elsevier), 307–328. doi: 10.1016/bs.mie.2014.12.023
- Bariola, P. A., Retelska, D., Stasiak, A., Kammerer, R. A., Fleming, A., Hijri, M., et al. (2004). Remorins form a novel family of coiled coil-forming oligomeric and filamentous proteins associated with apical, vascular and embryonic tissues in plants. *Plant Mol. Biol.* 55, 579–594. doi: 10.1007/s11103-004-1520-4
- Beck, J. G., Mathieu, D., Loudet, C., Buchoux, S., and Dufourc, E. J. (2007). Plant sterols in “rafts”: a better way to regulate membrane thermal shocks. *FASEB J.* 21, 1714–1723. doi: 10.1096/fj.06-7809com
- Bloom, M., Davis, J. H., and Mackay, A. L. (1981). Direct determination of the oriented sample NMR spectrum from the powder spectrum for systems with local axial symmetry. *Chem. Phys. Lett.* 80, 198–202. doi: 10.1016/0009-2614(81)80089-9
- Brown, M. F. (2017). Soft Matter in Lipid-Protein Interactions. *Annu. Rev. Biophys.* 46, 379–410. doi: 10.1146/annurev-biophys-070816-033843
- Cady, S. D., Schmidt-Rohr, K., Wang, J., Soto, C. S., DeGrado, W. F., and Hong, M. (2010). Structure of the amantadine binding site of influenza M2 proton channels in lipid bilayers. *Nature* 463, 689–692. doi: 10.1038/nature08722
- Davis, J. H. (1983). The description of membrane lipid conformation, order and dynamics by ²H-NMR. *Biochim. Biophys. Acta* 737, 117–171. doi: 10.1016/0304-4157(83)90015-1
- Davis, J. H., Jeffrey, K. R., Bloom, M., Valic, M. I., and Higgs, T. P. (1976). Quadrupolar echo deuterium magnetic resonance spectroscopy in ordered hydrocarbon chains. *Chem. Phys. Lett.* 42, 390–394. doi: 10.1016/0009-2614(76)80392-2
- Dufourc, E. J. (2008). Sterols and membrane dynamics. *J. Chem. Biol.* 1, 63–77. doi: 10.1007/s12154-008-0010-6
- Dufourc, E. J., Mayer, C., Stohrer, J., Althoff, G., and Kothe, G. (1992). Dynamics of phosphate head groups in biomembranes. Comprehensive analysis using phosphorus-31 nuclear magnetic resonance lineshape and relaxation time measurements. *Biophys. J.* 61, 42–57. doi: 10.1016/S0006-3495(92)81814-3
- Furt, F., König, S., Bessoule, J. J., Sargueil, F., Zallot, R., Stanislas, T., et al. (2010). Polyphosphoinositides are enriched in plant membrane rafts and form microdomains in the plasma membrane. *Plant Physiol.* 152, 2173–2187. doi: 10.1104/pp.109.149823
- Grecco, H. E., Schmick, M., and Bastiaens, P. I. (2011). Signaling from the living plasma membrane. *Cell* 144, 897–909. doi: 10.1016/j.cell.2011.01.029
- Grélaud, A., Guichard, P., Bonnafeous, P., Marco, S., Lambert, O., Manin, C., et al. (2013). Hepatitis B virus particles display both a fluid bilayer membrane and a strong resistance to freeze drying: a study by solid-state NMR, light scattering, and cryo-electron microscopy/tomography. *FASEB J.* 27, 4316–4326. doi: 10.1096/fj.13-232843
- Gronnier, J., Crowet, J.-M., Habenstein, B., Nasir, M. N., Bayle, V., Hosy, E., et al. (2017). Structural basis for plant plasma membrane protein dynamics and organization into functional nanodomains. *ELife* 6:e26404. doi: 10.7554/eLife.26404
- Habenstein, B., and Loquet, A. (2016). Solid-state NMR: an emerging technique in structural biology of self-assemblies. *Biophys. Chem.* 210, 14–26. doi: 10.1016/j.bpc.2015.07.003
- Huster, D. (2014). Solid-state NMR spectroscopy to study protein-lipid interactions. *Biochim. Biophys. Acta* 1841, 1146–1160. doi: 10.1016/j.bbalip.2013.12.002
- Javanainen, M., Martinez-Seara, H., and Vattulainen, I. (2017). Nanoscale membrane domain formation driven by cholesterol. *Sci. Rep.* 7:1143. doi: 10.1038/s41598-017-01247-9
- Kaiser, H.-J., Lingwood, D., Levental, I., Sampaio, J. L., Kalvodova, L., Rajendran, L., et al. (2009). Order of lipid phases in model and plasma membranes. *Proc. Natl. Acad. Sci. U.S.A.* 106, 16645–16650. doi: 10.1073/pnas.0908987106
- Kishore, A. I., and Prestegard, J. H. (2003). Molecular orientation and conformation of phosphatidylinositides in membrane mimetics using variable angle sample spinning (VASS) NMR. *Biophys. J.* 85, 3848–3857. doi: 10.1016/S0006-3495(03)74799-7
- Kooijman, E. E., King, K. E., Gangoda, M., and Gericke, A. (2009). Ionization properties of phosphatidylinositol polyphosphates in mixed model membranes. *Biochemistry* 48, 9360–9371. doi: 10.1021/bi9008616
- Ladizhansky, V. (2017). Applications of solid-state NMR to membrane proteins. *Biochim. Biophys. Acta Proteins Proteom.* 1865, 1577–1586. doi: 10.1016/j.bbapap.2017.07.004
- Lalli, D., Idso, M. N., Andreas, L. B., Hussain, S., Baxter, N., Han, S., et al. (2017). Proton-based structural analysis of a heptahelical transmembrane protein in lipid bilayers. *J. Am. Chem. Soc.* 139, 13006–13012. doi: 10.1021/jacs.7b05269
- Loquet, A., Tolchard, J., Berbon, M., Martinez, D., and Habenstein, B. (2017). Atomic scale structural studies of macromolecular assemblies by solid-state nuclear magnetic resonance spectroscopy. *J. Visualiz. Exp.* 17:e55779–e55779. doi: 10.3791/55779
- Mandala, V. S., Williams, J. K., and Hong, M. (2018). Structure and dynamics of membrane proteins from solid-state NMR. *Annu. Rev. Biophys.* 47, 201–222. doi: 10.1146/annurev-biophys-070816-033712
- Marin, M., Thallmair, V., and Ott, T. (2012). The intrinsically disordered N-terminal region of AtREM1.3 remorin protein mediates protein-protein interactions. *J. Biol. Chem.* 287, 39982–39991. doi: 10.1074/jbc.M112.414292
- Martinez, D., Legrand, A., Gronnier, J., Decossas, M., Gougnet, P., Lambert, O., et al. (2018). Coiled-coil oligomerization controls localization of the plasma membrane REMORINS. *J. Struct. Biol.* 206, 12–19. doi: 10.1016/j.jsb.2018.02.003
- McCabe, M. A., and Wassail, S. R. (1997). Rapid deconvolution of NMR powder spectra by weighted fast Fourier transformation. *Solid State Nucl. Magn. Res.* 10, 53–61. doi: 10.1016/S0926-2040(97)00024-6
- Molugu, T. R., Lee, S., and Brown, M. F. (2017). Concepts and methods of solid-state NMR spectroscopy applied to biomembranes. *Chem. Rev.* 117, 12087–12132. doi: 10.1021/acs.chemrev.6b00619
- Mongrand, S., Morel, J., Laroche, J., Claverol, S., Carde, J.-P., Hartmann, M.-A., et al. (2004). Lipid rafts in higher plant cells: purification and characterisation of triton X-100-insoluble microdomains from Tobacco plasma membrane. *J. Biol. Chem.* 279, 36277–36286. doi: 10.1074/jbc.M403440200
- Müller, M., Schiller, J., Petković, M., Zschörnig, O., Arnhold, J., and Arnold, K. (2004). Analysis of enzymatically generated phosphoinositides by ³¹P nuclear magnetic resonance spectroscopy. *Anal. Biochem.* 330, 167–171. doi: 10.1016/j.ab.2004.03.071
- Ott, T. (2017). Membrane nanodomains and microdomains in plant-microbe interactions. *Curr. Opin. Plant Biol.* 40, 82–88. doi: 10.1016/j.pbi.2017.08.008
- Perraki, A., Cacas, J.-L., Crowet, J.-M., Lins, L., Castroviejo, M., German-Retana, S., et al. (2012). Plasma membrane localization of solanum tuberosum remorin from group 1, Homolog 3 is mediated by conformational changes in a novel C-terminal anchor and required for the restriction of potato virus X movement]. *Plant Physiol.* 160, 624–637. doi: 10.1104/pp.112.200519
- Perraki, A., Gronnier, J., Gougnet, P., Boudsocq, M., Deroubaix, A.-F., Simon, V., et al. (2018). REM1.3's phospho-status defines its plasma membrane nanodomain organization and activity in restricting PVX cell-to-cell movement. *PLoS Pathog.* 14:e1007378. doi: 10.1371/journal.ppat.1007378
- Picas, L., Gaits-Iacovoni, F., and Goud, B. (2016). The emerging role of phosphoinositide clustering in intracellular trafficking and signal transduction. *F1000Res* 5:F1000. doi: 10.12688/f1000research.7537.1
- Pike, L. J. (2006). Rafts defined: a report on the Keystone symposium on lipid rafts and cell function. *J. Lipid Res.* 47, 1597–1598. doi: 10.1194/jlr.E600002-JLR200
- Raffaele, S., Bayer, E., Lafarge, D., Cluzet, S., German Retana, S., Boubekeur, T., et al. (2009). Remorin, a solanaceae protein resident in membrane rafts and plasmodesmata, impairs potato virus X movement. *Plant Cell Online* 21, 1541–1555. doi: 10.1105/tpc.108.064279
- Raffaele, S., Mongrand, S., Gamas, P., Niebel, A., and Ott, T. (2007). Genome-wide annotation of remorins, a plant-specific protein family: evolutionary and functional perspectives. *Plant Physiol.* 145, 593–600. doi: 10.1104/pp.107.108639
- Redfern, D. A., and Gericke, A. (2004). Domain formation in phosphatidylinositol monophosphate/phosphatidylcholine mixed vesicles. *Biophys. J.* 86, 2980–2992. doi: 10.1016/S0006-3495(04)74348-9
- Rueden, C. T., Schindelin, J., Hiner, M. C., DeZonia, B. E., Walter, A. E., Arena, E. T., et al. (2017). ImageJ2: ImageJ for the next generation of

- scientific image data. *BMC Bioinform.* 18:529. doi: 10.1186/s12859-017-1934-z
- Schindelin, J., Arganda-Carreras, I., Frise, E., Kaynig, V., Longair, M., Pietzsch, T., et al. (2012). Fiji: an open-source platform for biological-image analysis. *Nat. Methods* 9, 676–682. doi: 10.1038/nmeth.2019
- Sezgin, E., Levental, I., Mayor, S., and Eggeling, C. (2017). The mystery of membrane organization: composition, regulation and roles of lipid rafts. *Nat. Rev. Molecul. Cell Biol.* 18, 361–374. doi: 10.1038/nrm.2017.16
- Simons, K., and Ikonen, E. (1997). Functional rafts in cell membranes. *Nature* 387, 569–572. doi: 10.1038/42408
- Singer, S. J., and Nicolson, G. L. (1972). The fluid mosaic model of the structure of cell membranes. *Science* 175, 720–731. doi: 10.1126/science.175.4023.720
- Stanek, J., Andreas, L. B., Jaudzems, K., Cala, D., Lalli, D., Bertarello, A., et al. (2016). NMR spectroscopic assignment of backbone and side-chain protons in fully protonated proteins: microcrystals, sedimented assemblies, and amyloid fibrils. *Angew. Chem. Int. Ed. Engl.* 55, 15504–15509. doi: 10.1002/anie.201607084
- van Paridon, P. A., de Kruijff, B., Ouwerkerk, R., and Wirtz, K. W. (1986). Polyphosphoinositides undergo charge neutralization in the physiological pH range: a ³¹P-NMR study. *Biochim. Biophys. Acta* 877, 216–219. doi: 10.1016/0005-2760(86)90137-2
- Yao, H., and Hong, M. (2014). Conformation and lipid interaction of the fusion peptide of the paramyxovirus PIV5 in anionic and negative-curvature membranes from solid-state NMR. *J. Am. Chem. Soc.* 136, 2611–2624. doi: 10.1021/ja4121956

Conflict of Interest: The authors declare that the research was conducted in the absence of any commercial or financial relationships that could be construed as a potential conflict of interest.

Copyright © 2019 Legrand, Martinez, Grélard, Berbon, Morvan, Tawani, Loquet, Mongrand and Habenstein. This is an open-access article distributed under the terms of the Creative Commons Attribution License (CC BY). The use, distribution or reproduction in other forums is permitted, provided the original author(s) and the copyright owner(s) are credited and that the original publication in this journal is cited, in accordance with accepted academic practice. No use, distribution or reproduction is permitted which does not comply with these terms.

Supplemental information

Nanodomain clustering of the plant protein remorin by solid-state NMR

Anthony Legrand^{1,2}, Denis Martinez¹, Axelle Grélard¹, Melanie Berbon¹, Estelle Morvan³, Arpita Tawani¹, Antoine Loquet¹, Sébastien Mongrand², Birgit Habenstein^{1*}

¹ Institute of Chemistry & Biology of Membranes & Nanoobjects (UMR5248 CBMN), IECB, CNRS, Université Bordeaux, Institut Polytechnique Bordeaux, All. Geoffroy Saint-Hilaire, 33600 Pessac, France

² Laboratoire de Biogenèse Membranaire – UMR 5200 – CNRS, Université de Bordeaux, 71 Avenue Edouard Bourlaux, 33883 Villenave d'Ornon Cédex, France

³ European Institute of Chemistry and Biology – UMS3033/US001 – 2 Rue Robert Escarpit, 33607 Pessac, France

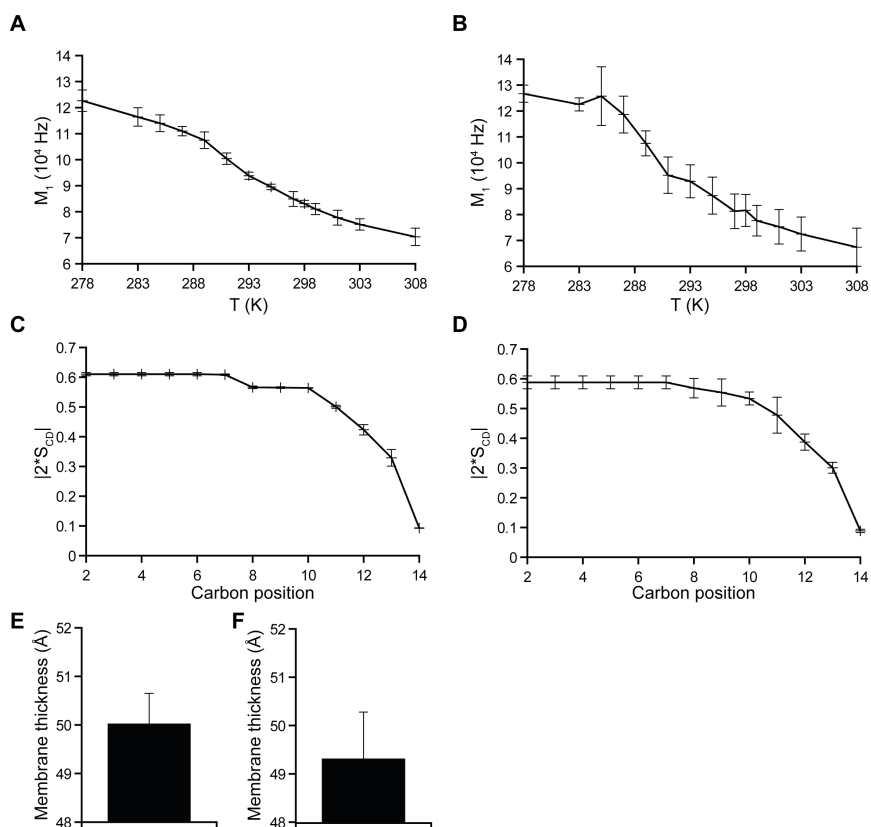


Figure S1. Estimation of the experimental errors for the peptide co-reconstitution method (A, C, E) or liposome preparation for protein constructs (B, D, F) for M_1 (A, B), $|2^*S_{CD}|$ (C, D) and membrane thickness assessment (E, F). Error bars are the standard deviations of three independent experiments, as described in section 2.2.

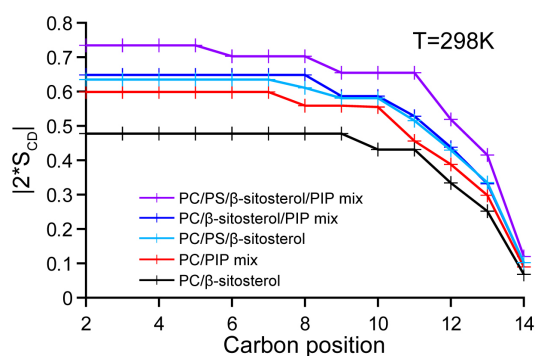


Figure S2. Comparison of the local order parameters $|2^*S_{CD}|$ as a function of the carbon position along the acyl chains of DMPC-d54 for the four lipid systems of this study, at 298K. Liposome compositions are: DMPC-d54/β-sitosterol 85/15, DMPC-d54/PIP mix 90/10, DMPC-d54/β-sitosterol/PIP mix 75/15/10, DMPC-d54/DMPS/β-sitosterol/PIP mix 65/10/15/10 (molar ratio) at pH=7-8. Representative error bars are shown in **Figure S1C**.

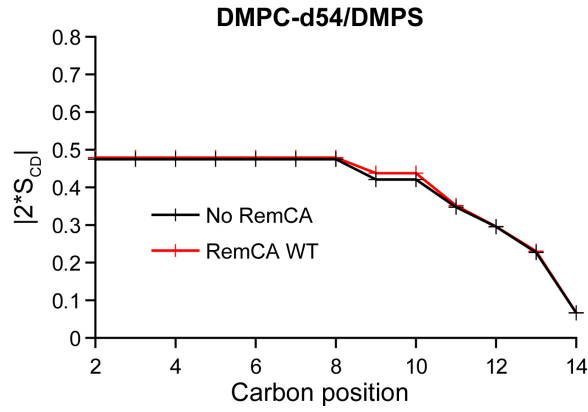


Figure S3. Local order parameters $|2^*S_{CD}|$ as a function of the carbon positions along the acyl chains of DMPC-d54 in absence (black) or presence (red) of RemCA WT. Liposome composition is DMPC-d54/DMPS 90/10 (molar ratio), at pH=7-8. Representative error bars are shown in **Figure S1C**.

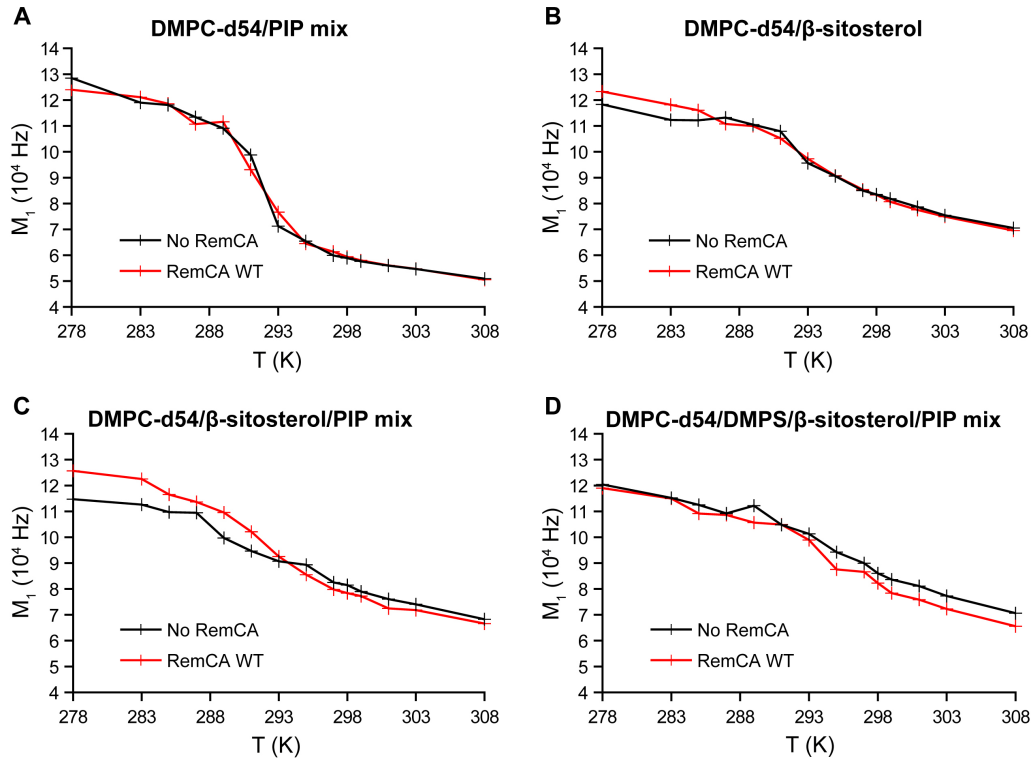


Figure S4. Variation of the first order spectral moments M_1 as a function of the temperature T in absence (black) or presence (red) of RemCA WT. Liposome compositions are (A) DMPC-d54/PIP mix 90/10, (B) DMPC-d54/ β -sitosterol 85/15, (C) DMPC-d54/ β -sitosterol/PIP mix 75/15/10, (D) DMPC-d54/DMPS/ β -sitosterol/PIP mix 65/10/15/10 (molar ratio), at pH=7-8. Representative error bars are shown in **Figure S1A**.

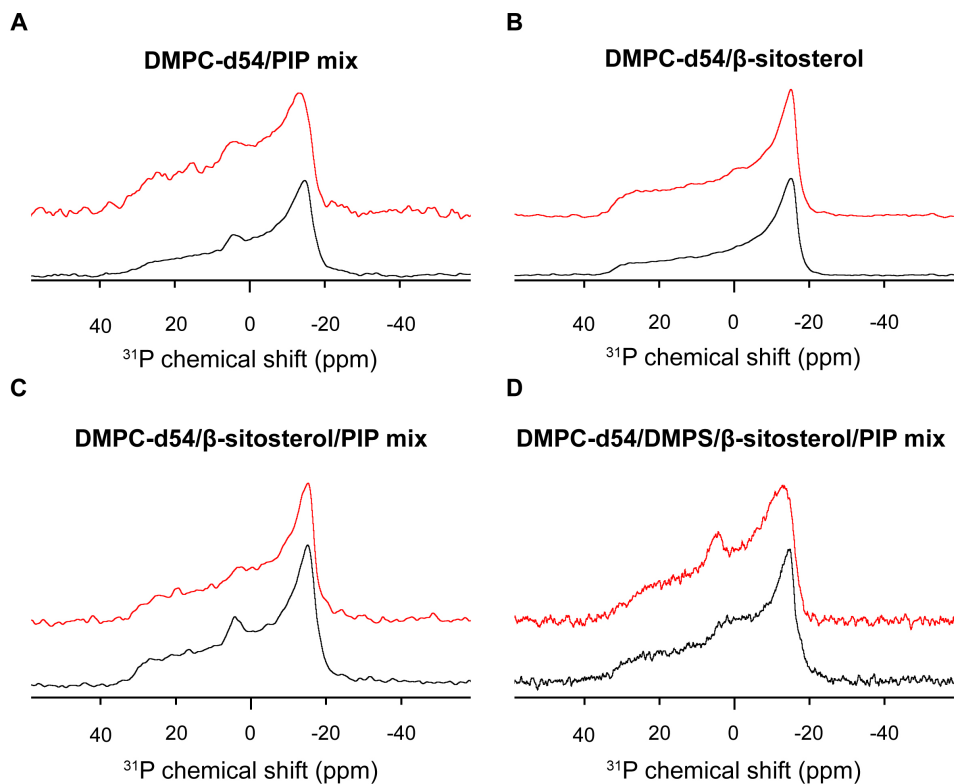


Figure S5. ^{31}P Hahn echo spectra in absence (black) or presence (red) of RemCA WT for different lipid systems. Liposome compositions are (A) DMPC-d54/PIP mix 90/10, (B) DMPC-d54/ β -sitosterol 85/15, (C) DMPC-d54/ β -sitosterol/PIP mix 75/15/10, (D) DMPC-d54/DMPS/ β -sitosterol/PIP mix 65/10/15/10 (molar ratio), at pH=7-8

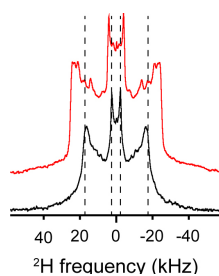


Figure S6. Comparison of ^2H quadrupolar spin echo spectra acquired at 298K in absence (black) or in presence (red) of RemCA WT in liposomes containing PIPs, hydrated with 1% acetate pH=3. The inner line pair indicates the Pake doublet frequency of the terminal CD_3 while the outer line pair indicates the plateau region (usually between positions 2 and 8). Liposome composition is: DMPC- $\text{d}54/\beta\text{-sitosterol}/\text{PIP}$ mix 75/15/10 (molar ratio), at pH=3

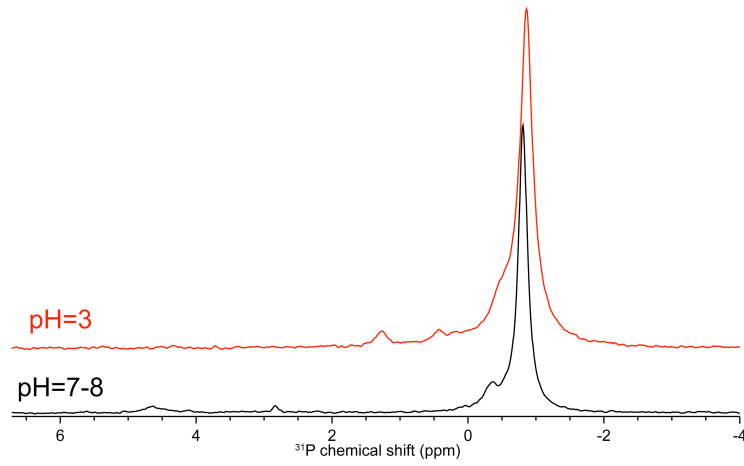


Figure S7. ^{31}P MAS ssNMR on DMPC-d54/ β -sitosterol/PIP mix 75/15/10 (molar ratio) in presence of RemCA WT at pH=7-8 (black) or pH=3 (red).

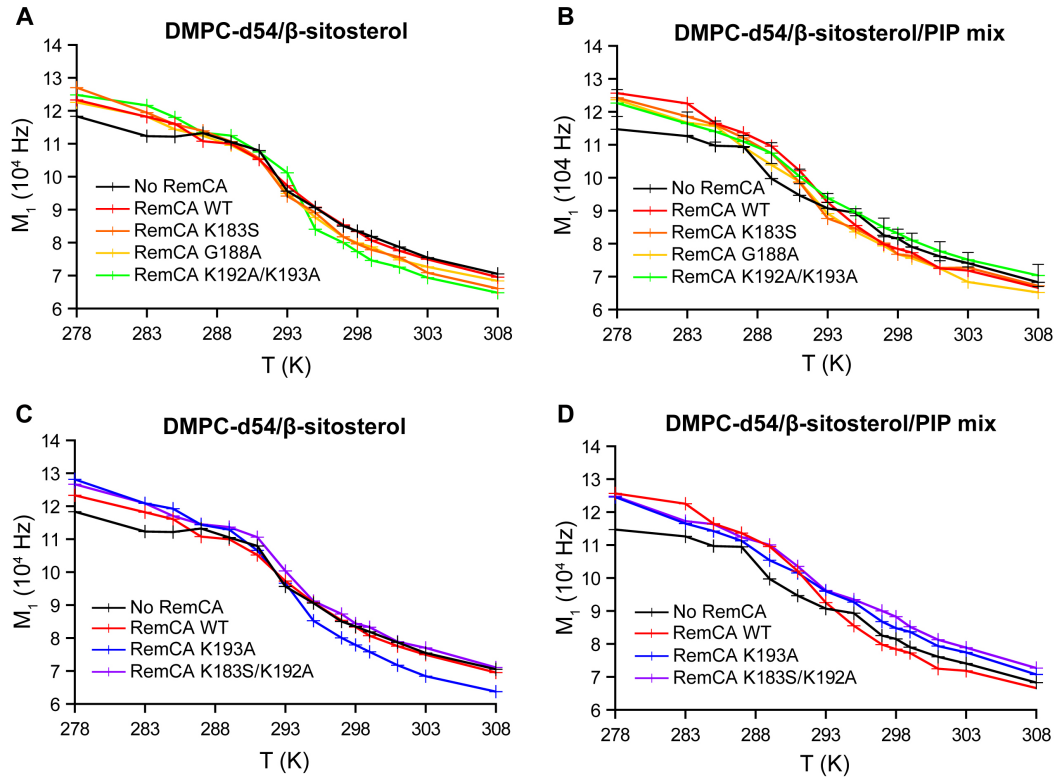


Figure S8. Variation of first order spectral moments M_1 as a function of the temperature T in presence of RemCA WT or mutated RemCA. Liposome compositions are (A, C) DMPC-d54/ β -sitosterol 85/15, (B, D) DMPC-d54/ β -sitosterol/PIP mix 75/15/10 (molar ratio), at pH=7-8. Representative error bars are shown in **Figure S1A**.

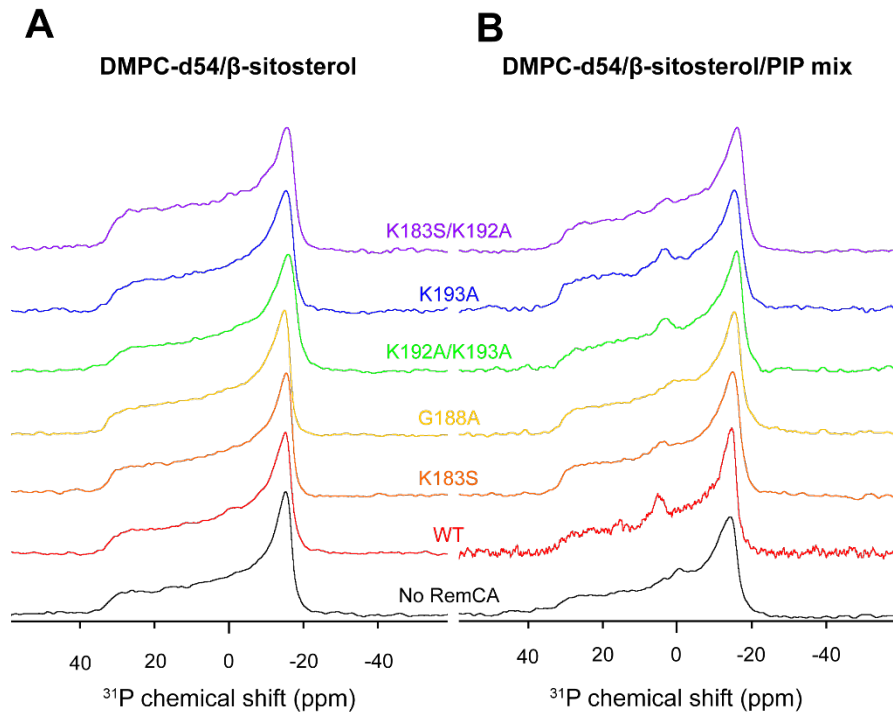


Figure S9. ^{31}P Hahn echo spectra in presence of various RemCA mutants. Liposome compositions are (A) DMPC-d54/ β -sitosterol 85/15 and (B) DMPC-d54/ β -sitosterol/PIP mix 75/15/10 (molar ratio), at pH=7-8.

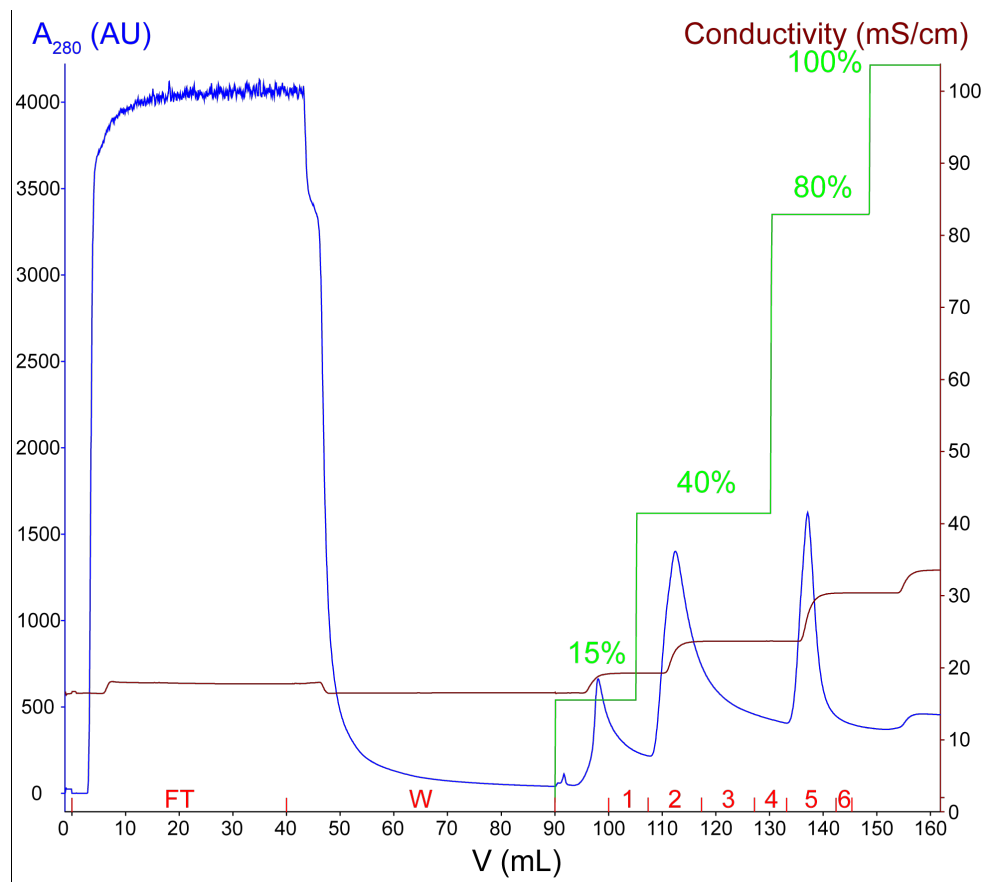


Figure S10. Histrap purification chromatogram of ^{15}N -, ^{13}C -labelled StREM1.3. FT: flow-through. W: wash. Blue curve: absorbance at 280 nm in arbitrary units. Brown curve: conductivity (mS/cm). Green curve: elution buffer percentage.

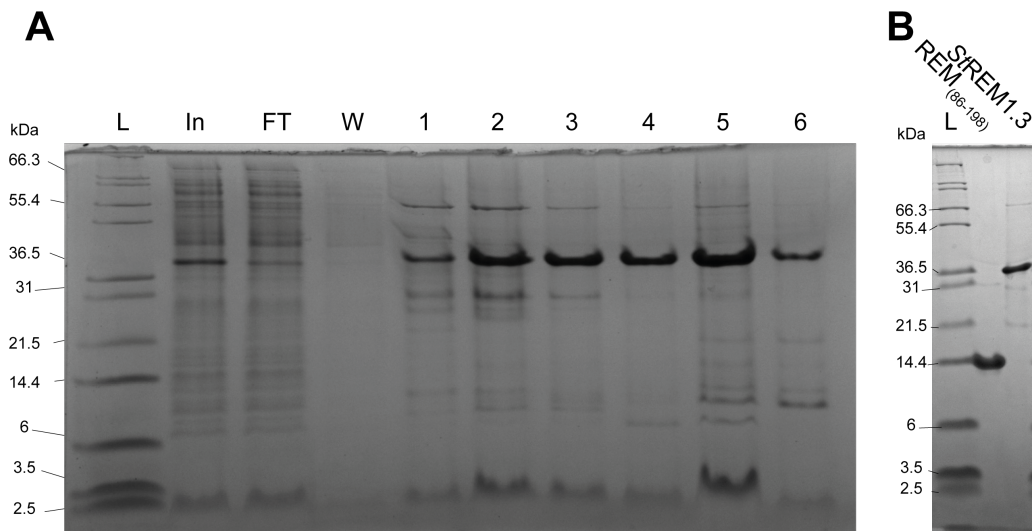


Figure S11. (A) SDS-PAGE of eluted fractions from figure S8. In: sample loaded into the column. 5 and 6 are pooled and purified further. (B) Example of pure protein samples for REM₈₆₋₁₉₈ and StREM1.3 analysed by SDS-PAGE. Coomassie-stained gels.

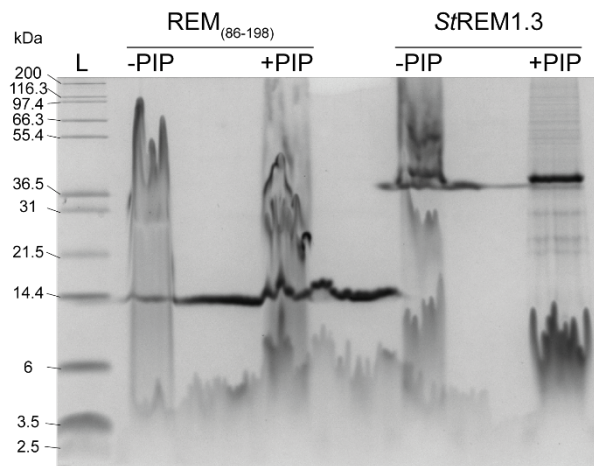


Figure S12. SDS-PAGE of liposomes containing, or not, PIP mix in presence of REM₍₈₆₋₁₉₈₎ or StREM1.3, at pH=7.4. Coomassie-stained gel.

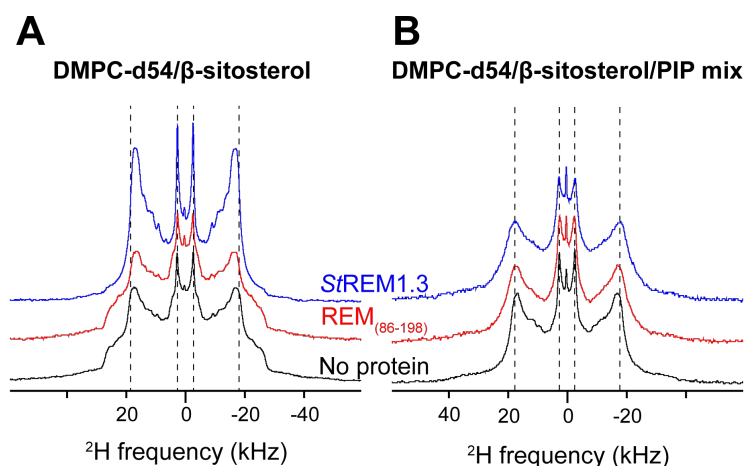


Figure S13. Comparison of ^2H quadrupolar spin echo spectra acquired at 298K in absence (black) or presence of REM_{86-198} (red) or StREM1.3 (blue). Inner line pairs indicate the Pake doublet frequency of the terminal CD_3 while outer line pairs indicate the plateau region (usually between positions 2 and 8). Liposome compositions are (A) DMPC-d54/ β -sitosterol 85/15 and (B) DMPC-d54/ β -sitosterol/PIP mix 75/15/10 (molar ratio), at pH=7.4.

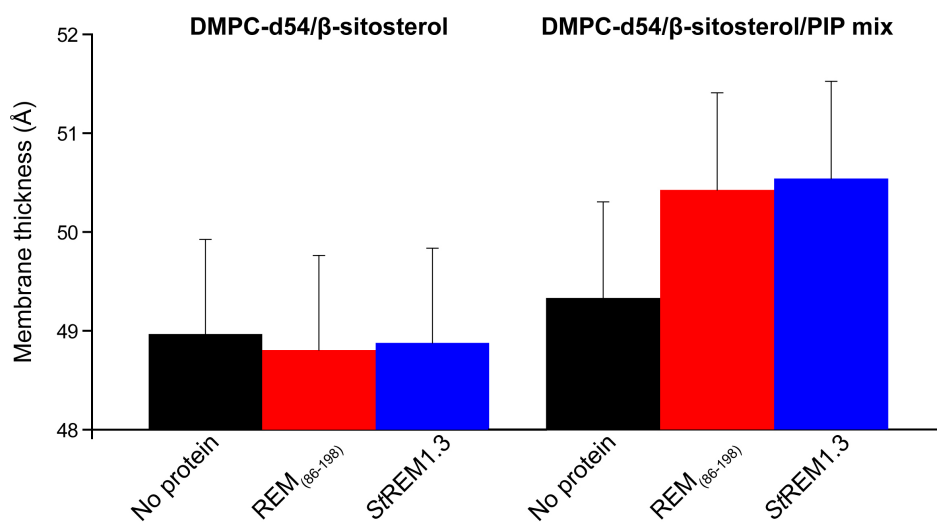


Figure S14. Membrane thickness at 298K calculated from the corresponding $[2 \cdot S_{\text{CD}}]$ (Figure 8). Liposome compositions are DMPC-d54/ β -sitosterol 85/15 and DMPC-d54/ β -sitosterol/PIP mix 75/15/10 (molar ratio), at pH=7.4. Error bars are assessed as described in Figure S1A, C, E.

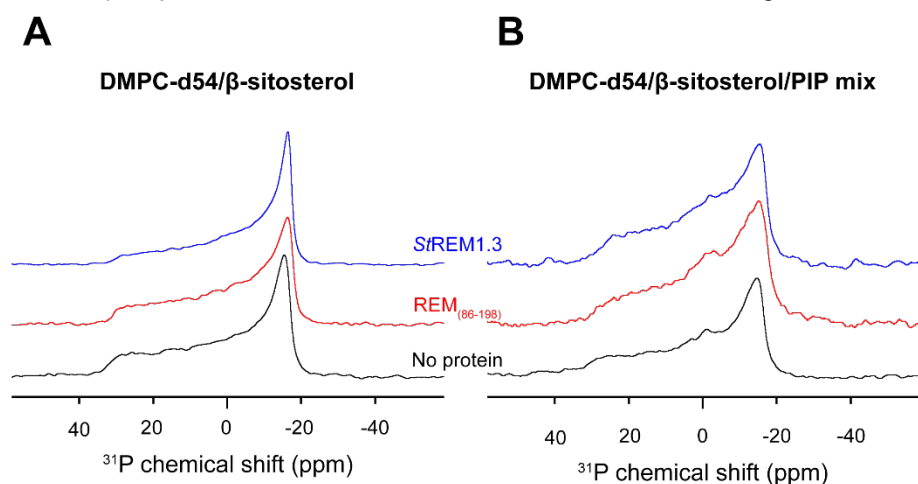


Figure S15. ^{31}P Hahn echo spectra in absence (black) or presence of REM_{86-198} (red) or StREM1.3 (blue). Liposome compositions are (A) DMPC-d54/ β -sitosterol 85/15 and (B) DMPC-d54/ β -sitosterol/PIP mix 75/15/10 (molar ratio), at pH=7.4.

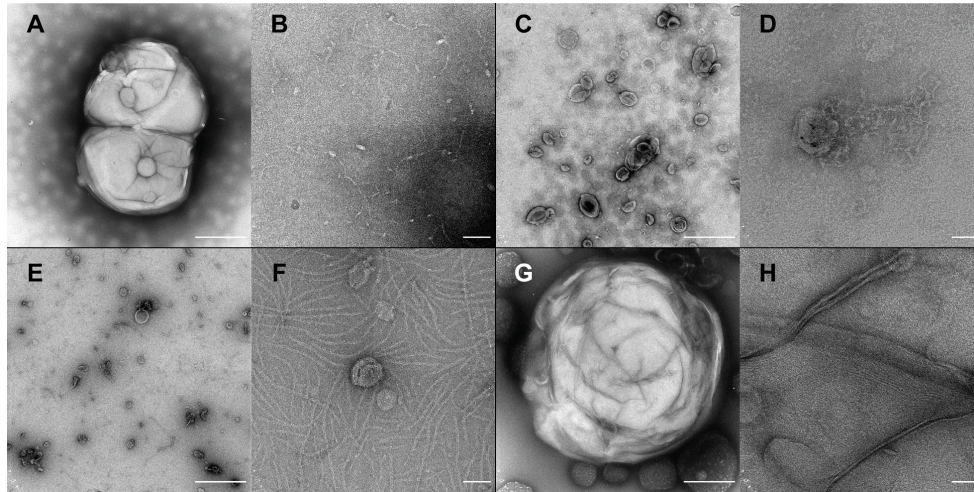


Figure S16. Negative staining electron microscopy of REM_{86-198} (A-D) and StREM1.3 (E-H) in liposomes DMPC-d54/ β -sitosterol 85/15 (A, B, E, F) and DMPC-d54/ β -sitosterol/PIP mix 75/15/10 (C, D, G, H) (molar ratio), at pH=7.4. Scale bars: (A, C, E, G) 500 nm or (B, D, F, H) 50 nm. Fewer filaments are observed for REM_{86-198} compared to StREM1.3 and the presence of PIP mix seems to reduce their number even more.

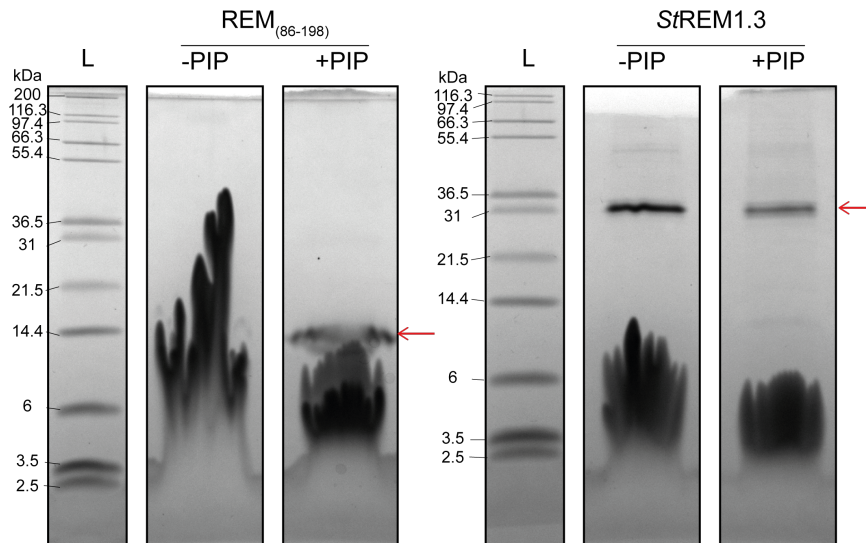


Figure S17. SDS-PAGE of liposomes containing, or not, PIP mix in presence of REM_{86-198} or StREM1.3 when attempting to remove filaments, at pH=7.4. For REM_{86-198} in liposomes in absence of PIP mix, the protein band might be hidden by the smear but the gel indicates a lack of a band. Red arrows indicate the expected molecular weight of each protein.

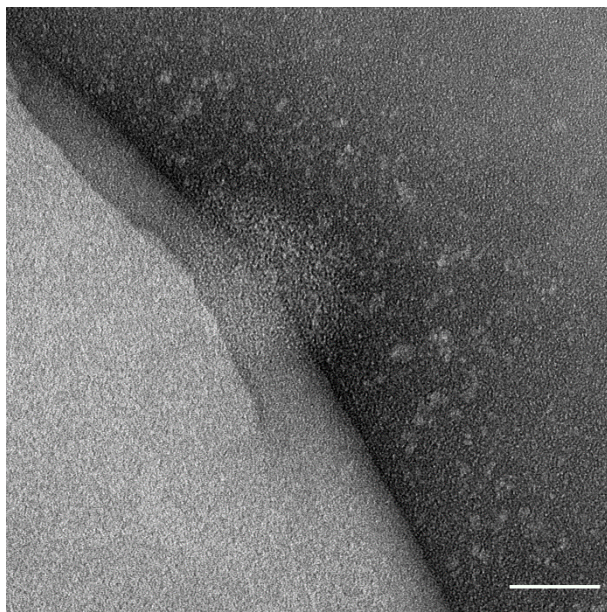


Figure S18. Negative staining electron microscopy of REM₈₆₋₁₉₈ in liposomes without filaments. Liposome composition is DMPC-d54/ β -sitosterol/PIP mix 75/15/10 (molar ratio), at pH=7.4.

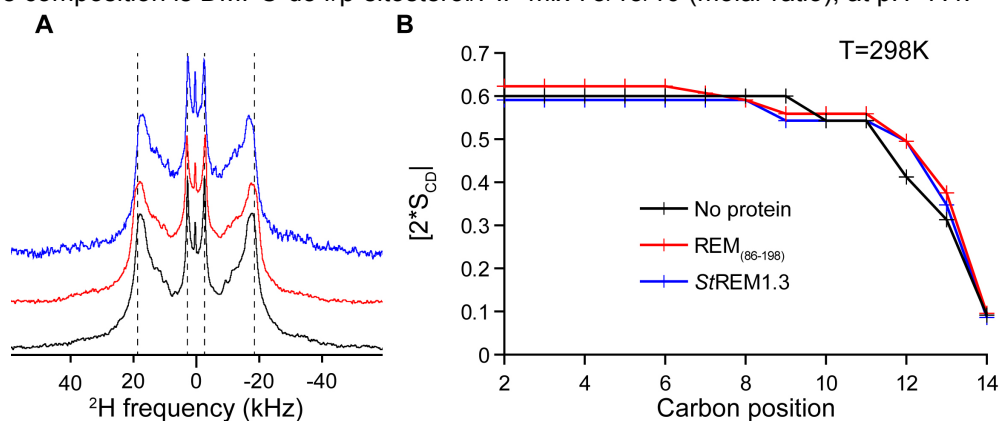


Figure S19. (A) Comparison of ^2H quadrupolar spin echo spectra acquired at 298K in absence (black) or presence of REM₈₆₋₁₉₈ (red) or StREM1.3 (blue) without filaments in either case. Inner line pairs indicate the Pake doublet frequency of the terminal CD_3 while outer line pairs indicate the plateau region (usually between positions 2 and 8). (B) Local order parameters $[2*S_{\text{CD}}]$ as function of carbon position along the acyl chains of DMPC-d54 from spectra in (A). Liposome composition is DMPC-d54/ β -sitosterol/PIP mix 75/15/10 (molar ratio), at pH=7.4. Representative error bars for (B) are shown in **Figure S1D**.

Article IV: addendum

In our study, we committed to sitosterol, which is the most abundant phytosterols in plant PM, with a role similar to cholesterol in ordering membranes above the phase transition temperature, where, by contrast, stigmasterol decreases the order membranes (Grosjean et al., 2015). What would it change, in terms of order and thermotropism, if we replaced sitosterol with stigmasterol? Lipid systems without and with PIP mix displayed a lesser M_1 in the fluid phase yet retained comparable M_1 in the gel phase, compared to their sitosterol counterparts (Figure 69). This loss of M_1 can be interpreted as a loss of global order parameter, which is confirmed by computing local order parameters $|2*S_{CD}|$. RemCA WT had no significant effect on liposomes made only of PC/stigmasterol but showed significant increase in global order parameters in the gel phase (figure 70). Due to the very large half-height widths of most peaks in the gel phase, computing $|2*S_{CD}|$ is difficult and very much prone to error. We did not compute them.

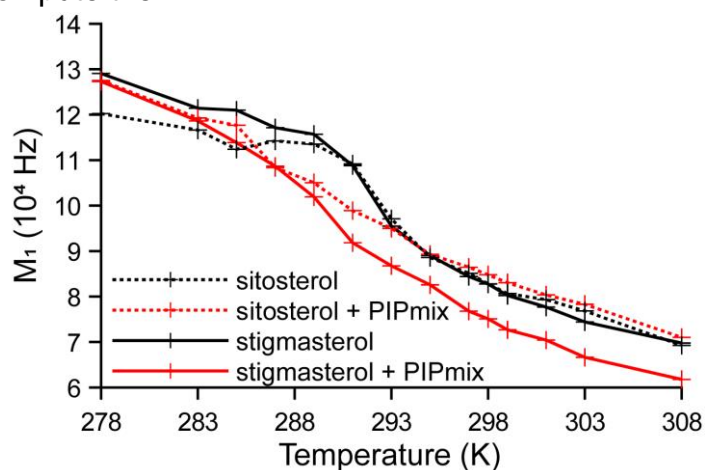


Figure 69

Comparison of first spectral moments M_1 between four different lipid systems as a function of temperature: 85/15 PC/sitosterol (black, dashed), 75/15/10 PC/sitosterol/PIPmix (red, dashed), 85/15 PC/stigmasterol (black, full), 75/15/10 PC/sitosterol/PIPmix (red, full). Data on systems with sitosterol comes from (Legrand et al., 2019).

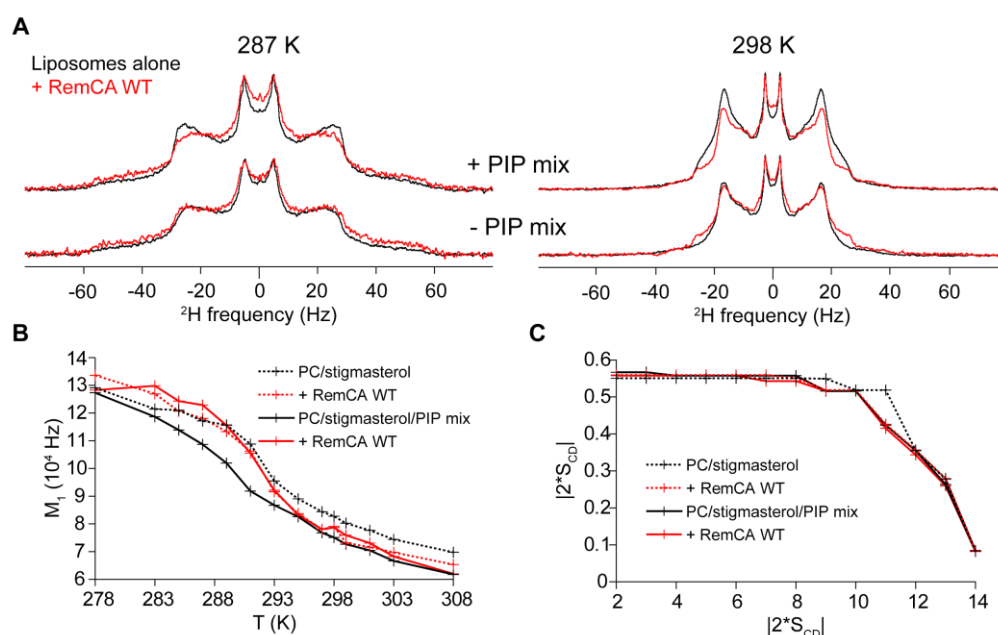


Figure 70

On the effect of RemCA WT in a PC/stigmasterol/PIPs lipid system. (A)

Superimposed ^2H quadrupolar echo spectra in the designed conditions. Black: liposomes alone. Red: liposomes with a 1/20 RemCA WT/lipid ratio. (B) M_1 as a function of temperature for without or with PIPmix (dashed vs full lines) and RemCA WT (black vs red). (C) $|2*S_{CD}|$ as a function of carbon position along the acyl chains of DMPC-d54. The legend is the same as (B).

So replacing sitosterol with stigmasterol modified the effect of a synthetic RemCA WT peptide on lipid order: with stigmasterol, there is no discernible effect on $|2*S_{CD}|$ in the fluid phase when there is a significant increase in $|2*S_{CD}|$ with sitosterol; whereas RemCA WT increased M_1 , and thus global order, in presence of stigmasterol in the gel phase while no effect was found in presence of sitosterol. This confirms that these two phytosterols have different effects on lipid order depending on temperature (section I.C.4) (Beck et al., 2007; Grosjean et al., 2015). More generally, the diversity and variability of plant sterols should always be accounted for when dealing with their behaviour in membranes.

Article V

This article is in a draft state. It is about reconstituting StREM1.3 nanodomains *in vitro*. Based on all the data and – partially – hypothetical models available on membrane attachment and clustering, we were confident enough to try to reconstruct these nanodomains in a minimal system. This would: (1) confirm our model (see Article IV) on StREM1.3' nanodomain clustering and (2) provide an *in vitro* platform for further investigations.

We started by assessing which lipids a GFP tagged REM₈₆₋₁₉₈ would bind to. By forming giant lipid vesicles (1-20 µm) labelled the fluorescent lipid rhodamine-PE (rhod-PE), we could, qualitatively, determine which negatively charged lipids (PS, PA, PIPs) are required for membrane binding. It appeared that StREM1.3 binds to any lipid bearing terminal phosphates, but notably not PS.

A next step was to disrupt REM₈₆₋₁₉₈'s coiled-coil oligomerisation domain to assess the effect of forcing a monomeric state on its membrane interactions, on giant vesicles, and biological activity, by assessing its ability to hinder the cell-to-cell propagation of the Potato Virus X (PVX). Though StREM1.3 was shown to interact with PIPs and PA, we observed the effect of PS synthase knockouts on StREM1.3 nanodomain organisation. At last, we attempted to reconstitute and observe nanodomains of StREM1.3 in a minimal system by cryoEM and AFM.

I performed the experiments involving giant vesicles. Marie-Dominique Jolivet performed all the *in vivo* assays, with coiled-coil mutants of StREM1.3 and PS synthase knockouts (*pss1*). I prepared samples for cryoEM and performed the observations with the tremendous help of both engineers of the CBMN EM platform: Dr Marion Decossas and Dr Tan Sisareuth. AFM was handled by collaborators, namely Dr Marisela Vélez for. The following draft was written by myself, figures included.

I. Introduction

Remorins belong to a multigenic family of plant proteins (Raffaele et al., 2007b). They display a broad range of functions and interactors: from protection against biotic and abiotic stress, inception of symbiosis to hormone signalling response (Gouguet et al., 2020). Their most well-known characteristic is to segregate into ~ 80 nm membrane nanodomains (Gronnier et al., 2017; Legrand et al., 2019) in the plasma membrane's (PM) inner leaflet. A model for the nanoclustering of StREM.3 has been proposed (Gouguet et al., 2020), in which homo-oligomeric remorins bind to phosphatidylinositol 4-phosphate (PI4P) negatively charged head groups via their remorin C-terminal anchors (RemCA) and recruit sterols and other remorins and PI4P in their vicinity to form a membrane nanodomain (Gronnier et al., 2017; Legrand et al., 2019; Perraki et al., 2012), while coiled-coil homo-oligomerisation ensures an efficient PM targeting (Martinez et al., 2018). This nanodomain organisation was shown to be cytoskeleton-dependent (Szymanski et al., 2015). StREM1.3's N-terminal intrinsically disordered domain (IDD) can be phosphorylated (Perraki et al., 2018) and is thought to mediate protein-ligand and protein-protein interactions (Khan et al., 2017; Nishi et al., 2013; Uversky, 2013).

Granted a sufficient understanding of StREM1.3's nanodomains, we will attempt to reconstitute these *in vitro* and to observe them by cryo-electron microscopy (cryoEM) and atomic force microscopy (AFM). This would confirm our proposed nanodomain formation model and provide us with a powerful tool for future biophysical studies.

II. Material and methods

A. Protein purification

REM₈₆₋₁₉₈ and StREM1.3 are produced and purified as described in (Legrand et al., 2019).

Production of GFP-REM₈₆₋₁₉₈ is identical to REM₈₆₋₁₉₈ and StREM1.3. Cells are broken by sonication and the supernatant is loaded onto a HisTrap affinity column controlled by an Atka Pure 25 HPLC system (GE Healthcare) equilibrated with equilibration buffer (20 mM HEPES 150 mM NaCl 20 mM imidazole 0.02% NaN₃ pH = 7.4) and eluted with a stepwise gradient of elution buffer (20 mM HEPES 150 mM NaCl 500 mM imidazole 0.02% NaN₃ pH = 7.4). Proteins eluted at 80% elution buffer was dialysed against 10 mM HEPES 150 mM NaCl 0.02% NaN₃ pH = 7.4 at 4°C overnight. The sample should turn turbid as GFP-REM₈₆₋₁₉₈ will assemble overnight (MARTINEZ). It is centrifuged at 100000 g 4°C 1h, the pellet, containing both GFP-REM₈₆₋₁₉₈ and contaminants, is resuspended then pelleted again. The last supernatant contains pure GFP-REM₈₆₋₁₉₈.

Production of REM₁₋₁₁₆ in BL21-DE3 cells is induced by 1 mM IPTG during 3h at 37°C. Cells are broken by sonication and the supernatant is loaded onto a HisTrap affinity column controlled by an Atka Pure 25 HPLC system (GE Healthcare) equilibrated with equilibration buffer and eluted with elution buffer (buffer compositions as described above). The eluted protein is adjusted to 0.5 mM EDTA and 1 mM DTT then TEV protease is added in a ~ 1/200 mass ratio. The mixture is incubated for 3h at RT then dialysed at 4°C overnight against 10 mM HEPES 50 mM NaCl 0.02% NaN₃

pH=7.5. Proteins were adjusted to 7M urea for 1h at room temperature before being loaded on a HisTrap column equilibrated with 20 mM HEPES 50 mM NaCl 7 M urea pH=7.4 and 20 mM HEPES 150 mM NaCl 7 M urea pH=7.4. TEV-cleaved REM₁₋₁₁₆ flowed through without binding to the resin and was desalted against 10 mM HEPES 150 mM NaCl 0.02% NaN₃ pH=7.4 using a HiPrep column (GE Healthcare).

B. Preparation and observation of giant vesicles (GVs)

200 µg of lipids, are mixed in solvent, adjusted to 0.1 mg/mL (final concentration) of rhodamine-dioleoyl-PE (RhodPE), spread drop-by-drop on a Teflon disk and dried for at least 1 h in a vacuum chamber. The remaining lipids are stored at -20°C for future use. The disk is pre-hydrated under a water-saturated nitrogen stream, covered with 5 mL of 300 mM sucrose and incubated at 34°C overnight. Observation chambers are coated with 5% BSA (w/v) for 20 min then rinsed three times with 10 mM HEPES 300 mM NaCl pH = 7.4. With large pipette tip, to avoid shearing, a drop of GV solution is added to the chamber, followed by $\sim 2 \cdot 10^{-12}$ moles of GFP-REM₈₆₋₁₉₈, WT or EEE, if necessary. Lipid systems were 0.5 / 0.26/0.08/0.16 dipalmitoyl-PC (DPPC)/di-linoleoyl-PC (DLPC)/sitosterol/anionic lipid (as indicated) plus rhodPE (molar ratio). All lipids were from obtained from Avanti.

C. Nanodomain reconstitution for cryoEM

Lipids are hydrated to 10 g/L with 10 mM HEPES 150 mM NaCl 0.02% NaN₃ pH = 7.4, submitted to five freeze-thaw-vortex cycles (liquid N₂, 42°C water bath), mixed with GFP-REM₈₆₋₁₉₈ to final concentrations of 0.5 g/L lipids and 1 µM GFP-REM₈₆₋₁₉₈ then incubated at room temperature for 1-2h. Samples are loaded on glow discharged cryoEM grids, blotted then frozen in liquid ethane using an EM-GP plunge freezer (Leica). Observed are carried out on an FEI20 (Tecnai) operating at 200 keV.

D. Agroninfiltration in *Nicotiana benthamiana*

Proteins were transiently expressed via infection with OD₆₀₀ = 0.2 *Agrobacterium tumefaciens* (strain GV3101) bearing pK7WGY2-StREM1.3-EEE (N-terminal YFP-tag) in four-weeks-old *Nicotiana benthamiana* plants grown at 22-24°C in a greenhouse. Leaves are observed 3 days post-infection by confocal microscopy.

E. Confocal microscopy

Observations were performed on a Leica SP5 confocal laser scanning microscopy system (Leica, Wetzlar, Germany) equipped with Argon, DPSS and He-Ne lasers and a hybrid detector. GFP was excited at 488 nm, YFP was excited at 514 nm and rhodPE was excited at 565 nm.

III. Results

A. StREM1.3 specifically binds to PA and PIPs, but not PS

To reconstruct a remorin nanodomain, its lipid binding specificity must be precisely assessed. StREM1.3 is located at the PM's inner leaflet, where most negatively charged lipids lie. Expression of SAC1 in *Nicotiana benthamiana* leaves, which

removes the last phosphate of PI4Ps, abolishes PM targeting (Gronnier et al., 2017). ^2H static ssNMR confirmed a specific interaction between StREM1.3, with or without its N-terminal IDD, and PIPs along with an overall increase in lipid order (Legrand et al., 2019).

A truncated GFP-tagged StREM1.3 (GFP-REM₈₆₋₁₉₈), without its N-terminal IDD, is mixed with GVs of defined lipid compositions, comprising some rhodamine-PE (rhoPE). Phase separation was favoured by mixing di-palmitoyl-phosphatidyl-choline (DPPC), di-linoleyl-phosphatidyl-choline (DLPC) and sitosterol. Using confocal microscopy, we assessed GFP-REM₈₆₋₁₉₈'s binding ability towards negatively charged lipids (Figure 71). GFP-REM₈₆₋₁₉₈ does not bind to neither PC nor PS, but does bind to PA and various phosphoinositides: PI4P, PI5P, PI(4,5)P₂, PI(3,4,5)P₃ and PIPs from bovine brain (PIPmix) (PIPmix is PS/PI/PI4P/PI4,5P₂ 50/20/15/15 (Gronnier et al., 2017)).

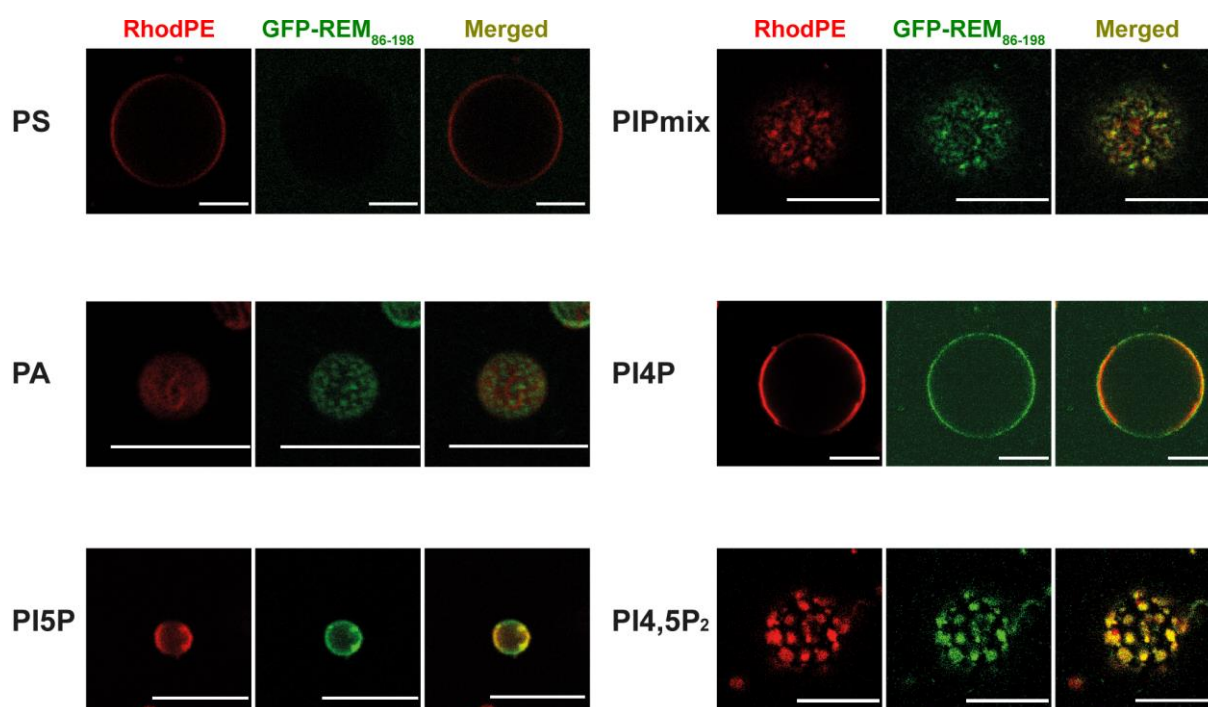


Figure 71

Liposome binding assay on GFP-REM₈₆₋₁₉₈. RhodPE (red) labels all liposomes. GFP-REM₈₆₋₁₉₈ (green) decorates liposomes it binds to. Scale bars: 10 μm .

To test whether PS could play an indirect role in the nanodomain clustering of StREM1.3, we assessed its distribution at the PM in epidermal cells of *Nicotiana benthamiana* leaves expressing wild-type (WT) function PS synthase (Platre et al., 2018) or a knocked-out (KO) version. Preliminary results show that StREM1.3 was still able to segregate into nanodomains at the PM, although these appear larger and more diffuse (Figure 72).

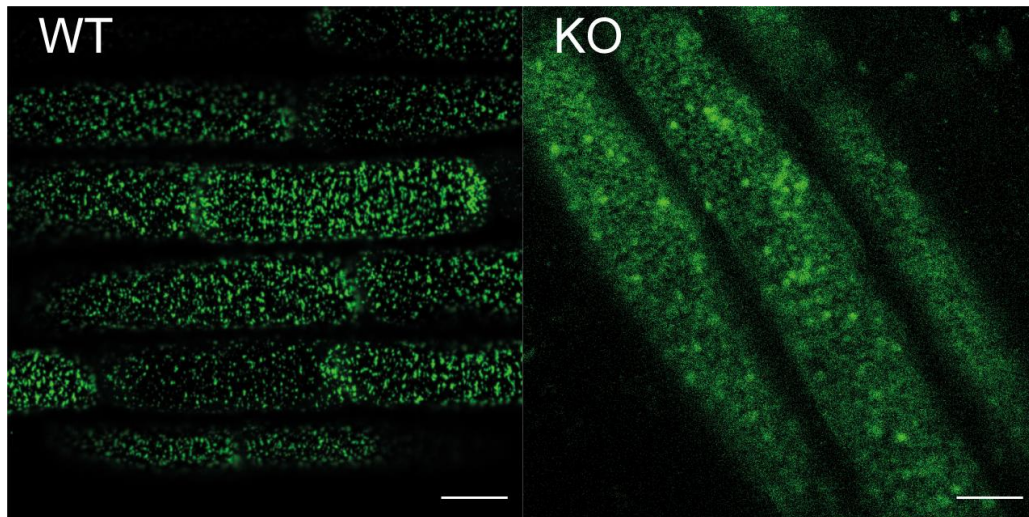


Figure 72

PM repartition of GFP-StREM1.3 in 5-days old seedling roots of *Arabidopsis thaliana* expressing WT or knocked-out (KO) pss. Scale bars: 10 μ m.

B. StREM1.3 must be oligomerised to ensure a tight membrane binding

Mutation of critical hydrophobic residues impairs PM targeting (Martinez et al., 2018). Here, leucines were mutated to glutamates, to remove hydrophobic residues at these positions, instead of prolines, to avoid disruption of coiled-coil helices.

Just like REM₈₆₋₁₉₈-PPP, REM₈₆₋₁₉₈-EEE displays a severely impaired PM targeting *in vivo* (Figure 73). Its biological activity, as assessed by its ability to slow down the cell-to-cell propagation of the Potato Virus X (Perraki et al., 2014, 2018; Raffaele et al., 2009b), remains to be tested. Binding of PIP-enriched vesicles by GFP-REM₈₆₋₁₉₈-EEE *in vitro* seems vastly reduced (Figure 74), although these observations should be repeated to make sure this result is reproducible (n = 2).

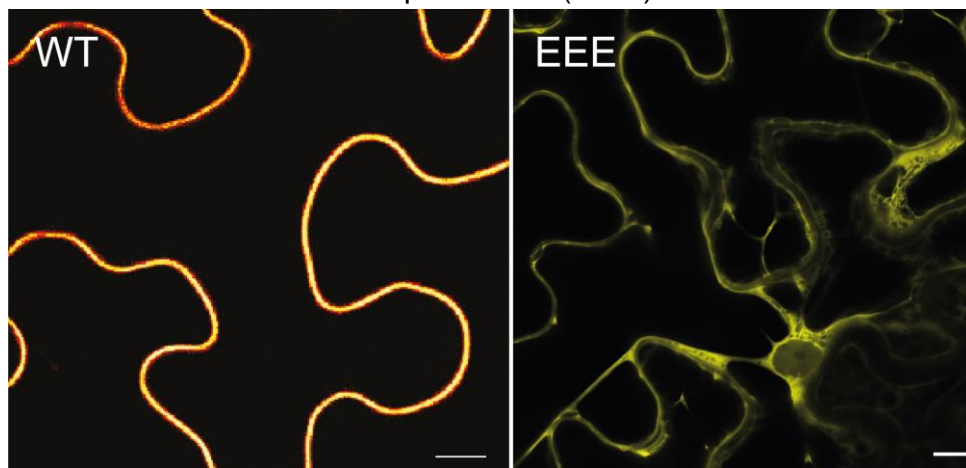


Figure 73

Cellular localisation of StREM1.3 WT (left) (Gronnier et al., 2017) and coiled-coil disrupted EEE (right). Scale bars: 10 μ m.

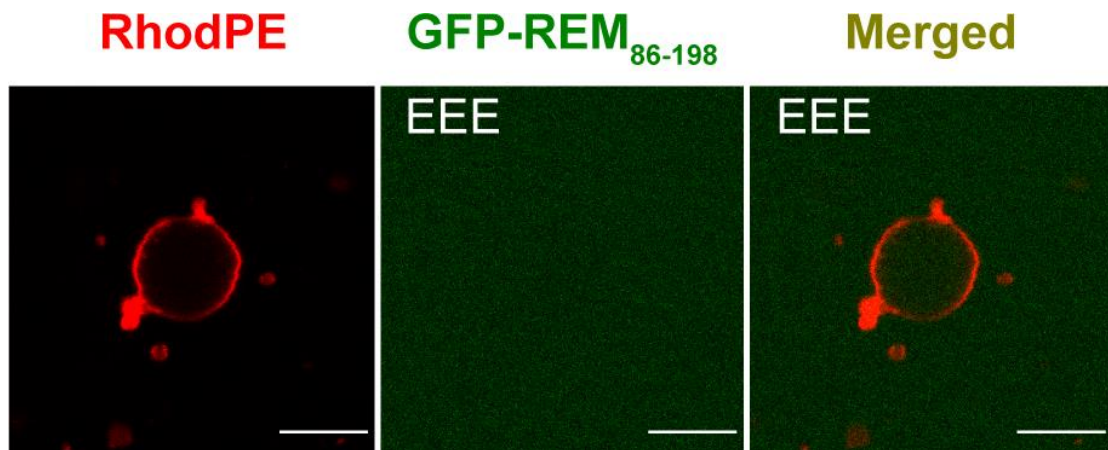


Figure 74

Liposome binding assay for GFP-REM₈₆₋₁₉₈-EEE on liposomes containing PIPmix. Notice the homogeneous background noise from the GFP and its absence of signal on the liposome. Scale bars: 10 μ m.

C. Close visual of synthetic remorin nanodomains

Considering the mass of structural data available on StREM1.3 nanodomains, both from previous sections and literature, we shall now attempt to reconstitute and observe them. Were the GVs from section 1 simply decorated with GFP-REM₈₆₋₁₉₈ or where they organised into nanodomains? Confocal microscopy does not allow to unambiguously distinguish nanodomains about 80 nm wide. Also, GVs, unless they are resting at the bottom of the observation chamber, which is rare, swim in solution. Yet, spt-PALM and STED super-resolution microscopies require an immobile sample. Other methodologies must be employed.

We turned ourselves towards cryoEM and AFM. All we should need are bulk lipids, here DPPC and DLPC, some sterols, here sitosterol, and some PIPs. For cryoEM, liposomes, mostly LUVs (100 - 1000 nm in diameter) and SUVs (< 100 nm in diameter) with some multilamellar vesicles as well, are pre-formed by five freeze-thaw-vortex cycles then mixed with GFP-REM₈₆₋₁₉₈. The rationale of choosing the GFP-tagged version was double: (1) the N-terminal IDD is not involved in membrane interactions (Legrand et al., 2019), (2) REM₈₆₋₁₉₈ alone is too small to be unambiguously detected by cryoEM (13 kDa), the GFP makes it 27 kDa bigger (total size: 40 kDa) and thus easier to spot.

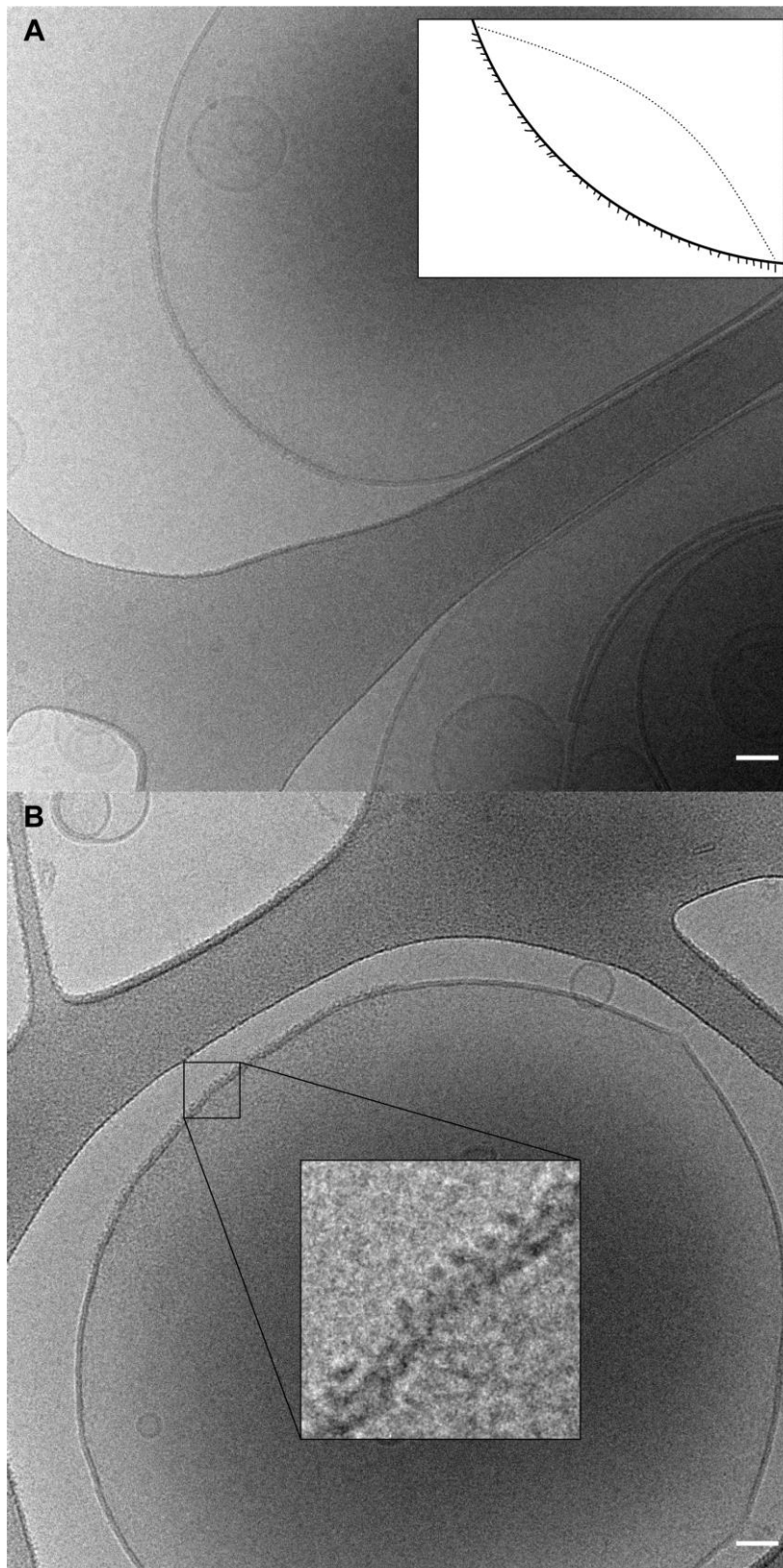


Figure 75

CryoEM images of GFP-REM₈₆₋₁₉₈ nanodomains. Notice how the protein decorates both liposomes with a heterogeneous repartition. (A) *Inlet*: schematic description of a GFP-REM₈₆₋₁₉₈ nanodomain. Proteins attach to the outer leaflet of the liposome and can be easily detected on the liposome's equatorial plane. A region

of the liposome surrounding this equatorial plane (dashed line) appears rippled: it could be the rest of the nanodomain outside the equatorial plane. (B) *Inlet*: closer view of a GFP-REM₈₆₋₁₉₈ nanodomain (X5 magnification). Scale bars: 50 nm.

We observe dense objects decorating patches of liposomes (Figure 75A, *inlet*). In these patches, one can distinguish small cylindrical objects directly and exclusively attached to the outer leaflet of liposomes (Figure 75A-B). Since these objects are absent of samples without GFP-REM₈₆₋₁₉₈, we conclude that these objects are GFP-REM₈₆₋₁₉₈ and these patchy structures are, or at least resemble closely to, GFP-REM₈₆₋₁₉₈ nanodomains. Tomography would be required to assess the distribution of angles between these objects and the bilayer they are attached to. In the top image, the membrane alone is 6.8 ± 0.3 nm thick and the nanodomain is 10.8 ± 1.3 nm thick. In the bottom image, thicknesses are 5.3 ± 0.1 nm for the membrane alone and 10.4 ± 0.3 nm for nanodomains. Thus, these nanodomains seem to be 4-5 nm thicker than the bulk membrane due to the presence of the remorin (Figure 75B, *inlet*).

In our quest to obtain a reliable reconstitution protocol, and to push the resolution barrier lower, we switched to atomic force microscopy (AFM) to study the products of our nanodomain reconstitution attempts, using the same molecular actors as for cryoEM. Experiments are still ongoing.

IV. Discussion

Membrane targeting of StREM1.3 relies on PA and PIPs but not PS (Figure 71). We should note that all three are available at PM's inner leaflet. Thus, the anionic phospholipid must bear a free terminal inorganic phosphate at its extremity to be targeted by RemCA through electrostatic interactions (Gronnier et al., 2017). Knocking out the production of PS provoked minor changes in nanoclustering that could be construed as a consequence of modifications to cell metabolism and signalling induced by the deprivation of PS, rather than implying an interaction between StREM1.3 and PS (Figure 72).

Disruption of the coiled-coil, as exemplified by StREM1.3-EEE *in vivo*, on *Nicotiana benthamiana* leaves (Figure 73), and GFP-REM₈₆₋₁₉₈-EEE *in vitro* on giant vesicles (Figure 74), greatly reduces membrane targeting. So, to reconstitute nanodomains of StREM1.3, the minimal set of partners seems to be: REM₈₆₋₁₉₈, i.e. three RemCA plus a coiled-coil domain to permit a homotrimerisation (Martinez et al., 2018), PIPs, sterols (Gronnier et al., 2017; Legrand et al., 2019) and bulk lipids, such as DPPC and DLPC.

With this minimal set of partners, we were able to decorate liposomes with patches of GFP-REM₈₆₋₁₉₈. These patches shared every expected feature of a nanodomain: (1) a finite width around a few hundred nanometres (roughly) so not all the liposome is covered and (2) it is enriched in GFP-REM₈₆₋₁₉₈ (Figure 75). The limitation in size of these nanodomains would come from the exhaustion of nanodomain components, particularly the protein and PIPs, in its vicinity.

V. Conclusion

We are currently attempting to improve the yield of our protocol for the reconstitution of StREM1.3 nanodomains. So far, we were able to reconstitute and observe GFP-REM₈₆₋₁₉₈ nanodomains using cryoEM, but analyses on REM₈₆₋₁₉₈ and StREM1.3, by both cryoEM and AFM are on their way. Once more thorough observations can be performed, studying the arrangement of these remorins inside a nanodomain will provide capital insights into their functioning. Another key methodology to achieve this goal would be electron cryotomography to reconstruct a 3D model of a remorin nanodomain.

Conclusion

1. What is the nanoclustering mechanism of StREM1.3?

As detailed in Article V, StREM1.3 binds to negatively charged phospholipids with the exception of PS. In other words, it targets phospholipids with a free terminal phosphate: PIPs and PA. StREM1.3 has an ordering effect on lipid membranes mimicking nanodomains (Article IV) (Legrand et al., 2019), which is an expected feature of nanodomains enriched in both cholesterol (Raffaele et al., 2009b) and PIPs with saturated acyl chains (Furt et al., 2010). Indeed, both PIPs and sterols seem important for RemCA to influence membrane dynamics (Article IV) (Legrand et al., 2019). And so we come back to wandering whether this nanoclustering is lipid-, protein- or interactome-driven. Even though PIP clusters may pre-exist (Bilkova et al., 2017; van den Bogaart et al., 2011; Ji et al., 2015), there is an undeniable effect of StREM1.3 on lipid dynamics that we attributed to protein-driven nanoclustering. Thus, both mechanisms, PIP- and StREM1.3-induced clustering seem at work. The influence of the interactome will be discussed in section 3.

Oligomerisation of StREM1.3 was proved to depend on the formation of a coiled-coil domain sustained by hydrophobic contacts, and whose integrity is needed to ensure an efficient PM targeting *in vivo* (Article I) (Martinez et al., 2018). In addition, these coiled-coil domains are the building blocks of StREM1.3 filaments. Moreover, the nanoclustering mechanism of StREM1.3 is linked to its ability to oligomerise: it cannot be summarised by RemCA alone, only by RemCA plus the coiled-coil domain, (the N-terminal IDD is dispensable). Yet, phosphorylation modifies PM mobility, hinting at a crucial influence of StREM1.3's interactome on its PM repartition (Article II) (Perraki et al., 2018). These interactions are postulated to happen mainly at the N-terminal IDD, challenging the idea that this domain would be completely irrelevant to the protein's behaviour at the PM. We will elaborate further on this line of thought in section 3.

Aside from StREM1.3 specifically, we still wonder what differences in nanoclustering mechanism produce such a variety of different remorin nanodomains in *Arabidopsis thaliana* (Jarsch et al., 2014). Reminiscing on the diversity of RemCA domains involved herein (Konrad et al., 2014), some of which are acylated or display a quite different repartition of basic, acidic and hydrophobic residues, or both, we could attribute some of these differences in PM repartition to differences in lipid specificity. However, AtREM6.1 and AtREM1.2 strongly anti-colocalise even though their RemCA domains both bear a rather basic N-terminal and a rather acidic C-terminal with two palmitoylation sites. In such a case, to test whether the RemCA is the sole determinant of their PM repartition, one could swap the RemCA of one remorin with the other and assess whether they would then colocalise. In the same vein, one could swap coiled-coil domains instead of RemCA: where would a hybrid oligomeric remorin be localised?

Alternatively, we can think that the RemCA is not the sole determinant in PM repartition and colocalisation or anti-colocalisation with other remorins. Once more, the answer we seek might lie within the interactome (section 3).

2. What is the minimal set of partners required to make StREM1.3 nanodomains?

The work towards the reconstitution of minimal StREM1.3 nanodomains *in vitro* has begun. We know that PIPs and PA but not PS interact StREM1.3 (Article V) and that sterols are essential partners of this nanodomain system (Article IV) (Legrand et al., 2019). Moreover, knockouts of PS synthase mutants, effectively removing all PS content from the cells, do not prevent the formation of StREM1.3 nanodomains.

For now, we hypothesise that the necessary partners for the formation of these nanodomains are: REM₈₆₋₁₉₈, a bulk phospholipid like PC, PIPs and sterols. The importance of acyl chain lengths and unsaturations, although important in a case like the Ras nanodomain system (Zhou et al., 2017), was not studied here: the combination of electrostatic interactions with PIPs and hydrophobic effects both involving the RemCA and the PM were already shown to be the major mechanisms of membrane targeting (Gronnier et al., 2017). Also, StREM1.3, unlike Ras, does not possess a farnesyl anchor, hence a lesser focus on a hypothetical acyl chain specificity.

3. How interactors of StREM1.3 may regulate its relationship with membranes and biological functions?

To understand how StREM1.3's interactome may influence its behaviour in membranes, particularly in regard to phosphorylation (Article II) (Perraki et al., 2018), we undertook the mapping of its phosphorylated residues (Article II: addenda). Working on the N-terminal domain REM₁₋₁₁₆, we described it is an IDP and remain an IDP even after phosphorylation by AtCPK3.

The question remains: why is StREM1.3-DDD, a mutant mimicking a constitutively phosphorylated protein, more mobile than StREM1.3-AAA, a mutant mimicking a constitutively not phosphorylated protein (Article II) (Perraki et al., 2018)? If we consider phosphorylation as a molecular switch, modifying the protein's interactome, it is tempting to view the changes in the mobility of StREM1.3-DDD as a consequence of interactors driving the protein out of nanodomains, while StREM1.3-AAA would remain strictly within. StREM1.3 has an intermediate phenotype, indicating either a turnover between non-phosphorylated and phosphorylated forms or, less likely, an inhibition of StREM1.3's phosphorylation when it is in nanodomains through an unknown mechanism.

With the goal of being more biologically relevant, it will be important to find what phosphorylates StREM1.3 in *Solanum tuberosum* (potato): the only remorin kinase we know of, for now, is AtCPK3 from *Arabidopsis thaliana* (Article II) (Perraki et al., 2018). Conversely, is there a phosphatase that can dephosphorylate pStREM1.3? Alternatively, we should switch to an AtREM to take advantage of the many genetic resources available on remorins in *Arabidopsis thaliana*.

One hypothesis to explain how the PM repartition of StREM1.3 could be influenced by its interactome should be investigated soon. Unpublished work by Dr Paul Gouguet and Dr Julien Gronnier identified the Actin Depolymerising Factor (ADF) as an interactor of StREM1.3-DDD, but not the WT, by both split ubiquitin assay and bi-

fluorescence complementation. ADF, as its name suggests, binds to filamentous F-actin and provokes its depolymerisation into G-actin monomers: it disrupts the actin cytoskeleton. Could it be that (1) nanodomains of non-phosphorylated StREM1.3 are pinned by actin and that (2) upon phosphorylation of StREM1.3, StADF is recruited, disrupting the actin cytoskeleton, therefore freeing StREM1.3 from pinning by actin and allowing it to escape the nanodomain, hence the higher PM mobility of StREM1.3-DDD (Article II) (Perraki et al., 2018)? (Szymanski et al., 2015) showed that disrupting the actin cytoskeleton modifies the PM repartition of AtREM1.2 and that AtREM1.2 and AtREM1.3, found to be enriched in DIMs under physiological conditions, target DSMs upon disruption of either the actin or the microtubule cytoskeleton. This interplay between StREM1.3 and actin would well illustrate the concept of fence and pickets as well as provide a plausible explanation to the difference in nanodomain localisation between different remorins (Jarsch et al., 2014), based on differences of interactome.

4. Final words

StREM1.3, likely as a homotrimer in the cytosol through a coiled-coil mediated oligomerisation (Article I) (Martinez et al., 2018), anchors to the inner leaflet of the PM using a combination of electrostatic interactions between the polar heads of PIPs, mostly PI4P, and two positively charged lysines of its three RemCA domains, as well as hydrophobic effects (Gronnier et al., 2017). More sitosterol and PIPs are then recruited to the nascent nanodomain where the lipid order parameter increases (Article IV) (Legrand et al., 2019). Phosphorylation of the N-terminal IDD influences the mobility of StREM1.3 at the PM (Article II and addenda) (Perraki et al., 2018).

The reconstitution of StREM1.3 nanodomains (Article V) and the study of its phosphorylation and interaction mechanism with StADF (Article II and addenda) (Perraki et al., 2018) are promising outlooks for future studies. The former will give access to a powerful platform to experiment upon nanodomain formation and validate our hypothetical nanoclustering model (Article IV) (Legrand et al., 2019). The latter will elaborate on the biological implications of StREM1.3, how they are performed and how they may impact its behaviour at the PM. New interactors could be studied using the same methodology.

At last, now that this manuscript is coming to an end and there is nothing left to spoil, I shall leave the reader with the revised draft of our review on remorins (Gouguet et al., 2020).

Annex: an up-to-date review on remorins

This review was the introduction of the PhD manuscript of Dr Paul Gouguet, my predecessor on the two decades long project to study remorins. It has recently been accepted for publication. From the very start, it was written with the intention to become the most comprehensive and up-to-date review on remorins. It covers all remorin groups and summarises all demonstrated biological functions along with putative ones. The history of their discovery and their biophysics are also discussed to their fullest extent. New axes of research are also discussed.

Most of the writing was done by Dr Paul Gouguet and reviewed by Dr Sébastien Mongrand. Among all the authors, Dr Birgit Habenstein and I stepped in to write about the biophysics of the remorins, and that of *StREM1.3* in particular. In conjunction with Dr Sébastien Mongrand, we also designed the related figure. A table summing up, in the light of this review, all established functions of remorins will be available; it is not part of the accepted manuscript.

Revised version:

Connecting the dots: from nanodomains to physiological functions of REMORINs

Plant-specific protein REMORINs

Paul Gouguet^{1,2}, Julien Gronnier³, Anthony Legrand^{1,4}, Artemis Perraki⁵, Marie-Dominique Jolivet¹, Anne-Flore Deroubaix¹, Sylvie German-Retana⁶, Marie Boudsocq⁷, Birgit Habenstein⁴, Sébastien Mongrand^{1*}, Véronique Germain^{1*}

¹, Laboratoire de Biogenèse Membranaire (LBM), Unité Mixte de Recherche UMR 5200, CNRS, Université de Bordeaux, Villenave d'Ornon, France

², ZMBP, Universität Tübingen, Auf der Morgenstelle 32 72076 Tübingen, Germany

³, Department of Plant and Microbial Biology University of Zürich, Zollikerstrasse, Zürich, Switzerland.

⁴, Institute of Chemistry & Biology of Membranes & Nanoobjects (UMR5248 CBMN), IECB, CNRS, Université de Bordeaux, Institut Polytechnique de Bordeaux, A11, Geoffroy Saint-Hilaire, Pessac, France

⁵, Department of Plant Sciences, University of Cambridge, Downing Street Cambridge, United Kingdom

⁶, Equipe de Virologie, Institut Scientifique de Recherche Agronomique and Université de Bordeaux, BP81, 33883 Villenave d'Ornon, France

⁷, Université Paris-Saclay, CNRS, INRAE, Université d'Evry, Institute of Plant Sciences Paris Saclay (IPS2), Université de Paris, Orsay, France

Present address Artemis Perraki: Institute of Molecular Biology and Biotechnology, Foundation for Research and Technology - Hellas, Heraklion, Crete, Greece.

* SM and VG are co-corresponding authors

Abstract

REMORINs (REMs) are a plant-specific protein family, proposed regulators of membrane-associated molecular assemblies and well-established markers of plasma membrane nanodomains. REMs have been shown to play a diverse set of functions in plant interactions with pathogens and symbionts, responses to abiotic stresses, hormones signaling and cell-to-cell communication. In this review, we highlight the established and more putative roles of REMs throughout the literature. We discuss the physiological functions of REMORINs, the mechanisms underlying their nanodomain-organization and their putative role as regulators of nanodomain-associated molecular assemblies. Furthermore, we discuss how REMORINs phosphorylation may regulate their functional versatility. Overall, through data-mining and comparative analysis of the literature, we suggest how to further study the molecular mechanisms underpinning the functions of REMs.

Advances Box

- REMORINs are plant-specific membrane-bound proteins family involved in response to biotic (bacteria, viruses, fungi, oomycetes, mycorrhizae) and abiotic stresses (cold, mannitol, salt...), as well as developmental cues.
- REMORINs are strongly embedded in the inner-leaflet of the plasma membrane by an unconventional mechanism involving anionic lipids and sterols
- REMORINs are proposed as nanodomain-organizing proteins.
- REMORINs are highly phosphorylated proteins containing putative intrinsically disordered regions, which likely play a role in scaffolding protein complexes.
- REMORINs regulate cell-to-cell connectivity through plasmodesmata.

Outstanding Questions Box

- How can REMORIN functional versatility be explained?
- What are the consequences of the phosphorylation(s) of REMORIN's putative intrinsically disordered regions in term of 3D structure, protein-protein interaction and nanodomain organization?
- How do REMORINs regulate cell-to-cell connectivity through plasmodesmata?

One-sentence summary

This review collates and discusses all the available information on the plant-specific plasma membrane-bound family of REMORIN proteins involved in a plethora of cellular processes, and discuss their role as potential scaffolding proteins.

REMORINS DISCOVERY

REMORINS LOCALIZE IN DIVERSE AND COEXISTING NANODOMAINS

Mechanisms of REMs' Association to PM Nanodomains

1. The unconventional membrane-anchoring domain REMORIN C-terminal Anchor (REM-CA) and S-acylation
2. REMORIN Oligomerization
3. REMORIN Association with the Cytoskeleton

THE BIOLOGICAL FUNCTIONS OF REMORINS

Established functions of REMORIN proteins

Data mining toward the putative functions of REMORIN

STRUCTURAL AND BIOLOGICAL IMPLICATIONS OF REMORIN PHOSPHORYLATION

PERSPECTIVES

- 1 Genetics
- 2 Protein-Protein Interactions
- 3 The PM's complexity

REFERENCES

REMORINS DISCOVERY

REMORINs were first identified in tomato (*Solanum lycopersicum*) and potato (*Solanum tuberosum*) by Edward Farmer, Gregory Pearce and Clarence Ryan in 1989, in a will of identifying molecular actors involved in the perception of polygalacturonides (PGA) by plant cells (Farmer et al., 1989). PGA are pectic polysaccharides present in the plant cell wall and released during wounding and pathogen attack to sensitize plant defense. (Voxeur and Höfte, 2016). By *in vitro* phosphorylation assays on isolated tomato and potato plasma membrane (PM), Farmer et al. found that PGA treatment caused the phosphorylation of a protein of 34 kilodaltons, named *phosphorylated protein of 34* kilodaltons or *pp34* (Farmer et al., 1989). Pp34 was then used as a marker of the plant response to wounding (Farmer et al., 1991). Unintuitively, the purification (Jacinto et al., 1993) and cloning of pp34 (Reymond et al., 1996) revealed that its sequence turned out to be one of a hydrophilic protein even though it is-tightly bound to the PM. Pp34 was then renamed REMORIN (later named StREM1.3 for *Solanum tuberosum* REMORIN of Group 1 isoform 3) in reference to remora or “suckerfish” depicted as attaching itself to vessels and larger fish described by J.L. Borges in “Book of Imaginary Beings” (*El libro de los seres imaginarios*, J.L. Borges, 1969), and reflecting REMORIN’s ability to bind to the PM whilst displaying an overall hydrophilic residue profile. Concurrently to the experiments of Farmer et al., Alliotte et al. isolated a similar protein in *Arabidopsis thaliana* termed DNA-binding protein (*dbp*). This gene would be later known as AtREM1.3 (At2g45820) and was first characterized as a DNA-binding protein due to its highly-hydrophilic nature permitting electrostatic interactions with DNA and its amino-acid composition similar to Histone 1 proteins (Alliotte et al., 1989).

Genome-wide analyses have shown that the REM family is specific to the land-plant lineage (Raffaele et al., 2007). REM proteins present a highly-conserved C-terminal domain and a divergent N-terminal domain, which has been the basis for their phylogenetic classification into 6 separate groups (Raffaele et al., 2007). For example, we count 19 OsREMs in rice *Oryza sativa* and 16 AtREMs in *Arabidopsis thaliana*.

Since their discovery in the late 1980’s, REMs have been the subject of ever-increasing attention. Be they directly the subject of studies or found in different screens of “omics” approaches, REMs are consistently found in a large variety of academic inquiries, providing grist to the mill to the idea that they could play a central role in plant development and adaptation. The first REMORIN protein identified in potato, which would be later named StREM1.3 for *Solanum tuberosum* REMORIN of Group 1 isoform 3. REMORIN’s polyanion

binding capacity, originally linked to binding cell wall compounds (Reymond et al., 1996) would be later mitigated by the discovery of REMORIN's presence in the inner-leaflet of the PM.

In this review, we address the different characteristics that have been described for REMs as well as an overview of the physiological roles that REMs may participate in. We will discuss how REMs are anchored to the PM and cluster into PM-nanodomains, how they are phosphorylated and the subsequent role of these post-translational modifications. Finally, we provide a number of perspectives on how REMs should be further studied in order to better understand the many physiological conditions involving REMs.

REMORINS LOCALIZE IN DIVERSE AND COEXISTING NANODOMAINS

REMORINs predominantly associate with the PM (Raffaele et al., 2009a; Marín et al., 2012; Jarsch et al., 2014; Konrad et al., 2014; Perraki et al., 2014). Moreover, isoforms from Group 1 and Group 6 REMs have been shown to be partially associated with the plasmodesmata (PD)-PM in rice and in *Solanaceae* (Raffaele et al., 2009a; Fernandez-Calvino et al., 2011; Gui et al., 2014; Perraki et al., 2018). Nonetheless, translocation into the nucleus upon interaction with α -importins (Marín et al., 2012) and re-localization to intracellular foci upon perception of an immunogenic epitope of bacterial flagellum (Albers et al., 2019) have been reported for Group 1 and Group 4 REMs, respectively. However, the ER-PM contact sites observed by bimolecular fluorescence complementation (BiFC) for StREM1.3 are likely artefactual and highlight the risk of using the BiFC to study membrane protein interactions in plants (Tao et al., 2019).

Concerning their PM localization, the identification of Group 1 REMs in tobacco detergent-resistant membrane fractions (DRM; a biochemical counterpart of membrane sub-compartmentalization) first suggested a lateral organization of REMs into clusters at the PM (Mongrand et al., 2004). REMs' co-purification with DRM appeared to be dependent on the presence of phytosterols as it was reported to be absent of DRM in the sterol methyl-transferase mutant *smt1* albeit still present in this fraction in the sterol glycosylation mutant *ugt80A2;B1* (Zauber et al., 2014).

In relation with the above biochemical data, electron microscopy immunolocalization, stimulated-emission depletion (STED) microscopy and photoactivated localization microscopy (PALM) studies have all showed that Group 1 REMs were organized into nanodomains around about 70-90 nm in diameter in *Arabidopsis* and *Solanaceae* species (Raffaele et al., 2009a; Demir and Horntrich, 2013; Gronnier et al., 2017). Members of other groups in *Arabidopsis*

and *Medicago* are organized in PM domains that can be distinguished in density, size and shape (Jarsch et al., 2014). Interestingly, evolutionary distant REMs (belonging to distinct groups *e.g.* groups 1 and 6) localize in separate nanodomains suggesting that distinct REMs cluster into separate domains in order to play independent functions (Jarsch et al., 2014; Bücherl et al., 2017). It must also be noted that not all REMs are found in DRM-fractions of different plant tissues (Stanislas et al., 2009; Keinath et al., 2010; Srivastava et al., 2013; Takahashi et al., 2013) hinting to a diversity of REM-associated PM-domains.

Mechanisms of REMs Association to PM Nanodomains

A number of works have been performed to understand how highly-hydrophilic REMs could be tightly anchored to the PM and the molecular interactions leading to the clustering of REMs into nanodomains. REMs are anchored to the PM inner-leaflet *via* the unconventional lipid-binding motif called REMORIN C-terminal Anchor (REM-CA) (Raffaele et al., 2009; Konrad et al., 2014; Perraki et al., 2012; Gronnier et al., 2017). In the past few years, several molecular determinants regulating REMs' nanodomain organization have emerged mostly for Group 1 and 2 REMs and need to be further studied to fully understand the diversity of REMs' clustering (Jarsch et al., 2014). There are at least four determinants: the lipid-binding properties of REM-CA domain, REM-CA S-acylation, REM-REM oligomerization and REM-cytoskeleton interactions. Here we review the knowledge obtained to explain the molecular mechanisms at play.

1. The unconventional membrane-anchoring REMORIN C-terminal Anchor domain (REM-CA) and S-acylation

REMs do not contain target-peptides or transmembrane domains (Raffaele et al., 2007) and attached to the PM independently of the conventional secretory pathway (Gui et al., 2015; Gronnier et al., 2017). StREM1.3, SYMREM1 (also termed MtREM2.2) as well as AtREM1.2, AtREM1.3, AtREM4.2, AtREM6.1 and AtREM6.4 have been described to be strictly PM localized thanks to their REM-CA moieties (Raffaele et al., 2009a; Lefebvre et al., 2010; Perraki et al., 2012; Raffaele, 2013; Jarsch et al., 2014; Konrad et al., 2014; Gronnier et al., 2017). In the case of StREM1.3, the last 28 amino acids (*i.e.* REM-CA) partially folds into an alpha helix in the presence of PI4P and sitosterol and also inserts itself into the hydrophobic core of the bilayer (Gronnier et al., 2017). This is driven by protein-lipid interactions between the REM-CA and the PM's inner-leaflet lipids: negatively-charged phosphoinositides (PIPs), notably phosphatidylinositol-4-phosphate (PI4P), and sterols, notably sitosterol (Raffaele et al.,

2009a; Legrand et al., 2019), (Figure 1). REM-CA binds to PI4P with a yet unknown stoichiometry through its Lysine/Arginine residues *via* electrostatic interactions. Association of StREM1.3's REM-CA with negatively-charged phospholipids regulates its nanodomain organization (Gronnier et al., 2017).

In mammals, PIPs have been reported to possess the ability to cluster *in vivo* to form nanodomains (van den Bogaart et al., 2011). It was also shown, *in vitro*, that cholesterol are found in the vicinity of saturated phospholipids rather than of unsaturated ones (Engberg et al., 2016). This mechanism creates a so-called Liquid-ordered domain in the lipid bilayer. In plants, the fact that PIPs bear mostly saturated acyl-chains suggest that phytosterols may also actively participate to the formation of nanodomains (Furt et al., 2010). REMs could be either targeted to pre-existing lipid-mediated nanodomains or participate in the organization of their own lipid environments. Both the latter and former possibilities for REMs' association to PM-nanodomains still remain open questions.

The presence of cysteine residues in the REM-CA of many REMs raised the possibility of membrane association due to S-acylation. AtREM1.2 was the first REM to be found to be S-acylated (Hemsley et al., 2013). AtREM1.2 and AtREM6.4, lost strict-PM localization when their REM-CA Cysteine residues were substituted by Alanine residues (Konrad et al., 2014). Altered localization when S-acylation is abolished *via* 2-bromopalmitate was also observed with the rice REM OsREM6.6 (Gui et al., 2015). This is reminiscent of the relocation observed for the S-acylation site mutant NbREM1.1^{C206A} to RFP-ATG8e-tagged vesicles (Fu et al., 2018). It is important to note that NbREM1.1^{C206A} is no longer organized in nanodomains, nor co-purifies with the DRM biochemical fraction (Fu et al., 2018). Yet for SYMREM1, the Cysteine substitution did not reduce its PM-localization and did not change its segregation pattern in the PM, hinting to a more complex PM association mechanism. Altogether, all of the above mentioned data highlight the importance of the REM-CA as a determinant of REM's general membrane affinity as well as REM's organization within these membranes. Interestingly, many REMs do not have predicted S-acylation sites in their REM-CA (Konrad et al., 2014; Gronnier et al., 2017), suggesting a degree of diversity in the mechanisms regulating REMs' PM targeting and nanodomain organization.

2. REM Oligomerization

REM oligomerization is highly important for its targeting and function. REMs were first proposed to form oligomeric structures. The first evidence of the oligomerization was reported in Bariola et al. (2004) where the group 1 REMORIN coiled-coil domain was described to participate in the formation of REM oligomers. Electron microscopy and glutaraldehyde

crosslinking assays evidenced REM multimerization *via* the C-terminal region of two Group 1 REMs *i.e.* StREM1.3 and SIREM1.2 (Bariola et al., 2004). Bariola et al. (2004) proposed *via* analytical ultracentrifugation of recombinant proteins and cross-linking experiments on isolated PM that Group 1 REMs associate into dimers, tetramers or higher-order oligomeric structures *via* their coiled-coil domains. Alternatively, Perraki et al. (2012) developed the hypothesis that StREM1.3 would trimerize either before or after the anchoring event at the PM. This hypothesis was upheld by gel filtration assays with the *E. coli* purified 6His-tagged full-length StREM1.3 protein (Perraki et al., 2012). The exact order of oligomerization of REMs *in planta* is still lacking (Jaillais and Ott, 2020).

In our current view, StREM1.3 is homo-trimeric in solution bundling three REM-CA domains together (Bariola et al., 2004; Martinez et al., 2018). This trimeric hypothesis was further developed in Martinez et al. (2018) upon *in silico* modelling confirmed by Solid-State NMR in conjunction with cryo-Electron Microscopy (cryo-EM) and *in vivo* observations of mutations in the coiled-coil domain that impair PM-association (Figure 1). These *in vivo* observations seem to corroborate the hypothesis that in a minimal state, the trimeric form is necessary for PM anchoring. Cryo-EM further revealed a possible lateral association of the trimeric REMs in the presence of an N-terminal 6His-tag (Martinez et al., 2018), yet the presence of a 6His-tag may also alter the oligomeric behavior of proteins (Amor-Mahjoub et al., 2006). This casts a doubt on the *in vivo* relevance of the trimer of StREM1.3 observed by gel filtration (Perraki et al., 2012). In any case, the existence *in vivo* of homo-oligomers and higher-order oligomers has not been invalidated by the latest data. Formation of higher-order oligomers, *i.e.* oligomers of trimers, as a mean to drive nanoclustering cannot be excluded but has yet to be tested. Interactions between neighboring REM trimers are likely to further stabilize nanodomain clustering.

Group 1 AtREMs have been found to form oligomers in a large-scale study of PM protein oligomerization in leaves (McBride et al., 2017). AtREM1.2, AtREM1.3 and AtREM1.4 were predicted to form oligomeric complexes according to their ratio of the calculated mass to the apparent mass (R_{app}) score which calculates a ratio between the predicted molecular mass of the monomer and the measured molecular mass of the complex in which the protein is found. AtREM1.2, AtREM1.3 and AtREM1.4 were found in different complexes to have a ratio of the calculated mass to the apparent mass scores (R_{app}) ranging on average from 35 to 60 for AtREM1.2, 25 for AtREM1.3 and 30 to 95 for AtREM1.4 (McBride et al., 2017). This data may suggest that in addition to being homo-oligomerized, Group 1 REMs are also forming multi-protein complexes. This idea has already been suggested in the literature, notably in

Lefebvre et al. (2010) where REMs are compared to caveolins considering the common properties they share: small, oligomeric, lipid raft-associated scaffold proteins that can form filamentous structures.

3. *REM Association with the Cytoskeleton*

In the seminal work of Jarsch et al. (2014), filamentous exclusion zones observed at the surface of the PM have led to think that REMs could be associated with the cortical cytoskeleton. A localization dependent on microtubule polymerization has been reported using the microtubule depolymerizing drug oryzalin. Oryzalin treatment substantially mislocalized AtREM1.2 that was originally at the PM in domains (Szymanski et al., 2015). Moreover, AtREM6.6, that localizes at fibrillar structures and to PM domains, has been shown to be affected in its fibrillar localization by oryzalin treatment (Jarsch et al., 2014; Konrad et al., 2014).

This interplay between the cortical cytoskeleton and PM-nanodomains fits with the “fences and pickets” paradigm (Kusumi et al., 2012), where REMs could play a role as a putative scaffold protein. This interplay with actin has been further demonstrated for other REMs such as SYMREM1. SYMREM1’s association to PM-nanodomains has been shown to be destabilized by the actin depolymerizing drug, latrunculin B, yet not by the microtubule depolymerizing drug, oryzalin. SYMREM1’s presence at the PM was also shown to be essential for the establishment of FLOT4-LYK3 domains that are dependent on the contact between FLOT4 and the actin cytoskeleton (Liang et al., 2018) (see Figure 2B). The rice Group 6 REM, OsREM6.6 (or GSD1 for grain setting defect 1, see below), has also been shown to associate with the actin cytoskeleton. Treatment with cytochalasin D (a potent inhibitor of actin polymerization) completely disrupted the punctate localization pattern of AtREM1.2 and AtREM1.3 to a more uniform distribution with smaller punctate patterns of lower intensity (Szymanski et al., 2015). Additionally, AtREM1.2 was shown to associate with the actin cytoskeleton under viral infection (Cheng et al., 2020). This data reveals the strong relationship between REMs’ anchoring to the PM and the actin cytoskeleton, although the functional mechanism remains to be tackled.

THE BIOLOGICAL FUNCTIONS OF REMORINS

Established functions of REMORIN proteins

Plant-Microbe Interactions

Numerous studies have reported the implication of REMs in plant interactions with microorganisms.

Viruses

The first REM to be shown as implicated in the context of viral infection has been StREM1.3. It has been demonstrated that its over-expression leads to the limiting of the cell-to-cell movement of *Potato Virus X* (PVX), and that its under-expression (RNAi lines) lead to an acceleration of the PVX movement (Raffaele et al., 2009) (Perraki et al., 2018). A general effect on the REM-dependent gating of PD was also shown in the presence of viral movement proteins such as 30K from the *Tobacco Mosaic Virus* (TMV) or Hc-Pro from the *Potato Virus Y* (PVY) (Perraki et al., 2014). In addition to limiting PVX cell-to-cell movement, StREM1.3 has also recently been shown to limit TMV cell-to-cell propagation (Perraki et al., 2018). Over-expression of StREM1.3 was shown not to impair the silencing suppressor activity of the PVX-encoded TRIPLE-GENE BLOCK protein 1 (TGBp1) (Perraki et al., 2012), but rather to induce the increase in callose accumulation at PD pit-fields (Perraki et al., 2018). Furthermore, StREM1.3's capacity in hindering PVX cell-to-cell movement has been shown to be abolished when REM-CA is mutated, thereby modifying its targeting to the PM (Gronnier et al., 2017). Additionally, StREM1.3 was shown to physically interact with the PVX movement protein TGBp1 with or without an impaired REM-CA domain (Perraki et al., 2012).

In Perraki et al., (2018), it was shown that PVX-activated kinases are responsible for StREM1.3's phosphorylation potentially on residues S74/T86/S91 and that expression of the phosphomimetic, but not the phosphoablative mutant of StREM1.3 hampered virus cell-to-cell propagation to similar levels with the wild type. Importantly, the calcium-dependent protein kinase AtCPK3, which could phosphorylate StREM1.3 *in vitro*, could also restrict PVX cell-to-cell movement in a REM-dependent manner. *In vitro*, the StREM1.3 phosphomutants were not phosphorylated by AtCPK3 (Perraki et al., 2018). This suggests that an AtCPK3 ortholog in potato could potentially regulate StREM1.3 *in vivo* for anti-viral defense. Moreover, the phosphorylation mutants had an impact on the localization of REM at PD and on callose deposition, associating phosphorylation status, protein mobility, PD permeability and cell-to-cell viral propagation (Perraki et al., 2018, Figure 2A).

Solanaceae Group 1 REMs have also been studied in the context of *Tenuivirus* infection. *N. benthamiana* NbREM1.1 and NbREM1.2 were shown to be degraded during *Rice Stripe Virus*

(RSV) infection in consequence to the interference of the RSV-encoded protein, NSvc4. The degradation of NbREM1.1 and NbREM1.2 *via* the autophagy pathway led to RSV circumventing NbREM1-associated resistance (Fu et al., 2018). In contrast, a recent study has underlined the effect of the tobacco REM NtREM1.2 on the cell-to-cell movement of a *Tobamovirus*, the *Tomato Mosaic Virus* (ToMV) (Sasaki et al., 2018). ToMV infection and the overexpression of ToMV movement proteins separately affected NtREM1.2's localization by inducing its aggregation at the PM. Dissimilarly to StREM1.3, which is known to localize in a patchy pattern at the PM and is present in PM-nanodomains, NtREM1.2 localized in a uniform fashion throughout the PM regardless of N-terminal or C-terminal fusion to fluorescent tags. Considering the high sequence conservation of the C-terminal region, this suggested that the N-terminal region was involved in NtREM1.2's characteristic localization. Interestingly, NtREM1.2 was shown to interact and colocalize with ToMV's 30-kDa movement protein at PD. *Agrobacterium*-mediated transient expression of NtREM1.2 was also shown to slightly increase ToMV infection foci size (Sasaki et al., 2018). Moreover, in ToMV infected cells, NtREM1.2 aggregates occur close to tubular ER structures and are associated with ToMV's 30-kDa movement protein bodies that appeared to be linked to the ER-Actin network (Sasaki et al., 2018). Finally, *A. thaliana* AtREM1.2 has been proposed to play a role in *Turnip Mosaic Virus* (TuMV) cell-to-cell movement by competing with the TuMV protein VPg in the actin-dependent regulation of PD aperture (Cheng et al., 2020).

Group 4 REMs have been reported as positive regulators of viral infection. AtREM4.1 and AtREM4.2 were shown to be susceptibility factors during *Beet Curly Top Virus* (BCTV) and *Beet Severe curly Top Virus* (BSCTV) infection. This was shown using single- and double-knock-out and overexpressing lines for AtREM4.1 and AtREM4.2. This effect of Group 4 REMs on geminiviral infection could be linked to SnRK1, an important positive regulator of plant stress involved in antiviral defense, which could phosphorylate AtREM4.1 *in vitro* (Son et al., 2014).

Bacterial Symbiosis

The Group 2 REMs merely constituted of a C_domain (c.f. Figure 1A) (Raffaele et al., 2007), have been characterized by their role in the establishment of infection threads (IT) during the symbiosis of *M. truncatula* and *Lotus japonicus* with *Rhizobiaceae* family bacteria by participating in the formation of root nodules (Lefebvre et al., 2010; Tóth et al., 2012). SYMREM1 has been shown to be specifically expressed in *M. truncatula* roots and nodules with an expression strongly induced by Nod factor treatment (Lefebvre et al., 2010), which are lipo-chitooligosaccharides produced by symbiotic bacteria in order to initiate symbiosis

(Oldroyd, 2013). Furthermore, SYMREM1 knock-down lines were shown to strongly reduce nodule establishment and growth (Lefebvre et al., 2010). Analogously, overexpression of Group 2 REM LjSYMREM1 significantly increased the number of nodules per root in *L. japonicus*, establishing these orthologs as key players for symbiosis in legumes (Tóth et al., 2012). In this context, SYMREM1 has been further characterized at the molecular level. It has been described as a scaffold protein due to its interaction with three receptor-like kinases (RLKs) essential for nodule establishment and maintenance *i.e.* NFP, DMI2 and LYK3 (Lefebvre et al., 2010). This could be a recruiting process of RLKs to specific nanodomains to initiate IT along with FLOT4 (Liang et al., 2018). SYMREM1 is believed to stabilize the interactions between FLOT4 and both NFP and LYK3 which would prevent the RLKs' endocytosis and ensure nodulation-promoting signaling (Liang et al., 2018; see Figure 2B).

Fungi and Oomycetes

REMs have been reported to be implicated in interactions with filamentous pathogens/symbionts. StREM1.3 has long been established as a marker of *Phytophthora infestans* extrahaustorial membrane (EHM) (Lu et al., 2012; Bozkurt et al., 2014). StREM1.3 has been observed to label haustoria, approximately 50 % of the time, and to specifically label non-callosic haustoria (Bozkurt et al., 2014). Moreover, the overexpression of StREM1.3 in *N. benthamiana* and tomato increased susceptibility to *P. infestans* infection (Bozkurt et al., 2014). The precise role of StREM1.3 during *P. infestans* has yet to be precisely determined. Interestingly, recent studies showed the specific recruitment of phosphoinositides (PIPs) to the plant-pathogen interfacial membrane during fungal infection (Qin et al., 2020). Different PIPs were found enriched at the EHM. Phosphatidylinositol 4,5-bisphosphate (PI(4,5)P₂) was shown to be dynamically up-regulated at powdery mildew infection sites and recruited to the EHM, whereas PI4P is absent in the EHM. Furthermore, the depletion of PI(4,5)P₂ in the *pip5k1 pip5k2* mutant lines inhibited fungal pathogen development and caused disease resistance, independent of cell death-associated defenses, involving impaired host susceptibility. The fact that REMs both bind to PIPs and are involved in immune responses to fungi incites to examine in detail the link between these two observations in future work.

The first report of a possible implication of REMs in plant-fungal interactions was a maize ZmREM6.3 that was found in a QTL (Quantitative Trait Loci) analysis for resistance to northern leaf blight caused by the fungal pathogen *Setosphaeria turcica* (Jamann et al., 2016). A recent study further highlighted the importance of REMs in the resistance to fungal pathogens by identifying ZmREM1.3 in a large scale proteomic analysis (Wang et al., 2019). The comparison between southern corn rust (*Puccinia polysora*) sensitive- and resistant-maize

inbred lines revealed that ZmREM1.3 protein amount was increased in the resistant line whereas it was decreased in the sensitive line. Genetic approaches (overexpression and KO) confirmed that ZmREM1.3 mediated maize resistance to *P. polysora*, through SA/JA signaling and defense gene up-regulation (Wang et al., 2019).

A recent study showed that overexpression of tomato (*Solanum lycopersicum*) SIREM1 increased susceptibility to the necrotrophic fungus *Botrytis cinerea* (Cai et al., 2020). Heterologous expression of SIREM1 increased ROS accumulation and triggered other cell-death regulators, suggesting a positive regulatory role of SIREM1 in programmed cell-death (PCD) and providing clues for understanding the PCD molecular regulatory networks in plants.

Hormone Signaling & Abiotic Stress

The rice (*Oryza sativa*) OsREM4.1 was shown to be up regulated by ABA treatment *via* the bZIP transcription factor OsZIP23, which can bind the OsREM4.1 promoter. OsREM4.1 overexpression inhibited BR signaling by inhibiting OsSERK1 and OsBRI1 complex formation. This REM effect is undermined by the phosphorylation of REM. Under high BR concentrations, BR stabilizes the OsSERK1/OsBRI1 complex, which activates the phosphorylation of OsREM4.1 by OsBRI1, thereby reducing OsREM4.1's affinity for OsSERK1 and enabling the BR signaling cascade. This signaling system maintains a dynamic equilibrium between ABA and BR signaling (Gui et al., 2016), see Figure 2C. In *A. thaliana*, AtREM1.2 and AtREM1.3 have been shown to organize lipid raft nanodomains in a salicylic acid (SA)-dependent fashion. Indeed, by interaction with GRF10, both REMs were shown to participate in PD closure after SA treatment (Huang et al., 2019). Moreover, AtREM1.2 was shown to be crucial for SA-induced asymmetric auxin flux during root gravitropic response as well as for the regulation of clathrin-mediated endocytosis (Ke et al., 2020).

The tomato SIREM1.2 has recently been shown to be involved in fruit ripening by interacting with the ethylene biosynthesis proteins. The overexpression of SIREM1.2 up-regulates key genes involved in ethylene, lycopene biosynthesis and ripening regulators resulting in an effective increase in the ethylene and lycopene content of fruit (Cai et al., 2018).

The functional characterization of a mulberry (*Morus indica*) Group 1 isoform MiREM1 evidenced its transcriptional upregulation under a number of abiotic stresses and hormone treatments. Gain of function *via* the heterologous overexpression of MiREM1 in *A. thaliana* conferred resistance to salt stress and drought (Checker and Khurana, 2013).

The Group 6 REM SiREM6 (*Setaria italica*, fox-tail millet) has been found to be transcriptionally up regulated under salt, cold, ABA and osmotic stress. Yet this up regulation

was weakly observed under drought stress and SiREM6 overexpression did not impact drought tolerance. SiREM6 overexpression in *A. thaliana* increased germination rate and seedling biomass as well as seedling survival under salt stress. These characteristics were linked to an increase in proline content and a reduction in electrolyte leakage. Additionally, overexpression of SiREM6 in *A. thaliana* enhanced sensitivity to ABA treatment (Yue et al., 2014). In rice (*Oryza sativa*), OsREM6.5 was also found to be highly upregulated during drought stress and ABA treatment (Wu et al., 2006)

In *Populus euphratica*, a salt-resistant poplar, PeREM6.5 was induced by NaCl stress. Interestingly, PeREM6.5 recombinant protein significantly increased the H⁺-ATPase hydrolytic activity and proton transport activity in *P. euphratica* PM vesicles. Yeast two-hybrid assays showed that PeREM6.5 interacted with RPM1-interacting protein 4 (PeRIN4). Notably, the increase of H⁺-ATPase activity induced by PeREM6.5 was further enhanced by PeRIN4 recombinant protein. Finally, overexpression of PeREM6.5 in *A. thaliana* improved salt tolerance. PeREM6.5, by regulating H⁺-ATPase activity in the PM, may therefore enhance the plant capacity to maintain ionic homeostasis under salinity (Zhang et al., 2020).

Cell-to-Cell connectivity *via* PD

The first direct evidence of the implication of REMs in cell-to-cell connectivity *via* PD was revealed by the ability of StREM1.3 to hinder PVX cell-to-cell movement as well as GFP diffusion in non-virally-infected plants in *N. benthamiana* leaf epidermal cells (Perraki et al., 2012; Perraki et al., 2014, Raffaele et al., 2009). REM transcript and protein levels were shown to increase in mature, ageing and senescing tissues, as well as in “source parts” of tobacco leaves (*i.e.* the tip of the leaf), where a majority of mature- and branched-PD are present (Raffaele et al., 2009b). These results suggest that tobacco Group 1 REMs predominantly associate with mature-branched-PD.

The Group 6 REM OsREM6.6 was shown to regulate PD permeability in rice leading to the filling of the seed. The mutant termed GSD-1 (grain setting defect 1) was shown to have an altered and ubiquitous expression of OsREM6.6, which is natively only expressed in phloem companion cells, thereby inducing an accumulation of starch and free-sugars in the leaf blades and consequently a reduction of starch accumulation in grains (Gui et al., 2014).

Data mining toward the putative functions of REMORINs

Throughout the relatively extensive literature that links REMs to biological functions (from transcriptomic, proteomic, phosphoproteomic data), several patterns may be found.

Considering the overlapping nature of these types of events, we summarize that data in Table 1 by grouping REMs by phylum and by putative function. These links remain to be further experimentally confirmed but deserve to be pointed out in order to pave the way in understanding the biological functions of REMs.

STRUCTURAL AND BIOLOGICAL IMPLICATIONS OF REM PHOSPHORYLATION

Since the first identification of REM as an *in vitro* phosphorylated protein, pp34 (Farmer et al., 1989), members of all REM groups have been detected in phosphoproteomes from diverse tissues and biological contexts, suggesting phosphorylation as a major *in vivo* regulatory mechanism of REMs (see Supplemental Table 1 for a compilation of REM phosphoproteomic data). A recent study established the phosphorylation pattern of 14 AtREMs in 30 different plant tissues (Mergner et al., 2020). Apart from this broad-scale analysis, other studies have shown that, for some residues, the phosphorylation of REMs is modulated by stress conditions such as flg22 and OG treatment, nitrogen deprivation, ABA, H₂O₂, cold, osmotic and salt stresses (Benschop et al., 2007; Kohorn et al., 2016; Menz et al., 2016; Nikonorova et al., 2018; Wang et al., 2020, see Supplemental Table 1), suggesting functional roles of phosphorylation that remain to be explored.

REMs are found to be phosphorylated *in vivo* mainly at the putatively intrinsically disordered region (IDR) located in the N-terminal domain (Figure 3) (Marín and Ott, 2012). IDR regions are flexible and extended protein segments that provide dynamic structural remodeling and protein-protein interaction plasticity (Iakoucheva et al., 2004; Dyson and Wright, 2005; Uversky, 2013). They are often regulated *via* phosphorylation that may act as a regulatory switch leading to structural changes such as folding and the sequestration of binding sites (Bah et al., 2015). Because they facilitate protein recognition and binding by acting as adaptable interaction surfaces, IDR regions may often found in hub proteins that link interaction networks and integrate signals (Kim et al., 2008). REMs' basal and signal-induced phosphorylation regions could putatively regulate interactions with its protein partners upon stimulus (Figure 3). This, and the fact that REMs participate in different plant signaling networks, ground the idea that they act as PM-bound-complex signaling “hubs” able to interact with many different proteins, at specific times and locations, and in response to specific stimuli. However, little is known about how REMs integrate diverse signaling cues in plants.

Only a few studies have drawn links between REM phosphorylation and intracellular signaling. Marín and Ott (2012) showed that AtREM1.3 phosphorylation at S66 located in the

IDR region led to a reduced affinity for importins in yeast two-hybrid assays. However, the impact of this phosphorylation on the structure, and subcellular localization of AtREM1.3 remains to be investigated. Furthermore, Gui et al. (2016) demonstrated the role of OsREM4.1 phosphorylation by OsBRI1 in activation of the brassinosteroid signaling pathway (Gui et al., 2016, Figure 2C). While the phosphosites remain to be identified, this model connects REM phosphorylation, hormone-signaling balance and rice development, giving an important insight on one of the functional roles of REM phosphorylation in rice. In Perraki *et al.*, 2018, it was shown that the phosphorylation of StREM1.3 on residues S74, T86, S91 was essential for its anti-viral function and dynamic nanodomain association (Perraki et al., 2018, Figure 2A). Yet, the *in vivo* phosphorylation at those sites in response to PVX infection still remains to be determined.

Although multiple REM phosphosites have been described in phosphoproteomes or with directed approaches, only few REM-associated kinases have been identified (see Supplemental table 1). A recent large-scale phosphoproteomic study identified 8 Arabidopsis kinases (CPK11, MPK6, OST1, SnRK2.4, SOS2, OXI1, CKL2, CRKL2) that could phosphorylate, *in vitro*, AtREM phosphopeptides generated *in vivo* (Wang et al., 2020). Additional kinases responsible for REM phosphorylation have been described in rice, *N. benthamiana*, *M. truncatula*, *L. japonicus* and *A. thaliana* (SnRK1.2, AtCPK3 and various RLKs) (Mehlmer et al., 2010; Tóth et al., 2012; Son et al., 2014; Gui et al., 2016; Perraki et al., 2018; Albers et al., 2019), see a summary in Figure 4. However, all these data have been obtained *in vitro* and will require further validation. Notably, *in vivo* interactions between REMs and protein kinases had already been reported for some of the kinases identified in Wang et al., (2020) (Tóth et al., 2012; Perraki et al., 2018; Albers et al., 2019). These kinases have been reported to phosphorylate a unique REM or several of them (Mehlmer et al., 2010; Tóth et al., 2012; Son et al., 2014; Gui et al., 2016; Perraki et al., 2018; Albers et al., 2019; Wang et al., 2020) (Supplemental Table 1). Interestingly, most of those kinases are associated with DRMs, (Majeran et al., 2018) but some of them are putatively soluble suggesting a PM recruitment.

This protein-protein interaction conferred by regions with high-scores of intrinsic disorder (Raffaele et al., 2007, Marín and Ott, 2012) and phosphorylation (Reymond et al., 1996; Marín and Ott, 2012; Gui et al., 2016; Kohorn et al., 2016; Perraki et al., 2018) (see Figure 3) are characteristics reminiscent of scaffold proteins, such as the 14-3-3 family of proteins. This analogy holds on the cases where REMs' interaction capacity was reported to differ upon phosphorylation of either the interaction partner(s) or the REM isoform itself (Gui et al., 2016; Liang et al., 2018). GRF10 (14-3-3 epsilon, At1g22300) was recently shown to interact with

and mediate AtREM1.2 and AtREM1.3 interaction (Huang et al., 2019). 14-3-3 family proteins are involved in phospho-relay events, preeminently in facilitating and hindering protein-protein interactions by binding to the phosphorylated residues of interaction partners (Lozano-Durán and Robatzek, 2015).

PERSPECTIVES

The amount of data that has been accumulated since the cloning of the first REM in 1989 on the characteristics and the cellular and physiological role of REMs is very heterogeneous. Although many articles have shown REMs expression as being correlated with a number of physiological processes, a clear role for the REM family has not yet arose. Nevertheless, many trails have emerged from the 30 years of research on REMs that show great promise in the search for REMs' functionalities. One of these functionalities stands out, considering the multiple instances where REMs are linked to intercellular connectivity. These instances reinforce the idea that the establishment of REMs as a genetic family could have been important for the adaptation of photosynthetic algae during the land plant invasion that occurred approximately 475 million years ago (Steemans et al., 2009). Indeed, the control of water and solute exchanges between cells and tissues was a major necessary adaptation in order to handle water fluxes in dry land. The development of complex PD along with a complex vasculature necessary for the establishment of root systems and hormone signaling were the fundamental developments that enabled adaptation and establishment of Embryophytes (Rensing et al., 2008). Moreover, the fact REMs are found to be involved in biotic interactions, notably with symbiotic fungi and bacteria is also a clue to their potential involvement in the conquest of land by plants considering the hypothetical importance of symbiotic microorganisms in helping the first rootless land plants to secure nutrients (for review Rensing 2018). (Raffaele et al., 2009a). The recent discovery of Group 1 REMs in a proteomic analysis of *A. thaliana* extracellular vesicles may potentially change our view of REMORIN's strictly-PM function (Rutter and Innes, 2017; Rutter and Innes, 2018).

1. Genetics

A major weakness in the functional study of REMs is the lack of genetic tools. Overall, REM single mutants have not yet been shown to display any striking or strong phenotypes although AtREM1.2 alone has recently been shown to be involved in SA-dependent gravitropism response (Ke et al., 2020). To study REMs, the most notable problematic is currently the lack

of multiple KO-lines for each isoform although the generation of these lines is currently ongoing with the recently published CRISPR-Cas9 KO-lines for two Group 1 REMs in *N. benthamiana* (Fu et al., 2018, Huang et al., 2019) and the quadruple CRISPR-Cas9 KO-line for all four Group 1 REMs in *A. thaliana* soon available (T. Ott, personal communication). KO lines for each REM Group will be essential for our understanding of the role played by each REM Group that could entail not only different possible cellular functions but also different tissue specificities (*e.g.* Gui et al., 2014). Nevertheless, we cannot exclude that REMs from different sub-groups are at least partially redundant or can functionally substitute for other REMs, even if in the wild-type situation they are doing a different function.

Several REM Groups such as Group 5 and Group 3 could consequently become less illusive as to their function. The generation of KO-lines should be combined with gain-of-function assays as those undertaken in the characterization of OsREM6.6 (or GSD1; Gui et al., 2014) and OsREM4.1 (Gui et al., 2016) in order to develop true functional approaches in deciphering the cellular and physiological purposes of REMs.

2. Protein-Protein Interactions

Phosphorylation of REMs are suspected to be involved in protein-protein interactions (Raffaele et al., 2007; Marín et al., 2012) (Figure 2, Supplemental Table 1). These characteristics are reminiscent of scaffold proteins, notably of 14-3-3 family proteins. Recently, GRF10 (14-3-3 epsilon) was shown to interact with AtREM1.2 and to be crucial for its partitioning at the PM (Huang et al., 2019). REMs and 14-3-3 family proteins could indeed co-depend on each other considering REMs' interaction capacity was reported to vary upon phosphorylation of either the interaction partner(s) or the REM isoform itself (Gui et al., 2016; Liang et al., 2018;). In both cases, the REM isoforms *i.e.* OsREM4.1 or SYMREM1 interact with receptor-like kinases (RLKs), OsSERK1 (Gui et al., 2016) and LYK3 and NFP (Liang et al., 2018), respectively (Figure 2B). The interplay between REMs and RLKs deserves to be further investigated particularly in view of the recent emerging role of RLK signaling in PD physiology (Grison et al., 2019; Cheval et al., 2020)

Considering that phosphorylation is at the center of the interaction events recorded for REMs, it seems crucial to develop phospho-dependent interactomic screens for REMs in order to understand their function. This type of screen should importantly be performed under different stress conditions and in different tissues as REMs' interactions with its cognate partners appear to be highly determined by plant development and stress.

3. The PM's complexity

Important advancements have recently been established in the deciphering of the PM-anchoring properties of REMs (Perraki et al., 2012; Gronnier et al., 2017; Martinez et al., 2018; Legrand et al., 2019). In as much as REMs are dependent of their C-terminal region or REM-CA for their anchoring to the PM, more must be developed in the understanding of the exact biophysical properties that govern this anchoring. Critically, decrypting the determinants of the PM-nanodomain association of REMs is a top priority, as it has already been shown to be a determining factor of REM function (Gronnier et al., 2017; Fu et al., 2018; Ke et al., 2020). In particular, affiliating the presence of Group 1 REMs in PM-nanodomains with their observed effect on the accumulation of callose at PD pit-fields (Gronnier et al., 2017; Perraki et al., 2018) raises a critical question: how does a protein, present in the PM inner-leaflet, influence enzymatic activities (*i.e.* callose synthesis/degradation) occurring in the cell wall or, at best in the PM outer-leaflet?

Several hypotheses may be explored to answer this question: 1) Can Group 1 REMs or their interaction partners regulate callose synthases or other partners of the callose synthesis complex present at PD pit-fields in order to stimulate callose deposition? 2) Can Group 1 REMs or their interaction partners regulate the activity or localization of β -1,3-glucanases? This latter question can be a particularly interesting hypothesis to investigate considering the different subcellular and extracellular localizations of β -1,3-glucanases (for review: (Zavaliev et al., 2011)). Group 1 REMs could potentially regulate the extracellular secretion of β -1,3-glucanases as it was reported in Zavaliev et al. 2013 in response to salicylic acid treatments. Yet some β -1,3-glucanases have been reported to be glycosylphosphatidylinositol (GPI)-anchored proteins within the PM outer-leaflet associated with PD (Levy et al., 2007). The enrichment of GPI-anchored proteins in the DRM biochemical fraction (for review on plant GPI-anchored proteins: Yeats et al., 2018) licenses the hypothesis that there could be trans-bilayer coupling between the inner-leaflet PM-domains containing REMs and the outer-leaflet PM-domains containing GPI-anchored β -1,3-glucanases. In this context, the concept of trans-bilayer coupling refers to the presence of each component in a common PM-domain that spans from one PM-leaflet to the other. There could therefore be interaction *in trans* between inner- and outer-leaflet proteins *via* the interdigitation of saturated and/or very-long-chain acyl chains of the lipids that are present in these PM-domains. This functional mechanism has been demonstrated in animal cells by showing the necessity of long-chain PS species with at least one long saturated chain in order to register a GPI-anchored protein to a lipid-protein complex that virtually anchored the

GPI-anchored protein to the actin cytoskeleton (Raghupathy et al., 2015; Skotland and Sandvig, 2019). The registration hypothesis is supported by the altered StREM1.3 PM-dynamics under a phosphorylated state (Perraki et al., 2018), which could be due to the regulation of StREM1.3's PM-lateral-segregation *via* the cortical cytoskeleton. This change in REM PM-patterning could affect the PM-dynamics of PM-outer-leaflet-associated proteins *e.g.* GPI-anchored β -1,3-glucanases. Ultimately, elucidating not only the protein-protein- but also the protein-lipid-interactions necessary for REMs' PM-nanodomain-association constitutes a great challenge that will participate in the unfurling of the complex and dynamic molecular mechanisms that govern REMs particular role(s) at the PM.

New methodologies must be developed in order to study the PM-based events and interactions: these methodologies should include: 1) cutting-edge proteomic and lipidomic techniques (*e.g.* identifying lipids in close interaction with proteins) including phosphoproteomics and the study of lipidated proteins (myristoylation, palmitoylation, isoprenylation, and GPI-anchoring; reviewed in Ray et al., 2017); 2) biophysical tools to study lipid-protein interactions *via* surface plasmon resonance (*e.g.* Lenarčič et al., 2017), liposome binding assays and lipid blotting assays (*e.g.* Perraki et al., 2012), solid-state NMR, cryo-electron microscopy, atomic force microscopy, computational modeling, Langmuir monolayer tensiometry, and Fourier transform infrared spectrometry (*e.g.* Gronnier et al., 2017; methods reviewed in Zhou & Hancock 2018); 3) to obtain the structure of these lipid-protein complexes for example by solid-state NMR; 4) generation of mutants impaired in PM-domain-association and the use of super-resolution imaging to visualize the *in vivo* segregation and dynamics of PM-components, which should be a focus in order to better understand the molecular interplay occurring at the protein and lipid clustering sites that are PM-domains. These important tools can considerably be assisted by *in silico* modeling such as molecular dynamics simulations (for review: Ulmschneider & Ulmschneider 2018). Overall, these techniques and methods have been used and described in numerous research articles and reviews that focus on understanding the function of PM-based proteins (Zhou et al., 2015; Zhou et al., 2017; Gronnier et al., 2018; Maxwell et al., 2018).

ACKNOWLEDGEMENTS

This work was sustained by CNRS (Centre National de la Recherche Scientifique) and the University of Bordeaux. This work has benefited from the facilities of the Bordeaux Metabolome/lipidome Facility-MetaboHUB (ANR-11-INBS-0010). AFD, AL, JG and PG were supported by grants from the French Ministère de l'Enseignement Supérieur et de la Recherche (MESR). JG was supported by EMBO LTF 438-2018 and ERC-2017-COG IMMUNO-PEPTALK ID: 773153. SM, BH, MB and VG are supported by ANR project Phospho-REM domain (ANR 2019). SG, SM, VG are supported by ANR project Potymove The IPS2 (MB) benefits from the support of the LabEx Saclay Plant Sciences-SPS (ANR-10-LABX-0040-SPS). BH was supported by the CNRS Momentum.

AUTHOR CONTRIBUTIONS

PG and JG developed the rationale of the review and wrote the text with the help of all the co-authors. AL and BH did the Figure 1 and wrote the corresponding text. PG did the Figure 2. AP did the Figures 3 and 4. MDJ and MB gathered the data for the Supplementary Table 1 and wrote the corresponding text. SM and VG supervised the writing and figures. All authors read and corrected the manuscript.

Table 1: Data mining toward the putative functions of REMORINs

Plant species	Group of REMs	Methods / Stimuli	Biological effect(s)	Putative associated function(s)	References
<i>Arabidopsis thaliana</i>	AtREM1.2	Protein-protein interaction (<i>in vivo</i> co-purification)	Interaction with RPM1-INTERACTING PROTEIN 4 (RIN4)	Bacterial immunity	(Mackey et al., 2002; Liu et al., 2009a; Lee et al., 2015)
	AtREM1.2	Proteomics and Phosphoproteomics / AvrRPM1	Increased protein amount and phosphorylation	Bacterial immunity	(Widjaja et al., 2009)
	AtREM1.2 AtREM1.3	Protein-protein interaction (<i>in vivo</i> Proximity-dependent biotin identification BioID)	Interaction with HopF2b ^{PRODC3000}	Bacterial immunity	(Khan et al., 2018)
	AtREM1.2 AtREM1.3	Proteomics	Presence in extracellular vesicles	Immunity	(Rutter and Innes, 2017)
	AtREM1.3	Phosphoproteomics / Flagellin (flg22)	Increased phosphorylation	Bacterial immunity	(Benschop et al., 2007)
	AtREM1.3	Transcriptomics / Water deficit, cold, mannitol, salt stress	Transcript up-regulation	Abiotic stress	(Reymond et al., 2000; Bray, 2002; Kreps et al., 2002)
	AtREM1.3	Transcriptomics / auxin	Transcript up-regulation	Development	(Alliotte et al., 1989)
	AtREM1.3	Protein-protein interaction (yeast two-hybrid)	Interaction with Arabidopsis response-regulator 4 (ARR4)	Cytokinin response	(Yamada et al., 1998)
	AtREM1.3	Affinity-based chromatography enrichment with immobilized ergosterol/ergosterol	Interaction with the fungal MAMP ergosterol	Fungal immunity	(Khoza et al., 2019)
	AtREM4.1 AtREM4.2	Transcriptomics / Drought, osmotic, salt stress and ABA treatment	Transcript up-regulation	Abiotic stress	(Reymond et al., 2000; Bray, 2002; Son et al., 2014).
	AtREM6.7	Transcriptomics / Overexpression of DAYSLEEPER	Transcript up-regulation	Flowering, PD connectivity in the meristematic zones	(Bundock and Hooykaas, 2005)
<i>Curcumis sativus</i>	Group 1 and 4 CsREM5	Quantitative trait loci and transcriptomics / <i>Podosphaera fusca</i>	Transcript up-regulation associated with increased fungal resistance	Fungal immunity	(Xu et al., 2017)
<i>Glycine max</i>	GmREM4	Transcriptomics / Drought treatment	Transcript up-regulation	Abiotic stress, circadian rhythm	(Marcolino-Gomes et al., 2014)

<i>Hordeum vulgare</i>	Group 1 REM	Transcriptomics / GA and ABA treatments	Transcript down-regulation	Hormone response	(Chen and An, 2006)
<i>Lotus japonicus</i>	Group 1 REMs	Transcriptomics / <i>Glomus intraradices</i>	Transcript up-regulation	Fungal symbiosis	(Kistner et al., 2005)
<i>Oryza sativa</i>	OsREM1.5	Transcriptomics / ABA, BR treatments	Transcript up-regulation	Hormone response	(Lin et al., 2003)
	OsREM5.3 (Long Panicle 1 LP1)	Quantitative trait loci	Strongly expressed in young panicle, associated with longer panicle	Panicle size	(Liu et al., 2016)
	OsREM4.1	Transcriptomics / overexpression of <i>Deschampsia antartica</i> C-repeat binding factor /dehydration-responsive element binding protein (CBF/DREB), DaCBF7	Transcript up-regulation	Stress adaptation, cold recovery	(Byun et al., 2015)
	OsREM6.5	drought stress and ABA treatment	Transcript up-regulation	Stress adaptation,	(Wu et al., 2006)
<i>Quercus robur</i>	QrREM4.1	Transcriptomics / <i>Piloderma croceum</i>	Transcript up-regulation	Ectomycorrhizal symbiosis	(Tarkka et al., 2013)
<i>Solanum tuberosum</i>	StREMa4	Transcriptomics / <i>Ralstonia solanacearum</i>	Transcript up-regulation	Bacterial immunity	(Kong et al., 2016)
	StREMa4	Transcriptomics/ ABA, SA, MeJa	Transcript up-regulation	Hormone response	(Kong et al., 2016)
<i>Solanum lycopersicum</i>	SIREM1.2	Tomato plants overexpressing CaPIF1	Transcript up-regulation	Enhanced resistance to cold stress	(Seong et al., 2007).
	SIREM1.2	Proteomics / <i>Verticillium dahlia</i>	Increased protein amount during incompatible interaction	Fungal immunity	(Hu et al., 2019)
<i>Triticum aestivum</i>	12 members of TaREM	Transcriptomics / Cold acclimation	Transcript up-regulation during early (7 TaREMs) and late (3 TaREMs) cold response, Transcript down-regulation (2 TaREM)	Cold adaptation	(Badawi et al., 2019)
<i>Zea mays</i>	ZmREM4.1	Transcriptomics / cold	Transcript down-regulation	Cold sensitivity	(Bilska-Kos et al., 2016).
	ZmREM4.1	Transcripts localized near PD linking cells from the Kranz mesophyll and the bundle sheath	Transcript localization	PD connectivity	(Bilska-Kos et al., 2016)

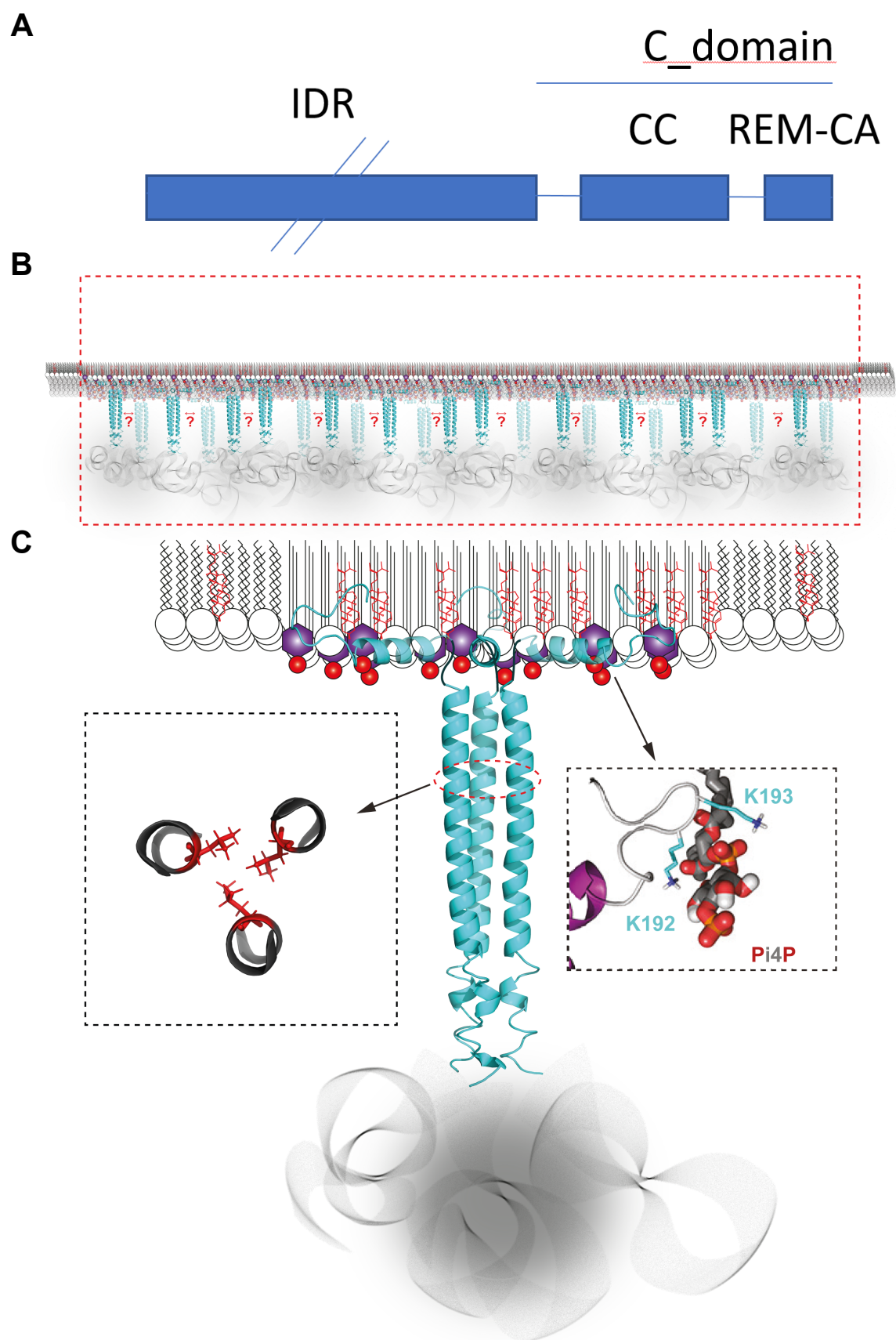


Figure 1

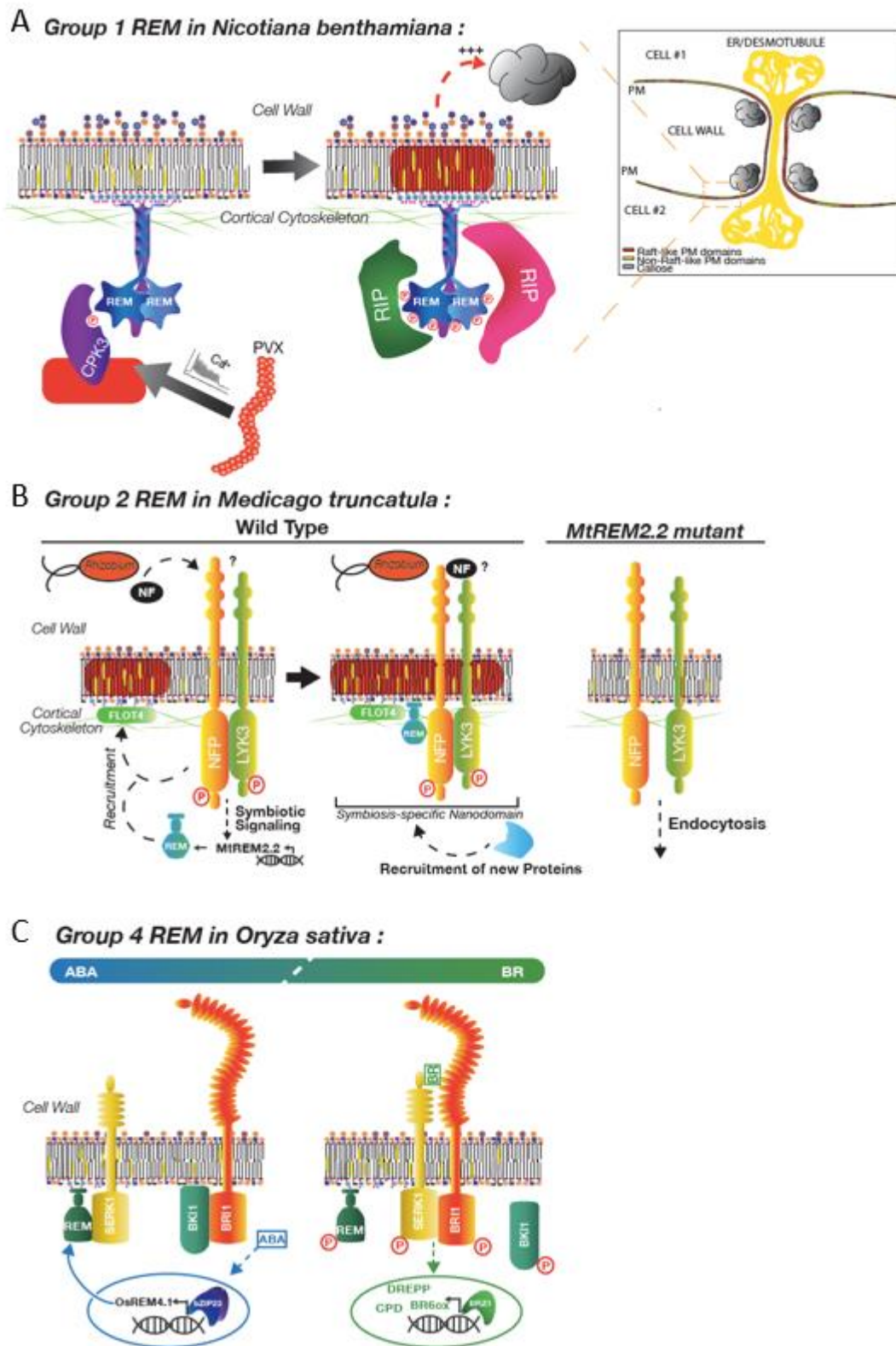


Figure 2

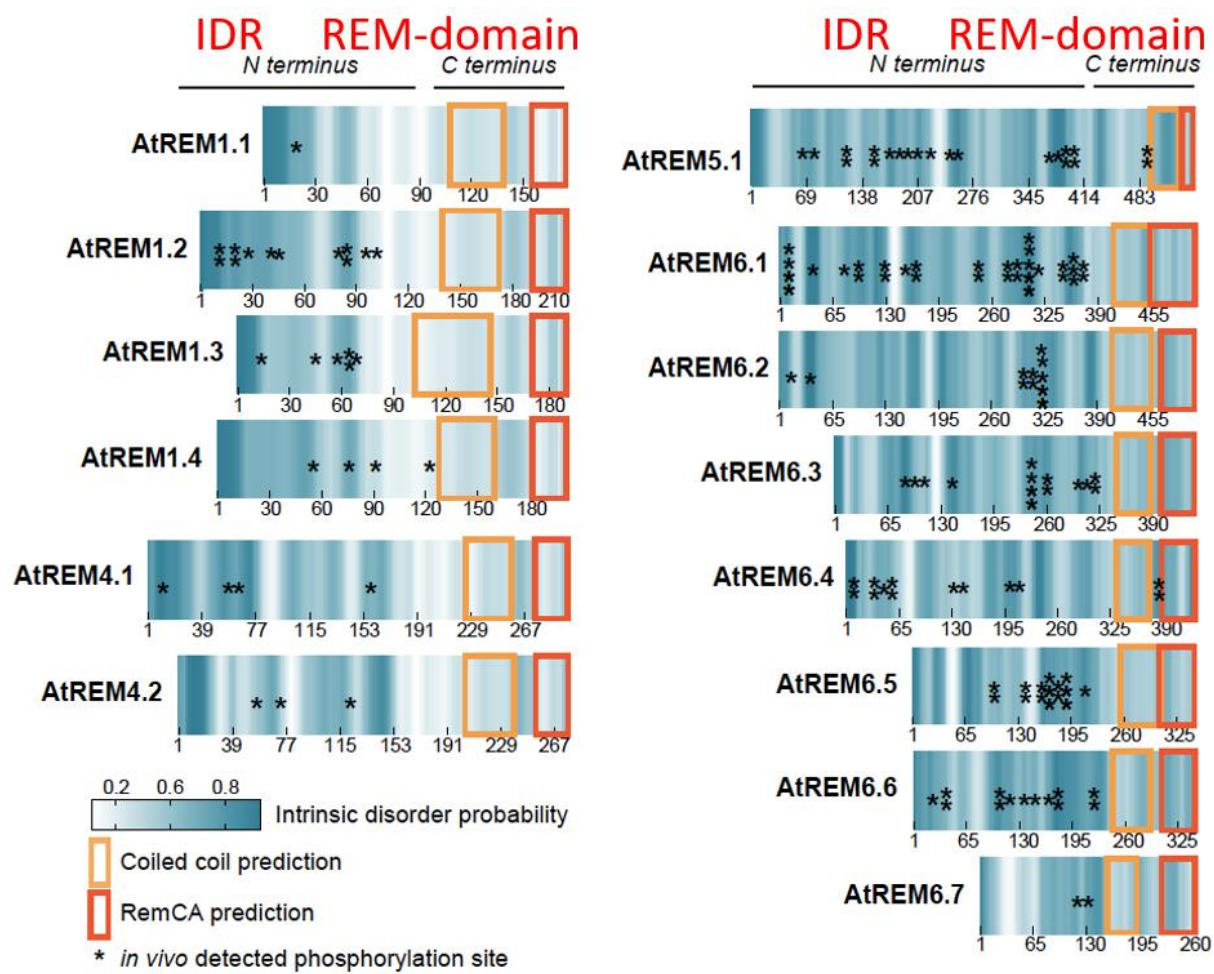


Figure 3

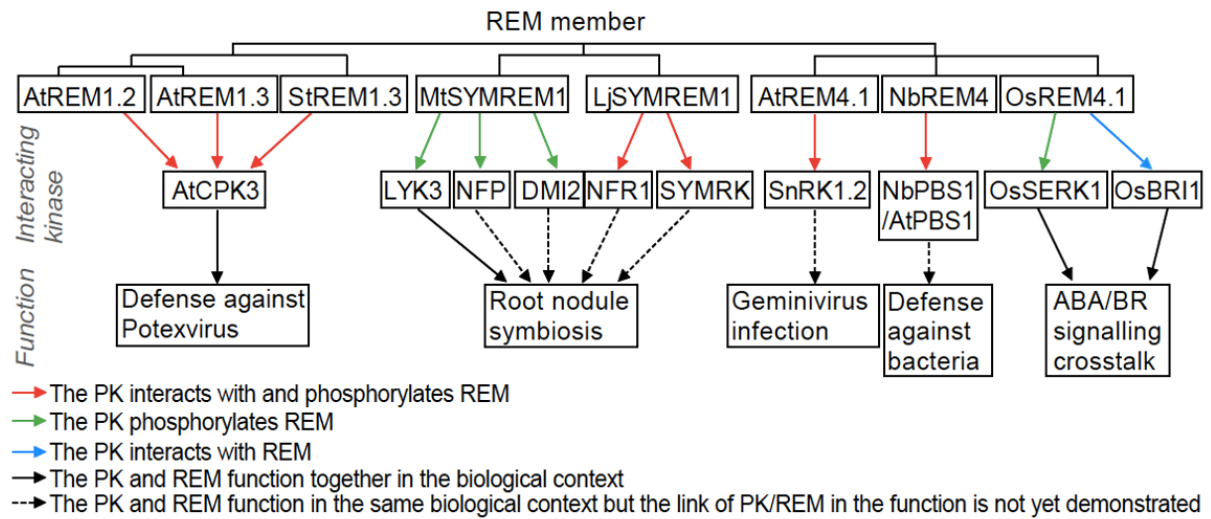


Figure 4

FIGURE LEGENDS

Figure 1: StREM1.3-enriched PM nanodomains based on structural analysis. (A) Sequence features of all REMs with Intrinsically Disordered Region (IDR) domain at the N-terminal highly variable in length, and a REM-C domain composed of a coiled-coil region (CC) and the REM-C-terminal anchor (REM-CA); (B) StREM1.3 (blue) clusters at the PM's inner leaflet into nanodomains (red rectangle) enriched in phytosterols and phosphoinositides, the most common being sitosterol and PI4P (Palta et al., 1993; Furt et al., 2010; Furt et al., 2011; Gronnier et al., 2017; Legrand et al., 2019). The overall REM orientation is likely to be perpendicular to the membrane plane to minimize steric hindrance, though the precise angle distribution is unknown. Lipids herein are more ordered than the bulk of the PM and the membrane therefore is slightly thicker even though the PM's complex composition may greatly attenuate this tendency (Gronnier et al., 2018, Legrand et al., 2019); (C) StREM1.3 forms homo-trimers through a coiled-coil domain (Martinez et al., 2018) bundling together three REM C-terminal membrane anchors (REM-CA) (Gronnier et al., 2017) and three intrinsically-disordered regions (IDR) bearing phosphorylation sites (Perraki et al., 2018). REM-CA binds to PI4P through electrostatic interactions involving, notably, positively charged amino-acids K192 and K193, as proposed in the right panel by molecular dynamics (Gronnier et al., 2017). The most C-terminal part (region 2) of REM-CA is embedded inside the inner leaflet, as supported by solid-state NMR and molecular dynamics (Gronnier et al., 2017). Nanodomain-associated PIPs being enriched in saturated acyl chains (Furt et al., 2010), sitosterol is also recruited. The left panel shows hydrophobic contacts between the three L155 residues (red), which are critical to the coiled-coil's structure, supporting membrane-association (Martinez et al. 2019). Membrane binding is accompanied by an enrichment in PI4P and sitosterol in the vicinity of the binding site (Legrand et al., 2019). A relative impoverishment in such lipids in the surrounding bulk membrane would therefore be a logical consequence. Note here that only REM molecules are presented, and the other PM proteins are omitted.

Figure 2. Proposed model for REM-mediated signaling. (A). Group 1 REM in *Nicotiana benthamiana*. Proposed model for the molecular mechanisms involved in the StREM1.3-dependent limiting of PVX cell-to-cell movement according to the data from (Raffaele et al. 2009; Perraki et al. 2012; Gronnier et al. 2017; Perraki et al. 2018). Perception of PVX leads to the production of a calcium burst that activates a group 2 calcium-dependent protein kinase (here CPK3), which in turns phosphorylates group 1 REMs. Group 1 REMs' phosphorylated

state increases its PM-mobility and interacts with phospho-REM Interacting Proteins (RIP). These interactions cause an increase in callose deposition at the plasmodesmata; (B) Group 2 REM in *Medicago truncatula*. Constitutively-expressed FLOT4 forms a primary PM-scaffold that is unable to recruit LYK3 in the absence of SYMREM1 (MtREM2.2). Nod factor (NF) perception by NFP and LYK3 PM-receptors triggers the activation of a symbiosis-specific signaling cascade that leads to the expression of SYMREM1. Due to its ability to directly bind LYK3, SYMREM1 actively recruits the receptor into the FLOT4 domain. In *symrem1* mutants, LYK3 is destabilized and endocytosed upon rhizobial inoculation. Illustrations adapted from Liang et al. 2018; (C) Group 4 REM in *Oryza sativa*. OsREM4.1 protein is PM-localized in association with OsBRI1-OsSERK1 complex. Upon elevated ABA levels, the ABA-responsive transcription factor OsbZIP23 is activated and upregulates OsREM4.1 expression. OsREM4.1 protein interacts with OsSERK1 and interferes with OsBRI1-OsSERK1 active complex formation, repressing therefore BR signaling initiation. Increased BR levels, causes the binding of BR to the extracellular domain of OsBRI1 and the activation of OsBRI1 kinase (BKI1) to phosphorylate OsREM4.1. The phosphorylated OsREM4.1, has lower binding affinity to OsSERK1, and therefore the OsREM4.1- OsSERK1 complex is dissociated. Therefore, OsSERK1 is able to interact with OsBRI1 to form the OsBRI1- OsSERK1 receptor kinase complex, and activate BR signaling. OsREM4.1 function is similar to BKI1, which upon BR binding to BRI1, is phosphorylated and released from the PM, allowing the BRI1/SERK1 complex to form. Illustrations adapted from Gui et al. 2016.

Figure 3. Phosphorylation of Arabidopsis REMs occurs mostly at putative intrinsically disordered regions at its N-terminus. Graphs show the intrinsic disorder probability on the Arabidopsis REM proteins that were found to be phosphorylated up to date by in vivo studies. In vivo phosphorylation site positions on REM sequences are indicated by asterisk. Intrinsic disorder predictions were calculated using the PrDOS-Protein disorder prediction server (<http://prdos.hgc.jp/cgi-bin/top.cgi>). Coiled-coil predictions were calculated using the COILS program (https://embnet.vital-it.ch/software/COILS_form.html). REM-CA prediction was estimated based on homology with the REM-CA protein from StREM1.3.

Figure 4. REM proteins are involved in independent signaling pathways and are phosphorylated by different kinases.

Schematic representation of all the known interactions between REM proteins from groups 1, 2, 4 and protein kinases, that were described in plant immunity, symbiosis and hormonal

signaling. Dotted lined arrow (i.e. Functional link to be determined) signifies that the given REM and kinases were identified as being involved in the given biological context yet direct experimental data has yet to be established. See text for details.

SUPPLEMENTAL INFORMATION

Table 1: Compilation of phosphoproteomic datasets on REMs of different plant species. (Nühse et al., 2004; Benschop et al., 2007; Niittylä et al., 2007; Nühse et al., 2007; Sugiyama et al., 2008; Whiteman et al., 2008; Li et al., 2009; Reiland et al., 2009; Chen et al., 2010; Grimsrud et al., 2010; Mehlmer et al., 2010; Nakagami et al., 2010; Reiland et al., 2011; Engelsberger and Schulze, 2012; Lan et al., 2012; Mayank et al., 2012; Tóth et al., 2012; Yang et al., 2013; Son et al., 2014; Wang et al., 2014; Choudhary et al., 2015; Hou et al., 2015; Lu et al., 2015; Marcon et al., 2015; Roitinger et al., 2015; Ye et al., 2015; Gui et al., 2016; Kohorn et al., 2016; Marondedze et al., 2016; Mattei et al., 2016; Nukarinen et al., 2016; Qiu et al., 2016; Vu et al., 2016; Xiang et al., 2016; Qiu et al., 2017; Nikonorova et al., 2018; Perraki et al., 2018; Song et al., 2018; Wang et al., 2018; Albers et al., 2019; Gupta et al., 2019; Wong et al., 2019; Cai et al., 2020; Mergner et al., 2020; Wang et al., 2020)

REFERENCES

- Albers P, Üstün S, Witzel K, Kraner M, Börnke F** (2019) A Remorin from *Nicotiana benthamiana* Interacts with the *Pseudomonas* Type-III Effector Protein HopZ1a and is Phosphorylated by the Immune-Related Kinase PBS1. *Mol Plant-Microbe Interact* **32**: 1229–1242
- Alliotte T, Tiré C, Engler G, Peleman J, Caplan a, Van Montagu M, Inzé D** (1989) An Auxin-Regulated Gene of *Arabidopsis thaliana* Encodes a DNA-Binding Protein. *Plant Physiol* **89**: 743–52
- Amor-Mahjoub M, Suppini JP, Gomez-Vrielyunck N, Ladjimi M** (2006) The effect of the hexahistidine-tag in the oligomerization of HSC70 constructs. *J Chromatogr B Anal Technol Biomed Life Sci* **844**: 328–334
- Badawi MA, Agharbaoui Z, Zayed M, Li Q, Byrns B, Zou J, Fowler DB, Danyluk J, Sarhan F** (2019) Genome-Wide Identification and Characterization of the Wheat Remorin (Ta REM) Family during Cold Acclimation. *Plant Genome* **12**: 180040
- Bah A, Vernon RM, Siddiqui Z, Krzeminski M, Muhandiram R, Zhao C, Sonenberg N, Kay LE, Forman-Kay JD** (2015) Folding of an intrinsically disordered protein by phosphorylation as a regulatory switch. *Nature* **519**: 106–109
- Bariola PA, Retelska D, Stasiak A, Kammerer RA, Fleming A, Hijri M, Frank S, Farmer EE** (2004) Remorins form a novel family of coiled coil-forming oligomeric and filamentous proteins associated with apical, vascular and embryonic tissues in plants. *Plant Mol Biol* **55**: 579–594
- Benschop JJ, Mohammed S, O’Flaherty M, Heck AJR, Slijper M, Menke FLH** (2007) Quantitative Phosphoproteomics of Early Elicitor Signaling in *Arabidopsis*. *Mol Cell Proteomics* **6**: 1198–1214
- Bilska-Kos A, Grzybowski M, Jończyk M, Sowiński P** (2016) In situ localization and changes in the expression level of transcripts related to intercellular transport and phloem loading in leaves of maize (*Zea mays* L.) treated with low temperature. *Acta Physiol Plant*. doi: 10.1007/s11738-016-2151-5
- van den Bogaart G, Meyenberg K, Risselada HJ, Amin H, Willig KI, Hubrich BE, Dier M, Hell SW, Grubmüller H, Diederichsen U, et al** (2011) Membrane protein sequestering by ionic protein–lipid interactions. *Nature* **479**: 552–555
- Bozkurt TO, Richardson A, Dagdas YF, Mongrand S, Kamoun S, Raffaele S** (2014) The Plant Membrane-Associated REMORIN1.3 Accumulates in Discrete Perihyphae Domains and Enhances Susceptibility to *Phytophthora infestans*. *Plant Physiol* **165**: 1005–1018
- Bray EA** (2002) Classification of genes differentially expressed during water-deficit stress in *Arabidopsis thaliana*: An analysis using microarray and differential expression data. *Ann Bot* **89**: 803–811
- Bücherl CA, Jarsch IK, Schudoma C, Segonzac C, Mbengue M, Robatzke S, MacLean D, Ott T, Zipfe C** (2017) Plant immune and growth receptors share common signalling components but localise to distinct plasma membrane nanodomains. *Elife* **6**: 1–28
- Byun MY, Lee J, Cui LH, Kang Y, Oh TK, Park H, Lee H, Kim WT** (2015) Constitutive expression of DaCBF7, an Antarctic vascular plant *Deschampsia antarctica* CBF homolog, resulted in improved cold tolerance in transgenic rice plants. *Plant Sci* **236**: 61–74
- Cai J, Chen T, Wang Y, Qin G, Tian S** (2020) SIREM1 triggers cell death by activating an oxidative burst and other regulators. *Plant Physiol* pp.00120.2020
- Cai J, Qin G, Chen T, Tian S** (2018) The mode of action of remorin1 in regulating fruit ripening at transcriptional and post-transcriptional levels. *New Phytol* **219**: 1406–1420
- Checker VG, Khurana P** (2013) Molecular and functional characterization of mulberry EST

- encoding remorin (MiREM) involved in abiotic stress. *Plant Cell Rep* **32**: 1729–41
- Chen K, An YQC** (2006) Transcriptional responses to gibberellin and abscisic acid in Barley aleurone. *J Integr Plant Biol* **48**: 591–612
- Chen Y, Hoehenwarter W, Weckwerth W** (2010) Comparative analysis of phytohormone-responsive phosphoproteins in *Arabidopsis thaliana* using TiO₂-phosphopeptide enrichment and mass accuracy precursor alignment. *Plant J* **63**: 1–17
- Cheng G, Yang Z, Zhang H, Zhang J, Xu J** (2020) Remorin interacting with PCaP1 impairs Turnip mosaic virus intercellular movement but is antagonised by VPg. *New Phytol* **225**: 2122–2139
- Cheval C, Samwald S, Johnston MG, de Keijzer J, Breakspear A, Liu X, Bellandi A, Kadota Y, Zipfel C, Faulkner C** (2020) Chitin perception in plasmodesmata characterizes submembrane immune-signaling specificity in plants. *Proc Natl Acad Sci U S A* **117**: 9621–9629
- Choudhary MK, Nomura Y, Wang L, Nakagami H, Somers DE** (2015) Quantitative circadian phosphoproteomic analysis of *Arabidopsis* reveals extensive clock control of key components in physiological, metabolic, and signaling pathways. *Mol Cell Proteomics* **14**: 2243–2260
- Demir F, Horntich C** (2013) *Arabidopsis* nanodomain-delimited ABA signaling pathway regulates the anion channel SLAH3. *Proc* doi: 10.6019/PXD000211
- Dyson HJ, Wright PE** (2005) Intrinsically unstructured proteins and their functions. *Nat Rev Mol Cell Biol* **6**: 197–208
- Engberg O, Hautala V, Yasuda T, Dehio H, Murata M, Slotte JP, Nyholm TKM** (2016) The Affinity of Cholesterol for Different Phospholipids Affects Lateral Segregation in Bilayers. *Biophys J* **111**: 546–556
- Engelsberger WR, Schulze WX** (2012) Nitrate and ammonium lead to distinct global dynamic phosphorylation patterns when resupplied to nitrogen-starved *Arabidopsis* seedlings. *Plant J* **69**: 978–995
- Farmer E, Pearce G, Ryan C** (1989) In vitro phosphorylation of plant plasma membrane proteins in response to the proteinase inhibitor inducing factor. *Proc ...* **86**: 1539–1542
- Farmer EE, Moloshok TD, Saxton MJ** (1991) Oligosaccharide Signaling in Plants. *Mol Biol* 0–5
- Fernandez-Calvino L, Faulkner C, Walshaw J, Saalbach G, Bayer E, Benitez-Alfonso Y, Maule A** (2011) *Arabidopsis* plasmodesmal proteome. *PLoS One*. doi: 10.1371/journal.pone.0018880
- Fu S, Xu Y, Li C, Li Y, Wu J, Zhou X** (2018) Rice Stripe Virus Interferes with S-acylation of Remorin and Induces Its Autophagic Degradation to Facilitate Virus Infection. *Mol Plant* **11**: 269–287
- Furt F, König S, Bessoule JJ, Sargueil F, Zallot R, Stanislas T, Noirot E, Lherminier J, Simon-Plas F, Heilmann I, et al** (2010) Polyphosphoinositides are enriched in plant membrane rafts and form microdomains in the plasma membrane. *Plant Physiol* **152**: 2173–2187
- Furt F, Mongrand S, Simon-Plas F** (2011) The Plant Plasma Membrane. *Plant Plasma Membr.* doi: 10.1007/978-3-642-13431-9
- Grimsrud PA, den Os D, Wenger CD, Swaney DL, Schwartz D, Sussman MR, Ané JM, Coon JJ** (2010) Large-scale Phosphoprotein analysis in *Medicago truncatula* roots provides insight into in vivo kinase activity in legumes. *Plant Physiol* **152**: 19–28
- Grisson MS, Kirk P, Brault ML, Wu XN, Schulze WX, Benitez-Alfonso Y, Immel F, Bayer EM** (2019) Plasma membrane-associated receptor-like kinases relocate to plasmodesmata in response to osmotic stress. *Plant Physiol* **181**: 142–160
- Gronnier J, Crowet JM, Habenstein B, Nasir MN, Bayle V, Hosy E, Platre MP, Gougnet**

- P, Raffaele S, Martinez D, et al** (2017) Structural basis for plant plasma membrane protein dynamics and organization into functional nanodomains. *Elife* **6**: 26404
- Gronnier J, Gerbeau-Pissot P, Germain V, Mongrand S, Simon-Plas F** (2018) Divide and Rule: Plant Plasma Membrane Organization. *Trends Plant Sci* **23**: 899–917
- Gui J, Liu C, Shen J, Li L** (2014) Grain setting defect1, Encoding a Remorin Protein, Affects the Grain Setting in Rice through Regulating Plasmodesmatal Conductance. *Plant Physiol* **166**: 1463–1478
- Gui J, Zheng S, Liu C, Shen J, Li J, Li L** (2016) OsREM4.1 Interacts with OsSERK1 to Coordinate the Interlinking between Absciscic Acid and Brassinosteroid Signaling in Rice. *Dev Cell* **38**: 201–213
- Gui J, Zheng S, Shen J, Li L** (2015) Grain setting defect1 (GSD1) function in rice depends on S-acylation and interacts with actin 1 (OsACT1) at its C-terminal. *Front Plant Sci* **6**: 1–11
- Gupta R, Min CW, Kim YJ, Kim ST** (2019) Identification of Msp1-induced signaling components in rice leaves by integrated proteomic and phosphoproteomic analysis. *Int J Mol Sci* **20**: 1–17
- Hemsley PA, Weimar T, Lilley KS, Dupree P, Grierson CS** (2013) A proteomic approach identifies many novel palmitoylated proteins in Arabidopsis. *New Phytol* **197**: 805–814
- Hou Y, Qiu J, Tong X, Wei X, Nallamilli BR, Wu W, Huang S, Zhang J** (2015) A comprehensive quantitative phosphoproteome analysis of rice in response to bacterial blight. *BMC Plant Biol* **15**: 1–15
- Hu X, Puri KD, Gurung S, Klosterman SJ, Wallis CM, Britton M, Durbin-Johnson B, Phinney B, Salemi M, Short DPG, et al** (2019) Proteome and metabolome analyses reveal differential responses in tomato -Verticillium dahliae-interactions. *J Proteomics* **207**: 103449
- Huang D, Sun Y, Ma Z, Ke M, Cui Y, Chen Z, Chen C, Ji C, Tran TM, Yang L, et al** (2019) Salicylic acid-mediated plasmodesmal closure via Remorin-dependent lipid organization. *Proc Natl Acad Sci U S A* **116**: 21274–21284
- Iakoucheva LM, Radivojac P, Brown CJ, O'Connor TR, Sikes JG, Obradovic Z, Dunker AK** (2004) The importance of intrinsic disorder for protein phosphorylation. *Nucleic Acids Res* **32**: 1037–1049
- Jacinto T, Farmer E, Ryan C** (1993) Purification of potato leaf plasma membrane protein pp34, a protein phosphorylated in response to oligogalacturonide signals for defense and development. *Plant Physiol* **139**: 1393–1397
- Jaillais Y, Ott T** (2020) The Nanoscale Organization of the Plasma Membrane and Its Importance in Signaling: A Proteolipid Perspective. *Plant Physiol* **182**: 1682–1696
- Jamann TM, Luo X, Morales L, Kolkman JM, Chung CL, Nelson RJ** (2016) A remorin gene is implicated in quantitative disease resistance in maize. *Theor Appl Genet* **129**: 591–602
- Jarsch IK, Konrad SSA, Stratil TF, Urbanus SL, Szymanski W, Braun P, Braun K-HK-H, Ott T** (2014) Plasma Membranes Are Subcompartmentalized into a Plethora of Coexisting and Diverse Microdomains in Arabidopsis and Nicotiana benthamiana. *Plant Cell* **26**: 1698–1711
- Ke M, Ma Z, Wang D, Sun Y, Wen C, Huang D, Chen Z, Yang L, Tan S, Li R, et al** (2020) Salicylic acid regulates PIN2 auxin transporter hyper-clustering and root gravitropic growth via Remorin-dependent lipid nanodomain organization in Arabidopsis thaliana. *New Phytol* **0**: 0–2
- Keinath NF, Kierszniowska S, Lorek J, Bourdais G, Kessler SA, Shimosato-Asano H, Grossniklaus U, Schulze WX, Robatzek S, Panstruga R** (2010) PAMP (Pathogen-associated Molecular Pattern)-induced changes in plasma membrane

- compartmentalization reveal novel components of plant immunity. *J Biol Chem* **285**: 39140–39149
- Khan M, Youn J-Y, Gingras A-C, Subramaniam R, Desveaux D** (2018) In planta proximity dependent biotin identification (BioID). *Sci Rep* **8**: 9212
- Khoza TG, Dubery IA, Piater LA** (2019) Identification of candidate ergosterol-responsive proteins associated with the plasma membrane of arabidopsis Thaliana. *Int J Mol Sci* **20**: 1–22
- Kim PM, Sboner A, Xia Y, Gerstein M** (2008) The role of disorder in interaction networks: A structural analysis. *Mol Syst Biol* **4**: 179
- Kistner C, Winzer T, Pitzschke A, Mulder L, Sato S, Kaneko T, Tabata S, Sandal N, Stoudgard J, Webb KJ, et al** (2005) Seven Lotus japonicus Genes Required for Transcriptional Reprogramming of the Root during Fungal and Bacterial Symbiosis. *Plant Cell* **17**: 2217–2229
- Kohorn BD, Hoon D, Minkoff BB, Sussman MR, Kohorn SL** (2016) Rapid Oligo-Galacturonide Induced Changes in Protein Phosphorylation in Arabidopsis. *Mol Cell Proteomics* **15**: 1351–1359
- Konrad SSA, Popp C, Stratil TF, Jarsch IK, Thallmair V, Folgmann J, Marín M, Ott T** (2014) S-acylation anchors remorin proteins to the plasma membrane but does not primarily determine their localization in membrane microdomains. *New Phytol* **203**: 758–769
- Kreps JA, Wu Y, Chang H, Zhu T, Wang X, Harper JF, Mesa T, Row M, Diego S, California JAK, et al** (2002) Transcriptome Changes for Arabidopsis in Response to Salt, Osmotic, and Cold Stress. *Plant Physiol* **130**: 2129–2141
- Kusumi A, Fujiwara TK, Chadda R, Xie M, Tsunoyama TA, Kalay Z, Kasai RS, Suzuki KGN** (2012) Dynamic Organizing Principles of the Plasma Membrane that Regulate Signal Transduction: Commemorating the Fortieth Anniversary of Singer and Nicolson's Fluid-Mosaic Model. *Annu Rev Cell Dev Biol* **28**: 215–250
- Lan P, Li W, Wen TN, Schmidt W** (2012) Quantitative phosphoproteome profiling of iron-deficient arabidopsis roots. *Plant Physiol* **159**: 403–417
- Lee D, Bourdais G, Yu G, Robatzek S, Coaker G** (2015) Phosphorylation of the Plant Immune Regulator RPM1-INTERACTING PROTEIN4 Enhances Plant Plasma Membrane H⁺-ATPase Activity and Inhibits Flagellin-Triggered Immune Responses in Arabidopsis. *Plant Cell* **27**: 2042–2056
- Lefebvre B, Timmers T, Mbengue M, Moreau S, Hervé C, Tóth K, Bittencourt-Silvestre J, Klaus D, Deslandes L, Godiard L, et al** (2010) A remorin protein interacts with symbiotic receptors and regulates bacterial infection. *Proc Natl Acad Sci U S A* **107**: 2343–8
- Legrand A, Martinez D, Grélard A, Berbon M, Morvan E, Tawani A, Loquet A, Mongrand S, Habenstein B** (2019) Nanodomain Clustering of the Plant Protein Remorin by Solid-State NMR. *Front Mol Biosci* **6**: 1–14
- Lenarčič T, Albert I, Böhm H, Hodnik V, Pirc K, Zavec AB, Podobnik M, Pahovnik D, Žagar E, Pruitt R, et al** (2017) Eudicot plant-specific sphingolipids determine host selectivity of microbial NLP cytolysins. *Science* (80-) **358**: 1431–1434
- Levy A, Erlanger M, Rosenthal M, Epel BL** (2007) A plasmodesmata-associated β -1,3-glucanase in Arabidopsis. *Plant J* **49**: 669–682
- Li H, Wai SW, Zhu L, Hong WG, Ecker J, Li N** (2009) Phosphoproteomic analysis of ethylene-regulated protein phosphorylation in etiolated seedlings of Arabidopsis mutant ein2 using two-dimensional separations coupled with a hybrid quadrupole time-of-flight mass spectrometer. *Proteomics* **9**: 1646–1661
- Liang P, Stratil TF, Popp C, Marín M, Folgmann J, Mysore KS, Wen J, Ott T** (2018)

- Symbiotic root infections in *Medicago truncatula* require remorin-mediated receptor stabilization in membrane nanodomains. *Proc Natl Acad Sci* **115**: 5289–5294
- Lin F, Xu SL, Ni WM, Chu ZQ, Xu ZH, Xue HW** (2003) Identification of ABA-responsive genes in rice shoots via cDNA macroarray. *Cell Res* **13**: 59–68
- Liu E, Liu Y, Wu G, Zeng S, Tran Thi TG, Liang L, Liang Y, Dong Z, She D, Wang H, et al** (2016) Identification of a Candidate Gene for Panicle Length in Rice (*Oryza sativa* L.) Via Association and Linkage Analysis. *Front Plant Sci* **7**: 1–13
- Liu J, Elmore JM, Coaker G** (2009a) Investigating the functions of the RIN4 protein complex during plant innate immune responses. *Plant Signal Behav* **4**: 1107–1110
- Liu J, Elmore JM, Fuglsang AT, Palmgren MG, Staskawicz BJ, Coaker G** (2009b) RIN4 functions with plasma membrane H⁺-ATPases to regulate stomatal apertures during pathogen attack. *PLoS Biol.* doi: 10.1371/journal.pbio.1000139
- Lozano-Durán R, Robatzek S** (2015) 14-3-3 Proteins in Plant-Pathogen Interactions. *Mol Plant-Microbe Interact* **28**: 511–518
- Lu Q, Ding S, Reiland S, Rödiger A, Roschitzki B, Xue P, Gruissem W, Lu C, Baginsky S** (2015) Identification and characterization of chloroplast casein kinase II from *Oryza sativa* (rice). *J Exp Bot* **66**: 175–187
- Lu YJ, Schornack S, Spallek T, Geldner N, Chory J, Schellmann S, Schumacher K, Kamoun S, Robatzek S** (2012) Patterns of plant subcellular responses to successful oomycete infections reveal differences in host cell reprogramming and endocytic trafficking. *Cell Microbiol* **14**: 682–697
- Mackey D, Iii BFH, Wiig A, Dangl JL, Hill C, Carolina N** (2002) RIN4 interacts with *Pseudomonas syringae* type III effector molecules and is required for RPM1-mediated resistance in *Arabidopsis*. *Cell* **108**: 743–754
- Majeran W, Le Caer JP, Ponnala L, Meinnel T, Giglione C** (2018) Targeted profiling of *Arabidopsis thaliana* subproteomes illuminates co- and posttranslationally N-terminal myristoylated proteins. *Plant Cell* **30**: 543–562
- Marcolino-Gomes J, Rodrigues FA, Fuganti-Pagliarini R, Bendix C, Nakayama TJ, Celaya B, Molinari HBC, De Oliveira MCN, Harmon FG, Nepomuceno A** (2014) Diurnal oscillations of soybean circadian clock and drought responsive genes. *PLoS One*. doi: 10.1371/journal.pone.0086402
- Marcon C, Malik WA, Walley JW, Shen Z, Paschold A, Smith LG, Piepho HP, Briggs SP, Hochholdinger F** (2015) A high-resolution tissue-specific proteome and phosphoproteome atlas of maize primary roots reveals functional gradients along the root axes. *Plant Physiol* **168**: 233–246
- Marín M, Ott T** (2012) Phosphorylation of intrinsically disordered regions in remorin proteins. *Front Plant Sci* **3**: 86
- Marín M, Thallmair V, Ott T** (2012) The intrinsically disordered N-terminal region of AtREM1.3 remorin protein mediates protein-protein interactions. *J Biol Chem* **287**: 39982–39991
- Marondedze C, Groen AJ, Thomas L, Lilley KS, Gehring C** (2016) A Quantitative Phosphoproteome Analysis of cGMP-Dependent Cellular Responses in *Arabidopsis thaliana*. *Mol Plant* **9**: 621–623
- Martinez D, Legrand A, Gronnier J, Decossas M, Gouguet P, Lambert O, Berbon M, Verron L, Grélard A, Germain V, et al** (2018) Coiled-coil oligomerization controls localization of the plasma membrane REMORINs. *J Struct Biol* 0–1
- Mattei B, Spinelli F, Pontiggia D, De Lorenzo G** (2016) Comprehensive Analysis of the Membrane Phosphoproteome Regulated by Oligogalacturonides in *Arabidopsis thaliana*. *Front Plant Sci.* doi: 10.3389/fpls.2016.01107
- Maxwell KN, Zhou Y, Hancock JF** (2018) Clustering of Rac1: Selective Lipid Sorting

- Drives Signaling. *Trends Biochem Sci* **43**: 75–77
- Mayank P, Grossman J, Wuest S, Boisson-Dernier A, Roschitzki B, Nanni P, Nühse T, Grossniklaus U** (2012) Characterization of the phosphoproteome of mature Arabidopsis pollen. *Plant J* **72**: 89–101
- McBride Z, Chen D, Reick C, Xie J, Szymanski DB** (2017) Global Analysis of Membrane-associated Protein Oligomerization Using Protein Correlation Profiling. *Mol Cell Proteomics* **16**: 1972–1989
- Mehlmer N, Wurzinger B, Stael S, Hofmann-Rodrigues D, Csaszar E, Pfister B, Bayer R, Teige M** (2010) The Ca²⁺-dependent protein kinase CPK3 is required for MAPK-independent salt-stress acclimation in Arabidopsis. *Plant J* **63**: 484–498
- Menz J, Li Z, Schulze WX, Ludewig U** (2016) Early nitrogen-deprivation responses in Arabidopsis roots reveal distinct differences on transcriptome and (phospho-) proteome levels between nitrate and ammonium nutrition. *Plant J* **88**: 717–734
- Mergner J, Frejno M, List M, Papacek M, Chen X, Chaudhary A, Samaras P, Richter S, Shikata H, Messerer M, et al** (2020) Mass-spectrometry-based draft of the Arabidopsis proteome. *Nature* **579**: 409–414
- Mongrand S, Morel J, Laroche J, Claverol S, Carde J-P, Hartmann M-A, Bonneau M, Simon-Plas F, Lessire R, Bessoule J-J** (2004) Lipid rafts in higher plant cells: purification and characterization of Triton X-100-insoluble microdomains from tobacco plasma membrane. *J Biol Chem* **279**: 36277–86
- Nakagami H, Sugiyama N, Mochida K, Daudi A, Yoshida Y, Toyoda T, Tomita M, Ishihama Y, Shirasu K** (2010) Large-scale comparative phosphoproteomics identifies conserved phosphorylation sites in plants. *Plant Physiol* **153**: 1161–1174
- Niittylä T, Fuglsang AT, Palmgren MG, Frommer WB, Schulze WX** (2007) Temporal analysis of sucrose-induced phosphorylation changes in plasma membrane proteins of Arabidopsis. *Mol Cell Proteomics* **6**: 1711–1726
- Nikonorova N, Van Den Broeck L, Zhu S, Van De Cotte B, Dubois M, Gevaert K, Inzé D, De Smet I** (2018) Early mannitol-triggered changes in the Arabidopsis leaf (phospho)proteome reveal growth regulators. *J Exp Bot* **69**: 4591–4607
- Nühse TS, Bottrill AR, Jones AME, Peck SC** (2007) Quantitative phosphoproteomic analysis of plasma membrane proteins reveals regulatory mechanisms of plant innate immune responses. *Plant J* **51**: 931–940
- Nühse TS, Stensballe A, Jensen ON, Peck SC** (2004) Phosphoproteomics of the arabidopsis plasma membrane and a new phosphorylation site database W inside box sign. *Plant Cell* **16**: 2394–2405
- Nukarinen E, Ngele T, Pedrotti L, Wurzinger B, Mair A, Landgraf R, Börnke F, Hanson J, Teige M, Baena-Gonzalez E, et al** (2016) Quantitative phosphoproteomics reveals the role of the AMPK plant ortholog SnRK1 as a metabolic master regulator under energy deprivation. *Sci Rep* **6**: 1–19
- Oldroyd GED** (2013) Speak, friend, and enter: Signalling systems that promote beneficial symbiotic associations in plants. *Nat Rev Microbiol* **11**: 252–263
- Palta JP, Whitaker BD, Weiss LS** (1993) Plasma membrane lipids associated with genetic variability in freezing tolerance and cold acclimation of Solanum species. *Plant Physiol* **103**: 793–803
- Perraki A, Binaghi M, Mecchia M a, Gronnier J, German-Retana S, Mongrand S, Bayer E, Zelada AM, Germain V** (2014) StRemorin1.3 hampers Potato virus X TGBp1 ability to increase plasmodesmata permeability, but does not interfere with its silencing suppressor activity. *FEBS Lett* **588**: 1699–705
- Perraki A, Cacas J-L, Crowet J-M, Lins L, Castroviejo M, German-Retana S, Mongrand S, Raffaele S** (2012) Plasma membrane localization of Solanum tuberosum

- remorin from group 1, homolog 3 is mediated by conformational changes in a novel C-terminal anchor and required for the restriction of potato virus X movement]. *Plant Physiol* **160**: 624–37
- Perraki A, Gronnier J, Gouguet P, Boudsocq M, Deroubaix F, Simon V, Legrand A, German-Retana S, Zipfel C, Bayer EMF, et al** (2018) REM1 .3's phospho-status defines its plasma membrane nanodomain organization and activity in restricting PVX cell-to-cell movement. *PLoS Pathog.*
- Qin L, Zhou Z, Li Q, Zhai C, Liu L, Quilichini TD, Gao P, Kessler SA, Jaillais Y, Datla R, et al** (2020) Specific Recruitment of Phosphoinositide Species to the Plant-Pathogen Interfacial Membrane Underlies Arabidopsis Susceptibility to Fungal Infection. *Plant Cell* **32**: tpc.00970.2019
- Qiu J, Hou Y, Tong X, Wang Y, Lin H, Liu Q, Zhang W, Li Z, Nallamilli BR, Zhang J** (2016) Quantitative phosphoproteomic analysis of early seed development in rice (*Oryza sativa* L.). *Plant Mol Biol* **90**: 249–265
- Qiu J, Hou Y, Wang Y, Li Z, Zhao J, Tong X, Lin H, Wei X, Ao H, Zhang J** (2017) A comprehensive proteomic survey of aba-induced protein phosphorylation in rice (*Oryza sativa* L.). *Int J Mol Sci* **18**: 1–16
- Raffaele S** (2013) The Remorin C-terminal Anchor was shaped by convergent evolution among membrane binding domains. *Plant Signal ...* 3–6
- Raffaele S, Bayer E, Lafarge D, Cluzet S, German Retana S, Boubekur T, Leborgne-Castel N, Carde J-P, Lherminier J, Noirot E, et al** (2009a) Remorin, a solanaceae protein resident in membrane rafts and plasmodesmata, impairs potato virus X movement. *Plant Cell* **21**: 1541–55
- Raffaele S, Bayer E, Mongrand S** (2009b) Upregulation of the plant protein remorin correlates with dehiscence and cell maturation: A link with the maturation of plasmodesmata? *Plant Signal Behav* **4**: 915–919
- Raffaele S, Mongrand S, Gamas P, Niebel A, Ott T** (2007) Genome-wide annotation of remorins, a plant-specific protein family: evolutionary and functional perspectives. *Plant Physiol* **145**: 593–600
- Raghupathy R, Anilkumar AA, Polley A, Singh PP, Yadav M, Johnson C, Suryawanshi S, Saikam V, Sawant SD, Panda A, et al** (2015) Transbilayer Lipid Interactions Mediate Nanoclustering of Lipid-Anchored Proteins. *Cell* **161**: 581–594
- Ray A, Jatana N, Thukral L** (2017) Lipidated proteins: Spotlight on protein-membrane binding interfaces. *Prog Biophys Mol Biol* **128**: 74–84
- Reiland S, Finazzi G, Endler A, Willig A, Baerenfaller K, Grossmann J, Gerrits B, Rutishauser D, Gruissem W, Rochaix JD, et al** (2011) Comparative phosphoproteome profiling reveals a function of the STN8 kinase in fine-tuning of cyclic electron flow (CEF). *Proc Natl Acad Sci U S A* **108**: 12955–12960
- Reiland S, Messerli G, Baerenfaller K, Gerrits B, Endler A, Grossmann J, Gruissem W, Baginsky S** (2009) Large-scale arabidopsis phosphoproteome profiling reveals novel chloroplast kinase substrates and phosphorylation networks1[w]. *Plant Physiol* **150**: 889–903
- Rensing SA** (2018) Great moments in evolution: the conquest of land by plants. *Curr Opin Plant Biol* **42**: 49–54
- Rensing SA, Lang D, Zimmer AD** (2008) Conquest of Land by Plants. *Science (80-)* **319**: 64–69
- Reymond P, Kunz B, Paul-Pletzer K, Grimm R, Eckerskorn C, Farmer EE** (1996) Cloning of a cDNA encoding a plasma membrane-associated, uronide binding phosphoprotein with physical properties similar to viral movement proteins. *Plant Cell ...* **8**: 2265–2276

- Reymond P, Weber H, Damond M, Farmer EE** (2000) Differential Gene Expression in Response to Mechanical Wounding and Insect Feeding in Arabidopsis. *Plant Cell* **12**: 707–720
- Roitinger E, Hofer M, Köcher T, Pichler P, Novatchkova M, Yang J, Schlögelhofer P, Mechtler K** (2015) Quantitative phosphoproteomics of the ataxia telangiectasia-mutated (ATM) and ataxia telangiectasia-mutated and Rad3-related (ATR) dependent DNA damage response in arabidopsis thaliana. *Mol Cell Proteomics* **14**: 556–571
- Rutter BD, Innes RW** (2018) Extracellular vesicles as key mediators of plant–microbe interactions. *Curr Opin Plant Biol* **44**: 16–22
- Rutter BD, Innes RW** (2017) Extracellular Vesicles Isolated from the Leaf Apoplast Carry Stress-Response Proteins. *Plant Physiol* **173**: 728–741
- Sasaki N, Takashima E, Nyunoya H** (2018) Altered Subcellular Localization of a Tobacco Membrane Raft-Associated Remorin Protein by Tobamovirus Infection and Transient Expression of Viral Replication and Movement Proteins. *Front Plant Sci* **9**: 1–16
- Seong ES, Baek KH, Oh SK, Jo SH, Yi SY, Park JM, Joung YH, Lee S, Cho HS, Choi D** (2007) Induction of enhanced tolerance to cold stress and disease by overexpression of the pepper CaPIF1 gene in tomato. *Physiol Plant* **129**: 555–566
- Skotland T, Sandvig K** (2019) The role of PS 18:0/18:1 in membrane function. *Nat Commun* **10**: 1–10
- Son S, Oh C, An C** (2014) Arabidopsis thaliana Remorins Interact with SnRK1 and Play a Role in Susceptibility to Beet Curly Top Virus and Beet Severe Curly Top Virus. *plant Pathol J* **30**: 269–278
- Song G, Brachova L, Nikolau BJ, Jones AM, Walley JW** (2018) Heterotrimeric G-Protein-Dependent Proteome and Phosphoproteome in Unstimulated Arabidopsis Roots. *Proteomics* **18**: 1–14
- Srivastava V, Malm E, Sundqvist G, Bulone V** (2013) Quantitative Proteomics Reveals that Plasma Membrane Microdomains From Poplar Cell Suspension Cultures Are Enriched in Markers of Signal Transduction, Molecular Transport, and Callose Biosynthesis. *Mol Cell Proteomics* **12**: 3874–3885
- Stanislas T, Bouyssie D, Rossignol M, Vesa S, Fromentin J, Morel J, Pichereaux C, Monsarrat B, Simon-Plas F** (2009) Quantitative Proteomics Reveals a Dynamic Association of Proteins to Detergent-resistant Membranes upon Elicitor Signaling in Tobacco. *Mol Cell Proteomics* **8**: 2186–2198
- Steehans P, Hérisse A Le, Melvin J, Miller MA, Paris F, Verniers J, Wellman CH** (2009) Origin and radiation of the earliest vascular land plants. *Science* (80-) **324**: 353
- Sugiyama N, Nakagami H, Mochida K, Daudi A, Tomita M, Shirasu K, Ishihama Y** (2008) Large-scale phosphorylation mapping reveals the extent of tyrosine phosphorylation in Arabidopsis. *Mol Syst Biol*. doi: 10.1038/msb.2008.32
- Szymanski WG, Zauber H, Erban A, Wu XN, Schulze WX** (2015) Cytoskeletal components define protein location to membrane microdomains. *Mol Cell Proteomics* **14**: 046904–
- Takahashi D, Kawamura Y, Uemura M** (2013) Detergent-resistant plasma membrane proteome to elucidate microdomain functions in plant cells. *Front Plant Sci* **4**: 27
- Tao K, Waletzsch JR, Arredondo F, Tyler BM** (2019) Manipulating endoplasmic reticulum-plasma membrane tethering in plants through fluorescent protein complementation. *Front Plant Sci* **10**: 1–16
- Tarkka MT, Herrmann S, Wubet T, Feldhahn L, Recht S, Kurth F, Mailänder S, Bönn M, Neef M, Angay O, et al** (2013) OakContigDF159.1, a reference library for studying differential gene expression in Quercus robur during controlled biotic interactions: Use for quantitative transcriptomic profiling of oak roots in ectomycorrhizal symbiosis. *New*

- Phytol **199**: 529–540
- Tóth K, Stratil TF, Madsen EB, Ye J, Popp C, Antolín-Llovera M, Grossmann C, Jensen ON, Schübler A, Parniske M, et al** (2012) Functional domain analysis of the remorin protein LjSYMREM1 in lotus japonicus. PLoS One. doi: 10.1371/journal.pone.0030817
- Ulmschneider JP, Ulmschneider MB** (2018) Molecular Dynamics Simulations Are Redefining Our View of Peptides Interacting with Biological Membranes. Acc Chem Res **51**: 1106–1116
- Uversky VN** (2013) A decade and a half of protein intrinsic disorder: Biology still waits for physics. Protein Sci **22**: 693–724
- Voxeur A, Höfte H** (2016) Cell wall integrity signaling in plants: “To grow or not to grow that’s the question.” Glycobiology **26**: 950–960
- Vu LD, Stes E, Van Bel M, Nelissen H, Maddelein D, Inzé D, Coppens F, Martens L, Gevaert K, De Smet I** (2016) Up-to-Date Workflow for Plant (Phospho)proteomics Identifies Differential Drought-Responsive Phosphorylation Events in Maize Leaves. J Proteome Res **15**: 4304–4317
- Wang K, Yang Z, Qing D, Ren F, Liu S, Zheng Q, Liu J, Zhang W, Dai C, Wu M, et al** (2018) Quantitative and functional posttranslational modification proteomics reveals that TREP1 plays a role in plant touch-delayed bolting. Proc Natl Acad Sci U S A **115**: E10265–E10274
- Wang K, Zhao Y, Li M, Gao F, Yang M kun, Wang X, Li S, Yang P** (2014) Analysis of phosphoproteome in rice pistil. Proteomics **14**: 2319–2334
- Wang P, Hsu CC, Du Y, Zhu P, Zhao C, Fu X, Zhang C, Paez JS, Macho AP, Andy Tao W, et al** (2020) Mapping proteome-wide targets of protein kinases in plant stress responses. Proc Natl Acad Sci U S A **117**: 3270–3280
- Wang S, Chen Z, Tian L, Ding Y, Zhang J, Zhou J, Liu P, Chen Y, Wu L** (2019) Comparative proteomics combined with analyses of transgenic plants reveal ZmREM1.3 mediates maize resistance to southern corn rust. Plant Biotechnol J **17**: 2153–2168
- Whiteman SA, Serazetdinova L, Jones AME, Sanders D, Rathjen J, Peck SC, Maathuis FJM** (2008) Identification of novel proteins and phosphorylation sites in a tonoplast enriched membrane fraction of Arabidopsis thaliana. Proteomics **8**: 3536–3547
- Widjaja I, Naumann K, Roth U, Wolf N, Mackey D, Dangl JL, Scheel D, Lee J** (2009) Combining subproteome enrichment and Rubisco depletion enables identification of low abundance proteins differentially regulated during plant defense. Proteomics **9**: 138–147
- Wong MM, Bhaskara GB, Wen TN, Lin WD, Nguyen TT, Chong GL, Verslues PE** (2019) Phosphoproteomics of Arabidopsis Highly ABA-Induced1 identifies AT-Hook-Like10 phosphorylation required for stress growth regulation. Proc Natl Acad Sci U S A **116**: 2354–2363
- Wu C-Q, Hu H-H, Zeng Y, Liang D-C, Xie K-B, Zhang J-W, Chu Z-H, Xiong L-Z** (2006) Identification of Novel Stress-responsive Transcription Factor Genes in Rice by cDNA Array Analysis. J Integr Plant Biol **48**: 1216–1224
- Xiang Y, Song B, Née G, Kramer K, Finkemeier I, Soppe WJJ** (2016) Sequence polymorphisms at the REDUCED DORMANCY5 pseudophosphatase underlie natural variation in Arabidopsis dormancy. Plant Physiol **171**: 2659–2670
- Xu Q, Xu X, Shi Y, Qi X, Chen X** (2017) Elucidation of the molecular responses of a cucumber segment substitution line carrying Pm5.1 and its recurrent parent triggered by powdery mildew by comparative transcriptome profiling. BMC Genomics **18**: 1–14
- Yamada H, Hanaki N, Imamura A, Ueguchi C, Mizuno T** (1998) An Arabidopsis protein that interacts with the cytokinin-inducible response regulator, ARR4, implicated in the His-Asp phosphorylay signal transduction. FEBS Lett **436**: 76–80

- Yang Z, Guo G, Zhang M, Liu CY, Hu Q, Lam H, Cheng H, Xue Y, Li J, Li N** (2013) Stable isotope metabolic labeling-based quantitative phosphoproteomic analysis of arabidopsis mutants reveals ethylene-regulated time-dependent phosphoproteins and putative substrates of constitutive triple response 1 kinase. *Mol Cell Proteomics* **12**: 3559–3582
- Ye J, Zhang Z, Long H, Zhang Z, Hong Y, Zhang X, You C, Liang W, Ma H, Lu P** (2015) Proteomic and phosphoproteomic analyses reveal extensive phosphorylation of regulatory proteins in developing rice anthers. *Plant J* **84**: 527–544
- Yeats TH, Bacic A, Johnson KL** (2018) Plant glycosylphosphatidylinositol anchored proteins at the plasma membrane-cell wall nexus. *J Integr Plant Biol* **60**: 649–669
- Yue J, Li C, Liu Y, Yu J** (2014) A remorin gene SiREM6, the target gene of SiARDP, from foxtail millet (*Setaria italica*) promotes high salt tolerance in transgenic Arabidopsis. *PLoS One* **9**: e100772
- Zauber H, Burgos A, Garapati P, Schulze WX** (2014) Plasma membrane lipid-protein interactions affect signaling processes in sterol-biosynthesis mutants in Arabidopsis thaliana. *Front Plant Sci* **5**: 1–18
- Zavaliev R, Levy A, Gera A, Epel BL** (2013) Subcellular dynamics and role of Arabidopsis β -1,3-glucanases in cell-to-cell movement of tobamoviruses. *Mol Plant Microbe Interact* **26**: 1016–30
- Zavaliev R, Ueki S, Epel BL, Citovsky V** (2011) Biology of callose (β -1,3-glucan) turnover at plasmodesmata. *Protoplasma* **248**: 117–130
- Zhang H, Deng C, Wu X, Yao J, Zhang Y, Zhang Y, Deng S, Zhao N, Zhao R, Zhou X, et al** (2020) *Populus euphratica* remorin 6.5 activates plasma membrane H⁺-ATPases to mediate salt tolerance. *Tree Physiol* 1–49
- Zhou Y, Hancock JF** (2018) Deciphering lipid codes: K-Ras as a paradigm. *Traffic* **19**: 157–165
- Zhou Y, Prakash P, Liang H, Cho K-J, Gorfe AA, Hancock JF** (2017) Lipid-Sorting Specificity Encoded in K-Ras Membrane Anchor Regulates Signal Output. *Cell* **168**: 239–251
- Zhou Y, Wong CO, Cho KJ, Van Der Hoeven D, Liang H, Thakur DP, Luo J, Babic M, Zinsmaier KE, Zhu MX, et al** (2015) Membrane potential modulates plasma membrane phospholipid dynamics and K-Ras signaling. *Science* (80-) **349**: 873–876

Organism	Remorin Group	Isoform	Functions	References
At	1	2	Slows TuMV by closing PD	Cheng 2019
.	.	.	Higher expression vs bacterial elicitor AvrRPM1	Widjaja 2009
.	.	.	Interacts with RIN4 (PAMP-immunity trigger vs <i>P. syringae</i>) and ERD4	Mackley 2002, Liu 2009, Lee 2015
.	.	.	In EVs during infection, with AtREM1.3 and RIN4	Meyer 2009, Micali 2011
.	.	.	SA-induced PD closure depends on PM targeting and organisation	Huang 2019
.	.	.	Binds OGA, OGA-induced phosphorylation	Reymond 1996, Kohorn 2016, Mattei 2016
.	.	.	Cytoskeleton-dependent PM organisation	Szymanski 2015
.	.	3	More phosphorylated vs bacterial elicitor flg22	Benschop 2007
.	.	.	In EVs during infection, with AtREM1.2 and RIN4	Meyer 2009, Micali 2011
.	.	.	Binds ergosterol (toxic for plants)	Khoza 2019
.	.	.	Expressed in response to water, cold and osmotic stresses	Reymond 2000, Bray 2002 Kreps 2022
.	.	.	Auxin-induced overexpression in dividing cells	Alliotte 1989
.	.	.	Interacts with ARR4	Verma 2015
.	.	.	Binds OGA, OGA-induced phosphorylation	Reymond 1996, Kohorn 2016, Mattei 2016
.	.	.	Cytoskeleton-dependent PM organisation	Szymanski 2015
.	4	1	Higher susceptibility vs BCT and BSCT	Son 2014
.	.	2		
.	.	1		
.	.	2		
.	.	1	Higher expression under drought- and osmotic-stresses	Reymond 2000, Bray 2002, Son 2014
.	.	2	Higher expression under ABA treatment	
Cs	1		Higher expression vs Powdery mildew	Xu and Xu 2017
.	4			
Gm	4		Circadian-dependent transcription under drought stress	Marcolino-Gomes 2014
Hv	1		Lower expression under ABA or GA treatment	Chen and an 2006
Lj	2	SYMREM1	More nodules/root	Toth 2012
Mi	1		Higher transcription in response to abiotic stress	Checker and Khurana 2013
.	.		Higher transcription ABA, SA or BR treatment	
Mt	2	2	Expressed in root nodules, response to Nod factors	Lefebvre 2010
.	.	.	Scaffold for nodulation-related receptor-like kinases NFP, DMI2, LYK3 and flotillin 4	Liang 2018
Nb	1	1	Slows RSV by closing PD	Fu 2018
.	.	2		
Nt	1	2	Speeds TumMV	Sasaki 2018
Os	1	5	Higher expression under ABA or BA treatment	Lin 2003
.	4	1	Upkeep of ABA/BR homeostat	Gui 2016
.	.	.	Higher expression induced by cold-resistance factor DaCBF7	Byun 2015
.	5	3	Size of panicles	Liu 2016
.	6	5	Higher expression under drought	Wu 2006
.	.	.	Higher expression under ABA treatment	
.	.	6	Grain Setting defect 1 (GSD1) mutant has plant-wide impaired starch and sugar metabolism	Gui 2014, 2015
Pe	6	5	Higher expression and resistance to salt stress	Zhang 2020
.	.	.	Higher H ⁺ -atpase activity	
.	.	.	Interacts with RIN4	
Qr	4	1	More expressed with <i>Piloderma croceum</i>	Tarkka 2013
Si	1		Higher susceptibility vs <i>Botrytis cinerea</i>	Cai 2020

Remorin Organism	Group	Isoform	Functions	References
.	.	.	Higher ROS accumulation Cell death trigger	Cai 2020
.	.	.	Lower susceptibility vs <i>Verticillium dahlia</i>	Hu 2019
.	6	.	Higher expression under salt, osmotic and cold stress Higher expression under ABA treatment Overexpression in <i>A. thaliana</i> increased germination rate, seedling biomass and drought resistance Overexpression in <i>A. thaliana</i> increased ABA sensitivity	Yue 2016
Sl	1	2	Interacts with SAM1, ACS2 and ACO1, promotes fruit ripening Favours ethylene and lycopene biosynthesis	Cai 2018
.	.	.	Higher transcription when CaPIF1 (resistance to bacterial infections and cold) is overexpressed	Seong 2007, Oh 2005
St	1	3	Slows PVX by closing PD Interacts with TGBp1 of PVX Promotes callose deposit at PD, even in absence of virus IDP is phosphorylated by AtCPK3 Enriched in Pms near haustoria (fungal protrusions into plant cells) May localise at PD Binds OGA, OGA-induced phosphorylation	Perraki 2014, Raffaele, 2009 Raffaele 2009 Perraki 2014, 2018 Perraki 2018 Lu and Schornack 2012, Bozkurt 2014 Gronnier 2017, Raffaele 2009
.	1	4	Higher expression vs <i>Ralstonia solanaceum</i> Higher transcription under ABA, SA or MeJa treatment	Reymond 1996, Kohorn 2016, Mattei 2016 Kong 2016 Kong 2016
Ta	.	.	Higher expression under cold stress	Badawi 2019
Zm	1	3	Lower susceptibility vs <i>Puccinia polyspora</i>	Wang 2019
.	4	1	Higher expression under cold stress	Bilska-Kos 2016
.	6	3	Genetic correlation with resistance vs <i>Steosphaeria turcica</i>	Jamann 2015

List of known biological involvement of remorins from (Gouguet et al., 2020), with colour code from Figure 29. Abbreviations: *At*, *Arabidopsis thaliana* (thale cress); *Cs*, *Cucumis sativus* (cucumber); *Gm*, *Glycine max* (soybean); *Hv*, *Hordeum vulgare* (barley); *Lj*, *Lotus japonicas*; *Mi*, *Morus indica* (mulberry); *Mt*, *Medicago truncatula* (barrel clover); *Nb*, *Nicotiana benthamiana* (australian tobacco); *Nt*, *Nicotiana tabacum* (common tobacco); *Os*, *Oryza sativa* (rice); *Pe*, *Populus euphratica* (poplar); *Qr*, *Quercus robur* (oak); *Sl*, *Solanum lycopersicum* (tomato); *St*, *Solanum tuberosum* (potato); *Ta*, *Triticum aestivum* (wheat); *Zm*, *Zea mays* (corn).

References

- Ackerman, D.G., and Feigenson, G.W. (2015). Multiscale Modeling of Four-Component Lipid Mixtures: Domain Composition, Size, Alignment, and Properties of the Phase Interface. *The Journal of Physical Chemistry B* 119, 4240–4250.
- Alia, A., Ganapathy, S., and de Groot, H.J.M. (2009). Magic angle spinning (MAS) NMR: a new tool to study the spatial and electronic structure of photosynthetic complexes. *Photosynth Res* 102, 415–425.
- Alliotte, T., Tiré, C., Engler, G., Peleman, J., Caplan, A., Montagu, M.V., and Inzé, D. (1989). An Auxin-Regulated Gene of *Arabidopsis thaliana* Encodes a DNA-Binding Protein. *Plant Physiology* 89, 743–752.
- Bach, J.N., and Bramkamp, M. (2013). Flotillins functionally organize the bacterial membrane. *Molecular Microbiology* 88, 1205–1217.
- Baker, D. (2019). What has de novo protein design taught us about protein folding and biophysics? *Protein Science* 28, 678–683.
- Bar, R.S., Deamer, D.W., and Cornwell, D.G. (1966). Surface Area of Human Erythrocyte Lipids: Reinvestigation of Experiments on Plasma Membrane. *Science* 153, 1010–1012.
- Bariola, P., Retelska, D., Stasiak, A., Kammerer, R., Fleming, A., Hijri, M., Frank, S., and Farmer, E. (2004). Remorins form a novel family of coiled coil-forming oligomeric and filamentous proteins associated with apical, vascular and embryonic tissues in plants. *Plant Molecular Biology* 55, 579–594.
- Beck, J.G., Mathieu, D., Loudet, C., Buchoux, S., and Dufourc, E.J. (2007). Plant sterols in “rafts”: a better way to regulate membrane thermal shocks. *The FASEB Journal* 21, 1714–1723.
- Benitez-Alfonso, Y., Faulkner, C., Ritzenthaler, C., and Maule, A.J. (2010). Plasmodesmata: gateways to local and systemic virus infection. *Mol. Plant Microbe Interact.* 23, 1403–1412.
- Benschop, J.J., Mohammed, S., O’Flaherty, M., Heck, A.J.R., Slijper, M., and Menke, F.L.H. (2007). Quantitative phosphoproteomics of early elicitor signaling in *Arabidopsis*. *Mol. Cell Proteomics* 6, 1198–1214.
- Benson, A.A. (1966). On the orientation of lipids in chloroplast and cell membranes. *Journal of the American Oil Chemists’ Society* 43, 265–270.
- Betzig, E., Patterson, G.H., Sougrat, R., Lindwasser, O.W., Olenych, S., Bonifacino, J.S., Davidson, M.W., Lippincott-Schwartz, J., and Hess, H.F. (2006). Imaging Intracellular Fluorescent Proteins at Nanometer Resolution. *Science* 313, 1642–1645.
- Bilkova, E., Pleskot, R., Rissanen, S., Sun, S., Czogalla, A., Cwiklik, L., Róg, T., Vattulainen, I., Cremer, P.S., Jungwirth, P., et al. (2017). Calcium Directly Regulates

Phosphatidylinositol 4,5-Bisphosphate Headgroup Conformation and Recognition. *J. Am. Chem. Soc.* **139**, 4019–4024.

Bilska-Kos, A., Szczepanik, J., and Sowiński, P. (2016). Cold induced changes in the water balance affect immunocytolocalization pattern of one of the aquaporins in the vascular system in the leaves of maize (*Zea mays* L.). *Journal of Plant Physiology* **205**, 75–79.

van den Bogaart, G., Meyenberg, K., Risselada, H.J., Amin, H., Willig, K.I., Hubrich, B.E., Dier, M., Hell, S.W., Grubmüller, H., Diederichsen, U., et al. (2011). Membrane protein sequestering by ionic protein–lipid interactions. *Nature* **479**, 552–555.

Borges, J.L., and Guerrero, M. (1969). *El Libro De Los Seres Imaginarios*. 69.

Bozkurt, T.O., Richardson, A., Dagdas, Y.F., Mongrand, S., Kamoun, S., and Raffaele, S. (2014). The Plant Membrane-Associated REMORIN1.3 Accumulates in Discrete Perihyphal Domains and Enhances Susceptibility to *Phytophthora infestans*[W]. *Plant Physiol* **165**, 1005–1018.

Bragina, N.A., and Chupin, V.V. (1997). Methods of synthesis of deuterium-labelled lipids. *Russ. Chem. Rev.* **66**, 975.

Braicu, C., Buse, M., Busuioc, C., Drula, R., Gulei, D., Raduly, L., Rusu, A., Irimie, A., Atanasov, A.G., Slaby, O., et al. (2019). A Comprehensive Review on MAPK: A Promising Therapeutic Target in Cancer. *Cancers (Basel)* **11**.

Bramkamp, M., and Lopez, D. (2015). Exploring the Existence of Lipid Rafts in Bacteria. *Microbiol. Mol. Biol. Rev.* **79**, 81–100.

Brown, R. (1833). On the Organs and Mode of Fecundation in Orchideæ and Asclepiadeæ. *Transactions of the Linnean Society of London* **16**, 685–738.

Brown, D.A., and Rose, J.K. (1992). Sorting of GPI-anchored proteins to glycolipid-enriched membrane subdomains during transport to the apical cell surface. *Cell* **68**, 533–544.

Buré, C., Cacas, J.-L., Mongrand, S., and Schmitter, J.-M. (2014). Characterization of glycosyl inositol phosphoryl ceramides from plants and fungi by mass spectrometry. *Anal Bioanal Chem* **406**, 995–1010.

Bureau International des Poids et Mesures (2006). Le système international d'unités (SI) =: The international system of units (SI) (Sèvres: BIPM).

Burnett, L.J., and Muller, B.H. (1971). Deuteron Quadrupole Coupling Constants in Three Solid Deuterated Paraffin Hydrocarbons: C₂D₆, C₄D₁₀, C₆D₁₄. *The Journal of Chemical Physics* **55**, 5829–5831.

Cacas, J.-L., Buré, C., Grosjean, K., Gerbeau-Pissot, P., Lherminier, J., Rombouts, Y., Maes, E., Bossard, C., Gronnier, J., Furt, F., et al. (2016). Revisiting Plant Plasma Membrane Lipids in Tobacco: A Focus on Sphingolipids. *Plant Physiology* **170**, 367–384.

Carter, W.G., and Hakomori, S. (1981). A new cell surface, detergent-insoluble glycoprotein matrix of human and hamster fibroblasts. The role of disulfide bonds in stabilization of the matrix. *J. Biol. Chem.* 256, 6953–6960.

Chavent, M., Duncan, A.L., and Sansom, M.S. (2016). Molecular dynamics simulations of membrane proteins and their interactions: from nanoscale to mesoscale. *Curr. Opin. Struct. Biol.* 40, 8–16.

Chazal, N., and Gerlier, D. (2003). Virus Entry, Assembly, Budding, and Membrane Rafts. *Microbiol. Mol. Biol. Rev.* 67, 226–237.

Cheesbrough, T.M., and Moore, T.S. (1980). Transverse Distribution of Phospholipids in Organelle Membranes from *Ricinus communis* L. var. Hale Endosperm. *Plant Physiol* 65, 1076–1080.

Clejan, S., Krulwich, T.A., Mondrus, K.R., and Seto-Young, D. (1986). Membrane lipid composition of obligately and facultatively alkalophilic strains of *Bacillus* spp. *J Bacteriol* 168, 334–340.

Collins, M.D., and Keller, S.L. (2008). Tuning lipid mixtures to induce or suppress domain formation across leaflets of unsupported asymmetric bilayers. *PNAS* 105, 124–128.

Cullis, P.R., and de Kruffy, B. (1976). ³¹P NMR studies of unsonicated aqueous dispersions of neutral and acidic phospholipids. Effects of phase transitions, p2H and divalent cations on the motion in the phosphate region of the polar headgroup. *Biochimica et Biophysica Acta (BBA) - Biomembranes* 436, 523–540.

Dahm, R. (2008). Discovering DNA: Friedrich Miescher and the early years of nucleic acid research. *Hum Genet* 122, 565–581.

Danielli, J.F., and Davson, H. (1935). A contribution to the theory of permeability of thin films. *Journal of Cellular and Comparative Physiology* 5, 495–508.

Daskalov, A., Habenstein, B., Martinez, D., Debets, A.J.M., Sabaté, R., Loquet, A., and Saupe, S.J. (2015). Signal Transduction by a Fungal NOD-Like Receptor Based on Propagation of a Prion Amyloid Fold. *PLOS Biology* 13, e1002059.

Daskalov, A., Habenstein, B., Sabaté, R., Berbon, M., Martinez, D., Chaignepain, S., Coulary-Salin, B., Hofmann, K., Loquet, A., and Saupe, S.J. (2016). Identification of a novel cell death-inducing domain reveals that fungal amyloid-controlled programmed cell death is related to necroptosis. *PNAS* 113, 2720–2725.

Demers, J.-P., Habenstein, B., Loquet, A., Kumar Vasa, S., Giller, K., Becker, S., Baker, D., Lange, A., and Sgourakis, N.G. (2014). High-resolution structure of the *Shigella* type-III secretion needle by solid-state NMR and cryo-electron microscopy. *Nature Communications* 5, 4976.

Demir, F., Horntrich, C., Blachutzik, J.O., Scherzer, S., Reinders, Y., Kierszniowska, S., Schulze, W.X., Harms, G.S., Hedrich, R., Geiger, D., et al. (2013). Arabidopsis nanodomain-delimited ABA signaling pathway regulates the anion channel SLAH3. *PNAS* 110, 8296–8301.

- Dempsey, G.T., Vaughan, J.C., Chen, K.H., Bates, M., and Zhuang, X. (2011). Evaluation of fluorophores for optimal performance in localization-based super-resolution imaging. *Nat Methods* 8, 1027–1036.
- Di Paolo, G., and De Camilli, P. (2006). Phosphoinositides in cell regulation and membrane dynamics. *Nature* 443, 651–657.
- Diener, A.C., Li, H., Zhou, W., Whoriskey, W.J., Nes, W.D., and Fink, G.R. (2000). STEROL METHYLTRANSFERASE 1 Controls the Level of Cholesterol in Plants. *The Plant Cell* 12, 853–870.
- Dinic, J., Ashrafzadeh, P., and Parmryd, I. (2013). Actin filaments attachment at the plasma membrane in live cells cause the formation of ordered lipid domains. *Biochimica et Biophysica Acta (BBA) - Biomembranes* 1828, 1102–1111.
- Donovan, C., and Bramkamp, M. (2009). Characterization and subcellular localization of a bacterial flotillin homologue. *Microbiology (Reading, Engl.)* 155, 1786–1799.
- Dufourc, E.J. (2008). Sterols and membrane dynamics. *J Chem Biol* 1, 63–77.
- Dupree, P., Parton, R. g., Raposo, G., Kurzchalia, T. v., and Simons, K. (1993). Caveolae and sorting in the trans-Golgi network of epithelial cells. *The EMBO Journal* 12, 1597–1605.
- Dwyer, J.J., Gittis, A.G., Karp, D.A., Lattman, E.E., Spencer, D.S., Stites, W.E., and García-Moreno E, B. (2000). High apparent dielectric constants in the interior of a protein reflect water penetration. *Biophys J* 79, 1610–1620.
- Einstein, A. (1920). *Relativity: The Special and General Theory*. Henry Holt and Company 184.
- Engberg, O., Hautala, V., Yasuda, T., Dehio, H., Murata, M., Slotte, J.P., and Nyholm, T.K.M. (2016). The Affinity of Cholesterol for Different Phospholipids Affects Lateral Segregation in Bilayers. *Biophys J* 111, 546–556.
- Erickson, H.P., and Klug, A. (1970). The Fourier Transform of an Electron Micrograph: Effects of Defocussing and Aberrations, and Implications for the Use of Underfocus Contrast Enhancement. *Berichte Der Bunsengesellschaft Für Physikalische Chemie* 74, 1129–1137.
- Ewers, H., Römer, W., Smith, A.E., Bacia, K., Dmitrieff, S., Chai, W., Mancini, R., Kartenbeck, J., Chambon, V., Berland, L., et al. (2010). GM1 structure determines SV40-induced membrane invagination and infection. *Nat Cell Biol* 12, 11–18.
- Farmer, E.E., Pearce, G., and Ryan, C.A. (1989). In vitro phosphorylation of plant plasma membrane proteins in response to the proteinase inhibitor inducing factor. *Proceedings of the National Academy of Sciences* 86, 1539–1542.
- Feigenson, G.W. (2006). Phase behavior of lipid mixtures. *Nature Chemical Biology* 2, 560–563.

Fischer, H., Polikarpov, I., and Craievich, A.F. (2004). Average protein density is a molecular-weight-dependent function. *Protein Sci* 13, 2825–2828.

Fogh, R.H., Boucher, W., Vranken, W.F., Pajon, A., Stevens, T.J., Bhat, T.N., Westbrook, J., Ionides, J.M.C., and Laue, E.D. (2005). A framework for scientific data modeling and automated software development. *Bioinformatics* 21, 1678–1684.

Frederix, P.L.T.M., Bosshart, P.D., and Engel, A. (2009). Atomic Force Microscopy of Biological Membranes. *Biophys J* 96, 329–338.

Friedman, R., Khalid, S., Aponte-Santamaría, C., Arutyunova, E., Becker, M., Boyd, K.J., Christensen, M., Coimbra, J.T.S., Concilio, S., Daday, C., et al. (2018). Understanding Conformational Dynamics of Complex Lipid Mixtures Relevant to Biology. *J Membr Biol* 251, 609–631.

Fujimoto, T., and Parmryd, I. (2017). Interleaflet Coupling, Pinning, and Leaflet Asymmetry—Major Players in Plasma Membrane Nanodomain Formation. *Front Cell Dev Biol* 4.

Fung, B.M., Khitritin, A.K., and Ermolaev, K. (2000). An Improved Broadband Decoupling Sequence for Liquid Crystals and Solids. *Journal of Magnetic Resonance* 142, 97–101.

Furt, F., König, S., Bessoule, J.J., Sargueil, F., Zallot, R., Stanislas, T., Noirot, E., Lherminier, J., Simon-Plas, F., Heilmann, I., et al. (2010). Polyphosphoinositides Are Enriched in Plant Membrane Rafts and Form Microdomains in the Plasma Membrane. *PLANT PHYSIOLOGY* 152, 2173–2187.

Futerman, A.H., and Hannun, Y.A. (2004). The complex life of simple sphingolipids. *EMBO Rep* 5, 777–782.

Garcia-Manyes, S., and Sanz, F. (2010). Nanomechanics of lipid bilayers by force spectroscopy with AFM: A perspective. *Biochimica et Biophysica Acta (BBA) - Biomembranes* 1798, 741–749.

Gorter, E., and Grendel, F. (1925). ON BIMOLECULAR LAYERS OF LIPOIDS ON THE CHROMOCYTES OF THE BLOOD. *J Exp Med* 41, 439–443.

Gouguet, P., Gronnier, J., Legrand, A., Perraki, A., Jolivet, M.-D., Deroubaix, A.-F., German-Retana, S., Boudsocq, M., Habenstein, B., Mongrand, S., et al. (2020). Connecting the dots: from nanodomains to physiological functions of REMORINS. *Plant Physiology*, *accepted*

Gramse, G., Dols-Perez, A., Edwards, M.A., Fumagalli, L., and Gomila, G. (2013). Nanoscale Measurement of the Dielectric Constant of Supported Lipid Bilayers in Aqueous Solutions with Electrostatic Force Microscopy. *Biophys J* 104, 1257–1262.

Grecco, H.E., Schmick, M., and Bastiaens, P.I.H. (2011). Signaling from the Living Plasma Membrane. *Cell* 144, 897–909.

Grélard, A., Guichard, P., Bonnafous, P., Marco, S., Lambert, O., Manin, C., Ronzon, F., and Dufourc, E.J. (2013). Hepatitis B subvirus particles display both a fluid bilayer

membrane and a strong resistance to freeze drying: a study by solid-state NMR, light scattering, and cryo-electron microscopy/tomography. *The FASEB Journal* 27, 4316–4326.

Grew, N. (1672). *The Anatomy Of Vegetables* (Royal Society).

Grille, S., Zaslawski, A., Thiele, S., Plat, J., and Warnecke, D. (2010). The functions of sterol glycosides come to those who wait: Recent advances in plants, fungi, bacteria and animals. *Progress in Lipid Research* 49, 262–288.

Gronnier, J., Crowet, J.-M., Habenstein, B., Nasir, M.N., Bayle, V., Hosy, E., Platre, M.P., Gouguet, P., Raffaele, S., Martinez, D., et al. (2017). Structural basis for plant plasma membrane protein dynamics and organization into functional nanodomains. *ELife* 6.

Gronnier, J., Gerbeau-Pissot, P., Germain, V., Mongrand, S., and Simon-Plas, F. (2018). Divide and Rule: Plant Plasma Membrane Organization. *Trends in Plant Science* 23, 899–917.

Grosjean, K., Mongrand, S., Beney, L., Simon-Plas, F., and Gerbeau-Pissot, P. (2015). Differential effect of plant lipids on membrane organization: specificities of phytosphingolipids and phytosterols. *J. Biol. Chem.* 290, 5810–5825.

Groves, J.T., and Kuriyan, J. (2010). Molecular mechanisms in signal transduction at the membrane. *Nat Struct Mol Biol* 17, 659–665.

Habenstein, B., and Loquet, A. (2016). Solid-state NMR: An emerging technique in structural biology of self-assemblies. *Biophysical Chemistry* 210, 14–26.

Habenstein, B., Bousset, L., Sourigues, Y., Kabani, M., Loquet, A., Meier, B.H., Melki, R., and Böckmann, A. (2012). A Native-Like Conformation for the C-Terminal Domain of the Prion Ure2p within its Fibrillar Form. *Angewandte Chemie International Edition* 51, 7963–7966.

Hancock, J.F. (2003). Ras proteins: different signals from different locations. *Nat Rev Mol Cell Biol* 4, 373–385.

Hannich, J.T., Umebayashi, K., and Riezman, H. (2011). Distribution and Functions of Sterols and Sphingolipids. *Cold Spring Harbor Perspectives in Biology* 3, a004762–a004762.

Heilmann, I. (2016). Phosphoinositide signaling in plant development. *Development* 143, 2044–2055.

Heinz, D.W., Essen, L.O., and Williams, R.L. (1998). Structural and mechanistic comparison of prokaryotic and eukaryotic phosphoinositide-specific phospholipases C. *J. Mol. Biol.* 275, 635–650.

Hell, S.W., and Wichmann, J. (1994). Breaking the diffraction resolution limit by stimulated emission: stimulated-emission-depletion fluorescence microscopy. *Opt. Lett.*, OL 19, 780–782.

Hooke, R. (1665). *Micrographia, or, Some physiological descriptions of minute bodies made by magnifying glasses :with observations and inquiries thereupon* / (London : Royal Society).

Hooper, N.M., and Turner, A.J. (1988). Ectoenzymes of the kidney microvillar membrane. Differential solubilization by detergents can predict a glycosyl-phosphatidylinositol membrane anchor. *Biochem J* 250, 865–869.

Hosaka, T., Okazaki, M., Kimura-Someya, T., Ishizuka-Katsura, Y., Ito, K., Yokoyama, S., Dodo, K., Sodeoka, M., and Shirouzu, M. (2017). Crystal structural characterization reveals novel oligomeric interactions of human voltage-dependent anion channel 1. *Protein Sci.* 26, 1749–1758.

Howard, A.R., Heppler, M.L., Ju, H.-J., Krishnamurthy, K., Payton, M.E., and Verchot-Lubicz, J. (2004). Potato virus X TGBp1 induces plasmodesmata gating and moves between cells in several host species whereas CP moves only in *N. benthamiana* leaves. *Virology* 328, 185–197.

Huang, W., and Levitt, D.G. (1977). Theoretical calculation of the dielectric constant of a bilayer membrane. *Biophys J* 17, 111–128.

Huff, J., Bergter, A., Birkenbeil, J., Kleppe, I., Engelmann, R., and Krzic, U. (2017). The new 2D Superresolution mode for ZEISS Airyscan. *Nature Methods* 14, 1223–1223.

Huster, D. (2014). Solid-state NMR spectroscopy to study protein–lipid interactions. *Biochimica et Biophysica Acta (BBA) - Molecular and Cell Biology of Lipids* 1841, 1146–1160.

Jacinto, T., Farmer, E.E., and Ryan, C.A. (1993). Purification of potato leaf plasma membrane protein pp34, a protein phosphorylated in response to oligogalacturonide signals for defense and development. *Plant Physiology* 103, 1393–1397.

Jaillais, Y., and Ott, T. (2020). The Nanoscale Organization of the Plasma Membrane and Its Importance in Signaling: A Proteolipid Perspective. *Plant Physiology* 182, 1682–1696.

Jamann, T.M., Poland, J.A., Kolkman, J.M., Smith, L.G., and Nelson, R.J. (2014). Unraveling Genomic Complexity at a Quantitative Disease Resistance Locus in Maize. *Genetics* 198, 333–344.

Jarsch, I.K., Konrad, S.S.A., Stratil, T.F., Urbanus, S.L., Szymanski, W., Braun, P., Braun, K.-H., and Ott, T. (2014). Plasma Membranes Are Subcompartmentalized into a Plethora of Coexisting and Diverse Microdomains in *Arabidopsis* and *Nicotiana benthamiana*. *The Plant Cell* 26, 1698–1711.

Javanainen, M., Martinez-Seara, H., and Vattulainen, I. (2017). Nanoscale Membrane Domain Formation Driven by Cholesterol. *Scientific Reports* 7.

Ji, C., Zhang, Y., Xu, P., Xu, T., and Lou, X. (2015). Nanoscale Landscape of Phosphoinositides Revealed by Specific Pleckstrin Homology (PH) Domains Using Single-molecule Superresolution Imaging in the Plasma Membrane. *J. Biol. Chem.* 290, 26978–26993.

- Jung, S.-H., Park, D., Park, J.H., Kim, Y.-M., and Ha, K.-S. (2010). Molecular imaging of membrane proteins and microfilaments using atomic force microscopy. *Exp Mol Med* 42, 597.
- Kamat, N.P., Tobé, S., Hill, I.T., and Szostak, J.W. (2015). Electrostatic Localization of RNA to Protocell Membranes by Cationic Hydrophobic Peptides. *Angewandte Chemie International Edition* 54, 11735–11739.
- Katritch, V., Cherezov, V., and Stevens, R.C. (2013). Structure-Function of the G Protein–Coupled Receptor Superfamily. *Annual Review of Pharmacology and Toxicology* 53, 531–556.
- Kauzmann, W. (1959). Some Factors in the Interpretation of Protein Denaturation. In *Advances in Protein Chemistry*, (Elsevier), pp. 1–63.
- Kavran, J.M., Klein, D.E., Lee, A., Falasca, M., Isakoff, S.J., Skolnik, E.Y., and Lemmon, M.A. (1998). Specificity and Promiscuity in Phosphoinositide Binding by Pleckstrin Homology Domains. *J. Biol. Chem.* 273, 30497–30508.
- Keeler, J. (2016). *Understanding NMR Spectroscopy* (2004).
- Kefala, G., Ahn, C., Krupa, M., Esquivies, L., Maslennikov, I., Kwiatkowski, W., and Choe, S. (2010). Structures of the OmpF porin crystallized in the presence of foscholine-12. *Protein Sci.* 19, 1117–1125.
- Khan, S.H., McLaughlin, W.A., and Kumar, R. (2017). Site-specific phosphorylation regulates the structure and function of an intrinsically disordered domain of the glucocorticoid receptor. *Sci Rep* 7, 1–8.
- Khoza, T.G., Dubery, I.A., and Piater, L.A. (2019). Identification of Candidate Ergosterol-Responsive Proteins Associated with the Plasma Membrane of *Arabidopsis thaliana*. *Int J Mol Sci* 20.
- Klotz, I.M., and Franzen, J.S. (1962). Hydrogen Bonds between Model Peptide Groups in Solution. *J. Am. Chem. Soc.* 84, 3461–3466.
- Koldsø, H., Shorthouse, D., Hélie, J., and Sansom, M.S.P. (2014). Lipid Clustering Correlates with Membrane Curvature as Revealed by Molecular Simulations of Complex Lipid Bilayers. *PLOS Computational Biology* 10, e1003911.
- Kong, C.-Y., Luo, Y., Duan, T.-T., Xue, Z., Gao, X.-D., Zhao, X., and Gao, G. (2016). Potato remorin gene StREMa4 cloning and its spatiotemporal expression pattern under *Ralstonia solanacearum* and plant hormones treatment. *Phytoparasitica* 44, 575–584.
- Konrad, S.S.A., Popp, C., Stratil, T.F., Jarsch, I.K., Thallmair, V., Folgmann, J., Marín, M., and Ott, T. (2014). S-acylation anchors remorin proteins to the plasma membrane but does not primarily determine their localization in membrane microdomains. *New Phytologist* 203, 758–769.
- Koynova, R., and Tenchov, B. (2013). Phase Transitions and Phase Behavior of Lipids. In *Encyclopedia of Biophysics*, G.C.K. Roberts, ed. (Berlin, Heidelberg: Springer), pp. 1841–1854.

Kusumi, A., Nakada, C., Ritchie, K., Murase, K., Suzuki, K., Murakoshi, H., Kasai, R.S., Kondo, J., and Fujiwara, T. (2005). Paradigm shift of the plasma membrane concept from the two-dimensional continuum fluid to the partitioned fluid: high-speed single-molecule tracking of membrane molecules. *Annu Rev Biophys Biomol Struct* 34, 351–378.

Lakowicz, J.R. (2006). *Principles of fluorescence spectroscopy* (New York: Springer).

Langmuir, I. (1917). THE CONSTITUTION AND FUNDAMENTAL PROPERTIES OF SOLIDS AND LIQUIDS. II. LIQUIDS.1. *J. Am. Chem. Soc.* 39, 1848–1906.

de Laurentiis, A., Donovan, L., and Arcaro, A. (2007). Lipid Rafts and Caveolae in Signaling by Growth Factor Receptors. *Open Biochem J* 1, 12–32.

Ledeen, R.W., and Wu, G. (2015). The multi-tasked life of GM1 ganglioside, a true factotum of nature. *Trends in Biochemical Sciences* 40, 407–418.

Lee, M., Morgan, C.A., and Hong, M. (2019). Fully hydrophobic HIV gp41 adopts a hemifusion-like conformation in phospholipid bilayers. *J. Biol. Chem.* 294, 14732–14744.

Leeuwenhoek, A. van, and Hoole, S. (1800). The select works of Antony van Leeuwenhoek : containing his microscopical discoveries in many of the works of nature / (London : G. Sidney,).

Lefebvre, B., Timmers, T., Mbengue, M., Moreau, S., Herve, C., Toth, K., Bittencourt-Silvestre, J., Klaus, D., Deslandes, L., Godiard, L., et al. (2010). A remorin protein interacts with symbiotic receptors and regulates bacterial infection. *Proceedings of the National Academy of Sciences* 107, 2343–2348.

Légrand, A., Martinez, D., Grélard, A., Berbon, M., Morvan, E., Tawani, A., Loquet, A., Mongrand, S., and Habenstein, B. (2019). Nanodomain Clustering of the Plant Protein Remorin by Solid-State NMR. *Front. Mol. Biosci.* 6.

Lenarčič, T., Albert, I., Böhm, H., Hodnik, V., Pirc, K., Zavec, A.B., Podobnik, M., Pahovnik, D., Žagar, E., Pruitt, R., et al. (2017). Eudicot plant-specific sphingolipids determine host selectivity of microbial NLP cytolysins. *Science* 358, 1431–1434.

Lenard, J., and Singer, S.J. (1966). PROTEIN CONFORMATION IN CELL MEMBRANE PREPARATIONS AS STUDIED BY OPTICAL ROTATORY DISPERSION AND CIRCULAR DICHROISM*. *Proc Natl Acad Sci U S A* 56, 1828–1835.

Lenoir, M., Grzybek, M., Majkowski, M., Rajesh, S., Kaur, J., Whittaker, S.B.-M., Coskun, Ü., and Overduin, M. (2015a). Structural Basis of Dynamic Membrane Recognition by trans-Golgi Network Specific FAPP Proteins. *Journal of Molecular Biology* 427, 966–981.

Lenoir, M., Kufareva, I., Abagyan, R., and Overduin, M. (2015b). Membrane and Protein Interactions of the Pleckstrin Homology Domain Superfamily. *Membranes (Basel)* 5, 646–663.

Léonard, A., Escrive, C., Laguerre, M., Pebay-Peyroula, E., Néri, W., Pott, T., Katsaras, J., and Dufourc, E.J. (2001). Location of Cholesterol in DMPC Membranes. A Comparative Study by Neutron Diffraction and Molecular Mechanics Simulation. *Langmuir* 17, 2019–2030.

Levitt, M.H. (2008). *Spin Dynamics: Basis of Nuclear Magnetic Resonance* (John Wiley & Sons, Ltd).

Leyser, O. (2018). Auxin Signaling. *Plant Physiology* 176, 465–479.

Liang, P., Stratil, T.F., Popp, C., Marín, M., Folgmann, J., Mysore, K.S., Wen, J., and Ott, T. (2018). Symbiotic root infections in *Medicago truncatula* require remorin-mediated receptor stabilization in membrane nanodomains. *Proceedings of the National Academy of Sciences* 115, 5289–5294.

Lide, D.R. (2010). *CRC Handbook of Chemistry and Physics*. 2760.

Lin, W.-C., Blanchette, C.D., Ratto, T.V., and Longo, M.L. (2006). Lipid Asymmetry in DLPC/DSPC-Supported Lipid Bilayers: A Combined AFM and Fluorescence Microscopy Study. *Biophysical Journal* 90, 228–237.

Lingwood, D., and Simons, K. (2010). Lipid Rafts As a Membrane-Organizing Principle. *Science* 327, 46–50.

Lins, L., Decaffmeyer, M., Thomas, A., and Brasseur, R. (2008). Relationships between the orientation and the structural properties of peptides and their membrane interactions. *Biochimica et Biophysica Acta (BBA) - Biomembranes* 1778, 1537–1544.

Lisanti, M.P., Tang, Z., Scherer, P.E., Kübler, E., Koleske, A.J., and Sargiacomo, M. (1995). Caveolae, transmembrane signalling and cellular transformation. *Molecular Membrane Biology* 12, 121–124.

Liu, Z., Lavis, L.D., and Betzig, E. (2015). Imaging Live-Cell Dynamics and Structure at the Single-Molecule Level. *Molecular Cell* 58, 644–659.

Loeb, J. (1906). *The Dynamics Of Living Things* (Columbia University Biological Series).

Lombard, J. (2014). Once upon a time the cell membranes: 175 years of cell boundary research. *Biol Direct* 9.

Lu, Y.-J., Schornack, S., Spallek, T., Geldner, N., Chory, J., Schellmann, S., Schumacher, K., Kamoun, S., and Robatzek, S. (2012). Patterns of plant subcellular responses to successful oomycete infections reveal differences in host cell reprogramming and endocytic trafficking. *Cell. Microbiol.* 14, 682–697.

MacCallum, J.L., Bennett, W.F.D., and Tieleman, D.P. (2007). Partitioning of Amino Acid Side Chains into Lipid Bilayers: Results from Computer Simulations and Comparison to Experiment. *J Gen Physiol* 129, 371–377.

Malpighii, M. (1675). *Anatome Plantarum* (Royal Society).

Mamode Cassim, A., Gouguet, P., Gronnier, J., Laurent, N., Germain, V., Grison, M., Boutté, Y., Gerbeau-Pissot, P., Simon-Plas, F., and Mongrand, S. (2019). Plant lipids: Key players of plasma membrane organization and function. *Progress in Lipid Research* 73, 1–27.

Marín, M., and Ott, T. (2012). Phosphorylation of Intrinsically Disordered Regions in Remorin Proteins. *Frontiers in Plant Science* 3.

Marin, M., Thallmair, V., and Ott, T. (2012). The Intrinsically Disordered N-terminal Region of AtREM1.3 Remorin Protein Mediates Protein-Protein Interactions. *Journal of Biological Chemistry* 287, 39982–39991.

Markham, J.E., Li, J., Cahoon, E.B., and Jaworski, J.G. (2006). Separation and Identification of Major Plant Sphingolipid Classes from Leaves. *Journal of Biological Chemistry* 281, 22684–22694.

Marquês, J.T., Marinho, H.S., and de Almeida, R.F.M. (2018). Sphingolipid hydroxylation in mammals, yeast and plants – An integrated view. *Progress in Lipid Research* 71, 18–42.

Marrink, S.J., Corradi, V., Souza, P.C.T., Ingólfsson, H.I., Tieleman, D.P., and Sansom, M.S.P. (2019). Computational Modeling of Realistic Cell Membranes. *Chem Rev* 119, 6184–6226.

Martinez, D., Legrand, A., Gronnier, J., Decossas, M., Gouguet, P., Lambert, O., Berbon, M., Verron, L., Grélard, A., Germain, V., et al. (2018). Coiled-coil oligomerization controls localization of the plasma membrane REMORINs. *J. Struct. Biol.*

McCabe, M.A., and Wassail, S.R. (1997). Rapid deconvolution of NMR powder spectra by weighted fast Fourier transformation. *Solid State Nuclear Magnetic Resonance* 10, 53–61.

van Meer, G., Voelker, D.R., and Feigenson, G.W. (2008). Membrane lipids: where they are and how they behave. *Nature Reviews Molecular Cell Biology* 9, 112–124.

Merk, A., Bartesaghi, A., Banerjee, S., Falconieri, V., Rao, P., Davis, M.I., Pragani, R., Boxer, M.B., Earl, L.A., Milne, J.L.S., et al. (2016). Breaking Cryo-EM Resolution Barriers to Facilitate Drug Discovery. *Cell* 165, 1698–1707.

Merutka, G., Dyson, H.J., and Wright, P.E. (1995). ‘Random coil’¹H chemical shifts obtained as a function of temperature and trifluoroethanol concentration for the peptide series GGXGG. *Journal of Biomolecular NMR* 5, 14–24.

Meyer, D., Pajonk, S., Micali, C., O’Connell, R., and Schulze-Lefert, P. (2009). Extracellular transport and integration of plant secretory proteins into pathogen-induced cell wall compartments. *The Plant Journal* 57, 986–999.

Micali, C.O., Neumann, U., Grunewald, D., Panstruga, R., and O’Connell, R. (2011). Biogenesis of a specialized plant-fungal interface during host cell internalization of *Golovinomyces orontii* haustoria. *Cell. Microbiol.* 13, 210–226.

- Mioka, T., Fujimura-Kamada, K., and Tanaka, K. (2014). Asymmetric distribution of phosphatidylserine is generated in the absence of phospholipid flippases in *Saccharomyces cerevisiae*. *MicrobiologyOpen* 3, 803–821.
- Mongrand, S., Morel, J., Laroche, J., Claverol, S., Carde, J.-P., Hartmann, M.-A., Bonneau, M., Simon-Plas, F., Lessire, R., and Bessoule, J.-J. (2004). Lipid Rafts in Higher Plant Cells: PURIFICATION AND CHARACTERIZATION OF TRITON X-100-INSOLUBLE MICRODOMAINS FROM TOBACCO PLASMA MEMBRANE. *Journal of Biological Chemistry* 279, 36277–36286.
- Moreau, R.A., Whitaker, B.D., and Hicks, K.B. (2002). Phytosterols, phytostanols, and their conjugates in foods: structural diversity, quantitative analysis, and health-promoting uses. *Progress in Lipid Research* 41, 457–500.
- Moreau, R.A., Nyström, L., Whitaker, B.D., Winkler-Moser, J.K., Baer, D.J., Gebauer, S.K., and Hicks, K.B. (2018). Phytosterols and their derivatives: Structural diversity, distribution, metabolism, analysis, and health-promoting uses. *Progress in Lipid Research* 70, 35–61.
- Mullock, B.M., and Luzio, J.P. (2013). *Theory of Organelle Biogenesis: A Historical Perspective* (Landes Bioscience).
- Munro, S. (2003). Lipid Rafts: Elusive or Illusive? *Cell* 115, 377–388.
- Nagawa, S., Xu, T., and Yang, Z. (2010). RHO GTPase in plants. *Small GTPases* 1, 78–88.
- Nakamura, Y. (2017). Plant Phospholipid Diversity: Emerging Functions in Metabolism and Protein–Lipid Interactions. *Trends in Plant Science* 22, 1027–1040.
- Nicolas, W.J., Grison, M.S., Trépout, S., Gaston, A., Fouché, M., Cordelières, F.P., Oparka, K., Tilsner, J., Brocard, L., and Bayer, E.M. (2017). Architecture and permeability of post-cytokinesis plasmodesmata lacking cytoplasmic sleeves. *Nature Plants* 3, 17082.
- Nilges, M., Bernard, A., Bardiaux, B., Malliavin, T., Habeck, M., and Rieping, W. (2008). Accurate NMR Structures Through Minimization of an Extended Hybrid Energy. *Structure* 16, 1305–1312.
- Nishi, H., Fong, J.H., Chang, C., Teichmann, S.A., and Panchenko, A.R. (2013). Regulation of protein–protein binding by coupling between phosphorylation and intrinsic disorder: analysis of human protein complexes. *Mol. BioSyst.* 9, 1620–1626.
- Noack, L.C., and Jaillais, Y. (2017). Precision targeting by phosphoinositides: how PIs direct endomembrane trafficking in plants. *Curr. Opin. Plant Biol.* 40, 22–33.
- Norkin, L.C., and Kuksin, D. (2005). The caveolae-mediated sv40 entry pathway bypasses the golgi complex en route to the endoplasmic reticulum. *Virol J* 2, 38.
- Nyström, L., Schär, A., and Lampi, A.-M. (2012). Steryl glycosides and acylated steryl glycosides in plant foods reflect unique sterol patterns. *Eur. J. Lipid Sci. Technol.* 114, 656–669.

- Oda, Y., and Fukuda, H. (2012). Initiation of Cell Wall Pattern by a Rho- and Microtubule-Driven Symmetry Breaking. *Science* 337, 1333–1336.
- Otero, S., Helariutta, Y., and Benitez-Alfonso, Y. (2016). Symplastic communication in organ formation and tissue patterning. *Curr. Opin. Plant Biol.* 29, 21–28.
- Pang, H., Le, P.U., and Nabi, I.R. (2004). Ganglioside GM1 levels are a determinant of the extent of caveolae/raft-dependent endocytosis of cholera toxin to the Golgi apparatus. *J. Cell. Sci.* 117, 1421–1430.
- Parton, R.G. (1994). Ultrastructural localization of gangliosides; GM1 is concentrated in caveolae. *J. Histochem. Cytochem.* 42, 155–166.
- Parton, R.G., and Simons, K. (2007). The multiple faces of caveolae. *Nature Reviews Molecular Cell Biology* 8, 185–194.
- Pata, M.O., Hannun, Y.A., and Ng, C.K.-Y. (2010). Plant sphingolipids: decoding the enigma of the Sphinx. *New Phytologist* 185, 611–630.
- Patterson, G.H., and Lippincott-Schwartz, J. (2002). A photoactivatable GFP for selective photolabeling of proteins and cells. *Science* 297, 1873–1877.
- Patton, J.L., and Lester, R.L. (1991). The phosphoinositol sphingolipids of *Saccharomyces cerevisiae* are highly localized in the plasma membrane. *J. Bacteriol* 173, 3101–3108.
- Perraki, A., Cacas, J.-L., Crowet, J.-M., Lins, L., Castroviejo, M., German-Retana, S., Mongrand, S., and Raffaele, S. (2012). Plasma Membrane Localization of *Solanum tuberosum* Remorin from Group 1, Homolog 3 Is Mediated by Conformational Changes in a Novel C-Terminal Anchor and Required for the Restriction of Potato Virus X Movement]. *PLANT PHYSIOLOGY* 160, 624–637.
- Perraki, A., Binaghi, M., Mecchia, M.A., Gronnier, J., German-Retana, S., Mongrand, S., Bayer, E., Zelada, A.M., and Germain, V. (2014). StRemorin1.3 hampers *Potato virus X* TGBp1 ability to increase plasmodesmata permeability, but does not interfere with its silencing suppressor activity. *FEBS Letters* 588, 1699–1705.
- Perraki, A., Gronnier, J., Gouguet, P., Boudsocq, M., Deroubaix, A.-F., Simon, V., German-Retana, S., Legrand, A., Habenstein, B., Zipfel, C., et al. (2018). REM1.3's phospho-status defines its plasma membrane nanodomain organization and activity in restricting PVX cell-to-cell movement. *PLOS Pathogens* 14, e1007378.
- Picas, L., Gaits-lacovoni, F., and Goud, B. (2016). The emerging role of phosphoinositide clustering in intracellular trafficking and signal transduction. *F1000Res* 5.
- Pike, L.J. (2006). Rafts defined: a report on the Keystone symposium on lipid rafts and cell function. *Journal of Lipid Research* 47, 1597–1598.
- Pimenta-Lopes, C., Suay-Corredera, C., Velázquez-Carreras, D., Sánchez-Ortiz, D., and Alegre-Cebollada, J. (2019). Concurrent atomic force spectroscopy. *Commun Phys* 2, 1–11.

Platre, M.P., Noack, L.C., Doumane, M., Bayle, V., Simon, M.L.A., Maneta-Peyret, L., Fouillen, L., Stanislas, T., Armengot, L., Pejchar, P., et al. (2018). A Combinatorial Lipid Code Shapes the Electrostatic Landscape of Plant Endomembranes. *Developmental Cell* 45, 465-480.e11.

Platre, M.P., Bayle, V., Armengot, L., Bareille, J., Marquès-Bueno, M.D.M., Creff, A., Maneta-Peyret, L., Fiche, J.-B., Nollmann, M., Miège, C., et al. (2019). Developmental control of plant Rho GTPase nano-organization by the lipid phosphatidylserine. *Science* 364, 57–62.

Pockels, A. (1891). Surface Tension. *Nature* 43, 437–439.

Pott, T., and Dufourc, E.J. (1995). Action of melittin on the DPPC-cholesterol liquid-ordered phase: a solid state ²H-and ³¹P-NMR study. *Biophys J* 68, 965–977.

Prior, I.A., Lewis, P.D., and Mattos, C. (2012). A Comprehensive Survey of Ras Mutations in Cancer. *Cancer Res* 72, 2457–2467.

Quillin, M.L., and Matthews, B.W. (2000). Accurate calculation of the density of proteins. *Acta Crystallogr. D Biol. Crystallogr.* 56, 791–794.

Raffaele, S., Mongrand, S., Gamas, P., Niebel, A., and Ott, T. (2007a). Genome-Wide Annotation of Remorins, a Plant-Specific Protein Family: Evolutionary and Functional Perspectives. *PLANT PHYSIOLOGY* 145, 593–600.

Raffaele, S., Mongrand, S., Gamas, P., Niebel, A., and Ott, T. (2007b). Genome-Wide Annotation of Remorins, a Plant-Specific Protein Family: Evolutionary and Functional Perspectives. *PLANT PHYSIOLOGY* 145, 593–600.

Raffaele, S., Bayer, E., Lafarge, D., Cluzet, S., German Retana, S., Boubekur, T., Leborgne-Castel, N., Carde, J.-P., Lherminier, J., Noirot, E., et al. (2009a). Remorin, a Solanaceae Protein Resident in Membrane Rafts and Plasmodesmata, Impairs Potato virus X Movement. *THE PLANT CELL ONLINE* 21, 1541–1555.

Raffaele, S., Bayer, E., Lafarge, D., Cluzet, S., German Retana, S., Boubekur, T., Leborgne-Castel, N., Carde, J.-P., Lherminier, J., Noirot, E., et al. (2009b). Remorin, a Solanaceae Protein Resident in Membrane Rafts and Plasmodesmata, Impairs Potato virus X Movement. *THE PLANT CELL ONLINE* 21, 1541–1555.

Raffaele, S., Perraki, A., and Mongrand, S. (2013). The Remorin C-terminal Anchor was shaped by convergent evolution among membrane binding domains. *Plant Signaling & Behavior* 8, e23207.

Raghupathy, R., Anilkumar, A.A., Polley, A., Singh, P.P., Yadav, M., Johnson, C., Suryawanshi, S., Saikam, V., Sawant, S.D., Panda, A., et al. (2015). Transbilayer Lipid Interactions Mediate Nanoclustering of Lipid-Anchored Proteins. *Cell* 161, 581–594.

Ray, S., Kassan, A., Busija, A.R., Rangamani, P., and Patel, H.H. (2016). The plasma membrane as a capacitor for energy and metabolism. *Am J Physiol Cell Physiol* 310, C181–C192.

Reichman, J. (2013). Handbook of Optical Filters for Fluorescence Microscopy.

Reymond, P., Kunz, B., Paul-Pletzer, K., Grimm, R., Eckerskorn, C., and Farmer, E.E. (1996). Cloning of a cDNA encoding a plasma membrane-associated, uronide binding phosphoprotein with physical properties similar to viral movement proteins. *The Plant Cell* 8, 2265–2276.

Rieping, W., Habeck, M., and Nilges, M. (2005). Modeling Errors in NOE Data with a Log-normal Distribution Improves the Quality of NMR Structures. *Journal of the American Chemical Society* 127, 16026–16027.

Rieping, W., Habeck, M., Bardiaux, B., Bernard, A., Malliavin, T.E., and Nilges, M. (2007). ARIA2: Automated NOE assignment and data integration in NMR structure calculation. *Bioinformatics* 23, 381–382.

Rinia, H.A., Snel, M.M.E., Eerden, J.P.J.M. van der, and Kruijff, B. de (2001). Visualizing detergent resistant domains in model membranes with atomic force microscopy. *FEBS Letters* 501, 92–96.

Rivera-Milla, E., Stuermer, C.A.O., and Málaga-Trillo, E. (2006). Ancient origin of reggie (flotillin), reggie-like, and other lipid-raft proteins: convergent evolution of the SPFH domain. *Cell. Mol. Life Sci.* 63, 343–357.

Robertson, J.D. (1957). New Observations on the Ultrastructure of the Membranes of Frog Peripheral Nerve Fibers. *J Biophys Biochem Cytol* 3, 1043–1048.

Rolland, N., Ferro, M., Seigneurin-Berny, D., Garin, J., Block, M., and Joyard, J. (2009). The Chloroplast Envelope Proteome and Lipidome. In *The Chloroplast*, A.S. Sandelius, and H. Aronsson, eds. (Berlin, Heidelberg: Springer Berlin Heidelberg), pp. 41–88.

Ross-Elliott, T.J., Jensen, K.H., Haaning, K.S., Wager, B.M., Knoblauch, J., Howell, A.H., Mullendore, D.L., Monteith, A.G., Paultre, D., Yan, D., et al. (2017). Phloem unloading in *Arabidopsis* roots is convective and regulated by the phloem-pole pericycle. *Elife* 6.

Rust, M.J., Bates, M., and Zhuang, X. (2006). Sub-diffraction-limit imaging by stochastic optical reconstruction microscopy (STORM). *Nat. Methods* 3, 793–795.

Sako, Y., and Kusumi, A. (1994). Compartmentalized structure of the plasma membrane for receptor movements as revealed by a nanometer-level motion analysis. *The Journal of Cell Biology* 125, 1251–1264.

Santos, A.X.S., and Riezman, H. (2012). Yeast as a model system for studying lipid homeostasis and function. *FEBS Letters* 586, 2858–2867.

Sargiacomo, M., Sudol, M., Tang, Z., and Lisanti, M.P. (1993). Signal transducing molecules and glycosyl-phosphatidylinositol-linked proteins form a caveolin-rich insoluble complex in MDCK cells. *J. Cell Biol.* 122, 789–807.

Sassa, T., and Kihara, A. (2014). Metabolism of Very Long-Chain Fatty Acids: Genes and Pathophysiology. *Biomol Ther (Seoul)* 22, 83–92.

Scarff, C.A., Fuller, M.J.G., Thompson, R.F., and Iadanza, M.G. (2018). Variations on Negative Stain Electron Microscopy Methods: Tools for Tackling Challenging Systems. *J Vis Exp*.

Schroeder, R., London, E., and Brown, D. (1994). Interactions between saturated acyl chains confer detergent resistance on lipids and glycosylphosphatidylinositol (GPI)-anchored proteins: GPI-anchored proteins in liposomes and cells show similar behavior. *Proceedings of the National Academy of Sciences* *91*, 12130–12134.

Schuck, S., Honsho, M., Ekroos, K., Shevchenko, A., and Simons, K. (2003). Resistance of cell membranes to different detergents. *PNAS* *100*, 5795–5800.

Schwertner, H.A., and Biale, J.B. (1973). Lipid composition of plant mitochondria and of chloroplasts. *8*.

Seelig, J. (1977). Deuterium magnetic resonance: theory and application to lipid membranes. *Quarterly Reviews of Biophysics* *10*, 353.

Shogomori, H., and Brown, D.A. (2003). Use of Detergents to Study Membrane Rafts: The Good, the Bad, and the Ugly. *Biological Chemistry* *384*, 1259–1263.

Simon, M.L.A., Platre, M.P., Assil, S., van Wijk, R., Chen, W.Y., Chory, J., Dreux, M., Munnik, T., and Jaillais, Y. (2014). A multi-colour/multi-affinity marker set to visualize phosphoinositide dynamics in Arabidopsis. *The Plant Journal* *77*, 322–337.

Simons, K., and Ikonen, E. (1997). Functional rafts in cell membranes. *Nature* *387*, 569.

Simons, K., and Van Meer, G. (1988). Lipid sorting in epithelial cells. *Biochemistry* *27*, 6197–6202.

Simons, K., and Wandinger-Ness, A. (1990). Polarized sorting in epithelia. *Cell* *62*, 207–210.

Singer, S.J. (2004). Some Early History of Membrane Molecular Biology. *Annu. Rev. Physiol.* *66*, 1–27.

Singer, S.J., and Nicolson, G.L. (1972). The Fluid Mosaic Model of the Structure of Cell Membranes. *Science* *175*, 720–731.

Smith, W. (2014). *Elements of Molecular Dynamics*. 460.

Smith, S.A., Palke, W.E., and Gerig, J.T. (1992a). The Hamiltonians of NMR. part I. Concepts in Magnetic Resonance *4*, 107–144.

Smith, S.A., Palke, W.E., and Gerig, J.T. (1992b). The Hamiltonians of NMR. Part II. Concepts in Magnetic Resonance *4*, 181–204.

Smokvarska, M., Francis, C., Platre, M.P., Fiche, J.B., Alcon, C., Dumont, X., Nacry, P., Bayle, V., Nollmann, M., Maurel, C., et al. (2020). A plasma membrane nanoplateform ensures signal specificity during osmotic signaling in plants (*Plant Biology*).

- Solanko, L.M., Sullivan, D.P., Sere, Y.Y., Szomek, M., Lunding, A., Solanko, K.A., Pizovic, A., Stanchev, L.D., Pomorski, T.G., Menon, A.K., et al. (2018). Ergosterol is mainly located in the cytoplasmic leaflet of the yeast plasma membrane. *Traffic* 19, 198–214.
- Speranza, A. (2010). Into the world of steroids. *Plant Signaling & Behavior* 5, 940–943.
- Spira, F., Mueller, N.S., Beck, G., Olshausen, P. von, Beig, J., and Wedlich-Söldner, R. (2012). Patchwork organization of the yeast plasma membrane into numerous coexisting domains. *Nat Cell Biol* 14, 640–648.
- Steck, T.L., and Lange, Y. (2018). Transverse distribution of plasma membrane bilayer cholesterol: Picking sides. *Traffic* 19, 750–760.
- Stier, A., and Sackmann, E. (1973). SPIN LABELS AS ENZYME SUBSTRATES. *Biochimica et Biophysica Acta (BBA) - Biomembranes* 9.
- Szymanski, W.G., Zauber, H., Erban, A., Gorka, M., Wu, X.N., and Schulze, W.X. (2015). Cytoskeletal components define protein location to membrane microdomains. *Molecular & Cellular Proteomics* 14, 2493–2509.
- Tagawa, A., Mezzacasa, A., Hayer, A., Longatti, A., Pelkmans, L., and Helenius, A. (2005). Assembly and trafficking of caveolar domains in the cell: caveolae as stable, cargo-triggered, vesicular transporters. *J. Cell Biol.* 170, 769–779.
- Tarkka, M.T., Herrmann, S., Wubet, T., Feldhahn, L., Recht, S., Kurth, F., Mailänder, S., Bönn, M., Neef, M., Angay, O., et al. (2013). OakContigDF159.1, a reference library for studying differential gene expression in *Quercus robur* during controlled biotic interactions: use for quantitative transcriptomic profiling of oak roots in ectomycorrhizal symbiosis. *New Phytologist* 199, 529–540.
- Theillet, F.-X., Rose, H.M., Liokatis, S., Binolfi, A., Thongwichian, R., Stuiver, M., and Selenko, P. (2013). Site-specific NMR mapping and time-resolved monitoring of serine and threonine phosphorylation in reconstituted kinase reactions and mammalian cell extracts. *Nature Protocols* 8, 1416–1432.
- Thomsen, P., Roepstorff, K., Stahlhut, M., and van Deurs, B. (2002). Caveolae are highly immobile plasma membrane microdomains, which are not involved in constitutive endocytic trafficking. *Mol. Biol. Cell* 13, 238–250.
- Thuman-Commike, P.A., and Chiu, W. (2000). Reconstruction principles of icosahedral virus structure determination using electron cryomicroscopy. *Micron* 31, 687–711.
- Thureau, P., Mollica, G., Ziarelli, F., and Viel, S. (2014). Solid-State ^1H NMR Studies of Homonuclear Dipolar Couplings. In *Annual Reports on NMR Spectroscopy*, (Elsevier), pp. 217–249.
- Thurlkill, R.L., Grimsley, G.R., Scholtz, J.M., and Pace, C.N. (2006). pK values of the ionizable groups of proteins. *Protein Science* 15, 1214–1218.

Tian, T., Harding, A., Inder, K., Plowman, S., Parton, R.G., and Hancock, J.F. (2007). Plasma membrane nanoswitches generate high-fidelity Ras signal transduction. *Nature Cell Biology* 9, 905–914.

Tjellström, H., Hellgren, L.I., Wieslander, Å., and Sandelius, A.S. (2010). Lipid asymmetry in plant plasma membranes: phosphate deficiency-induced phospholipid replacement is restricted to the cytosolic leaflet. *The FASEB Journal* 24, 1128–1138.

Tóth, K., Stratil, T.F., Madsen, E.B., Ye, J., Popp, C., Antolín-Llovera, M., Grossmann, C., Jensen, O.N., Schüßler, A., Parniske, M., et al. (2012). Functional Domain Analysis of the Remorin Protein LjSYMREM1 in *Lotus japonicus*. *PLoS One* 7.

Tsuji, A., and Ohnishi, S. (1986). Restriction of the lateral motion of band 3 in the erythrocyte membrane by the cytoskeletal network: dependence on spectrin association state. *Biochemistry* 25, 6133–6139.

Uversky, V.N. (2013). A decade and a half of protein intrinsic disorder: Biology still waits for physics. *Protein Science* 22, 693–724.

Valdez-Taubas, J., and Pelham, H.R.B. (2003). Slow diffusion of proteins in the yeast plasma membrane allows polarity to be maintained by endocytic cycling. *Curr. Biol.* 13, 1636–1640.

Vicidomini, G., Bianchini, P., and Diaspro, A. (2018). STED super-resolved microscopy. *Nat Methods* 15, 173–182.

Villasmil, M.L., Gallo-Ebert, C., Liu, H.-Y., Francisco, J., and Nickels, J.T. (2017). A link between very long chain fatty acid elongation and mating-specific yeast cell cycle arrest. *Cell Cycle* 16, 2192–2203.

Virtanen, J.A., Cheng, K.H., and Somerharju, P. (1998). Phospholipid composition of the mammalian red cell membrane can be rationalized by a superlattice model. *Proc Natl Acad Sci U S A* 95, 4964–4969.

Vranken, W.F., Boucher, W., Stevens, T.J., Fogh, R.H., Pajon, A., Llinas, M., Ulrich, E.L., Markley, J.L., Ionides, J., and Laue, E.D. (2005). The CCPN data model for NMR spectroscopy: Development of a software pipeline. *Proteins: Structure, Function, and Bioinformatics* 59, 687–696.

Wang, Y. (2002). Probability-based protein secondary structure identification using combined NMR chemical-shift data. *Protein Science* 11, 852–861.

Weise, K., Kapoor, S., Denter, C., Nikolaus, J., Opitz, N., Koch, S., Triola, G., Herrmann, A., Waldmann, H., and Winter, R. (2011). Membrane-Mediated Induction and Sorting of K-Ras Microdomain Signaling Platforms. *J. Am. Chem. Soc.* 133, 880–887.

Wewer, V., Dombrink, I., Dorp, K. vom, and Dörmann, P. (2011). Quantification of sterol lipids in plants by quadrupole time-of-flight mass spectrometry. *J. Lipid Res.* 52, 1039–1054.

Whited, A.M., and Park, P.S.-H. (2014). Atomic force microscopy: A multifaceted tool to study membrane proteins and their interactions with ligands. *Biochimica et Biophysica Acta (BBA) - Biomembranes* 1838, 56–68.

Widjaja, I., Lassowskat, I., Bethke, G., Eschen-Lippold, L., Long, H.-H., Naumann, K., Dangl, J.L., Scheel, D., and Lee, J. (2010). A protein phosphatase 2C, responsive to the bacterial effector AvrRpm1 but not to the AvrB effector, regulates defense responses in Arabidopsis. *The Plant Journal* 61, 249–258.

Williams, T.M., and Lisanti, M.P. (2005). Caveolin-1 in oncogenic transformation, cancer, and metastasis. *Am. J. Physiol., Cell Physiol.* 288, C494-506.

Williamson, J.J., and Olmsted, P.D. (2015). Registered and Antiregistered Phase Separation of Mixed Amphiphilic Bilayers. *Biophysical Journal* 108, 1963–1976.

Wishart, D.S., Sykes, B.D., and Richards, F.M. (1992). The chemical shift index: a fast and simple method for the assignment of protein secondary structure through NMR spectroscopy. *Biochemistry* 31, 1647–1651.

Wishart, D.S., Bigam, C.G., Yao, J., Abildgaard, F., Dyson, H.J., Oldfield, E., Markley, J.L., and Sykes, B.D. (1995). ¹H, ¹³C and ¹⁵N chemical shift referencing in biomolecular NMR. *J. Biomol. NMR* 6, 135–140.

Wisnieski, B.J., Williams, R.E., and Fox, C.F. (1973). Manipulation of Fatty Acid Composition in Animal Cells Grown in Culture. *Proceedings of the National Academy of Sciences* 70, 3669–3673.

Wu, S., O'Leary, R., Xu, M., Sang, Y., Chen, X., Yu, Q., and Gallagher, K.L. (2016). Symplastic signaling instructs cell division, cell expansion, and cell polarity in the ground tissue of Arabidopsis thaliana roots. *Proc. Natl. Acad. Sci. U.S.A.* 113, 11621–11626.

Yamada, E. (1955). The fine structure of the gall bladder epithelium of the mouse. *J Biophys Biochem Cytol* 1, 445–458.

Yu, J., Fischman, D.A., and Steck, T.L. (1973). Selective solubilization of proteins and phospholipids from red blood cell membranes by nonionic detergents. *Journal of Supramolecular Structure* 1, 233–248.

Yuan, C., and Johnston, L.J. (2001). Atomic force microscopy studies of ganglioside GM1 domains in phosphatidylcholine and phosphatidylcholine/cholesterol bilayers. *Biophys J* 81, 1059–1069.

Zachowski, A. (1993). Phospholipids in animal eukaryotic membranes: transverse asymmetry and movement. *Biochem J* 294, 1–14.

Zeng, G., Duan, Y., Besenbacher, F., and Dong, M. (2012). Nanomechanics of Amyloid Materials Studied by Atomic Force Microscopy. In *Atomic Force Microscopy Investigations into Biology - From Cell to Protein*, C. Frewin, ed. (InTech), p.

Zhendre, V., Grélard, A., Garnier-LHomme, M., Buchoux, S., Larijani, B., and Dufourc, E.J. (2011). Key Role of Polyphosphoinositides in Dynamics of Fusogenic Nuclear Membrane Vesicles. *PLoS ONE* 6, e23859.

Zhou, Y., and Hancock, J.F. (2015). Ras nanoclusters: Versatile lipid-based signaling platforms. *Biochimica et Biophysica Acta (BBA) - Molecular Cell Research* 1853, 841–849.

Zhou, A., Rohou, A., Schep, D.G., Bason, J.V., Montgomery, M.G., Walker, J.E., Grigorieff, N., and Rubinstein, J.L. (2015). Structure and conformational states of the bovine mitochondrial ATP synthase by cryo-EM. *ELife* 4, e10180.

Zhou, Y., Prakash, P., Liang, H., Cho, K.-J., Gorfe, A.A., and Hancock, J.F. (2017). Lipid-Sorting Specificity Encoded in K-Ras Membrane Anchor Regulates Signal Output. *Cell* 168, 239-251.e16.

Zickermann, V., Wirth, C., Nasiri, H., Siegmund, K., Schwalbe, H., Hunte, C., and Brandt, U. (2015a). Mechanistic insight from the crystal structure of mitochondrial complex I. *Science* 347, 44–49.

Zickermann, V., Wirth, C., Nasiri, H., Siegmund, K., Schwalbe, H., Hunte, C., and Brandt, U. (2015b). Mechanistic insight from the crystal structure of mitochondrial complex I. *Science* 347, 44–49.

Kragelund, B., and Skriver K. (2020). *Intrinsically Disordered Proteins: Methods and Protocols* (New York, NY: Springer US).